frontiers | Research Topics

Biofilm-biomaterial interactions: Understanding, preventing, and eradicating attachment in infection

Edited by
Jessica Amber Jennings, Lauren B. Priddy and Mark Smeltzer

Published in
Frontiers in Microbiology

ISSN 1664-8714
ISBN 978-2-83250-974-6
DOI 10.3389/978-2-83250-974-6

About Frontiers

Frontiers is more than just an open access publisher of scholarly articles: it is a pioneering approach to the world of academia, radically improving the way scholarly research is managed. The grand vision of Frontiers is a world where all people have an equal opportunity to seek, share and generate knowledge. Frontiers provides immediate and permanent online open access to all its publications, but this alone is not enough to realize our grand goals.

Frontiers journal series

The Frontiers journal series is a multi-tier and interdisciplinary set of open-access, online journals, promising a paradigm shift from the current review, selection and dissemination processes in academic publishing. All Frontiers journals are driven by researchers for researchers; therefore, they constitute a service to the scholarly community. At the same time, the *Frontiers journal series* operates on a revolutionary invention, the tiered publishing system, initially addressing specific communities of scholars, and gradually climbing up to broader public understanding, thus serving the interests of the lay society, too.

Dedication to quality

Each Frontiers article is a landmark of the highest quality, thanks to genuinely collaborative interactions between authors and review editors, who include some of the world's best academicians. Research must be certified by peers before entering a stream of knowledge that may eventually reach the public - and shape society; therefore, Frontiers only applies the most rigorous and unbiased reviews. Frontiers revolutionizes research publishing by freely delivering the most outstanding research, evaluated with no bias from both the academic and social point of view. By applying the most advanced information technologies, Frontiers is catapulting scholarly publishing into a new generation.

What are Frontiers Research Topics?

Frontiers Research Topics are very popular trademarks of the *Frontiers journals series*: they are collections of at least ten articles, all centered on a particular subject. With their unique mix of varied contributions from Original Research to Review Articles, Frontiers Research Topics unify the most influential researchers, the latest key findings and historical advances in a hot research area.

Find out more on how to host your own Frontiers Research Topic or contribute to one as an author by contacting the Frontiers editorial office: frontiersin.org/about/contact

Biofilm-biomaterial interactions: Understanding, preventing, and eradicating attachment in infection

Topic editors

Jessica Amber Jennings — University of Memphis, United States
Lauren B. Priddy — Mississippi State University, United States
Mark Smeltzer — University of Arkansas for Medical Sciences, United States

Citation

Jennings, J. A., Priddy, L. B., Smeltzer, M., eds. (2022). *Biofilm-biomaterial interactions: Understanding, preventing, and eradicating attachment in infection*. Lausanne: Frontiers Media SA. doi: 10.3389/978-2-83250-974-6

Table of contents

05 Virtual Screening for Novel SarA Inhibitors to Prevent Biofilm Formation of *Staphylococcus aureus* in Prosthetic Joint Infections
Jinlong Yu, Feng Jiang, Feiyang Zhang, Yunqi Pan, Jianqiang Wang, Pei Han, Jin Tang and Hao Shen

16 Pulse Dosing of Antibiotic Enhances Killing of a *Staphylococcus aureus* Biofilm
Kirsten J. Meyer, Hannah B. Taylor, Jazlyn Seidel, Michael F. Gates and Kim Lewis

26 *In vitro* Evaluation of Medihoney Antibacterial Wound Gel as an Anti-biofilm Agent Against Ventricular Assist Device Driveline Infections
Yue Qu, David McGiffin, Christina Kure, Janelle McLean, Courtney Duncan and Anton Y. Peleg

36 Influence of High Intensity Focused Ultrasound on the Microstructure and c-di-GMP Signaling of *Pseudomonas aeruginosa* Biofilms
Lakshmi Deepika Bharatula, Enrico Marsili, Scott A. Rice and James J. Kwan

50 An Improved 2-Aminoimidazole Based Anti-Biofilm Coating for Orthopedic Implants: Activity, Stability, and *in vivo* Biocompatibility
Guglielmo Attilio Coppola, Jolien Onsea, T. Fintan Moriarty, Dirk Nehrbass, Caroline Constant, Stephan Zeiter, Merve Kübra Aktan, Annabel Braem, Erik V. Van der Eycken, Hans P. Steenackers and Willem-Jan Metsemakers

61 Azithromycin Exhibits Activity Against *Pseudomonas aeruginosa* in Chronic Rat Lung Infection Model
Manoj Kumar, Madhvi Rao, Tarun Mathur, Tarani Kanta Barman, Vattan Joshi, Tridib Chaira, Smita Singhal, Manisha Pandya, Souhaila Al Khodor, Dilip J. Upadhyay and Nobuhisa Masuda

70 *Staphylococcus aureus* Floating Biofilm Formation and Phenotype in Synovial Fluid Depends on Albumin, Fibrinogen, and Hyaluronic Acid
Samantha Knott, Dylan Curry, Neil Zhao, Pallavi Metgud, Sana S. Dastgheyb, Caroline Purtill, Marc Harwood, Antonia F. Chen, Thomas P. Schaer, Michael Otto and Noreen J. Hickok

83 *In vitro* Activity of Antimicrobial Wound Dressings on *P. aeruginosa* Wound Biofilm
Ewa Klara Stuermer, Isabell Plattfaut, Michael Dietrich, Florian Brill, Andreas Kampe, Vanessa Wiencke, Anna Ulatowski, Maria Geffken, Julian-Dario Rembe, Ella Alexandrovna Naumova, Sebastian Eike Debus and Ralf Smeets

93 Understanding How Staphylococcal Autolysin Domains Interact With Polystyrene Surfaces
Radha P. Somarathne, Emily R. Chappell, Y. Randika Perera, Rahul Yadav, Joo Youn Park and Nicholas C. Fitzkee

106 Bacterial Biofilm Growth on 3D-Printed Materials
Donald C. Hall Jr., Phillip Palmer, Hai-Feng Ji, Garth D. Ehrlich and Jarosław E. Król

119 2-Heptylcyclopropane-1-Carboxylic Acid Disperses and Inhibits Bacterial Biofilms
Zoe L. Harrison, Rukhsana Awais, Michael Harris, Babatunde Raji, Brian C. Hoffman, Daniel L. Baker and Jessica Amber Jennings

130 One-Pot Microwave-Assisted Synthesis of Carbon Dots and *in vivo* and *in vitro* Antimicrobial Photodynamic Applications
María Paulina Romero, Fernanda Alves, Mirian Denise Stringasci, Hilde Harb Buzzá, Heloísa Ciol, Natalia Mayumi Inada and Vanderlei Salvador Bagnato

143 Adaptation of the Start-Growth-Time Method for High-Throughput Biofilm Quantification
Lara Thieme, Anita Hartung, Kristina Tramm, Julia Graf, Riccardo Spott, Oliwia Makarewicz and Mathias W. Pletz

frontiers in Microbiology

ORIGINAL RESEARCH
published: 05 November 2020
doi: 10.3389/fmicb.2020.587175

Virtual Screening for Novel SarA Inhibitors to Prevent Biofilm Formation of *Staphylococcus aureus* in Prosthetic Joint Infections

Jinlong Yu[1], Feng Jiang[1], Feiyang Zhang[1], Yunqi Pan[2], Jianqiang Wang[2], Pei Han[1], Jin Tang[2]* and Hao Shen[1]**

[1] Department of Orthopedics, Shanghai Sixth People's Hospital, Shanghai Jiao Tong University, Shanghai, China,
[2] Department of Clinical Laboratory, Shanghai Sixth People's Hospital, Shanghai Jiao Tong University, Shanghai, China

OPEN ACCESS

Edited by:
Mark Smeltzer, University of Arkansas for Medical Sciences, United States

Reviewed by:
Jessica Amber Jennings, University of Memphis, United States
Zaixiang Lou, Jiangnan University, China

***Correspondence:**
Pei Han
hanpei_cn@163.com
Jin Tang
tangjin6ph@163.com
Hao Shen
shenhao7212@sina.com

Specialty section:
This article was submitted to Antimicrobials, Resistance and Chemotherapy, a section of the journal Frontiers in Microbiology

Received: *25 July 2020*
Accepted: *15 October 2020*
Published: *05 November 2020*

Citation:
Yu J, Jiang F, Zhang F, Pan Y, Wang J, Han P, Tang J and Shen H (2020) Virtual Screening for Novel SarA Inhibitors to Prevent Biofilm Formation of Staphylococcus aureus in Prosthetic Joint Infections. Front. Microbiol. 11:587175. doi: 10.3389/fmicb.2020.587175

Staphylococcus aureus is one of the predominant causes of periprosthetic joint infections (PJIs). Bacterial adhesion and biofilm formation are important factors in the pathogenesis of PJIs. *S. aureus* biofilm formation is regulated by several factors, including *S. aureus* regulator A (SarA). Previous studies have found that SarA mutants have limited ability to develop biofilms. In this study, we identified a SarA-targeting antibiofilm compound, ZINC00990144, and evaluated its efficacy and toxicity. According to static biofilm assay, the antibiofilm ability of the compound was concentration dependent. ZINC00990144 reduced biofilm in multiple strains by 40–86% at a concentration of 11.5 μM. Additionally, ZINC00990144 inhibited biofilm formation on different orthopedic implant materials including Titanium and UHMWPE disc. Furthermore, quantitative polymerase chain reaction results demonstrated that ZINC00990144 upregulated the expression of *S. aureus* exoproteases to inhibit the formation of biofilms. Moreover, ZINC00990144 prevented biofilm formation when exposed to sub-inhibitory doses of vancomycin, which is known to promote biofilm formation. CCK-8 results demonstrated ZINC00990144 has no significant effect on cell viability at concentration of 11.5 μM or below. Finally, we verified the antibiofilm function of the compound *in vivo* using implant infection mice model with/without exposure to sub-inhibitory vancomycin. In conclusion, ZINC00990144 acts by modulating between biofilm and planktonic state of *S. aureus* instead of being bactericidal. Therefore, it has the potential to be used in combination with other antibiotics to prevent PJIs.

Keywords: *Staphylococcus aureus*, biofilm, prosthetic joint infection, antibiofilm, virtual screening

INTRODUCTION

Biofilms are a consortium of microbial communities, such as bacteria, that are attached to each other as well as a surface and are surrounded by extracellular matrix (ECM), including proteins, exopolysaccharides, and extracellular DNA (eDNA) (Le et al., 2014; Moormeier and Bayles, 2017). In contrast to their planktonic state, bacteria in a biofilm are more recalcitrant to the host immune system and antimicrobial therapy (Figueiredo et al., 2017; Ricciardi et al., 2018). The formation of

biofilms within the human body and on the surface of implanted medical devices can be extremely devastating. Additionally, as the use of implanted medical devices continues to increase, implant infection cases will also continue to rise.

Periprosthetic joint infection, a devastating complication after arthroplasty, is the main cause of arthroplasty revisions (20–36.1%) (Kapadia et al., 2016; Postler et al., 2018; Kokko et al., 2019). Patients with PJI face poor prognosis and huge economic burden. Although the microbiological epidemiology of PJIs varies from country to country, the most common pathogen responsible for PJIs is *Staphylococcus aureus* (Fernandes and Dias, 2013). Patients with *S. aureus* PJI have a poor prognosis (Lourtet-Hascoet et al., 2016). Given the frequent emergence of multidrug resistant strains, antibiotics alone are inadequate for PJI treatment, thus, emphasizing the need for development of antibiofilm drugs for combinatorial therapy (Ciofu et al., 2017).

Staphylococcal accessory regulator A, a global regulator, controls the transcription of a range of virulence genes by binding to the promotor region of its target genes. It has been reported that SarA mutations limit biofilm formation under both *in vivo* and *in vitro* conditions (Trotonda et al., 2005; Abdelhady et al., 2014). Inspired by this phenomenon, Balamurugan and Rekha (Arya and Princy, 2013; Arya et al., 2015; Balamurugan et al., 2017) designed 13 SarAIs as antibiofilm compounds. Both studies used *de novo* computer-assisted drug design methods based on SarA amino acid residues—DER (D88, E89, R90), a highly conserved amino acid sequence among the SarA family members (Liu et al., 2006). However, Liu et al. (2006) showed that R84 residue is also critical for DNA binding. Therefore, we propose that R84 should also be considered when carrying out *in silico* drug design.

In this study, we screened several drug-like compounds for their antibiofilm property. The compound with the best antibiofilm activity, ZINC00990144, was selected for experimentation. It is known that subinhibitory doses of antibiotics (e.g., vancomycin) can induce *S. aureus* biofilm formation. Hence, we investigated whether ZINC00990144 could inhibit *S. aureus* biofilm stimulated by sub-MIC vancomycin. We investigated the cytotoxicity of the compound via CCK-8 cytotoxicity assay. We also studied its efficacy in a mouse subcutaneous model of implant-associated infection.

MATERIALS AND METHODS

Virtual Screening for SarA Inhibitors

The crystal structure of SarA (PDB ID: 2frh) was downloaded from the Protein Data Bank database. The conserved residues R84, D88, E99, and R90 of the SarA family were determined via multi-sequence alignment using ClustalW (Larkin et al., 2007) and the result was displayed via Jalview1.8. A compound library from Specs database[1] containing 316,044 drug-like molecules was chosen for screening. We used Autodock Vina 1.1.2 program for structure-based virtual screening of SarAIs. The docking grid box was centered on the conserved residues to encompass all the important residues. The energy range and exhaustiveness were set at 3 and 8, respectively.

Bacterial Strains and Compound Preparation

Staphylococcus aureus strains involved in this study were either maintained by our laboratory or isolated from PJI prosthesis. To construct a fluorescence labeled strain, pCM29 (Pang et al., 2010) plasmid with superfolder green fluorescent protein (sfGFP) reporter system was introduced into *S. aureus* competent cells RN4220 via electroporation and maintained using chloromycetin (10 μg/mL). Next, the plasmid was transformed into *S. aureus* ST1792 isolated from infectious prosthesis with bacteriophage11. Detailed strain information is listed in **Table 1**.

All the compounds were acquired from Specs[1] and dissolved in dimethyl sulfoxide (DMSO) at concentration of 12.8 mg/mL for storage. During the experiment, the storage solution was diluted with culture medium (in the case of *in vitro* experiment) or normal saline (in the case of *in vivo* part) according to the dilution ratio.

In vitro Static Biofilm Assays

All bacterial strains involved in this study were cultured at 37°C overnight in TSBG, and the culture was serially diluted to a concentration of ∼1×10^6 colony forming units/mL (CFU/mL); the serially diluted bacterial cells (200 μL) were inoculated in a 96-well plate and the plate was incubated at 37°C for 24 h. The culture was aspirated from each well, and the wells were washed gently thrice with 200 μL of PBS to remove the non-adherent cells. After fixation with methanol, the plate was air-dried and the biofilm was stained with 200 μL of crystal violet. The biofilm biomass at the bottom of the well was dissolved in 200 μL of 33%

[1]www.specs.net

TABLE 1 | Strains used in this study*.

Strain name	Antibiotic resistance	Description
ST1792[#]	MSSA	Isolated from PJIs patients
ST239[&]	MRSA	Isolated from PJIs patients
USA300	MRSA	CA-pneumonia
RN4220	MSSA	Restriction minus and modification plus strain
PJI_32	MRSA	Isolated from PJIs patients
PJI_27	MRSA	Isolated from PJIs patients
PJI_18	MRSA	Isolated from PJIs patients
PJI_55	MSSA	Isolated from PJIs patients
PJI_58	MSSA	Isolated from PJIs patients
PJI_57	MSSA	Isolated from PJIs patients
RN4220-sfGFP	MSSA	Fluorescence labeled strain
ST1792-sfGFP	MSSA	Fluorescence labeled strain

All of the strains are grown in TSBG at 37°C.[#]MLST type 1792.[&]MLST type 239.

Abbreviations: MIC, minimum inhibitory concentration; MLST, multilocus sequence typing; PIA, polysaccharide intercellular adhesion; PJI, periprosthetic joint infection; SarA, Staphylococcal accessory regulator A; SarAI, SarA inhibitor; TSBG, tryptic soy broth supplied with 0.5% glucose; UHMWP, ultra high molecular weight polyethylene.

acetic acid, and 100 μL aliquot from each well was transferred into a new 96-well plate. Optical absorbance was measured at 590 nm with a microplate reader (BioTek Instrument, Inc., United States) to quantify the biofilm biomass. For biofilm formation on Titanium disc or UHMWPE disc, bacteria were incubated with the material at 37°C overnight in TSBG.

To investigate whether protein is indispensable in biofilm matrix, proteinase K (Beyotime, China) was added to TSBG at a final concentration of 100 μg/mL to eliminate proteins as described previously (Moormeier et al., 2014). Bacteria were cultured overnight and biofilm biomass was quantified using crystal violet staining as described above.

Confocal Laser Scanning Microscopy (CLSM)

Biofilms were cultured overnight at 37°C in TSBG as described above. The supernatant was removed gently, and the biofilm mass that remained at the bottom of the well was stained with the Live/Dead BacLight bacteria viability kit (Invitrogen, United States) according to the instructions of the manufacturer. Live (stained with green fluorescent dye Syto9) and dead (stained with red fluorescent dye propidium iodide) cells were viewed with CLSM (Leica TCS SP8, Germany).

S. aureus Growth Curve

A final concentration of 11.5 μM ZINC00990144 in TSBG was incubated with *S. aureus* USA300 (∼1×10^6 CFU/mL) at 37°C overnight, and the OD600 of the cells was measured every 2 h until it reached the stationary phase.

CCK-8 Cytotoxicity Assay

HFF-1 (human foreskin fibroblasts) were pre-incubated to ∼80% convergence in DMEM containing 10% FBS and penicillin-streptomycin in a 96-well plate (∼10,000 cells/well) at 37°C, 5% CO_2. The supernatant was then removed and 100 μL culture medium with either 23, 11.5, or 5.73 μM ZINC00990144, respectively, was added. After incubation for 24 h, the culture medium was removed and 100 μL of culture medium with 10 μL CCK-8 solution (Dojindo, Japan) was added to each well. The plate was incubated for 1.5 h in an incubator at 37°C (Thermo Fisher Heracell, United States), and the optical absorbance was measured at 450 nm with a microplate reader (BioTek Instrument, Inc., United States).

S. aureus RNA Isolation and qRT-PCR

To investigate the expression of genes regulated by SarA, *S. aureus* was cultured overnight in TSBG with or without 11.5 μM ZINC00990144. The bacterial cells were harvested and transferred to a tissuelyser (50 Hz, 30 s) to physically disrupt the cell wall. Then the RNeasy Mini kit (Qiagen, Germany) was used to isolate RNA according to the manufacturer's instructions. RNA with 260 nm/280 nm > 2.0 (Nanodrop, Thermo Fisher Scientific, United States) was used for reverse transcription. Fresh RNA was immediately reverse transcribed into cDNA using an RT-PCR kit (Takara, Dalian, China). cDNA was used as the DNA template for real-time PCR (Takara, Dalian, China). The primers used in this study are summarized in **Table 2**. Relative gene expression level was quantified using the $2^{-\Delta\Delta Ct}$ method (Livak and Schmittgen, 2001) with *gyrB* as the internal reference. Each group contained three independent replicates.

Anti-biofilm Efficacy in Mice Implant Infection Model

Mice handling and related procedures in this study were reviewed and approved by the Animal Care and Ethics Committee of Sixth People's Hospital affiliated to Shanghai Jiao Tong University, China.

The effect of inhibitors was assessed in a murine model of implant infection. Forty adult male C57BL/6 mice were randomly divided into four groups. To construct an implant infection model, a titanium disc was implanted into the dorsal area subcutaneously, and ∼1×10^6 CFU of strain ST1792 were inoculated around the metal disc. Two groups were treated with DMSO (n = 10) or sub-MIC vancomycin (n = 10) and were set as control. SarAI-treated groups with (n = 10) or without (n = 10) sub-MIC vancomycin exposure were chosen as experimental groups. To observe the *in vivo* biofilm structure, we used sfGFP labeled *S. aureus* (RN4220-sfGFP/ST1792-sfGFP) to construct the mouse model. All treatments for this strain were performed as with strain ST1792 as described above. All the mice were euthanized 7 days after infection. Peri-implant tissues were harvested and homogenized in 1 mL sterile saline before CFU counting. The biofilm on the titanium discs was either observed under fluorescence microscope (Leica DMI8, Germany) (in the case of strain RN4220/ST1792-sfGFP) or sonicated in 1 mL sterile saline for further bacterial load quantification (in the case of strain ST1792).

TABLE 2 | qPCR Primers used in this study.

Primer name	Sequence (5′–3′)
gyrB_F	TTGGTACAGGAATCGGTGGC
gyrB_R	TCCATCCACATCGGCATCAG
aur_F	ATGGTGATGGTGATGGTCGC
aur_R	TTGACATGCTGCGTAAAGCG
sspA_F	CGCAGTCAAGCAAACAGCAA
sspA_R	CCTACAACTACACCGGAAGCA
sspB_F	ACGGTAAATCACAAGGCAGAGA
sspB_R	AGCGCATGTCCTAAATGTGG
splA_F	CCCGGAAAAGAAGACCTTGC
splA_R	TTTCACTTTTGCTCCGTCTGC
splB_F	GGCAGGGGCTAAAGCTGGTG
splB_R	TCTACTGACATCACAGGGCCAG
splc_F	TGCAGTCGTTGAAGAGACACA
splc_R	CACCGTTTGGATGGGCAGTA
splD_F	GGCAGCTCTGGTTCACCTAT
splD_R	ACCTTGTACTTTCACCTGTTGGT
splE_F	AACCAGGCAACTCAGGTTCAG
splE_R	TATTTCCAGGGCCGTTTCCAC

Statistical Analysis

Statistical analysis was performed using GraphPad prism 7. The data are expressed as mean ± standard deviation. Student's *t*-test was used for normally distributed data. Bonferroni–Dunn method was used to correct for multiple comparisons. Statistical significance level was defined as a two-tailed $p < 0.05$.

RESULTS

Identification of Candidate SarA Inhibitors

We aligned different SarA family proteins (UniProt accession numbers in parenthesis): SarX (Q2G0D1), SarA (Q7A1N5), SarS (Q2G1N7), SarU (Q2G1T7), SarT (Q2G2B1), SarR (Q9F0R1), and SarV (Q2FVY9) to identify the most conserved amino acids of the active site of SarA protein; L40, K82, R84, D88, and R90 were the most conserved amino acid residues (**Supplementary Figure 1**). According to previous reports (Liu et al., 2006), R84, D88, E89, and R90 are critical for the activity of SarA. Therefore, we selected R84, D88, E89, and R90 as the target sites for biofilm inhibition and conducted a virtual screening of the known inhibitors. Among 3,160,144 drug-like molecules, our virtual screening program revealed a set of new potential SarAIs that were different from those reported in previous studies. The candidate inhibitors were ranked according to their binding affinity to the target sites. Finally, we purchased top 23 compounds (Specs[2]) for the biological assays (**Supplementary Table 1**).

In vitro Evaluation of Potential SarA Inhibitors

In our preliminary trial (**Supplementary Figure 2**), all the compounds were used at a concentration of 1.28 mg/mL. Microtiter plate biofilm assay showed that most of the compounds could inhibit *S. aureus* biofilm formation (approximately 15.47–55.9%), while ZINC00990144 exhibited significant ($p < 0.001$) ability to inhibit biofilm formation (approximately 68.3%). Since ZINC00990144 had outstanding biofilm inhibition ability, it was chosen for further experiments.

The chemical structure of ZINC00990144 was shown in **Figure 1C**. Predicted binding mode with SarA revealed that ZINC00990144 blocked the active site residues of SarA protein (**Figures 1A,B**).

Exploring the Best Concentration for Usage

We diluted the compound serially and repeated the microtiter plate biofilm assay as described above. The result showed that the antibiofilm ability was concentration dependent (**Figure 2A**). Briefly, concentration as low as 2.3 μM (1:1000 dilution) was enough to produce observable effects and a

[2]www.specs.net

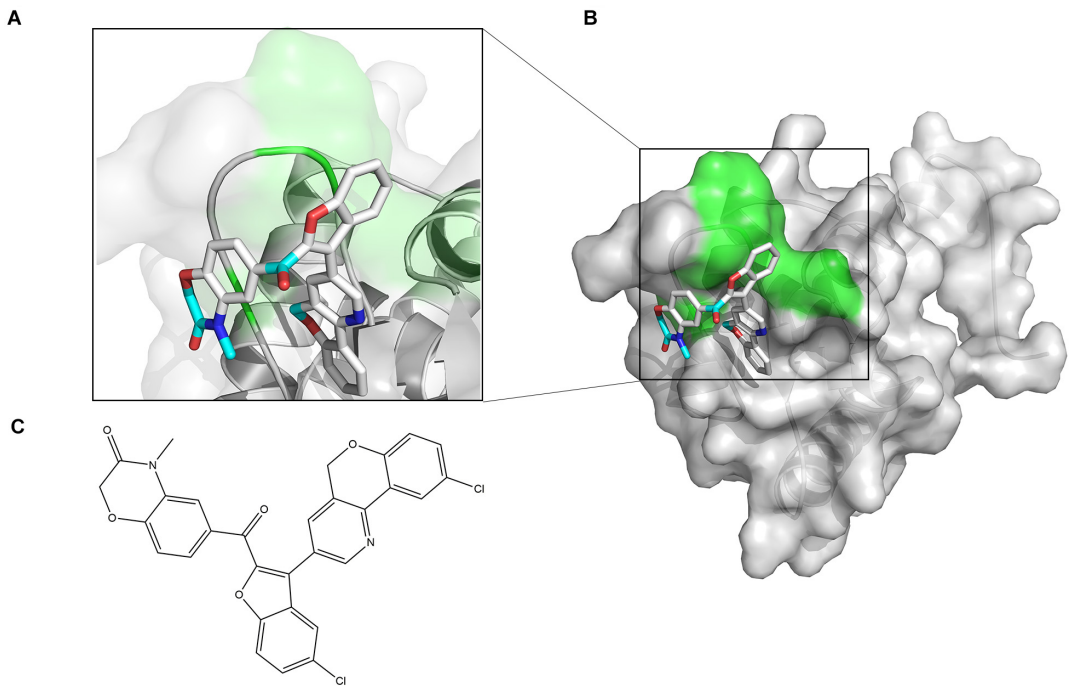

FIGURE 1 | Computational model of compound ZINC00990144 bound to SarA revealed by docking simulations. **(A)** SarA proteins are shown in cartoon mode with conservative residues marked with green and labeled. ZINC00990144 is displayed as stick. Light blue: carbon, dark blue: nitrogen, gray: hydrogen, and red: oxygen. **(B)** Protein surfaces are shown in gray and predicted binding sites are marked with green. **(C)** Structure of ZINC00990144.

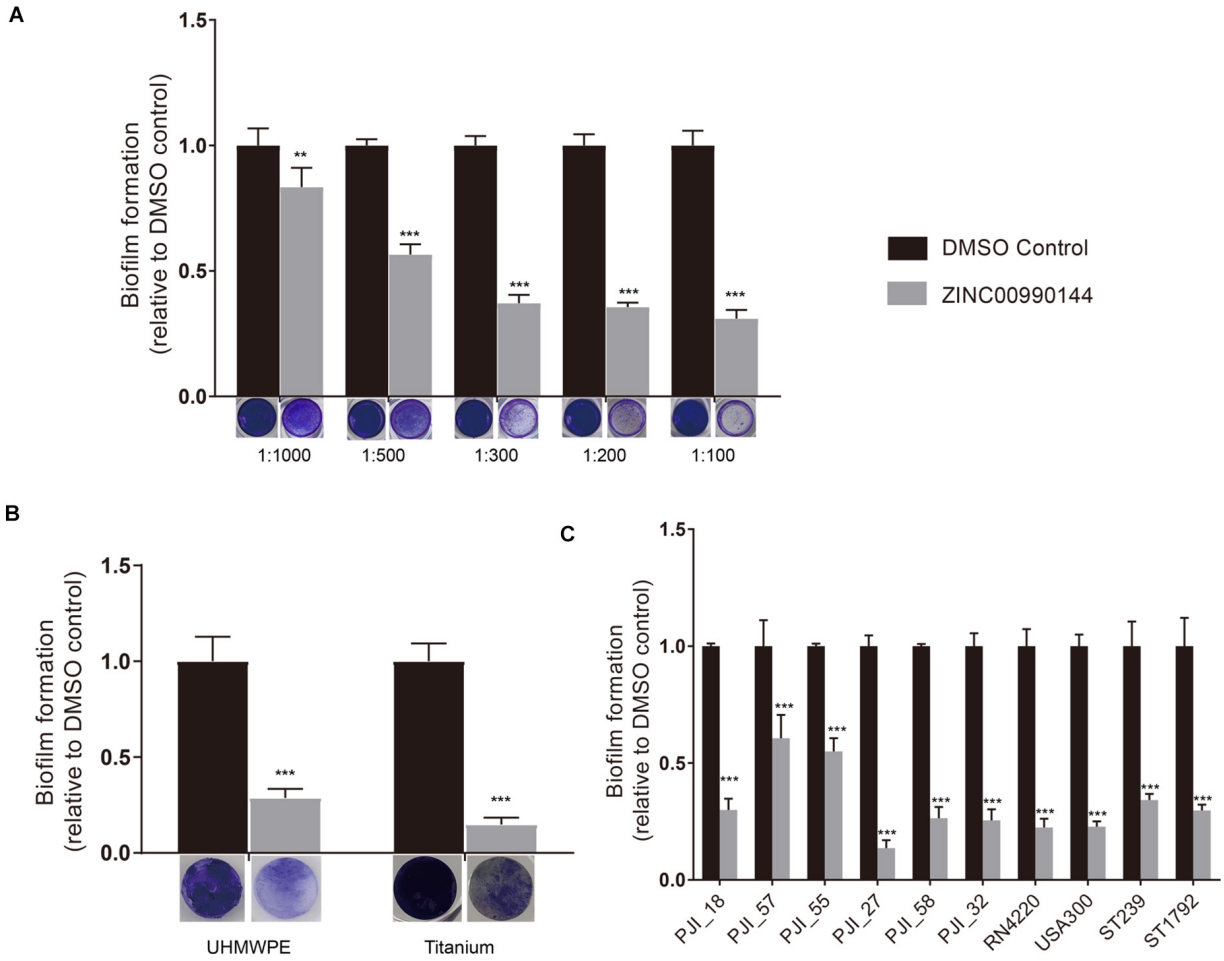

FIGURE 2 | Concentration gradient of ZINC00990144 on the inhibition biofilm formation **(A)**. Biofilm inhibition potency of ZINC00990144 on different materials **(B)** and against different *S. aureus* strains **(C)**. **(A)** The significance of biofilm inhibition increased with the increment of concentration in strain USA300. Biofilm was stained with crystal violet and quantified by measuring 590 nm absorbance. Dilution ratio is relative to storage solution. (For example: 1:1000 represents 2.3 μM compound or 0.1% DMSO). **(B)** USA300 biofilm formation on UHMWPE and titanium are significantly prevented by ZINC00990144 administration at the concentration of 11.5 μM (dilution ratio 1:200). Representative gross image of UHMWPE and titanium implant are shown under the *x*-axis. **(C)** ZINC00990144 at concentration of 11.5 μM is effective to all of the *S. aureus* isolates we tested. Biofilm was quantified with crystal violet staining method. $^{**}P < 0.01$, $^{***}P < 0.001$ comparing to DMSO control.

concentration of 11.5 μM (1:200 dilution) was close to its maximum function. As a result, the inhibitor was used at a concentration of 11.5 μM (dilution ratio 1:200) for further experiments.

Anti-biofilm Function on Different Materials and Different *S. aureus* Strains

In artificial joint implants, the most used materials are titanium alloy and UHMPWE. Compared to untreated materials, biofilms on both materials could be efficiently inhibited by 11.5 μM concentration of ZINC00990144 (**Figure 2B**, $p < 0.001$).

Furthermore, we selected eight *S. aureus* strains isolated from PJIs prosthesis and two most used *S. aureus* strains (strains USA300 and RN4220) for analysis. Although the sensitivity to ZINC00990144 varied among the strains, they were still susceptible to ZINC00990144 (**Figure 2C**). In addition, both MRSA and MSSA strains were susceptible to ZINC00990144.

Observation of the Structure of Biofilms via CLSM

The biofilms were further subjected to live/dead staining. As shown in **Figures 3A,B** strain USA300 forms a robust biofilm with a thickness of up to ∼12 μm after 12 h of incubation in TSBG, most of the cells are alive with propidium iodide-labeled dead cells (red) scattered among the biofilm. On the other hand, treatment with ZINC00990144 significantly affected the biofilm forming ability of strain USA300. Mature biofilm was not observed in most of the observation fields, while small

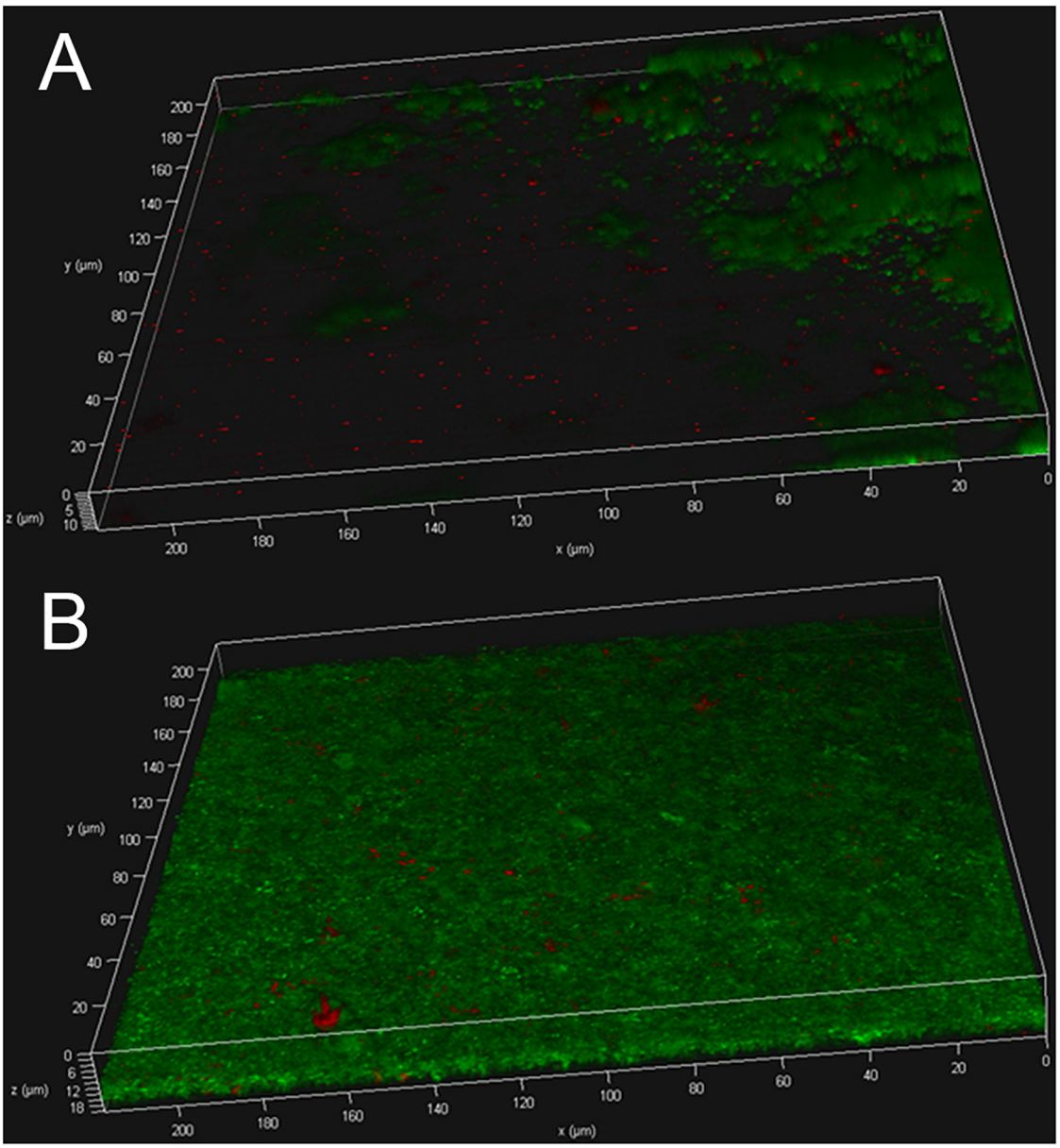

FIGURE 3 | USA300 biofilm with **(A)** or without **(B)** ZINC00990144 treatment was observed under CLSM after live/dead staining.

clusters of bacteria were occasionally detected. The thickness of the bacterial clusters displayed high variation, ranging from ∼3 to ∼12 μm.

qPCR Analysis for Genes Regulated by SarA

Agnieszka et al. (Zielinska et al., 2012) reported that SarA mediated proteases are closely correlated with decreased biofilm formation. We used qPCR to explore whether ZINC00990144 influenced the transcription of the reported extracellular proteases (*aur*, *sspA*, *sspB*, *splA*, *splB*, *splC*, *splD*, *splE*). In comparison to the control, a 5.25-fold, 2.56-fold, and 2.56-fold increase in *sspA*, *sspB*, and *splB* transcription, respectively, was observed due to SarAI treatment (**Figure 4**).

SarAI Prevents Sub-MIC Vancomycin Induced Biofilm Formation

When exposed to sub-MIC vancomycin, *S. aureus* biofilm formation was slightly promoted compared with the controls without exposure to vancomycin (**Figures 5A,B**), though the difference was not remarkable. In addition, *S. aureus* subjected to SarAI (with/without vancomycin) exhibited a significant reduction in biofilm formation

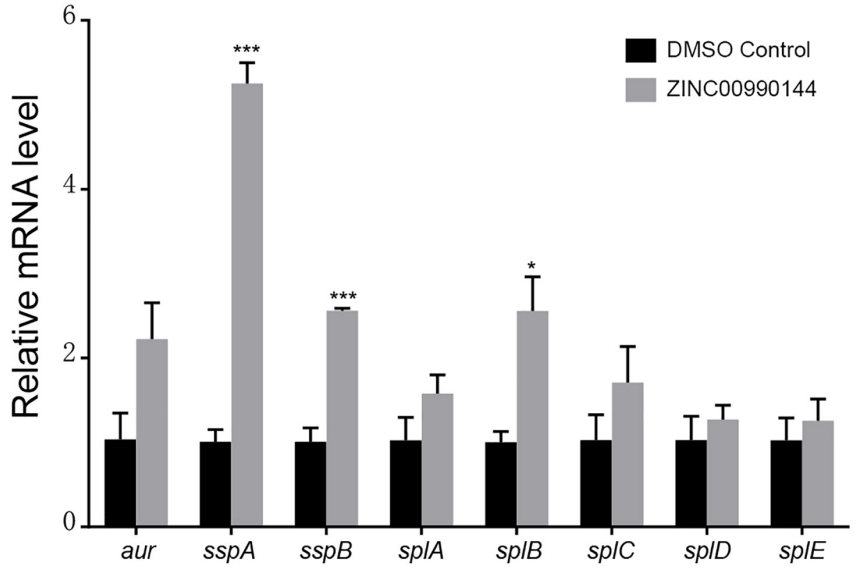

FIGURE 4 | Transcriptional changes of selected biofilm-associated genes after ZINC00990144 treatment. Following ZINC00990144 treatment, transcription levels of *aur*, *sspA*, *sspB*, *splA*, *splB*, *splC*, *splD*, and *splE* were investigated by qPCR in strain USA300. Each group contains three independent replicates. The fold change was in relative to the untreated samples. $^{*}P < 0.05$, $^{***}P < 0.001$ comparing with DMSO control.

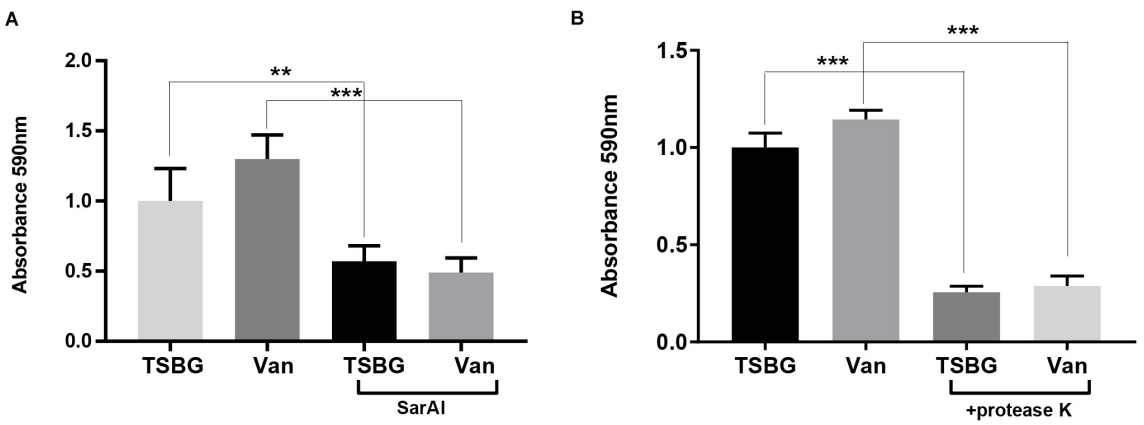

FIGURE 5 | Anti-biofilm function of ZINC00990144 **(A)** and proteinase K **(B)**. **(A)** ZINC00990144 is effective to USA300 biofilm with/without exposure to sub-MIC vancomycin. **(B)** Sub-MIC vancomycin promotes biofilm formation. Proteinase K (100 μg/mL) added at the initiation of the experiment inhibited biofilm formation completely, regardless of whether vancomycin is present. Van: sub-MIC vancomycin (0.5 μg/mL), SarAI: ZINC00990144, TSBG: TSB medium supplied with 0.5% glucose, $^{**}P < 0.01$, $^{***}P < 0.001$ comparing with corresponding control.

(**Figure 5A**) ($p < 0.01$/$p < 0.001$ for groups with/without vancomycin, respectively).

Protein Is Essential in *S. aureus* Biofilm Development

In order to investigate the role of protein in biofilm development, Proteinase K was added in TSBG to eliminate proteins. The result showed that addition of exogenous proteases exhibited significant biofilm clearance with/without exposure to sub-MIC vancomycin ($p < 0.001$) (**Figure 5B**).

Cytotoxicity and Bactericidal Effects of ZINC00990144

The cytotoxicity of ZINC00990144 was evaluated at concentrations ranging from 6.75 to 23 μM (dilution ratio ranging from 1:400 to 1:100, **Figure 6A**). ZINC00990144 at concentrations of 6.75 and 11.5 μM had no observable effects on cell growth. However, concentration of 23 μM (relative cell viability 89 ± 1.5%) and its corresponding DMSO control (1%) exhibited cell toxicity (relative cell viability 75.7 ± 4.8%) when comparing to blank control.

By analyzing the growth curve of *S. aureus*, ZINC00990144 treated group did not inhibit the growth of *S. aureus* (**Figure 6B**).

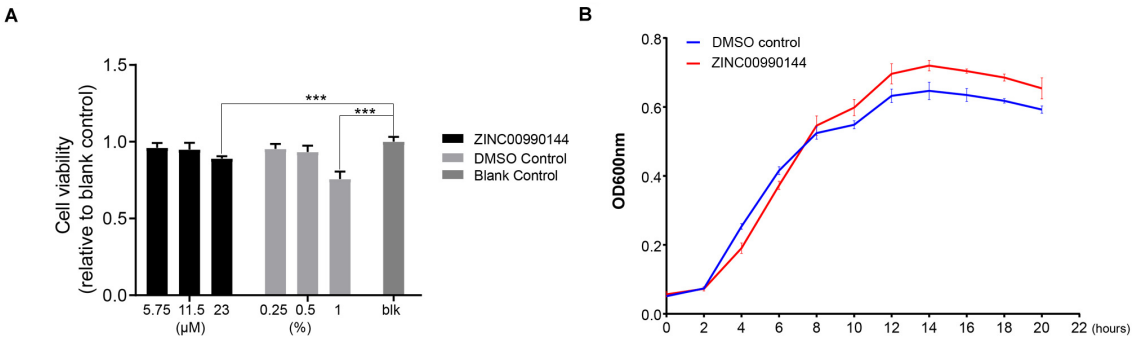

FIGURE 6 | Cytotoxicity of ZINC00990144 to HFF-1 cell line **(A)** and *S. aureus* **(B)**. **(A)** No significant difference detected between untreated (blank control) and treated group at 5.75 and 11.5 μM concentrations of ZINC00990144 by CCK-8 assay. 23 μM ZINC00990144 exhibits slight cytotoxicity which could be attributed to the solvent when comparing with the DMSO control. 5.75,11.5, 23 μM ZINC00990144 contains 0.25, 0.5, 1% DMSO, respectively. **(B)** ZINC00990144 does not hamper the growth of USA300. ***$P < 0.001$ comparing to blank group.

Instead, it slightly promoted *S. aureus* proliferation during the stationary phase.

Role of ZINC00990144 in Mice Model of Implant Infection

In a mouse model of implant infection, intervention was given at specific time points as described in **Figure 7A**. All mice ($n = 40$) were euthanatized 7 days after infection. When mice were not exposed to sub-MIC vancomycin, SarAI treated group showed a 0.864 log CFU reduction ($p < 0.05$) in adherent bacterial count compared with control group. Similarly, when sub-MIC vancomycin was presented, SarAI also reduced adherent bacteria by 1.011 log CFU ($P < 0.001$) compared to the control (**Figures 7C,E**). However, the peri-implant bacterial load had no significant difference among the four groups (**Figures 7B,D**).

We also inoculated the implant infection mice model with sfGFP labeled strains and the titanium discs were collected for observation (**Figure 8**). Green fluorescence was sparsely dispersed in the treatment group (SarAI with or without sub-MIC concentration of vancomycin). Some of the bacteria adhered to the surface of the titanium disc in single cell state, but some aggregated together to form bacterial clusters. In contrast, the groups without SarAI intervention formed typical mature biofilms surrounded by a clear border; in these groups, green fluorescence labeled *S. aureus* cells were densely distributed and existed in aggregation.

DISCUSSION

In this study, we adopted virtual screening method and screened a list of potential antibiofilm molecules by targeting *S. aureus* regulator SarA. It has been widely reported that SarA mutants have attenuated biofilm formation. Previously, Arya and Princy (2013) discovered 13 potential SarAIs by employing computer-assisted *de novo* drug design method with the software LUDI (Bohm, 1992). Two of the potential inhibitors were evaluated *in vitro* or *in vivo*, and both showed remarkable antibiofilm effect (Arya et al., 2015; Balamurugan et al., 2017). Different from *de novo* drug design, which designs new molecules from scratch, virtual screening identifies potential ligands from existing chemical compound databases. In this study, the compound library was obtained from Specs database, and all compounds complied with the Lipinski's rule of drug-likeness (also known as rule of five, Ro5) (Lipinski et al., 2001).

According to the predicted binding mode between ZINC00990144 and SarA protein (**Figures 1A,B**), ZINC00990144 blocked the promoter binding region of SarA protein. However, there is no molecular force such as hydrogen bond or van der waals force observed between SarA and ZINC00990144. Further optimization of ZINC00990144 to increase binding force may improve its potency. SarA down-stream gene transcription analysis shows that SarA negatively regulated protease was upregulated in ZINC00990144 treated group (**Figure 4**). It also supports ZINC00990144 as an SarAI.

In Orthopedics, vancomycin is one of the commonly used antibiotics in bone cement for infection treatment and prevention. However, antibiotics in cement are always explosively released and the concentration rapidly reduces over time. When the concentration of vancomycin drops under the MIC concentration, it promotes *S. aureus* biofilm formation (Hsu et al., 2011; Abdelhady et al., 2014), our results also verified this phenomenon (**Figures 5A,B**). It has been reported Staphylococcus biofilm could be divided into PIA-dependent and PIA-independent biofilm (proteinaceous biofilm) (Rohde et al., 2007). Previous studies have demonstrated that vancomycin promotes biofilm formation by inducing PIA production (Hsu et al., 2011; Abdelhady et al., 2014). Since ZINC00990144 prevent biofilm formation by upregulating protease and degrading protein, we speculated proteinaceous biofilm would be more susceptible to ZINC00990144 than PIA-dependent biofilm such as sub-MIC vancomycin induced biofilm. However, our study found that ZINC00990144 efficiently inhibited sub-MIC induced biofilm which demonstrated ZINC00990144 is also potent toward PIA-dependent biofilm (**Figure 5A**). Previously studies (Mootz et al., 2013; Moormeier et al., 2014) revealed that protein is essential for *S. aureus* biofilm integrity and adhesion/multiplication process. Taken these

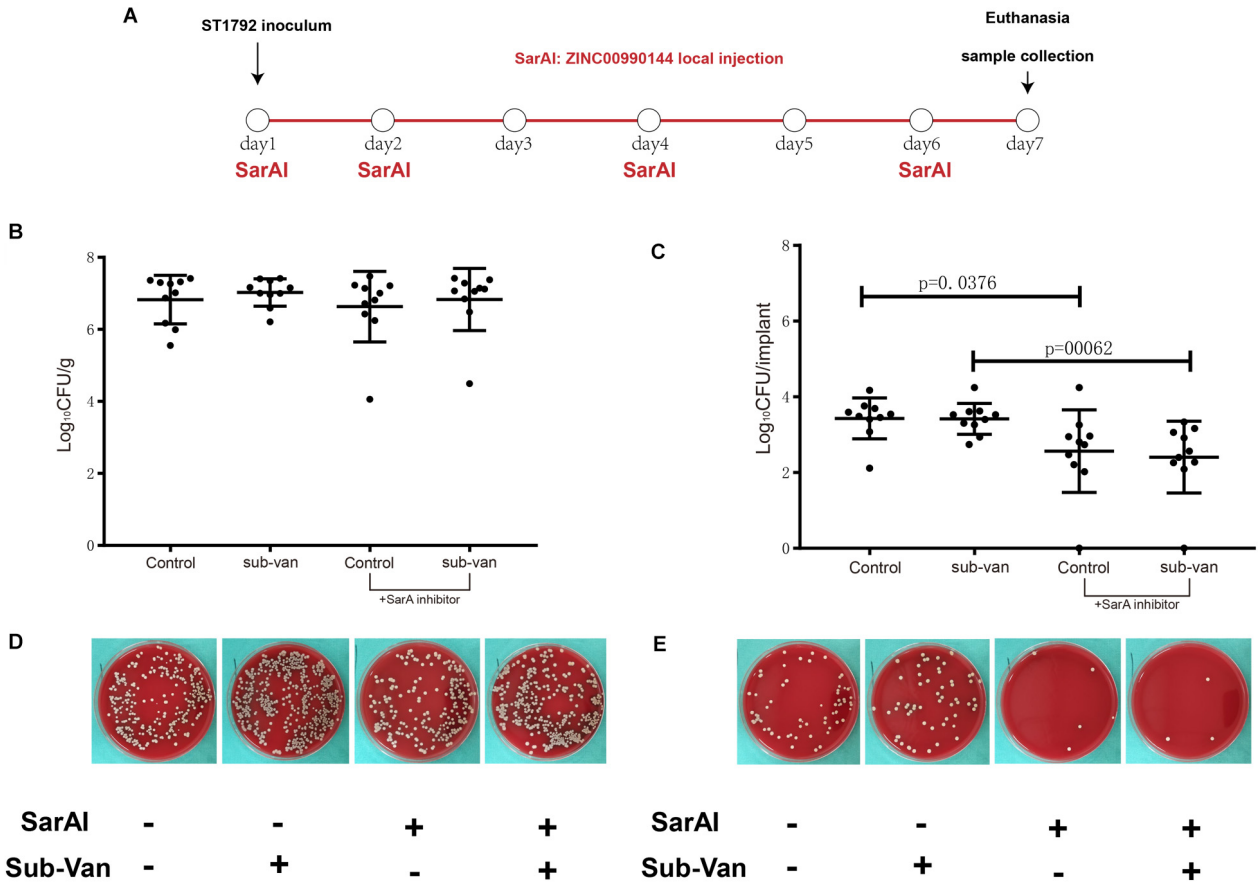

FIGURE 7 | Role of ZINC00990144 in the mice model of implant infection. **(A)** Schematic diagram for process of *in vivo* experiment. SarA inhibitor was used in implant infection mice model at day1, 2, 4, 6. All of the mice were sacrificed at day 7. **(B–E)** Quantification of bacterial load for the implant and surrounding infected tissue. **(B,D)** Bacteria count on surrounding tissues. **(C,E)** Bacteria count on implant and representative photos.

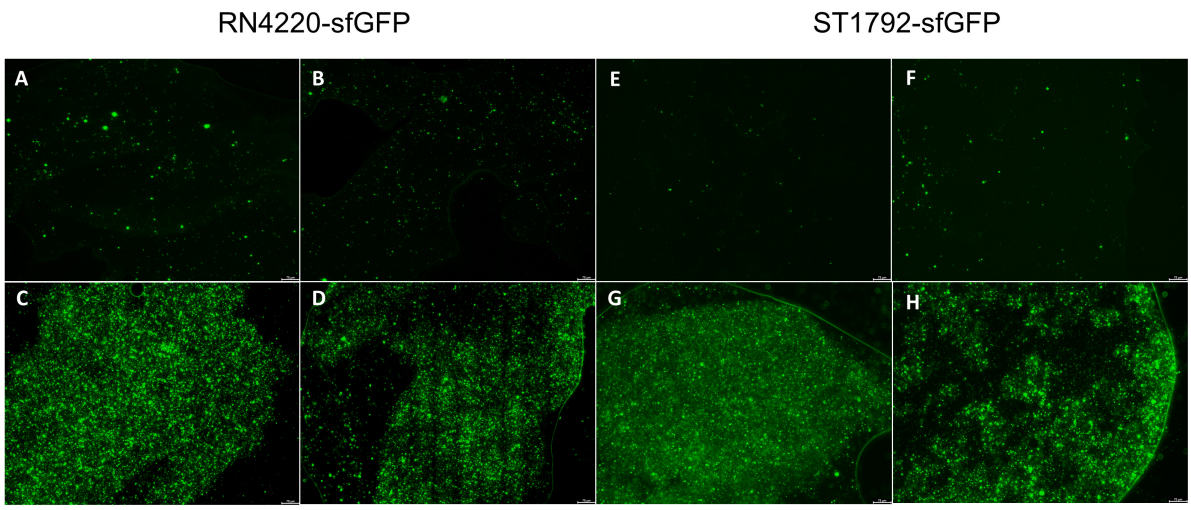

FIGURE 8 | Representative fluorescence images of biofilm *in vivo*. Titanium discs was harvested on seventh day since infection and observed under microscope. Green fluorescence represents sfGFP labeled RN4220 **(A–D)** and ST1792 **(E–H)**. **(A,E)** Mice model given SarA inhibitor ZINC00990144. **(B,F)** Mice model given ZINC00990144 and sub-MIC vancomycin. **(C,G)** Control mice model without sub-MIC vancomycin. **(D,H)** Mice model given sub-MIC vancomycin. Scale bar = 75 μm.

findings into consideration, the underlying mechanism could be explained by the hypothesis that protein is equally important in PIA-dependent and PIA-independent biofilm. According to our result, exogenous proteases efficiently inhibited sub-MIC vancomycin induced biofilm (**Figure 5B**). This result combined with previous reports demonstrated protein is an indispensable part both in PIA-dependent/independent biofilm. Strategies targeting proteins could be an effective way to limit biofilm formation.

In our study, ZINC00990144 presented anti-biofilm ability in a concentration-dependent mode and concentration at 11.5 μM is close to its maximum function (**Figure 2A**). Comparing with previous reported SarAIs, of which the effective concentration is 2.5 μM (Balamurugan et al., 2017), ZINC00990144 is still not an ideal inhibitor and needs optimization. Moreover, our results show that ZINC00990144 is highly effective toward different *S. aureus* strains including both MRSA and MSSA (**Figure 2C**), it is also functional on different materials such as titanium and UHMWPE (**Figure 2B**), which are widely used in arthroplasty, all of this together endows ZINC00990144 promising applications in a wide range of fields.

As for cytocompatibility, ZINC00990144 had a slight cytotoxicity effect when concentration reaches 23 μM (**Figure 6A**). However, it is still unclear whether the toxicity was from compound itself or the solvent (DMSO), because the corresponding DMSO control group (1%) also exhibits cytotoxicity. In this study, most of the experiment was carried out at concentration of 11.5 μM which has no cytotoxicity according to our result; hence, ZINC00990144 has good cytocompatibility at its effective concentration.

Despite the effective potency of the compound toward biofilm inhibition, our study had some limitations. First, the most suitable dose for treatment was around 11.5 μM; such a high concentration cannot be easily orally administered, therefore, we adopted local injection when conducting *in vivo* experiments. However, local injection cannot maintain the concentration at an effective level for a long duration because molecules are rapidly absorbed and metabolized by the body. Thus, selecting a drug delivery system for slow-release is necessary, such as nanoemulsions, lipid or polymeric nanoparticles, and liposomes (Shi et al., 2010). Second, the compound we identified cannot eliminate already existing mature biofilms, indicating its role in prophylaxis rather than therapy. Moreover, in consideration of its non-bactericidal effect, it should be regarded as an adjuvant compound for combinatorial usage. Besides, the *in vivo* experiment in our study only investigated early stage biofilm at a single time point and the implant infection model was soft tissue related instead of bone related. Thus, it may not truly reflect the disease process of PJI.

Although we found ZINC00990144 has an impact on SarA-associated phenotypes, it is not a direct demonstration that ZINC00990144 inhibits SarA function because many other *S. aureus* regulatory loci are known to impact these phenotypes. In order to directly investigate the function of SarA, several other assays could be adopted in the future. First, since SarA functions by binding to DNA regions, electrophoretic mobility shift assay (EMSA) is the most effective assay investigating SarA function. Second, a Luciferase reporter system governed by a known SarA binding promoter is also an alternative approach to reflect SarA activity. These methods are commonly adopted by researchers to evaluate the transcription factor activity.

In summary, here we identified a new SarA targeted anti-biofilm leading compound using virtual screening method and testified its potency *in vivo* using implant infection mice model. As an anti-biofilm compound without bactericidal effects, ZINC00990144 can be used in combination with other bactericidal antibiotics.

DATA AVAILABILITY STATEMENT

The raw data supporting the conclusions of this article will be made available by the authors, without undue reservation.

ETHICS STATEMENT

The animal study was reviewed and approved by the Animal Care and Experiment Committee of Shanghai Jiao Tong University Affiliated Sixth People's Hospital.

AUTHOR CONTRIBUTIONS

JLY contributed to the concept of the study, performed virtual screening, and wrote the manuscript. FJ and FYZ contributed to the qPCR experiment and cell culture. YQP performed the biofilm assay. JT and JQW collected clinical strains and performed antibiotic susceptibility testing. JLY, FJ, and FYZ performed the *in vivo* experiment and data acquisition. PH contributed to data analysis and data interpretation. HS contributed to study design and manuscript editing and revision. All authors contributed to the article and approved the submitted version.

FUNDING

This study was supported by the National Natural Science Foundation of China (Grant No. 81772364) and Medical Guidance Scientific Research Support Project of Shanghai Science and Technology Commission (Grant No. 19411962600).

SUPPLEMENTARY MATERIAL

The Supplementary Material for this article can be found online at: https://www.frontiersin.org/articles/10.3389/fmicb.2020.587175/full#supplementary-material

Supplementary Figure 1 | Multiple alignment result for SarA family. Seven SarA family members are aligned using clustalW. The color depth represents conservative amino acid residues.

Supplementary Figure 2 | *In vitro* static biofilm assays for all purchased 23 compounds. All of the compounds except ZINC00969968 could inhibit biofilm with varied extent. Among all of the compounds, compound ZINC00990144 shows excellent anti-biofilm performance. $^{***}P < 0.001$ comparing to DMSO control.

REFERENCES

Abdelhady, W., Bayer, A. S., Seidl, K., Moormeier, D. E., Bayles, K. W., Cheung, A., et al. (2014). Impact of vancomycin on sarA-mediated biofilm formation: role in persistent endovascular infections due to methicillin-resistant Staphylococcus aureus. *J. Infect. Dis.* 209, 1231–1240. doi: 10.1093/infdis/jiu007

Arya, R., and Princy, S. A. (2013). Computational approach to design small molecule inhibitors and identify SarA as a potential therapeutic candidate. *Med. Chem. Res.* 22, 1856–1865. doi: 10.1007/s00044-012-0185-9

Arya, R., Ravikumar, R., Santhosh, R. S., and Princy, S. A. (2015). SarA based novel therapeutic candidate against Staphylococcus aureus associated with vascular graft infections. *Front. Microbiol.* 6:416. doi: 10.3389/fmicb.2015.00416

Balamurugan, P., Praveen Krishna, V., Bharath, D., Lavanya, R., Vairaprakash, P., and Adline Princy, S. (2017). Staphylococcus aureus Quorum Regulator SarA Targeted Compound, 2-[(Methylamino)methyl]phenol Inhibits Biofilm and Down-Regulates Virulence Genes. *Front. Microbiol.* 8:1290. doi: 10.3389/fmicb.2017.01290

Bohm, H. J. (1992). The computer program LUDI: a new method for the de novo design of enzyme inhibitors. *J. Comput. Aided Mol. Des.* 6, 61–78. doi: 10.1007/BF00124387

Ciofu, O., Rojo-Molinero, E., Macia, M. D., and Oliver, A. (2017). Antibiotic treatment of biofilm infections. *APMIS* 125, 304–319. doi: 10.1111/apm.12673

Fernandes, A., and Dias, M. (2013). The Microbiological Profiles of Infected Prosthetic Implants with an Emphasis on the Organisms which Form Biofilms. *J. Clin. Diagn. Res.* 7, 219–223. doi: 10.7860/jcdr/2013/4533.2732

Figueiredo, A. M. S., Ferreira, F. A., Beltrame, C. O., and Cortes, M. F. (2017). The role of biofilms in persistent infections and factors involved in ica-independent biofilm development and gene regulation in Staphylococcus aureus. *Crit. Rev. Microbiol.* 43, 602–620. doi: 10.1080/1040841X.2017.1282941

Hsu, C. Y., Lin, M. H., Chen, C. C., Chien, S. C., Cheng, Y. H., Su, I. N., et al. (2011). Vancomycin promotes the bacterial autolysis, release of extracellular DNA, and biofilm formation in vancomycin-non-susceptible Staphylococcus aureus. *FEMS Immunol. Med. Microbiol.* 63, 236–247. doi: 10.1111/j.1574-695X.2011.00846.x

Kapadia, B. H., Berg, R. A., Daley, J. A., Fritz, J., Bhave, A., and Mont, M. A. (2016). Periprosthetic joint infection. *Lancet* 387, 386–394. doi: 10.1016/S0140-6736(14)61798-0

Kokko, M. A., Abdel, M. P., Berry, D. J., Butler, R. D., and Van Citters, D. W. (2019). A retrieval analysis perspective on revision for infection. *Arthroplasty Today* 5, 362–370. doi: 10.1016/j.artd.2019.03.007

Larkin, M. A., Blackshields, G., Brown, N. P., Chenna, R., McGettigan, P. A., McWilliam, H., et al. (2007). Clustal W and Clustal X version 2.0. *Bioinformatics* 23, 2947–2948. doi: 10.1093/bioinformatics/btm404

Le, K. Y., Dastgheyb, S., Ho, T. V., and Otto, M. (2014). Molecular determinants of staphylococcal biofilm dispersal and structuring. *Front. Cell Infect. Microbiol.* 4:167. doi: 10.3389/fcimb.2014.00167

Lipinski, C. A., Lombardo, F., Dominy, B. W., and Feeney, P. J. (2001). Experimental and computational approaches to estimate solubility and permeability in drug discovery and development settings. *Adv. Drug Deliv. Rev.* 46, 3–26. doi: 10.1016/s0169-409x(00)00129-0

Liu, Y., Manna, A. C., Pan, C. H., Kriksunov, I. A., Thiel, D. J., Cheung, A. L., et al. (2006). Structural and function analyses of the global regulatory protein SarA from Staphylococcus aureus. *Proc. Natl. Acad. Sci. U S A* 103, 2392–2397. doi: 10.1073/pnas.0510439103

Livak, K. J., and Schmittgen, T. D. (2001). Analysis of relative gene expression data using real-time quantitative PCR and the 2(-Delta Delta C(T)) Method. *Methods* 25, 402–408. doi: 10.1006/meth.2001.1262

Lourtet-Hascoet, J., Bicart-See, A., Felice, M. P., Giordano, G., and Bonnet, E. (2016). Staphylococcus lugdunensis, a serious pathogen in periprosthetic joint infections: comparison to Staphylococcus aureus and Staphylococcus epidermidis. *Int. J. Infect. Dis.* 51, 56–61. doi: 10.1016/j.ijid.2016.08.007

Moormeier, D. E., and Bayles, K. W. (2017). Staphylococcus aureus biofilm: a complex developmental organism. *Mol. Microbiol.* 104, 365–376. doi: 10.1111/mmi.13634

Moormeier, D. E., Bose, J. L., Horswill, A. R., and Bayles, K. W. (2014). Temporal and stochastic control of Staphylococcus aureus biofilm development. *mBio* 5, 1314–1341e. doi: 10.1128/mBio.01341-14

Mootz, J. M., Malone, C. L., Shaw, L. N., and Horswill, A. R. (2013). Staphopains modulate Staphylococcus aureus biofilm integrity. *Infect. Immun.* 81, 3227–3238. doi: 10.1128/iai.00377-13

Pang, Y. Y., Schwartz, J., Thoendel, M., Ackermann, L. W., Horswill, A. R., and Nauseef, W. M. (2010). agr-Dependent interactions of Staphylococcus aureus USA300 with human polymorphonuclear neutrophils. *J. Innate. Immun.* 2, 546–559. doi: 10.1159/000319855

Postler, A., Lutzner, C., Beyer, F., Tille, E., and Lutzner, J. (2018). Analysis of Total Knee Arthroplasty revision causes. *BMC musculoskelet. Disord.* 19:55. doi: 10.1186/s12891-018-1977-y

Ricciardi, B. F., Muthukrishnan, G., Masters, E., Ninomiya, M., Lee, C. C., and Schwarz, E. M. (2018). Staphylococcus aureus Evasion of Host Immunity in the Setting of Prosthetic Joint Infection: Biofilm and Beyond. *Curr. Rev. Musculoskelet. Med.* 11, 389–400. doi: 10.1007/s12178-018-9501-4

Rohde, H., Burandt, E. C., Siemssen, N., Frommelt, L., Burdelski, C., Wurster, S., et al. (2007). Polysaccharide intercellular adhesin or protein factors in biofilm accumulation of Staphylococcus epidermidis and Staphylococcus aureus isolated from prosthetic hip and knee joint infections. *Biomaterials* 28, 1711–1720. doi: 10.1016/j.biomaterials.2006.11.046

Shi, J., Votruba, A. R., Farokhzad, O. C., and Langer, R. (2010). Nanotechnology in drug delivery and tissue engineering: from discovery to applications. *Nano Lett.* 10, 3223–3230. doi: 10.1021/nl102184c

Trotonda, M. P., Manna, A. C., Cheung, A. L., Lasa, I., and Penades, J. R. (2005). SarA positively controls bap-dependent biofilm formation in Staphylococcus aureus. *J. Bacteriol.* 187, 5790–5798. doi: 10.1128/JB.187.16.5790-5798.2005

Zielinska, A. K., Beenken, K. E., Mrak, L. N., Spencer, H. J., Post, G. R., Skinner, R. A., et al. (2012). sarA-mediated repression of protease production plays a key role in the pathogenesis of Staphylococcus aureus USA300 isolates. *Mol. Microbiol.* 86, 1183–1196. doi: 10.1111/mmi.12048

Conflict of Interest: The authors declare that the research was conducted in the absence of any commercial or financial relationships that could be construed as a potential conflict of interest.

frontiers in Microbiology

ORIGINAL RESEARCH
published: 09 November 2020
doi: 10.3389/fmicb.2020.596227

Pulse Dosing of Antibiotic Enhances Killing of a *Staphylococcus aureus* Biofilm

*Kirsten J. Meyer†, Hannah B. Taylor†, Jazlyn Seidel, Michael F. Gates and Kim Lewis**

Department of Biology, Antimicrobial Discovery Center, Northeastern University, Boston, MA, United States

OPEN ACCESS

Edited by:
Mark Smeltzer, University of Arkansas for Medical Sciences, United States

Reviewed by:
Paul Stoodley, The Ohio State University, United States
Philip S. Stewart, Montana State University, United States
Marta Zapotoczna, University of Warsaw, Poland

***Correspondence:**
Kim Lewis
k.lewis@neu.edu;
k.lewis@northeastern.edu

†Present address:
Kirsten J. Meyer, Department of Biochemistry, University of Toronto, Toronto, ON, Canada
Hannah B. Taylor, Proteomics Platform, Broad Institute, Boston, MA, United States

Specialty section:
This article was submitted to Antimicrobials, Resistance and Chemotherapy, a section of the journal Frontiers in Microbiology

Received: *18 August 2020*
Accepted: *16 October 2020*
Published: *09 November 2020*

Citation:
Meyer KJ, Taylor HB, Seidel J, Gates MF and Lewis K (2020) Pulse Dosing of Antibiotic Enhances Killing of a Staphylococcus aureus Biofilm. Front. Microbiol. 11:596227. doi: 10.3389/fmicb.2020.596227

Biofilms are highly tolerant to antibiotics and underlie the recalcitrance of many chronic infections. We demonstrate that mature *Staphylococcus aureus* biofilms can be substantially sensitized to the treatment by pulse dosing of an antibiotic – in this case, oxacillin. Pulse (periodic) dosing was compared to continuous application of antibiotic and was studied in a novel *in vitro* flow system which allowed for robust biofilm growth and tractable pharmacokinetics of dosing regimens. Our results highlight that a subpopulation of the biofilm survives antibiotic without becoming resistant, a population we refer to as persister bacteria. When oxacillin was continuously present the persister level did not decline, but, importantly, providing correctly timed periodic breaks decreased the surviving population. We found that the length of the periodic break impacted efficacy, and there was an optimal length that sensitized the biofilm to repeat treatment without allowing resistance expansion. Periodic dosing provides a potential simple solution to a complicated problem.

Keywords: biofilm treatment, *Staphylococcus aureus*, antibiotic tolerance, persister resuscitation, intermittent dosing, periodic dosing, pulse dosing, oxacillin

INTRODUCTION

Biofilms, multicellular communities of bacteria, can be highly tolerant to antibiotics (Spoering and Lewis, 2001). Inside the biofilm, bacterial cells are closely packed together and surrounded by an extracellular matrix. The tolerance of biofilms to antibiotics is linked to many physiological factors. Low nutrient and oxygen availability, upregulation of innate resistance factors, cell-cell signaling, heterogeneity in population gene expression profiles, the extracellular matrix, stress responses, and cell dormancy have all been implicated (Mah et al., 2003; Walters et al., 2003; Rani et al., 2007; Mulcahy et al., 2008; Macia et al., 2011; Nguyen et al., 2011; Kirby et al., 2012; Koch et al., 2014; Van Acker et al., 2014; Stewart, 2015; Ciofu et al., 2017; Hall and Mah, 2017; Stewart et al., 2019). Moreover, the extracellular matrix protects bacteria in biofilms from clearance by the immune system (Otto, 2018; Yan and Bassler, 2019). Biofilm-based infections are a major health burden, leading to treatment failure and chronic relapsing infections (Lewis, 2008, 2019). This is exemplified by the endless rounds of treatment and substantial morbidity and mortality associated with *Pseudomonas aeruginosa* biofilms in cystic fibrosis (Costerton et al., 1999) and staphylococcal biofilms on prosthetic joint and device-related infections (Otto, 2018).

Biofilms, even of the same bacterial species, can differ widely in structure and matrix composition depending on environmental conditions. *In vitro* under lab conditions, broth nutrient components and biofilm age strongly impact antibiotic tolerance, with increasing tolerance as the biofilm

matures (Anwar et al., 1992; Haagensen et al., 2015). Experiments with *P. aeruginosa* and *S. aureus* have shown that in mature biofilms, oxygen concentration rapidly decreases from the surface of the biofilm to the deeper layers of cells (Xu et al., 1998; Walters et al., 2003; Rani et al., 2007). This correlates with the metabolic activity of cells, with high transcription rates restricted to exposed surface layers, and with the remainder of the biofilm being slow growing or even dormant. These regions of metabolic activity in the biofilm also correspond to the regions of efficacy of antibiotics (Walters et al., 2003; Haagensen et al., 2015; Stewart, 2015). Slow growth and dormancy lead to tolerance with multiple classes of antibiotics as most require active cell processes to corrupt for efficacy (Lewis, 2008; Conlon et al., 2016; Shan et al., 2017). Growth in biofilms enriches for such antibiotic tolerant cells, termed persisters (Roberts and Stewart, 2005; Lewis, 2010; Conlon et al., 2015; Waters et al., 2016). This tolerance due to low metabolic state is distinct from resistance, as at the population level there is no shift in the minimal inhibitory concentration (MIC) of antibiotics. Instead, these cells have the ability to survive a prolonged presence of antibiotic and resume growth following treatment (Balaban et al., 2019).

We and others have reasoned that as persister cells resuscitate post-treatment to generate antibiotic susceptible cells, intermittent or pulse dosing is a viable strategy for reducing the persister burden (Bigger, 1944; Cogan, 2006; Lewis, 2008; Sharma et al., 2015; Carvalho et al., 2018). Within a biofilm, there will be two populations of cells – susceptible and tolerant to the antibiotic. Applying antibiotic will kill the susceptible cells, while the tolerant population remains. Removing the antibiotic in the presence of nutrients will allow a portion of the dormant tolerant cells to resuscitate and transition to be susceptible. Therefore, if antibiotic is reapplied before new persister formation, the new susceptible portion can be removed, and the process can be repeated until all the tolerant population have been resuscitated and killed. Periodic dosing against planktonic batch cultures have found varying effects on persister levels (Bigger, 1944; Sharma et al., 2015; Cogan et al., 2016; Feng et al., 2016), and periodic application of biocides against environmental biofilms has demonstrated the importance of timing for efficacy (Grant and Bott, 2005). Several groups have modeled *in silico* the effects of varying the period of antibiotic dosing against biofilms (Cogan et al., 2013; Imran and Smith, 2014; Zhao et al., 2016; Carvalho et al., 2018), but to our knowledge, *in vitro* experimental studies systematically testing this approach have been lacking. Using *S. aureus* biofilms, we examined this experimentally with oxacillin and found that indeed providing a periodic break from antibiotic was able to dramatically improve efficacy of treatment.

MATERIALS AND METHODS

Reagents and Cell Lines

Staphylococcus aureus HG003 containing a chromosomal *lux* operon (*luxABCDE* modified from *Photorhabdus luminescens*) and a chloramphenicol resistance marker (moved by phage transduction from Newman-*lux* strain; Plaut et al., 2013) was used for all experiments. The lux strain had the same growth rate as parent (**Supplementary Figure S1A**), and was used with the intention of luminescence being a read out for biofilm metabolic activity (**Supplementary Figure S1B**), but the noise from the change in environmental conditions (e.g., temperature and oxygen) on luminescence quantification in the biofilm was unfortunately greater than the experimental signal. Single colonies were streaked on to brain heart infusion (BHI; BD BBL) agar plates from glycerol stocks, and were put into overnight culture in BHI broth (shaking 200 rpm, 37°C), before being diluted and used for experiments. Antibiotic stock solutions were stored at −20°C: oxacillin (TCI), vancomycin (Sigma), and gentamicin (Acros Organics) in water; rifampicin (Sigma) in DMSO. Oxacillin MIC was 0.125 μg/ml.

Biofilm Flow System

Input bottles, silicone tubing (Tygon 3/32" ID × 5/32" OD, Masterflex 3/16" ID × 5/16" OD, and Ismatec Tygon S3 0.89 mm ID, Cole Parmer), glass segments (7 cm long, Borosilicate 4 mm ID × 6 mm OD, Amazon), and waste bottles were autoclaved for sterilization. Tubing segments were connected *via* polypropylene Luer connectors or barbed fittings (Cole Parmer). Sterile 14G polyurethane I.V. catheters (SurFlash Terumo) were cut into 1 cm segments (approximate outer and inner surface area combined 120 mm^2), transferred to a microcentrifuge tube, and submerged in FBS (ATCC) overnight at 37°C, to promote bacterial adherence. Individual segments were then transferred to 1 ml of OD_{600} 0.01 *S. aureus* suspension in BHI + 1% glucose broth in microcentrifuge tubes, and were incubated for 24 h at 37°C. The medium was supplemented with glucose to stimulate biofilm formation and to rapidly achieve mature and tolerant biofilms (Mack et al., 1992). Catheters were transferred to fresh BHI + 1% glucose for 24 h, and then placed in triplicate inside sterile glass segments. The glass segments were connected inline to the flow system *via* tight sealing silicone tubing (ID 3/16") and Luer connectors. The tubing portion containing the glass segments (hosting the catheters) were set inside a 37°C incubator. The tubing lines and glass segments were filled with BHI + 1% glucose from input bottles *via* peristaltic pumps, and the flow rate was set to 0.1 ml/min. This regimen was maintained for 16–21 h, and then, antibiotic treatment was initiated by the addition of antibiotic to input bottles. To achieve periodic regimens, input bottles were either changed to antibiotic free BHI + 1% glucose for set intervals of time, or antibiotic was steadily diluted out of input bottles by the addition of fresh broth at the same rate as liquid removal (0.1 ml/min). Syringe pumps (New Era) controlled by programmable electronic timers (Cole Parmer) were used to regularly inject antibiotic into input bottles to achieve dosing schedules. At the end of an experiment, glass segments were disconnected from tubing, catheters removed, and rinsed in saline (0.9% NaCl). Catheters were then sonicated in 1 ml of saline for 5 min, followed by 30 s of vigorous vortexing, and this was repeated three times to disrupt biofilms. The resulting suspension was serially diluted by 10x dilutions and plated on BHI agar plates (in duplicate), then incubated at 37°C, to enumerate colony forming units (CFUs). CFU plating was performed on BHI alone or BHI containing antibiotic to establish resistance expansion. Plates were examined for CFU 24 and 72 h after plating.

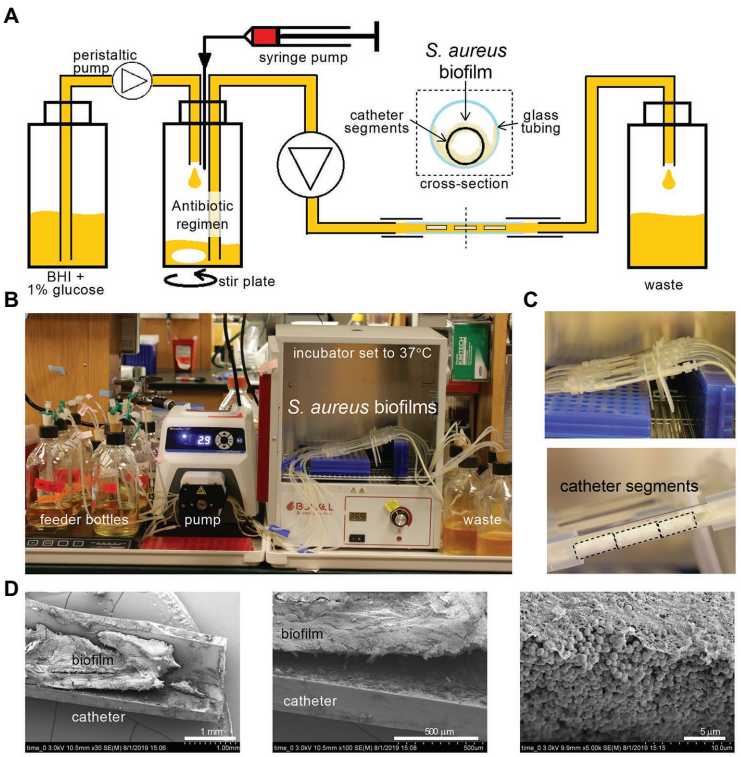

FIGURE 1 | A tractable constant flow system for *Staphylococcus aureus* biofilms. **(A)** Schematic of the flow system. Antibiotic regimens are created in a central bottle *via* injection syringe pumps and dilution with fresh medium [brain heart infusion (BHI) supplemented with 1% glucose], and pumped continuously through a piece of glass tubing containing three 1 cm catheter segments hosting *S. aureus* biofilms, then to a waste container. **(B)** Photograph of one experiment set-up with bottles, tubing, peristaltic pump, glass tubing, and waste bottles. The glass tubing sections hosting the biofilms on catheters are placed inside a 37°C incubator. **(C)** Close up of the glass tubes from **(B)** show thick white *S. aureus* biofilms. Black dotted lines outline catheter segments. **(D)** Catheters were removed from the flow system (Day 0, after 16–21 h of BHI + 1% glucose flow), halved longitudinally, and imaged by scanning electron microscopy. A dense mat of *S. aureus* biofilm can be seen inside the catheter.

Scanning Electron Microscopy

Catheters were removed from the flow system and were rinsed in 1 ml saline. Catheters were left intact or split using a razor, and were moved to a solution of 2.5% glutaraldehyde in 0.1 M sodium cacodylate containing 0.15% alcian blue and 0.15% safranin O for 24 h at 4°C for fixing and staining. Catheters were washed in 0.1 M sodium cacodylate for 10 min, infiltrated with 1% osmium tetroxide for 30 min, and then washed three times in 0.1 M sodium cacodylate. Biofilms were dehydrated by sequential submersion in 30, 50, 70, 85, and 95%, and then 100% ethanol for 5–10 min at each level. Submersion in absolute ethanol was repeated three times, and then the catheters were placed in a SAMDRI-PVT-3D (Tousimis) for critical point drying using liquid CO_2. Catheters were mounted on aluminum sample mounts using double-sided conductive carbon adhesive tape and sputter coated with 5 nm of platinum (Cressington 208HR). They were imaged on a Hitachi S-4800 SEM at 3.0 kV.

Phamacokinetic Confirmation

Samples were taken at intervals from the input bottles, or from the tubing line just prior to glass segments, to check oxacillin concentration. Oxacillin concentration was measured using a bioassay – samples were serially diluted in 96-well plates in BHI and incubated with *S. aureus* OD_{600} 0.001 at 37°C overnight (static), and compared to a standard curve run in parallel with known oxacillin levels. Turbidity was examined by eye and OD_{600} measurement (Biotek Synergy H1), and oxacillin concentration for samples was calculated by multiplying 0.5xMIC concentration (from the standard curve) by the dilution factor of samples that allowed growth to occur. The assay was run on 7 separate days with a total of 15 standard curves. Across days the standard curves displayed a mean MIC of 0.14 µg/ml, SD 0.04 µg/ml, $n = 7$, and a within day mean SD of 0.01 µg/ml (two standard curves differed in their MIC by 2-fold on 1 day, all other standard curves run on the same day shared the same MIC).

RESULTS

Catheter Biofilm Flow System

To robustly compare the effect of different antibiotic dosing regimens on biofilms, we desired a system with constant liquid flow, so that nutrients could be continually provided and antibiotics

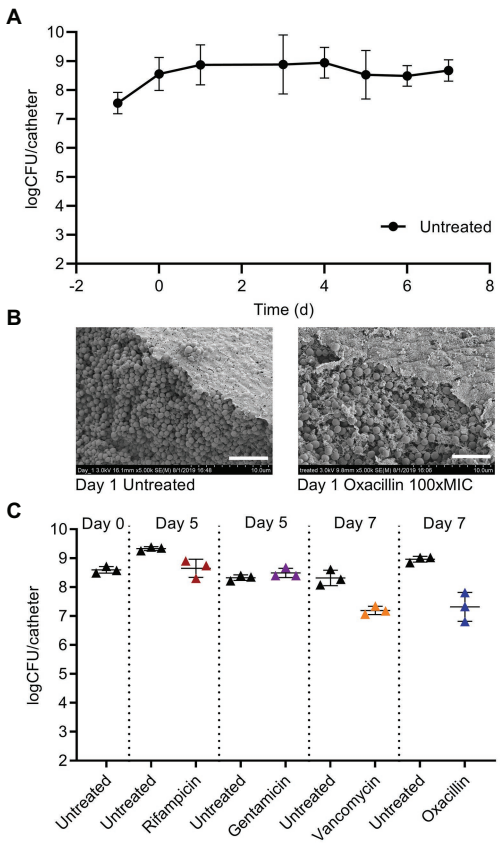

FIGURE 2 | Mature *S. aureus* biofilms on catheters are highly tolerant to antibiotics. **(A)** Catheters carrying 5×10^7 colony forming unit (CFU) of *S. aureus* are placed into the flow system on Day-1, and then fed continuously with BHI + 1% glucose. The CFU per catheter rises to 5×10^8 and stays steady over 1 week of medium flow. Symbols are means of multiple experiments on different days, $2 \leq n \leq 17$, error bars are SD. **(B)** SEM on Day 1 of untreated biofilms, or biofilms treated for 24 h with 12.5 μg/ml oxacillin [100x minimal inhibitory concentration (MIC), planktonic]. White bar, 5 μm. **(C)** Treatment beginning on Day 0 with 2 μg/ml of rifampicin, 50 μg/ml of gentamicin, 100 μg/ml of vancomycin, or 12.5 μg/ml oxacillin (100x the planktonic MICs) and continued for multiple days is ineffective at clearing *S. aureus* biofilms. Data are obtained from representative experiments, and are separated by dotted vertical lines. Symbols represent one catheter, and lines are mean and SD.

adjusted without physical disruption to the biofilm. We began by using the CDC bioreactor (Goeres et al., 2005), but the large volume of medium required for experiments led us to design a smaller system for higher throughput. Catheter segments, 1 cm long, were chosen as the vehicle for the biofilms, providing a reproducible surface area and medically relevant substrate (Kadurugamuwa et al., 2003). The segments were coated with FBS, then inoculated with methicillin-sensitive *S. aureus* (HG003-*lux*, **Supplementary Figure S1**) in microcentrifuge tubes, and biofilms were allowed to mature for 48 h in rich medium (BHI + 1% glucose). The biofilm-carrying catheters were then placed in triplicate inside glass tubing, and were subjected to a constant flow of medium (**Figures 1A,B**). All biofilms first received nutrients for 16–21 h (BHI + 1% glucose, 37°C) to allow adjustment to flow conditions and for final maturation, then antibiotic regimens were applied (Day 0). The catheter segments developed robust biofilms, which could be seen by eye (**Figure 1C**; **Supplementary Figure S1B**). Scanning electron microscopy revealed dense packing of *S. aureus* into thick mats, covered with a fibrous matrix, on both the inside and outside of the catheters (**Figure 1D**; **Supplementary Figure S2**).

To enumerate bacterial density of biofilms, catheters were removed from the glass tubing, rinsed, sonicated, and vortexed in saline, and then the saline suspension was plated for CFU. At Day 0, the biofilms averaged 3.5×10^8 CFU/catheter, and without antibiotic treatment maintained a similar burden over 7 days of providing continuous medium (**Figure 2A**). The *S. aureus* biofilms grown in this system were highly tolerant to multiple classes of antibiotics. Treatment began on Day 0 with addition of antibiotics to the medium and was provided in a continuous flow past the biofilms. Scanning electron microscopy of biofilms treated for 24 h with oxacillin at 12.5 μg ml^{-1}, 100x the planktonic MIC, showed no obvious changes compared to untreated controls (**Figure 2B**). Even with 7 days of continuous treatment with 12.5 μg ml^{-1} (100xMIC) of oxacillin, there was a maximum of 1.5 log of CFU reduction (**Figure 2C**). Likewise, the biofilm was stable for multiple days under continuous flow of 100x the planktonic MIC of gentamicin (50 μg ml^{-1}), and vancomycin (100 μg ml^{-1}; **Figure 2C**). The biofilm also withstood 100xMIC of rifampicin (2 μg ml^{-1}; **Figure 2C**) but, in this case, the treatment led to the selection for resistance and by Day 5, the biofilm was composed entirely of rifampicin resistant cells. However, for gentamicin, vancomycin, and oxacillin, the treatment did not lead to a substantial increase in resistance compared to untreated biofilms (**Supplementary Figure S3**).

Providing Breaks From Oxacillin Can Sensitize Biofilms to Treatment

For methicillin sensitive *S. aureus*, oxacillin is frequently used in the clinic, and so we chose to focus on oxacillin for studying periodic dosing. We began by providing a regular break from oxacillin each day. *S. aureus* biofilms on catheters were treated for 6 days with either continuous oxacillin (1.25 μg ml^{-1}, 10xMIC), or with a 2–5 h break each day by changing the source bottle to antibiotic free broth for the specified interval (**Figure 3**). Untreated control biofilms had on average 3×10^8 CFU/catheter at the end of 6 days (**Figure 3**). Continuous oxacillin treatment for 6 days was only able to reduce the biofilms on average 1 log to 5×10^7 CFU/catheter (the 0 h break/day point in **Figure 3**). A 2 h break each day from the oxacillin made no significant difference to biofilm burdens. Encouragingly, providing a 3 h break each day decreased biofilm survival, with 2–3 logs of the biofilm cleared by the end of the experiment. There was a greater variability in response to breaks of 4 or 5 h; on some experimental rounds, biofilms withstood the treatment, and in others, biofilms were decreased.

Modeling *in vivo* Half-Lives to Provide a Periodic Break

Typically, antibiotics are given orally or by injection, and the bacteria are exposed to an antibiotic pharmacokinetic (PK)

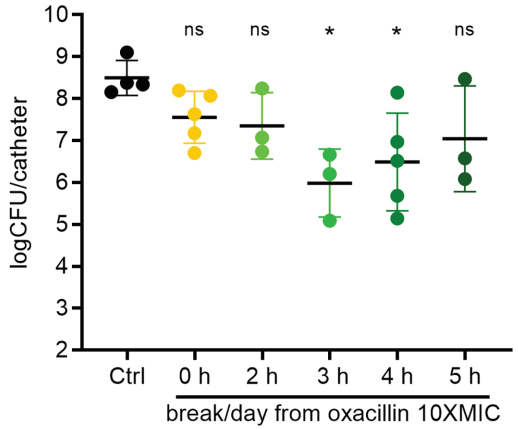

FIGURE 3 | Treatment breaks from constant oxacillin can sensitize biofilms. Biofilms were treated with constant oxacillin at 1.25 μg/ml (10x MIC) for 6 days, with a 0–5 h treatment break each day and plated for CFU. Symbols represent mean of three catheters from one experiment. Lines are means and SD of symbols (repeat experiments). Group means (of the log transformed data) were compared with an ordinary one-way ANOVA, followed by multiple-comparison of all means using Tukey's test (Prism 8.4.2). The ANOVA found a significant difference between means, $p = 0.019$, and oxacillin treated biofilms with a 3 or 4 h break each day were assessed as different than the control mean with adjusted p values of 0.018 and 0.035, respectively. All other comparisons did not reach significance.

profile that has a peak and then decays over time. To begin to examine the effect of periodic dosing on biofilms using dynamic PK profiles and to enable further translational studies, we simulated oxacillin regimens based on *in vivo* mouse pharmacokinetics. Oxacillin was dosed into the central bottle that feeds the catheters by syringe pump, and then constantly diluted by the addition of fresh medium (**Figure 1A**) to achieve a half-life of 1.3 h (Jo et al., 2011). To provide a 3–4 h break below the planktonic MIC of oxacillin, 0.125 μg ml^{-1}, every dosing period, a regimen was modeled with a peak of 12.5 μg ml^{-1} (100xMIC) given every 12 h, and compared to continuous treatment with 12.5 μg ml^{-1} (100xMIC) oxacillin (**Figure 4A**, PK sample check **Supplementary Figure S4**). Encouragingly, in four out of five experiments over 7 days, dramatically improved efficacy was seen in the periodic treatment compared to constant oxacillin, with the periodic regimen clearing 3–5 log more than continuous antibiotic (**Figure 4B**). In two experiments, the periodic regimen cleared the biofilm almost to the limit of detection (**Figure 4B**). When this was expanded with further experiments, including endpoints at 3 and 5 days, it appeared that continuous oxacillin (12.5 μg ml^{-1}, 100xMIC) cleared 1.5 log of the biofilm between 3 and 5 days of treatment, with an average remaining persister burden of 5% (10^7 CFU remaining) at 7 days (**Figure 4C**). In comparison, the periodic regimen caused continuous decline leading to a greater reduction in biofilm burden by Day 7 (**Figure 4C**). The response was variable, suggesting variation in the slope of biofilm decline between experiments, but the average decline was log-linear and achieved 4 log reduction over 7 days (**Figure 4C**).

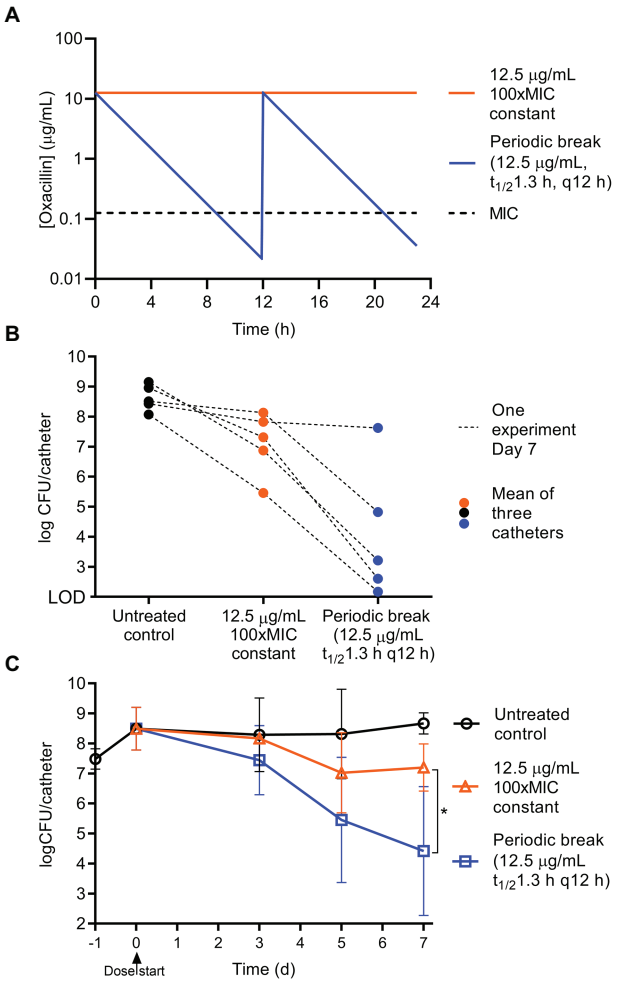

FIGURE 4 | Periodic oxacillin with half-life is more effective than constant regimen. To achieve a 3–4 h periodic break below the MIC, oxacillin was given as a peak of 12.5 μg/ml (100xMIC) with a $t_{1/2}$ of 1.3 h (the half-life in mice) every 12 h, and compared to constant 12.5 μg/ml oxacillin. **(A)** Modeled pharmacokinetics. **(B)** Day 7 results from five matched experiments, symbols represent the mean of triplicate catheters, and lines connect the results of treatment groups from one experiment. **(C)** Efficacy of regimens on biofilm CFU over time. Symbols are means of repeat experiments, $3 \leq n \leq 14$, lines SD. Day 7 results (log transformed CFU) for constant and periodic oxacillin were compared with an unpaired t-test, $p = 0.023$, with Welch's correction for unequal variance (Prism 8.4.2).

Break Length Has a U-Shaped Response Curve

The length of the effective break from oxacillin was modulated by decreasing and increasing the peak concentration of each dose, and by decreasing and increasing the interval of doses, while comparing these regimens to constant oxacillin (**Figure 5**, PK sample check **Supplementary Figure S4**). These experiments highlighted the impressive tolerance of mature biofilms – 10^7 CFU/catheter (5% of untreated biofilms) remained after constant oxacillin at 6.25, 12.5, 25, or 62.5 μg ml^{-1} (50x, 100x, 200x, or 500xMIC, respectively) for 7 days (**Figure 5A**). Periodic dosing was able to decrease the final biofilm burden, but had a steep U-shaped

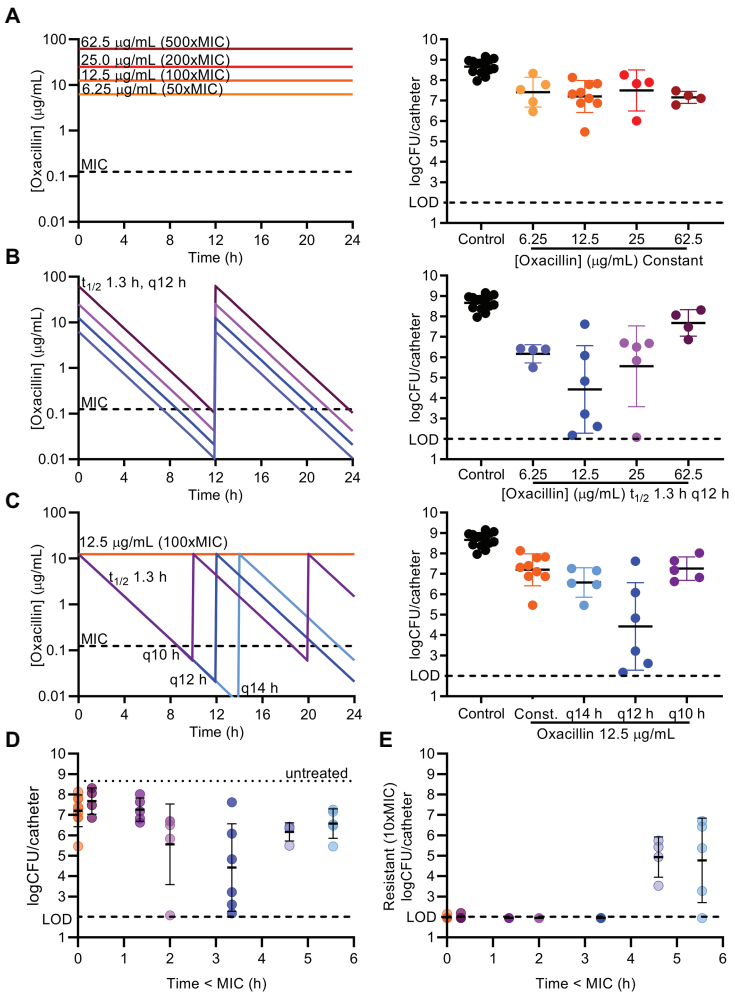

FIGURE 5 | Length of periodic break gives U-shaped dose response curve. Oxacillin was given as constant regimens of 6.25, 12.5, 25, or 62.5 µg/ml (50, 100, 200, or 500x MIC; **A**) or as periodic regimens with a $t_{1/2}$ of 1.3 h, and given every (*q*) 10, 12, or 14 h **(B,C)** for 7 days. Programmed oxacillin regimens are depicted on the left. Biofilm suspensions were plated on BHI to determine total CFU/catheter after 7 days (right). Untreated controls, 12.5 µg/ml (100xMIC) constant, or 12.5 µg/ml (100x MIC) q12 h are the same data **(A–C)** visually repeated for purposes of comparison. **(D)** CFU results for each periodic regimen, and 12.5 µg/ml (100xMIC) constant for comparison, are displayed with the time oxacillin was below the planktonic MIC 0.125 µg/ml (Time < MIC) in the programmed conditions. **(E)** Biofilm suspensions were plated on agar containing 10xMIC oxacillin to determine resistant CFU, and only those periodic regimens with the greatest Time < MIC allowed resistance expansion above the limit of detection (LOD). Symbols represent mean of three catheters from one experiment. Lines are mean and SD of symbols (repeat experiments). LOD, limit of detection.

dose response curve. The optimal periodic regimen was the originally tested peak of 12.5 µg ml^{-1} (100xMIC) of oxacillin given every 12 h, decreasing the biofilm down to 10^4 CFU/catheter on average (0.006% of the untreated biofilm) after 7 days (**Figures 5B,C**). Decreasing or increasing the peak concentration by 2-fold was less effective, leaving 10^6 CFU/catheter (0.2% of the untreated biofilm) remaining (**Figure 5B**). Shifting the dosing frequency 2 h likewise gave a U-shaped dose response curve (**Figure 5C**). These results correlate with the time oxacillin was below MIC (0.125 µg ml^{-1}) in the modeled regimens (Time < MIC), with the best efficacy achieved with a break from oxacillin of 3–4 h below the MIC (**Figure 5D**). To assess selection for oxacillin resistance, at the end of every experiment, biofilm suspensions were also plated on plates containing 10xMIC oxacillin. Encouragingly, resistance expansion did not occur in the optimal regimen, and remained below the level of detection (**Figure 5E**). The regimens providing the longest break, 5–6 h below the planktonic MIC, arising from a peak of 6.25 µg ml^{-1} (50xMIC) oxacillin given every 12 h or 12.5 µg ml^{-1} (100xMIC) given every 14 h, allowed a resistant subpopulation to expand and reach levels of 10^5 CFU/catheter over 7 days (**Figure 5E**). Under our conditions of rich medium and very mature biofilms, the optimal break is 3–4 h below the planktonic MIC of the antibiotic to allow reversal of biofilm tolerance but prevent resistance expansion.

DISCUSSION

Biofilms are a critical problem in health care, leading to chronic recurring infections despite lengthy treatment with antibiotics.

Our *in vitro* flow system allowed us to grow mature *S. aureus* biofilms and expose them to a constant flow of nutrients and to various antibiotic dosing regimens (**Figure 1**). The system is simple and tractable, and minimizes medium use compared to other macroscopic biofilm flow systems available, although experiments remain time-consuming given the impressive antibiotic tolerance of mature biofilms. For motile bacteria, the system could be adjusted with an air break, or equivalent measure, to prevent movement of the bacteria against the direction of flow. A limitation of the system is the use of catheters that likely restrict the flow of liquid through the lumen, and alternative flat substrates could be explored. Despite the complexity of the nature of biofilm tolerance to antibiotics, we found that simply providing a periodic and correctly timed break from an antibiotic (oxacillin) can sensitize a *S. aureus* biofilm to treatment (**Figure 4**). Although inclination to improve antibiotic efficacy is often to treat with a larger dose of drug for longer, we demonstrate that periodic absence of antibiotic, or the time below a critical threshold (e.g., MIC), can be important for efficacy of regimens against biofilms.

Our study leads to several conclusions. First, it is consistent with previous research and clinical experience and shows that a mature biofilm remains tolerant to antibiotic treatment over multiple days, even while provided with a continuous supply of nutrients (**Figure 2C**; Parra-Ruiz et al., 2012; Barber et al., 2015). This occurred without selection for resistance in the case of gentamicin, vancomycin, and oxacillin (**Figure 2C**; **Supplementary Figure S3**). For simplicity, we refer to this tolerant subpopulation as persisters, despite likely complexity in the mechanisms of tolerance, as these cells withstood antibiotic in the biofilm but when removed from the biofilm were able to regrow in the absence of antibiotic. The levels of persisters in our study were comparable to persister/tolerant subpopulation levels observed in previous studies of mature staphylococcal biofilms and cell-wall inhibiting antibiotics (Anwar et al., 1992; Parra-Ruiz et al., 2012; Barber et al., 2015; Butini et al., 2019). For constant oxacillin, under rich medium conditions, the persister level in our study was remarkably stable across five dose levels from 1.25 to 62.5 μg ml^{-1} (10xMIC–500xMIC) and averaged 5 ± 2% of the total (mean and SD; **Figures 3–5**).

Second, providing a periodic break from oxacillin for short periods could reverse biofilm tolerance and lead to sensitization to repeated applications of oxacillin (**Figures 3–5**). Presumably, a subset of the persisters exit dormancy and resuscitate when the antibiotic is not present. Conversely, this suggests that maintaining the presence of antibiotic prolongs dormancy. This may be cellular stress response related, or the direct action of the antibiotic, inhibiting the function of key cellular machinery, which, in the case of oxacillin, is the inhibition of penicillin binding proteins preventing the formation of peptidoglycan.

Third, the extent of sensitization and the rate of removal to a given periodic regimen had considerable variation (**Figures 3–5**), likely reflecting a heterogeneity in biofilm maturity and response between different experiments even when conditions were replicated. This variation may also have come from the outer and inner surfaces of the catheter experiencing different flow rates.

Finally, under our rich medium conditions, the effective break window from oxacillin was narrow and adjusting the period of oxacillin dosing by 2 h in either directions substantially decreased efficacy. We speculate that too short a break does not allow for adequate persister resuscitation, whereas too long a break allows for population expansion (including resistant cells) and perhaps produces new persisters. This narrow window under our rich medium conditions may also explain the high variability in response to periodic dosing. With the caveat that concentrations in the microenvironment of the biofilm may have been different than in the bulk flow system broth, our models suggest the effective break from oxacillin required 3–4 h of the antibiotic below the planktonic MIC (**Figures 3–5**). Further research is needed to explore optimal dosing regimens for other antibiotics and for biofilms grown under different medium conditions or *in vivo*.

These are among the first experimental results, that we are aware of, which demonstrate that providing the optimal break from antibiotics can indeed sensitize biofilms to treatment. The observed U-shaped response curve around the break from antibiotic agrees with theoretical modeling studies on biofilm removal by intermittent application (Cogan et al., 2013, 2016; Zhao et al., 2016; Acar and Cogan, 2019). The optimal length of break likely depends on the time to resuscitation of dormant cells (Carvalho et al., 2018; Butini et al., 2019), which will be a function of both unique effects of the antibiotic used (pharmacodynamics) and the nutrient availability across the biofilm. This concept is similar to that of the post-antibiotic effect (PAE), but is subtly different, as it is the time to resuscitation not to regrowth. We have correlated this with the PK-PD variable of Time below MIC, Time < MIC, not to be confused with the PK-PD parameters of beta-lactams required for growth inhibition or bactericidal activity, which are usually Time > MIC. The planktonic MIC may not be the threshold concentration at which persisters resuscitate in the biofilm, but is used for simplicity as a concentration at which to quantify the antibiotic "break." We found that under rich medium conditions, a relatively short break from oxacillin was optimal (3–4 h below the planktonic MIC in the broth treating the biofilms). If the break was extended, a population resistant to oxacillin began to expand. This resistant subpopulation may have been able to expand in sub-MIC antibiotic concentrations, and then survive repeated applications of antibiotic by virtue of slow-growth rate or being present in pockets of the biofilm experiencing low concentrations of oxacillin (Lee et al., 2018). Encouragingly, resistant cells did not expand in the optimally sensitizing regimen of oxacillin (**Figure 5**), suggesting a therapeutic window for biofilm efficacy with periodic break dosing.

Biofilms, and more generally persisters, are notoriously difficult to treat. Treatment strategies shown to activate dormant cells through providing alternative metabolites (Borriello et al., 2006; Meylan et al., 2018; Li et al., 2019), or targeting signaling pathways (Marques et al., 2014; Koo et al., 2017), are promising, as are approaches that use antibiotics that kill dormant cells (Defraine et al., 2018), such as ADEP4, with an ATP independent mechanism to kill dormant *S. aureus* (Conlon et al., 2013),

or colistin to kill dormant *P. aeruginosa* (Pamp et al., 2008). Our result of achieving efficacy against biofilms with a single antibiotic by providing periodic breaks is encouraging in its simplicity. More sobering was the narrow window of effective break, and the variability in sensitization, that we observed against *S. aureus* biofilms with oxacillin. This narrow effective window may also explain why intermittent dosing is not necessarily more effective than continuous infusion in animal models of endocarditis (Robaux et al., 2001; Jacqueline et al., 2002). With individual variation in antibiotic PK, a correctly timed periodic break would be challenging to achieve clinically with oral or parental oxacillin treatment. However, potential applications may exist for wound treatment with topical antibiotics or for antimicrobial lock therapy for catheters, where tight control of antibiotic levels is maintained. Increasing the frequency of applied breaks may also improve efficacy, and deserves future exploration. Our experiments were conducted under rich medium conditions with very mature and dense biofilms, and further research is needed to study the effective break period and frequency under alternative conditions. It is intriguing to consider the possibility of removing the antibiotic, supplying a short interval of nutrients to activate the biofilm, and then reapplying antibiotic, achieving greater control over the time to resuscitation of persisters (Acar and Cogan, 2019). Several strategies to increase the range of the break window also suggest themselves, such as sequential treatment with different antibiotics (Butini et al., 2019), or searching for antibiotic pairs that exhibit cellular hysteresis (Roemhild et al., 2018) in regard to persister resuscitation and sensitivity, or exploiting collateral sensitivity to maximize clearance of resistant cells with the second antibiotic (Baym et al., 2016). We expect that the use of compounds such as teixobactin, for which there is no detectable resistance (Ling et al., 2015), will allow for more relaxed regimens with a broader window between antibiotic applications.

Using a clinically approved antibiotic, we were able to achieve efficacy against mature *S. aureus* biofilms by providing short and repeated breaks where the antibiotic was below a critical threshold. Targeting the dormant portion of a biofilm can be achieved by correct timing of dosing, relying on resuscitation during drops in the antibiotic. Biofilms are indeed difficult to treat; their dormancy is their shield, but knowing this allows us to exploit and undermine it.

DATA AVAILABILITY STATEMENT

The raw data supporting the conclusions of this article will be made available by the authors, without undue reservation.

AUTHOR CONTRIBUTIONS

KM and KL designed the study and wrote the manuscript. KM performed the experiments and analyzed results. HT, JS, and MG assisted with experiments and revised the manuscript. All authors contributed to the article and approved the submitted version.

FUNDING

This study was supported by NIH grant R01 AI141966 to KL.

ACKNOWLEDGMENTS

We thank Samantha Niles and Meghan Ghiglieri for technical support. We thank William H. Fowle of the Electron Microscopy Core at Northeastern University for assistance with the scanning electron microscopy. We thank Sylvie Manuse and Nadja Leimer for reading the manuscript and providing helpful advice.

SUPPLEMENTARY MATERIAL

The Supplementary Material for this article can be found online at: https://www.frontiersin.org/articles/10.3389/fmicb.2020.596227/full#supplementary-material

REFERENCES

Acar, N., and Cogan, N. G. (2019). Enhanced disinfection of bacterial populations by nutrient and antibiotic challenge timing. *Math. Biosci.* 313, 12–32. doi: 10.1016/j.mbs.2019.04.007

Anwar, H., Strap, J. L., and Costerton, J. W. (1992). Eradication of biofilm cells of *Staphylococcus aureus* with tobramycin and cephalexin. *Can. J. Microbiol.* 38, 618–625. doi: 10.1139/m92-102

Balaban, N. Q., Helaine, S., Lewis, K., Ackermann, M., Aldridge, B., Andersson, D. I., et al. (2019). Definitions and guidelines for research on antibiotic persistence. *Nat. Rev. Microbiol.* 17, 441–448. doi: 10.1038/s41579-019-0196-3

Barber, K. E., Smith, J. R., Ireland, C. E., Boles, B. R., Rose, W. E., and Rybak, M. J. (2015). Evaluation of ceftaroline alone and in combination against biofilm-producing methicillin-resistant *Staphylococcus aureus* with reduced susceptibility to daptomycin and vancomycin in an in vitro pharmacokinetic/pharmacodynamic model. *Antimicrob. Agents Chemother.* 59, 4497–4503. doi: 10.1128/aac.00386-15

Baym, M., Stone, L. K., and Kishony, R. (2016). Multidrug evolutionary strategies to reverse antibiotic resistance. *Science* 351:aad3292. doi: 10.1126/science.aad3292

Bigger, J. (1944). Treatment of staphylococcal infections with penicillin by intermittent sterilisation. *Lancet* 244, 497–500. doi: 10.1016/S0140-6736(00)74210-3

Borriello, G., Richards, L., Ehrlich, G. D., and Stewart, P. S. (2006). Arginine or nitrate enhances antibiotic susceptibility of *Pseudomonas aeruginosa* in biofilms. *Antimicrob. Agents Chemother.* 50, 382–384. doi: 10.1128/aac.50.1.382-384.2006

Butini, M. E., Abbandonato, G., Di Rienzo, C., Trampuz, A., and Di Luca, M. (2019). Isothermal microcalorimetry detects the presence of persister cells in a *Staphylococcus aureus* biofilm after vancomycin treatment. *Front. Microbiol.* 10:332. doi: 10.3389/fmicb.2019.00332

Carvalho, G., Balestrino, D., Forestier, C., and Mathias, J. D. (2018). How do environment-dependent switching rates between susceptible and persister cells affect the dynamics of biofilms faced with antibiotics? *NPJ Biofilms Microbiomes* 4:6. doi: 10.1038/s41522-018-0049-2

Ciofu, O., Rojo-Molinero, E., Macia, M. D., and Oliver, A. (2017). Antibiotic treatment of biofilm infections. *APMIS* 125, 304–319. doi: 10.1111/apm.12673

Cogan, N. G. (2006). Effects of persister formation on bacterial response to dosing. *J. Theor. Biol.* 238, 694–703. doi: 10.1016/j.jtbi.2005.06.017

Cogan, N. G., Rath, H., Kommerein, N., Stumpp, S. N., and Stiesch, M. (2016). Theoretical and experimental evidence for eliminating persister bacteria by

manipulating killing timing. *FEMS Microbiol. Lett.* 363:fnw264. doi: 10.1093/femsle/fnw264

Cogan, N. G., Szomolay, B., and Dindos, M. (2013). Effect of periodic disinfection on persisters in a one-dimensional biofilm model. *Bull. Math. Biol.* 75, 94–123. doi: 10.1007/s11538-012-9796-z

Conlon, B. P., Nakayasu, E. S., Fleck, L. E., LaFleur, M. D., Isabella, V. M., Coleman, K., et al. (2013). Activated ClpP kills persisters and eradicates a chronic biofilm infection. *Nature* 503, 365–370. doi: 10.1038/nature12790

Conlon, B. P., Rowe, S. E., Gandt, A. B., Nuxoll, A. S., Donegan, N. P., Zalis, E. A., et al. (2016). Persister formation in *Staphylococcus aureus* is associated with ATP depletion. *Nat. Microbiol.* 1:16051. doi: 10.1038/nmicrobiol.2016.51

Conlon, B. P., Rowe, S. E., and Lewis, K. (2015). Persister cells in biofilm associated infections. *Adv. Exp. Med. Biol.* 831, 1–9. doi: 10.1007/978-3-319-09782-4_1

Costerton, J. W., Stewart, P. S., and Greenberg, E. P. (1999). Bacterial biofilms: a common cause of persistent infections. *Science* 284, 1318–1322. doi: 10.1126/science.284.5418.1318

Defraine, V., Fauvart, M., and Michiels, J. (2018). Fighting bacterial persistence: current and emerging anti-persister strategies and therapeutics. *Drug Resist. Updat.* 38, 12–26. doi: 10.1016/j.drup.2018.03.002

Feng, J., Zhang, S., Shi, W., and Zhang, Y. (2016). Ceftriaxone pulse dosing fails to eradicate biofilm-like microcolony *B. burgdorferi* persisters which are sterilized by daptomycin/doxycycline/cefuroxime without pulse dosing. *Front. Microbiol.* 7:1744. doi: 10.3389/fmicb.2016.01744

Goeres, D. M., Loetterle, L. R., Hamilton, M. A., Murga, R., Kirby, D. W., and Donlan, R. M. (2005). Statistical assessment of a laboratory method for growing biofilms. *Microbiology* 151, 757–762. doi: 10.1099/mic.0.27709-0

Grant, D. M., and Bott, T. R. (2005). Biocide dosing strategies for biofilm control. *Heat Transf. Eng.* 26, 44–50. doi: 10.1080/01457630590890166

Haagensen, J. A., Verotta, D., Huang, L., Spormann, A., and Yang, K. (2015). New in vitro model to study the effect of human simulated antibiotic concentrations on bacterial biofilms. *Antimicrob. Agents Chemother.* 59, 4074–4081. doi: 10.1128/aac.05037-14

Hall, C. W., and Mah, T. F. (2017). Molecular mechanisms of biofilm-based antibiotic resistance and tolerance in pathogenic bacteria. *FEMS Microbiol. Rev.* 41, 276–301. doi: 10.1093/femsre/fux010

Imran, M., and Smith, H. L. (2014). A model of optimal dosing of antibiotic treatment in biofilm. *Math. Biosci. Eng.* 11, 547–571. doi: 10.3934/mbe.2014.11.547

Jacqueline, C., Batard, E., Perez, L., Boutoille, D., Hamel, A., Caillon, J., et al. (2002). In vivo efficacy of continuous infusion versus intermittent dosing of linezolid compared to vancomycin in a methicillin-resistant *Staphylococcus aureus* rabbit endocarditis model. *Antimicrob. Agents Chemother.* 46, 3706–3711. doi: 10.1128/aac.46.12.3706-3711.2002

Jo, D. S., Montgomery, C. P., Yin, S., Boyle-Vavra, S., and Daum, R. S. (2011). Improved oxacillin treatment outcomes in experimental skin and lung infection by a methicillin-resistant *Staphylococcus aureus* isolate with a vraSR operon deletion. *Antimicrob. Agents Chemother.* 55, 2818–2823. doi: 10.1128/aac.01704-10

Kadurugamuwa, J. L., Sin, L., Albert, E., Yu, J., Francis, K., DeBoer, M., et al. (2003). Direct continuous method for monitoring biofilm infection in a mouse model. *Infect. Immun.* 71, 882–890. doi: 10.1128/iai.71.2.882-890.2003

Kirby, A. E., Garner, K., and Levin, B. R. (2012). The relative contributions of physical structure and cell density to the antibiotic susceptibility of bacteria in biofilms. *Antimicrob. Agents Chemother.* 56, 2967–2975. doi: 10.1128/aac.06480-11

Koch, G., Yepes, A., Forstner, K. U., Wermser, C., Stengel, S. T., Modamio, J., et al. (2014). Evolution of resistance to a last-resort antibiotic in *Staphylococcus aureus* via bacterial competition. *Cell* 158, 1060–1071. doi: 10.1016/j.cell.2014.06.046

Koo, H., Allan, R. N., Howlin, R. P., Stoodley, P., and Hall-Stoodley, L. (2017). Targeting microbial biofilms: current and prospective therapeutic strategies. *Nat. Rev. Microbiol.* 15, 740–755. doi: 10.1038/nrmicro.2017.99

Lee, A. J., Wang, S., Meredith, H. R., Zhuang, B., Dai, Z., and You, L. (2018). Robust, linear correlations between growth rates and beta-lactam-mediated lysis rates. *Proc. Natl. Acad. Sci. U. S. A.* 115, 4069–4074. doi: 10.1073/pnas.1719504115

Lewis, K. (2008). Multidrug tolerance of biofilms and persister cells. *Curr. Top. Microbiol. Immunol.* 322, 107–131. doi: 10.1007/978-3-540-75418-3_6

Lewis, K. (2010). Persister Cells. *Annu. Rev. Microbiol.* 64, 357–372. doi: 10.1146/annurev.micro.112408.134306

Lewis, K. (Ed.) (2019). *Persister cells and infectious disease*. (Switzerland, AG: Springer Nature).

Li, M., Kang, E. T., Chua, K. L., and Neoh, K. G. (2019). Sugar-powered nanoantimicrobials for combating bacterial biofilms. *Biomater. Sci.* 7, 2961–2974. doi: 10.1039/c9bm00471h

Ling, L. L., Schneider, T., Peoples, A. J., Spoering, A. L., Engels, I., Conlon, B. P., et al. (2015). A new antibiotic kills pathogens without detectable resistance. *Nature* 517, 455–459. doi: 10.1038/nature14098

Macia, M. D., Perez, J. L., Molin, S., and Oliver, A. (2011). Dynamics of mutator and antibiotic-resistant populations in a pharmacokinetic/pharmacodynamic model of *Pseudomonas aeruginosa* biofilm treatment. *Antimicrob. Agents Chemother.* 55, 5230–5237. doi: 10.1128/aac.00617-11

Mack, D., Siemssen, N., and Laufs, R. (1992). Parallel induction by glucose of adherence and a polysaccharide antigen specific for plastic-adherent *Staphylococcus epidermidis*: evidence for functional relation to intercellular adhesion. *Infect. Immun.* 60, 2048–2057. doi: 10.1128/IAI.60.5.2048-2057.1992

Mah, T. F., Pitts, B., Pellock, B., Walker, G. C., Stewart, P. S., and O'Toole, G. A. (2003). A genetic basis for *Pseudomonas aeruginosa* biofilm antibiotic resistance. *Nature* 426, 306–310. doi: 10.1038/nature02122

Marques, C. N., Morozov, A., Planzos, P., and Zelaya, H. M. (2014). The fatty acid signaling molecule cis-2-decenoic acid increases metabolic activity and reverts persister cells to an antimicrobial-susceptible state. *Appl. Environ. Microbiol.* 80, 6976–6991. doi: 10.1128/aem.01576-14

Meylan, S., Andrews, I. W., and Collins, J. J. (2018). Targeting antibiotic tolerance, pathogen by pathogen. *Cell* 172, 1228–1238. doi: 10.1016/j.cell.2018.01.037

Mulcahy, H., Charron-Mazenod, L., and Lewenza, S. (2008). Extracellular DNA chelates cations and induces antibiotic resistance in *Pseudomonas aeruginosa* biofilms. *PLoS Pathog.* 4:e1000213. doi: 10.1371/journal.ppat.1000213

Nguyen, D., Joshi-Datar, A., Lepine, F., Bauerle, E., Olakanmi, O., Beer, K., et al. (2011). Active starvation responses mediate antibiotic tolerance in biofilms and nutrient-limited bacteria. *Science* 334, 982–986. doi: 10.1126/science.1211037

Otto, M. (2018). Staphylococcal biofilms. *Microbiol. Spectr.* 6:GPP3-0023-2018. doi: 10.1128/microbiolspec.GPP3-0023-2018

Pamp, S. J., Gjermansen, M., Johansen, H. K., and Tolker-Nielsen, T. (2008). Tolerance to the antimicrobial peptide colistin in *Pseudomonas aeruginosa* biofilms is linked to metabolically active cells, and depends on the pmr and mexAB-oprM genes. *Mol. Microbiol.* 68, 223–240. doi: 10.1111/j.1365-2958.2008.06152.x

Parra-Ruiz, J., Bravo-Molina, A., Pena-Monje, A., and Hernandez-Quero, J. (2012). Activity of linezolid and high-dose daptomycin, alone or in combination, in an in vitro model of *Staphylococcus aureus* biofilm. *J. Antimicrob. Chemother.* 67, 2682–2685. doi: 10.1093/jac/dks272

Plaut, R. D., Mocca, C. P., Prabhakara, R., Merkel, T. J., and Stibitz, S. (2013). Stably luminescent *Staphylococcus aureus* clinical strains for use in bioluminescent imaging. *PLoS One* 8:e59232. doi: 10.1371/journal.pone.0059232

Rani, S. A., Pitts, B., Beyenal, H., Veluchamy, R. A., Lewandowski, Z., Davison, W. M., et al. (2007). Spatial patterns of DNA replication, protein synthesis, and oxygen concentration within bacterial biofilms reveal diverse physiological states. *J. Bacteriol.* 189, 4223–4233. doi: 10.1128/jb.00107-07

Robaux, M. A., Dube, L., Caillon, J., Bugnon, D., Kergueris, M. F., Navas, D., et al. (2001). In vivo efficacy of continuous infusion versus intermittent dosing of ceftazidime alone or in combination with amikacin relative to human kinetic profiles in a *Pseudomonas aeruginosa* rabbit endocarditis model. *J. Antimicrob. Chemother.* 47, 617–622. doi: 10.1093/jac/47.5.617

Roberts, M. E., and Stewart, P. S. (2005). Modelling protection from antimicrobial agents in biofilms through the formation of persister cells. *Microbiology* 151, 75–80. doi: 10.1099/mic.0.27385-0

Roemhild, R., Gokhale, C. S., Dirksen, P., Blake, C., Rosenstiel, P., Traulsen, A., et al. (2018). Cellular hysteresis as a principle to maximize the efficacy of antibiotic therapy. *Proc. Natl. Acad. Sci. U. S. A.* 115, 9767–9772. doi: 10.1073/pnas.1810004115

Shan, Y., Brown Gandt, A., Rowe, S. E., Deisinger, J. P., Conlon, B. P., and Lewis, K. (2017). ATP-dependent persister formation in *Escherichia coli*. *mBio* 8, e02267–e02316. doi: 10.1128/mBio.02267-16

Sharma, B., Brown, A. V., Matluck, N. E., Hu, L. T., and Lewis, K. (2015). *Borrelia burgdorferi*, the causative agent of Lyme disease, forms drug-tolerant persister cells. *Antimicrob. Agents Chemother.* 59, 4616–4624. doi: 10.1128/aac.00864-15

Spoering, A. L., and Lewis, K. (2001). Biofilms and planktonic cells of *Pseudomonas aeruginosa* have similar resistance to killing by antimicrobials. *J. Bacteriol.* 183, 6746–6751. doi: 10.1128/jb.183.23.6746-6751.2001

Stewart, P. S. (2015). Antimicrobial tolerance in biofilms. *Microbiol. Spectr.* 3:MB-0010-2014. doi: 10.1128/microbiolspec.MB-0010-2014

Stewart, P. S., White, B., Boegli, L., Hamerly, T., Williamson, K. S., Franklin, M. J., et al. (2019). Conceptual model of biofilm antibiotic tolerance that integrates phenomena of diffusion, metabolism, gene expression, and physiology. *J. Bacteriol.* 201, e00307–e00319. doi: 10.1128/JB.00307-19

Van Acker, H., Van Dijck, P., and Coenye, T. (2014). Molecular mechanisms of antimicrobial tolerance and resistance in bacterial and fungal biofilms. *Trends Microbiol.* 22, 326–333. doi: 10.1016/j.tim.2014.02.001

Walters, M. C. III, Roe, F., Bugnicourt, A., Franklin, M. J., and Stewart, P. S. (2003). Contributions of antibiotic penetration, oxygen limitation, and low metabolic activity to tolerance of *Pseudomonas aeruginosa* biofilms to ciprofloxacin and tobramycin. *Antimicrob. Agents Chemother.* 47, 317–323. doi: 10.1128/aac.47.1.317-323.2003

Waters, E. M., Rowe, S. E., O'Gara, J. P., and Conlon, B. P. (2016). Convergence of *Staphylococcus aureus* persister and biofilm research: can biofilms be defined as communities of adherent persister cells? *PLoS Pathog.* 12:e1006012. doi: 10.1371/journal.ppat.1006012

Xu, K. D., Stewart, P. S., Xia, F., Huang, C. T., and McFeters, G. A. (1998). Spatial physiological heterogeneity in *Pseudomonas aeruginosa* biofilm is determined by oxygen availability. *Appl. Environ. Microbiol.* 64, 4035–4039. doi: 10.1128/AEM.64.10.4035-4039.1998

Yan, J., and Bassler, B. L. (2019). Surviving as a community: antibiotic tolerance and persistence in bacterial biofilms. *Cell Host Microbe* 26, 15–21. doi: 10.1016/j.chom.2019.06.002

Zhao, J., Seeluangsawat, P., and Wang, Q. (2016). Modeling antimicrobial tolerance and treatment of heterogeneous biofilms. *Math. Biosci.* 282, 1–15. doi: 10.1016/j.mbs.2016.09.005

Conflict of Interest: The authors declare that the research was conducted in the absence of any commercial or financial relationships that could be construed as a potential conflict of interest.

frontiers in Microbiology

ORIGINAL RESEARCH
published: 23 November 2020
doi: 10.3389/fmicb.2020.605608

In vitro Evaluation of Medihoney Antibacterial Wound Gel as an Anti-biofilm Agent Against Ventricular Assist Device Driveline Infections

*Yue Qu[1,2], David McGiffin[3,4], Christina Kure[3,4], Janelle McLean[5], Courtney Duncan[5] and Anton Y. Peleg[1,2]**

[1]Infection and Immunity Theme, Monash Biomedicine Discovery Institute, Department of Microbiology, Monash University, Clayton, VIC, Australia, [2]Department of Infectious Diseases, The Alfred Hospital and Central Clinical School, Monash University, Melbourne, VIC, Australia, [3]Department of Cardiothoracic Surgery, The Alfred Hospital and Monash University, Melbourne, VIC, Australia, [4]Department of Medicine, Central Clinical School, Monash University, Melbourne, VIC, Australia, [5]Transplant Services, The Alfred Hospital and Monash University, Melbourne, VIC, Australia

OPEN ACCESS

Edited by:
Jessica Amber Jennings,
University of Memphis, United States

Reviewed by:
László Majoros,
University of Debrecen, Hungary
Carolina Dos Anjos,
University of São Paulo, Brazil

***Correspondence:**
Anton Y. Peleg
anton.peleg@monash.edu

Specialty section:
This article was submitted to Antimicrobials, Resistance and Chemotherapy, a section of the journal Frontiers in Microbiology

Received: 12 September 2020
Accepted: 30 October 2020
Published: 23 November 2020

Citation:
Qu Y, McGiffin D, Kure C, McLean J, Duncan C and Peleg AY (2020) In vitro Evaluation of Medihoney Antibacterial Wound Gel as an Anti-biofilm Agent Against Ventricular Assist Device Driveline Infections. Front. Microbiol. 11:605608. doi: 10.3389/fmicb.2020.605608

Objectives: In adult ventricular assist device (VAD) programs in Australian hospitals, Medihoney Antibacterial Wound Gel (MAWG) is routinely used at the skin exit-site of VAD drivelines to prevent infections; however, its effectiveness remains unclear. Our aim was to assess antimicrobial activity of Medihoney wound gel, using *in vitro* models that mimic clinical biofilms grown at the driveline exit-site.

Methods: Antimicrobial susceptibility testing of MAWG was performed for 24 clinical isolates grown under planktonic conditions, and four representative strains grown as biofilms. Different antimicrobial mechanisms of MAWG were assessed respectively for their relative contribution to its anti-biofilm activity. A colony biofilm assay and a drip-flow biofilm reactor assay mimicking the driveline exit-site environment were used to evaluate the activity of MAWG against biofilm growth at the driveline exit-site.

Results: MAWG demonstrated species-specific activity against planktonic cultures [minimum inhibitory concentrations (MICs), 5–20% weight/volume (W/V) for *Staphylococcus* species, 20–>40% (W/V) for *Pseudomonas aeruginosa* and *Candida* species]. Higher concentrations [MICs, 30–>80% (W/V)] were able to inhibit biofilm growth, but failed to eradicate pre-established biofilms. The anti-biofilm properties of MAWG were multi-faceted, with the often-advertised "active" ingredient methylglyoxal (MGO) playing a less important role. The colony biofilm assay and the drip-flow biofilm reactor assay suggested that MAWG was unable to kill biofilms pre-established in a driveline exit-site environment, or effectively prevent planktonic cells from forming adherent monolayers and further developing mature biofilms.

Conclusion: Our work suggests a suboptimal effectiveness of MAWG in preventing driveline infections due to biofilm development.

Keywords: Medihoney Antibacterial Wound Gel, anti-biofilm, methylglyoxal, ventricular assistant device, driveline infections

INTRODUCTION

Medical-grade honeys have been used for the treatment of infection in chronic wounds and persistent diabetic ulcers (Soffer, 1976; Dunwoody and Acton, 2008). They have also been used for prophylactic indications such as prevention of peritoneal dialysis catheter exit-site infection (Forbes et al., 2016). Documented merits of honey as an antimicrobial agent include effectiveness against both planktonic cultures and biofilms (Lu et al., 2019), activity against multi-drug resistant microorganisms (Tirado et al., 2014), broad-spectrum antimicrobial activities (Israili, 2014), strain- and antibiotic-specific synergy with conventional antibiotics (Liu et al., 2017; Hayes et al., 2018), and a reported low risk of developing antimicrobial resistance (Lu et al., 2014). Antimicrobial and anti-biofilm effects of medical-grade honey have been attributed to various factors working either singularly or synergistically, including the production of hydrogen peroxide, the presence of specific antimicrobial agents, such as flavonoids, bee peptides and phenolic compounds [methylglyoxal (MGO)], special physiochemical properties including a low pH and exertion of high osmotic pressure, and its impact on the infection environment, such as desiccation of the wound (Osato et al., 1999; Israili, 2014; Cokcetin et al., 2016; Sowa et al., 2017).

Medihoney Antibacterial Wound Gel (MAWG, Comvita Ltd.) has been advertised by the manufacturer to be effective for all minor wounds including burns, cuts, grazes, and ulcers. Several *in vitro* studies have found that its main component, Manuka-type honey, is highly effective against bacterial biofilms (Cooper et al., 2014; Lu et al., 2014, 2019). As a consequence, MAWG has been used in all four Australian hospitals that perform adult ventricular assist device (VAD) implantation to prevent driveline infections by application at the driveline exit-site. Large randomized controlled trials, however, report only marginal effects of MAWG in preventing device-related infection in patients with percutaneous medical devices when compared with standard care with or without additional prophylaxis (Johnson et al., 2014; Zhang et al., 2015). The discrepancy between the *in vitro* efficacy of Manuka-type honey and *in vivo* efficacy of MAWG against biofilms may be partially due to the use of over-simplified microplate-based biofilm assays by many other *in vitro* studies (Cooper et al., 2014; Hammond et al., 2014; Lu et al., 2019). Microplate-based biofilm assays often neglect the impact of the clinical environment and might not adequately reflect infections at the unique skin exit-site of percutaneous medical devices (Buhmann et al., 2016).

The purpose of this study was to assess the antimicrobial efficacy of MAWG against biofilms causing VAD driveline infections, using *in vitro* assays that closely mimic driveline exit-site environments. The results of the study might determine if there is sufficient experimental support for the clinical use of MAWG to prevent driveline infections.

MATERIALS AND METHODS

Medihoney Antibacterial Wound Gel, Other Media, and Drivelines

Medihoney Antibacterial Wound Gel™ (simplified as MAWG for this study, Comvita Australia Pty Ltd.) was used for this study. This licensed commercial product is specifically formulated combining 80% Medihoney™ Antibacterial Honey derived from the *Leptospermum scoparium* plant in New Zealand and 20% natural waxes and oils. MAWG solution was prepared by dissolving the gel into a standard microbial growth medium such as Muller-Hinton broth (MHB; Oxoid, Hampshire, UK) or Roswell Park Memorial Institute 1640 medium (RPMI 1640; Oxoid, Hampshire, UK) to reach concentrations of 0–80% [weight/volume (w/v); increments of 10%, equivalent to Medihoney™ Antibacterial Honey of 0–64% with increments of 8%]. To assess the contribution of different antimicrobial mechanisms of MAWG to its anti-biofilm properties, other media preparations were used. Mixed sugar solution comprising 45% glucose (w/v), 48% fructose, and 1% sucrose was prepared as described by others (Liu et al., 2014). This mixed sugar solution has the same osmolarity as pure Manuka honey and was diluted to match that of MAWG (containing 80% Medihoney Antibacterial Honey). MGO solution (40% in H_2O) was purchased from Sigma Australia and was further diluted into the growth medium to a concentration the same as that found in MAWG (MGO: 620 mg/kg = 776 mg/kg × 80%; Liu et al., 2014; Lu et al., 2014). Microbiological growth media of different pH (pH = 7.0, 6.0, 5.0, and 4.0) were prepared by adding 5 M hydrogen chloride or sodium hydroxide. HeartMate III drivelines were provided by Abbott Medical, United States and were used for driveline biofilm experiments. Driveline silicone tubes (smooth section) were cut, and then transected into pieces of ~3 × 5 mm^2. Prior to use in each experiment, the cut-out driveline sections were sterilized with ethylene oxide (Steritech, VIC, Australia).

Microbial Strains

Twenty clinical isolates and four reference strains from three microbial genera frequently causing VAD driveline and other medical device related infections were selected for this study, including coagulase-negative *staphylococci*, *Staphylococcus aureus*, *Pseudomonas aeruginosa*, and *Candida* spp. (**Table 1**; Qu et al., 2010a, 2016, 2020; Wu et al., 2019). The clinical reference strains included *Staphylococcus epidermidis* RP62A (ATCC35984), *S. aureus* ATCC25923, *P. aeruginosa* PAO1, and *Candida albicans* SC5314. These reference strains were used to study the

TABLE 1 | Antimicrobial activity of Medihoney Antibacterial Wound Gel (MAWG) against clinical isolates grown as planktonic cultures.[1]

Microbial species	Source	References	Antimicrobial activities	
			MIC[2]	MBC/MFC[3]
Staphylococcus aureus				
ATCC25923	Reference strain	Qu et al., 2020	10%	20%
APS 18	The Alfred Hospital	Unpublished	10%	20%
APS 19	The Alfred Hospital	Unpublished	20%	40%
APS 27	The Alfred Hospital	Unpublished	20%	20%
APS 28	The Alfred Hospital	Unpublished	10%	20%
APS 29	The Alfred Hospital	Unpublished	20%	20%
CoNS				
Staphylococcus epidermidis RP62A	Reference strain	Qu et al., 2020	20%	20%
Staphylococcus epidermidis RCH3	RCH[4], Melbourne	Qu et al., 2010a	5%	10%
Staphylococcus epidermidis RCH 5	RCH, Melbourne	Qu et al., 2010a	10%	20%
Staphylococcus capitis RCH 6	RCH, Melbourne	Qu et al., 2010a	10%	20%
Staphylococcus epidermidis RCH 7	RCH, Melbourne	Qu et al., 2010a	20%	20%
Staphylococcus epidermidis RCH 12	RCH, Melbourne	Qu et al., 2010a	10%	10%
Pseudomonas aeruginosa				
PAO1	Reference strain	Qu et al., 2020	40%	40%
A0064	The Alfred Hospital	Unpublished	40%	40%
B0021	The Alfred Hospital	Unpublished	40%	40%
D0108	The Alfred Hospital	Unpublished	40%	40%
L0024	The Alfred Hospital	Unpublished	20%	20%
E0033	The Alfred Hospital	Unpublished	40%	40%
Candida spp.				
Candida albicans SC5314	Reference strain	Qu et al., 2020	20%	40%
Candida albicans APY49	The Alfred Hospital	Qu et al., 2016	40%	40%
Candida albicans VVC2	WMU[5]	Wu et al., 2019	40%	40%
Candida albicans VVC4	WMU	Wu et al., 2019	40%	40%
Candida glabrata	The Alfred Hospital	Unpublished	>40%	>40%
Candida parapsilosis	The Alfred Hospital	Unpublished	>40%	>40%

[1]*Antimicrobial activity of MAWG against clinical isolates was determined using broth microdilution assays, and the results were determined by viable counts, instead of examining turbidity or optical density.*
[2]*MIC, minimum inhibitory concentration.*
[3]*MBC/MFC, minimum bactericidal concentration/minimum fungicidal concentration.*
[4]*RCH, The Royal Children's hospital.*
[5]*Wenzhou Medical University, China.*

anti-biofilm efficacy of MAWG as they are well-known biofilm producers, they were representative of the clinical isolates in their sensitivity to MAWG under planktonic conditions, and they have been widely used in other *in vitro* studies, and parallel comparisons were possible.

Antimicrobial Activity of MAWG Against Planktonic Cells

Antimicrobial activity of MAWG against all 24 clinical and reference strains were evaluated by determining the minimum inhibitory concentrations (MICs) and minimum bactericidal or fungicidal concentrations (MBCs/MFCs), following Clinical and Laboratory Standards Institute (CLSI) guidelines with modification (Clinical and Laboratory Standards Institute, 2012, 2017). Viable counts were performed before and after overnight incubation, replacing turbidity-based growth assessment because of the cloudiness of MAWG solutions after incubation. Four concentrations of MAWG solutions (5, 10, 20, and 40%) were tested. MICs refer to the lowest concentration of MAWG at which no increase in microbial density was observed. The minimum concentrations of MAWG that reduced bacterial numbers by at least 3 log (99.9%) or fungal density by at least 1 log (90%) were defined as MBCs and MFCs. Three biological repeats in triplicates were carried out to determine the MIC, MBC, and MFC.

Antimicrobial Activity of MAWG and Its Key Components Against Biofilms

Although microplate-based biofilm assays are not the best *in vitro* model to study driveline infections, they are ideal for

quantitative examination of concentration-dependent effect of antimicrobials on inhibiting or killing biofilms. Single biofilms of *S. aureus* ATCC 25923, *S. epidermidis* RP62A, *P. aeruginosa* PAO1, and *C. albicans* SC5314 were set-up in 96-well microplates as previously described (Qu et al., 2016). Two hundred microliters of freshly prepared solutions, including that of MAWG, mixed sugar solution, and MGO in MHB or RPMI-1640 at increment concentrations were added into each microwell and treatments lasted for 24 h. Two anti-biofilm activity endpoints were assessed (Macia et al., 2014). Biofilm MICs ($BMIC_{50}$) referred to the lowest concentration of agents that inhibit biofilm growth by 50%, as determined by 2,3-bis-(2-methoxy-4-nitro-5-sulfophenyl)-2H-tetrazolium-5-carboxanilide (XTT) readings (see below). Minimum biofilm eradication concentration (MBEC) referred to the lowest concentration that led to complete eradication of viable cells embedded in biofilms and were determined as described previously (Qu et al., 2010b).

Biofilm XTT Assay

The XTT assay was adopted to assess the viability of biofilm cells after antimicrobial treatment (Qu et al., 2016). After treating established biofilms with MAWG solution, mixed sugar solution, and MGO at different concentrations, the suspensions were removed, and the microwells were washed twice with phosphate-buffered saline (PBS). Two hundred microliters of XTT solution (0.5 mg/ml) was added into each microwell, and the microplate was incubated at 37°C in the dark for 2 h. One hundred microliters of XTT solution was then transferred to a new microplate and read at OD_{492}. The ratio of cell survival (OD_{492} after antimicrobial treatment) relative to antimicrobial-free culture (OD_{492} of the drug-free biofilms × 100) was calculated. Biofilm reduction was calculated as (1-cell survival%). The experiment was carried out in three biological repeats in triplicate.

Agar Colony Biofilm Assay

The colony biofilm assay replicates some of the environmental conditions required for biofilm growth on a "relatively dry" wound bed of the driveline exit-site, by allowing microorganisms to grow on a filter membrane supplied with nutrients and oxygen but little shear stress (Hammond et al., 2011). In short, overnight microbial cultures were harvested by centrifuge, washed twice with PBS, and resuspended in MHB (for *S. epidermidis*, *S. aureus*, and *P. aeruginosa*, OD_{600} = 0.1), or RPMI 1640 (for *C. albicans*, OD_{600} = 1.0). Around 100 µl of each microbial suspension was seeded on sterile nitrocellulose filter membranes (diameter, 25 mm; pore size, 0.22 µm, Merck Millipore Ltd.,). The membranes were transferred onto either Muller-Hinton agar (MHA) or RPMI 1640 agar plates in a humid chamber and were incubated at 37°C for 2 h to grow early adherent monolayers or 24 h for mature biofilms (Merritt et al., 2005). Our preliminary scanning electron microscopy (SEM) assay suggested that 2 h incubation resulted in the attachment of a single layer of microorganisms to the filter membrane and 24 h incubation led to the growth of clusters of cells embedded in extracellular polymeric substances (EPSs). The filter membrane with early adherent monolayers or mature biofilms was completely covered with another filter membrane infused with 0.2 g of MAWG. This was to mimic the clinical application of MAWG in combination with wound dressings. The treatment lasted for 24 h. Both filter membranes were placed in a 15 ml falcon tube containing 5 ml of PBS and were sonicated for 10 min using a sonication bath (42 kHz, Branson 1510), followed by vortex at the highest speed for 2 min (30" × 4). The suspensions were serially diluted and plated on nutrient agar plates or yeast peptone dextrose (YPD) agar plates for viable counts. The experiment was carried out in three biological repeats in duplicate.

Microbial Adherence Assay and Drip-Flow Biofilm Assay Using Clinical Drivelines

To assess the effectiveness of MAWG in preventing planktonic cultures from growing early adherent monolayers on driveline materials, MAWG was applied on the surface of driveline cutouts and a microbial adherence assay was carried out (Qu et al., 2020). A drip-flow biofilm reactor was then used to evaluate the effectiveness of MAWG in preventing adherent monolayer on drivelines from further developing into mature biofilms (Goeres et al., 2009; Qu et al., 2020). This drip-flow biofilm reactor mimics a "wet" driveline exit-site environment by providing continuous flow of oxygen and nutrients and grows biofilms under low shear at the air-liquid interface (Goeres et al., 2009). Driveline cut-outs with attached microorganisms, prepared in the microbial adherence assay, were placed on the absorbent pads (25 mm, Millipore, Billerica, MA) with MAWG infused in the biofilm incubation chamber. Around 10% TSB as growth media were pumped through the system at 5 ml/h/channel. Biofilms were allowed to grow for 72 h at room temperature. The samples were washed three times with PBS, and were quantitatively analyzed for CFUs. The experiment was carried out in three biological repeats in duplicate.

Statistical Analyses

One-way ANOVA test or a non-parametric Mann–Whitney method (depending on the data distribution) was performed to analyze differences in biofilm formation under different conditions, using Minitab 16 for Windows (Pennsylvania State University, United States) and a significance level of 0.05.

RESULTS

Antimicrobial Activity of MAWG Against Planktonic and Biofilm Microorganisms Grown in 96-Well Microplates

Twenty-four clinically relevant isolates from three microbial genera were tested for their sensitivity to MAWG. Both *S. aureus* and coagulase-negative staphylococci were sensitive to MAWG when grown as planktonic cultures, with most isolates having MICs and MBCs of 10–20% (**Table 1**). *P. aeruginosa* and *Candida* spp. showed relatively higher resistance to MAWG, with MICs and MBCs/MFCs of 20–40%

TABLE 2 | Susceptibility of microplate-based biofilms to MAWG and its active components.

	Staphylococcus aureus ATCC 25923		*Staphylococcus epidermidis* RP62A		*Pseudomonas aeruginosa* PAO1		*Candida albicans* SC5314	
	$MBIC_{50}$	MBEC	$MBIC_{50}$	MBEC	$MBIC_{50}$	MBEC	$MBIC_{50}$	MBEC
MAWG	30%	>80%	50%	>80%	>80%	>80%	30%	>80%
Mixed sugar	>80%	>80%	70%	>80%	>80%	>80%	70%	>80%
MGO	>80%	>80%	>80%	>80%	>80%	>80%	>80%	>80%

The biofilm MIC ($BMIC_{50}$) refers to the lowest concentration of antimicrobials that is resulted in a 50% reduction of biofilm growth. Minimum biofilm eradication concentration (MBEC) refers to the lowest concentration of antimicrobial agents that completely kill embedded biofilm cells, showing no visible growth in the recovery medium used to collect biofilm cells after revival (Macia et al., 2014).

or even higher. To assess the efficacy of MAWG against microbial biofilms, we tested the $BMIC_{50}$. MAWG at concentrations of 30, 50, >80, and 30% (W/V) were needed to inhibit biofilm growth by 50% for *S. aureus*, *S. epidermidis*, *P. aeruginosa*, and *C. albicans*, respectively (**Table 2**, see $BMIC_{50}$). MAWG at the highest concentration used in this study [80% (W/V)], was unable to fully eradicate mature biofilms pre-formed by any of these microorganisms (**Table 2**, see MBECs).

MGO Plays a Less Important Role in the Multi-Faceted Anti-biofilm Activity of MAWG

To assess the contribution of the individual antimicrobial mechanisms of MAWG to its overall anti-biofilm properties, $BMIC_{50}$ and MBECs of MGO and a mixed sugar solution with high-osmolarity were determined, respectively (**Table 2**). For all pathogens, MGO showed a minor effect on biofilms, with the highest concentration (equivalent to 496 mg/kg) used in this study being unable to inhibit biofilm growth by 50% (**Table 2**). We then quantitated the actual viable cell reduction in biofilms achieved by varying concentrations of MGO (**Figure 1**). MGO at a concentration equivalent to that found in 80% (W/V) MAWG (MGO: 496 mg/kg) reduced the viability of biofilms of *S. aureus* by up to 30%, and by up 20% for *C. albicans* and *P. aeruginosa* (**Figure 1**). No evident activity of MGO was seen for *S. epidermidis* cells embedded in biofilms. In contrast to MAWG, mixed sugar solution conferring the high osmolarity had impaired activity in inhibiting biofilm growth, showing higher $BMIC_{50}$ for *S. aureus*, *S. epidermidis*, and *C. albicans* (**Table 2**). Direct quantification of biofilm reduction showed that the mixed sugar solution had some activity against embedded biofilm cells of *S. epidermidis* and *C. albicans*, while only minor activity was seen for *S. aureus* and *P. aeruginosa* biofilms (**Figure 1**). MAWG solution at 80% (W/V) is acidic with a pH of ~4. A growth medium at pH = 4, but not the other pH values, showed some effects against biofilms pre-formed by *S. aureus*, *S. epidermidis*, and *C. albicans* (~30% inhibition; **Figure 1**). No significant effect of pH was found for biofilms formed by *P. aeruginosa* (**Figure 1**). None of the above-mentioned components of MAWG was able to eradicate biofilm cells of any of the four microorganisms, with MBECs beyond the highest concentration tested. Anti-biofilm activities of MGO in combination with other antimicrobial mechanisms were not studied due to little effect of MGO was observed against established biofilms.

MAWG Has Minimal Activity on Biofilms Grown on the Exit-Site Wound Bed Mimics

A colony biofilm assay in combination with MAWG-infused filter membrane (**Figure 2A**) was used to determine whether MAWG kills pre-established monolayers and biofilms mimicking those grown on the wound bed at the driveline exit-site, or interferes with the developmental process of biofilm formation. It was found that the MAWG-infused filter membrane had little effect on adherent monolayers of any of the tested microorganisms. All adherent monolayers grew into mature biofilms within a 24 h period on the agar plates and their biomass increased by 3 log (for *C. albicans*) or 4 log (for bacteria; **Figure 2B**). Biofilms of a high cellular density of ~10^9 CFU/membrane (for bacteria) or ~10^7 CFU/membrane (for *Candida*) were recovered (**Figure 2B**). For already established mature biofilms, MAWG only slightly reduced biomass of bacterial biofilms upon treatment, lowering the CFU by ~1 log (**Figure 2B**). No effect was observed for biofilms formed by the fungal pathogen *C. albicans* (**Figure 2B**).

MAWG Has Minimal Activity Against Biofilms Growth on Drivelines at the Exit-Site

An early adherent monolayer assay and the drip-flow biofilm reactor assay were adopted to determine whether MAWG prevents planktonic cells from growing into adherent monolayers on the smooth tube section of drivelines and subsequently establishing biofilms. Covering driveline cutouts with MAWG lowered the biomass of adherent monolayers of *S. aureus*, *S. epidermidis* and *P. aeruginosa* by 12.9, 9.8, and 13.4%, respectively, as measured by viable counts (**Figure 3A**); a substantial number of adherent monolayers [2.7–4.6 log (CFU/cm^2)] were stilled recovered from the MAWG-coated drivelines. Exposing adherent monolayers to MAWG in the drip-flow biofilm reactor did not result in a lower microbial density (log CFU/ml) of mature biofilms formed by *S. aureus*, *S. epidermidis*, and *C. albicans*, in comparison with the non-MAWG control (**Figure 3B**). One-log reduction in microbial

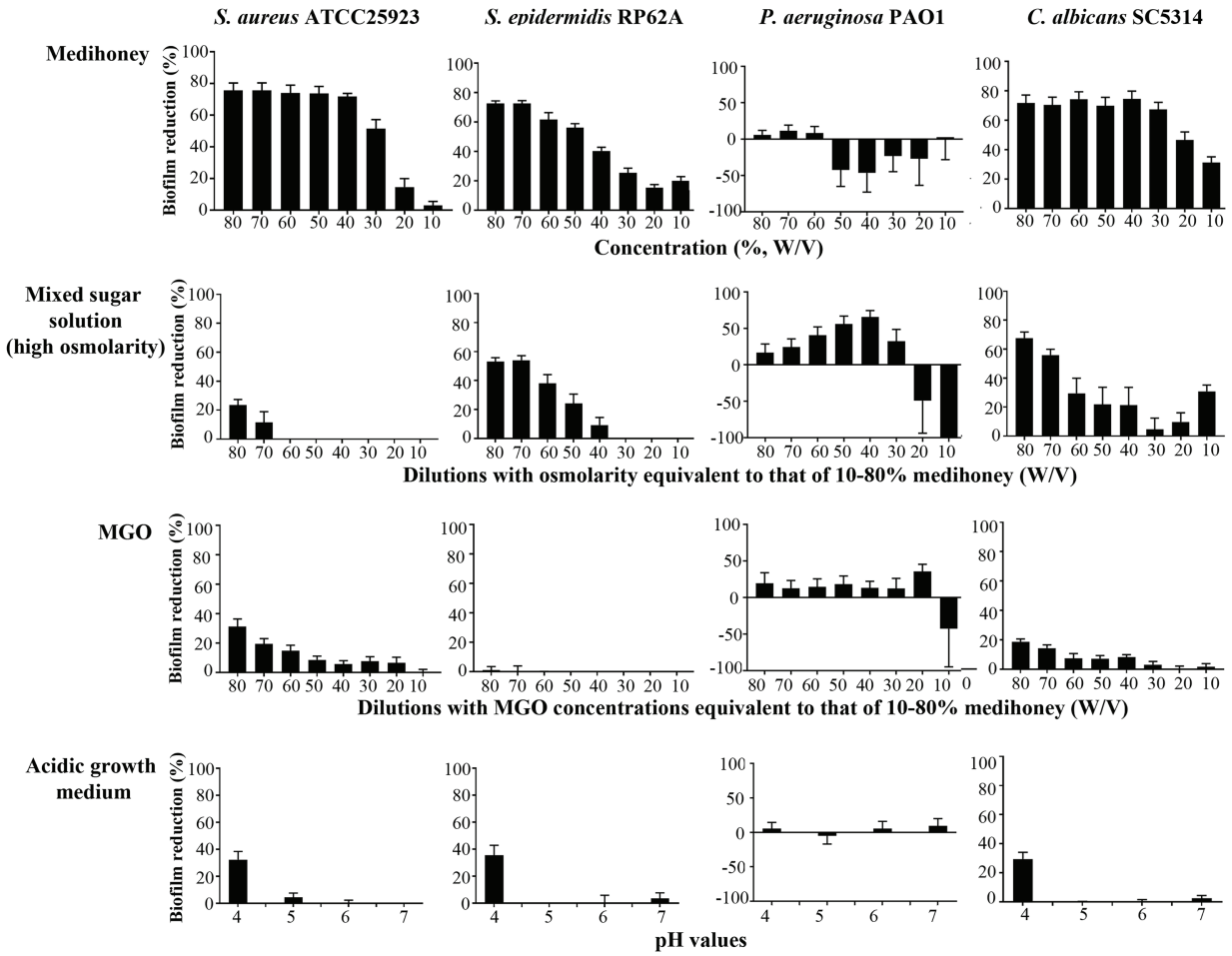

FIGURE 1 | Assessment of the anti-biofilm activity of individual components of MAWG using microplate-based biofilms. Biofilms were established in 96-well microplates and were treated with MAWG solution, mixed sugar solution, methylglyoxal (MGO) solution at different concentrations, and growth media prepared at different pH. 2,3-bis-(2-methoxy-4-nitro-5-sulfophenyl)-2H-tetrazolium-5-carboxanilide (XTT) was used to detect the percentage of survivor biofilm cells after the treatment relative to untreated control. XTT readings at OD_{492} for untreated control biofilms were as below: *S. aureus* ATCC 25923, 0.94 ± 0.09 (mean ± SD); *S. epidermidis* RP62A, 0.89 ± 0.22; *P. aeruginosa* PA01, 0.25 ± 0.06, and *C. albicans*, 2.50 ± 0.50. The ratio of cell survival (OD_{492} after antimicrobial treatment) relative to antimicrobial-free culture (OD_{492} of the drug-free biofilms × 100) was calculated. Biofilm reduction was calculated as (1-cell survival%). Error bars indicate the standard error of the mean.

density of mature biofilms was found when an adherent monolayer of *P. aeruginosa* was exposed to MAWG (**Figure 3B**).

DISCUSSION

Biofilm formation on percutaneous drivelines or surrounding tissues at the driveline exit-site is one of the most important factors contributing to the establishment of VAD-associated infections (Qu et al., 2020). This specific growth mode renders infections less responsive to antimicrobial treatments and is believed to be the root of the persistence of driveline infections (Qu et al., 2020). MAWG is routinely used for prophylaxis in all adult VAD programs in Australian hospitals. Despite the "excellent" *in vitro* anti-biofilm efficacy of Medihoney™ Antibacterial Honey, the main component of MAWG, reported by others (Muller et al., 2013; Cooper et al., 2014; Liu et al., 2017), driveline infections occurred frequently in VAD patients in these Australian hospitals. To clarify this discrepancy, a comprehensive assessment was conducted, using *in vitro* biofilm models that mimic the clinical environment of driveline exit-site. This study has shown that (1) MAWG inhibited and killed microorganisms under planktonic conditions in a species-specific manner, and had less inhibitory and microbicidal effect on biofilms pre-established in 96-well microplates, (2) the anti-biofilm activity of MAWG was mediated by multiple factors, with the often-advertised antimicrobial ingredient MGO only playing a minor role, and (3) under conditions that mimic the clinical environment, MAWG was neither able to kill monolayers or biofilms pre-established on tissue bed mimics, nor to prevent planktonic cells from growing mature biofilms on drivelines.

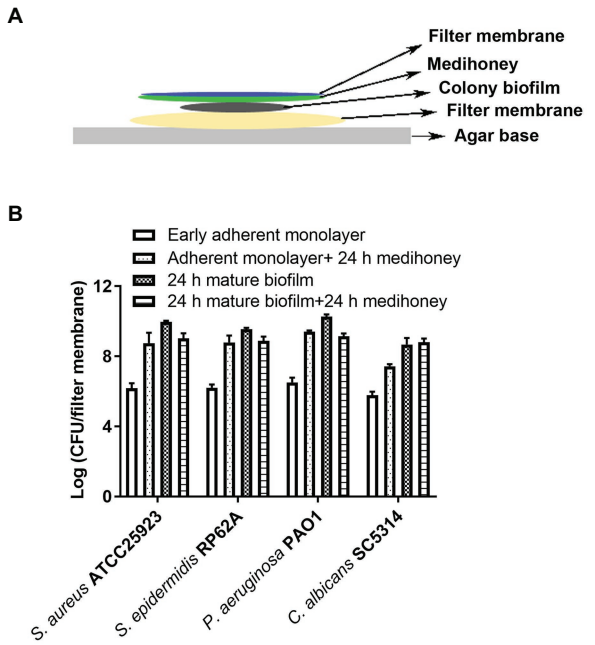

FIGURE 2 | Assessment of activities of MAWG against colony biofilms at different developmental stages. **(A)** Schematic description of the colony biofilm assay. **(B)** Antibiofilm activities of MAWG against early adherent monolayer and mature biofilms. MAWG was found unable to effectively kill adherent monolayers; adherent monolayers developed into mature biofilms [2–5 log (CFU/cm^2)] after overnight treatment. Only ~1 log reduction in CFU per colony biofilm was found when MAWG was used to challenge mature biofilms formed by *S. aureus*, *S. epidermidis*, and *P. aeruginosa*. No effect was observed for biofilms formed by *C. albicans*. Error bars indicate the standard error of the mean.

The driveline skin exit-site poses a huge risk of infections for VAD patients. Proper driveline exit-site care is considered effective in preventing infections during the healing period (Nienaber et al., 2013). Octenidine, dihydrochloride, chlorhexidine, and povidone-iodine have all been used to clean the skin around the driveline exit-site (Nienaber et al., 2013). Australian hospitals have often used 0.5% chlorhexidine in 70% alcohol solution to clean the driveline exit-site, followed by the application of MAWG as a prophylactic agent on the skin around the driveline exit-site and driveline dressing closure. While the use of prophylactic antibiotics has also been suggested peri-VAD implantation (Nienaber et al., 2013), no consensus has been reached regarding the optimal antimicrobial prophylaxis – either regime or duration (Walker et al., 2011; Nienaber et al., 2013). The prophylactic antimicrobial practice varies among different institutions and mostly relies on the team's experience and preference (Nienaber et al., 2013). The general concept is to effectively cover common causative organisms of driveline infections, and to include agents for Gram-positive bacteria, Gram-negative bacteria, and fungi. The effectiveness of using conventional antibiotics in preventing driveline infections has been questioned (Stulak et al., 2013), and a major concern of the development of resistance to conventional antimicrobials has promoted the use of MAWG (Lu et al., 2014).

The broth microdilution method has been chosen by many others for the assessment of antimicrobial activity of medical-grade honeys against planktonic cells (Cooper et al., 2014; Osés et al., 2016). This assay yields more reproducible and informative results in comparison with other testing methods such as agar well diffusion or disk diffusion methods (Osés et al., 2016). Using the broth microdilution method, we also found potent species-specific antimicrobial activities of MAWG against

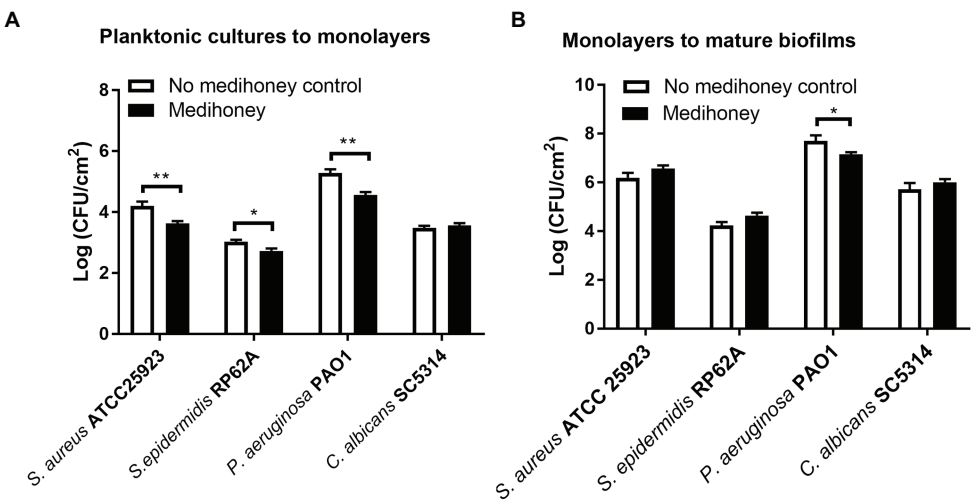

FIGURE 3 | Determination of anti-biofilm activity of MAWG using a drip-flow biofilm reactor and driveline materials. **(A)** Adherent monolayers of microorganisms were formed on driveline smooth tube cut-outs pre-conditioned with MAWG. Driveline cut-outs received no treatment were used as a control. **(B)** Adherent monolayers formed on driveline cutouts (without MAWG conditioning) were transferred into a drip-flow biofilm reactor for further cultivation. Driveline cutouts with microbial monolayer were placed on absorbent pads infused with or without MAWG. Biofilm formation on driveline cutouts were assessed by viable counts after 72 h. Error bars indicate the standard error of the mean. *$p < 0.05$; **$p < 0.01$.

planktonic cells. MAWG was highly effective against *S. epidermidis* and *S. aureus*, but not *P. aeruginosa* or *Candida* spp.. The role of individual components of honey in combating planktonic microorganisms has been extensively studied and seemed to be microorganism-specific (Kwakman and Zaat, 2012). Osato et al. (1999) found that the osmotic effect of honey was the most important mechanism for killing *Helicobacter pylori*, while hydrogen peroxide only played a minor role (Osato et al., 1999). Wasfi et al. (2016) studied Egyptian honeys and found their antibacterial activity against *Escherichia coli* was mostly caused by the production of hydrogen peroxide (Wasfi et al., 2016). Mavric et al. (2008) attributed the antibacterial potency of Manuka honey directly to the presence of MGO (Mavric et al., 2008). Using the microplate biofilm assay, we compared different components of MAWG that might contribute to its anti-biofilm potency and found that its anti-biofilm activities cannot be explained by one single antimicrobial mechanism. Unfavorable local environmental conditions resulted from the presence of honey including high-osmolarity and acidity, and other adverse effects occurring due to honey, such as desiccation (Park et al., 2016), might have hindered microbial biofilm growth. Notably, MGO, "the major antimicrobial effector" advertised by Comvita Ltd., failed to demonstrate a potent anti-biofilm effect in the current study. In support of our findings, Lu et al. (2014, 2019) reported that MGO in Manuka-type honey alone was inadequate in killing biofilms formed by *S. aureus* or *P. aeruginosa*.

In contrast to previous *in vitro* studies that reported outstanding anti-biofilm activities of Medihoney Antibacterial Honey (Muller et al., 2013; Cooper et al., 2014; Liu et al., 2017), the high-quality randomized controlled Honeypot trial recently found no superiority of MAWG in preventing biofilm-related peritoneal-dialysis-related infections or exit-site infections when compared with standard care (Johnson et al., 2014; Zhang et al., 2015). We speculated that the anti-biofilm effectiveness reported by other *in vitro* studies might be overly optimistic, partially due to the use of *in vitro* assays with minimum clinical relevance, such as the microplate-based biofilm assay (Lu et al., 2014; Buhmann et al., 2016; Liu et al., 2017; Piotrowski et al., 2017). Biofilms grown in 96-well microplate might not adequately reflect those found in a more complicated scenario such as driveline infections, where biofilms were often grown at a liquid-solid-air interface with low shear force and moisture. Our study used *in vitro* models that closely mimic the clinical environment of the driveline exit-site and evaluated MAWG as a therapeutic agent and a prophylactic agent for driveline infections, respectively. The colony biofilm assay showed that MAWG-infused filter membranes that mimic topical dressings with MAWG impregnated were unable to inhibit or kill pre-established adherent monolayers or biofilms, questioning the value of MAWG in treating driveline exit-site wounds. Our drip-flow biofilm reactor assay also found limited efficacy of MAWG in preventing biofilm formation on drivelines, supporting the conclusion from the large-scale Honeypot clinical trial (Zhang et al., 2015). We noticed differences in the anti-biofilm efficacy of MAWG against *P. aeruginosa* PAO1 when microplate-based biofilm assay and the drip-flow biofilm assay reactor assay were carried out. This can be explained by different environmental factors of these two biofilm assays that might affect the anti-biofilm activity of MAWG (Buhmann et al., 2016). We concede that two non-microplate-based *in vitro* biofilm assays chosen for this study could not completely duplicate the complexity of the clinical environment, but we managed to include some environmental factors such as local oxygen availability and low shear at the air-liquid-solid interface that are critical for biofilm development at the driveline exit-site or important for the assessment of anti-biofilm agents. A large-scale randomized-controlled clinical trial will facilitate a better understanding of the effectiveness of MAWG in preventing driveline infections in VAD patients.

CONCLUSION

Taken together, our data showed little success of MAWG in killing biofilms grown on tissue bed mimics, or in preventing biofilm formation on driveline materials, suggesting suboptimal effectiveness of MAWG as a therapeutic or prophylactic agent against biofilm-related driveline infections. Though routine application of MAWG might partially prevent microbial contamination of the driveline exit-site, supported by its effectiveness against planktonic microorganisms, caution must be exercised when relying on MAWG to prevent or treat driveline infections in patients with a VAD.

DATA AVAILABILITY STATEMENT

The raw data supporting the conclusions of this article will be made available by the authors, without undue reservation.

AUTHOR CONTRIBUTIONS

YQ, DM, and AP conceived and designed the study. YQ carried out the experiments. YQ, CK, JM, and CD performed data analysis. YQ and DM wrote up the manuscript. AP edited the manuscript. All authors contributed to the article and approved the submitted version.

FUNDING

This work was supported by the Alfred Foundation and the Australian National Health and Medical Research Council (NHMRC; APP1079421 and APP1117940) CRE ACTIONS. AP also acknowledges support from an Australian NHMRC Practitioner Fellowship. The contents of the published material are solely the responsibility of individual authors and do not reflect the views of NHMRC.

ACKNOWLEDGMENTS

The authors would like to thank Abbott Medical, United States for providing HeartMate III drivelines for this study.

REFERENCES

Buhmann, M. T., Stiefel, P., Maniura-Weber, K., and Ren, Q. (2016). In vitro biofilm models for device-related infections. *Trends Biotechnol.* 34, 945–948. doi: 10.1016/j.tibtech.2016.05.016

Clinical and Laboratory Standards Institute (2012). "Methods for dilution antimicrobial susceptibility tests for bacteria that grow aerobically: Approved standard-nineth edition M07-A9." In CLSI, (PA, USA: Wayne).

Clinical and Laboratory Standards Institute (2017). "Reference method for broth dilution antifungal susceptibility testing of yeasts, M27, 4th Edition." In CLSI, (PA, USA: Wayne).

Cokcetin, N. N., Pappalardo, M., Campbell, L. T., Brooks, P., Carter, D. A., Blair, S. E., et al. (2016). The antibacterial activity of Australian leptospermum honey correlates with methylglyoxal levels. *PLoS One* 11:e0167780. doi: 10.1371/journal.pone.0167780

Cooper, R., Jenkins, L., and Hooper, S. (2014). Inhibition of biofilms of *Pseudomonas aeruginosa* by Medihoney in vitro. *J. Wound Care* 23, 93–96. doi: 10.12968/jowc.2014.23.3.93

Dunwoody, G., and Acton, C. (2008). The use of medical grade honey in clinical practice. *Br. J. Nurs.* 17, S38–S44. doi: 10.12968/bjon.2008.17.Sup9.31665

Forbes, T. A., Shaw, L., and Quinlan, C. (2016). Topical honey in the management of pediatric peritoneal dialysis exit sites. *Perit. Dial. Int.* 36, 684–687. doi: 10.3747/pdi.2014.00350

Goeres, D. M., Hamilton, M. A., Beck, N. A., Buckingham-Meyer, K., Hilyard, J. D., Loetterle, L. R., et al. (2009). A method for growing a biofilm under low shear at the air-liquid interface using the drip flow biofilm reactor. *Nat. Protoc.* 4, 783–788. doi: 10.1038/nprot.2009.59

Hammond, E. N., Donkor, E. S., and Brown, C. A. (2014). Biofilm formation of *Clostridium difficile* and susceptibility to Manuka honey. *BMC Complement. Altern. Med.* 14:329. doi: 10.1186/1472-6882-14-329

Hammond, A. A., Miller, K. G., Kruczek, C. J., Dertien, J., Colmer-Hamood, J. A., Griswold, J. A., et al. (2011). An in vitro biofilm model to examine the effect of antibiotic ointments on biofilms produced by burn wound bacterial isolates. *Burns* 37, 312–321. doi: 10.1016/j.burns.2010.09.017

Hayes, G., Wright, N., Gardner, S. L., Telzrow, C. L., Wommack, A. J., and Vigueira, P. A. (2018). Manuka honey and methylglyoxal increase the sensitivity of *Staphylococcus aureus* to linezolid. *Lett. Appl. Microbiol.* 66, 491–495. doi: 10.1111/lam.12880

Israili, Z. H. (2014). Antimicrobial properties of honey. *Am. J. Ther.* 21, 304–323. doi: 10.1097/MJT.0b013e318293b09b

Johnson, D. W., Badve, S. V., Pascoe, E. M., Beller, E., Cass, A., Clark, C., et al. (2014). Antibacterial honey for the prevention of peritoneal-dialysis-related infections (HONEYPOT): a randomized trial. *Lancet Infect. Dis.* 14, 23–30. doi: 10.1016/S1473-3099(13)70258-5

Kwakman, P. H., and Zaat, S. A. (2012). Antibacterial components of honey. *IUBMB Life* 64, 48–55. doi: 10.1002/iub.578

Liu, M. Y., Cokcetin, N. N., Lu, J., Turnbull, L., Carter, D. A., Whitchurch, C. B., et al. (2017). Rifampicin-Manuka honey combinations are superior to other antibiotic-Manuka honey combinations in eradicating *Staphylococcus aureus* biofilms. *Front. Microbiol.* 8:2653. doi: 10.3389/fmicb.2017.02653

Liu, M., Lu, J., Muller, P., Turnbull, L., Burke, C. M., Schlothauer, R. C., et al. (2014). Antibiotic-specific differences in the response of *Staphylococcus aureus* to treatment with antimicrobials combined with Manuka honey. *Front. Microbiol.* 5:779. doi: 10.3389/fmicb.2014.00779

Lu, J., Cokcetin, N. N., Burke, C. M., Turnbull, L., Liu, M., Carter, D. A., et al. (2019). Honey can inhibit and eliminate biofilms produced by *Pseudomonas aeruginosa*. *Sci. Rep.* 9:18160. doi: 10.1038/s41598-019-54576-2

Lu, J., Turnbull, L., Burke, C. M., Liu, M., Carter, D. A., Schlothauer, R. C., et al. (2014). Manuka-type honeys can eradicate biofilms produced by *Staphylococcus aureus* strains with different biofilm-forming abilities. *PeerJ* 2:e326. doi: 10.7717/peerj.326

Macia, M. D., Rojo-Molinero, E., and Oliver, A. (2014). Antimicrobial susceptibility testing in biofilm-growing bacteria. *Clin. Microbiol. Infect.* 20, 981–990. doi: 10.1111/1469-0691.12651

Mavric, E., Wittmann, S., Barth, G., and Henle, T. (2008). Identification and quantification of methylglyoxal as the dominant antibacterial constituent of Manuka (*Leptospermum scoparium*) honeys from New Zealand. *Mol. Nutr. Food Res.* 52, 483–489. doi: 10.1002/mnfr.200700282

Merritt, J. H., Kadouri, D. E., and O'toole, G. A. (2005). Growing and analyzing static biofilms. *Curr. Protoc. Microbiol.* 22, 1B.1.1–1B.1.18. doi: 10.1002/9780471729259.mc01b01s00

Muller, P., Alber, D. G., Turnbull, L., Schlothauer, R. C., Carter, D. A., Whitchurch, C. B., et al. (2013). Synergism between Medihoney and rifampicin against methicillin-resistant *Staphylococcus aureus* (MRSA). *PLoS One* 8:e57679. doi: 10.1371/journal.pone.0080282

Nienaber, J., Wilhelm, M. P., and Sohail, M. R. (2013). Current concepts in the diagnosis and management of left ventricular assist device infections. *Expert Rev. Anti-Infect. Ther.* 11, 201–210. doi: 10.1586/eri.12.163

Osato, M. S., Reddy, S. G., and Graham, D. Y. (1999). Osmotic effect of honey on growth and viability of *Helicobacter pylori*. *Dig. Dis. Sci.* 44, 462–464. doi: 10.1023/A:1026676517213

Osés, S. M., Pascual-Maté, A., de La Fuente, D., de Pablo, A., Fernández-Muiño, M. A., and Sancho, M. T. (2016). Comparison of methods to determine antibacterial activity of honeys against *Staphylococcus aureus*. *NJAS* 78, 29–33. doi: 10.1016/j.njas.2015.12.005

Park, E., Long, S. A., Seth, A. K., Geringer, M., Xu, W., Chavez-Munoz, C., et al. (2016). The use of desiccation to treat *Staphylococcus aureus* biofilm-infected wounds. *Wound Repair Regen.* 24, 394–401. doi: 10.1111/wrr.12379

Piotrowski, M., Karpinski, P., Pituch, H., Van Belkum, A., and Obuch-Woszczatynski, P. (2017). Antimicrobial effects of Manuka honey on in vitro biofilm formation by *Clostridium difficile*. *Eur. J. Clin. Microbiol. Infect. Dis.* 36, 1661–1664. doi: 10.1007/s10096-017-2980-1

Qu, Y., Daley, A. J., Istivan, T. S., Garland, S. M., and Deighton, M. A. (2010a). Antibiotic susceptibility of coagulase-negative staphylococci isolated from very low birth weight babies: comprehensive comparisons of bacteria at different stages of biofilm formation. *Ann. Clin. Microbiol. Antimicrob.* 9:16. doi: 10.1186/1476-0711-9-16

Qu, Y., Daley, A. J., Istivan, T. S., Rouch, D. A., and Deighton, M. A. (2010b). Densely adherent growth mode, rather than extracellular polymer substance matrix build-up ability, contributes to high resistance of *Staphylococcus epidermidis* biofilms to antibiotics. *J. Antimicrob. Chemother.* 65, 1405–1411. doi: 10.1093/jac/dkq119

Qu, Y., Locock, K., Verma-Gaur, J., Hay, I. D., Meagher, L., and Traven, A. (2016). Searching for new strategies against polymicrobial biofilm infections: guanylated polymethacrylates kill mixed fungal/bacterial biofilms. *J. Antimicrob. Chemother.* 71, 413–421. doi: 10.1093/jac/dkv334

Qu, Y., Mcgiffin, D., Kure, C., Ozcelik, B., Fraser, J., Thissen, H., et al. (2020). Biofilm formation and migration on ventricular assist device drivelines. *J. Thorac. Cardiovasc. Surg.* 159, 491–502. doi: 10.1016/j.jtcvs.2019.02.088

Soffer, A. (1976). Editorial: chihuahuas and laetrile, chelation therapy, and honey from Boulder, Colo. *Arch. Intern. Med.* 136, 865–866. doi: 10.1001/archinte.1976.03630080007003

Sowa, P., Grabek-Lejko, D., Wesolowska, M., Swacha, S., and Dzugan, M. (2017). Hydrogen peroxide-dependent antibacterial action of *Melilotus albus* honey. *Lett. Appl. Microbiol.* 65, 82–89. doi: 10.1111/lam.12749

Stulak, J. M., Maltais, S., Cowger, J., Joyce, L. D., Daly, R. C., Park, S. J., et al. (2013). Prevention of percutaneous driveline infection after left ventricular assist device implantation: prophylactic antibiotics are not necessary. *ASAIO J.* 59, 570–574. doi: 10.1097/MAT.0b013e3182a9e2a5

Tirado, D. J., Hudson, N. R., and Maldonado, C. J. (2014). Efficacy of medical grade honey against multidrug-resistant organisms of operational significance: part I. *J. Trauma Acute Care Surg.* 77, S204–S207. doi: 10.1097/TA.0000000000000324

Walker, P. C., Depestel, D. D., Miles, N. A., and Malani, P. N. (2011). Surgical infection prophylaxis for left ventricular assist device implantation. *J. Card. Surg.* 26, 440–443. doi: 10.1111/j.1540-8191.2011.01262.x

Wasfi, R., Elkhatib, W. F., and Khairalla, A. S. (2016). Effects of selected Egyptian honeys on the cellular ultrastructure and the gene expression profile of *Escherichia coli*. *PLoS One* 11:e0150984. doi: 10.1371/journal.pone.0150984

Wu, X., Zhang, S., Xu, X., Shen, L., Xu, B., Qu, W., et al. (2019). RAFT-derived polymethacrylates as a superior treatment for recurrent vulvovaginal candidiasis by targeting biotic biofilms and persister cells. *Front. Microbiol.* 10:2592. doi: 10.3389/fmicb.2019.02592

Zhang, L., Badve, S. V., Pascoe, E. M., Beller, E., Cass, A., Clark, C., et al. (2015). The effect of exit-site antibacterial honey versus nasal mupirocin prophylaxis on the microbiology and outcomes of peritoneal dialysis-associated peritonitis and exit-site infections: a sub-study of the honeypot trial. *Perit. Dial. Int.* 35, 712–721. doi: 10.3747/pdi.2014.00206

Conflict of Interest: DM is an Abbott proctor for implantation of the Heartmate III VAD.

The remaining authors declare that the research was conducted in the absence of any commercial or financial relationships that could be construed as a potential conflict of interest.

frontiers in Microbiology

ORIGINAL RESEARCH
published: 15 December 2020
doi: 10.3389/fmicb.2020.599407

Influence of High Intensity Focused Ultrasound on the Microstructure and c-di-GMP Signaling of *Pseudomonas aeruginosa* Biofilms

Lakshmi Deepika Bharatula[1,2], Enrico Marsili[2,3], Scott A. Rice[2,4] and James J. Kwan[5]**

[1] School of Chemical and Biomedical Engineering, Nanyang Technological University, Singapore, Singapore, [2] Singapore Centre for Environmental Life Sciences Engineering, Nanyang Technological University, Singapore, Singapore, [3] Department of Chemical and Materials Engineering, Nazarbayev University, Nur-Sultan, Kazakhstan, [4] School of Biological Sciences, Nanyang Technological University, Singapore, Singapore, [5] Department of Engineering Science, University of Oxford, Oxford, United Kingdom

OPEN ACCESS

Edited by:
Jessica Amber Jennings, University of Memphis, United States

Reviewed by:
Cesar de la Fuente-Nunez, University of Pennsylvania, United States
Raheleh Miralami, Mississippi State University, United States

***Correspondence:**
Scott A. Rice
RSCOTT@ntu.edu.sg
James J. Kwan
james.kwan@eng.ox.ac.uk

Specialty section:
This article was submitted to Antimicrobials, Resistance and Chemotherapy, a section of the journal Frontiers in Microbiology

Received: *27 August 2020*
Accepted: *23 November 2020*
Published: *15 December 2020*

Citation:
Bharatula LD, Marsili E, Rice SA and Kwan JJ (2020) Influence of High Intensity Focused Ultrasound on the Microstructure and c-di-GMP Signaling of Pseudomonas aeruginosa Biofilms. Front. Microbiol. 11:599407. doi: 10.3389/fmicb.2020.599407

Bacterial biofilms are typically more tolerant to antimicrobials compared to bacteria in the planktonic phase and therefore require alternative treatment approaches. Mechanical biofilm disruption from ultrasound may be such an alternative by circumventing rapid biofilm adaptation to antimicrobial agents. Although ultrasound facilitates biofilm dispersal and may enhance the effectiveness of antimicrobial agents, the resulting biological response of bacteria within the biofilms remains poorly understood. To address this question, we investigated the microstructural effects of *Pseudomonas aeruginosa* biofilms exposed to high intensity focused ultrasound (HIFU) at different acoustic pressures and the subsequent biological response. Confocal microscopy images indicated a clear microstructural response at peak negative pressures equal to or greater than 3.5 MPa. In this pressure amplitude range, HIFU partially reduced the biomass of cells and eroded exopolysaccharides from the biofilm. These pressures also elicited a biological response; we observed an increase in a biomarker for biofilm development (cyclic-di-GMP) proportional to ultrasound induced biofilm removal. Cyclic-di-GMP overproducing mutant strains were also more resilient to disruption from HIFU at these pressures. The biological response was further evidenced by an increase in the relative abundance of cyclic-di-GMP overproducing variants present in the biofilm after exposure to HIFU. Our results, therefore, suggest that both physical and biological effects of ultrasound on bacterial biofilms must be considered in future studies.

Keywords: ***Pseudomonas aeruginosa*, biofilm, HIFU, microstructural effect, cyclic-di-GMP**

INTRODUCTION

Bacterial biofilms are microstructured bacterial consortia. These bacterial cells display a high degree of physiological and topographical heterogeneity and grow on abiotic surfaces (e.g., biomedical devices) or biological surfaces (e.g., lung tissue) (Flemming et al., 2016). Bacteria within biofilms are more tolerant to antimicrobials compared to planktonic bacterial cells due to self-produced biofilm matrix consisting of extracellular polymeric substance (EPS), high bacterial concentration,

exchange of genetic information in biofilms, differences in growth states of bacteria across the biofilm, and the expression of genes associated with tolerance or resistance to antimicrobial agents (Stewart and Costerton, 2001; Flemming and Wingender, 2010; Høiby et al., 2010). Given the increased tolerance of biofilms to antimicrobials, there remains a growing need for more effective antibiotics and new approaches to target biofilm infections. Developing novel antibiotics, however, is costly and time consuming. Thus, there have been increased efforts toward alternative approaches to induce cell death and/or promote dispersion of biofilms (Koo et al., 2017; Pinto et al., 2020).

One particularly promising approach for biofilm disruption is the use of therapeutic ultrasound, a non-invasive and cost-effective technique that provides targeted and localized mechanical effects (Erriu et al., 2014). Past research on the effect of ultrasound on biofilms has widely focused on low intensity ultrasound combined with antibiotics and/or cavitation agents (e.g., microbubbles). These studies showed that ultrasound-enhanced antibiotic treatment improved antibiotic efficacy, increased cell death, and reduced biofilm thickness (Lattwein et al., 2020). Interestingly, the application of ultrasound with microbubbles alone under these exposure conditions had minimal to no effect on biofilm removal (LuTheryn et al., 2019; Lattwein et al., 2020). In contrast, high intensity focused ultrasound (HIFU) without the addition of cavitation agents has also induced bacterial detachment from the substratum and left behind a patchy biofilm compared to the untreated control (Bigelow et al., 2009; Xu et al., 2012; Iqbal et al., 2013). Though HIFU alone was capable of disrupting biofilms, the biological effect on bacterial signaling molecules and/or cellular activity triggered by ultrasound exposure has not yet been investigated.

Here, we report on the physical and biological effects of HIFU on biofilms formed by *Pseudomonas aeruginosa*. The microstructural effects of HIFU were investigated through live/dead analysis, exopolysaccharide-lectin binding analysis, crystal violet assay and electrochemical response. Further, we investigated the impact of HIFU on the secondary messenger signaling system, cyclic diguanylate (c-di-GMP), which is a central regulator of the transition from the planktonic state to the biofilm and vice versa. In our study, we used a fluorescent bio-reporter strain of *P. aeruginosa* to quantify the effects of HIFU on biofilm formation and c-di-GMP signaling (Rybtke et al., 2012; Nair et al., 2017).

MATERIALS AND METHODS

Biofilm Formation

A non-mucoid, green fluorescent protein marked strain of *P. aeruginosa* PAO1 (PAO1 Gfp) and a double labeled mutant strain of *P. aeruginosa* PAO1 that uses Gfp as indicator of the intracellular concentration of c-di-GMP and cyan fluorescent protein (Cfp) as a biomass indicator [PAO1 Tn7-Gm-eCFP $P_{cdrA:Gfp}$ (ASV)] were used for the experiments (Lee et al., 2014; Nair et al., 2017). The mutant strains and their applications have been summarized in **Table 1**. The bacterial cultures and biofilms were grown as previously described (Bharatula et al., 2020). Briefly, two sheets of 15 × 15 mm ITO:PET [UV-sterilized and cleaned with 70% ethanol (v/v)] were glued onto a sterile petri dish with silicone sealant (Selleys, Singapore). After curing, the petri dish was filled with 15 mL minimal medium with 6.9 mM glucose (ABTG) and inoculated with bacteria. The ABTG minimal medium (excluding casamino acids) was prepared according to the previous report (Chua et al., 2015a). To prepare the bacterial inoculum, *P. aeruginosa* was grown overnight in 10 mL of Luria Bertani Lennox (LB) broth for 16 h at 37°C and 200 rpm shaking (Zhu et al., 2019). Furthermore, the culture was centrifuged for 5 min and 4,629×*g* and re-suspended in 10 mL fresh ABTG medium. After inoculating at an optical density equivalent to 0.02 at 600 nm (UV-1280, Shimadzu UV-vis spectrophotometer), the petri dishes with ITO:PET sheets were incubated at 37°C and 50 rpm shaking for 72 h. The medium was replaced every 24 h with fresh medium.

TABLE 1 | *Pseudomonas aeruginosa* strains used in this report.

Strain	Application	References
PAO1 *Gfp*	Analysis of biofilm viability using confocal microscopy (live/dead), crystal violet assay and electrochemistry for studies investigating the role of HIFU exposure at various acoustic pressures	Holloway et al., 1979
PAO1 P*cdrA*:*Gfp* (ASV)	Mutant where *cdrA* gene is fused with unstable Gfp plasmid; (i) Used for c-di-GMP quantification in biofilms after HIFU exposure (ii) Used for biomass determination in EPS staining study	Nair et al., 2017
PAO1 Δ*wspF* P*cdrA*:*Gfp* (ASV)	Mutant overproducing c-di-GMP; Used to study the role of c-di-GMP in biofilm after HIFU-treatment	Nair et al., 2017

Acoustic Characterization of Biofilms

A leak proof, custom-made sample chamber was used to hold the biofilm coated ITO:PET sheets. The sample chamber with biofilm layer at the bottom was filled with ABTG medium and sealed with a Mylar sheet (**Supplementary Figure 1**). For HIFU treatment, 0.5 MHz transducer (H107, Sonic Concepts, Bothell, WA, United States) attached to a coupling cone was used in our experiments.

A needle hydrophone (0.2 mm diameter, Precision Acoustics, Dorset, United Kingdom) coupled with a submersible pre-amplifier and DC coupler was used to calibrate the measured pressure amplitude whereas, 1 mm diameter hydrophone (Onda Corporation, Sunnyvale, CA, United States) was used to study acoustic wave propagation for non-linearity determination. The hydrophone was adjusted, such that it coincided with the geometric focus of 0.5 MHz transducer (63.2 mm). For pressure calibration, the signal was triggered at varying input voltage ranging from 10 to 100 mV_{pp} for 20 cycles with a burst period of 10 ms. The resulting output voltage at each point was used to calculate the peak negative pressure using the following equation:

$$\text{Pressure (MPa)} = \frac{\text{Output Voltage}}{2 \times \text{Hydrophone Sensitivity}}$$

Here, hydrophone sensitivity as defined by Precision Acoustics was 55.6 mV/MPa. For, non-linearity studies, the acoustic wave at peak negative pressure ranging from 0.5 to 5.5 MPa (as calculated from hydrophone calibration) was recorded.

For the biofilm exposure experiments, acoustic setup similar to previous study was adapted (Su et al., 2019). In short, sinusoidal wave electrical signal was triggered by function generator (Keysight 33210A) and amplified by high power RF amplifier (Electronics and Innovation, Rochester, NY, United States). The output signal was then converted to acoustic waves and transmitted to the target area by the HIFU transducer. An impedance matching network (Sonic Concepts, Bothell, WA, United States) was used to match the impedance of the HIFU to the output signal from the RF amplifier. The output emissions were received by a 7.5 MHz passive cavitation detector (PCD) (V320, Olympus, Singapore) aligned axially and laterally with HIFU transducer. The data was then collected by an oscilloscope (DSOX3032A, Keysight Technologies, Netherlands) or data acquisition board (DAQ) (PCI-5122, National Instruments, Texas, United States) (**Supplementary Figure 1**).

The biofilms were exposed for 3 min at 10% duty cycle and 50,000 cycles. The peak negative pressure amplitude was varied from 0.5 to 5.5 MPa (as calculated from hydrophone calibration). A sham sample was used as a control for all the HIFU exposed samples. The post processing of acoustic emissions to obtain power spectral density curve has been previously described (Jonnalagadda et al., 2020). Briefly, the post-processing involved extraction of power content from the fast Fourier transform of the received voltage signal. The power spectral density (PSD) differentiated between the presence of harmonics and broadband signal (Paliwal and Mitragotri, 2006). The presence of harmonics, sub-harmonics, and hyper-harmonics are typical for non-inertial cavitation whereas, broadband noise is usually indicative of inertial cavitation.

Confocal Imaging of Biofilms

Following HIFU exposure, independent replicates were imaged to quantify the live/dead cells ratio, exopolysaccharide content and c-di-GMP response. The biofilm samples, irrespective of stains used were imaged as z-stacks under confocal laser scanning microscope (CLSM) (Zeiss LSM 780 inverted microscope; 20× resolution) at five separate locations within the region of acoustic focus. The 3 dimensional (3D) projections of the z-stacks were reconstructed using Imaris (Bitplane, Oxford Instruments).

Live/Dead Cell Staining

To monitor bacterial cell viability, the biofilm samples (PAO1 *Gfp*) were stained with 8 μL of the *Baclight* live/dead stain and imaged by CLSM. The stock solution was made by adding 3 μL of both SYTO 9 (Excitation/Emission: 485/498) and propidium iodide (Excitation/Emission: 585/617) to 1 mL DI water.

cdrA Correlated C-di-GMP Response

PAO1 P_{cdrA}:*Gfp* and Δ*wspF* P_{cdrA}:*Gfp* mutants were used to quantify the relative amounts of c-di-GMP in HIFU treated and control biofilms (Nair et al., 2017). Following HIFU exposure, the amount of cell biomass [cyan fluorescent protein (Cfp), Excitation/Emission: 435/485] and *cdrA* response [green fluorescent protein (Gfp), Excitation/Emission: 488/510], which is directly correlated to the amount of c-di-GMP, were imaged by CLSM. The Gfp/Cfp ratio, i.e., the *cdrA* correlated c-di-GMP response signal per biomass was quantified.

Exopolysaccharide Staining

The PAO1 P_{cdrA}:*Gfp* mutant was used for these studies. The Cfp label of the mutant was used to image the biofilm cells. One mg/mL fluorescein isothiocyanate (FITC) conjugated concanavalin-A (con-A) (from *Canavalia ensiformis*, Sigma Aldrich, Singapore) in deionized water and calcofluor white stain (CWR) (Sigma Aldrich, Singapore), mixed with 10% KOH solution in a 1:1 ratio were prepared as stock solutions. Four microliter of con-A (Excitation/Emission: 492/518) and CWR (Excitation/Emission: 365/435) each were added to the biofilms to stain α polysaccharides and β polysaccharides, respectively. The biofilms were set aside for 30 min after addition of each stain.

Image Processing and Quantification

All calculations were performed using MATLAB (Mathworks Inc.). Prior to any calculation, all the images were split into separate channels. Image processing steps involved Otsu's image thresholding followed by image filtering using 2D median filtering (filter size = 5) (Yang et al., 2001; Beyenal et al., 2004b). The volumetric parameters were calculated as described by Beyenal et al. (2004a). We looked at parameters such as biovolume, porosity, and run-length. In summary, the biovolume was calculated from the following equation:

$$\text{Biovolume } (\mu m^3) = \sum_{x=1}^{N_x}\sum_{y=1}^{N_y}\sum_{z=1}^{N_z} \textit{Image Stack } (x, y, z) \textit{ voxel size}$$

The porosity of the biofilms was calculated as follows:

$$\text{Porosity } = \frac{\text{Total no. of void pixels}}{\text{Total no. of pixels}}$$

Run-length in a given direction is defined as the number of continuous biomass pixels. From these values, the aspect ratio was calculated in each axis as:

$$\text{Aspect Ratio} = \frac{\text{X Run} - \text{length}}{\text{Z Run} - \text{length}}$$

The quantification of Gfp/Cfp ratio (c-di-GMP per biovolume) and corresponding ratio images were obtained as suggested by previous report (Nair et al., 2017). To calculate the amount of c-di-GMP per cell biomass, the z-stacks of Cfp and Gfp channels corresponding to biomass and c-di-GMP were analyzed separately. A mask was created by thresholding and filtering the Cfp channel. This mask was multiplied with both Gfp channel and Cfp (graylevel) channel and a sum of the matrices was obtained. The ratio was calculated by dividing the Gfp value with Cfp value. This ratio was considered as the c-di-GMP per cells. The resulting heatmap from this ratio was termed as "ratiometric image." The final ratio was further normalized with respect to the untreated control. For MATLAB code snippets see **Supplementary Information**.

Crystal Violet Assay

The biofilm samples after HIFU test were washed with phosphate buffer saline (PBS) solution and further stained with 0.1% (v/v) crystal violet solution for 15 min. This was followed by washing the sheets with PBS, addition of 2 mL absolute ethanol and the measurement of absorbance at 550 nm using a microplate reader (TECAN M200, Switzerland).

Electrochemical Monitoring

The setup previously described in Bharatula et al. (2020) was used. Briefly, a VSP or VMP3 multi-channel potentiostat (Bio-Logic, France) was connected to a three-electrode setup. The 15 × 15 mm ITO:PET sheet was used as working electrode and connected to a Pt sheet electrode holder as current collector (Latech, Singapore). The auxiliary and reference electrodes were a coiled titanium wire (Sigma Aldrich, Singapore) and Ag/AgCl standard electrode (Latech, Singapore), respectively. The three electrodes immersed in 15 mL fresh ABTG medium with 5 mM potassium ferricyanide as an exogenous redox mediator were connected to the potentiostat controlled by EC-Lab software (Bio-Logic, France). Electrochemical Impedance Spectroscopy (EIS) was carried out at open circuit potential (OCP), in the frequency range from 100 kHz to 30 mHz with sinusoidal potential of 10 mV amplitude. Furthermore, bias potential in the range to 50–500 mV vs. Ag/AgCl was applied to gain additional information on the biofilm electrochemical signature. The impedance data were fitted to an equivalent circuit model consisting of two resistor—constant phase element (CPE) blocks and an additional resistor in series using the Z-Fit feature in the EC-lab software (Bharatula et al., 2020).

Colony Morphology Analysis

An area, representative of the acoustic focus in the samples exposed to HIFU and the untreated control sample was scraped and mixed in LB medium. Further, the solution was serially diluted till 10^5 dilution was reached. Final volume of 100 μL of each dilution was individually plated on LB agar plates and incubated at 30°C for 24 h. After incubation, the colony forming units (CFU) were quantified using the formula:

$$\text{CFU} = \frac{\text{No. of counted colonies}}{\text{Dilution factor} \times \text{droplet volume}}$$

Here, circular and wrinkled morphologies were counted separately. The percentage of CFU with wrinkled morphology was quantified as follows:

$$\%\ \text{of wrinkled colonies} = \frac{\text{CFU of wrinkled morphology}}{\text{Total CFU}} \times 100$$

Furthermore, both the morphologies were imaged by light microscope (Carl Zeiss Primo star) at 4× magnification.

RESULTS

Effect of HIFU on Biomass

To determine if HIFU induced a microstructural response in the biofilm, we quantified the biofilms formed by PAO1 mutant labeled with Cfp. **Figures 1**, **2** describe the qualitative and quantitative analysis of biovolume for untreated control and biofilms exposed to 0.5–5.5 MPa, respectively. Due to the heterogeneous nature of the biofilms and associated high variation in biomass values between replicates, a biovolume loss of 20% or more was arbitrarily considered as an estimate for the lower limit threshold for biofilm loss due to HIFU. Accordingly, a significant loss in biovolume, especially at high pressure amplitudes (4.5 and 5.5 MPa), was observed (**Figures 1F–G**, **2A**). Further probing into volumetric properties revealed increase in porosity (**Figure 2B**) and decrease in aspect ratio in X vs. Z direction (**Figure 2C**) with respect to loss of biovolume on the substratum.

Effect of HIFU on Biofilm Viability and EPS Components

Biofilms are comprised of cells as well as the extracellular matrix that holds them together and thus, biofilm control strategies may affect one or both components of the biofilm. As suggested by previous results, HIFU was able to disrupt the biomass yet its influence on the viability and the biofilm matrix remains unclear. Therefore, the effects of three pressure amplitudes on both the components were studied using confocal imaging, crystal violet assay, and electrochemical monitoring.

Figure 3 shows 3D reconstructions of confocal images of biofilms exposed to HIFU and the subsequent effect of HIFU on cell viability marked by live/dead staining. Based on 3D reconstructions (**Figures 3A–D**) and image quantification (**Figure 3E**) of the untreated biofilm and HIFU treated biofilms, there was no significant effect of HIFU at 0.5 and 2.5 MPa on live biofilm biomass. When the pressure was increased to 4.5 MPa, there was a reduction in live biomass. Interestingly, the dead biomass was also reduced alongside the live biomass especially after exposure at 4.5 MPa (**Figure 3F**).

Next, we investigated the effect of HIFU treatment on the distribution and quantity of polysaccharides that comprise part of the *P. aeruginosa* biofilm matrix (**Figure 4**). Two fluorescent dyes were used to distinguish between two broad classes of polysaccharides. Specifically, Con-A was used to visualize and quantify the α-polysaccharides and CWR was used to identify the β-polysaccharides. Based on 3D reconstructions of the biofilm (**Figures 4A–D**) it was observed that the bacterial cells (blue) were always surrounded by the α-polysaccharides (red) at the bottom and β-polysaccharides (yellow) on top irrespective of the HIFU pressure applied. Quantitative image analysis (**Figure 4E**) indicated a positive linear relationship between relative α-polysaccharides biovolume and the remaining biofilm cells. This observation suggested that α-polysaccharides were removed with the bacterial cells after HIFU exposure.

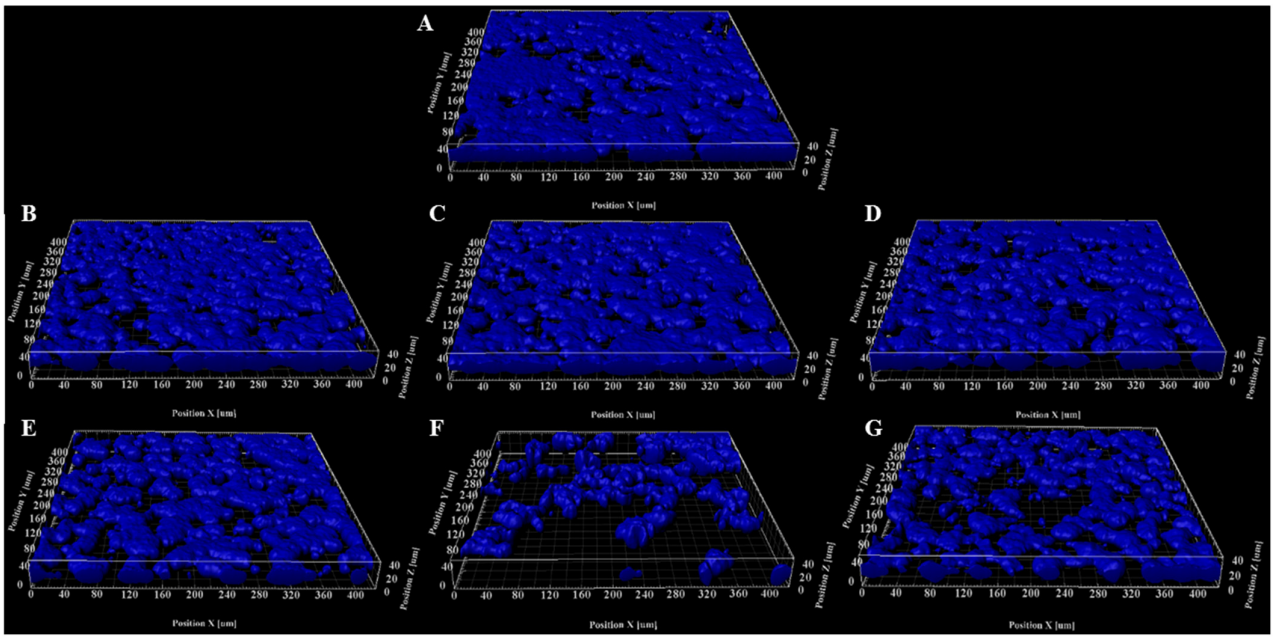

FIGURE 1 | Representative 3D reconstructions of biofilms formed by PAO1 P_{cdrA}:*Gfp* exposed to HIFU at **(A)** 0 MPa (Sham). **(B)** 0.5 MPa. **(C)** 1.5 MPa. **(D)** 2.5 MPa. **(E)** 3.5 MPa. **(F)** 4.5 MPa. **(G)** 5.5 MPa. The CFP channel of the confocal images of biofilms grown for 3 days and exposed to HIFU were converted to 3D reconstructions to observe the change in biomass.

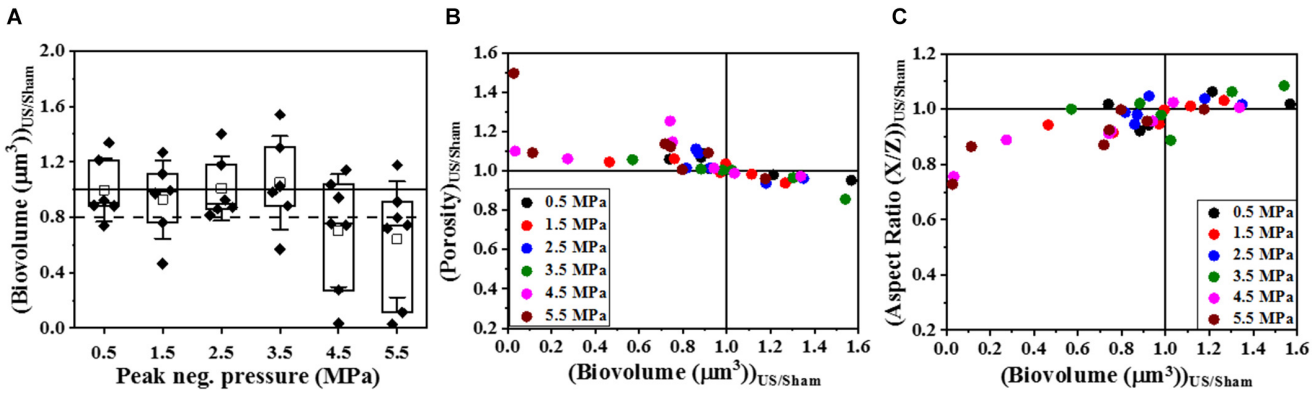

FIGURE 2 | The quantitative analysis of volumetric changes in biofilms formed by PAO1 P_{cdrA}:*Gfp* exposed to HIFU. **(A)** Change in biovolume with respect to acoustic pressure amplitude. An arbitrary threshold of 20% loss or more was considered significant. **(B)** Effect on biofilm porosity as the biovolume changed. **(C)** Effect on biofilm aspect ratio in X/Z direction as the biovolume changed.

In contrast, the relative β-polysaccharides volume was less reduced, suggesting that β-polysaccharides may remain in the biofilm micro-environment irrespective of cell biomass loss (**Figure 4F**).

Crystal violet assay and electrochemical monitoring (**Figure 5**) were used to corroborate the effect of HIFU exposure on the viability and biofilm matrix. In contrast to confocal imaging which analyzed smaller areas, these techniques allowed us to investigate the entire surface area exposed to HIFU. The crystal violet assay (**Figure 5A**) indicated no apparent effect of HIFU at any given pressure on the crystal violet absorbance. EIS allows for the rapid measurement of microstructural changes in the biofilm after ultrasound exposure through the variation of parameters such as interfacial resistance under open circuit potential conditions and current output at controlled electrode potential. Here, a marked yet, statistically insignificant increase in the interfacial resistance with respect to the sham (**Figure 5B**) was observed at all pressures. Even so, there was no significant difference between the current for sham and HIFU treated biofilms (**Figure 5C**), there was a slight (albeit not statistically significant) increase in current for 4.5 MPa exposed biofilms.

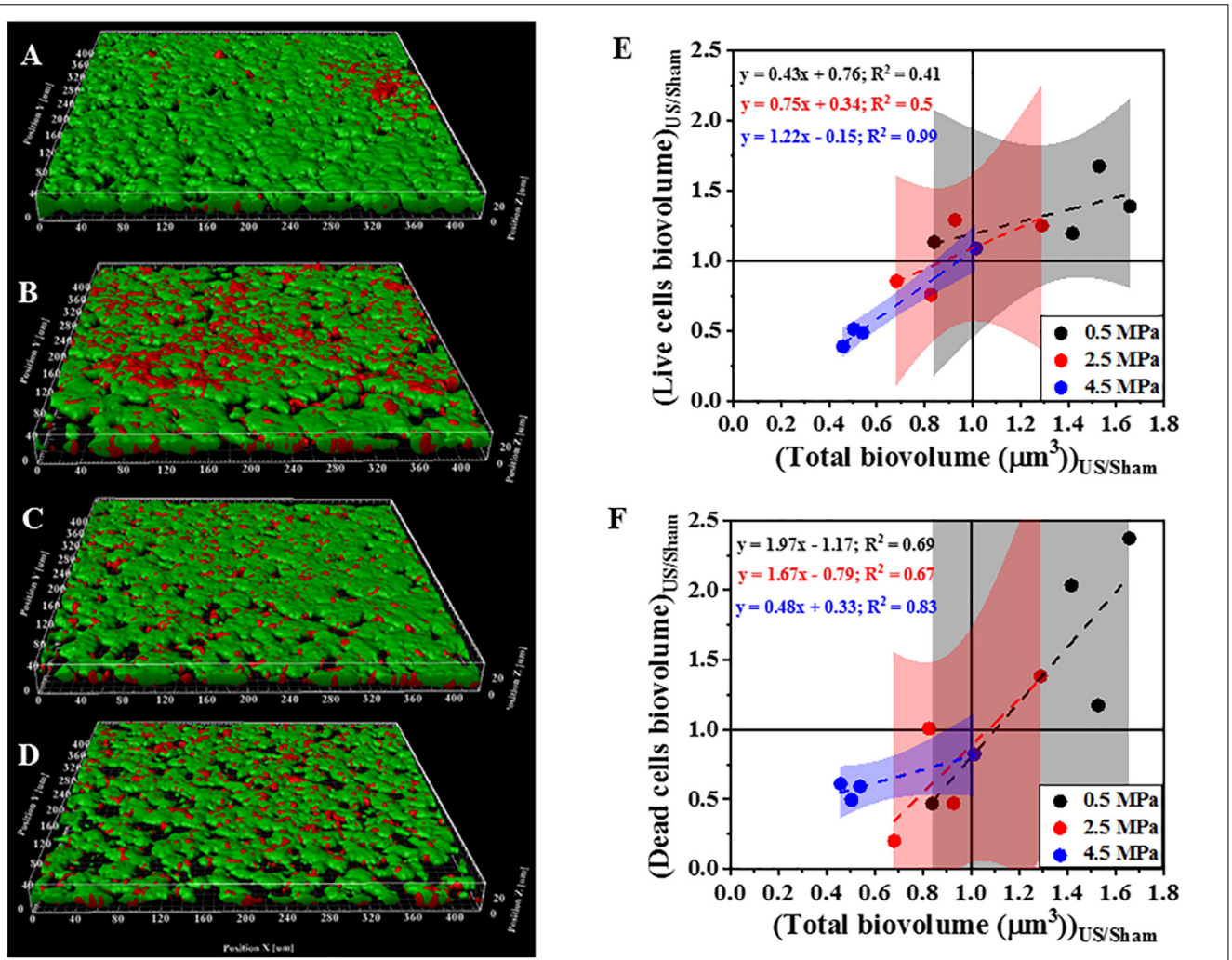

FIGURE 3 | Representative 3D reconstructions from confocal images of biofilms formed by PAO1 *Gfp* exposed to HIFU stained at **(A)** 0 MPa (Sham). **(B)** 0.5 MPa. **(C)** 2.5 MPa. **(D)** 4.5 MPa. Green = live cells, Red = Dead cells. **(E)** Effect on biovolume of live cells with respect to change in total biovolume. **(F)** Effect on biovolume of dead cells with respect to change in total biovolume. The method was adapted to study role of HIFU on biofilm viability by staining with SYTO9 and PI. Here, SYTO9 stained live cells whereas, PI stained the dead cells. The quantification established a linear relationship between Live/dead cells biovolume and total cells biovolume. The linear equation and R^2-value for individual regressions are indicated in the plots.

Effect of HIFU on *cdrA* Correlated c-di-GMP per Biovolume Ratio

To determine whether the loss in biovolume was a result of a purely physical effect or due to changes in gene regulation that controls biofilm formation, the response of the Gfp channel corresponding to the Cfp channel (seen in **Figure 1**) was analyzed using an indirect c-di-GMP quantification technique. Here, the *cdrA*-Gfp signal is a proxy for the intracellular c-di-GMP concentration. Quantitative image analysis (**Figure 6**) of the confocal images revealed the dependence of change in ratiometric signal on the loss of biofilm biomass. **Figures 6A–F** shows the scatter plot of Gfp/Cfp ratio with respect to remaining cell biovolume at six different acoustic pressure amplitudes. The increase in the ratio was evident in most samples (∼ 4 out of 7 samples) exposed at 4.5 and 5.5 MPa especially when the biovolume loss was above the 20% biovolume loss threshold. Statistical significance was not the best way to characterize the changes in these experiments as both cavitation and biofilm growth are subject to have levels of variability. To better understand the influence of acoustic pressure amplitude on the relationship between biovolume and Gfp/Cfp ratio, the data points were fit linearly at individual pressures. A negative correlation between biovolume and ratio was significant at 4.5 and 5.5 MPa whereas biofilms exposed to HIFU at pressure amplitudes below 4.5 MPa did not show any substantial change in Gfp signal per cell of the remaining cells in the biofilm. At $p = 0.05$, only the slope of 4.5 MPa response was statistically different from zero. All the p-values are shown in the respective plots along with the linear equation.

Next, we compared the effect of HIFU induced biofilm removal at 4.5 MPa and subsequent effect on *cdrA* correlated

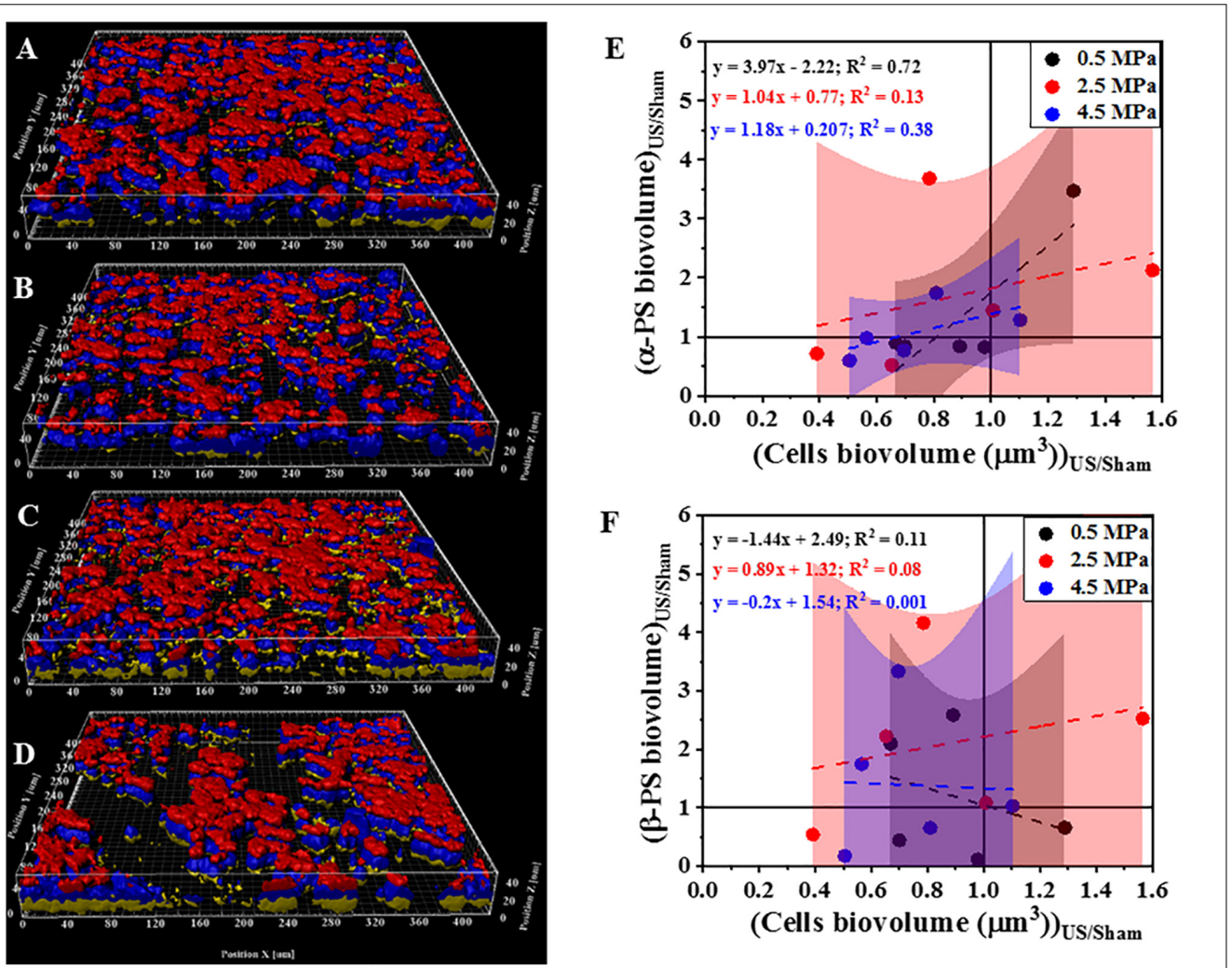

FIGURE 4 | Representative 3D reconstructions of confocal images of biofilms formed by PAO1 P_{cdrA}:*Gfp* and exposed to HIFU at **(A)** 0 MPa (Sham). **(B)** 0.5 MPa. **(C)** 2.5 MPa **(D)** 4.5 MPa. Blue = Biofilm cells, Red = Con-A, Yellow = CWR. **(E)** Effect on biovolume of α-polysaccharides with respect to bacterial cells biovolume. **(F)** Effect on biovolume of β-polysaccharides with respect to cell biovolume. PS in plots refers to polysaccharides. The method was adapted to study role of HIFU on biofilm exopolysaccharides by staining with Con-A and CWR. The CFP channel of the PAO1 P_{cdrA}:*Gfp* biofilms indicated the change in biomass whereas, Con-A stained α-polysaccharides and CWR stained the β-polysaccharides. The quantification established a linear relationship between α-/β-polysaccharides biovolume and total cells biovolume. The linear equation and R^2-value for individual regressions are indicated in the plots.

c-di-GMP response in wild type-PAO1 P_{cdrA}:*Gfp* and a Δ*wspF* mutant that overproduces c-di-GMP as a consequence of the mutation, i.e., PAO1 Δ*wspF* P_{cdrA}:*Gfp* (**Figure 7**). It is to be noted that the Δ*wspF* biofilms were thicker than the ones formed by wild type strain (**Supplementary Figure 3**). **Supplementary Figure 3** shows the comparison of biofilm growth by wild type and Δ*wspF* strains. Here, the Δ*wspF* biofilms both untreated (**Supplementary Figure 3C**) and HIFU-treated (**Supplementary Figure 3D**) were approximately four times thicker than the ones formed by wild type strain (**Supplementary Figures 3A,B**). The biovolume quantification (**Supplementary Figure 3E**) shows that HIFU exposure decreased the biovolume in both strains yet, contrary to wild type that removed cells from the base, in Δ*wspF* just layers of cells were removed from the top.

Figures 7A,B shows the qualitative analysis in the form of representative ratiometric images of Gfp per Cfp signal expressed by untreated biofilms and HIFU-treated biofilms for PAO1 P_{cdrA}:*Gfp* and PAO1 Δ*wspF* P_{cdrA}:*Gfp*, respectively. Inspection of images in **Figure 7A** indicated that the ratiometric signal in wild type biofilms gradually increased as HIFU acoustic pressures amplitude increased to 4.5 MPa. The ratiometric images of biofilms at other acoustic pressure amplitudes is shown in **Supplementary Figure 2**. In contrast, the qualitative image (**Figure 7B**) analysis of Δ*wspF* mutant biofilms at 4.5 MPa showed no increase in the ratiometric signal compared to wild type biofilms (**Figure 7A**). The same was reflected in the quantitative Gfp/Cfp ratio and biovolume relationship (**Figure 7C**). Here, the curve of PAO1 P_{cdrA}:*Gfp* is the same as **Figure 6E**; it was added here for a better comparison.

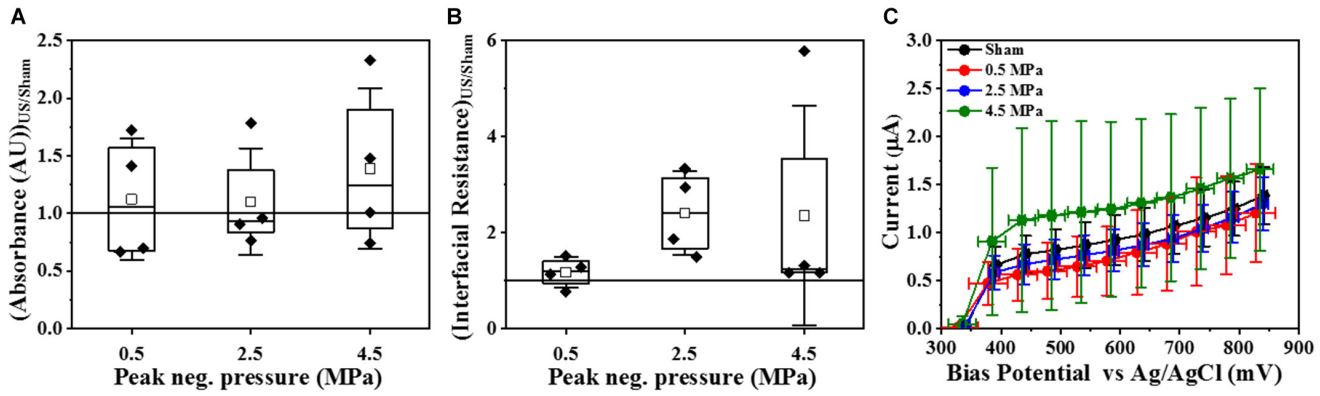

FIGURE 5 | Effect of HIFU on the entire biofilm surface. **(A)** Crystal violet absorbance at 550 nm for biofilms formed by PAO1 *Gfp* exposed to HIFU at various acoustic pressures. **(B)** Interfacial Resistance obtained by EIS and fit to an equivalent circuit and **(C)** Faradaic current characteristics at increasing bias potential for biofilms formed by PAO1 *Gfp* exposed to HIFU at various acoustic pressures. The results are statistically insignificant.

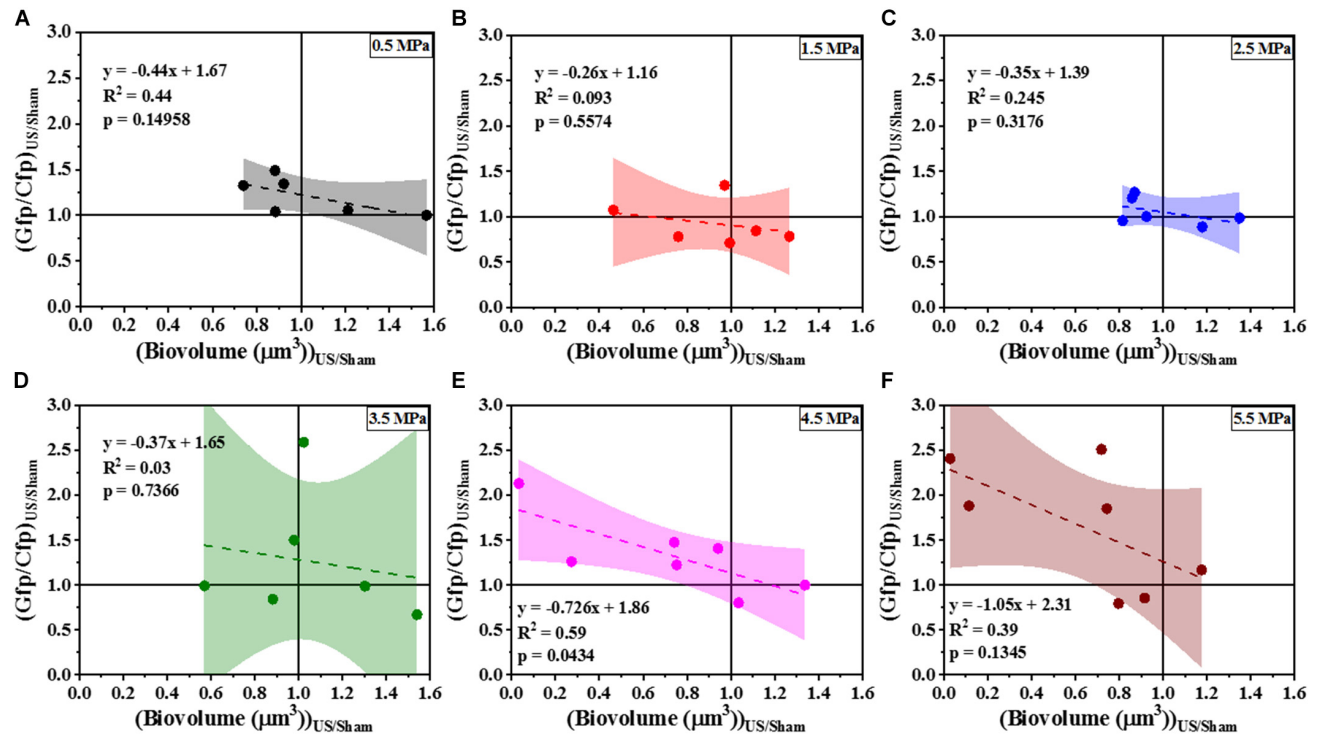

FIGURE 6 | The correlation of Gfp/Cfp ratio and biofilm biovolume at various pressure amplitudes normalized to the sham—**(A)** 0.5 MPa. **(B)** 1.5 MPa. **(C)** 2.5 MPa. **(D)** 3.5 MPa. **(E)** 4.5 MPa. **(F)** 5.5 MPa. The quantification established a linear relationship between Gfp/Cfp ratio (indicative of *cdrA* correlated c-di-GMP per unit cell biovolume) and cells biovolume. The linear equation, R^2-value and *p*-value for individual regressions are indicated in the plots. Here *p*-value is the significance level at which the obtained slope is statistically different from zero.

Figure 7D shows the slope obtained from the linear regression for various acoustic pressure amplitudes. Here, the slope of linear regression was always less than zero indicating an increase in the Gfp/Cfp even at the lowest acoustic pressure. Nonetheless, a decreasing trend was observed as the pressure increased. Interestingly, the slope tracked back to zero for the biofilms formed by Δ*wspF* mutant.

To corroborate the changes in c-di-GMP, we further investigated the genotypic composition of the biofilms by colony morphology analysis. Specifically, we looked for the presence of wrinkled colony morphology variants indicative of high c-di-GMP production due to mutations in the *wsp* pathway (**Figure 8A**). A positive correlation between the percentage of wrinkled colonies (**Figure 8B**) and total CFU was observed for

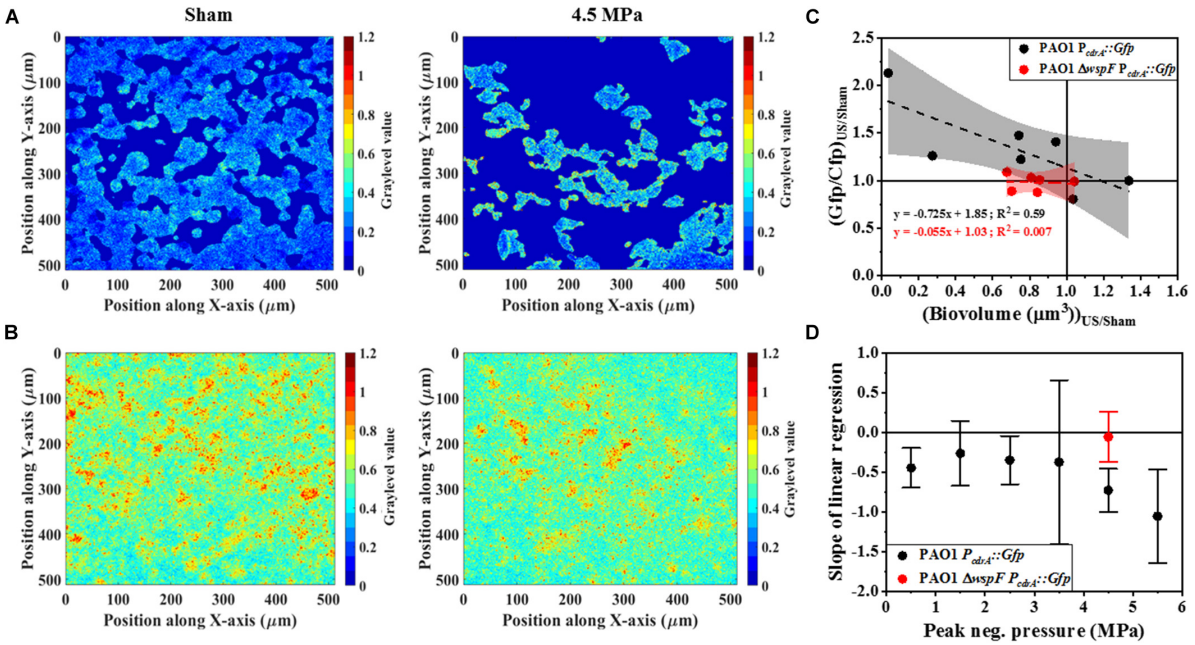

FIGURE 7 | Representative ratiometric images (i.e., images of Gfp channel per Cfp channel) of biofilms formed by **(A)** PAO1 P$_{cdrA}$*:Gfp* exposed to HIFU at 0 MPa (Sham) and 4.5 MPa. **(B)** Representative ratiometric images of biofilms formed by c-di-GMP overproducing PAO1 Δ*wspF* P$_{cdrA}$*:Gfp* exposed to HIFU at 0 MPa (Sham) and 4.5 MPa. The colorbar shows the graylevel value, i.e., the Gfp/Cfp ratio in the spatial plane. **(C)** The correlation of Gfp/Cfp ratio and biofilm biovolume for biofilms formed by PAO1 P$_{cdrA}$*:Gfp* and PAO1 Δ*wspF* P$_{cdrA}$*:Gfp* exposed to HIFU at 4.5 MPa and normalized to the sham. The linear equation and R^2-value for individual regressions are indicated in the plots. **(D)** Variation in the slope of linear regression with increasing acoustic pressure amplitude for biofilms formed by PAO1 P$_{cdrA}$*:Gfp* and PAO1 Δ*wspF* P$_{cdrA}$*:Gfp*.

4.5 MPa treated biofilms whereas, the slope of untreated biofilms was not significantly different from zero. This suggests that at the higher acoustic pressure, where loss of the biofilm was observed, the remaining biofilm appears to have a higher relative abundance of wrinkled variants that overproduce c-di-GMP. This may explain the observations above (**Figure 7**) where we observe an increase in relative c-di-GMP production after exposure to increased acoustic pressures.

Role of HIFU Properties in Microstructural and Biological Changes

Since our aim was to determine the influence of ultrasound alone on the biofilm, we used HIFU to achieve the desired effects. Introducing a coupling cone to the experimental system exhibited more intense power at the focus (**Supplementary Figure 4A**) compared to free-field (**Supplementary Figure 4B**). This pressure distribution calibration in presence of coupling cone also shows that the HIFU focus is limited to ∼3 mm in the radial plane.

Furthermore, the changes in acoustic properties at the pressures with maximum microstructural and biological response was apparent. The cavitation properties were investigated using PSD curve. For the frequency content, the raw data obtained from the oscilloscope was post processed and converted to a PSD curve. Here, inertial cavitation response was observed at 3.5 MPa and higher, in the representative PSD (**Supplementary Figure 5**). It is to be noted that this analysis just described inertial cavitation and there was a possibility of non-inertial cavitation which was revealed in the frequency content of the unfiltered signal. Investigations of unfiltered data revealed sub-harmonic signal at higher pressures indicating stable cavitation (**Supplementary Figure 6**).

Emergence of a non-linear acoustic wave was also investigated as a possible mechanism for the changes in biofilm. In contrast to the wave propagation in free-field (**Supplementary Figure 7A**), the distortion of rarefactional acoustic waves above 4.5 MPa indicating non-linear wave propagation was evident in a coupling cone setup (**Supplementary Figure 7B**).

DISCUSSION

Using therapeutic ultrasound on bacterial biofilms is gaining momentum as an efficient treatment strategy. To observe any effects, the choice of acoustic parameters is crucial (Brayman et al., 2017). While low intensity ultrasound in combination with microbubbles and antibiotics is intended to kill bacteria, HIFU treatment specifically breaks down and disrupts the biofilm, but does not necessarily rely on killing to achieve these effects (Erriu et al., 2014). At low acoustic intensity, exposing *P. aeruginosa* biofilms to varying ultrasonic frequency did not show any significant change in biofilm viability (Qian et al., 1997). In contrast, previous studies at high intensity have shown that varying parameters such as duty cycle, burst period and exposure time of HIFU cause loss of biomass in *P. aeruginosa* and

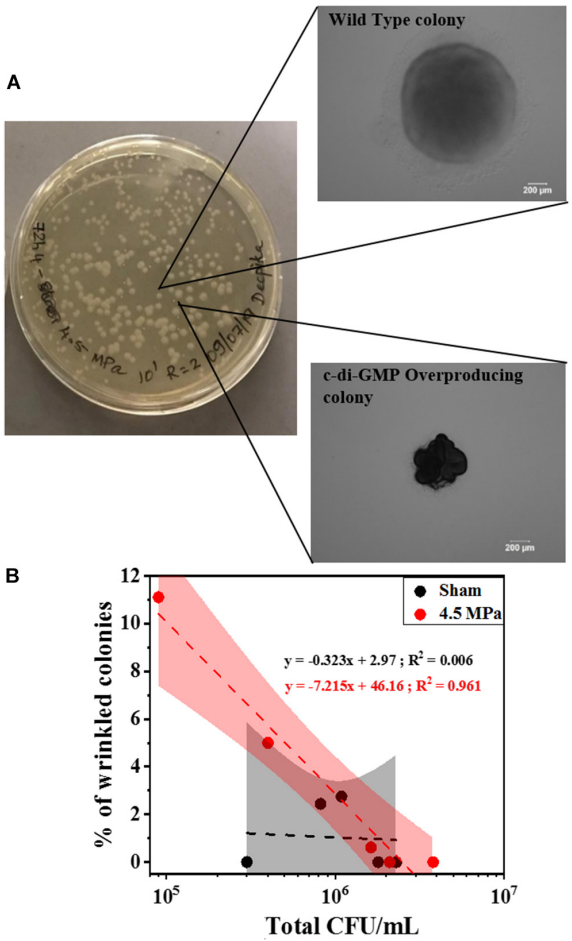

FIGURE 8 | This analysis is related to emergence of wrinkled colonies (indicative of c-di-GMP overproduction) after HIFU exposure at 4.5 MPa. **(A)** Representative optical images of various colony variants found in the biofilms formed by PAO1 P_{cdrA}:*Gfp* after exposure to HIFU at 4.5 MPa. **(B)** Linear relationship between total CFU and % of wrinkled colonies after sham and 4.5 MPa HIFU treatment. The linear equation and R^2-value for individual regressions are indicated in the plots.

Enterococcus faecalis biofilms (Xu et al., 2012; Iqbal et al., 2013). All of these studies revealed a vital role of acoustic intensity in the disruption of biofilms. Since our aim was to determine the influence of ultrasound alone on the biofilm we used HIFU to achieve the desired effects.

Furthermore, the mechanical effects of HIFU such as cavitation and acoustic streaming that might drive the disruption process rely strongly on the peak negative pressure (Mo et al., 2012). However, further investigation is required in the role of varying acoustic pressure amplitude on biofilms (Vyas et al., 2019). A study on acoustic pressure variation on *Escherichia coli* biofilms showed a reduction in CFU at relatively high pressures (Bigelow et al., 2009). Our studies showed biovolume loss at higher pressures and were consistent with Bigelow et al. (2009). Additional volumetric parameters such as porosity and aspect ratio gave a better understanding of the mechanical changes in biofilms after HIFU exposure (Lewandowski and Beyenal, 2007). The increase in porosity evidenced by the 3D reconstructions and quantification of biofilms indicated that HIFU penetrated the biofilm and uprooted the cells from the base of the substratum. Furthermore, the change in the aspect ratio of the run lengths confirmed that HIFU distorted the microcolonies in z-direction (Beyenal et al., 2004a).

Once we established that HIFU influenced the biofilm cells, we investigated the contribution of viable/non-viable cells and EPS to the microstructural change. Our findings showed that HIFU was able to detach both live and dead cells from the ITO:PET surface especially at 4.5 MPa. The biofilm detachment by HIFU was in agreement with previous studies (Bigelow et al., 2009; Xu et al., 2012; Iqbal et al., 2013). Additionally, there was no drastic increase in the dead cells after HIFU exposure; cell death was not a primary consequence of HIFU in contrast to the effects observed in presence of external agents such as microbubbles and antibiotics (Erriu et al., 2014; Cai et al., 2017; Lattwein et al., 2020). Our results therefore suggest that acoustic intensity was linked to the physical disruption of biofilms.

Next, we investigated the effect of ultrasound on exopolysaccharides. In addition to the bacterial cells, the biofilm matrix forms a major part of a biofilm (Flemming and Wingender, 2010). Previously, it has been suggested that low intensity ultrasound significantly affected polysaccharide synthesis expression in *Staphylococcus epidermidis* and *P. aeruginosa* biofilms (Zhu et al., 2013; Zhang et al., 2019). A positive correlation between EPS (stained by con-A) and biomass loss after low intensity ultrasound exposure in presence of microbubbles has also been determined (Agarwal et al., 2014). However, the impact of HIFU on the biofilm matrix has not yet been well studied (Pinto et al., 2020). In our study, con-A and CWR stains were used to study the role of HIFU on biofilm exopolysaccharides (Baird et al., 2012). These are general lectin-based polysaccharide stains and have been previously used to study exopolysaccharides in both biofilms (Baird et al., 2012) and aerobic granules (Chen et al., 2007).

In principle, each monosaccharide unit in the biofilm carbohydrates consist of α and β glycosidic linkages that bond with another monosaccharide or molecule (for e.g., lectins). Here, α and β linkages are stereoisomers where, the α-glycosidic bond is formed when the binding carbons have the same stereochemistry and β-glycosidic bond occurs when the two carbons have different stereochemistry. The biofilm exopolysaccharides are rich in such α and β linkages that bind to con-A and CWR, respectively (Baird et al., 2012).

In *P. aeruginosa*, biofilms formed by the non-mucoid PAO1 strain primarily consist of two exopolysaccharides namely, Pel, a glucose rich polysaccharide and Psl, a pentasaccharide repeat structure consisting of mannose, glucose and galactose (Mann and Wozniak, 2012). Here, con-A has a binding specificity toward α-mannose and α-glucose (Strathmann et al., 2002). Similarly, *P. aeruginosa* consists of cellulose-resembling β-1,4 and β-1,3 glucose units that binds with CWR (Stewart et al., 1995). To this effect, con-A and CWR stains are not specific to Pel or Psl, rather they give a combined

response of both the exopolysaccharides by bonding with α and β-glycosidic link in the structure of the sugar.

Our findings revealed that HIFU was able to remove the bacterial cells and the α-polysaccharides linked to them, whereas removal of β-polysaccharides located at the top of the biofilm did not depend on the biovolume removal. This indicated two possible effects of HIFU on α-polysaccharides: (i) HIFU interacted with biofilm exopolysaccharides and degraded them or (ii) they were simply removed from the surface along with the bacterial cells due to their strong linking as a result of active or passive dispersal; both resulting in destabilizing the biofilm microstructure (Kaplan, 2010; Agarwal et al., 2014). Based on the aforementioned indication, con-A bonded with two major glycosyl units in *P. aeruginosa,* i.e., mannose (formed ∼20% of Psl structure) and glucose (dominant in Pel and formed ∼13% of Psl) (Ma et al., 2007; Jennings et al., 2015). As a result, the disruption of α-polysaccharides suggested the ability of HIFU to affect both Pel and Psl exopolysaccharides in *P. aeruginosa*.

Although we investigated the effect of HIFU on cells and EPS sugars, these changes alone do not hint at total biofilm removal because the microstructure of a biofilm is dynamic and complex (Flemming and Wingender, 2010). Therefore, to further understand the relationship between HIFU and total biofilm dispersal, we used a common method for quantifying acoustic-biofilm interactions, crystal violet assay (He et al., 2011; Zhu et al., 2013; Dong et al., 2017; Koibuchi et al., 2018). Crystal violet is known to stain the entire biofilm, i.e., live cells, dead cells, and extracellular matrix (Merritt et al., 2005). We also utilized EIS to characterize changes in the biofilm biomass and structure as it has been found to be an efficient tool to detect the growth and disruption of biofilms on conductive surfaces (Dominguez-Benetton et al., 2012). The EIS response of *P. aeruginosa* biofilms grown on ITO:PET substrate suggested that interfacial resistance and current characteristics indirectly measure the viability of the biofilm (Bharatula et al., 2020). The current characteristics are also influenced by Psl in the EPS. The interfacial resistance agreed with the live/dead stain results. Based on the non-removal of β-polysaccharides in confocal analysis, crystal violet assay, and current at bias potential, no significant change in biofilms with respect to acoustic pressure indicated that biofilm matrix components remained on the substratum.

Another possibility for the insignificant changes in the crystal violet assay and electrochemical monitoring was that the microstructural effects were a localized phenomenon. The beam focus of a 0.5 MHz HIFU transducer is 3 mm in radial diameter (as observed by the pressure distribution map), resulting in an exposure area of ∼7 mm^2 (Bazan-Peregrino et al., 2012). Although this is a relatively small area compared to the entire area covered by biofilm (225 mm^2), it is easily visualized using confocal microscopy. Crystal violet assay and EIS, however, analyze an area that extends beyond the focus of the HIFU beam Thus, these sampling methods provide insight on the effects of HIFU on regions within and beyond the focus of the HIFU, and thus suggested that the results we observed were restricted to only biofilm within the acoustic focus of HIFU.

From the microstructural results, HIFU removed large regions of the biofilm, however, the biological mechanism behind such observation remains undefined. A previous study has suggested that changes in genetic factors such as quorum sensing, protein metabolism, and motility are possible after exposure to low intensity ultrasound (Zhang et al., 2019). We focused on the impact of HIFU on a key regulatory system that controls biofilm formation and dispersal and is known to be linked to cellular responses to environmental cues such as changes in oxygen, nutrient concentrations, as well as nitric oxide that lead to dispersal (Valentini and Filloux, 2016). C-di-GMP is a secondary messenger that plays a key role in regulating the shift between planktonic and biofilm bound cells (Ha and O'Toole, 2015). Moreover, c-di-GMP is crucial in regulating the stress response in *P. aeruginosa* (Chua et al., 2015b). The intracellular c-di-GMP was quantified using a reporter strain that responds to changes in c-di-GMP concentrations by inducing Gfp production from the promoter of the *cdrA* gene (Nair et al., 2017). The fluorescent bio-reporter used in this study was specifically developed for the indirect characterization of the c-di-GMP from planktonic bacteria and biofilms using confocal microscopy (Rybtke et al., 2012; Nair et al., 2017). Previous optimization of the bio-reporter strain showed that the data gathered from the confocal microscope correlated well with the chemical quantification (Nair et al., 2017). This correlation confirmed that the bio-reporter used was an efficient indicator of the c-di-GMP levels within the cells in different parts of the biofilms and at different time. Moreover, the c-di-GMP concentration may vary throughout the biofilm due to physiological heterogeneity. Therefore, this characterization technique provided information about the spatial and temporal distribution of c-di-GMP.

In principle, the amount of c-di-GMP per biovolume is independent to the amount of biomass loss due to HIFU if the removal of biofilm is truly non-specific. At low acoustic pressure amplitudes before 3.5 MPa, this principle held true. However, our findings revealed an increase in *cdrA* dependent c-di-GMP response per remaining biomass at acoustic pressure amplitudes at and above 4.5 MPa, which corresponded to more consistent biofilm removal. It was therefore possible that the biofilm had c-di-GMP hot-spots that were detectable when "weaker" portions of the biomass was removed.

One possible mechanism for this change entirely relies on mechanical disruption of either the matrix or cells to cause biofilm disaggregation. Alternatively, the cells actively respond to the acoustic stresses from ultrasound to disperse suggesting ultrasound may induce changes in gene expression that result in active dispersal of the bacterial cells from the biofilm (Kaplan, 2010). The mechanism of the changes was tested by treating biofilms formed by Δ*wspF* mutation that overproduce c-di-GMP. Such biofilms often contain spontaneous mutants that do not disperse as effectively as the wild-type cells and are characterized by small colony variants with wrinkled morphology (Hickman et al., 2005).

The response from biofilms formed by Δ*wspF* mutation did not show any change in c-di-GMP despite the removal of bacterial cells. Here, the lack of dispersal suggested that the genetic signal cascade that regulated the dispersal was blocked.

In comparison, a clear change was observed in biofilms formed by wild type strain indicating the influence of a biological mechanism as opposed to a purely mechanical one. Moreover, the increase in c-di-GMP per biomass ratio (Gfp/Cfp ratio) in the wild type biofilms after HIFU treatment suggested a slow transition toward PAO1 Δ*wspF* biofilm condition. Hence, an understanding of the response of high c-di-GMP producing biofilms toward HIFU was necessary. The lack of c-di-GMP response in PAO1 Δ*wspF* biofilms indicated that biofilms may develop resilience to HIFU as they become stronger.

Furthermore, the colony morphology studies corroborated the confocal microscopy findings where an increase in c-di-GMP was observed in wild type biofilms. Our findings revealed the c-di-GMP response was a consequence of an increase in genotypic variants (in the form of wrinkled colonies) with naturally high c-di-GMP production. Here, it is possible that HIFU induced dispersal of wild type cells, leaving behind the wrinkled variants that overproduced c-di-GMP. Several consequences of changes in c-di-GMP concentration in a biofilm have been previously reported. In *P. aeruginosa*, changes in c-di-GMP resulted in functional changes in LapG, which then cleaved *cdrA* from the surface of the cell. Since Pel is also attached to *cdrA*, this polysaccharide is then released from the cell surface to enable dispersal (Rybtke et al., 2015). Moreover, increased c-di-GMP levels were also shown to inversely affect the quorum sensing regulated *rhl* and *pqs* systems (Chua et al., 2017). Thus, it is plausible that biofilms have a biological response to the mechanical stress from HIFU.

Our investigations also revealed that the mechanical stress by HIFU at higher pressures was probably due to two independent mechanisms: (i) non-linearity of the acoustic wave and (ii) inertial and stable cavitation leading to fluid streaming effects and acoustic radiation forces that exert shear stress on the biofilms (Nyborg, 2006; Stride and Coussios, 2019). Previously, the application of external shear in the form of fluid flow has shown increase in the c-di-GMP levels in planktonic *P. aeruginosa* and was associated with increased biofilm development (Rodesney et al., 2017). Thus, it is possible that HIFU was sensed through similar mechanosensing mechanisms. However, studies on bacterial mechanosensing are limited to the planktonic cells and its effect on biofilm is unknown (Gordon and Wang, 2019). It has been suggested that either changes in rotation of the flagella or the membrane protein PilYI may act as mechanosensors in *P. aeruginosa* and further work is needed to determine if these bacterial components are also involved in HIFU sensing (Siryaporn et al., 2014; Luo et al., 2015).

Although the results are promising, there are few limitations to our study. As the characterization techniques used were destructive, a before and after effect of ultrasound on the same sample was not possible. Instead, an untreated biofilm grown from the same overnight culture was considered as a control. This control may not exactly resemble the treated sample resulting in variability in our observations. Additionally, there were limitations for the transcriptomic and/or nucleotide analysis of the HIFU-treated biofilms (which may give more insight into the biological response) due to the amount of biomass available in the test system. HIFU is used in biological applications to focus sound waves to create a small volume of intense acoustic energy, thereby avoiding off-target side effects. Here, the focus is not a point in space but a small elliptical volume resembling a grain of rice with maximum intensity at the center. To reiterate, for a 0.5 MHz transducer, the focus has a 3 mm radial diameter (Bazan-Peregrino et al., 2012). Therefore, we believe that the microstructural and biological changes were localized to this area as was evident from the electrochemical and crystal violet data. Therefore, we are constrained to the volume of biofilm exposed to HIFU to study its effects. This localization amounted to a miniscule volume of bacteria extracted and post-processed for biological characterization thereby, limiting a direct quantification of c-di-GMP levels in the system. As a result, an indirect although efficient fluorescent bio-reporter was used. Future studies (beyond the scope of this report) will explore: (i) other acoustic parameters (duty cycle, HIFU frequency), (ii) different HIFU transducers (for e.g., multi-element transducers with focus of 6 mm radial diameter), (iii) introduction of cavitation agents (for e.g., polymeric nano-cups or multi-cavity shells) (Kwan et al., 2015; Su et al., 2019), and (iv) switching to a relatively dynamic flow-cell system for biofilm growth (Sternberg and Tolker-Nielsen, 2006) to address the limitations.

CONCLUSION

In summary, acoustic pressures equal to or greater than 4.5 MPa were optimal to observe HIFU-biofilm interactions. The cell viability studies showed that HIFU at 4.5 MPa removed bacteria from the surface although the complete removal was never achieved. Staining the exopolysaccharides revealed that HIFU penetrated the β-polysaccharides and was able to remove and/or degrade α-polysaccharides. Although, biofilm cells were removed from the surface, components of biofilm matrix still remained as observed from crystal violet and EIS studies. The most prominent observation was increase in the c-di-GMP signal after HIFU exposure suggesting that the remaining biofilms have a biological response to HIFU. Therefore, while investigating mechanical/physical approaches on biofilm, looking at the removal of biomass and change in microstructure is not sufficient. It is vital to track the transcriptomic response of the surviving biofilm in the future and our results are a first step toward showing the importance of such biological changes.

DATA AVAILABILITY STATEMENT

The raw data supporting the conclusions of this article will be made available by the authors, without undue reservation.

AUTHOR CONTRIBUTIONS

LDB, SR, and JK conceptualized the experiments for **Figures 1–4**, **6–8**. LDB, EM, and JK conceptualized and analyzed the experiments in **Figure 5**. LDB performed the experiments, produced **Figures 1–8** and wrote the manuscript. JK and LDB

wrote the MATLAB codes for confocal image analysis. All authors reviewed and edited the manuscript.

FUNDING

This work was financially supported by the Nanyang Technological University Start-Up Grant (04INS000246C110) and Singapore Centre for Environmental Life Sciences Engineering (SCELSE), whose research is supported by the National Research Foundation Singapore, Ministry of Education, Nanyang Technological University and National University of Singapore, under its Research Centre of Excellence Programme. This research is also supported by the Singapore Ministry of Health's National Medical Research Council under its NMRC/OFYIRG/0034/2017. EM was supported by the grant FDCRGP 110119FD4537, Nazarbayev University, Kazakhstan.

ACKNOWLEDGMENTS

We thank Mr. Chow Wai Hoong (Bobby) (School of Chemical and Biomedical engineering, NTU) for manufacturing the sample chambers used in the experiments. We also thank Dr. Umesh Jonnalagadda, Mr. Noel Sng, and Ms. Yifan Li (School of Chemical and Biomedical engineering, NTU) for their help. This work is part of thesis submitted to the Nanyang Technological University.

SUPPLEMENTARY MATERIAL

The Supplementary Material for this article can be found online at: https://www.frontiersin.org/articles/10.3389/fmicb.2020.599407/full#supplementary-material

REFERENCES

Agarwal, A., Jern, Ng, W., and Liu, Y. (2014). Removal of biofilms by intermittent low-intensity ultrasonication triggered bursting of microbubbles. *Biofouling* 30, 359–365. doi: 10.1080/08927014.2013.876624

Baird, F. J., Wadsworth, M. P., and Hill, J. E. (2012). Evaluation and optimization of multiple fluorophore analysis of a *Pseudomonas aeruginosa* biofilm. *J. Microbiol. Methods* 90, 192–196. doi: 10.1016/j.mimet.2012.05.004

Bazan-Peregrino, M., Arvanitis, C. D., Rifai, B., Seymour, L. W., and Coussios, C. C. (2012). Ultrasound-induced cavitation enhances the delivery and therapeutic efficacy of an oncolytic virus in an in vitro model. *J. Control. Release* 157, 235–242. doi: 10.1016/j.jconrel.2011.09.086

Beyenal, H., Donovan, C., Lewandowski, Z., and Harkin, G. (2004a). Three-dimensional biofilm structure quantification. *J. Microbiol. Methods* 59, 395–413. doi: 10.1016/j.mimet.2004.08.003

Beyenal, H., Lewandowski, Z., and Harkin, G. (2004b). Quantifying biofilm structure: facts and fiction. *Biofouling* 20, 1–23. doi: 10.1080/0892701042000191628

Bharatula, L. D., Marsili, E., and Kwan, J. J. (2020). Impedimetric detection of *Pseudomonas aeruginosa* attachment on fl exible ITO-coated polyethylene terephthalate substrates. *Electrochim. Acta* 332:135390. doi: 10.1016/j.electacta.2019.135390

Bigelow, T. A., Northagen, T., Hill, T. M., and Sailer, F. C. (2009). The destruction of *Escherichia coli* biofilms using high-intensity focused ultrasound. *Ultrasound Med. Biol.* 35, 1026–1031. doi: 10.1016/j.ultrasmedbio.2008.12.001

Brayman, A. A., MacConaghy, B. E., Wang, Y. N., Chan, K. T., Monsky, W. L., McClenny, A. J., et al. (2017). Inactivation of planktonic *Escherichia coli* by focused 2-MHz ultrasound. *Ultrasound Med. Biol.* 43, 1476–1485. doi: 10.1016/j.ultrasmedbio.2017.03.009

Cai, Y., Wang, J., Liu, X., Wang, R., and Xia, L. (2017). A review of the combination therapy of low frequency ultrasound with antibiotics. *Biomed Res. Int.* 2017:2317846. doi: 10.1155/2017/2317846

Chen, M. Y., Lee, D. J., Tay, J. H., and Show, K. Y. (2007). Staining of extracellular polymeric substances and cells in bioaggregates. *Appl. Microbiol. Biotechnol.* 75, 467–474. doi: 10.1007/s00253-006-0816-815

Chua, S. L., Hultqvist, L. D., Yuan, M., Rybtke, M., Nielsen, T. E., Givskov, M., et al. (2015a). In vitro and in vivo generation and characterization of *Pseudomonas aeruginosa* biofilm–dispersed cells via c-di-GMP manipulation. *Nat. Protoc.* 10, 1165–1180. doi: 10.1038/nprot.2015.067

Chua, S. L., Sivakumar, K., Rybtke, M., Yuan, M., Andersen, J. B., Nielsen, T. E., et al. (2015b). C-di-GMP regulates *Pseudomonas aeruginosa* stress response to tellurite during both planktonic and biofilm modes of growth. *Sci. Rep.* 5:10052. doi: 10.1038/srep10052

Chua, S. L., Liu, Y., Li, Y., Ting, H. J., Kohli, G. S., Cai, Z., et al. (2017). Reduced intracellular c-di-GMP content increases expression of quorum sensing-regulated genes in *Pseudomonas aeruginosa*. *Front. Cell. Infect. Microbiol.* 7:451. doi: 10.3389/fcimb.2017.00451

Dominguez-Benetton, X., Sevda, S., Vanbroekhoven, K., and Pant, D. (2012). The accurate use of impedance analysis for the study of microbial electrochemical systems. *Chem. Soc. Rev.* 41, 7228–7246. doi: 10.1039/c2cs35026b

Dong, Y., Xu, Y., Li, P., Wang, C., Cao, Y., and Yu, J. (2017). Antibiofilm effect of ultrasound combined with microbubbles against *Staphylococcus epidermidis* biofilm. *Int. J. Med. Microbiol.* 307, 321–328. doi: 10.1016/j.ijmm.2017.06.001

Erriu, M., Blus, C., Szmukler-Moncler, S., Buogo, S., Levi, R., Barbato, G., et al. (2014). Microbial biofilm modulation by ultrasound: current concepts and controversies. *Ultrason. Sonochem.* 21, 15–22. doi: 10.1016/j.ultsonch.2013.05.011

Flemming, H., and Wingender, J. (2010). The biofilm matrix. *Nat. Rev. Microbiol.* 8, 623–633. doi: 10.1038/nrmicro2415

Flemming, H. C., Wingender, J., Szewzyk, U., Steinberg, P., Rice, S. A., and Kjelleberg, S. (2016). Biofilms: an emergent form of bacterial life. *Nat. Rev. Microbiol.* 14, 563–575. doi: 10.1038/nrmicro.2016.94

Gordon, V. D., and Wang, L. (2019). Bacterial mechanosensing: the force will be with you, always. *J. Cell Sci.* 132:jcs227694. doi: 10.1242/jcs.227694

Ha, D.-G., and O'Toole, G. A. (2015). c-di-GMP and its effects on biofilm formation and dispersion: a *Pseudomonas Aeruginosa* review. *Microbiol. Spectr* 3:MB-0003-2014. doi: 10.1128/microbiolspec.mb-0003-2014

He, N., Hu, J., Liu, H., Zhu, T., Huang, B., Wang, X., et al. (2011). Enhancement of vancomycin activity against biofilms by using ultrasound-targeted microbubble destruction. *Antimicrob. Agents Chemother.* 55, 5331–5337. doi: 10.1128/AAC.00542-511

Hickman, J. W., Tifrea, D. F., and Harwood, C. S. (2005). A chemosensory system that regulates biofilm formation through modulation of cyclic diguanylate levels. *Proc. Natl. Acad. Sci. U S A.* 102, 14422–14427. doi: 10.1073/pnas.0507170102

Høiby, N., Bjarnsholt, T., Givskov, M., Molin, S., and Ciofu, O. (2010). Antibiotic resistance of bacterial biofilms. *Int. J. Antimicrob. Agents* 35, 322–332. doi: 10.1016/j.ijantimicag.2009.12.011

Holloway, B. W., Krishnapillai, V., and Morgan, A. F. (1979). Chromosomal genetics of *Pseudomonas*. *Microbiol. Rev.* 43, 73–102. doi: 10.1128/mmbr.43.1.73-102.1979

Iqbal, K., Ohl, S. W., Khoo, B. C., Neo, J., and Fawzy, A. S. (2013). Effect of high-intensity focused ultrasound on enterococcus faecalis planktonic suspensions and biofilms. *Ultrasound Med. Biol.* 39, 825–833. doi: 10.1016/j.ultrasmedbio.2012.12.006

Jennings, L. K., Storek, K. M., Ledvina, H. E., Coulon, C., Marmont, L. S., Sadovskaya, I., et al. (2015). Pel is a cationic exopolysaccharide that cross-links extracellular DNA in the *Pseudomonas aeruginosa* biofilm matrix. *Proc. Natl. Acad. Sci. U S A.* 112, 11353–11358. doi: 10.1073/pnas.1503058112

Jonnalagadda, U. S., Nguyen, T. M., Li, F., Lee, J. H. C., Liu, X., Goto, A., et al. (2020). Sol–Gel transitions of comb-like polymethacrylate copolymers by mechano-thermal stimuli in water. *Macromol. Chem. Phys.* 221:2000088. doi: 10.1002/macp.202000088

Kaplan, J. B. (2010). Biofilm dispersal: mechanisms, clinical implications, and potential therapeutic uses. *Crit. Rev. Oral Biol. Med.* 89, 205–218. doi: 10.1177/0022034509359403

Koibuchi, H., Fujii, Y., Hirai, Y., Mochizuki, T., Masuda, K., Kotani, K., et al. (2018). Effect of ultrasonic irradiation on bacterial biofilms. *J. Med. Ultrason.* 45, 25–29. doi: 10.1007/s10396-017-0801-x

Koo, H., Allan, R. N., Howlin, R. P., Stoodley, P., and Hall-Stoodley, L. (2017). Targeting microbial biofilms: current and prospective therapeutic strategies. *Nat. Rev. Microbiol.* 15, 740–755. doi: 10.1038/nrmicro.2017.99

Kwan, J. J., Myers, R., Coviello, C. M., Graham, S. M., Shah, A. R., Stride, E., et al. (2015). Ultrasound-Propelled nanocups for drug delivery. *Small* 11, 5305–5314. doi: 10.1002/smll.201501322

Lattwein, K. R., Shekhar, H., Kouijzer, J. J. P., van Wamel, W. J. B., Holland, C. K., and Kooiman, K. (2020). Sonobactericide: an emerging treatment strategy for bacterial infections. *Ultrasound Med. Biol.* 46, 193–215. doi: 10.1016/j.ultrasmedbio.2019.09.011

Lee, K. W. K., Periasamy, S., Mukherjee, M., Xie, C., Kjelleberg, S., and Rice, S. A. (2014). Biofilm development and enhanced stress resistance of a model, mixed-species community biofilm. *ISME J.* 6, 1137–1147. doi: 10.1038/ismej.2013.194

Lewandowski, Z., and Beyenal, H. (2007). *Fundamentals of Biofilm Research*. Boca Raton: CRC Press.

Luo, Y., Zhao, K., Baker, A. E., Kuchma, S. L., Coggan, K. A., Wolfgang, M. C., et al. (2015). A hierarchical cascade of second messengers regulates *Pseudomonas aeruginosa* surface behaviors. *MBio* 6:e02456-14. doi: 10.1128/mBio.02456-2414

LuTheryn, G., Glynne-Jones, P., Webb, J. S., and Carugo, D. (2019). Ultrasound-mediated therapies for the treatment of biofilms in chronic wounds: a review of present knowledge. *Microb. Biotechnol.* 13, 613–628. doi: 10.1111/1751-7915.13471

Ma, L., Lu, H., Sprinkle, A., Parsek, M. R., and Wozniak, D. J. (2007). *Pseudomonas aeruginosa* Psl is a galactose- and mannose-rich exopolysaccharide. *J. Bacteriol.* 189, 8353–8356. doi: 10.1128/JB.00620-627

Mann, E. E., and Wozniak, D. J. (2012). *Pseudomonas* biofilm matrix composition and niche biology. *FEMS Microbiol. Rev.* 36, 893–916. doi: 10.1111/j.1574-6976.2011.00322.x

Merritt, J. H., Kadouri, D. E., and O'Toole, G. A. (2005). ""Growing and analyzing static biofilms,"," in *Current Protocols in Microbiology*, eds R. Coico, T. Kowalik, J. Quarles, B. Stevenson, and R. Taylor (Hoboken, NJ: J. Wiley & Sons), doi: 10.1002/9780471729259.mc01b01s22

Mo, S., Coussios, C.-C., Seymour, L., and Carlisle, R. (2012). Ultrasound-enhanced drug delivery for cancer. *Exp. Opin. Drug Deliv.* 9, 1525–1538. doi: 10.1517/17425247.2012.739603

Nair, H. A. S., Periasamy, S., Yang, L., Kjelleberg, S., and Rice, S. A. (2017). Real Time, spatial, and temporal mapping of the distribution of c-di-GMP during biofilm development. *J. Biol. Chem.* 292, 477–487. doi: 10.1074/jbc.M116.746743

Nyborg, W. L. (2006). Ultrasound, contrast agents and biological cells; a simplified model for their interaction during in vitro experiments. *Ultrasound Med. Biol.* 32, 1557–1568. doi: 10.1016/j.ultrasmedbio.2006.05.032

Paliwal, S., and Mitragotri, S. (2006). Ultrasound-induced cavitation: applications in drug and gene delivery. *Exp. Opin. Drug Deliv.* 3, 713–726. doi: 10.1517/17425247.3.6.713

Pinto, R. M., Soares, F. A., Reis, S., Nunes, C., and Van Dijck, P. (2020). Innovative strategies toward the disassembly of the EPS matrix in bacterial biofilms. *Front. Microbiol.* 11:952. doi: 10.3389/fmicb.2020.00952

Qian, Z., Sagers, R. D., and Pitt, W. G. (1997). The effect of ultrasonic frequency upon enhanced killing of *P. aeruginosa* biofilms. *Ann. Biomed. Eng.* 25, 69–76. doi: 10.1007/BF02738539

Rodesney, C. A., Roman, B., Dhamani, N., Cooley, B. J., Katira, P., Touhami, A., et al. (2017). Mechanosensing of shear by *Pseudomonas aeruginosa* leads to increased levels of the cyclic-di-GMP signal initiating biofilm development. *Proc. Natl. Acad. Sci. U.S.A.* 114, 5906–5911. doi: 10.1073/pnas.1703255114

Rybtke, M., Berthelsen, J., Yang, L., Høiby, N., Givskov, M., and Tolker-Nielsen, T. (2015). The LapG protein plays a role in *Pseudomonas aeruginosa* biofilm formation by controlling the presence of the CdrA adhesin on the cell surface. *Microbiologyopen* 4, 917–930. doi: 10.1002/mbo3.301

Rybtke, M. T., Borlee, B. R., Murakami, K., Irie, Y., Hentzer, M., Nielsen, T. E., et al. (2012). Fluorescence-based reporter for gauging cyclic Di-GMP levels in *Pseudomonas aeruginosa*. *Appl. Environ. Microbiol.* 78, 5060–5069. doi: 10.1128/AEM.00414-412

Siryaporn, A., Kuchma, S. L., O'Toole, G. A., Gitai, Z., and Ausubel, F. M. (2014). Surface attachment induces *Pseudomonas aeruginosa* virulence. *Proc. Natl. Acad. Sci. U.S.A.* 111, 16860–16865. doi: 10.1073/pnas.1415712111

Sternberg, C., and Tolker-Nielsen, T. (2006). Growing and analyzing biofilms in flow cells. *Curr. Protocols Microbiol.* Chapter 1:Unit1B.210. doi: 1002/9780471729259.mc01b02s00

Stewart, P. S., and Costerton, J. W. (2001). Antibiotic resistance of bacteria in biofilms. *Lancet* 358, 135–138. doi: 10.1016/s0140-6736(01)05321-5321

Stewart, P. S., Murga, R., Srinivasan, R., and de Beer, D. (1995). Biofilm structural heterogeneity visualized by three microscopic methods. *Water Res.* 29, 2006–2009. doi: 10.1016/0043-1354(94)00339-339

Strathmann, M., Wingender, J., and Flemming, H. C. (2002). Application of fluorescently labelled lectins for the visualization and biochemical characterization of polysaccharides in biofilms of *Pseudomonas aeruginosa*. *J. Microbiol. Methods* 50, 237–248. doi: 10.1016/S0167-7012(02)00032-35

Stride, E., and Coussios, C. (2019). Nucleation, mapping and control of cavitation for drug delivery. *Nat. Rev. Phys.* 1, 495–509. doi: 10.1038/s42254-019-0074-y

Su, X., Thomas, R. G., Bharatula, L. D., and Kwan, J. J. (2019). Remote targeted implantation of sound-sensitive biodegradable multi-cavity microparticles with focused ultrasound. *Sci. Rep.* 9:9612. doi: 10.1038/s41598-019-46022-46020

Valentini, M., and Filloux, A. (2016). Biofilms and cyclic di-GMP (c-di-GMP) signaling: lessons from *Pseudomonas aeruginosa* and other bacteria. *J. Biol. Chem.* 291, 12547–12555. doi: 10.1074/jbc.R115.711507

Vyas, N., Manmi, K., Wang, Q., Jadhav, A. J., Barigou, M., Sammons, R. L., et al. (2019). Which parameters affect biofilm removal with acoustic cavitation? a review. *Ultrasound Med. Biol.* 45, 1044–1055. doi: 10.1016/j.ultrasmedbio.2019.01.002

Xu, J., Bigelow, T. A., Halverson, L. J., Middendorf, J. M., and Rusk, B. (2012). Minimization of treatment time for in vitro 1.1 MHz destruction of Pseudomonas aeruginosa biofilms by high-intensity focused ultrasound. *Ultrasonics* 52, 668–675. doi: 10.1016/j.ultras.2012.01.013

Yang, X., Beyenal, H., Harkin, G., and Lewandowski, Z. (2001). Evaluation of biofilm image thresholding methods. *Water Res.* 35, 1149–1158. doi: 10.1016/S0043-1354(00)00361-364

Zhang, C., Zhu, X., Li, F., Gao, F., Tu, J., and Zhang, D. (2019). Enhanced eradication of *Pseudomonas aeruginosa* bio-films by using ultrasound combined with neutrophil and antibiotics. *Appl. Acoust.* 152, 101–109. doi: 10.1016/j.apacoust.2019.03.028

Zhu, C., He, N., Cheng, T., Tan, H., Guo, Y., Chen, D., et al. (2013). Ultrasound-targeted microbubble destruction enhances human β-defensin 3 activity against antibiotic-resistant staphylococcus biofilms. *Inflammation* 36, 983–996. doi: 10.1007/s10753-013-9630-9632

Zhu, X., Rice, S. A., and Barraud, N. (2019). Nitric oxide and iron signaling cues have opposing effects on biofilm development in *Pseudomonas aeruginosa*. *Appl. Environ. Microbiol.* 85:e02175-02118. doi: 10.1128/AEM.02175-2118

Conflict of Interest: The authors declare that the research was conducted in the absence of any commercial or financial relationships that could be construed as a potential conflict of interest.

frontiers in Microbiology

ORIGINAL RESEARCH
published: 21 April 2021
doi: 10.3389/fmicb.2021.658521

An Improved 2-Aminoimidazole Based Anti-Biofilm Coating for Orthopedic Implants: Activity, Stability, and *in vivo* Biocompatibility

Guglielmo Attilio Coppola[1,2†], Jolien Onsea[3,4†], T. Fintan Moriarty[5], Dirk Nehrbass[5], Caroline Constant[5], Stephan Zeiter[5], Merve Kübra Aktan[6], Annabel Braem[6], Erik V. Van der Eycken[1,7], Hans P. Steenackers[2*] and Willem-Jan Metsemakers[3,4*]*

[1] KU Leuven – Department of Chemistry, Laboratory for Organic & Microwave-Assisted Chemistry (LOMAC), Leuven, Belgium, [2] KU Leuven – Department of Microbial and Molecular Systems, Centre of Microbial and Plant Genetics (CMPG), Leuven, Belgium, [3] Department of Trauma Surgery, University Hospitals Leuven, Leuven, Belgium, [4] KU Leuven – Department of Development and Regeneration, Leuven, Belgium, [5] AO Research Institute, Davos, Switzerland, [6] KU Leuven – Department of Materials Engineering (MTM), Biomaterials and Tissue Engineering Research Group, Leuven, Belgium, [7] Peoples' Friendship University of Russia, Moscow, Russia

Orthopedic device-related infections remain a serious challenge to treat. Central to these infections are bacterial biofilms that form on the orthopedic implant itself. These biofilms shield the bacteria from the host immune system and most common antibiotic drugs, which renders them essentially antibiotic-tolerant. There is an urgent clinical need for novel strategies to prevent these serious infections that do not involve conventional antibiotics. Recently, a novel antibiofilm coating for titanium surfaces was developed based on 5-(4-bromophenyl)-*N*-cyclopentyl-1-octyl-1*H*-imidazol-2-amine as an active biofilm inhibitor. In the current study we present an optimized coating protocol that allowed for a 5-fold higher load of this active compound, whilst shortening the manufacturing process. When applied to titanium disks, the newly optimized coating was resilient to the most common sterilization procedures and it induced a 1 log reduction in biofilm cells of a clinical *Staphylococcus aureus* isolate (JAR060131) *in vitro*, without affecting the planktonic phase. Moreover, the antibiofilm effect of the coating in combination with the antibiotic cefuroxime was higher than cefuroxime treatment alone. Furthermore, the coating was successfully applied to a human-scale fracture fixation device resulting in a loading that was comparable to the titanium disk model. Finally, an *in vivo* biocompatibility and healing study in a rabbit osteotomy model indicated that these coated implants did not negatively affect fracture healing or osteointegration. These findings put our technology one step closer to clinical trials, confirming its potential in fighting orthopedic infections without compromising healing.

Keywords: antibiofilm, titanium, implants, 2-aminoimidazole, coating, *Staphylococcus aureus*

OPEN ACCESS

Edited by:
Jessica Amber Jennings, University of Memphis, United States

Reviewed by:
Hariprasada Reddy Kanna Reddy, Curza Global, United States
Connor James Frapwell, Consultant, Bristol, United Kingdom

***Correspondence:**
Erik V. Van der Eycken
erik.vandereycken@kuleuven.be
Hans P. Steenackers
hans.steenackers@kuleuven.be
Willem-Jan Metsemakers
willem-jan.metsemakers@uzleuven.be

† These authors have contributed equally to this work and share first authorship

Specialty section:
This article was submitted to Antimicrobials, Resistance and Chemotherapy, a section of the journal Frontiers in Microbiology

Received: *25 January 2021*
Accepted: *19 March 2021*
Published: *21 April 2021*

Citation:
Coppola GA, Onsea J, Moriarty TF, Nehrbass D, Constant C, Zeiter S, Aktan MK, Braem A, Van der Eycken EV, Steenackers HP and Metsemakers W-J (2021) An Improved 2-Aminoimidazole Based Anti-Biofilm Coating for Orthopedic Implants: Activity, Stability, and in vivo Biocompatibility. Front. Microbiol. 12:658521. doi: 10.3389/fmicb.2021.658521

INTRODUCTION

Implanted devices are extensively used in orthopedic and trauma surgery to restore function and aid healing of broken bones. These interventions offer more rapid and accurate restoration of function and greatly improve the quality of life for the affected patient. Nonetheless, orthopedic device-related infection (ODRI) represents a major threat to the success of these surgical interventions. The incidence of ODRI ranges from 1 or 2% in case of elective joint replacement (Tande and Patel, 2014) up to 30% in complex open fractures where the protective barrier of the skin is breached (Papakostidis et al., 2011). *Staphylococcus aureus* and *Staphylococcus epidermidis* are the major pathogens in ODRI, accounting for more than half of all ODRIs (Moriarty et al., 2016).

The surface of the implant in fact serves as a substrate for bacterial attachment and the formation of biofilms, which are significantly more tolerant to antibiotics. The bacteria within the biofilm produce an extracellular polymeric substance (EPS), which can serve as a matrix that limits the penetration of antimicrobials and host immune cells into the biofilm. Therefore, intravenous antibiotic therapy alone is rarely successful in treating biofilm infections. Furthermore, exposure to low antibiotic concentrations exerts selective pressure which can lead to resistance development (Liu et al., 2011; Stanton et al., 2020).

ODRI imposes a significant burden on patients and healthcare systems due to the need for surgical revisions, long duration of antibiotic therapy, functional loss, and, sometimes, even the need for salvage procedures such as amputation of the affected limb or establishment of a continuous fistula (Metsemakers et al., 2016a). As a result, there is clear clinical need for innovative infection prevention strategies that do not rely on conventional antibiotic therapy. In this context, local delivery systems, such as antibacterial coatings or antibiotic loaded biomaterials have emerged as attractive means to support improved infection prevention (Metsemakers et al., 2020). Currently, most orthopedic implants are made out of metals such as stainless steel or titanium alloys, which lack an active antimicrobial surface that can prevent biofilm formation (Zhang et al., 2014; Metsemakers et al., 2016b). In addition to containing antibacterial components that are effective in preventing bacterial colonization and biofilm formation, active antimicrobial coatings should be biocompatible and should not elicit a significant foreign-body response. Furthermore, such a coating should not interfere with bone healing, and should display sufficient mechanical stability, so that it does not detach from the surface when placed under mechanical stress, as may be experienced during implant placement (Zhang et al., 2014). Finally, in times where antibiotic resistance is acknowledged as a worldwide problem, the development of non-antibiotic coatings seems crucial (Metsemakers et al., 2021). Numerous coatings have been developed over the years containing various bactericidal materials and molecules, such as silver-coated implants, implants coated with disinfectants like chlorhexidine and iodine, and antibiotic-coated implants (Zhang et al., 2014; Kuehl et al., 2016). Nonetheless, novel strategies focusing on biofilm formation and dispersal are gaining attention as their integration with conventional antimicrobial therapies could potentially lower the risk of toxicity and resistance development (Qvortrup et al., 2019).

Recently, we reported a 5-aryl-2-aminoimidazole (2-AI)-based antibiofilm coating specifically targeting biofilm formation (Peeters et al., 2019). The in-house discovered compound 1-(8-aminooctyl)-5-(4-bromophenyl)-*N*-cyclopentyl-1*H*-imidazol-2-amine (LC0024-NH_2) was successfully linked to a titanium surface resulting in a reduction in biofilm formation without affecting the planktonic phase. The mechanism of action has been partially elucidated in a study on *Salmonella* (Robijns et al., 2014) where 2-AIs strongly reduced the expression of genes (i.e., *csgD*, *csgB*, and *adrA*) involved in the production of the EPS. Inhibition of public goods such as EPS, without affecting cell viability, is less likely to impose a strong selective pressure for resistance (Allen et al., 2014). Consistently, our *in vitro* evolution and competition experiments showed that strains resistant to 2-AIs are counter selected, proving this strategy to be resilient to resistance development (Dieltjens et al., 2020). Since the ability to form mature biofilms is hindered in the presence of 2-AIs, perioperative contamination is less likely to result in biofilm formation on the surface of the coated device. Moreover, this strategy has the potential to prevent the life-long risk of hematogenous ODRI (Rakow et al., 2019), as the active compound is covalently bonded to the implant surface and is not released, like is the case for many other implant coatings.

In the present study, we aimed to optimize the 2-AI coating protocol to achieve a higher surface loading, a more efficient synthesis process and a higher coating stability, both for titanium disks and commercially available titanium fracture fixation devices. In addition, we evaluated the compatibility of the coating with the most common sterilization procedures and performed an *in vivo* safety study in a rabbit fracture model to determine the impact of the coating on fracture healing.

MATERIALS AND METHODS

Bacterial Strain and Chemicals

The bacterial strain *S. aureus* JAR060131, a clinical isolate originally cultured from a human patient with ODRI, was used in this study (culture collection of Switzerland number CCOS 890). Overnight cultures of *S. aureus* JAR060131 were grown in Lysogeny broth (LB), in test tubes at 37°C in shaking conditions. *In vitro* biofilm assays were performed using a 1/20 dilution of Tryptic Soy Broth (TSB 1/20). Phosphate-buffered saline (PBS) was prepared by combining 8.8 gL^{-1} NaCl, 1.24 gL^{-1} K_2HPO_4, and 0.39 gL^{-1} KH_2PO_4 (pH 7.4). LC0024-NH_2 was prepared as previously reported (Peeters et al., 2019). All other chemicals were purchased from commercial sources and used without further purification.

2-AI Covalent Binding on Titanium Disks, Locking Compression Plates, and Screws

Coating Procedure

Round titanium disks (Ti6Al4V alloy, grade 5; height: 4 mm; diameter: 12 mm, total surface area: 3.77 cm^2) were purchased from Salomon's Metalen bv (Groningen, Netherlands) and used for coating optimization and *in vitro* activity testing. Prior to functionalization, the disks were roughened by bead blasting with high purity Al_2O_3 particles (Elysee Dental Belgium NV). The surface was cleaned and activated by chemical etching using a 20 wt% HNO_3 and 4 wt% HF aqueous solution, followed by thorough washing with demineralized water and acetone. These disks without further functionalization are called control-Ti. To covalently bind the active compound, the surface was functionalized with amine groups by treatment with Fmoc-protected 3-aminopropyltriethoxy silane (Fmoc-APTES), followed by deprotection with tetrahydrofuran (THF)/piperidine (90:10) and thorough washing with THF. The silanization protocol was repeated three times. The hydrolysis solution was kept for the quantification of -NH_2 groups *via* UV-Vis spectroscopy. After drying, the aminated disks were placed in a 15 ml falcon tube containing a n-hexane/hexamethylene diisocyanate (HMDI; 85:15) solution (1 mL/disk), agitated for 3 h at room temperature with the aid of a roller mixer and then rinsed with *n*-hexane. Next, the disks were transferred to a solution of LC0024-NH_2 in DMSO, agitated for 16 h and rinsed with demineralized water and afterward with acetone. The rinsed samples were then dried at room temperature for 1 h. These disks are further referred to as LC0024-Ti. The titanium locking compression plates (LCPs) and screws, used in the *in vivo* study, were obtained from Depuy Synthes; Johnson & Johnson Co. Inc., NJ, United States. LCPs and screws were also etched and coated with LC0024-NH_2, as described above. Control LCPs and screws did not receive any treatment.

Quantification of -NH_2 Groups

The hydrolysis solutions from the Fmoc-deprotection procedure were used for quantification of the –NH_2 groups by means of UV-Vis spectroscopy (Carey 5000, Varian, United States). To this end, the solution was diluted ten times with THF/piperidine (90:10) and the absorbance at 300 nm was measured against a pure THF/piperidine (90:10) solution.

LC0024-NH_2 Loading Quantification

Quantification of the LC0024-NH_2 loading was performed, as previously reported (Peeters et al., 2019), by hydrolysis and detachment from the linker followed by analysis of the hydrolysis solution *via* fluorescence spectroscopy. Briefly, the coated supports were fully immersed in the appropriate amount of hydrolysis solution composed of deionized water, isopropanol, and triethylamine in 1:0.5:1 volume ratio. The mixture was heated at 60°C for 1 h. Fluorescence absorbance of LC0024-NH_2 of the hydrolysis solution was measured with a fluorescence spectrophotometer (FLS 920, Edinburgh Instruments, Photonics division) at excitation and emission wavelengths of 380 and 462 nm, respectively. The LC0024-NH_2 loading was calculated according to a calibration curve obtained from serial dilutions of known standards in the hydrolysis solvent.

Sterilization Procedures

The coated and non-coated LCPs and screws were double packed in sterilization foil (Steriking, Wipac medical, Bomlitz, Germany) and steam sterilized in a steam autoclave (Vapofix 3-3-6 VS1, Belimed, Zug, Switzerland). The sterilization cycle used saturated steam generated from de-ionized water and maintained at 134°C for 6 min at 3,100 mbar. The same protocol was applied to the titanium disks. Ethylene oxide sterilization of titanium disks was performed by 2 h exposure at 55°C and negative pressure (at least 80 mbar below atmospheric pressure).

In vitro Biofilm Inhibition Assay and Antibiotic Co-Administration

To compare the *in vitro* antibiofilm activity of the LC0024-Ti disks with the control-Ti, the LC0024-Ti disks were inoculated with *S. aureus* for 24 h and the number of colony forming units (CFUs) on the surface of the disks (biofilm) and in the supernatant (planktonic) were determined. The disks were sterilized by immersion in ethanol solution for 10 min and dried under a laminar flow. Afterward, the disks were wrapped with Teflon tape and fitted snuggly into silicon rubber rings placed in the wells of a 12-well plate to prevent biofilm formation on the sides and bottoms. A first preconditioning step was performed by pouring 400 μL of bovine serum albumin (BSA, Sigma-Aldrich, Europe) in the wells, sealing the plate with a sterile semi-permeable membrane and wrapping it with parafilm to prevent evaporation, and incubating it overnight at 37°C in a closed plastic bag. Thereafter, the BSA solutions were removed, and the exposed surfaces washed with PBS. Overnight cultures of *S. aureus* were diluted in TSB 1/20 medium and 400 μL of a 1×10^4 cells/mL suspension was poured over each disk and the plate was covered with a semipermeable membrane. After static incubation for 24 h at 37°C, the supernatants were removed, diluted and plated on LB plates. The disks were carefully washed with sterile PBS to remove loose cells and transferred to falcon tubes filled with 2 mL PBS. The tubes with the disks were vigorously vortexed for 1 min, sonicated for 10 min at 45,000 Hz in a water bath sonicator (VWR USC 300-T) and vortexed again for 1 min. The resulting bacterial suspensions were passed through a 25G needle to disrupt any remaining aggregates, diluted, and plated on LB plates. After 24 h of incubation at 37°C, the numbers of CFU/ml were determined by plate counting. Finally, CFU/cm^2 values were calculated accordingly by multiplying with the dispersion volume (2 ml) and dividing by the area of the exposed surface (1,13 cm^2). The *in vitro* activity of steam sterilized disks was assessed using the same protocol.

Additional biofilm experiments were performed as mentioned above, except for the addition of cefuroxime to evaluate the impact of the coating in the presence of a conventionally used antibiotic. In these experiments, after a 24-h incubation period, the supernatant was replaced with a 0,004 μg/ml cefuroxime solution in TSB 1/20 for the treated samples and regular TSB 1/20

for the control disks. A second incubation period of 24 h followed and afterward the disks were handled as described above.

Visualization of Biofilm

Biofilms were grown onto control-Ti and LC0024-Ti disks as described above. The samples were prepared for scanning electron microscopy (SEM) by fixation with glutaraldehyde, as previously described (De Brucker et al., 2015). After removal of loosely attached cells by gentle immersion of the disks in PBS, the samples were fixed with 2.5% glutaraldehyde (2.5% glutaraldehyde in cacodylate buffer [0.1 M, pH 7.4]) for 30 min and rinsed 3 times with PBS. Dehydration was performed through a series of ethanol washes (30, 50, 70, and 90% ethanol for 20 min each) followed by soaking in 100% ethanol for 20 min – each three times – and drying. Finally, the surface of the samples was sputter-coated with Pt (Q150/S, Quorum Technologies) and analyzed by SEM, operated at standard high-vacuum settings, and using a 4.8-mm working distance and 5-keV accelerating voltage using back-scattered electron (BSE) imaging.

Evaluation of Fracture Healing in a Rabbit Model

The impact of the LC0024 coating on fracture healing was evaluated *in vivo* in a rabbit model. The study was approved by the ethical committee of the canton of Grisons in Switzerland (approval number TVB_ 07_19). All procedures were performed in an Association for Assessment and Accreditation of Laboratory Animal Care International (AAALAC)-approved facility and according to Swiss animal protection law and regulations.

The model involved the creation of a mid-diaphyseal osteotomy in a rabbit humerus with plate fixation as previously described (Arens et al., 2015). The osteotomy was performed using a 0.44 mm Gigly saw (RISystem, Switzerland) and fixed with a 7-hole (coated or uncoated) titanium LCP and (coated or uncoated) six locking screws (central plate hole was left empty).

Animals

Nine skeletally mature female New Zealand white rabbits (Charles River, Sulzfeld, Germany) were used in this study. All animals underwent clinical examination and were found healthy prior to inclusion in this study. The animals were divided in two groups and implanted with coated (6 animals) or uncoated (3 animals) fracture fixation devices (LCPs). After 8 weeks, the animals were euthanized using intravenously administered pentobarbital (200 mg/kg; Esconarkon).

Clinical Observations

An animal caretaker checked the rabbits three times a day for the first post-operative week. Thereafter, all animals were monitored daily. Their general and eating behavior as well as weight-bearing on the operated leg was scored. The surgical incision, respiration, eyes, fur and feces were also monitored and logged. Blood samples were taken preoperatively, at day 3 and day 7 postoperatively, and were continued once a week thereafter. Blood and serum were used to measure white blood cell count (VET ABC, Scil animal care, Viernheim, Germany) and C-reactive protein (CRP; rabbit CRP ELISA Kit, ICL Inc. Portland, OR, United States), respectively. The weight of each animal was determined at the same timepoints. Radiographs of the operated limbs were taken in anteroposterior and lateral views postoperatively and every 2 weeks until euthanasia.

Histopathology

A post-mortem high-resolution contact radiograph was taken of the humerus of each animal in two directions (caudocranial and lateromedial). All humeri were fixed for a minimum of 2 weeks in 70% methanol. After fixation, samples were dehydrated through an ascending series of ethanol (70%, 96%, absolute ethanol) with two changes for each step, every 4–7 days. Samples were transferred to xylene and finally to methylmethacrylate (MMA) for embedding. The polymerized samples were trimmed on a butcher saw and glued to beracryl holders and sectioned using a Leica 1600 saw microtome. A high-resolution contact radiograph was taken of the sectioned bones. Sections were then stained with Giemsa Eosin. Imaging of the Giemsa Eosin stained sections was performed using brightfield illumination. A veterinary histopathologist performed a semi-quantitative histopathological analysis using a six-point grading system (grade 0: change absent, grade 1: minimal change, grade 2: slight change; grade 3: moderate change; grade 4: marked change; and grade 5: massive change). Median grades were calculated per group (coated vs. uncoated). Due to the different number of animals per group, the severity and incidence of changes was calculated per animal.

Statistical Analysis

All *in vitro* experiments were carried out in technical triplicates and were independently repeated at least three times. Statistical significance of the *in vitro* data was determined by applying a two-sided ratio paired *t*-test using GraphPad Prism version 9 (GraphPad Software, United States).

RESULTS

Improved Coating Procedure and Loading Analysis

An optimized protocol for the attachment of the active compound LC0024-NH_2 (**Figure 1A**) to titanium surfaces was developed. A schematic representation of the coating is presented in **Figure 1B**. The first step of the coating procedure consisted in functionalizing the titanium surface with Fmoc-APTES. When the reaction was carried out in an inert atmosphere the loading showed a slight increase compared to standard conditions. Nonetheless, higher surface loading could be obtained by multiple repetitions of the coating procedure. The graph in **Figure 1C** shows the increased loading following the increased number of repetitions. After cleavage of the Fmoc groups, LC0024-NH_2 was covalently bonded to the aminated surface using HMDI as a linker. This shortened the synthetic protocol with one step as compared to our previous report (Peeters et al., 2019). The amount of LC0024-NH_2 was measured by fluorescence spectroscopy

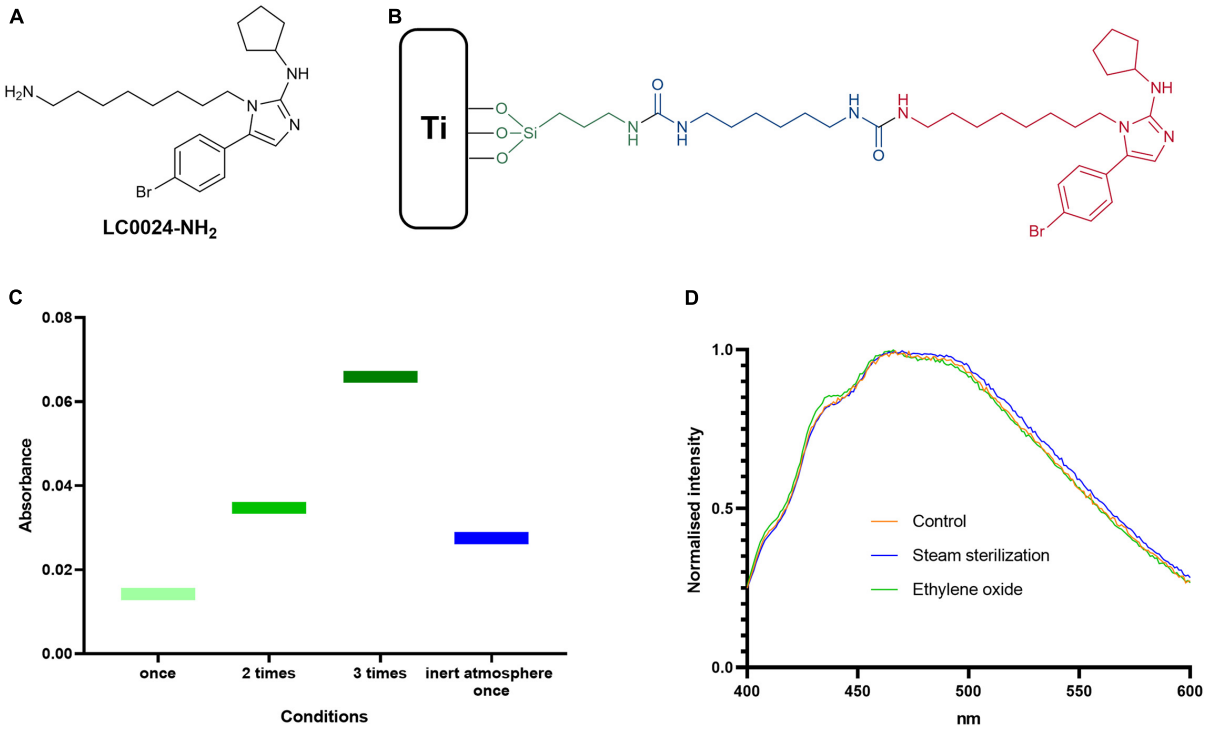

FIGURE 1 | Optimized coating and chemical analyses. **(A)** Schematic structure of LC0024-NH_2; **(B)** schematic representation of the coating sub-units; **(C)** results from the silanization step optimization; and **(D)** fluorescence emission profiles of the sterilized samples compared to the control disks.

as described in the Materials and Methods and resulted in a final loading of 50 nmol/cm^2. The presence of LC0024-NH_2 was also confirmed by scanning electron microscopy with associated energy-dispersive X-ray spectroscopy (SEM-EDX) (**Supplementary Table 2**). Stability of the coating was evaluated against two common sterilization procedures, steam sterilization and exposure to ethylene oxide. Therefore, the LC0024-Ti disks were sterilized using both techniques. After sterilization, the active compound was detached from the titanium surface by hydrolysis and the resultant solutions were analyzed *via* fluorescence spectroscopy. The fluorescence emission profiles of the two sterilization procedures did not show a significant difference compared to the profile of the control disks (**Figure 1D**).

In vitro Antibiofilm Activity Evaluation

After optimizing the coating procedure, we continued with *in vitro* evaluation of the antibiofilm activity. In order to provide relevant data for future *in vivo* studies, a clinical isolate of *S. aureus* (JAR06.01.31), was chosen. As shown in **Figure 2A**, biofilm formation after 24 h was significantly affected with an average decrease of biofilm cells with 1 log (92% reduction; remaining cells: 1,06 × 10^5 CFU/cm^2) for LC0024-Ti compared to the control-Ti, whilst planktonic cells were not affected. Similarly, SEM pictures, of fixed biofilms showed a strong difference in biofilm growth (**Figures 2D,E**). The surface of LC0024-Ti disks was populated mainly by isolated cells whereas aggregates of biofilm cells were visible on the control-Ti disks (**Figures 2D,E**). This finding is in accordance with the described mechanism of action of 2-AI, i.e., inhibiting matrix production (Robijns et al., 2014; Peeters et al., 2019).

A second set of experiments was carried out to evaluate the combined activity of the coating and a classic antibiotic. Biofilms were set to grow for 24 h on coated and uncoated titanium disks, after which the biofilms were submerged in a cefuroxime solution at 0.004 μg/ml in TSB 1/20 for an additional 24 h. For the untreated control group, the supernatant was replaced with fresh TSB 1/20. The treatment with cefuroxime alone caused a 80% reduction in biofilm cells (remaining cells: 8.28 × 10^4 CFU/cm^2; **Figure 2B**) while the coating alone caused a 90% reduction (remaining cells: 3,64 × 10^4 CFU/cm^2) demonstrating resilience to biofilm formation also after 48 h. The combined effect of the two treatments resulted in a significant ($p = 0.0498$) further reduction of 14% (-5.28 × 10^4 CFU/cm^2) compared to cefuroxime alone and the remaining biofilm cells accounted for only ∼6% (94% reduction; remaining cells: 3.02 × 10^4 CFU/cm^2) compared to the control. The activity of the antibiotic against cells on the Control-Ti surface [79.45% ± 6.17 (SE) reduction upon cefuroxime treatment] and the LC0024-Ti surface [24.81% ± 36.91 (SE) reduction upon cefuroxime treatment] did not significantly differ ($p = 0.2182$). Before attempting the *in vivo* experiments, activity retention after sterilization was tested *in vitro* using steam sterilized disks. The results showed that activity was retained (93 and 92%

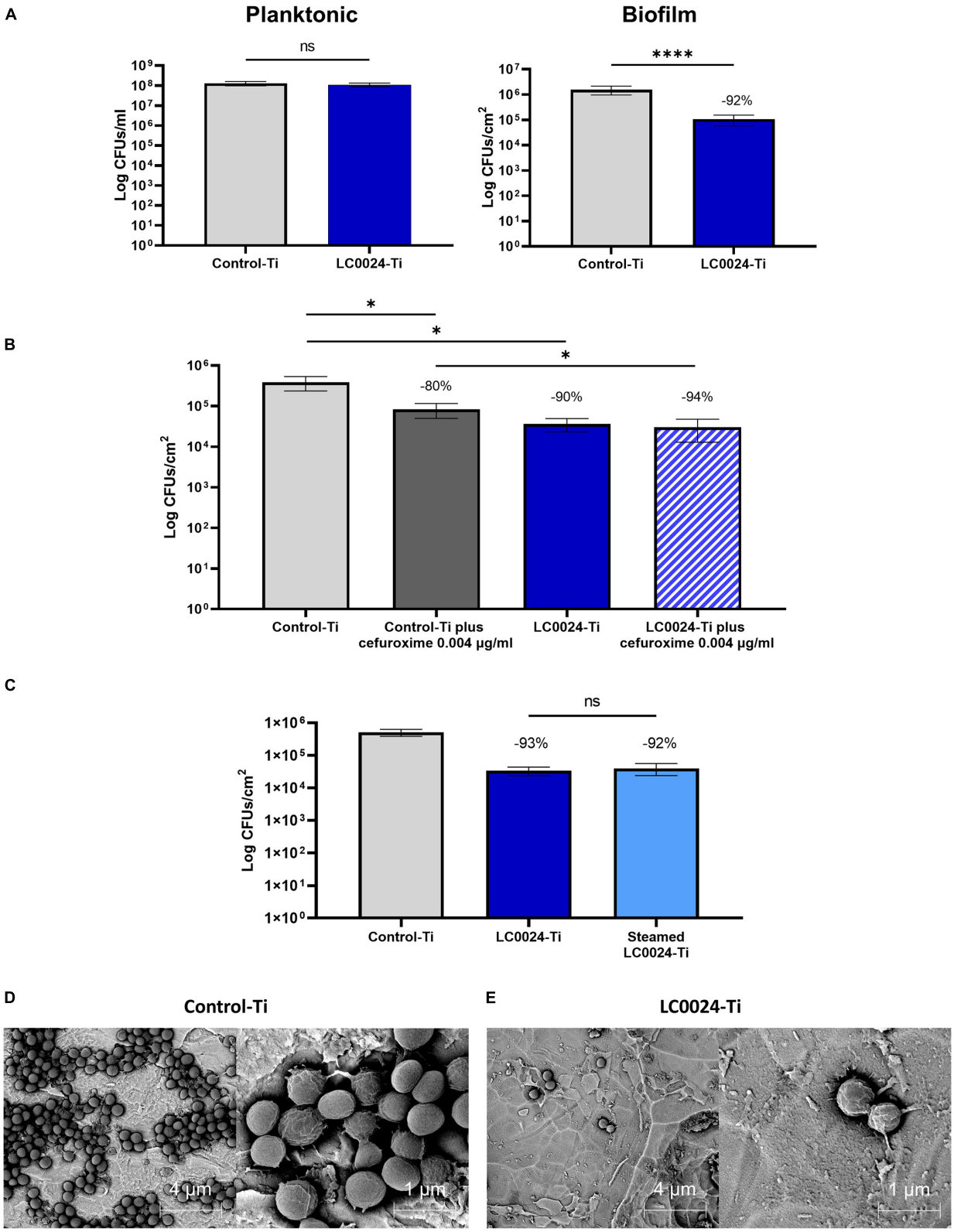

FIGURE 2 | Overview of *in vitro* activity evaluation. **(A)** *In vitro* characterization of planktonic growth and biofilm formation of *S. aureus* JAR060131 on LC0024-Ti disks. Data represent the mean of at least three independent experiments, the error bars show the standard error of the mean (SE). Statistical significance was determined by applying a two-sided ratio paired *t*-test using GraphPad Prism (ns, not significant; ****$p < 0.0001$), the average relative reduction compared to the

(Continued)

FIGURE 2 | Continued
untreated Control-Ti is reported as percentage; **(B)** *In vitro* evaluation of the effect of low concentration of cefuroxime (0.004 μg/ml) on biofilm cells present on the surface of the LC0024-Ti disks as compared to the control-Ti disks. Data represent the mean of three independent experiments, the error bars show the standard error of the mean (SE). Statistical significance was determined by applying two-sided ratio paired *t*-test using GraphPad Prism (*$p < 0.05$), the average relative reduction compared to the untreated Control-Ti is reported as percentage; **(C)** *In vitro* evaluation of the effect of steam sterilization on the LC0024-Ti disks as compared to the control-Ti disks and non-sterilized LC0024-Ti disks. Averages of biofilm cells from three technical replicates are reported. Data represent the mean of three independent experiments, the error bars show the standard error of the mean (SE). Statistical significance was determined by applying a two-sided ratio paired *t*-test using GraphPad Prism (ns, not significant), the average relative reduction compared to the untreated Control-Ti is reported as percentage; **(D)** Representative SEM-BSE images of a fixed biofilm grown on control-Ti disks; and **(E)** Representative SEM-BSE images of a fixed biofilm grown on LC0024-Ti disks.

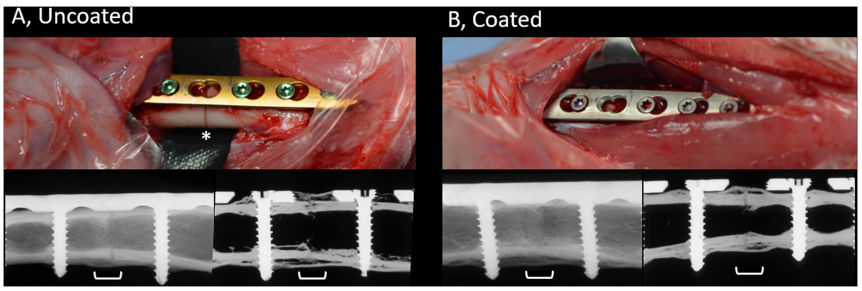

FIGURE 3 | Appearance of uncoated **(A)** and 2-AI-based coated **(B)** plates during placement and radiographic appearance of healing at time of study completion. Upper row, intra-operative pictures of the surgical site prior to wound closure showing LCPs being fixed to the bone. Skeletally mature rabbits received a 7-hole LCP and six screws. Note the position of the osteotomy beneath the empty screw hole on left hand side image (asterisk). The uncoated plates and screws are as purchased with coloring due to anodization. The color of the coated plates and screws match, due to the coating process that was applied. Lower row, post-mortem contact radiographs of the bone (left) or after sectioning (right), centered on the osteotomy (white bracket). Note the complete bridging of the osteotomy gap and the formation of periosteal callus at the osteotomy site. The osteotomy is still visible indicative of ongoing healing. Images were randomly selected as representative of the entire group.

reduction for LC0024-Ti and steamed sterilized LC0024-Ti disks, respectively; **Figure 2C**).

Histopathological and Radiographical Evaluation

The contact radiographs of rabbits in the coated and uncoated groups 8 weeks after osteotomy are shown in **Figure 3**. In the uncoated group (**Figure 3A**), where rabbits received commercially available medical grade titanium LCPs, healing progressed well and there was bridging of the osteotomy and a physiological presence of periosteal callus at the osteotomy site. Similarly, rabbits in the coated group (**Figure 3B**) also displayed healing of the osteotomy and a similar periosteal callus appearance as the uncoated group. In both the coated and uncoated groups, healing was not yet totally completed, as revealed by sections through the bone (lower right-hand image in **Figures 3A,B**), and no differences were observed between the groups based on visual inspection of contact radiographs.

The semi-quantitative histological evaluation of coated/non-coated plates and screws and the local tissues is shown in **Figure 4**. The data points from each evaluation showed a rather homogenous response among the different animals. The few scores that notably differ are due to inherent variability of the model as they are not attributable to the discordant response of one single animal. This variability can be associated with mechanical effects caused by minor differences in plate and screw placement, as well as intrinsic limitations in the sampling method whereby a three-dimensional object is scored on a single longitudinal section. In general, the score for fracture healing (**Figure 4A**) shows equivalent healing in both groups at both the *cis* and *trans* cortex, consistent with the radiographic appearance shown in **Figure 3**. Similarly, periosteal callus (**Figure 4B**) at both the *cis* and *trans* side were similar between groups, and at a moderate to high grade consistent with the radiographic signs. A moderate increase of cortical porosity near the osteotomy site and a minimal to moderate cortical thinning (attributed to stress-shielding) was found in both groups.

Direct osteointegration (segments with direct bone-implant contact) was also comparable between both groups, with a relatively low score in both groups for both the plates and screws (**Figure 4C**). Microscopic images of the Giemsa Eosin-stained sections show the osteointegration of plates and screws in the uncoated group [**Figure 5A** (magnified in B) and C, respectively] and in the coated group [**Figure 5E** (magnified in F) and G]. There was greater direct bone-implant contact around the screws compared to the plates, without any marked differences between the coated and uncoated groups.

The severity of the inflammatory cell infiltration was also scored (**Figure 4D**) and microscopic images are shown in **Figures 5D,H** for the uncoated and coated groups, respectively). Any observed inflammation was either serous (formation of fluid- and cell-filled space) and/or mononuclear (lymphoplasmacellular cell infiltration). Generally, it was relatively low and broadly equivalent between both groups. No inflammatory cell infiltration was recorded in the osteotomy gap or bone marrow (not shown).

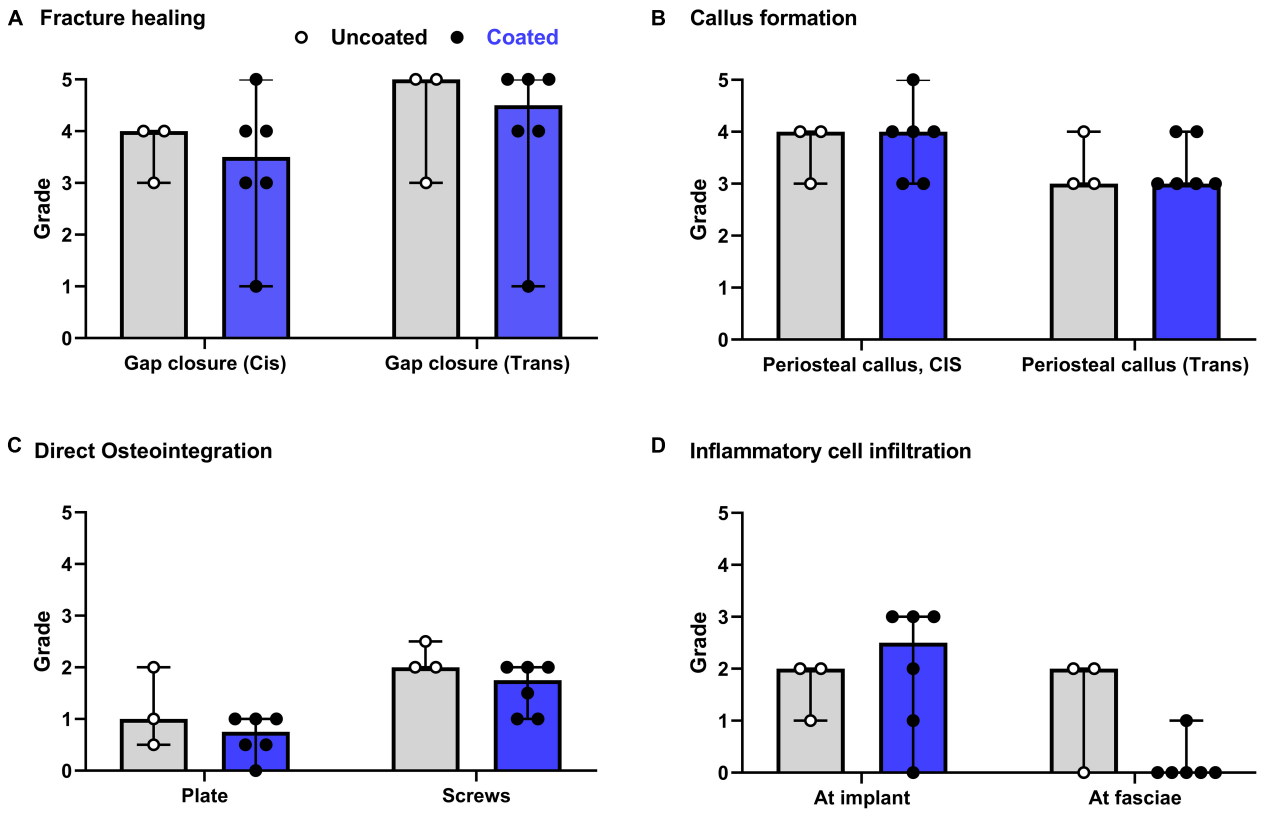

FIGURE 4 | Overview of histological evaluation of rabbits receiving coated and uncoated screws. **(A)** Fracture healing; **(B)** callus formation; **(C)** direct osteointegration; **(D)** inflammatory cell infiltration. Rabbits were euthanized 8 weeks after osteotomy and fixation with uncoated (gray bars [median/group], white dots [individual values]) or coated (blue bars, black dots) LCPs and screws. The entire operated bone was fixed, embedded in polymethylmethacrylate (PMMA), sectioned and stained with Giemsa Eosin. Semi-quantitative histological scores (0–5) were given by a blinded veterinary pathologist for a group of $n = 6$ rabbits receiving coated implants and $n = 3$ rabbits receiving uncoated implants. Features were scored for the entire section. Error bars represent the range. No statistical comparisons made.

DISCUSSION

The eradication of ODRI is challenging due to the presence of a biofilm that forms a physical and chemical barrier, thereby protecting bacteria from antibiotics and host defenses. Moreover, reduced metabolic activity of bacteria within the biofilm further reduces the activity of certain antibiotics. Biofilms also offer protection against phagocytes by offering mechanical protection and preventing the engulfment process as described for *S. aureus* (Thurlow et al., 2011). In addition, treatment of ODRI becomes challenging when compromised vascularization at the surgical site hampers the penetration of antibiotics and vital components of the immune system. Therefore, biofilm formation should be considered the key target in tackling ODRI. As an example, surface modification by covalent attachment of an antibiofilm-specific compound has shown to prevent ODRI by inhibiting bacterial colonization while on the other hand allowing tissue integration (Seebach and Kubatzky, 2019).

This study presents our latest progress regarding the development of an antibiofilm coating for titanium implants *via* covalent binding of 2-AI LC0024-NH_2. Recently, we reported our first results regarding the application of 2-AI in the prevention of *S. aureus* biofilm formation on titanium surfaces (Peeters et al., 2019). *In vitro* experiments and *in vivo* data in a biomaterial-associated murine infection model proved the retention of activity of the LC0024-NH_2 when covalently bonded onto titanium. In the present work we have optimized the coating procedure by shortening the synthetic route by one step, and achieved a 5-fold increase in surface density as compared to our earlier results. The previously adopted procedure for covalent binding LC0024-NH_2 onto the titanium surface consisted of functionalization with carboxylic moieties followed by amide coupling with LC0024-NH_2 *via* a four step synthesis (Peeters et al., 2019). Specifically, amination of the titanium oxide layer was performed *via* a single step of silanization using APTES. The aminated surface was then reacted with HMDI, followed by reaction with a 6-aminohexanoic acid solution for 16 h. HMDI hereby acted as a linker between aminopropyl silane and 6-aminohexanoic acid. Finally, LC0024-NH_2 was bonded *via* amide synthesis to the carboxylic moieties hanging from the surface. This resulted in a LC0024-NH_2 loading of 10.1 nmol/cm^2. In the present study, we attempted to improve several steps in this coating procedure and increase the loading. We started with the optimization of the silanization step. Literature studies

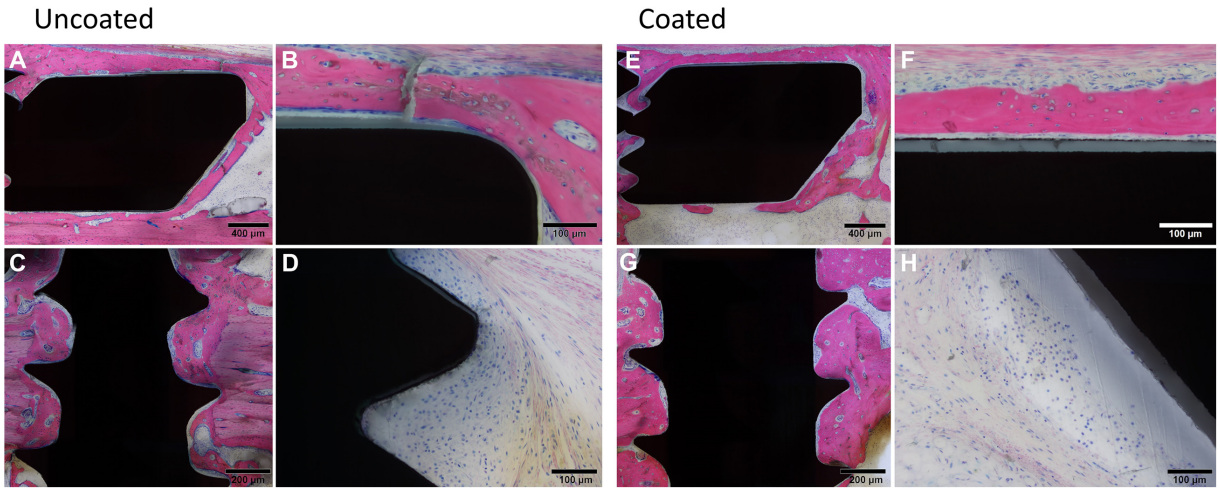

FIGURE 5 | Histological images of rabbits receiving Left, uncoated, or Right, coated LCPs and screws. At euthanasia, 8 weeks after surgery, rabbits were submitted for histopathological processing and evaluation. Giemsa Eosin-stained sections of the plate **(A,E)** and screws **(C,G)** are shown that are indicative of typical findings. **(B,F)** show higher magnification images of **(A,E)**, respectively. Note the greater bone-implant contact for the screws relative to the plates and a lack of significant differences between the groups. Low to moderate grade infiltration with inflammatory cells was also observed (uncoated, **D** and coated **H**) again without marked differences between the groups. Images were selected as representative of features observed.

suggested that an inert atmosphere could have a positive effect on the attachment of silanes onto surfaces (Zhu et al., 2012). Degassing and purging nitrogen gas into the Fmoc-APTES solution indeed caused a slight increase in loading (**Figure 1C**). Nonetheless, simple repetition of the standard procedure without use of an inert atmosphere resulted in an even higher surface density. To simplify later upscaling of the coating procedure, the inert atmosphere option was not further adopted. Furthermore, since LC0024-NH_2 could potentially react directly with HMDI without the need for adding the aminoacidic linker, we speculated that this lengthy step could be avoided. This was indeed confirmed by the observed increase in overall yield. Moreover, the absence of the hydrolysable amide bond associated with the aminoacidic linker can have the additional benefit of making the coating more resistant to deactivation processes (i.e. chemical or enzymatic hydrolysis) and thus retaining activity for a longer period. Nonetheless, reduction in the chain length, and possibly flexibility, could have an effect on the biological activity. Therefore, *in vitro* experiments were carried out to ensure retention of activity.

In vitro antibiofilm activity of the newly optimized LC0024-Ti disks was assessed against the clinical *S. aureus* isolate JAR06.01.31. The number of biofilm cells onto LC0024-Ti disks surface was reduced on average with more than 90% compared to the uncoated control-Ti disks. In our previous report, LC0024-NH_2 coating led to a 47% reduction in biofilm cells (Peeters et al., 2019). These results also confirmed that the reduction in length of the chain was not detrimental to activity. As the viability of planktonic cells was not significantly affected, this enhanced activity solely targeted biofilm formation. To gain further insights in our strategy, we compared the effect of antibiotic treatment on biofilms grown onto LC0024-Ti and control-Ti disks. Since 2-AIs target EPS production, the integrity of the biofilm matrix is expected to be compromised (Mongkolrob et al., 2015). Consequently, antibiotic treatment might show a stronger effect in the presence of the coating. This would have a beneficial impact on the resolution of ODRIs allowing for shorter antibiotic therapies at lower concentrations. Cefuroxime was the antibiotic of choice in this study as it is commonly employed in daily clinical practice and well tolerated by rabbits. We selected a cefuroxime concentration of 0.004 μg/ml that is much lower than the MBC and MBEC (**Supplementary Table 3**), because at such suboptimal antibiotic concentration the tolerance effects of the biofilm, and thus potential effects of the antibiofilm coating on antibiotic efficacy, are expected to be most pronounced. We observed a similar activity of the antibiotic against bacterial cells on the antibiofilm coated and uncoated surface. The combined effect of cefuroxime with the coating (94% reduction compared control-Ti) was therefore higher than that of cefuroxime alone (80% reduction compared to control-Ti). The anticipated higher efficacy of the antibiotic against cells on the anti-biofilm surface, which we previously reported for *Salmonella* (Dieltjens et al., 2020), was, however, not observed. This might be related to the difference in bacterial target species, but also to the longer antibiotic treatment period in the current experiment [24 h vs 1 h in our previous report (Dieltjens et al., 2020)] which might have introduced additional effects such as partial antibiotic degradation, re-attachment of dispersed bacterial cells and/or antibiotic resistance. The current study focused on effects of the coating on early colonization and early stage biofilm formation (up to 48 h). In future studies we plan to implement flow-cell devices for biofilm formation and monitoring. Continuous flow of fresh medium ensures the constant supply of nutrients for prolonged periods of time. This will allow us to study the effect of the coating on biofilm maturation. Moreover, we aim to extend

our focus on other clinically relevant strains and species (e.g., *S. epidermidis)*.

Before proceeding with the preparation of the LCPs for the *in vivo* evaluation, stability of the coating to conventional sterilization procedures was assessed. Heat treatment as well as chemical sterilization can affect coating activity by hydrolysis of the active compound or the linker (Duncan et al., 1998; Preem et al., 2019). Other undesired reactions such as oxidation or radical formation can also compromise the coating activity. The coating was therefore challenged with steam sterilization and exposure to ethylene oxide, two commonly used procedures for implant sterilization. Analysis of the hydrolysis solutions from sterilized samples did not show significant variations compared to the untreated LC0024-Ti disks. Moreover, antibiofilm activity of steam sterilized LC0024-Ti disks was confirmed *in vitro*. These results are of crucial importance prior to preclinical validation in living animals. Finally, the coating procedure was applied to LCPs and screws and the presence of the active compound on the surface was confirmed by fluorescence spectrophotometry.

Implant biocompatibility is of crucial importance for the success of orthopedic procedures and patient outcome. Although it is true that fracture fixation devices may be removed after fracture healing, which makes direct osteointegration less important, biomechanical stability of the implant plays a crucial role in fracture healing. Moreover, stability is an important aspect with respect to prevention and treatment of infection, due to a vicious cycle between instability, ongoing soft tissue trauma and osteolysis (Foster et al., 2021). Stability of the fractured bone, that is provided by fracture fixation devices (e.g., plates and screws), requires a biocompatible surface that does not lead to inflammation or loss of local bone (i.e., osteolysis) at the bone-implant interface. The interaction of host and implant is significantly impacted by the surface of the implant and is first of all influenced by an initial conditioning layer of host proteins, followed later by fibroblast adhesion and later bone forming cells (osteoprogenitor cells and osteoblasts; Nuss and Rechenberg, 2008). Interference with any of these phases due to physicochemical properties of the implant surface can undermine the success of the surgery, and, therefore, needs careful evaluation. In our previous study, evaluation of the *in vitro* osteointegration potential [use of human bone marrow-derived stromal cells (MSC) and human microvascular endothelial cells (HMVEC)] and *in vivo* osteointegration in a rat model showed a positive outcome (Peeters et al., 2019). To further validate the applicability, the current study provides evidence for the biocompatibility of the coating in a rabbit fracture model. Histological evaluation showed that the grade of osteotomy gap closure and of periosteal callus formation were high and comparable for both groups. This confirms that the 2-AI coating does not interfere with fracture healing. Furthermore, both groups showed a low and similar amount of inflammatory cell infiltration.

In conclusion, this study reported on an optimized coating procedure to covalently bind the antibiofilm compound LC0024-NH_2 on titanium surfaces. This resulted in higher loading and an enhanced activity *in vitro*. When applied to fracture fixation devices the coating did not negatively affect fracture healing in a rabbit fracture model. These positive results pave the way for future translational studies where we aim to confirm the effectiveness of the optimized coating against infection *in vivo*. Furthermore, they put our technology one step closer to clinical trials, confirming its potential in fighting ODRI without inducing local toxicity.

DATA AVAILABILITY STATEMENT

The raw data supporting the conclusions of this article will be made available by the authors, without undue reservation.

ETHICS STATEMENT

The animal study was reviewed and approved by ethical committee of the canton of Grisons in Switzerland (approval number TVB_ 07_19).

AUTHOR CONTRIBUTIONS

GC performed the synthesis, chemical analysis, and *in vitro* activity tests. JO prepared and contributed to the surgeries and performed dissections. SZ and CC performed the surgeries. MK performed SEM analysis. DN performed the histopathological and radiographical evaluation. GC, JO, TM, HS, and W-JM wrote and revised the manuscript. EV, CC, SZ, and AB revised the manuscript. EV, HS, and W-JM contributed to project administration and funding acquisition. All authors contributed to the article and approved the submitted version.

FUNDING

This work was supported by the KU Leuven Research Fund (C32/17/020), by FWO-Vlaanderen under grant 3G046318, and grant FWO-SBO S007019N (Bisceps). EV acknowledges the support by the RUDN University Strategic Academic Leadership Program. AB acknowledges the receipt of a starting grant from Internal Funds KU Leuven (STG/17/024).

SUPPLEMENTARY MATERIAL

The Supplementary Material for this article can be found online at: https://www.frontiersin.org/articles/10.3389/fmicb.2021.658521/full#supplementary-material

Supplementary Table 1 | SEM-EDX analysis of control-Ti.

Supplementary Table 2 | SEM-EDX analysis of LC0024-Ti.

Supplementary Table 3 | Susceptibility of *S. aureus* JAR060131 to cefuroxime.

REFERENCES

Allen, R. C., Popat, R., Diggle, S. P., and Brown, S. P. (2014). Targeting virulence: can we make evolution-proof drugs? *Nat. Rev. Microbiol.* 12, 300–308. doi: 10.1038/nrmicro3232

Arens, D., Wilke, M., Calabro, L., Hackl, S., Zeiter, S., Zderic, I., et al. (2015). A rabbit humerus model of plating and nailing osteosynthesis with and without *Staphylococcus aureus* osteomyelitis. *Eur. Cell. Mater.* 30, 148–162. doi: 10.22203/ecm.v030a11

De Brucker, K., Tan, Y., Vints, K., De Cremer, K., Braem, A., Verstraeten, N., et al. (2015). Fungal -1,3-Glucan increases ofloxacin tolerance of *Escherichia coli* in a polymicrobial *E. coli*/*Candida albicans* biofilm. *Antimicrob. Agents Ch.* 59, 3052–3058. doi: 10.1128/AAC.04650-14

Dieltjens, L., Appermans, A., Lissens, M., Lories, B., Kim, W., Van der Eycken, E. V., et al. (2020). Inhibiting bacterial cooperation is an evolutionarily robust anti-biofilm strategy. *Nat. Commun.* 11:107. doi: 10.1038/s41467-019-13660

Duncan, M. R., Wang, P., and Moldenhauer, J. E. (1998). Determining the capability of a drug product to be terminally sterilized: a case study involving a heat-sensitive. *Oxygen Sens. Drug Product. Pharm. Dev. Technol.* 3, 527–534. doi: 10.3109/10837459809028635

Foster, A. L., Moriarty, T. F., Zalavras, C., Morgenstern, M., Jaiprakash, A., Crawford, R., et al. (2021). The influence of biomechanical stability on bone healing and fracture-related infection: the legacy of Stephan Perren. *Injury* 52, 43–52. doi: 10.1016/j.injury.2020.06.044

Kuehl, R., Brunetto, P. S., Woischnig, A. K., Varisco, M., Rajacic, Z., Vosbeck, J., et al. (2016). Preventing implant-associated infections by silver coating. *Antimicrob. Agents Chemother.* 60, 2467–2475. doi: 10.1128/AAC.02934-15

Liu, A., Fong, A., Becket, E., Yuan, J., Tamae, C., Medrano, L., et al. (2011). Selective advantage of resistant strains at trace levels of Antibiotics: a simple and ultrasensitive color test for detectionof antibiotics and genotoxic agents. *Antimicrob. Agents Chemother.* 55, 204–1210. doi: 10.1128/AAC.01182-10

Metsemakers, W. J., Fragomen, A. T., Moriarty, T. F., Morgenstern, M., Egol, K. A., Zalavras, C., et al. (2020). Evidence-based recommendations for local antimicrobial strategies and dead space management in fracture-related infection. *J. Orthop. Trauma.* 34, 18–29. doi: 10.1097/BOT.0000000000001615

Metsemakers, W. J., Kuehl, R., Moriarty, T. F., Richards, R. G., Verhofstad, M. H., Borens, O., et al. (2016a). Infection after fracture fixation: current surgical and microbiological concepts. *Injury* 49, 511–522. doi: 10.1016/j.injury.2016.09.019

Metsemakers, W. J., Schmid, T., Zeiter, S., Ernst, M., Keller, I., Cosmelli, N., et al. (2016b). Titanium and steel fracture fixation plates with different surface topographies: Influence on infection rate in a rabbit fracture model. *Injury* 47, 633–639. doi: 10.1016/j.injury.2016.01.011

Metsemakers, W. J., Zalavras, C., Schwarz, E., Chen, A., Trampuz, A., and Moriarty, T. F. (2021). Antimicrobial resistance, the COVID-19 pandemic, and lessons for the orthopaedic community. *J. Bone Joint Surg. Am.* 103, 4–9. doi: 10.2106/JBJS.20.01214

Mongkolrob, R., Taweechaisupapong, S., and Tungpradabkul, S. (2015). Correlation between biofilm production, antibioticsusceptibility and exopolysaccharide compositionin *Burkholderia pseudomallei* bpsI, ppk, andrpo Smutant strains. *Microbiol. Immunol.* 59, 653–663. doi: 10.1111/1348-0421.12331

Moriarty, T. F., Kuehl, R., Coenye, T., Metsemakers, W. J., Morgenstern, M., Schwarz, E. M., et al. (2016). Orthopaedic device-related infection: current and future interventions for improved prevention and treatment. *EFORT Open. Rev.* 1, 89–99. doi: 10.1302/2058-5241.1.000037

Nuss, K. M. R., and Rechenberg, B. V. (2008). Biocompatibility issues with modern implants in bone – A review for clinical orthopedics. *Open Orthop. J.* 2, 66–78. doi: 10.2174/1874325000802010066

Papakostidis, C., Kanakaris, N. K., Pretel, J., Faour, O., Morell, D. J., and Giannoudis, P. V. (2011). Prevalence of complications of open tibial shaft fractures stratified as per the Gustilo-Anderson classification. *Injury* 42, 1408–1415. doi: 10.1016/j.injury.2011.10.015

Peeters, E., Hooyberghs, G., Robijns, S., De Weerdt, A., Kucharíková, S., Tournu, H., et al. (2019). An antibiofilm coating of 5-aryl-2-aminoimidazole covalently attached to a titanium surface. *J. Biomed. Mater. Res. B Appl. Biomater.* 107, 1908–1919. doi: 10.1002/jbm.b.34283

Preem, L., Vaarmets, E., Meos, A., Jõgi, I., Putrinš, M., Tenson, T., et al. (2019). Effects and efficacy of different sterilization and disinfection methods on electrospun drug delivery systems. *Int. J. Pharm.* 567:118450. doi: 10.1016/j.ijpharm.2019.118450

Qvortrup, K., Hultqvist, L. D., Nilsson, M., Jakobsen, T. H., Jansen, C. U., Uhd, J., et al. (2019). Small molecule anti-biofilm agents developed on the basis of mechanistic understanding of biofilm formation. *Front. Chem.* 7:742. doi: 10.3389/fchem.2019.00742

Rakow, A., Perka, C., Trampuz, A., and Renz, N. (2019). Origin and characteristics of haematogenous periprosthetic joint infection. *Clin. Microbiol. Infect.* 25, 845–850. doi: 10.1016/j.cmi.2018.10.010

Robijns, S. C. A., Roberfroid, S., Van Puyvelde, S., De Pauw, B., Uceda Santamaría, E., De Weerdt, A., et al. (2014). A GFP promoter fusion library for the study of *Salmonella* biofilm formation and the mode of action of biofilm inhibitors. *Biofouling* 30, 605–625. doi: 10.1080/08927014.2014.907401

Seebach, E., and Kubatzky, K. F. (2019). Chronic implant-related bone infections—can immune modulation be a therapeutic strategy? *Front. Immunol.* 10:1724. doi: 10.3389/fimmu.2019.01724

Stanton, I. C., Murray, A. K., Zhang, L., Snape, J., and Gaze, W. H. (2020). Evolution of antibiotic resistance at low antibiotic concentrations including selection below the minimal selective concentration. *Commun. Biol.* 3:467. doi: 10.1038/s42003-020-01176-w

Tande, A. J., and Patel, R. (2014). Prosthetic joint infection. *Clin. Microbiol. Rev.* 27, 302–345. doi: 10.1128/CMR.00111-13

Thurlow, L. R., Hanke, M. L., Fritz, T., Angle, A., Aldrich, A., and Williams, S. H. (2011). *Staphylococcus aureus* biofilms prevent macrophage phagocytosis and attenuate inflammation in vivo. *J. Immunol.* 186, 6585–6596. doi: 10.4049/jimmunol.1002794

Zhang, B. G., Myers, D. E., Wallace, G. G., Brandt, M., and Choong, P. F. (2014). Bioactive coatings for orthopaedic implants-recent trends in development of implant coatings. *Int. J. Mol. Sci.* 15, 11878–11921.

Zhu, M., Lerum, M. Z., and Chen, W. (2012). Bioactive coatings for orthopaedic implants-recent trends in development of implant coatings. *Langmuir* 28, 416–423. doi: 10.1021/la203638g

Conflict of Interest: The authors declare that the research was conducted in the absence of any commercial or financial relationships that could be construed as a potential conflict of interest.

frontiers in Microbiology

ORIGINAL RESEARCH
published: 23 April 2021
doi: 10.3389/fmicb.2021.603151

Azithromycin Exhibits Activity Against *Pseudomonas aeruginosa* in Chronic Rat Lung Infection Model

Manoj Kumar[1,2†], Madhvi Rao[1†], Tarun Mathur[1], Tarani Kanta Barman[1], Vattan Joshi[1], Tridib Chaira[3], Smita Singhal[1], Manisha Pandya[1], Souhaila Al Khodor[2], Dilip J. Upadhyay[1] and Nobuhisa Masuda[1]*

[1] Department of Microbiology, Daiichi Sankyo India Pharma Private Limited, Gurgaon, India, [2] Research Department, Sidra Medicine, Doha, Qatar, [3] Department of Pharmacokinetics and Metabolism, Daiichi Sankyo India Pharma Private Limited, Gurgaon, India

Pseudomonas aeruginosa forms biofilms in the lungs of chronically infected cystic fibrosis patients, which are tolerant to both the treatment of antibiotics and the host immune system. Normally, antibiotics are less effective against bacteria growing in biofilms; azithromycin has shown a potent efficacy in cystic fibrosis patients chronically infected with *P. aeruginosa* and improved their lung function. The present study was conducted to evaluate the effect of azithromycin on *P. aeruginosa* biofilm. We show that azithromycin exhibited a potent activity against *P. aeruginosa* biofilm, and microscopic observation revealed that azithromycin substantially inhibited the formation of solid surface biofilms. Interestingly, we observed that azithromycin restricted *P. aeruginosa* biofilm formation by inhibiting the expression of *pel* genes, which has been previously shown to play an essential role in bacterial attachment to solid-surface biofilm. In a rat model of chronic *P. aeruginosa* lung infection, we show that azithromycin treatment resulted in the suppression of quorum sensing-regulated virulence factors, significantly improving the clearance of *P. aeruginosa* biofilms compared to that in the placebo control. We conclude that azithromycin attenuates *P. aeruginosa* biofilm formation, impairs its ability to produce extracellular biofilm matrix, and increases its sensitivity to the immune system, which may explain the clinical efficacy of azithromycin in cystic fibrosis patients.

Keywords: Gram-negative bacteria, PA-14, PAO1, multidrug resistance, respiratory tract infection, *pel* genes, extracellular biofilm matrix, quorum sensing molecule

OPEN ACCESS

Edited by:
Mark Smeltzer, University of Arkansas for Medical Sciences, United States

Reviewed by:
Giuseppantonio Maisetta, University of Pisa, Italy
Oana Ciofu, University of Copenhagen, Denmark

***Correspondence:**
Manoj Kumar
mkumar@sidra.org

† These authors have contributed equally to this work

Specialty section:
This article was submitted to Antimicrobials, Resistance and Chemotherapy, a section of the journal Frontiers in Microbiology

Received: *05 September 2020*
Accepted: *15 March 2021*
Published: *23 April 2021*

Citation:
Kumar M, Rao M, Mathur T, Barman TK, Joshi V, Chaira T, Singhal S, Pandya M, Al Khodor S, Upadhyay DJ and Masuda N (2021) Azithromycin Exhibits Activity Against Pseudomonas aeruginosa in Chronic Rat Lung Infection Model. Front. Microbiol. 12:603151. doi: 10.3389/fmicb.2021.603151

INTRODUCTION

Pseudomonas aeruginosa is the most common bacterial pathogen that causes biofilm-mediated chronic lung infections among cystic fibrosis (CF) patients (Faure et al., 2018; Maurice et al., 2018). *P. aeruginosa* has an innate propensity to attach to different solid surfaces and form biofilms, which enables the bacteria to resist both the host's innate immune system and treatments with antibiotics (Mulcahy et al., 2014). The treatment options for nosocomial Gram-negative infections are very limited. The antibiotics of choice for Gram-negative pathogens are parenteral carbapenems, such asimipenem and meropenemor quinolones (Bassetti et al., 2018). However, the poor activities of these antibiotics on bacterial biofilms and the increasing prevalence of multidrug-resistant

P. aeruginosa (Cabot et al., 2012; Ciofu and Tolker-Nielsen, 2019; Kumar et al., 2019) leave the physicians with very limited choices to effectively treat these patients.

Although macrolides are commonly used for Gram-positive pathogens, azithromycin is being extensively used to treat chronic respiratory tract infections caused by *P. aeruginosa* especially in cystic fibrosis patients (Hansen et al., 2005; Wagner et al., 2005). In addition to the direct anti-pseudomonas effects (Tateda et al., 1996; Marvig et al., 2012), multiple clinical studies have highlighted the beneficial non-antibiotic effects of azithromycin, including modulation of the aberrant immune response and improving lung function in CF patients (Equi et al., 2002; Saiman et al., 2003; Clement et al., 2006; Principi et al., 2015; Cogen et al., 2018). Taken together, multiple mechanisms of azithromycin have been suggested, such as inhibiting biofilm formation by modulating the synthesis of quorum sensing (QS) molecules (Nalca et al., 2006; Swatton et al., 2016) or stimulating the anti-inflammatory effect during prolonged exposure (Zimmermann et al., 2018).

P. aeruginosa poses different QS signaling systems (LasI/LasR and Rh1I/Th1R)that regulate different cellular processes, including cell-to-cell communication, extracellular matrix synthesis, and biofilm formation (de Kievit and Iglewski, 2000; Smith and Iglewski, 2003). A large number of genes, including those involved in virulence and biofilm formation, are modulated by two acyl-homoserine lactone molecules synthesized by QS systems, namely, 3-O-C12homoserine lactone (HSL) synthesized by *lasI* and C4-HSL synthesized by *Rh1I* (Ding et al., 2018). The QS signaling molecule 3-O-C12 HSL has been shown to be essential for extracellular matrix modulation and biofilm formation since the *lasI* mutant was found to be defective in extracellular biofilm matrix and biofilm formation (Sakuragi and Kolter, 2007). In contrast, the Rh1I/Rh1R signaling system was found to be important for the survival of bacterial cells during anaerobic conditions in biofilms (Yoon et al., 2002; Sakuragi and Kolter, 2007). Interestingly, an increasing level of 3-O-C12 HSL has been reported in both *P. aeruginosa* biofilm formed *in vitro* and in CF patients chronically infected with *P. aeruginosa* (Geisenberger et al., 2000; Singh et al., 2000; Barr et al., 2015). Azithromycin has been shown to inhibit the synthesis of 3-O-C12 HSL signaling QS molecules (Favre-Bonte et al., 2003) without influencing the growth of planktonic cells (Chalmers, 2017).

However, data concerning the mechanism of biofilm inhibition by azithromycin and *in vivo* efficacy in chronic pulmonary infection, to support the clinical utilities of azithromycin in CF patients, are scarce. In this study, we evaluated the efficacy of azithromycin against *in vitro* and *in vivo* *P. aeruginosa* biofilm formation in a chronic pulmonary rat infection model at a human-equivalent dose. Our study revealed the potential mechanism of biofilm inhibition by azithromycin.

MATERIALS AND METHODS

Bacterial Strains and Antibiotics

P. aeruginosa strain PAO1, PA-14 (highly virulent clinical isolate), and ATCC 700829 (standard strain for biofilm formation) were used for all *in vitro* and *in vivo* biofilm experiments. A recombinant *P. aeruginosa* G2 strain having a single chromosomal copy of promoterless *lacZ* gene, under promoter control of the *pelA* gene, was used for the mechanism of action studies. The bacterial isolates were obtained from the American Type Culture Collection (Manassas, VA, United States) or from our proprietary collection of clinical isolates. Levofloxacin was synthesized at Daiichi Sankyo Co., Tokyo. Azithromycin and clindamycin were obtained from a commercial source. All strains were stored at −80°C in 20% glycerol in trypticase soy broth (TSB) (Becton, Dickinson, and Company, Cockeysville, MD). All bacteriological media were procured from Becton Dickinson and Company; the reagents and chemicals were purchased from Sigma-Aldrich Co., LLC, United States.

In vitro Biofilm Activity

The effect of azithromycin and clindamycin on *P. aeruginosa* biofilm formation was assessed as described previously (Sharma et al., 2009; Barman et al., 2016; Kumar et al., 2019). Briefly, the overnight-grown culture of *P. aeruginosa* PAO1 in TSB was pelleted and resuspended in Luria–Bertani broth containing 0.2% glucose (10^7 CFU/ml). The bacterial suspension was spiked with different concentrations (16–0.015 μg/ml) of azithromycin or clindamycin in 96-well plates and incubated at 26 ± 2°C. The effects of azithromycin and clindamycin on inhibition of biofilm formation were assayed after 24 h of exposure. The wells were emptied and washed three times with phosphate-buffered saline (PBS; pH 7.3), and the adherent biofilm was stained with 200 μl of 1% crystal violet for 30 min and rinsed with distilled water. The adherent biofilm in the wells was solubilized with 200 μl of 30% acetic acid, and the optical density at 600 nm (OD_{600}) was measured to quantify the formed biofilms. Each experiment was performed thrice, and the mean percent inhibition and standard deviations were calculated. The relative inhibition of biofilms, expressed as a mean percentage, was determined using the following formula:

$$\text{Percent inhibition} = 100 - \left\{ \left(\frac{OD_{600}\ of\ drug\ well}{OD_{600}\ of\ positive} - \text{control well} \right) \times 100 \right\}$$

The efficacy of azithromycin was also evaluated on a pre-formed biofilm of *P. aeruginosa* PAO1 to assess the therapeutic or eradicative effect of azithromycin as described earlier (Macia et al., 2014). The bacterial suspension was prepared as described above and inoculated at 200 μl/well in a 96-well plate. After 24 h of incubation, the wells were emptied and washed with PBS and then spiked with different concentrations (16–0.015 μg/ml) of azithromycin prepared in LB broth containing 0.2% glucose. The plate was further incubated for 24 h, and the effect of azithromycin was assessed as described above.

To further evaluate the effect of azithromycin on planktonic cells and biofilm formation, a time-kill kinetic study was performed. Briefly, 10 ml of LB broth containing 0.2% glucose and a sterile 2-cm-long piece of the catheter were pre-warmed at 26 ± 2°C in reaction tubes, and the different concentrations of

azithromycin (2 or 16 μg/ml) were added to tubes. The bacterial inoculum of *P. aeruginosa* PA-14 was prepared as described above and added to the tubes to achieve a final inoculum of $\sim 1 \times 10^5$ CFU/ml. The tubes were incubated at 26 ± 2°C. The planktonic cell counts were determined at various time-points by serial dilution plating onto a trypticase soy agar plate. After 24 h of incubation, the catheter pieces from each tube were removed, non-adherent bacteria were washed from the catheter pieces, and the number of CFU embedded in biofilm per catheter was determined as described earlier (Kumar et al., 2016, 2019). The experiment was performed in triplicate, and the mean $\log_{10}$ killing of planktonic cells and biofilm inhibition were calculated for each concentration. To further assess biofilm formation in the absence (drug-free control) or presence of azithromycin, the catheter pieces were also sectioned and processed for scanning electron microscopy (SEM).

β-Galactosidase Activity

To understand the molecular mechanism of biofilm inhibition, a recombinant mutant *P. aeruginosa* G2-containing promoterless *lacZ* gene under promoter control of *pelA* was gifted to us by Prof. Kilter (Sakuragi and Kolter, 2007). The β-galactosidase activity was performed in the absence and presence of different concentrations of azithromycin and levofloxacin, as described earlier (Sakuragi and Kolter, 2007).

In vivo Studies

Specific pathogen-free female Sprague–Dawley (SD) rats, weighing 200 ± 20 g (age 8 weeks), were used for the study. The rats were procured from Vivo Biotech Pvt. Ltd., Hyderabad, India. The animals were housed in a pathogen-free animal facility and allowed 5 days of acclimatization in the study room before initiating the experiment. Feed and water were provided *ad libitum* during acclimatization and the study periods. All animal studies were approved by the institutional animal ethics committee. The animal studies were conducted under the strict guidelines of the committee for the Purpose of Control and Supervision of Experiments on Animals, Ministry of Environment, Forests and Climate Change, New Delhi, Government of India, and under the supervision of the institutional committee.

To determine the *in vivo* efficacy of azithromycin, a chronic biofilm model *of P. aeruginosa* was established in SD rats, which mimic the human chronic infection (Hoover et al., 2017; Chawanpaiboon et al., 2019). A semisolid 0.25% w/v agar beads suspension was prepared and autoclaved a day before the *in vivo* experiment and stored overnight at 4°C. To cause a chronic biofilm infection, *P. aeruginosa* PA-14 was grown overnight on Mueller–Hinton agar (MHA; Becton, Dickinson and Company), and three to four isolated bacterial colonies were picked and suspended in PBS buffer to prepare the bacterial suspension. The turbidity of bacterial suspension was adjusted to 1 McFarland, diluted 1:10 with PBS. To prepare the inoculum, bacterial suspension was embedded in agar beads as detailed in a previously described method, which yield beads of mean size approximately 200–300 μm and a bead suspension of 2.5×10^7 CFU/ml (Hraiech et al., 2012).The animals were anesthetized by injecting 100 μl of xylazine (5 mg/kg) and ketamine (100 mg/kg) mixture intramuscularly. Using an 18-gauge blunt needle, 150 μl of bead suspension was injected intratracheally as described earlier (Barman et al., 2011). To cause a chronic biofilm infection, the animals were kept untreated for 3 days. Before starting the treatment, the animals were randomized using their body weight, and $n = 6$ animals were kept in each group. Azithromycin was administered orally using agavage at 75 mg/kg, q24h for 4 days. The rats were then euthanized 22 h after the last dose, and the lungs' bacterial load was determined by plating diluted lung homogenates on MHA.

Pharmacokinetics Studies of Azithromycin in *P. aeruginosa*-Infected Rats

The concentrations of azithromycin were assessed in the plasma and lung epithelial lining fluid (ELF) of the rats infected with *P. aeruginosa* PA-14. Intratracheal infection in rats was performed as described above. A single dose of 75 mg/kg of azithromycin was administered orally through gavage. Blood and broncho-alveolar lavage (BAL) fluid (with 2 ml of normal saline wash) were collected at different time-points up to 24 h post-dose from each animal by gross dissection. For the collection of BAL, 2 ml of sterile cold PBS was infused into the animal through the trachea and into the bronchial cavity and aspirated out. Plasma was harvested from blood samples by centrifugation. The azithromycin concentrations in plasma and BAL samples were determined using liquid chromatography with tandem mass spectrometry. The apparent volume of ELF (V_{ELF}) in BAL fluid was determined by the urea dilution method using the urea assay kit from BioChain (Hayward, CA). The concentration of azithromycin in ELF (C_{ELF}) was determined as

$$C_{ELF} = C_{BAL} \times \frac{V_{BAL}}{V_{ELF}}$$

where C_{BAL} is the measured concentration of azithromycin in BAL fluid.

Statistical Analysis

All data were analyzed using GraphPad Prism (version 8; GraphPad Software, San Diego, CA, United States). The statistical significance of the difference between the numbers of viable organisms recovered from the lungs of the treated group and those for the untreated control group or biofilm inhibition as compared to control (no drug control) was evaluated by non-parametric Mann–Whitney analysis. A difference between the treated group and the untreated control group was considered to be statistically significant if the $P < 0.05$.

RESULTS

In vitro Biofilm Activity

Azithromycin exhibited a potent activity against biofilms produced by different isolates of *P. aeruginosa*. Azithromycin showed a strong biofilm inhibition as compared to the drug-free

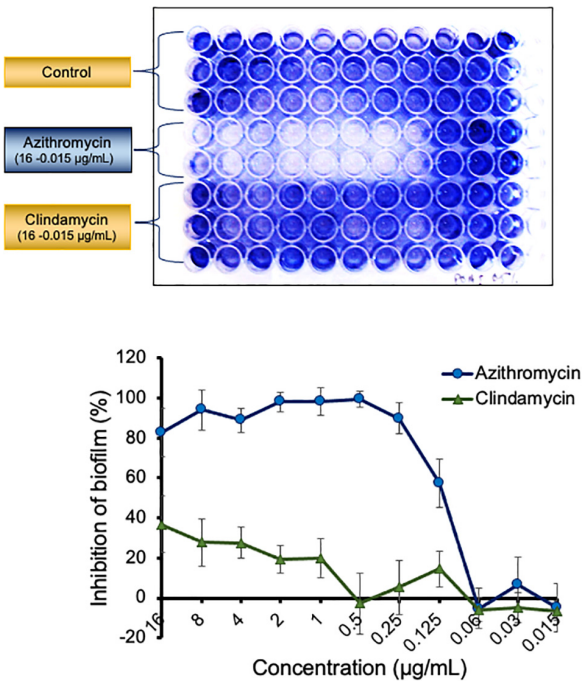

FIGURE 1 | Activity of azithromycin and clarithromycin against biofilm of *P. aeruginosa* PAO1 The adherent biofilm in presence of azithromycin, clindamycin or in control well (drug free) was stained with 1% crystal violet and measured by OD_{600} after dissolving in 30% acetic acid. The inhibition of biofilm in presence of antibiotics was calculated by comparing the biofilm formation in control well. Values shown in the figure are average of three independent experiments.

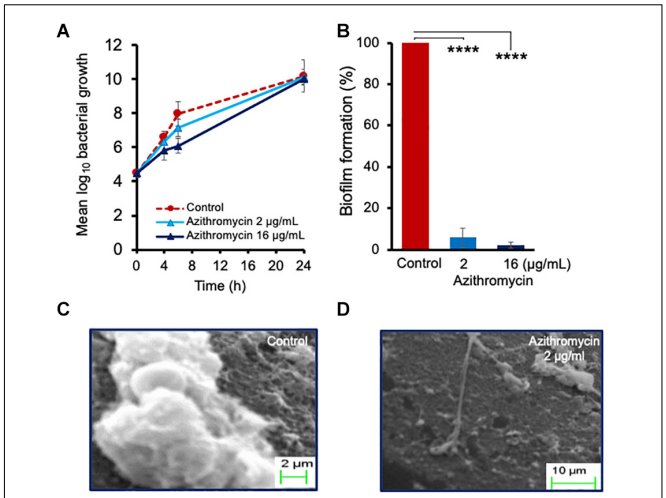

FIGURE 2 | Activity of azithromycin against planktonic cells of *P. aeruginosa* PA14 **(A)**, and biofilm formation **(B)** at 24 h. Scanning electron micrographs revealing biofilm formation at 24 h in absence of drug **(C)** or in presence of azithromycin **(D)**. The catheter piece in drug-free control well shows production of extracellular matrix and biofilm formation, while no extracellular biofilm matrix and biofilm formation observed in presence of azithromycin. Each value is the average of triplicate assay where presented data is mean ± SD. Statistical analysis were calculated using one way ANOVA and ****$p < 0.0001$ ($n = 3$).

control and clindamycin with a biofilm preventive concentration (BPC_{50}) value of 0.122 µg/ml against *P. aeruginosa* PAO1 (**Figure 1**) and also exhibited a similar biofilm activity against *P. aeruginosa* ATCC 700829 (standard strain used for biofilm formation) (**Supplementary Figure 1**). In contrast, azithromycin exhibited a comparatively reduced activity against the pre-formed biofilm with a minimum biofilm eradication concentration ($MBEC_{50}$) value of 7.49 µg/ml against *P. aeruginosa* PAO1 (**Supplementary Figure 2**).

To further determine the effect of azithromycin against planktonic cells and biofilm formation on a solid surface, we performed a time-kill kinetic study using a catheter piece as a solid surface objective, as described earlier (Kumar et al., 2019), although azithromycin showed a substantial 1.86 $\log_{10}$ reduction in planktonic cell counts at 6 h as compared to the drug-free control and but no effect at 24 h post-incubation (**Figure 2A** and **Supplementary Figure 3**). Possibly, over-expression of multidrug efflux pumps could be the reason of its poor activity against *P. aeruginosa* in LB media, as potent-activity of azithromycin has been observed in the presence of known efflux pump inhibitors or eukaryotic media (RPMI 1640) (Buyck et al., 2012). Despite the high bacterial cell counts in LB media (**Figure 2A**), azithromycin exhibited a strong activity against *P. aeruginosa* PA-14 biofilm (**Figure 2B**). A simple macroscopic and quantitative analysis 24 h after incubation revealed that *P. aeruginosa* PA-14 formed a strong solid-surface biofilm on catheter pieces (**Figures 2C,D**), whereas in the presence of azithromycin, no solid-surface biofilm formed, suggesting that, despite having a limited activity against the planktonic cells of *P. aeruginosa* in LB media, azithromycin efficiently impeded the planktonic cells from leading to biofilm formation, possibly by inhibiting the synthesis of the extracellular biofilm matrix required for solid-surface biofilm formation. To confirm our hypothesis, we used SEM to visualize biofilm formation at the cellular level in a drug-free control and the presence of azithromycin. As shown in **Figure 2C**, *P. aeruginosa* cells were embedded in an extracellular matrix to form a solid-surface biofilm in a drug-free control, whereas no extracellular matrix was observed in the presence of azithromycin (**Figure 2D**). Hence, biofilm formation was significantly inhibited. These lines of evidence support the hypothesis that azithromycin inhibits biofilm formation by impairing the ability of *P. aeruginosa* to produce its biofilm matrix.

Development of the solid-surface-associated biofilm is controlled by *pel* genes in *P. aeruginosa*, as a *pel* gene mutant was found defective in synthesizing an extracellular biofilm matrix and biofilm formation (Sakuragi and Kolter, 2007), and the expression of *pel* genes is regulated by 3-O-C_{12} homoserine lactone (autoinducer of the *las* QS signaling system, synthesized by *lasI*) (Sakuragi and Kolter, 2007).

To understand the biofilm inhibition mechanism of azithromycin, we evaluated the β-galactosidase activity of a recombinant mutant containing a promoter less *lacZ* gene under promoter control of *pel* gene (Sakuragi and Kolter, 2007), in the absence and presence of different azithromycin

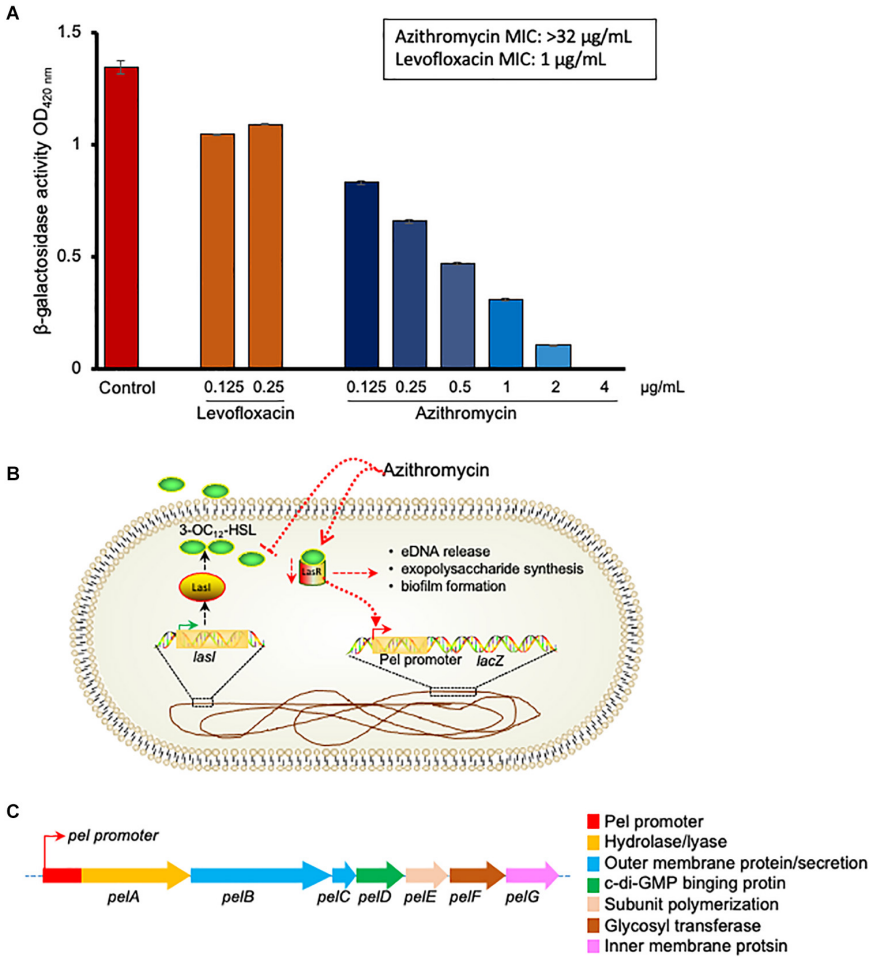

FIGURE 3 | p-galactosidase activity of *P. aeruginosa*G2 recombinant construct containing pel promoter-lacZ transcriptional fusion in presence of different concentration of azithromycin, levofloxacin or no-drug control **(A)**. The MIC of azithromycin and levofloxacin was > 32 and 1 ng/mL, respectively, against *P. aeruginosa*G2. Proposed mechanism of biofilm and *pel* genes inhibition by azithromycin **(B)**.Genetic structure of *pel* genes in *P. aeruginosa* **(C)**.

concentrations. Azithromycin showed a dose-dependent inhibition of β-galactosidase activity with IC_{50} 0.170 µg/ml (**Figure 3**). In addition, to confirm the selectively of azithromycin from the Las QS system, we also evaluated the sub-MIC concentrations of levofloxacin. As expected, levofloxacin did not influence the β-galactosidase activity of mutant (**Figure 3A**). Taken together, these results indicate that azithromycin inhibits *pel* gene transcription by inhibiting the *las* QR signaling system (**Figures 3B,C**), resulting in the inhibition of *P. aeruginosa* biofilm formation.

In vivo Efficacy Against *P. aeruginosa* in a Rat Biofilm Model

The experimental plan used for testing the efficacy of azithromycin at a human-equivalent dose is shown in **Figure 4**. The treatment was implemented 3 days post-infection and given once daily for a period of 4 days (**Figure 4A**). All the infected animals in the control group exhibited consistent bacterial counts. At 4 days, the placebo treatment resulted in no significant change in bacterial load, whereas treatment with azithromycin at 75 mg/kg, q24h resulted in a significant 1.67 log_{10} reduction in bacterial counts as compared to the placebo control (**Figure 4B**).

Pharmacokinetics of Azithromycin in *P. aeruginosa*-Infected Rats

The plasma and lung tissue kinetics of azithromycin in the SD rats infected with *P. aeruginosa* PA-14 are presented in **Figure 4C** and **Table 1**. The plasma and lung tissues were harvested from infected animals at different time-points of up to 24 h post-dosing, and the stimulated plasma and lung tissue (EFL) profile was prepared to understand the pharmacokinetics of azithromycin in infected animals. Although C_{max} in plasma and lung tissues was observed 2 h after administration, azithromycin showed comparatively higher concentrations in lung tissues. The lung ELF/plasma ratios of C_{max} and AUC_{inf} were 81.05 and 85.96, respectively. The graph shows that the simulated lung concentrations of azithromycin

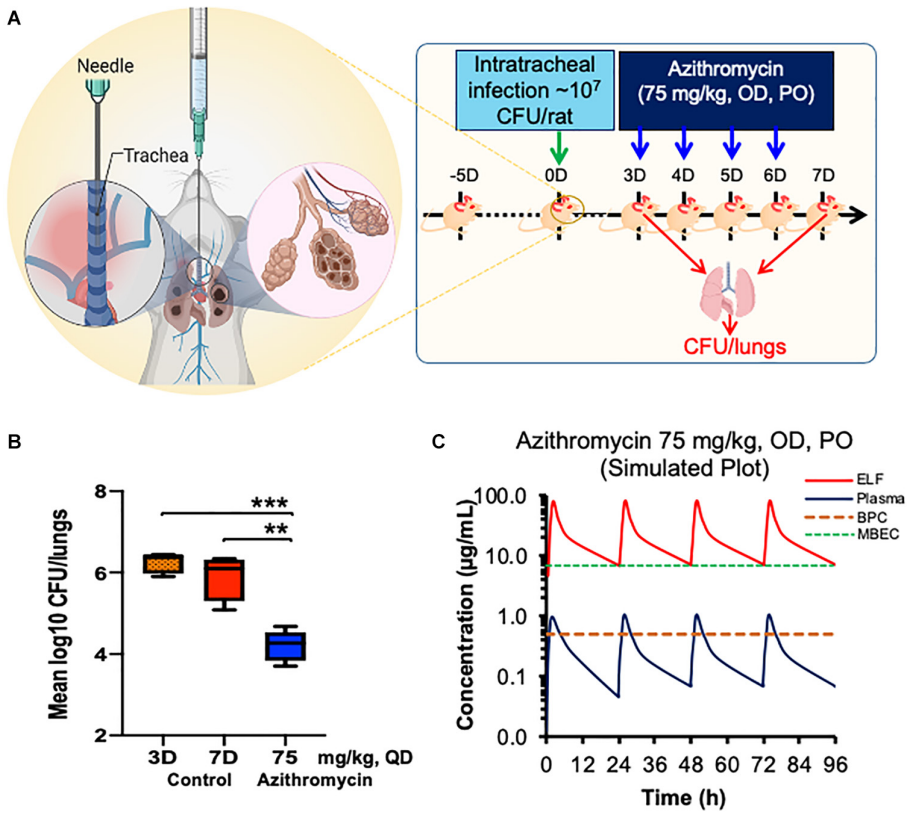

FIGURE 4 | Efficacy of azithromycin in chronic rat pulmonary infection model of P. *aeruginosa* PA-14.Chronic pulmonary was caused using *P aeruginosa*PA-14 in rats via the intratracheally route and treatment was started 3 days post infection with azithromycin by PO route **(A)**. Bacterial lungs loads were determined post 22 h of last dose and compared with those of placebo treated **(B)**. Stimulated plasma and ELF concentration of azithromycin at 75 mg/kg, PO for 4 days was calculated using WinNonlin **(C)**. The asterisks indicates a significant difference compared with those of control group (**$P < 0.01$, ***$P < 0.001$). CFU, Colony Forming Unit; OD, Once a Day; PO, Per Orem (Oral administration); ELF, Epithelial Lining Fluid; BPC, Biofilm Preventive Concentration; MBEC, Minimal Biofilm Eradication Concentration.

at 75 mg/kg, q24h dose were substantially higher than the BPC and MBEC values of *P. aeruginosa* biofilms throughout the treatment (**Figure 4C**).

DISCUSSION

Biofilm formation within the lungs of CF patients is the hallmark of *P. aeruginosa* pathogenesis (Singh et al., 2000), as it substantially reduced the bacterial susceptibility to antimicrobial agents and the host immune system compared to planktonic cells (Smith and Iglewski, 2003; Mulcahy et al., 2014). Biofilm infections (including CF infections) tend to be chronic and difficult to eradicate and remain a matter of great concern, which has generated the need for alternative treatment strategies. The most striking findings with azithromycin in the present investigation were its capacity to inhibit *P. aeruginosa* biofilm formation and reduce the solid-surface biofilm attachment almost to a lower detection limit. Interestingly, the SEM of solid-surface biofilm in the presence of azithromycin shows a substantially reduced extracellular biofilm matrix and attachment to a solid surface to form a biofilm, which is in accordance with the findings of other studies (Mizukane et al., 1994; Ichimiya et al., 1996). Although azithromycin is well known to show a potent activity against *P. aeruginosa* biofilm, its evaluation in chronic respiratory *P. aeruginosa* biofilm infection model has been relatively understudied. There is a pressing need to determine its bactericidal activity on biofilms to facilitate its clinical use.

To evaluate the potential mechanism of azithromycin to inhibit biofilm formation, we developed a refined and chronic lung rat model of *P. aeruginosa* to mimic the clinical and chronic *P. aeruginosa* infection conditions in patients

TABLE 1 | Pharmacokinetic parameters of azithromycin at 75 mg/kg, PO dose in Wister rats infected with *P. aeruginosa* PA-14.

Parameters	Azithromycin Plasma	Lung ELF
c_{max}(µg/L)	0.95 ± 0.30	82.00 ± 26.10
Tmax (h)	2.00 ± 0.00	2.00 ± 0.00
$AUC_{0\text{-}24}$ (µg.h/L)	5.91 ± 0.62	508.11 ± 53.54
AUC_{inf} (µg.h/L)	6.92 ± 0.91	594.88 ± 77.68

Values are presented as mean ± SD, n = 3.

(Hraiech et al., 2012; Chawanpaiboon et al., 2019). The most important features of the rat chronic *P. aeruginosa* infection model were consistent and reproducible bacterial lung counts in infected animals with no acute morbidity but only delayed mortality of infected rats within 7–14 days if left untreated (data not shown), which makes it ideal to evaluate efficacy against chronic disease. These findings align with those of CF patients who suffer from chronic *P. aeruginosa* infections and show high mortalities. In this study, we evaluated the efficacy of azithromycin at 75 mg/kg, once daily, which was equivalent to 500 mg every 24 h in humans (Beringer et al., 2005; Cipolli et al., 2012; Dalhoff, 2014). To mimic the clinical chronic infection conditions, the treatment was initiated 3 days post-infection with 75 mg/kg, q24h of azithromycin for 4 days by the PO route. This treatment regimen resulted in a significant reduction in the lungs' bacterial counts compared to the placebo-treated control.

To understand the pharmacodynamics of potent *in vivo* activity of azithromycin, we performed pharmacokinetics of azithromycin in the SD rats infected with *P. aeruginosa*. Interestingly, we observed a significantly higher concentration of azithromycin in the lungs of the infected animals, which was found to be well above the BPC and MBEC values of azithromycin. This explains the potent *in vivo* efficacy of azithromycin in treating the chronic lung infection model of *P. aeruginosa*. Our data are in accordance with the clinical findings that azithromycin treatment improves lung function in CF patients chronically infected with *P. aeruginosa* either by inhibiting biofilm formation (Saiman et al., 2003; Hansen et al., 2005) or suppressing the growth of susceptible bacteria.

The bacterial biofilm matrix is generally composed of exopolysaccharides, proteins (Sutherland, 2001), and e-DNA (Cherny and Sauer, 2019), which is required for both structural integrity and protective barrier to the harsh environment (Mulcahy et al., 2014). Three main exopolysaccharides (*psl*, *pel*, and alginate) have been identified in *P. aeruginosa* (Sutherland, 2001). Among these, *pel* gene cluster regulated by LasI/LasR (3-O-C_{12} HSL molecule synthesized by *lasI*) was found important for bacterial attachment to solid surfaces and biofilm formation (Sakuragi and Kolter, 2007). A dose-dependent inhibition of the *pel* promoter by azithromycin in our study suggests that azithromycin affects biofilm formation by inhibiting the synthesis of the QS molecule (3-O-C_{12}). In addition to the regulation of *in vitro* biofilm, the QS molecules are also critical for the infectivity of *P. aeruginosa*, as QS mutant showed impaired chronic infectivity compared to wild-type *P. aeruginosa* (Willcox et al., 2008). Interestingly, a comparatively reduced level of QS molecules (a marker of biofilm formation) in the ELF of animals treated with azithromycin further suggests the important role of the QS system during chronic *P. aeruginosa* infection (**Figure 5**) and indicates that azithromycin modulates the biofilm by inhibiting the synthesis of 3-O-C12 HSL, a known marker of biofilm formation (Barr et al., 2015). Our results with rats with chronic *P. aeruginosa* infection demonstrated that azithromycin significantly improved the pulmonary *P. aeruginosa* clearance, possibly by interfering with QS systems and crippling of the exopolysaccharides of the biofilm synthesized by the *pel* proteins.

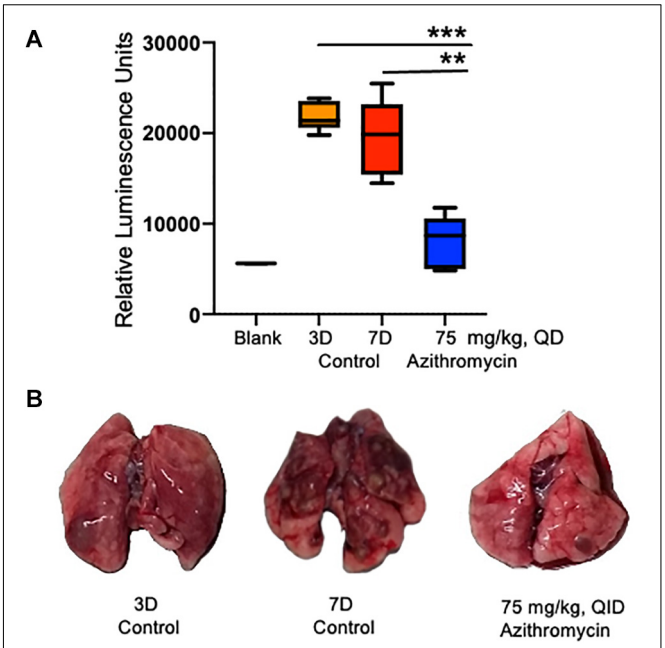

FIGURE 5 | Detection of QS molecule in the epithelial lining fluid (ELF) of infected rats. QS molecule was determined 3 days post-infection, when the treatment was started and at 7 days post-infection in the placebo control and azithromycin treated rats **(A)**. Representative lungs photos of 3D, 7D and azithromycin treated rats **(B)**. The asterisks indicates a significant difference compared with those of 7D control group (**$P < 0.01$, ***$P < 0.001$).

Besides inhibiting the virulence factors, azithromycin is known to have multiple effects against *P. aeruginosa*: (a) enhanced activity in the presence of serum, which could contribute to bacterial killing during chronic pulmonary infection (Lucchi et al., 2008), (b) anti-inflammatory activity that could help to reduce the inflammation at infection sites (Zeng et al., 2016; Zimmermann et al., 2018), (c) biofilm inhibitory or eradicative activity by modulating the synthesis of signaling molecules, such as the QS system, ci-di-GMP, and AHL (Favre-Bonte et al., 2003; Nalca et al., 2006; Barr et al., 2015; Ghosh et al., 2020), and (d) anti-virulence activity that could impair *P. aeruginosa* cells to produce extracellular biofilm matrix. These multiple effects of azithromycin could together be important mediators for its potent *in vivo* efficacy, or is there something else that drives the efficacy against *P. aeruginosa* in chronic CF patients? Could it be that host immune modulation leads to killing of bacterial cells or inhibition/eradication of biofilm and exposing the bacterial cells to an accumulated azithromycin concentration in the lung? These could be interesting avenues for investigation for future research.

In the present study, we reported the detailed biofilm preventive effect of azithromycin. However, our study has several limitations. First, the *in vitro* biofilm assays revealed that azithromycin shows better BPC than the MPEC, which was also supported by the reduced production of extracellular biofilm matrix in the presence of azithromycin, while the *in vivo* efficacy of azithromycin was evaluated against chronic *P. aeruginosa* infection

(preformed biofilms). Second, the *in vivo* study was performed only at a single human-equivalent dose. Therefore, further detailed studies are required to access the preventive and eradicative biofilm effect of azithromycin at multiple doses to understand its clinical utilities in CF patients.

In summary, we demonstrated that azithromycin repressed the expression of 3-O-C_{12} (QS system) and inhibits biofilm matrix production by influencing the expression of *pel* genes. Furthermore, azithromycin treatment of rats with chronic *P. aeruginosa* infection significantly improved the bacterial clearance from chronic infection compared to placebo controls. Taken together, the repression of bacterial virulence, the bactericidal effect on biofilm formation, and the enhanced serum sensitivity after a prolonged exposure to azithromycin may be responsible for the potent efficacy observed in our rats with chronic infection and in patients with CF.

DATA AVAILABILITY STATEMENT

The original contributions presented in the study are included in the article/**Supplementary Material**, further inquiries can be directed to the corresponding author/s.

ETHICS STATEMENT

The animal study was reviewed and approved by the Institutional Animal Ethics Committee at Daiichi Sankyo Pharma Pvt. Ltd., Gurgaon.

AUTHOR CONTRIBUTIONS

MK and MR conceived the study, performed statistical analyses, and generated graphs. MK, MR, TM, TKB, VJ, SS, and MP performed the *in vitro* and *in vivo* studies. TC performed the PK studies. MP, DJU, and NM did the project management. MK, MR, and SA wrote the first draft of manuscript. All authors contributed to manuscript editing, discussed the results, and approved the final submitted version.

FUNDING

We declare that this study received funding from Daiichi Sankyo Pharma Pvt., Ltd., Gurgaon. The funder was not involved in the study design, the collection, analysis, and interpretation of data, the writing of this article, or the decision to submit it for publication. We obtained permission for the publication of this manuscript from the funder before submitting the manuscript to the journal. We thank Daiichi Sankyo Co., Ltd., for financial assistance and support to this project.

ACKNOWLEDGMENTS

We thank the Institute of Genomics and Integrative Biology, Delhi, India, for performing SEM studies and their interpretation. We were also grateful to Prof. Kilter of Harvard Medical School, 200 Longwood Avenue, Boston, for providing the *P. aeruginosa* G2.

SUPPLEMENTARY MATERIAL

The Supplementary Material for this article can be found online at: https://www.frontiersin.org/articles/10.3389/fmicb.2021.603151/full#supplementary-material

REFERENCES

Barman, T. K., Kumar, M., Mathur, T., Chaira, T., Ramkumar, G., Kalia, V., et al. (2016). In vitro and in vivo activities of a Bi-Aryl Oxazolidinone. RBx 11760, against Gram-Positive Bacteria. *Antimicrob. Agents Chemother.* 60, 7134–7145.

Barman, T. K., Rao, M., Bhati, A., Kishore, K., Shukla, G., Kumar, M., et al. (2011). Non invasive real-time monitoring of bacterial infection & therapeutic effect of anti-microbials in five mouse models. *Indian J. Med. Res.* 134, 688–695.

Barr, H. L., Halliday, N., Camara, M., Barrett, D. A., Williams, P., Forrester, D. L., et al. (2015). *Pseudomonas aeruginosa* quorum sensing molecules correlate with clinical status in cystic fibrosis. *Eur. Respir. J.* 46, 1046–1054.

Bassetti, M., Vena, A., Croxatto, A., Righi, E., and Guery, B. (2018). How to manage *Pseudomonas aeruginosa* infections. *Drugs Context* 7:212527.

Beringer, P., Huynh, K. M., Kriengkauykiat, J., Bi, L., Hoem, N., Louie, S., et al. (2005). Absolute bioavailability and intracellular pharmacokinetics of azithromycin in patients with cystic fibrosis. *Antimicrob. Agents Chemother.* 49, 5013–5017. doi: 10.1128/aac.49.12.5013-5017.2005

Buyck, J. M., Plesiat, P., Traore, H., Vanderbist, F., Tulkens, P. M., and Van Bambeke, F. (2012). Increased susceptibility of *Pseudomonas aeruginosa* to macrolides and ketolides in eukaryotic cell culture media and biological fluids due to decreased expression of oprM and increased outer-membrane permeability. *Clin. Infect. Dis.* 55, 534–542. doi: 10.1093/cid/cis473

Cabot, G., Ocampo-Sosa, A. A., Dominguez, M. A., Gago, J. F., Juan, C., Tubau, F., et al. (2012). Genetic markers of widespread extensively drug-resistant *Pseudomonas aeruginosa* high-risk clones. *Antimicrob. Agents Chemother.* 56, 6349–6357. doi: 10.1128/aac.01388-12

Chalmers, J. D. (2017). Macrolide resistance in *Pseudomonas aeruginosa*: implications for practice. *Eur. Respir. J.* 49:1700689. doi: 10.1183/13993003.00689-2017

Chawanpaiboon, S., Vogel, J. P., Moller, A. B., Lumbiganon, P., Petzold, M., Hogan, D., et al. (2019). Global, regional, and national estimates of levels of preterm birth in 2014: a systematic review and modelling analysis. *Lancet Glob. Health* 7, e37–e46.

Cherny, K. E., and Sauer, K. (2019). *Pseudomonas aeruginosa* requires the DNA-specific endonuclease EndA to degrade extracellular genomic DNA to disperse from the biofilm. *J. Bacteriol.* 201:e00059-19.

Ciofu, O., and Tolker-Nielsen, T. (2019). Tolerance and resistance of *Pseudomonas aeruginosa* biofilms to antimicrobial agents-how *P. aeruginosa* can escape antibiotics. *Front. Microbiol.* 10:913. doi: 10.3389/fmicb.2019.00913

Cipolli, M., Cazzola, G., Novelli, A., Cassetta, M. I., Fallani, S., and Mazzei, T. (2012). Azithromycin concentrations in serum and bronchial secretions of patients with cystic fibrosis. *Clin. Drug Invest.* 21, 353–360. doi: 10.2165/00044011-200121050-00005

Clement, A., Tamalet, A., Leroux, E., Ravilly, S., Fauroux, B., and Jais, J. P. (2006). Long term effects of azithromycin in patients with cystic fibrosis: a double blind, placebo controlled trial. *Thorax* 61, 895–902.

Cogen, J. D., Onchiri, F., Emerson, J., Gibson, R. L., Hoffman, L. R., Nichols, D. P., et al. (2018). Chronic Azithromycin use in cystic fibrosis and risk of treatment-emergent respiratory pathogens. *Ann. Am. Thorac. Soc.* 15, 702–709.

Dalhoff, A. (2014). Pharmacokinetics and pharmacodynamics of aerosolized antibacterial agents in chronically infected cystic fibrosis patients. *Clin. Microbiol. Rev.* 27, 753–782. doi: 10.1128/cmr.00022-14

de Kievit, T. R., and Iglewski, B. H. (2000). Bacterial quorum sensing in pathogenic relationships. *Infect. Immun.* 68, 4839–4849. doi: 10.1128/iai.68.9.4839-4849.2000

Ding, F., Oinuma, K. I., Smalley, N. E., Schaefer, A. L., Hamwy, O., Greenberg, E. P., et al. (2018). The *Pseudomonas aeruginosa* orphan quorum sensing signal receptor QscR regulates global quorum sensing gene expression by activating a single linked operon. *mBio* 9: e01274-18.

Equi, A., Balfour-Lynn, I. M., Bush, A., and Rosenthal, M. (2002). Long term azithromycin in children with cystic fibrosis: a randomised, placebo-controlled crossover trial. *Lancet* 360, 978–984. doi: 10.1016/s0140-6736(02)11081-6

Faure, E., Kwong, K., and Nguyen, D. (2018). *Pseudomonas aeruginosa* in chronic lung infections: how to adapt within the host? *Front. Immunol.* 9:2416. doi: 10.3389/fimmu.2018.02416

Favre-Bonte, S., Kohler, T., and Van Delden, C. (2003). Biofilm formation by *Pseudomonas aeruginosa*: role of the C4-HSL cell-to-cell signal and inhibition by azithromycin. *J. Antimicrob. Chemother.* 52, 598–604. doi: 10.1093/jac/dkg397

Geisenberger, O., Givskov, M., Riedel, K., Hoiby, N., Tummler, B., and Eberl, L. (2000). Production of N-acyl-L-homoserine lactones by *P. aeruginosa* isolates from chronic lung infections associated with cystic fibrosis. *FEMS Microbiol. Lett.* 184, 273–278. doi: 10.1016/s0378-1097(00)00059-8

Ghosh, A., Jayaraman, N., and Chatterji, D. (2020). Small-molecule inhibition of bacterial biofilm. *ACS Omega* 5, 3108–3115. doi: 10.1021/acsomega.9b03695

Hansen, C. R., Pressler, T., Koch, C., and Hoiby, N. (2005). Long-term azitromycin treatment of cystic fibrosis patients with chronic *Pseudomonas aeruginosa* infection; an observational cohort study. *J. Cyst. Fibros.* 4, 35–40. doi: 10.1016/j.jcf.2004.09.001

Hoover, J. L., Lewandowski, T. F., Mininger, C. L., Singley, C. M., Sucoloski, S., and Rittenhouse, S. (2017). A robust pneumonia model in immunocompetent rodents to evaluate antibacterial efficacy against *S. pneumoniae*, *H. influenzae*, *K. pneumoniae*, *P. aeruginosa* or *A. baumannii*. *J. Vis. Exp.* 119:e55068. doi: 10.3791/55068

Hraiech, S., Bregeon, F., Brunel, J. M., Rolain, J. M., Lepidi, H., Andrieu, V., et al. (2012). Antibacterial efficacy of inhaled squalamine in a rat model of chronic *Pseudomonas aeruginosa* pneumonia. *J. Antimicrob. Chemother.* 67, 2452–2458. doi: 10.1093/jac/dks230

Ichimiya, T., Takeoka, K., Hiramatsu, K., Hirai, K., Yamasaki, T., and Nasu, M. (1996). The influence of azithromycin on the biofilm formation of *Pseudomonas aeruginosa* in vitro. *Chemotherapy* 42, 186–191. doi: 10.1159/000239440

Kumar, M., Rao, M., Barman, T. K., Pandya, M., Dube, S., and Purnapatre, K. P. (2016). In-vivo efficacy of a novel Leu-t-RNA synthatase inhibitor compound a against MDR *Pseudomonas aeruginosa* 1594965 in a foreign body associated urinary tract infection model. *Int. J. Infect. Dis.* 45:129. doi: 10.1016/j.ijid.2016.02.320

Kumar, M., Rao, M., Purnapatre, K. P., Barman, T. K., Joshi, V., Kashyap, A., et al. (2019). DS86760016, a Leucyl-tRNA synthetase inhibitor with activity against *Pseudomonas aeruginosa*. *Antimicrob. Agents Chemother.* 63: e02122-18.

Lucchi, M., Damle, B., Fang, A., de Caprariis, P. J., Mussi, A., Sanchez, S. P., et al. (2008). Pharmacokinetics of azithromycin in serum, bronchial washings, alveolar macrophages and lung tissue following a single oral dose of extended or immediate release formulations of azithromycin. *J. Antimicrob. Chemother.* 61, 884–891. doi: 10.1093/jac/dkn032

Macia, M. D., Rojo-Molinero, E., and Oliver, A. (2014). Antimicrobial susceptibility testing in biofilm-growing bacteria. *Clin. Microbiol. Infect.* 20, 981–990. doi: 10.1111/1469-0691.12651

Marvig, R. L., Sondergaard, M. S., Damkiaer, S., Hoiby, N., Johansen, H. K., Molin, S., et al. (2012). Mutations in 23S rRNA confer resistance against azithromycin in *Pseudomonas aeruginosa*. *Antimicrob. Agents Chemother.* 56, 4519–4521. doi: 10.1128/aac.00630-12

Maurice, N. M., Bedi, B., and Sadikot, R. T. (2018). *Pseudomonas aeruginosa* biofilms: host response and clinical implications in lung infections. *Am. J. Respir. Cell Mol. Biol.* 58, 428–439.

Mizukane, R., Hirakata, Y., Kaku, M., Ishii, Y., Furuya, N., Ishida, K., et al. (1994). Comparative in vitro exoenzyme-suppressing activities of azithromycin and other macrolide antibiotics against *Pseudomonas aeruginosa*. *Antimicrob. Agents Chemother.* 38, 528–533. doi: 10.1128/aac.38.3.528

Mulcahy, L. R., Isabella, V. M., and Lewis, K. (2014). *Pseudomonas aeruginosa* biofilms in disease. *Microb. Ecol.* 68, 1–12.

Nalca, Y., Jansch, L., Bredenbruch, F., Geffers, R., Buer, J., and Haussler, S. (2006). Quorum-sensing antagonistic activities of azithromycin in *Pseudomonas aeruginosa* PAO1: a global approach. *Antimicrob. Agents Chemother.* 50, 1680–1688. doi: 10.1128/aac.50.5.1680-1688.2006

Principi, N., Blasi, F., and Esposito, S. (2015). Azithromycin use in patients with cystic fibrosis. *Eur. J. Clin. Microbiol. Infect. Dis.* 34, 1071–1079.

Saiman, L., Marshall, B. C., Mayer-Hamblett, N., Burns, J. L., Quittner, A. L., Cibene, D. A., et al. (2003). Azithromycin in patients with cystic fibrosis chronically infected with *Pseudomonas aeruginosa*: a randomized controlled trial. *JAMA* 290, 1749–1756. doi: 10.1001/jama.290.13.1749

Sakuragi, Y., and Kolter, R. (2007). Quorum-sensing regulation of the biofilm matrix genes (pel) of *Pseudomonas aeruginosa*. *J. Bacteriol.* 189, 5383–5386. doi: 10.1128/jb.00137-07

Sharma, S., Khan, I. A., Ali, I., Ali, F., Kumar, M., Kumar, A., et al. (2009). Evaluation of the antimicrobial, antioxidant, and anti-inflammatory activities of hydroxychavicol for its potential use as an oral care agent. *Antimicrob. Agents Chemother.* 53, 216–222. doi: 10.1128/aac.00045-08

Singh, P. K., Schaefer, A. L., Parsek, M. R., Moninger, T. O., Welsh, M. J., and Greenberg, E. P. (2000). Quorum-sensing signals indicate that cystic fibrosis lungs are infected with bacterial biofilms. *Nature* 407, 762–764. doi: 10.1038/35037627

Smith, R. S., and Iglewski, B. H. (2003). *Pseudomonas aeruginosa* quorum sensing as a potential antimicrobial target. *J. Clin. Invest.* 112, 1460–1465. doi: 10.1172/jci200320364

Sutherland, I. (2001). Biofilm exopolysaccharides: a strong and sticky framework. *Microbiology* 147, 3–9. doi: 10.1099/00221287-147-1-3

Swatton, J. E., Davenport, P. W., Maunders, E. A., Griffin, J. L., Lilley, K. S., and Welch, M. (2016). Impact of Azithromycin on the quorum sensing-controlled proteome of *Pseudomonas aeruginosa*. *PLoS One* 11:e0147698. doi: 10.1371/journal.pone.0147698

Tateda, K., Ishii, Y., Matsumoto, T., Furuya, N., Nagashima, M., Matsunaga, T., et al. (1996). Direct evidence for antipseudomonal activity of macrolides: exposure-dependent bactericidal activity and inhibition of protein synthesis by erythromycin, clarithromycin, and azithromycin. *Antimicrob. Agents Chemother.* 40, 2271–2275. doi: 10.1128/aac.40.10.2271

Wagner, T., Soong, G., Sokol, S., Saiman, L., and Prince, A. (2005). Effects of azithromycin on clinical isolates of *Pseudomonas aeruginosa* from cystic fibrosis patients. *Chest* 128, 912–919. doi: 10.1378/chest.128.2.912

Willcox, M. D. P., Zhu, H., Conibear, T. C. R., Hume, E. B. H., Givskov, M., Kjelleberg, S., et al. (2008). Role of quorum sensing by *Pseudomonas aeruginosa* in microbial keratitis and cystic fibrosis. *Microbiology (Reading)* 154, 2184–2194. doi: 10.1099/mic.0.2008/019281-0

Yoon, S. S., Hennigan, R. F., Hilliard, G. M., Ochsner, U. A., Parvatiyar, K., Kamani, M. C., et al. (2002). *Pseudomonas aeruginosa* anaerobic respiration in biofilms: relationships to cystic fibrosis pathogenesis. *Dev. Cell* 3, 593–603.

Zeng, J., Zhang, N., Huang, B., Cai, R., Wu, B., E, S., et al. (2016). Mechanism of azithromycin inhibition of HSL synthesis in *Pseudomonas aeruginosa*. *Sci. Rep.* 6:24299.

Zimmermann, P., Ziesenitz, V. C., Curtis, N., and Ritz, N. (2018). The immunomodulatory effects of macrolides-A systematic review of the underlying mechanisms. *Front. Immunol.* 9:302. doi: 10.3389/fimmu.2018.00302

Conflict of Interest: MK, MR, TM, TKB, VJ, TC, SS, MP, DJU, and NM were employed by the company Daiichi Sankyo Pharma Pvt. Ltd., Gurgaon.

The remaining author declares that the research was conducted in the absence of any commercial or financial relationships that could be construed as a potential conflict of interest.

frontiers in Microbiology

ORIGINAL RESEARCH
published: 29 April 2021
doi: 10.3389/fmicb.2021.655873

Staphylococcus aureus Floating Biofilm Formation and Phenotype in Synovial Fluid Depends on Albumin, Fibrinogen, and Hyaluronic Acid

*Samantha Knott[1†‡], Dylan Curry[1†‡], Neil Zhao[1], Pallavi Metgud[1], Sana S. Dastgheyb[1†], Caroline Purtill[1], Marc Harwood[2], Antonia F. Chen[3], Thomas P. Schaer[4], Michael Otto[5] and Noreen J. Hickok[1]**

[1] Department of Orthopaedic Surgery, Sidney Kimmel Medical College of Thomas Jefferson University, Philadelphia, PA, United States, [2] Rothman Orthopaedic Institute, Philadelphia, PA, United States, [3] Department of Orthopaedic Surgery, Brigham and Women's Hospital, Boston, PA, United States, [4] Department of Clinical Studies, New Bolton Center, School of Veterinary Medicine, University of Pennsylvania, Kennett Square, PA, United States, [5] Pathogen Molecular Genetics Section, Laboratory of Human Bacterial Pathogenesis, National Institute of Allergy and Infectious Diseases, National Institutes of Health, Bethesda, MD, United States

Biofilms are typically studied in bacterial media that allow the study of important properties such as bacterial growth. However, the results obtained in such media cannot take into account the bacterial localization/clustering caused by bacteria–protein interactions *in vivo* and the accompanying alterations in phenotype, virulence factor production, and ultimately antibiotic tolerance. We and others have reported that methicillin-resistant or methicillin-susceptible *Staphylococcus aureus* (MRSA or MSSA, respectively) and other pathogens assemble a proteinaceous matrix in synovial fluid. This proteinaceous bacterial aggregate is coated by a polysaccharide matrix as is characteristic of biofilms. In this study, we identify proteins important for this aggregation and determine the concentration ranges of these proteins that can reproduce bacterial aggregation. We then test this protein combination for its ability to cause marked aggregation, antibacterial tolerance, preservation of morphology, and expression of the phenol-soluble modulin (PSM) virulence factors. In the process, we create a viscous fluid that models bacterial behavior in synovial fluid. We suggest that our findings and, by extension, use of this fluid can help to better model bacterial behavior of new antimicrobial therapies, as well as serve as a starting point to study host protein–bacteria interactions characteristic of physiological fluids.

Keywords: *Staphylococcus aureus*, biofilm, synovial fluid, antibiotic tolerance, virulence factors

OPEN ACCESS

Edited by:
Mark Smeltzer,
University of Arkansas for Medical Sciences, United States

Reviewed by:
Phil Giffard,
Charles Darwin University, Australia
Raiane Cardoso Chamon,
Fluminense Federal University, Brazil
K. Urish,
University of Pittsburgh, United States

***Correspondence:**
Noreen J. Hickok
Noreen.Hickok@jefferson.edu

†Present address:
Samantha Knott,
Bluebird Bio, Cambridge, MA, United States
Dylan Curry,
Association of Public Health Laboratories Fellow, Utah Public Health Laboratory, Salt Lake City, UT, United States
Sana S. Dastgheyb,
Department of Radiation Oncology, Hospital of the University of Pennsylvania, Philadelphia, PA, United States

‡*These authors have contributed equally to this work*

Specialty section:
This article was submitted to Antimicrobials, Resistance and Chemotherapy, a section of the journal Frontiers in Microbiology

Received: *19 January 2021*
Accepted: *19 March 2021*
Published: *29 April 2021*

Citation:
Knott S, Curry D, Zhao N, Metgud P, Dastgheyb SS, Purtill C, Harwood M, Chen AF, Schaer TP, Otto M and Hickok NJ (2021) Staphylococcus aureus Floating Biofilm Formation and Phenotype in Synovial Fluid Depends on Albumin, Fibrinogen, and Hyaluronic Acid. Front. Microbiol. 12:655873. doi: 10.3389/fmicb.2021.655873

INTRODUCTION

Despite aggressive treatment and the use of local supratherapeutic concentration of antimicrobials, joint infections can persist (Kunutsor et al., 2018), even in the absence of implants. The presence of synovial fluid in the joint fosters the formation of dense, proteinaceous, free-floating biofilm aggregates (Dastgheyb et al., 2015a,b; Crosby et al., 2016; Gilbertie et al., 2019; Pestrak et al., 2020), the removal of which is required for successful treatment of infection. The bacteria–protein

interactions in these aggregates induce alterations in phenotype, virulence factor production, and ultimately marked antibiotic tolerance (Dastgheyb et al., 2015a,b,c), akin to what has been described for adherent biofilms.

Under conditions that mimic the physiological environment, bacterial aggregation also occurs *in vitro*, where microscopic clusters are seen in serum and microscopic and macroscopic clusters are visible in synovial fluid (Dastgheyb et al., 2015a; Crosby et al., 2016). We and others have reported that in synovial fluid, methicillin-resistant or methicillin-susceptible *Staphylococcus aureus* (MRSA or MSSA, respectively) and other pathogens assemble a proteinaceous matrix that is coated by polysaccharides as is characteristic of biofilms (Dastgheyb et al., 2015b; Perez and Patel, 2015; Gilbertie et al., 2019). Aggregation depends on microbial surface components recognizing adhesive matrix molecules (MSCRAMMs) and the master biofilm regulator accessory gene regulator (Agr) (Dastgheyb et al., 2015b). Agr-regulated virulence factors, specifically phenol-soluble modulins (PSMs), are downregulated in synovial fluid. This downregulation appears to have consequences on bacterial aggregation, as we found that overexpression of any type of PSM (PSMα, PSMβ, and delta toxin) abrogated synovial fluid-induced aggregation. These findings support the notion that suppression of Agr and the concomitant strong suppression of PSM production are critical for MRSA aggregation (Dastgheyb et al., 2015c). Thus, these reports challenge whether drugs that act through inhibition of *agr*-mediated gene expression, such as production of proteins important for quorum sensing, will result in a benefit to the host during periprosthetic joint infection (PJI) (Piewngam et al., 2020). In light of these findings, we reasoned that it would be important to begin mapping the components of these aggregates to allow better modeling both for implant development as well as for combatting joint infection.

Synovial fluid is central to aggregation and is a protein-rich viscous fluid composed of proteins filtered from blood and secreted proteins/proteoglycans from cells (predominantly synovium and cartilage). In our studies, we have recognized that synovial fluid shows donor variability, perhaps where composition reflects disease state (Mateos et al., 2012; Noh et al., 2014). To circumvent this limitation, we have established equine or porcine synovial fluid as a readily available source of "normal" synovial fluid that reproduces the reported aggregatory behavior and phenotype over multiple bacterial species (Gilbertie et al., 2019).

In this study, we set out to determine which proteins in synovial fluid were predominantly responsible for staphylococcal aggregation. To do that, the abundant proteins sequestered in synovial fluid bacterial aggregates were identified and their roles were investigated. Based on these determinations, we next evaluated if the presence of these proteins/proteoglycans could reproduce the phenotype of synovial fluid bacterial aggregates, where our criteria were (1) morphology, (2) composition, (3) antimicrobial tolerance, and (4) virulence factor production. As a consequence of these studies, we have developed a "pseudo" synovial fluid (pSynF) that embodies many of the characteristics of native synovial fluid and serves as a readily accessible means to study bacterial behavior in fluids that more closely approximate *in vivo* biofilm characteristics.

MATERIALS AND METHODS

Ethics Statement

Human synovial fluid and other surgical waste were obtained from therapeutically necessary joint aspirations or operations. This material, designated as "waste" (no identifiers), was retrieved and designated as "not human research" by the Thomas Jefferson University Office of Human Research Protections in keeping with the revised Federal Policy for the Protection of Human Subjects (revised Common Rule, 2018).

Bacterial Strains and Growth

MSSA ATCC®25923™ and MRSA LAC USA300 [parent strain, giving rise to LAC *psm*α-lux, LAC *psm*β-lux, or LAC P3-lux strains (Dastgheyb et al., 2015c)] were grown from a single colony in Trypticase Soy Broth (TSB; Becton-Dickinson, Sparks, MD) overnight (ON), 37°C, 180 rpm. ON cultures were diluted by comparison to a 0.5 McFarland standard [$\sim 10^8$ colony-forming unit (CFU)/ml for *S. aureus*].

Clinical Samples

Except for the PJI samples, synovial fluid used in this manuscript was collected as discarded material from routine office aspirations from patients with sterile fluid excess. Eight of those were used without pooling for determination of MSSA aggregate characteristics by sodium dodecyl sulfate–polyacrylamide gel electrophoresis (SDS-PAGE) and Western blotting. Otherwise, 2–5 samples were pooled to allow volumes large enough to perform the various activity/expression assays throughout the rest of the manuscript. The infected samples were collected as waste from revision surgeries for treatment of confirmed PJI and represented implant-adherent biofilm and non-attached biofilm. A small sample was scraped from the implant (biofilm sample), and another sample was retrieved from the discarded fluid material that was flushed from the bone cavity (floating aggregate). Material was placed into labeled 50-ml conical tubes, fixed by incubation in formalin, and, after rinsing, prepared for imaging by scanning electron microscopy (SEM). The identity of the bacterial strain causing PJI was not supplied with the fixed samples.

Biofilm Formation

To form biofilms *in vitro*, MSSA (10^5 CFU/ml) were incubated in TSB or human synovial fluid for 24 h, 37°C, without agitation using 1 cm × 2 mm Ti6Al4V coupons (kind gift of Zimmer). Surfaces were gently rinsed 3 × with phosphate buffered saline (PBS) and fixed with 4% paraformaldehyde, ON, 4°C. Samples were then prepared for SEM. Clinical examples were composed of samples of infected reamings from a PJI patient as well as several scrapings from the implant removed during the patient's treatment. From this formalin-fixed material, at least three samples were removed and rinsed and solid material was affixed to a slide followed by dehydration, sputter coating, and

SEM analysis. Micrographs were compared for fibrous material, presence of blood cells, and apparent biofilm-like structures that could be attributed to bacteria. Images representative of these are shown.

Determination of Interplay of Synovial Fluid Components on Methicillin-Susceptible *Staphylococcus aureus* Aggregation and Formation of Pseudo Synovial Fluid

Hyaluronic acid (HA; *Streptococcus equi*, 91% high molecular weight (MW); Alfar Aesar, Tewksbury, MA) was dissolved (ON, 4°C) to 4.05 mg/ml in sterile TSB. Fibrinogen (Fg; Alfa Aesar, Tewksbury, MA, United States) was dissolved to 60, 90, and 120 mg/ml in PBS, pH 8.5, by incubation at 37°C, 3 min, followed by vortexing. Albumin (Alb; Fisher Scientific, Pittsburgh, PA, United States) was dissolved to 60, 120, and 180 mg/ml in PBS, pH 8.5. All stocks were sterile filtered (0.2 μm filter) and stored at 4°C for up to 2 days.

A concentration matrix of Fg, Alb, and HA was created in 96-well plates. TSB (140 μl) containing 0, 1.5, or 3.0 mg/ml HA was added to each well; 20 μl of Fg stocks were added to give 0, 6, 9, or 12 mg/ml and 20 μl of Alb stocks to yield 0, 6, 12, and 18 mg/ml. Lastly, 20 μl of 10^8 CFU/ml MSSA in sterile PBS were added into each well to yield 10^7 CFU/ml. Plates were incubated, 37°C, 180 rpm, 90 min to allow bacterial aggregation. Samples were serially diluted, followed by plating on Petrifilms; reduced bacterial counts were considered aggregation events (1 CFU would equal one aggregate in that instance). Each individual condition was determined in triplicate, with three independent experiments to yield an $n = 8$ or 9 for each condition. The combination of 3.0 mg/ml HA, 9 mg/ml Fg, and 10 mg/ml Alb in TSB was referred to as pSynF.

Bacterial Aggregate Formation and Antibiotic Treatment

Pooled synovial fluid was formed by combining 2–5 samples from individual donors to better allow reproducibility. Here, 0.2, 1.0, or 3.0 ml of human synovial fluid (≥90% final volume), pSynF, human serum (Sigma, not heat inactivated) or TSB in 6-, 24-, or 96-well tissue culture plates (Med Supply Partners, Atlanta, GA), respectively, were inoculated with 10^7 or 10^8 CFU/ml MSSA or MRSA and incubated for a minimum of 90 min, 37°C, 125 rpm. Either during or after aggregation, amikacin (AMK) was added (0–200 μg/ml) and incubated for 6 h. At 6 h, bacteria were pelleted and washed [when aggregate dispersal was used, the resulting pellet was treated with 1 ml of 0.25% trypsin (Corning), 37°C, 180 rpm, 20 min, and pelleted again]. All pellets were then washed with PBS, resuspended by pipetting/vortexing and, after serial dilution, plated on 3M™ Petrifilm™ aerobic count plates (3M Corporation, St. Paul, MN), followed by direct counting (countable range, 30–300 CFU/spot). This dispersal method was validated by the (1) disappearance of visible aggregates and (2) equivalence of CFU (after Trypsin) with CFU recovered from TSB using an equal bacterial inoculum.

Scanning Electron Microscopy

Bacterial aggregates were fixed with 4% paraformaldehyde, room temperature (RT), 10 min, and dehydrated by sequential incubation (RT, 10 min) with 10, 30, 50, 70, 90, and 100% ethanol in PBS. Samples were dried ON, sputter-coated with gold, and imaged using a Hitachi TM-1000 SEM.

Fractionation by Sodium Dodecyl Sulfate–Polyacrylamide Gel Electrophoresis: Pseudo Synovial Fluid or Human Synovial Fluid

Synovial fluid samples were obtained from individual donors ($n = 8$), each separately labeled with a different number. Before fractionation, samples were diluted to 3% with sterile PBS. Aggregates formed as above were pelleted at 13,000 × g, 3 min, washed, and resuspended in 1 ml PBS by repeated vortexing and pipetting. Laemmli sample buffer with β-mercaptoethanol was added (1:1), samples heated at 70°C for 10 min, placed on ice, and fractionated (105 V, ∼70 min) on an SDS-polyacrylamide gel (7.5%), using the discontinuous buffer system of Laemmli (1970). MW standards (10–250 kDa; Precision Plus Protein™ Dual Color Standards, Bio-Rad, Hercules, CA, United States) were run on the same gel, as were serum, Fg (Alfa Aesar), and Alb (Thermo Fisher Scientific).

Western Blotting

Following fractionation, protein bands were transferred (1.3 A, 25V, 7 min) to nitrocellulose membranes (Bio-Rad) using the Trans Blot Turbo Transfer System (BioRad) with Turbo transfer buffer. Membranes were blocked by incubation in 10% nonfat milk (BioRad) in Tris-Buffered Saline (1×) containing 0.5% Tween-20 (10% TTBS), 60 min, followed by incubation with mouse anti-Fg (1:1,000; Sigma-Aldrich F9902) or rabbit anti-Alb (1:1,000; Sigma-Aldrich, SAB4200656) antibody, in 5% TTBS, 4°C, ON, with shaking. The blot was then washed 3× with 10% TTBS, incubated in horseradish peroxidase (HRP)-linked goat anti-mouse (Bio-Rad; 1:10,000) or HRP-linked goat anti-rabbit antibody (Abcam, Cambridge, MA; 1:20,000), RT, 2 h, washed 3×, followed by visualization using Pierce™ ECL Western Blotting Substrate (Thermo Fisher Scientific, Rockford, IL, United States). In all gels and blots, results were repeated using additional aggregates formed in the same or different synovial fluid sample with similar appearances. Densitometry was performed using three different exposures of each blot. The amount of Fg in samples was calculated by comparison to the band area in 100 μg Fg control for each of the exposures.

Synovial Fluid Fractionation

Pooled synovial fluid was formed by combining 2–5 samples from individual donors to better allow reproducibility. Protein was precipitated from pooled human synovial fluid (Qiu et al., 2003) by addition of 200 proof (100%) absolute ethanol, 4°C, to a final concentration of 10%, followed by ON incubation, 4°C. Protein precipitates were collected, 1,100 × g, 5 min, 4°C, where the pellet represented a Fg-enriched fraction (ppt) and the

supernatant, a Fg-depleted synovial fluid (depSynF). SDS-PAGE and Western blotting were used to determine the extent of Fg depletion. Upon Fg re-addition, the concentrations added were 6, 9, and 12 mg/ml.

Viscosity Determination

The viscosity of pooled synovial fluid and pSynF was measured by a homemade viscometer (Tang, 2016) using the following equation:

$$\eta = \frac{d^2 (\rho_b - \rho_l) g \sin\theta}{18L} T$$

T = time (s) for a 2-mm diameter (d) ball bearing to traverse 0.1 m (L) of liquid in a 2-ml serological pipette. η = viscosity, ρ_b = 5156.6 kg/m^3 = ball density; ρ_l = 1,000, 1,002, or 1,034 kg/m^3, which are the density of water, synovial fluid, or pSynF, respectively; g = 9.8 m/s^2 = gravitational acceleration; $\theta = \pi/3$ radians = angle of the pipette with respect to the horizontal. Finally, all values were adjusted by multiplied by the ratio of the established viscosity of water over the viscosity of water in this experiment (Tang, 2016).

Wheat Germ Agglutinin Staining

Bacterial aggregates were rinsed three times with sterile PBS, fixed with 4% paraformaldehyde, 37°C, 15 min, rinsed three times with sterile PBS, and stained with 5 μg/ml AlexaFluor®488 conjugated wheat germ agglutinin (WGA; Invitrogen), 10 min, RT. Stained aggregates were rinsed three times with sterile PBS and imaged at 488 nm using a confocal laser scanning microscope (Zeiss LSM800).

Phenol-Soluble Modulin Luminescence Assay

LAC *psm*α-lux, LAC *psm*β-lux, or LAC P3-lux strains of USA300 MRSA were inoculated ($C_f \sim 10^6$ CFU/ml) in TSB, human serum, pooled synovial fluid, or pSynF to a final volume of 5.0 ml, followed by incubation for up to 24 h (225 rpm, 37°C). Every 2 h, while maintaining temperature, samples were vortexed, 2 × 100 μl were removed and placed in clear bottom white plates, and luminescence was measured using a Veritas™ microplate luminometer (Turner Biosystems, Sunnyvale, CA, United States). In parallel, absorbance (λ = 600 nm) was measured on the same samples to determine bacterial growth (Tecan Infinite M1000 plate reader). Luminescent values were normalized to the absorbance at 600 nm and expressed as relative luminescent units (RLUs). Each point was determined in duplicate in a minimum of three independent experiments.

Statistics

Statistical significance was determined using the Student's t-test or the Mann–Whitney U-test for simple comparisons. More complex comparisons were analyzed by one-way or two-way ANOVA with a Tukey's *post hoc* test. Alpha values were set to 0.05, and the statistical analyses were performed using SPSS IBM®SPSS® Statistics Version 26 or Prism GraphPad 9.0.1.

RESULTS

Staphylococcus aureus Aggregates in Human Synovial Fluid Are Rich in Fibrinogen and Albumin

We started our investigation by asking if the aggregates and biofilms formed *in vitro* in human synovial fluid approximated the aggregates formed in an infected joint. By SEM (**Figure 1A**; all *in vitro* images are representative of at least three samples), the adherent biofilm retrieved from an implant in a case of clinically confirmed PJI was rich in proteins and even showed the presence of red blood cells. *In vitro*, MSSA biofilm formed in human synovial fluid on smooth titanium alloy (Ti6Al4V) was relatively sparse and much simpler than the PJI biofilm. The major similarity was that bacteria/biofilm showed clear fibers within and between biofilm clusters. In TSB, MSSA was largely clustered and covered by biofilm; any underlying fibrils were not as apparent as on Ti6Al4V. The non-adherent aggregate retrieved from the PJI fluid (clinical aggregate) showed large globular bacterial aggregates immobilized on a fibrous matrix and encased in biofilm. Like the PJI aggregate, large, globular, floating MSSA aggregates were formed *in vitro* in human synovial fluid from a single donor; individual bacteria were also visible and many of these were obscured by biofilm coating (**Figure 1A**). Because MSSA does not aggregate in TSB, no clear picture was able to be taken.

Based on our previous work (Dastgheyb et al., 2015b,c; Gilbertie et al., 2019), the abundant serum protein Fg was likely an important component of aggregates. We asked if we could identify the most abundant proteins in the aggregate, if they included Fg among other proteins, and if protein abundance was similar to the parent synovial fluid. Based on electrophoretic fractionation, the size distribution and relative amounts of human synovial fluid proteins from individual donors (SynF1, 2, 3) largely mirrored those found in human serum (**Figure 1B**; aggregates from the samples were fractionated on at least three gels). Proteins in the 50–75 kDa were most abundant in all samples, whereas high-MW components, which would include fibronectin (Fn), were not sufficiently abundant to be apparent with Coomassie staining of these gels. Based on staining intensity, bacterial aggregates formed in synovial fluid appeared to be composed predominantly of the same abundant proteins found in the parent synovial fluid.

Fg and Alb are both abundant in osteoarthritic synovial fluid (Fitowska et al., 2012; Mateos et al., 2012; Ritter et al., 2013). Thus, we investigated if the intense bands noted in the bacterial aggregates in **Figure 1B** could be associated with Fg and Alb. Both synovial fluid and their corresponding bacterial aggregates showed clear presence of Fg and Alb by Western blotting (**Figure 1C**). In the left-hand blot, the Alb content of three different synovial fluid samples (SynF 6, 7, 8) and their corresponding macroscopic aggregates are shown. In the right-hand blot, the Fg content of three additional human synovial fluid samples (SynF 3, 4, 5), along with the Fg content of aggregates formed in those synovial fluids, are shown. Both blots demonstrated that Alb and Fg were

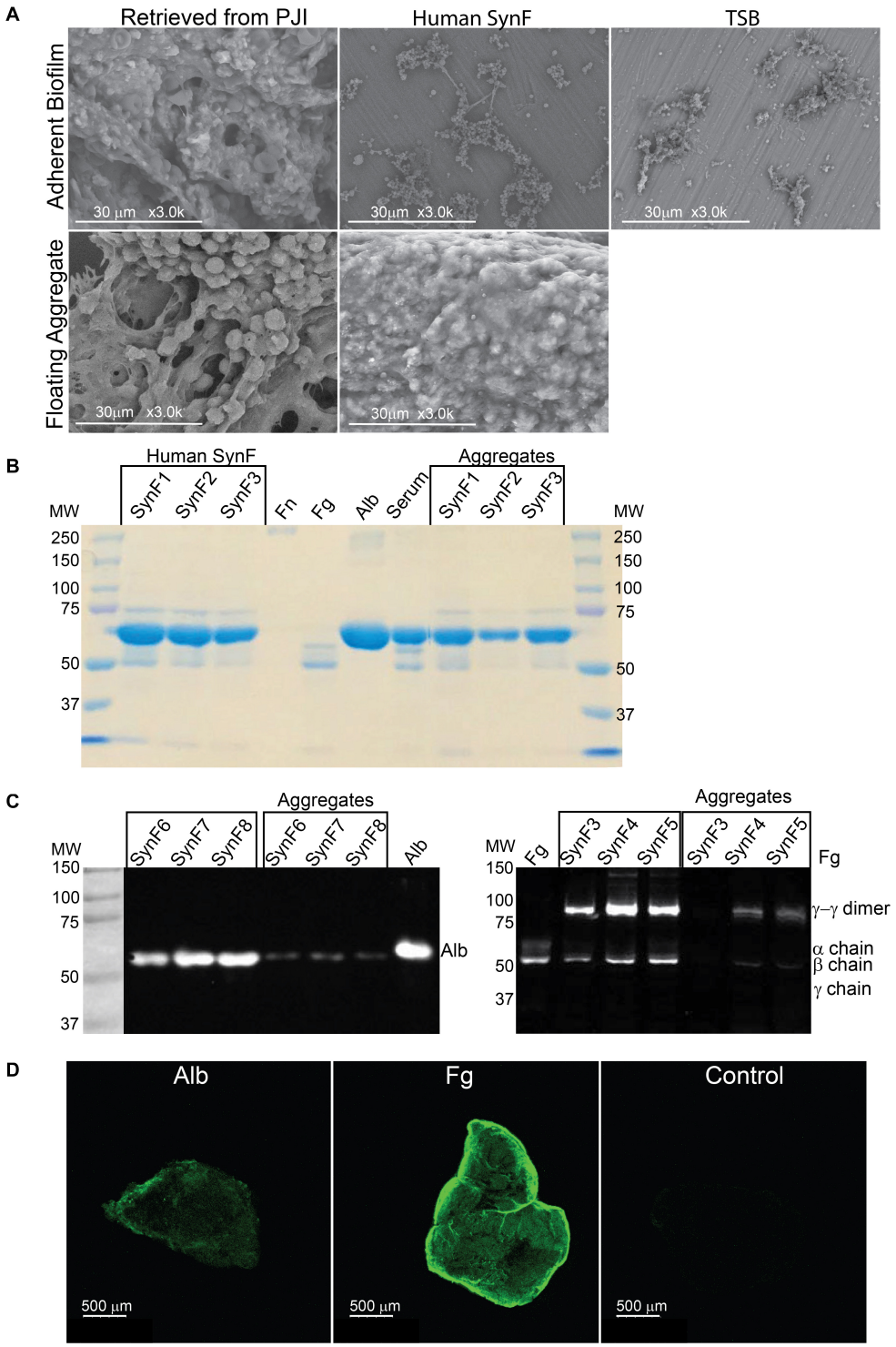

FIGURE 1 | Synovial fluid aggregate morphology and composition. **(A) (Top)** Using SEM, biofilm morphology in samples retrieved from an infected knee replacement [periprosthetic joint infection (PJI)] or formed on titanium using methicillin-susceptible *Staphylococcus aureus* (MSSA) in human synovial fluid (SynF) or Trypticase Soy Broth (TSB). **(Bottom)** Floating aggregates retrieved from an infected knee replacement or floating aggregates formed with MSSA in human synovial fluid. **(B)** Sodium dodecyl sulfate–polyacrylamide gel electrophoresis (SDS-PAGE) gel stained with Coomassie Blue. The gel shows the composition of human synovial fluid and of synovial fluid MSSA aggregates from three separate samples of synovial fluid, as compared to fibronectin (Fn), fibrinogen (Fg), albumin (Alb), and serum controls. **(C)** Western blot analysis of MSSA aggregates from synovial fluid for Alb **(left)** and for Fg **(right)**. The γ – γ dimer and α chain are indicated, as compared with human synovial fluid, Fg, and Alb standards. Lanes represent human synovial fluid samples and resulting aggregates from different samples. **(D)** MSSA aggregates stained for Alb, Fg, or secondary antibody alone (Control). All images are representative images of at least three samples.

components of the bacterial synovial fluid aggregate. We also confirmed the presence of Fg and Alb in bacterial aggregates formed in pooled synovial fluid by immunostaining (**Figure 1D**). Using antibodies to the two proteins, Fg or Alb staining was clearly visible on the outside of the aggregates (in contrast to the control staining with secondary antibody; confirmed by microscopy of three aggregates). Collectively, these results established the basic components of bacterial aggregates, guiding our development of a viscous fluid for modeling bacterial behavior in synovial fluid.

Fibrinogen Is Necessary for Bacterial Aggregation in Human Synovial Fluid

We next sought to explore the involvement of Fg in bacterial aggregation. To test its role, we ethanol-precipitated proteins from pooled human synovial fluid to deplete Fg (among other proteins; n = 3) (Qiu et al., 2003). By Western blotting (**Figure 2A**), the Fg content of ethanol-precipitated human synovial fluid (depSynF) was reduced compared with the parent pooled synovial fluid; the precipitate (Ppt) had faint bands corresponding to Fg. Approximate Fg concentrations were determined by densitometric comparisons of band intensities for Fg standards with experimental bands. Precipitation depleted the Fg content of synovial fluid by ∼50%, depending on the experiment.

To be able to determine the effect of altered Fg content on bacterial aggregation, we set up a trypsin dispersal assay. Specifically, we tested the ability of trypsin to digest surface proteins and other proteinaceous components that facilitate bacterial clustering in TSB and aggregation in pooled synovial fluid [**Figure 2B**; n = 9 (TSB), 12–13 (SynF)]. MSSA that typically exists in small clusters within TSB showed no significant increase in CFU after trypsin treatment. In synovial fluid, CFU were ∼1 log lower than the measured inoculum; trypsin treatment resulted in an ∼1.5 log increase in CFU. Thus, (1) synovial fluid aggregation reduced the number of retrieved CFU by counting one large cluster as one colony, and (2) trypsin treatment dispersed the aggregates to release the bacteria from the aggregates. This trypsin dispersal resulted in numbers of CFU consistent with those measured for the same inoculum in TSB.

We asked if the Fg-depleted synovial fluid (depSynF) supported MSSA aggregation (**Figure 2C**). No visible aggregation was observed with depSynF, and the CFUs were approximately equal to the initial inoculum (red dashed line). Addition of 6, 9, or 12 mg/ml of Fg caused a decrease in CFU, consistent with increased aggregation. Notably, 9 and 12 mg/ml Fg caused the largest decreases. In summary, we have demonstrated that

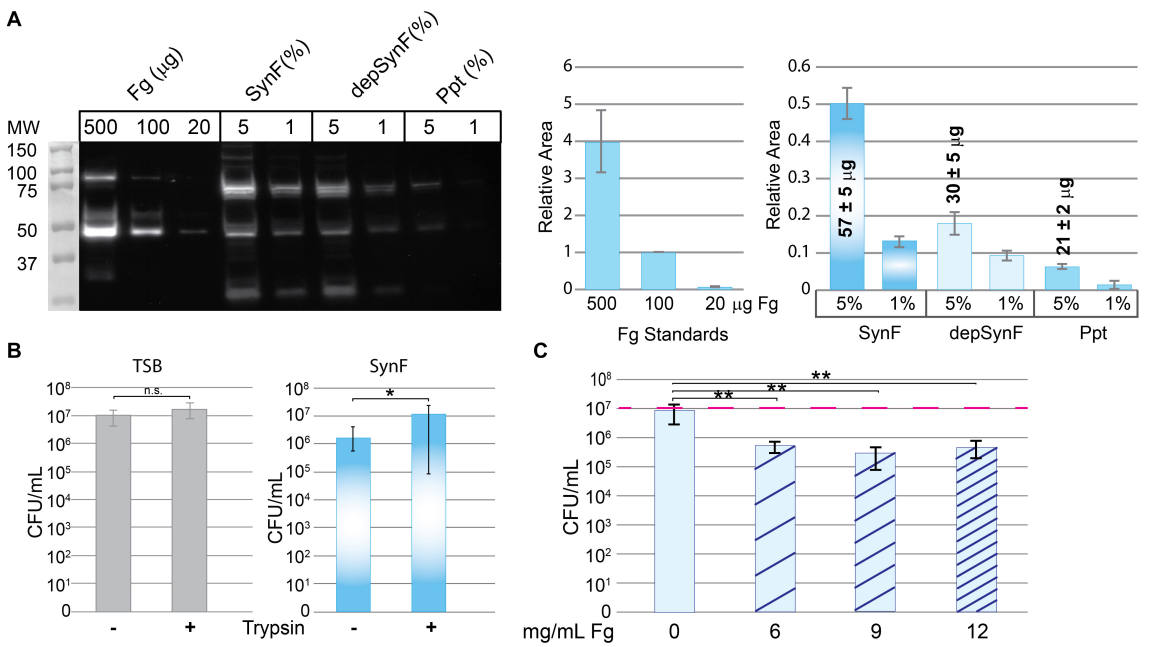

FIGURE 2 | Effects of fibrinogen (Fg) on aggregation. **(A)** Western blot showing Fg standards, amount of Fg detected in pooled human synovial fluid (equal amounts added; percentage of synovial fluid in solution indicated), and amount remaining in synovial fluid after ethanol depletion of proteins including Fg (depSynF) and amount in the Fg-enriched precipitate (ppt) (>3 blots with similar results). Densitometry of this Western blot is shown on the right using varying exposures. Fg standards are plotted in the first graph and used to calculate Fg contained in the 5% samples. Areas associated with the experimental Fg samples were determined and normalized to the 100-µg sample. **(B)** Effects of aggregation in pooled synovial fluid on colony-forming units (CFUs)/ml. Minus indicates no dispersion and reflects counts obtained by dilution and counting. Plus indicates the counts after treatment of the cultures with trypsin to disperse aggregates. Values graphed are means ± SD {*$p \leq 0.05$; n = 9 [Trypticase Soy Broth (TSB)], 12–13 (Synovial fluid)}. **(C)** Re-addition of Fg to depSynF causes reacquisition of aggregation at 90 min, as demonstrated by decreased CFU/ml. Red dashed line indicates the initial inoculum. Values graphed are means ± SD (*$p \leq 0.05$; **$p \leq 0.01$; n = 6 for each condition; representative experiment of three with similar results for each).

Fg is crucial for visible (macroscopic) *S. aureus* aggregation in synovial fluid.

Combinations of Albumin, Fibrinogen, and Hyaluronic Acid Can Recreate the Aggregatory Phenotype

In keeping with the presence of Fg and Alb in MSSA/MRSA aggregates, we investigated if both Fg and Alb contributed to the aggregatory antimicrobial-tolerant bacterial phenotype. Because HA contributes to the viscosity of synovial fluid (Park et al., 2014), HA was also tested. A matrix of Alb, Fg, and HA concentrations was created (**Figure 3**).

To measure aggregation, we looked at the dependence of component concentration on total CFU, where decreases in CFU were interpreted as increased aggregation. The addition of HA visibly increased viscosity and aggregation for all Alb, Fg concentrations/combinations. However, only 6 and 12 mg/ml Alb contained HA concentrations that were statistically different from 0 mg/ml HA (see statistical analysis in **Supplementary Material A1**). Among the conditions containing 6 mg/ml Alb, only 3.0 mg/ml HA (n = 36) resulted in lower CFU when compared to 0 mg/ml HA (n = 35; $p < 0.05$). When the Alb concentration was increased to 12 mg/ml, both 1.5 mg/ml (n = 34; $p < 0.001$) and 3.0 mg/ml HA (n = 36; $p < 0.0001$) resulted in greater aggregation, as manifested by lower CFU. Significantly greater aggregation occurred with (a) 12 mg/ml Alb in the presence of 1.5 or 3.0 mg/ml HA or (b) 3.0 mg/ml HA in the presence of 6 or 12 mg/ml Alb. We focused on the combination that formed the intersection of the two groups, 12 mg/ml Alb and 3.0 mg/ml HA. Addition of Fg caused some MSSA aggregation (n = 9; $p < 0.001$), as measured by decreased CFU. While addition of Fg always increased bacterial aggregation, a clear demarcation between the different Fg concentrations was not consistent. Ultimately, based on similarities to synovial fluid, we chose 12 mg/ml of Alb, 3 mg/ml HA, 10 mg/ml of Fg dissolved in TSB for the final concentrations. This choice was based on (a) 12 mg/ml Fg was not suitable, as it caused acquisition of a gel-like consistency to the bacteria-containing fluid (data not shown); (b) there was no difference in bacterial aggregation between 6 and 9 mg/ml Fg; and (c) known range of Fg concentrations in synovial fluid (Kushner and Somerville, 1971; Mateos et al., 2012; Bennike et al., 2014). Statistical analyses are in table form (**Supplementary Material A1**). We referred to this fluid as pSynF and asked if it could model bacterial behavior in human native synovial fluid.

Methicillin-Susceptible *Staphylococcus aureus* in Pseudo Synovial Fluid Aggregate and Display Amikacin Tolerance

To determine if the proteins contained within pSynF were able to reproduce the known characteristics of synovial fluid, we first examined the morphology of a synovial fluid aggregate

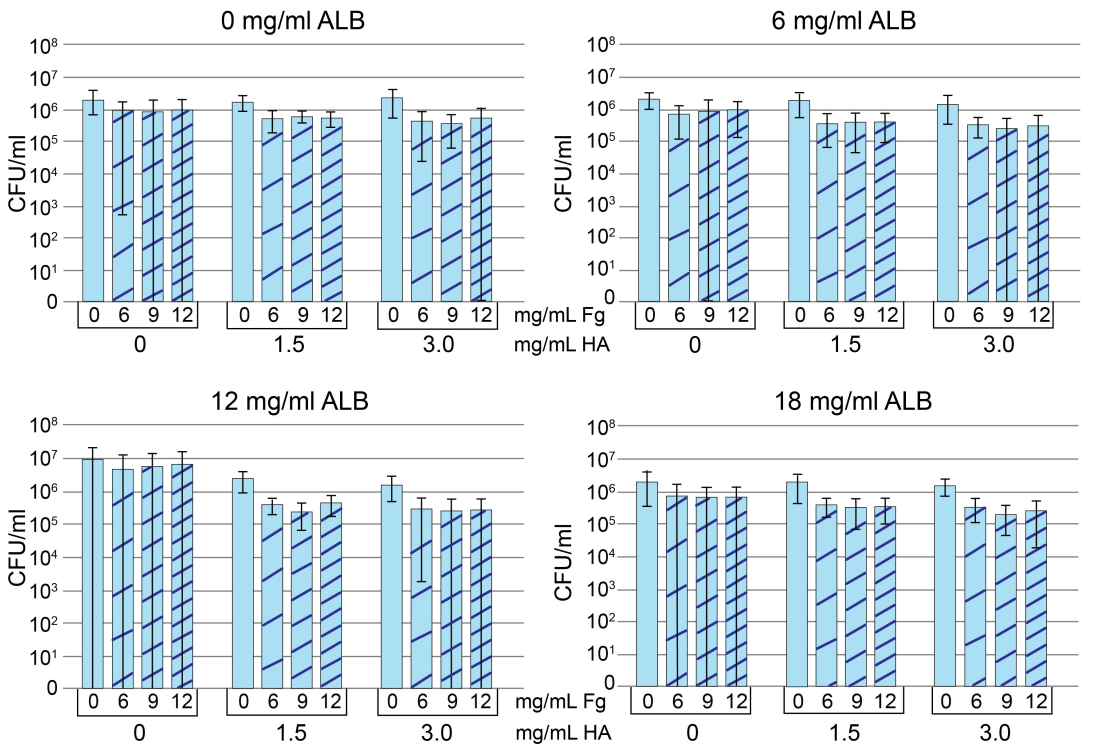

FIGURE 3 | Protein addition assay. Methicillin-susceptible *Staphylococcus aureus* (MSSA) CFU/ml after growth in Trypticase Soy Broth (TSB) containing 0, 6, 12, or 18 mg/ml albumin (Alb). Increasing concentrations of hyaluronic acid (HA) and fibrinogen (Fg) are indicated in each panel. Decreased CFU/ml is a marker of increased aggregation. Values graphed are means ± SD. Statistical analyses are included in the **Supplementary Material A1** (n = 8–9/condition).

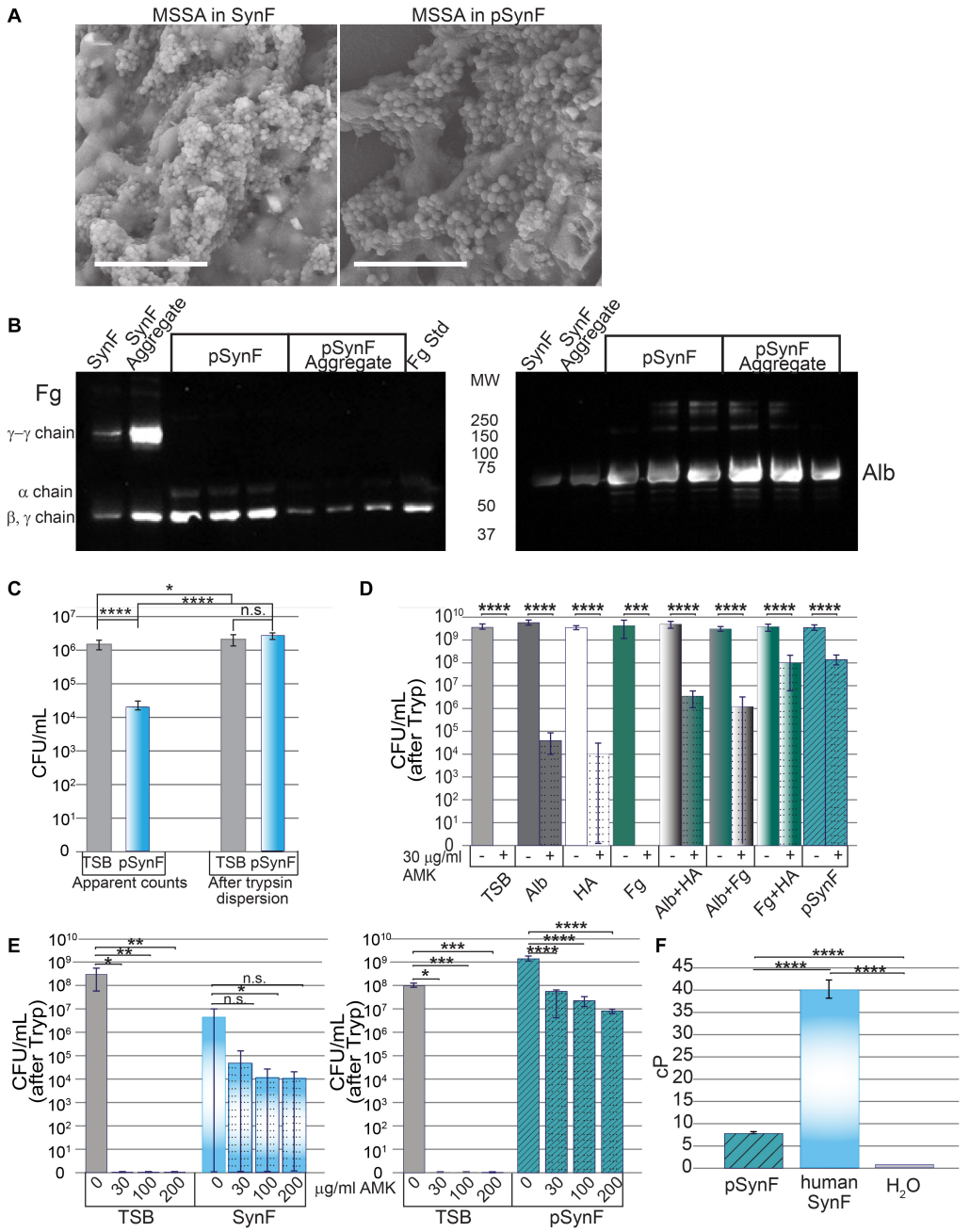

FIGURE 4 | Effects of pseudo synovial fluid (pSynF) on methicillin-susceptible *Staphylococcus aureus* (MSSA). **(A)** Comparison of MSSA aggregates in human synovial fluid (SynF) vs. pSynF using SEM. Magnification: scale bar = 15 μm. **(B)** Fibrinogen (Fg) **(left)** and albumin (Alb) **(right)** content of pSynF and pSynF aggregates compared to aggregates formed in synovial fluid by Western blotting. **(C)** Graphs showing CFU/ml in Trypticase Soy Broth (TSB) and pSynF before trypsin dispersion vs. CFU/ml after trypsin dispersion [("after Tryp" in subsequent graphs) $n = 12$ for each condition]. **(D)** Effects of amikacin (AMK) on fluids containing protein/proteoglycan concentrations found in pSynF. Controls are TSB alone and complete pSynF ($n = 8$–9 for each condition). All components were dissolved in TSB. **(E)** Dose response of MSSA to AMK in TSB vs. synovial fluid (left; $n = 9$/condition) and of TSB vs. pSynF (right; $n = 12$/condition). **(F)** Viscosity of pSynF compared to that of synovial fluid and H_2O using a ball velocity method ($n = 10$/condition). Values graphed are means ± SD. Viscosity is expressed as centiPoise (cP). In panels **(A–F)**, $^*p < 0.05$; $^{**}p < 0.01$; $^{***}p < 0.001$; $^{****}p < 0.0001$.

compared to that of pSynF (**Figure 4A**). By SEM, large floating aggregates were formed in pooled synovial fluid and in pSynF. These aggregates were partially covered with a biofilm layer that obscured the finer details of the underlying aggregate; distinct fibers were only occasionally visible for either aggregate. By Western blotting, pSynF aggregates showed the presence of Fg and Alb (**Figure 4B**; independent replicates are shown on the blot), as was observed in the synovial fluid aggregates. The α, β,

and γ Fg monomers were present in pSynF. γ-γ dimers, which were abundant in synovial fluid and synovial fluid aggregates, were sparse in the pSynF aggregates.

We next wanted to test the effects of each of the components apart and together on the antibiotic tolerance of bacteria. First, we established that, like synovial fluid, aggregation resulted in a decrease in CFU (**Figure 4C**; $n = 12$). Similarly, trypsin treatment caused release of MSSA from the aggregates to reach levels indistinguishable from those measured for the same inoculum in TSB.

We then tested the effect of each of the different components of pSynF when added to TSB on MSSA tolerance to AMK, an aminoglycoside antibiotic important for severe infections (**Figure 4D**; $n = 8$–9). In this experiment, all aggregates were dispersed by trypsin before enumeration [CFU (after Tryp)]. In TSB, 30 μg/ml of AMK eradicated MSSA (∼9 log decrease). In 12 mg/ml Alb + TSB, or 3 mg/ml HA +TSB, AMK tolerance increased so that there was only an ∼5–5.5 log decrease. It is notable that MSSA in Fg + TSB exhibited full sensitivity to AMK. MSSA in either Alb + HA + TSB or Fg + Alb + TSB showed intermediate tolerance (∼3 log decrease). MSSA exhibited the greatest tolerance to AMK in Fg + HA + TSB and the complete pSynF (HA + Fg + Alb + TSB) where 30 μg/ml AMK could only decrease MSSA levels by ∼1.5 log.

We then compared MSSA antibiotic responsiveness in pooled synovial fluid to that in pSynF (**Figure 4E**). In TSB, MSSA was eradicated at all doses of AMK tested. In synovial fluid, 2–3 log decreases were measured with increasing doses of AMK, although no differences were significant presumably due to incomplete dispersion of the fibrous aggregates resulting in a large variance. Increasing AMK levels in pSynF caused dose-dependent 1.5–2.5 log decreases in MSSA CFU/ml ($p < 0.001$).

To complete these analyses, we measured the viscosity of pSynF, an important property of the proteoglycan-rich synovial fluid. While the viscosity of the pSynF (∼7.5 cP) was much greater than that of water (∼1 cP), it was lower than the viscosity of human synovial fluid, which was measured as ∼40 cP in our system (**Figure 4F**). Collectively, these results indicate that pSynF manifests similar bacterial aggregation and antibiotic tolerance abilities to those seen in human synovial fluid.

Virulence Factor Expression in Pseudo Synovial Fluid and Synovial Fluid

Previously, we showed that both MSSA and MRSA aggregates, i.e., floating biofilms, formed in synovial fluid were covered with a polysaccharide intercellular adhesin (PIA) matrix (Dastgheyb et al., 2015a,b,c; Gilbertie et al., 2019). We thus examined WGA staining of the biofilm matrix (**Figure 5A**). Staining was sparse in bacteria grown in TSB. WGA staining was more intense in both synovial fluid (pooled) and pSynF and similar in intensity, suggesting similar levels of PIA production.

S. aureus virulence factor expression, which is under the control of the *agr* operon, is also highly influenced by the microenvironment. We have previously shown that virulence factor production in *S. aureus* is downregulated in synovial fluid (Dastgheyb et al., 2015c). We therefore sought to measure expression levels of virulence factors under the control of agr, PSMs alpha and beta, as well as the P3 promoter. The RLUs of MRSA LAC USA300 strains that expressed luciferase under control of *psm*α, *psm*β, or P3 were determined by normalization of the measured luminescence with the corresponding OD of the growing cultures in TSB, serum, pooled synovial fluid, and pSynF (**Figure 5B**; $n = 6$). P3 luc expression in TSB showed a rapid and marked rise over time, whereas the expression in serum and synovial fluid was only minimally detectable. However, P3 luc expression in pSynF fell between that of synovial fluid and TSB, despite the presence of aggregation. For both *psm*α and *psm*β, luc expression in TSB showed a marked steep rise over time, similar to the expression patterns of P3 in TSB. As we had observed previously, both serum and synovial fluid showed very low levels of *psm*α and *psm*β luc activity. Importantly, *psm*α and *psm*β luc expression patterns in pSynF were very similar to those measured for serum and synovial fluid.

DISCUSSION

We have suggested that the phenotype of bacteria in the joint directly impacts the ability of antimicrobials to combat PJI, a devastating complication of joint replacements. In previous work, we showed that synovial fluid, the lubricious fluid within the joint space, causes aggregation of many bacterial species, including MSSA and MRSA. Furthermore, we established that proteinase K and tissue plasminogen activator (tPA), presumably through activation of the serine protease plasmin, can inhibit aggregate formation, disperse the floating MSSA or MRSA aggregates formed in synovial fluid, and restore antibiotic sensitivity (Dastgheyb et al., 2015a,b; Gilbertie et al., 2019). These observations were given further rigor by examining MRSA USA300 strains from the Nebraska transposon bank, with which we previously showed (Dastgheyb et al., 2015b) that macroscopic aggregation could be abrogated in strains that had insertions in fibronectin-binding proteins A and B (FnbA and FnbB), the fibrinogen-binding Clumping factor A and B (ClfA and ClfB), and RsbU and TRAP, which are regulatory proteins (Dastgheyb et al., 2015c). Others have suggested a role for Fg and Fn in this aggregation (Walker et al., 2013; Pestrak et al., 2020). In this study, we characterized the protein content of these aggregates and set about testing which components of these aggregates were critical for this bacterial association. MSSA aggregation was dependent on increased viscosity, Alb, and Fg. We used both MSSA and MRSA strains in this work as their aggregation behavior is similar and importantly, so that our measurements of virulence factor production could be compared with our previously published work in synovial fluid (Dastgheyb et al., 2015c). Ultimately, we formulated a pSynF that could be used to study this aggregation and its effects on bacterial virulence factor production.

In the infected joint, macroscopic mucinous aggregates are routinely present and have morphological similarities to the aggregates formed *in vitro* in synovial fluid. While these aggregates show many normal components of a biofilm, based on our earlier work, the degradation of PIA or extracellular

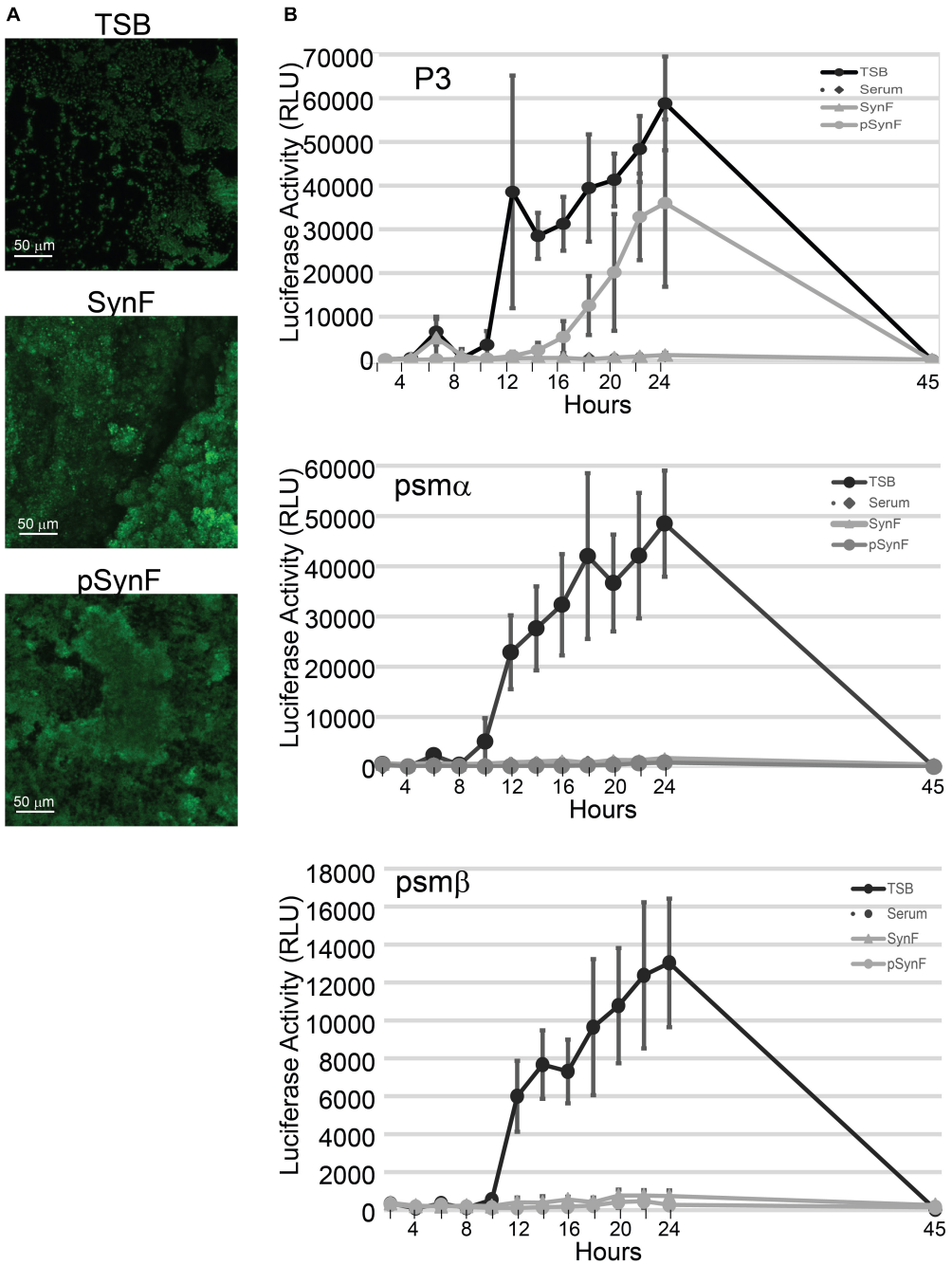

FIGURE 5 | Biofilm and virulence factor expression as a function of medium. **(A)** Comparison of wheat germ agglutinen staining of polysaccharide intercellular adhesin (PIA) in methicillin-susceptible *Staphylococcus aureus* (MSSA) grown in Trypticase Soy Broth (TSB), pooled synovial fluid, or pseudo synovial fluid (pSynF). **(B)** Expression of luciferase under control of P3, *psm*α, or *psm*β promoters using MRSA LAC300 strains in TSB, serum, pooled synovial fluid, and pSynF. Each line represents the average of three independent experiments performed in duplicate. Values graphed are means ± SD. Statistics are available in **Supplementary Material A2**.

DNA is insufficient to disrupt the aggregates – a proteinase is required (Dastgheyb et al., 2015b). We thus set out to examine the components of synovial fluid aggregates. Synovial fluid is a filtrate of human serum and is enriched with proteoglycans produced by synoviocytes and chondrocytes. We used both individual and pooled samples of human synovial fluid, with similar results on aggregation, protein composition, and antibiotic tolerance. Unlike synovial fluid, serum aggregates tend to be small except in end-stage sepsis (Iskander et al., 2013). *In vitro*, aggregation in serum, albeit microscopic, does occur

(Walker et al., 2013; Dastgheyb et al., 2015a), but it is worth noting that laboratory serum has had Fg precipitated or cross-linking inhibited during the process of collection and isolation. Taken together, we thought that Fg and perhaps proteoglycans, specifically HA, would be necessary for recapitulating the aggregatory phenotype. In fact, others have shown that Fg and Fn can cause bacterial aggregation when added to ideal media (Pestrak et al., 2020), which is consistent with our earlier experiments with aggregate dispersion.

Using aggregates from three independent human synovial fluid samples, the aggregate protein content and concentrations were determined to be similar to those of the parent synovial fluid by SDS-PAGE. Furthermore, the apparent protein distribution mirrored the pattern of human serum (within the limits of Coomassie blue staining) (Lyngbye and Krøll, 1971). Based on known proteins in serum and synovial fluid and their relative abundance (Ritter et al., 2013; Bennike et al., 2014), we identified Alb and Fg as major components of the aggregate, with a number of minor components that we did not identify. While our previous work and that of others using tPA suggested a critical role for Fg (Dastgheyb et al., 2015a,b; Gilbertie et al., 2019; Pestrak et al., 2020), only through Fg complementation could its role be established. Thus, we depleted pooled synovial fluid of Fg by ethanol precipitation of proteins. Nevertheless, the ethanol precipitation, while enriching the precipitate for Fg, precipitated other proteins that could also play a role in the bacterial response to synovial fluid, e.g., aggregation. However, addition of Fg back to the ethanol-precipitated synovial fluid restored visible aggregation and supported its proposed role, in keeping with our published work and work by others (Walker et al., 2013; Dastgheyb et al., 2015a,b,c; Pestrak et al., 2020). Bacterial binding to these proteins would use the MSCRAMMs that, through use of MRSA USA300 strains from the Nebraska transposon bank, we previously showed moderated macroscopic aggregation (Dastgheyb et al., 2015b). Specifically, aggregation could be abrogated in strains that had insertion mutations in FnbA and FnbB, the ClfA and ClfB, prominent MSCRAMMs, and RsbU and TRAP, which are regulatory proteins (Dastgheyb et al., 2015c).

Interestingly, Alb and HA were also important for aggregation, as demonstrated in the combinatorial addition experiments. Within the range of 1.5–3.0 mg/ml HA, 6–12 mg/ml Alb, and 6–12 mg/ml Fg, MSSA and MRSA aggregated, as evidenced by decreased CFU. Furthermore, if only one of the components was present, the ability to reproduce the characteristic antibiotic tolerance was attenuated. Interestingly, antibiotic tolerance measured in HA + Fg + TSB was similar to that in pSynF, despite the dependence on Alb that aggregation was shown to have. It is interesting that the Fg concentration showed an upper limit as the 12 mg/ml Fg concentrations started to become more gel-like (rather than distinct aggregates) in the presence of MSSA. Importantly, we chose the concentrations of the different components based on statistical tests using aggregation, antibiotic tolerance, and ultimately literature values for human synovial fluid (which fell within the ranges we had determined) (Mateos et al., 2012; Bennike et al., 2014).

The proteins sequestered within the MSSA aggregates formed in pSynF approximated the protein composition of that in human synovial fluid, although individual and cross-linked chains of Fg were not always equivalent in the pSynF vs. synovial fluid aggregates, perhaps pointing to the absence of the Fg cross-linking cascade in pSynF. When aggregates were viewed without magnification, the pSynF aggregates were uniformly smaller than those formed in synovial fluid and in clinical cases where we have observed retrieval of more mucinous aggregates. It is of course probable that other proteins will have roles in subtly modifying the stability, antibiotic sensitivity, and morphology of the aggregates. We would suggest either the localization of additional proteoglycans found in synovial fluid or greater production of PIA, as well as perhaps additional proteins, that modifies the density of the aggregate. Possibilities would include collagen that binds to the same MSCRAMMs previously identified and Fn, a protein that decorates most extracellular matrices; all are present in synovial fluid. Interestingly, the Fg and Alb content of synovial fluid increases in the osteoarthritic joint (Mateos et al., 2012; Bennike et al., 2014). We similarly expect an increase in the infected joint, making them more available for bacterial aggregation. Nevertheless, both human synovial fluid and pSynF conferred marked antibiotic tolerance to MSSA aggregates, with similar decreases when compared to the untreated control.

While clinically relevant joint-lubricating fluids (Adams et al., 1995; Neustadt et al., 2005; Mathies, 2006; Petterson and Plancher, 2019), as well as those for the study of rheology (Radin et al., 1971; Takadama and Mizuno, 2006; Bortel et al., 2015), have been formulated, our goal was to study bacterial responses to synovial fluid proteins. Interestingly, the viscosity of pSynF, while ∼7× that of water, was still lower than that which we measured for native synovial fluid, even though the concentrations of HA tested were informed by known amounts of HA in synovial fluid. A number of proteoglycans produced in the joint capsule contribute to this viscosity, including the MW of the HA itself and an important role played by the lubricin macromolecule (Jay et al., 2007). Importantly, despite the difference in viscosity, both pSynF and synovial fluid caused marked antibiotic tolerance. An important role for viscosity/polarity of the medium was indicated by the requirement for HA to obtain the full antibiotic tolerance associated with Fg or Fg + Alb. The importance, however, of understanding the underpinnings of this antibiotic tolerance remains focused on restoring antibiotic susceptibility, especially as the mechanism is likely to be the same poorly defined bacterial metabolism and protein expression changes that characterize the biofilm phenotype. By defining the importance of the three components within pSynF, we also define targets for therapeutic interventions. One such possibility already exists with our reports of tPA dispersal (and restoration of antibiotic susceptibility) to the MSSA aggregates.

Further emphasizing the similarity of these aggregates to biofilms, both synovial fluid and pSynF formed PIA-encased aggregates that were similar in morphology and apparent intensity of WGA staining. Furthermore, expression levels of PSM-α and -β reporter plasmids suggested that Fg, Alb, and HA are key mediators of bacterial behavior in synovial fluid, especially as similar magnitudes and kinetics of expression were noted in serum, synovial fluid, and pSynF. However,

it is not clear if the lower viscosity, or perhaps the use of TSB as the reconstituting medium, led to a difference in P3 expression by MRSA USA300. Finally, we used P3 expression as a readout of Agr regulation. As Agr regulates quorum sensing, as well as the expression of a subset of virulence factors (Dastgheyb and Otto, 2015), it becomes important to elucidate the additional components that suppress P3 expression and, by implication, Agr activity in human physiological fluid. Finally, we would suggest that the overall reproduction of aggregation, biofilm slime, antibiotic resistance, and PSM expression suggests that these three components are critical mediators of bacterial phenotype and in the process furnish an important tool to determine bacterial/biomaterial interactions in a system that more faithfully reproduces the *in vivo* environment.

In summary, we have identified Fg, Alb, and HA as critical components responsible for bacterial aggregation in synovial fluid and that together, as presented in pSynF, these proteins interact with MSSA and MRSA to recapitulate the majority of the properties of MSSA or MRSA in synovial fluid aggregates. Importantly, as we have previously shown, both serum and synovial fluid cause marked decreases in virulence factor expression, in contrast to many studies suggesting an apparent increase in Agr-controlled genes associated with infections (Le and Otto, 2015). Our studies emphasize the importance of using physiological and model physiological fluids such as this pSynF in studying bacteria–biomaterial interactions. This formulated pSynF can, in fact, be used as a reasonable alternative for studying *in vitro* models of PJI and septic arthritis, as well as providing a more realistic medium for the development of antimicrobial strategies/materials for implants.

DATA AVAILABILITY STATEMENT

The raw data supporting the conclusions of this article will be made available by the authors, without undue reservation.

AUTHOR CONTRIBUTIONS

SK and DC contributed to the methodology, formal analysis, investigation, writing, review, and editing, visualization, and writing the final approved version. NZ contributed to the validation, formal analysis, investigation, writing, review, and editing, and writing the final approved version. PM contributed to the methodology, investigation, visualization, and writing the final approved version. SD contributed to the methodology, investigation, writing, review, and editing, and writing the final approved version. CP contributed to the validation, investigation, writing, review, and editing, and writing the final approved version. MH and AC contributed to the resources, writing, review, and editing, and writing the final approved version. TS contributed to the conceptualization, resources, writing, review, and editing, funding acquisition, and writing the final approved version. MO contributed to the methodology, resources, writing, review, and editing, visualization, funding acquisition, and writing the final approved version. NH contributed to the conceptualization, writing the original draft, writing, review, and editing, visualization, supervision, funding acquisition, and writing the final approved version. All authors contributed to the article and approved the submitted version.

FUNDING

Research reported in this publication was supported by the National Institutes of Health (NIH) under award numbers R01 AR069119, R01 AR072513, and RO1 AR076941 (NH and TS) and the Intramural Research Program of the National Institute of Allergy and Infectious Diseases (NIAID), NIH under project number 1 ZIA AI001080 (MO). The content is solely the responsibility of the authors and does not necessarily represent the official views of the National Institutes of Health.

ACKNOWLEDGMENTS

We thank Catherine Gurr for her help in data presentation.

SUPPLEMENTARY MATERIAL

The Supplementary Material for this article can be found online at: https://www.frontiersin.org/articles/10.3389/fmicb.2021.655873/full#supplementary-material

REFERENCES

Adams, M. E., Atkinson, M. H., Lussier, A. J., Schulz, J. I., Siminovitch, K. A., Wade, J. P., et al. (1995). The role of viscosupplementation with hylan G-F 20 (Synvisc) in the treatment of osteoarthritis of the knee: a Canadian multicenter trial comparing hylan G-F 20 alone, hylan G-F 20 with non-steroidal anti-inflammatory drugs (NSAIDs) and NSAIDs alone. *Osteoarthr. Cartil.* 3, 213–225.

Bennike, T., Ayturk, U., Haslauer, C. M., Froehlich, J. W., Proffen, B. L., Barnaby, O., et al. (2014). A normative study of the synovial fluid proteome from healthy porcine knee joints. *J. Proteome Res.* 13, 4377–4387. doi: 10.1021/pr500587x

Bortel, E. L., Charbonnier, B., and Heuberger, R. (2015). Development of a synthetic synovial fluid for tribological testing. *Lubricants* 3, 664–686. doi: 10.3390/lubricants3040664

Crosby, H. A., Kwiecinski, J., and Horswill, A. R. (2016). *Staphylococcus aureus* aggregation and coagulation mechanisms, and their function in host-pathogen interactions. *Adv. Appl. Microbiol.* 96, 1–41. doi: 10.1016/bs.aambs.2016.07.018

Dastgheyb, S. S., and Otto, M. (2015). Staphylococcal adaptation to diverse physiologic niches: an overview of transcriptomic and phenotypic changes in different biological environments. *Fut. Microbiol.* 10, 1981–1995. doi: 10.2217/fmb.15.116

Dastgheyb, S. S., Hammoud, S., Ketonis, C., Liu, A. Y., Fitzgerald, K., Parvizi, J., et al. (2015a). Staphylococcal persistence due to biofilm formation in synovial fluid containing prophylactic cefazolin. *Antimicrob Agents Chemother.* 59, 2122–2128. doi: 10.1128/aac.04579-14

Dastgheyb, S. S., Parvizi, J., Shapiro, I. M., Hickok, N. J., and Otto, M. (2015b). Effect of biofilms on recalcitrance of staphylococcal joint infection to antibiotic treatment. *J. Infect. Dis.* 211, 641–650. doi: 10.1093/infdis/jiu514

Dastgheyb, S. S., Villaruz, A. E., Le, K. Y., Tan, V. Y., Duong, A. C., Chatterjee, S. S., et al. (2015c). Role of phenol-soluble modulins in formation of *Staphylococcus aureus* biofilms in synovial fluid. *Infect. Immun.* 83, 2966–2975. doi: 10.1128/iai.00394-15

Fitowska, A., Ostalowska, A., Dobrakowski, M., Hapeta, B., Kasperczyk, A., Stoltny, T., et al. (2012). Protein metabolism in the synovial membrane in the hip osteoarthritis. *Pol. Orthop. Traumatol.* 77, 21–26.

Gilbertie, J. M., Schnabel, L. V., Hickok, N. J., Jacob, M. E., Conlon, B. P., Shapiro, I. M., et al. (2019). Equine or porcine synovial fluid as a novel ex vivo model for the study of bacterial free-floating biofilms that form in human joint infections. *PLoS One* 14:e0221012. doi: 10.1371/journal.pone.0221012

Iskander, K. N., Osuchowski, M. F., Stearns-Kurosawa, D. J., Kurosawa, S., Stepien, D., Valentine, C., et al. (2013). Sepsis: multiple abnormalities, heterogeneous responses, and evolving understanding. *Physiol. Rev.* 93, 1247–1288. doi: 10.1152/physrev.00037.2012

Jay, G. D., Torres, J. R., Warman, M. L., Laderer, M. C., and Breuer, K. S. (2007). The role of lubricin in the mechanical behavior of synovial fluid. *Proc. Natl. Acad. Sci. U.S.A.* 104:6194. doi: 10.1073/pnas.0608558104

Kunutsor, S. K., Whitehouse, M. R., Blom, A. W., Board, T., Kay, P., Wroblewski, B. M., et al. (2018). One- and two-stage surgical revision of peri-prosthetic joint infection of the hip: a pooled individual participant data analysis of 44 cohort studies. *Eur. J. Epidemiol.* 33, 933–946. doi: 10.1007/s10654-018-0377-9

Kushner, I., and Somerville, J. A. (1971). Permeability of human synovial membrane to plasma proteins. Relationship to molecular size and inflammation. *Arthrit. Rheum.* 14, 560–570. doi: 10.1002/art.1780140503

Laemmli, U. K. (1970). Cleavage of structural proteins during the assembly of the head of bacteriophage T4. *Nature* 227, 680–685. doi: 10.1038/227680a0

Le, K. Y., and Otto, M. (2015). Quorum-sensing regulation in staphylococci-an overview. *Front. Microbiol.* 6:1174.

Lyngbye, J., and Krøll, J. (1971). Quantitative immunoelectrophoresis of proteins in serum from a normal population: season-, age-, and sex-related variations. *Clin. Chem.* 17, 495–500. doi: 10.1093/clinchem/17.6.495

Mateos, J., Lourido, L., Fernández-Puente, P., Calamia, V., Fernández-López, C., Oreiro, N., et al. (2012). Differential protein profiling of synovial fluid from rheumatoid arthritis and osteoarthritis patients using LC-MALDI TOF/TOF. *J. Proteom.* 75, 2869–2878. doi: 10.1016/j.jprot.2011.12.042

Mathies, B. (2006). Effects of Viscoseal, a synovial fluid substitute, on recovery after arthroscopic partial meniscectomy and joint lavage. *Knee Surg. Sports Traumatol. Arthrosc.* 14, 32–39. doi: 10.1007/s00167-005-0625-x

Neustadt, D., Caldwell, J., Bell, M., Wade, J., and Gimbel, J. (2005). Clinical effects of intraarticular injection of high molecular weight hyaluronan (Orthovisc) in osteoarthritis of the knee: a randomized, controlled, multicenter trial. *J. Rheumatol.* 32, 1928–1936.

Noh, R., Park, S. G., Ju, J. H., Chi, S. W., Kim, S., Lee, C. K., et al. (2014). Comparative proteomic analyses of synovial fluids and serums from rheumatoid arthritis patients. *J. Microbiol. Biotechnol.* 24, 119–126. doi: 10.4014/jmb.1307.07046

Park, J. Y., Duong, C. T., Sharma, A. R., Son, K. M., Thompson, M. S., Park, S., et al. (2014). Effects of hyaluronic acid and gamma-globulin concentrations on the frictional response of human osteoarthritic articular cartilage. *PLoS One* 9:e112684. doi: 10.1371/journal.pone.0112684

Perez, K., and Patel, R. (2015). Biofilm-Like aggregation of *Staphylococcus epidermidis* in synovial fluid. *J. Infect. Dis.* 212, 335–336. doi: 10.1093/infdis/jiv096

Pestrak, M. J., Gupta, T. T., Dusane, D. H., Guzior, D. V., Staats, A., Harro, J., et al. (2020). Investigation of synovial fluid induced *Staphylococcus aureus* aggregate development and its impact on surface attachment and biofilm formation. *PLoS One* 15:e0231791. doi: 10.1371/journal.pone.0231791

Petterson, S. C., and Plancher, K. D. (2019). Single intra-articular injection of lightly cross-linked hyaluronic acid reduces knee pain in symptomatic knee osteoarthritis: a multicenter, double-blind, randomized, placebo-controlled trial. *Knee Surg. Sports Traumatol. Arthrosc.* 27, 1992–2002. doi: 10.1007/s00167-018-5114-0

Piewngam, P., Chiou, J., Chatterjee, P., and Otto, M. (2020). Alternative approaches to treat bacterial infections: targeting quorum-sensing. *Exp. Rev. Anti Infect. Ther.* 18, 499–510. doi: 10.1080/14787210.2020.1750951

Qiu, L. L., Levinson, S. S., Keeling, K. L., and Elin, R. J. (2003). Convenient and effective method for removing fibrinogen from serum specimens before protein electrophoresis. *Clin. Chem.* 49(6 Pt 1), 868–872. doi: 10.1373/49.6.868

Radin, E. L., Paul, I. L., and Weisser, P. A. (1971). Joint lubrication with artificial lubricants. *Arthr. Rheumat.* 14, 126–129. doi: 10.1002/art.1780140116

Ritter, S. Y., Subbaiah, R., Bebek, G., Crish, J., Scanzello, C. R., Krastins, B., et al. (2013). Proteomic analysis of synovial fluid from the osteoarthritic knee: comparison with transcriptome analyses of joint tissues. *Arthr. Rheumat.* 65, 981–992. doi: 10.1002/art.37823

Takadama, H., and Mizuno, M. A. (2006). Simulated synovial fluid for wear characterization of artificial hip joints by a hip joint simulator. *Key Eng. Mater.* 309-311, 1273–1276. doi: 10.4028/www.scientific.net/kem.309-311.1273

Tang, J. X. (2016). Measurements of fluid viscosity using a miniature ball drop device. *Rev. Sci. Instrum.* 87:054301. doi: 10.1063/1.4948314

Walker, J. N., Crosby, H. A., Spaulding, A. R., Salgado-Pabón, W., Malone, C. L., Rosenthal, C. B., et al. (2013). The *Staphylococcus aureus* ArlRS Two-component system is a novel regulator of agglutination and pathogenesis. *PLoS Pathog.* 9:e1003819. doi: 10.1371/journal.ppat.1003819

Conflict of Interest: The authors declare that the research was conducted in the absence of any commercial or financial relationships that could be construed as a potential conflict of interest.

frontiers in Microbiology

ORIGINAL RESEARCH
published: 14 May 2021
doi: 10.3389/fmicb.2021.664030

In vitro Activity of Antimicrobial Wound Dressings on *P. aeruginosa* Wound Biofilm

Ewa Klara Stuermer[1], Isabell Plattfaut[2], Michael Dietrich[2], Florian Brill[3], Andreas Kampe[3], Vanessa Wiencke[3], Anna Ulatowski[3], Maria Geffken[4], Julian-Dario Rembe[5], Ella Alexandrovna Naumova[6], Sebastian Eike Debus[1] and Ralf Smeets[7,8]*

[1] Department of Vascular Medicine, University Heart Center, University Medical Center Hamburg-Eppendorf (UKE), Hamburg, Germany, [2] Institute of Virology and Microbiology, Faculty of Health, Centre for Biomedical Education and Research (ZBAF), Witten/Herdecke University, Witten, Germany, [3] Dr. Brill + Partner GmbH, Institute for Hygiene and Microbiology, Hamburg, Germany, [4] Institute for Transfusion Medicine, University Medical Center Hamburg-Eppendorf, Hamburg, Germany, [5] Department of Vascular and Endovascular Surgery, Heinrich-Heine University Düsseldorf, Düsseldorf, Germany, [6] Department of Biological and Material Sciences in Dentistry, Faculty of Health, School of Dentistry, Witten/Herdecke University, Witten, Germany, [7] Department of Oral and Maxillofacial Surgery, University Medical Center Hamburg-Eppendorf, Hamburg, Germany, [8] Department of Oral and Maxillofacial Surgery, Division of Regenerative Orofacial Medicine, University Medical Center Hamburg Eppendorf, Hamburg, Germany

OPEN ACCESS

Edited by:
Mark Smeltzer, University of Arkansas for Medical Sciences, United States

Reviewed by:
Ajmal Khan, University of Nizwa, Oman
Alexia Hapeshi, University of Warwick, United Kingdom

***Correspondence:**
Ewa Klara Stuermer
e.stuermer@uke.de

Specialty section:
This article was submitted to Antimicrobials, Resistance and Chemotherapy, a section of the journal Frontiers in Microbiology

Received: *04 February 2021*
Accepted: *19 April 2021*
Published: *14 May 2021*

Citation:
Stuermer EK, Plattfaut I, Dietrich M, Brill F, Kampe A, Wiencke V, Ulatowski A, Geffken M, Rembe J-D, Naumova EA, Debus SE and Smeets R (2021) In vitro Activity of Antimicrobial Wound Dressings on P. aeruginosa Wound Biofilm. Front. Microbiol. 12:664030. doi: 10.3389/fmicb.2021.664030

The treatment of acute and chronic infected wounds with residing biofilm still poses a major challenge in medical care. Interactions of antimicrobial dressings with bacterial load, biofilm matrix and the overall protein-rich wound microenvironment remain insufficiently studied. This analysis aimed to extend the investigation on the efficacy of a variety of antimicrobial dressings using an *in vitro* biofilm model (lhBIOM) mimicking the specific biofilm-environment in human wounds. Four wound dressings containing polyhexanide (PHMB), octendine di-hydrochloride (OCT), cadexomer-iodine (C-IOD) or ionic silver (AG) were compared regarding their antimicrobial efficacy. Quantitative analysis was performed using a quantitative suspension method, separately assessing remaining microbial counts within the solid biofilm as well as the dressing eluate (representing the absorbed wound exudate). Dressing performance was tested against *P. aeruginosa* biofilms over the course of 6 days. Scanning electron microscopy (SEM) was used to obtain qualitative visualization on changes in biofilm structure. C-IOD demonstrated superior bacterial reduction. In comparison it was the only dressing achieving a significant reduction of more than 7 $\log_{10}$ steps within 3 days. Neither the OCT- nor the AG-containing dressing exerted a distinct and sustained antimicrobial effect. PHMB achieved a non-significant microbicidal effect (1.71 ± 0.31 $\log_{10}$ steps) at day 1. Over the remaining course (6 days) it demonstrated a significant microbistatic effect compared to OCT, AG and the control. Quantitative results in the dressing eluate correlate with those of the solid biofilm model. Overall, AG- and OCT-containing dressings did not achieve the expected anti-biofilm efficacy, while C-IOD performed best. Chemical interaction with the biofilms extrapolymeric substance (EPS), visualized in the SEM, and dressing configuration (agent concentration and release pattern) are

suspected to be responsible. The unexpected low and diverse results of the tested antimicrobial dressings indicate a necessity to rethink non-debridement anti-biofilm therapy. Focussing on the combination of biofilm-disruptive (for EPS structure) and antimicrobial (for residing microorganisms) features, as with C-IOD, using dehydration and iodine, appears reasonably complementary and an optimal solution, as suggested by the here presented *in vitro* data.

Keywords: wound biofilm, wound dressing, antimicrobials, wound infection, PHMB, silver, octenidine dihydrochloride, iodine

INTRODUCTION

Infected wounds, especially chronic wounds populated with biofilm, are one of the greatest challenges in modern wound care (Bowler et al., 2001; James et al., 2008; Demidova-Rice et al., 2012; Magill et al., 2014). Antimicrobial agents often fail in effective biofilm eradication (Percival et al., 2019b; Besser et al., 2020). This results from the symbiotic, multi-species society formed in biofilms by microorganisms, encasing themselves in a protective extrapolymeric substance (EPS), which acts as a shield against biochemical penetration by antimicrobial agents. Lateral resistance gene transfer between species and sub-species, dorment persister cells in the depth of biofilm and tissue as well as an effective biochemical diffusion barrier for active agents are further aspects contributing to the high resilience of microbial biofilms (Percival et al., 2015; Kirketerp-Møller et al., 2020). Even if an antimicrobial substance is capable of effectively eradicating a bacterial strain in its planctonic state, a deep enough penetration to achieve the same reductive efficacy, cannot be ensured in a complex biofilm scenario (Rembe et al., 2020).

Dressings and solutions containing silver, PHMB, octenidine or iodine have demonstrated favorable antimicrobial activity in several *in vitro* and clinical studies (Koburger et al., 2010; Storm-Versloot et al., 2010; Sibbald et al., 2011; Daeschlein, 2013; To et al., 2016; Dissemond et al., 2017). Anti-biofilm effects are often postulated alongside or were investigated in simple *in vitro* models, but are lacking validation in more complex test settings or clinical studies (O'Meara et al., 2000, 2013). To reduce the individual patient's burden caused by chronic and infected wounds, prevention and treatment of pathogenic biofilm formation in wounds is a serious and relevant challenge in everyday clinical practice (Guest et al., 2017; Guest et al., 2018). Modern antimicrobial wound dressings represent promising therapeutic options in aiding to master this challenge (Daeschlein, 2013).

Mostly, *in vitro* evaluation of anti-biofilm activity is performed in models and settings less suited to sufficiently mimic a wound biofilm and the interactions with the human wound microenvironment. Such models and settings include simple single-species-biofilms, lower protein challenge than in clinical wounds, non-human matrix material (e.g., plastic or stainless steel surface) and one-dimensional biofilm structures (Brackman and Coenye, 2016; Shukla et al., 2020). In addition, most studies are not performed with dressings, but with antimicrobial solutions to prove the efficacy of a compound. However, solutions exhibit an entirely different biochemical and biophysical pattern of distribution, penetration and concentration in contact with a wounds micro-environment and biofilm residing in this environment, compared to wound dressings.

Thus, it is currently unclear whether the anti-biofilm activity of antimicrobial agents embedded in wound dressings is comparable to its antimicrobial liquid counterpart in the wound microenvironment. The presented work addresses this question *in vitro* using a modified human plasma-based biofilm model (lhBIOM) developed and described earlier by the authors (Besser et al., 2020; Rembe et al., 2020; Stuermer et al., 2021). The model mimics the condition of a wound biofilm by consisting of a bacteria-incorporating, matured, three-dimensional (3D) gel-like biofilm structure surrounded by bacteria-rich human plasma, which is similar to the composition of wound exudate in terms of protein content, carbohydrates, enzymes and bacterial breakdown products (Demidova-Rice et al., 2012; Stuermer et al., 2021).

MATERIALS AND METHODS

Test Organism and Nutrient Solutions

Pseudomonas aeruginosa (DSM-939) was cultivated on casein/soy peptone agar plates (CSA) following standard procedures (DIN EN 13727). The first subculture was used for testing. The bacterial suspension was adjusted to a 0.5 McFarland standard (approx. 1.5×10^8 cfu/mL) using a densitometer (Grant Bio^{TM} DEN-1B, Grant Instruments Ltd.; Cambs SG8 6GB, England). Bacterial counts were determined by spreading untreated controls of each experiment onto agar plates allowing exact calculations of surviving microorganisms as well as reduction rates.

Test Wound Dressings and Preparation of Specimen

Five commercial dressings were investigated, four antimicrobial dressings containing either octenidine di-hydochloride (OCT), polyhexanide (PHMB), cadexomer-iodine (C-IOD) or ionic silver (AG) and an agent-free control dressing. Detailed data on dressing composition, contained active agent and concentration are displayed in **Table 1**. For all dressings, round pieces with a diameter of 2.2 cm ($A = 3.8$ cm^2) were prepared in an aseptic manner fitting press-fit in one well of a standard 12-well-plate

TABLE 1 | Investigated dressings.

	Manufacturer	Material	Active agent (concentration)
UrgoClean®	Urgo GmbH, Chenôve, France	Cohesive polyabsorbent polyacrylate fibers; TLC wound matrix®; non-adhesive	None
Sorelex®	Contipro C, Dolní Dobrouč, Czech Republic	Permeable, gel-forming bioactive gauze, releases octenidine hydrochloride, and sodium hyluronat; non-adhesive	Octenidine di-hydrochloride (not indicated)
Suprasorb® P + PHMB	Lohmann&Rauscher GmbH, Rengsdorf, Germany; Vienna, Austria	Semi permeable top film on polyurethane foam layer impregnated with and releasing PHMB; non-adhesive	Polyhexanide (0.25–0.65 mg/cm^2)
UrgoClean® Ag	Urgo GmbH, Chenôve, France	Cohesive polyabsorbent polyacrylate fibers; TLC wound matrix®; silver ion coating; non-adhesive	Ionic silver (0.50 mg/cm^2)
IODOSORB™ Dressing	Smith & Nephew GmbH, Hull, England	Beats of cadexomer (dextrin and epichlorhydrin) on gauze backing release iodine; non-adhesive	Iodine (0.90% w/w)

Data of manufacturer, material, mechanism of action and contained substance concentration. Information has been obtained from the manufacturer.

(Sarstedt, Nuembrecht, Germany). For analyses, pieces of each dressing were placed in 12-well plates containing the lhBIOM and surrounding bacteria-rich serum, to create a wound-like scenario with direct contact to the biofilm.

Preparation of Leucocyte Rich Human Plasma Biofilm Model (lhBIOM)

The preparation of the lhBIOM was performed as described previously (Besser et al., 2020; Stuermer et al., 2021). In brief, fresh frozen plasma (FFP) of blood type AB (citrate buffered) and one LRS® chamber of leukocyte apheresis (Trima Accel®; Terumo BCT Inc., Lakewood, United States) were obtained from the Institute for Transfusion Medicine (University Medical Center Hamburg-Eppendorf, Germany). Preparation of the lhBIOM was initiated on the same day of blood product donation. In brief, FFP was thawed, adjusted to 250 mL and the "immunocompetence" in form of leukocytes from the LRS® chamber was added. The immune cells were obtained by using a special automated blood collection system for apheresis (Terumo BCT design, Trima Accel® LRS® Platelet, Plasma Set, REF number 82300; Terumo BCT Inc., Lakewood, United States), which removes nearly all leukocytes of the donor from the platelet sample, so that its concentration is equivalent to about 40×10^3 leukocytes/μL. The content of one LRS® chamber was placed in a tube, washed out with 3 mL of the FFP to remove any residual leukocytes, the wash-out added to the tube and centrifuged at 1,610 g. The layer of erythrocytes was gently removed and the remaining plasma-leukocyte mix added to the remaining FFP at room temperature. After gentle mixing, the bacterial suspension was added resulting in a final concentration of 1.5×10^6 cfu/model. Next 18.26 μL $CaCl_2$ (500 mM) per mL plasma was added to the bacteria-plasma-mix to induce coagulation. The resulting biofilm mixture was immediately transferred into 12-well plates (1.5 mL per model/well). Well plates were placed on a rotation shaker and incubated for 12 h at 60 rpm and 37.0°C to polymerize and form an extracellular matrix. After this period, stable biofilm discs with integrated test organisms resulted. Procedures of blood product collection are in accordance with "good clinical practice" standards and all donors gave their informed and written consent for the use of their blood products.

Dressing Performance on *P. aeruginosa* Biofilm and Quantification of Bacterial Load

After 12 h of biofilm maturation in the lhBIOM (**Figure 1**), the test dressings were placed on the models as described above under "specimen preparation." Treatment with dressings was performed for 1, 3, or 6 days without dressing change. After the specified treatment periods, wound dressings were carefully removed so that neither residues of the dressing remained on the model, nor biofilm substance was lost. Plastic beakers (50 mL) were filled with glass beads (D = 3–4 mm), so that the bottom was slightly covered. 10 mL neutralizer solution TLSNt-SDS (6% polysorbate 80, 6% saponin, 0.8% lecithin, 2% sodium dodecyl sulfat, 0.6% sodium thiosulfat in Aqua dest.) was added. The wound dressings were placed in the neutralizer solution. After shaking for 10 min at 200 rpm, extracts were plated out in 10-fold dilutions on CSA and incubated at 37°C under aerobic conditions for 48 h before quantification of colony forming units using a digital colony counter (NSCA 436000, VWR International GmbH; Germany).

Antimicrobial activity in the wells was neutralized by adding 300 μL of the neutralizing solution TLSNt-SDS to each well. Plates were subsequently placed on a rotation shaker for 5 min at room temperature for incubation of neutralizing agent. Subsequently, biofilm models were dissolved using bromelain (Bromelain from pineapple, Serva Electrophoresis GmbH; Heidelberg, Germany). Bromelain solution was prepared using 2.1 g powder, dissolved in 100 mL phosphate buffered saline (PBS) and 1.5 mL was added to each well containing a biofilm model. The biofilms were punctured with sterile pipette tips several times to ensure and accelerate complete dissolution of the model. After 3 h incubation (37°C; aerobic conditions) the biofilm models were completely dissolved with the exception of the iodine wound dressing models. These left insoluble residues. The microbial counts in the dissolved models were quantified in the same manner as the dressing eluates.

Qualitative Evaluation by Scanning Electron Microscopy (SEM)

To visualize the antimicrobial effects of the wound dressings on biofilm morphology and structure, scanning electron microscopy

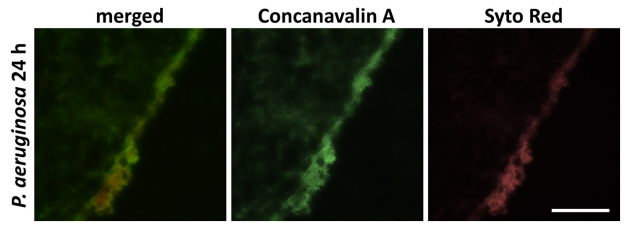

FIGURE 1 | Immunohistochemical carbohydrates-staining of the glycocalyx of 24 h maturated biofilm produced by *P. aeruginosa*. Carbohydrates were detected with FITC-conjugated Con A, cellular and bacterial nucleic acids with SYTO Red staining (scale bar: 100 μm).

(SEM) was performed. All dressings were carefully removed prior to further preparation of the models and antimicrobial activity were neutralized using the TLSNt-SDS neutralizing solution. Biofilm models were fixed with a glutaraldehyde/PVP-solution containing 2.5% glutaraldehyde, 2% polyvinylpyrrolidone (PVP) and 0.5% $NaNO_2$ in 0.1 M cacodylate buffer for 1 h at 4°C. After washing three times (0.1M cacodylate buffer) they were prepared with liquid nitrogen to get freeze fracture fragments and stored in 0.1M cacodylate buffer. In order to stain the glycoxalyx, the samples were incubated for 18 h at RT in an arginine-HCl solution (solution with 2% arginine-HCL, glycine, sucrose and sodium glutamate). Next samples were rinsed again three times for 5 min with aqua dest. and subsequently stored for 5.5 h at RT in a mixture of 2% tannic acid and guanidine-HCL. After storage, samples were again rinsed once with aqua dest (5 min incubation) and three times with 0.1M cacodylate buffer (5 min incubation) and incubated overnight at 4°C. After overnight incubation, samples were placed in a 1% OsO_4 solution for 30 min at RT followed by three rinsing steps with 0.1 M cacodylate buffer (10 min incubation) and stored again over night at 4°C. Last, samples were dehydrated in an isopropanol series (50, 70, 90, and 100%) for 15 min each followed by an acetone series (50, 75, and 100%) also each for 15 min. The drying step was completed by a final treatment in the critical point dryer (BAL-TEC AG, Balzers, Liechtenstein). With a sputter coater (BAL-TEC AG, Balzers, Liechtenstein), samples were sputtered with gold palladium and afterward analyzed by Zeiss Sigma VP SEM (Zeiss, Oberkochen, Germany) at 2 kV acceleration voltages using the in-lens and SE detectors.

Statistical Analysis

Data is expressed as means ± standard error of the mean (SEM) based on triplicates derived from six different anonymous blood donors (FFP and leukocytes) at different time-points. Microbial reduction rates (in $\Delta\log_{10}$ cfu/mL) were calculated and analyzed using the statistics program GraphPad PRISM (Version 9.0; GraphPad Software Inc., La Jolla, United States). For analysis of statistical significance a two-way repeated-measures ANOVA, followed by Tukey *post hoc* test for evaluation of multiple comparisons was applied. A *p*-value of $p \leq 0.05$ was considered statistically significant.

RESULTS

Quantitative Microbial Load in Wound Dressing Eluate

Over the examined treatment course of a total of 6 days, the microbial counts in the wound dressing eluate followed a directly proportional pattern to the microbial load in the solid biofilm itself. Under treatment with octenidine di-hydrochloride (OCT) and ionic silver (AG), a gradual increase of microbial counts on days 1, 3 and 6 were observed (**Figure 2**). Such increasing microbial counts also occurred in the control dressing (CTRL) with no antimicrobial agent, consequently showing no anti-biofilm activity of OCT and AG on the wound dressing eluate. PHMB demonstrated a statistically non-significant decrease in microbial counts of the eluate on day 1 (0.62 ± 0.16 $\log_{10}$ steps) compared to initial counts. Subsequently, the PHMB dressing maintained the level of microbial counts over the remaining course of 6 days compared to the increasing counts in the control dressing (**Figure 2**), demonstrating a bacteriostatic effect.

On day 1, treatment with the C-IOD dressing resulted in a statistically non-significant reduction of 1.51 ± 0.41 $\log_{10}$ steps compared to initial bacterial counts in the dressing eluate. After 3 and 6 days of treatment, C-IOD achieved a significant reduction of microbial counts in the eluate compared to initial counts of 2.93 ± 0.29 $\log_{10}$ steps ($p = 0.0207$) and 6.92 ± 0.58 $\log_{10}$ steps ($p = 0.0154$), respectively. Compared to the control dressing this accounts for a significantly reduced bacterial burden of 1.41 ± 0.24 $\log_{10}$ steps on day 1 ($p = 0.0254$), 3.51 ± 0.42 $\log_{10}$ steps on day 3 ($p = 0.0069$) and 7.62 ± 0.60 $\log_{10}$ steps on day 6 ($p = 0.0077$; **Figure 2**).

Anti-biofilm Activity of Antimicrobial Wound Dressings on the lhBIOM

Regarding the antimicrobial effect on bacteria within the biofilm model, the results demonstrated an overall similar trend for wound dressings and dressing eluate (**Figure 2**). Treated with an OCT-containing dressing over a 6-day-period, microbial counts within the lhBIOM showed a continued increase with no observable antimicrobial effect. The AG-containing dressing demonstrated similar results, with the exception of an initial significant decrease in microbial counts on day 1 of 3.33 ± 1.50 $\log_{10}$ steps ($p = 0.013$) compared to initial counts. On day 3 however the initial reductive effect had worn off and microbial re-growth above initial counts had occurred.

After an initial non-significant reduction on day 1, the PHMB-impregnated dressing maintained a prolonged bacteriostatic effect. This was observed for the biofilm itself as well as in the dressing eluate. PHMB reduced the initial bacterial counts by 1.71 ± 0.31 $\log_{10}$ steps, subsequently keeping it at the reduced level over the course of 6 days without occurring re-growth (**Figure 2**). Compared to the control dressing, PHMB obtained a significant reduction in bioburden of 2.36 ± 0.12 $\log_{10}$ steps on day 3 ($p = 0.0028$) and 2.66 ± 0.19 $\log_{10}$ steps on day 6 ($p = 0.0010$) in the lhBIOM. The reduction on day 1 compared to the control dressing, however, was not statistically significant.

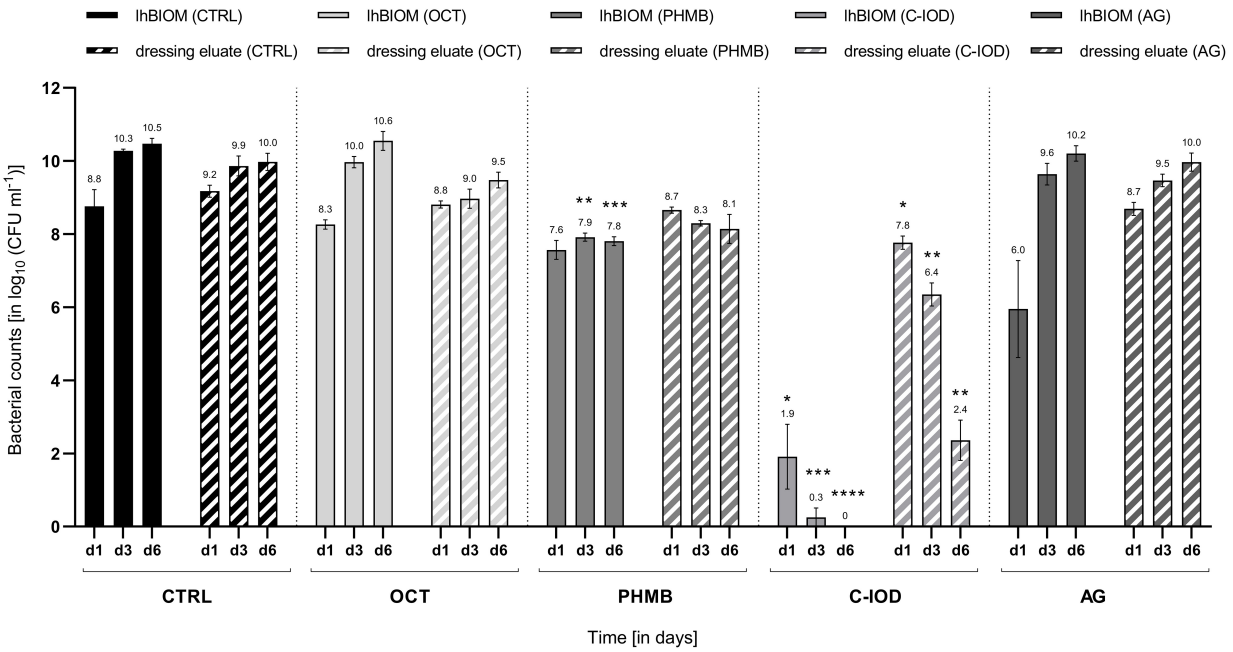

FIGURE 2 | Comparison of the antimicrobial efficacy of wound dressings containing antimicrobial agents in the *P. aerugionosa* biofilm model lhBIOM. Reduction rates of bacteria (in $\log_{10}$ cfu/mL) are outlined after 1, 3, and 6 days of treatment with agent-free wound dressings (CTRL) and dressings containing octenidine (OCT), polyhexanide (PHMB), cadexomer-iodine (C-IOD), or ionic silver (AG). Bacterial content of the biofilm (solid bars) and in the dressing eluate (striped bars) are shown (values expressed as mean ± SEM. *$p \leq 0.05$ vs. CTRL; **$p \leq 0.01$ vs. CTRL, ***$p \leq 0.001$ vs. CTRL, and ****$p \leq 0.0001$ vs. CTRL).

The C-IOD containing dressing showed the highest antibiofilm activity. On day 1, bacterial counts in the biofilm were significantly reduced by 7.37 ± 0.99 $\log_{10}$ steps ($p = 0.0387$) compared to initial counts. On day 3 the initial bacterial load was reduced by 9.03 ± 0.45 $\log_{10}$ steps ($p = 0.0054$) and on day 6 no quantifiable microrganisms were retrieved, representing a complete reduction of initial microbial counts (9.28 ± 0.24 $\log_{10}$ steps; $p = 0.0015$; **Figure 2**).

Visual Analysis of Dressing Effects on the lhBIOM Using Scanning Electron Microscopy (SEM)

SEM analysis of *P. aeruginosa* biofilm treated with wound dressings for 3 days (**Figure 3**) showed a distinct modification of the biofilm surface for all models compared to the untreated biofilm (**Figure 3A**). Whereas with drug-free wound dressings only an undulating fissuring with an almost intact surface was visible (**Figure 3B**), those containing antimicrobials induced an increased porosity. This was most prominent in the cadexomer-iodine dressing (**Figure 3E**). The former induced a shotgun-like change in the biofilm surface reflecting the penetration of iodine from the cadexomer beads into deeper layers. The OCT- (**Figure 3C**) and PHMB-containing wound dressings (**Figure 3D**) showed a smooth surface with multiple isolated but rather big holes and their structural appearances were quite similar. The AG-containing dressing seemed to induce a more pronounced roughening of the biofilm surface with, however, fewer entry holes and an overall lower porosity (**Figure 3F**).

DISCUSSION

In guidelines, local antimicrobials such as different silver formulations, polyhexanide (PHMB), octenidine, dihydrochloride or iodine are rated as equally efficient (AWMF, 2012). Consensus about advantages and disadvantages in direct comparison, recommendations and independent analyses of efficacies in complex test scenarios or clinical conditions are, however, rare (Kramer et al., 2018). Even though several studies addressed this issue, most concluded that further analyses are mandatory to gain evidence-based recommendations for the daily use of antimicrobial dressings (Storm-Versloot et al., 2010; Daeschlein, 2013; Forster and Pagnamenta, 2015; Wu et al., 2015; Norman et al., 2016). Using a complex 3D model designed to mimic the micro-environment of a human wound biofilm (lhBIOM), composed of human material (plasma, platelets and leukocytes), this study aimed to extend the knowledge-base on efficacy profiles of antimicrobial wound dressings in a more transferable, "closer-to-reality" test scenario (Besser et al., 2020; Rembe et al., 2020; Stuermer et al., 2021). In this model, the incorporated bacteria encounter not only a milieu similar to the wound exudate (Loeffler et al., 2013), but also a certain immunological competence represented by leukocytes, so a biofilm matrix has to be produced under the challenge of a donor's immunocompetence (**Figure 1**).

The obtained results of the investigated wound dressings regarding antimicrobial efficacy partly contrast what is currently considered best-practice knowledge and has been previously reported. In case of the iodine-containing product (C-IOD), a

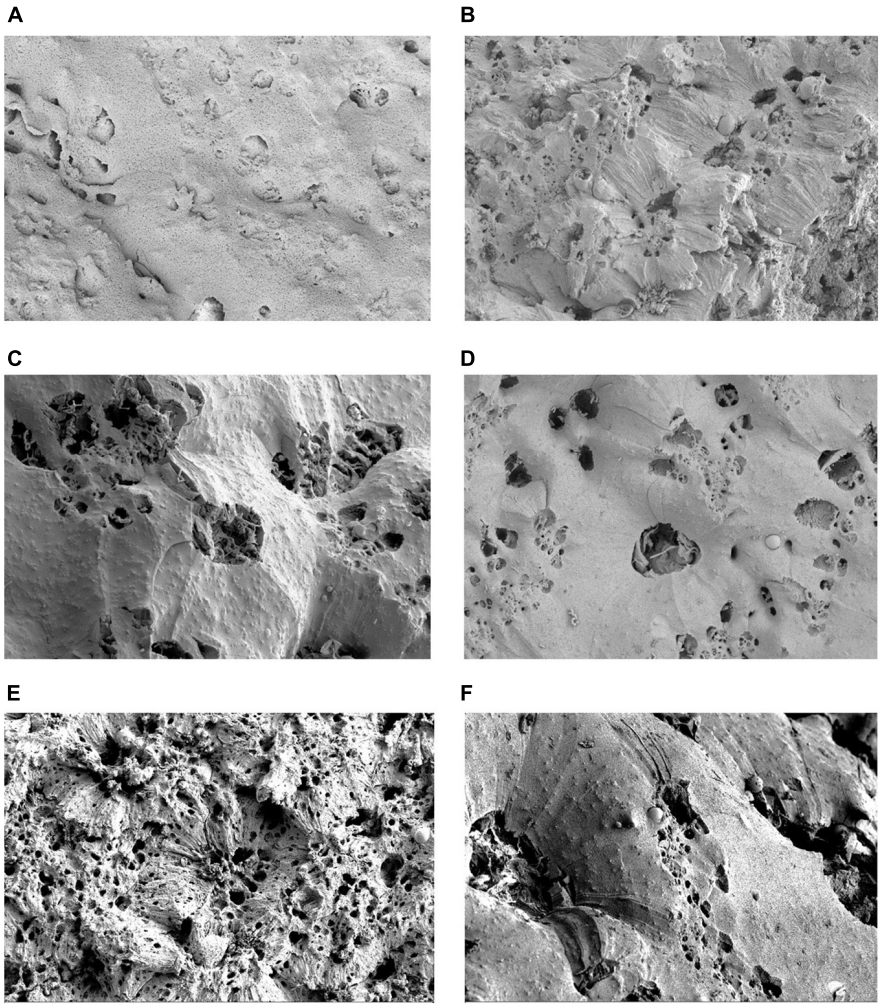

FIGURE 3 | Scanning electron microscopy (SEM) visualization of *P. aerugionosa* biofilm surface (lhBIOM) after 3 days under control conditions **(A)** and after treatment with commercial wound dressings: **(B)** polyurethane dressing with no active agent; **(C)** with octenidin (OCT); **(D)** with polyhexanide (PHMB); **(E)** with cadexomer-iodine (C-IOD) and **(F)** ionic silver. The untreated biofilm model **(A)** shows a densely connected surface structure. After treatment with cadexomer-iodine **(E)**, surface structure appears rugged and "broken-open" with several holes as potential new entry points for iodine. After treatment with OCT **(C)** and PHMB **(D)** biofilm surface remains more dense though several holes are visible. Silver **(F)** induced the least changes.

distinct and continuous antimicrobial effect was observed in this study with a successive microbial reduction within 3 days (**Figure 2**), confirming previous *in vitro* and clinical studies (Phillips et al., 2015; Fitzgerald et al., 2017; Roche et al., 2019). It should be emphasized, however, that under treatment with the cadexomer-iodine dressing, the biofilm model was not completely dissolved in bromelain. This most likely arises from the proposed dehydrative effect caused by the cadoxmer agent (Akiyama et al., 2004; Fitzgerald et al., 2017). Judging by the reductive pattern in the solid biofilm model (lhBIOM), it seems, that the cadexomer-proportion of the dressing degrades and increases the porosity of the biofilm structure. Combined with iodine it acts partly lethal on exposed bacteria, while partly binding microorganisms within the dressing. This offers an explanation for the higher remaining microbial counts within the eluate on day 1 (**Figure 2**): Released microorganisms from the degraded biofilm structure are initially bound and subsequently reduced by the continued release of iodine. The simultaneous continued, slow release of iodine molecules into the degraded biofilm also reaches deeper structures and works against dorment bacteria. This approach is also supported by the SEM images, showing a failure of the closed protective EPS shield due to the impact of cadexomer-iodine.

Evaluations regarding the anti-biofilm activity of polyhexanide-containing wound dressings (PHMB) are rarely found in the literature (Huebner and Kramer, 2010; Huebner et al., 2010; Lenselink and Andriessen, 2011; Davis et al., 2017; Kramer et al., 2018); for the octenidine-containing wound dressing (OCT) no data at all could be found. Most efficacy assumptions and statements are transferred from analyses performed on microorganisms in a planktonic state or from evaluations of the antiseptic solution counterparts. Regarding

the PHMB dressing, a reductive efficacy (˜2 $\log_{10}$ steps) with a subsequent bacteriostatic effect could be demonstrated in this work, presumably due to the comparably high concentration of PHMB (0.65 mg/cm^2) embedded in and released by the wound dressing (**Figure 2** and **Table 1**). These results are in accordance with the results of earlier analyses of our working group, demonstrating a good efficacy for PHMB-containing antiseptics and antimicrobial irrigation solutions (Brackman and Coenye, 2016; Rembe et al., 2020). However, this positive quantitative effect is not reflected in the SEM images, since only slightly changes to the surface of the biofilm can be observed.

For the here tested silver-containing wound dressing (AG), the expected high antimicrobial efficacy could not be verified. While several *in vitro* evaluations in planktonic or simpler biofilm models demonstrated a good antimicrobial and anti-biofilm efficacy (O'Meara et al., 2000; Desroche et al., 2016; Percival et al., 2019b), these results could not be reproduced in a more complex *in vitro* biofilm scenario used here (**Figure 2**). Similar discrepancies and debates arise from various previous clinical studies of critically colonized or infected wounds, resulting in the necessity for further investigations (Lo et al., 2009; O'Meara et al., 2013; Dissemond et al., 2017). Even though a initial bacterial reduction was observed after 1 day of treatment, re-growth occurred over the following course of 6 days treatment, ultimately displaying similar microbial counts as the control dressing. Analyzing the eluate of the silver dressing, as a surrogate for the absorbed microorganism-containing wound exudate, there was also no reduction of the microbial load. These findings are contrary to previous descriptions by Desroche et al. (2016), stating that it "reduces the bacterial population and the biofilm of *P. aeruginosa* and MRSA up to 4 log steps within 24 h for 7 days" (collagen I-coated surface with no human components). The AG-impregnated wound dressing contains ionic silver coated to the specific surface matrix in a comparably low concentration (0.50 mg/cm^2; **Table 1**). Besides the low concentration of the active agent, the composition of the milieu seemed to impede silver to exert its full antimicrobial effect. The relevance of its chemical structure has already been proven in previous studies. The loss of efficacy was pointed out for nanocrystalline silver (Gnanadhas et al., 2013; Rembe et al., 2018) more than for ionic silver, however, interactions with the wound microenvironment such as pH value or protein content have been described for both several times (Hirsch et al., 2011; Kapalschinski et al., 2013; Wiegand et al., 2015; Rembe et al., 2018). This emphasizes the need for human-adapted analyses *in vitro*, as the here tested dressing containing ionic silver demonstrates an overall loss of antimicrobial efficacy in a complex, protein-rich, human-adapted microenvironment.

Surprisingly, the octenidine-impregnated dressing showed no antimicrobial or anti-biofilm efficacy in the performed experiments, while the antiseptic solution tested in a similar complex model (hpBIOM) in previous studies, demonstrated the highest efficacy compared to other antimicrobial solutions (Besser et al., 2020; Rembe et al., 2020). In many previous studies, both against planktonic bacteria as well as biofilm, the active agent of the disinfectant Octenisept® has repeatedly proven to be highly effective (Brackman and Coenye, 2016; Rembe et al., 2020), even though the onset of its full efficacy was shown to be delayed in complex biofilm scenarios (up to 48 h). The missing antimicrobial activity of the OCT dressing might therefore be attributed to the dressing configuration with a retained release of the active agent into the wound (here biofilm model) or an insufficient amount of active agent embedded and released to achieve an impact. Unfortunately, the exact amount of octenidine di-hydrochloride in the dressing is not provided in the literature or by the manufacturer. However, the question of substance concentration has shown differences in antimicrobial dressing performance in previous studies, with lower concentrations yielding lower reduction rates (Rembe et al., 2018). Another restrictive factor of the dressing configuration might be the combination of octenidine, dihydrochloride and hyaluronic acid in the wound contact layer, which upon contact with wound exudate forms a gelling structure. This can lead to an "entrapment" of the active agent OCT in the gelling layer with the main antimicrobial activity exerted on microorganisms absorbed with the wound exudate into this layer and therefore low release of the agent into the wound and biofilm. Additionally, in the here tested dressing, only octenidine di-hydrochloride is embedded, in contrast to the highly effective liquid antiseptic Octenisept®, which contains a combination of octenidine di-hydrochloride and phenoxyethanol. The additive phenoxyethanol, however, exerts additional antimicrobial effects and further contained additives as well as alcohols have been specifically attributed with biofilm degrading properties (Percival et al., 2017a,b, 2019a), therefore offering another explanatory factor for the missing antimicrobial and anti-biofilm efficacy in the presented results. The question whether a daily or 2-day dressing change, would enhance the performance of the less effective test dressings (AG and OCT) cannot be conclusively answered herein. In relation, however, the more effective dressings (PHMB and C-IOD) would expectedly also profit from a more frequent change regimen, therefore not altering the comparative performance.

The aspects regarding active substance concentration and physicochemical release patterns as well as specific interactions due to dressing and microenvironment composition are transferable and applicable to all here tested wound dressings. Supposedly, the specific constellation of such factors for individual dressings dictate the overall antimicrobial and anti-biofilm efficacy observed in the presented results. Here, the polyhexanide-containing (PHMB) and especially the cadexomer-iodine containing dressing (C-IOD) proved to be most active against *P. aeruginosa* biofilm compared to other antimicrobial wound dressing formulations. However, only cadexomer-iodine achieved an actual relevant bactericidal effect. This is also reflected in the SEM showing an increased porosity and a distinct alteration of the biofilm surface pattern. Similar results were observed in earlier research approaches regarding its anti-biofilm activity (Phillips et al., 2015). As mentioned earlier, the combined cadexomer-iodine dressing exerts its effect by two main aspects: Cadexomer directly destroys biofilm structures by collapsing the bacterial glycocalyx (EPS) which is composed of 99% water (Lapping-Scott et al., 2014) by dehydration through water absorbtion, while iodine as an antimicrobial agent can subsequently eliminate bacteria (here

P. aeruginosa) released and exposed from the damaged biofilm structure (Akiyama et al., 2004).

Naturally, the presented results are limited as to the fact that they are *in vitro* results, calling for a careful consideration in terms of translation to clinical situations. Due to the experimental setup using a complex, human material based approach, the evaluations have been moved one step closer to clinical reality, however, still need to be interpreted with caution and in relation. The here used model allows for far more precise interpretations of results in terms of transferability into reality than simpler models. Still, even more complex test settings (incorporating human cell lines and three-dimensional tissue structures) will be required in the future to even better interpret complex efficacy interactions of antimicrobial products. The same goes for well-designed, sufficiently powered randomized controlled clinical trial to back *in vitro* findings and establish long-sought evidence-based clinical guidelines. The present results, however, show that these are urgently needed to clarify indications and support correct choice of wound care products.

Further limitations include the intentional disregard of the negative aspect of cytotoxicity potentially caused to the regenerating wound by excessive release of antimicrobial substances from wound dressings, as well as the evaluation of only one dressing per agent group with only a single combination of substance concentration and dressing formation per group investigated. Cytotoxic aspects were intentionally not addressed in this work due to focus being placed on bactericidal effects against biofilms, which untreated would exert potentially more harm to the healing wound than a confined cytotoxic impact derived from an antimicrobial treatment.

Finally, questions regarding the relevance of physicochemical release patterns and the specific composition and placement of the active agent within the dressing would be better addressed comparing differently manufactured dressings. However, in most cases (OCT, C-IOD, and PHMB) only very limited or even no further dressings containing the specific antimicrobial agents are commercially available and therefore need to be specifically manufactured as prototypes. This represents a continuous future endeavor in the field of material science, to identify and reliably validate the best combination of wound dressing material and active antimicrobial agent.

CONCLUSION

In this *in vitro* study the challenge a wound biofilm poses for antimicrobial agents becomes evident once again. The iodine- and polyhexanide-containing dressings perform as expected with a high bactericidal effect of C-IOD and a sustained bacteriostatic effect of PHMB over the course of 6 days even though not all surviving bacteria were counted due to incomplete lysis of the biofilm under C-IOD. The silver- and octenidine-containing wound dressings on the contrary did not show a bactericidal or bacteriostatic activity in the employed complex biofilm model (lhBIOM). In all wound dressings, the overall composition of the dressing, the concentration of the active substance and the form of interaction with the microenvironment are postulated to be crucial factors. For future anti-biofilm treatment strategies, especially dressings should be sought out, that exhibit biofilm/EPS degrading as well as antimicrobial properties, either in a single active substance or combinations. Therefore, biocompatible active agents or additives, that are readily and continuously released into the wound to interact with the biofilm need to be further investigated.

DATA AVAILABILITY STATEMENT

The raw data supporting the conclusions of this article will be made available by the authors, without undue reservation.

AUTHOR CONTRIBUTIONS

ES, FB, and RS designed the study. IP, VW, AU, MD, and MG carried out the experiments. ES, J-DR, AK, and RS analyzed the results and performed statistical analysis. IP, MD, and EN made the REM pictures and figures. ES, J-DR, SD, and RS drafted the manuscript. All authors contributed to the article and approved the submitted version.

FUNDING

The presented work was funded by the German Initiative Chronische Wunden e.V. (ICW).

ACKNOWLEDGMENTS

We would like to thank Mrs. A. Borger for her support in generating the blood agents, and B. Haußmann for preparation of the biofilm models for SEM analyzes.

REFERENCES

Akiyama, H., Oono, T., Saito, M., and Iwatsuki, K. (2004). Assessment of cadexomer iodine against *Staphylococcus aureus* biofilm in vivo and in vitro using confocal laser scanning microscopy. *J. Dermatol.* 31, 529–534. doi: 10.1111/j.1346-8138.2004.tb00549.x

AWMF. (2012). *Local therapy of chronic wounds in patients with the risk of peripheral arterial disease, diabetes or chronic venous insufficiency. Reg.-No. 091-001*. Available Online at: www.awmf.org/leitlinien/detail/ll/091-001.html

Besser, M., Dietrich, M., Weber, L., Rembe, J. D., and Stuermer, E. K. (2020). Efficiency of antiseptics in a novel 3-dimensional human plasma biofilm model (hpBIOM). *Sci. Rep. Nat. Res.* 10:4792. doi: 10.1038/s41598-020-61728-2

Bowler, P. G., Duerden, B. I., and Armstrong, D. G. (2001). Wound microbiology and associated approaches to wound management. *Clin. Microbiol. Rev.* 14, 244–269.

Brackman, G., and Coenye, T. (2016). In vitro and in vivo biofilm wound models and their application. *Adv. Exp. Med. Biol.* 897, 15–32.

Daeschlein, G. (2013). Antimicrobial and antiseptic strategies in wound management. *Int. Wound J.* 10, 9–14.

Davis, S. C., Harding, A., Gil, J., Parajon, F., Valdes, J., Solis, M., et al. (2017). Effectiveness of a polyhexanide irrigation solution on methicillin-resistant *Staphylococcus aureus* biofilms in a porcine wound model. *Int. Wound J.* 14, 937–944. doi: 10.1111/iwj.12734

Demidova-Rice, T. N., Hamblin, M. R., and Herman, I. M. (2012). Acute and impaired wound healing: pathophysiology and current methods for drug delivery, part 1: normal and chronic wounds: biology, causes, and approaches to care. *Adv. Skin Wound Care* 25, 304–314. doi: 10.1097/01.ASW.0000416006.55218.d0

Desroche, N., Dropet, C., Janod, P., and Guzzo, J. (2016). Antibacterial properties and reduction of MRSA biofilm with a dressing combining polyabsorbent fibres and a silver matrix. *J. Wound Care.* 25, 577–584. doi: 10.12968/jowc.2016.25.10.577

Dissemond, J., Boettrich, J. G., Braunwarth, H., Hilt, J., Wilken, P., and Münter, K. C. (2017). Evidence for silver in wound care - meta-analysis of clinical studies from 2000-2015. *J. Dtsch. Dermatol. Ges.* 15, 524–535. doi: 10.1111/ddg.13233

Fitzgerald, D. J., Renick, P. J., Forrest, E. C., Tetens, S. P., Earnest, D. N., and McMillan, J. (2017). Cadexomer iodine provides superior efficacy against bacterial wound biofilms in vitro and in vivo. *Wound Repair. Regen.* 25, 13–24. doi: 10.1111/wrr.12497

Forster, R., and Pagnamenta, F. (2015). Dressings and topical agents for arterial leg ulcers. *Cochrane Database Syst. Rev.* 6:CD001836.

Gnanadhas, D. P., Thomas, M., Thomas, R., Raichur, A. M., and Chakravortty, D. (2013). Interaction of silver nanoparticles with serum proteins affects their antimicrobial activity in vivo. *Antimicrob. Agent. Chemother.* 57, 4945–4955. doi: 10.1128/AAC.00152-13

Guest, J. F., Ayoub, N., McIlwraith, T., Uchegbu, I., Gerrish, A., Weidlich, D., et al. (2017). Health economic burden that different wound types impose on the UK's national health service. *Int. Wound J.* 14, 322–330. doi: 10.1111/iwj.12603

Guest, J. F., Fuller, G. W., and Vowden, P. (2018). Diabetic foot ulcer management in clinical practice in the UK: costs and outcomes. *Int. Wound J.* 5, 43–52.

Hirsch, T., Limoochi-Deli, S., Lahmer, A., Jacobsen, F., Goertz, O., Steinau, H. U., et al. (2011). Antimicrobial activity of clinically used antiseptics and wound irrigating agents in combination with wound dressings. *Plast. Reconstr. Surg.* 127, 1539–1545. doi: 10.1097/PRS.0b013e318208d00f

Huebner, N. O., and Kramer, A. (2010). Review on the efficacy, safety and clinical applications of polihexanide, a modern wound antiseptic. *Skin Pharmacol. Physiol.* 23, 17–27. doi: 10.1159/000318264

Huebner, N. O., Matthes, R., Koban, I., Raendler, C., Mueller, G., Bender, C., et al. (2010). Efficacy of chlorhexidine, polihexanide and tissue-tolerable plasma against *Pseudomonas aeruginosa* biofilms grown on polystyrene and silicone materials. *Skin. Pharmacol. Physiol.* 23, 28–34. doi: 10.1159/000318265

James, G. A., Swogger, E., Wolcott, R., Pulcini, E., Secor, P., Sestrich, J., et al. (2008). Biofilms in chronic wounds. *Wound Repair. Regen.* 16, 37–44.

Kapalschinski, N., Seipp, H. M., Onderdonk, A. B., Goertz, O., Daigeler, A., Lahmer, A., et al. (2013). Albumin reduces the antibacterial activity of polyhexanide-biguanide-based antiseptics against Staphylococcus aureus and MRSA. *Burns* 39, 1221–1225. doi: 10.1016/j.burns.2013.03.003

Kirketerp-Møller, K., Stewart, P. S., and Bjarnsholt, T. (2020). The zone model: a conceptual model for understanding the microenvironment of chronic wound infection. *Wound Repair. Regen.* 28, 593–599. doi: 10.1111/wrr.12841

Koburger, T., Hubner, N. O., Braun, M., Siebert, J., and Kramer, A. (2010). Standardized comparison of antiseptic efficacy of triclosan, PVP-iodine, octenidine dihydrochloride, polyhexanide and chlorhexidine digluconate. *J. Antimicrob. Chemother.* 65, 1712–1719.

Kramer, A., Dissemond, J., Kim, S., Willy, C., Mayer, D., Papke, R., et al. (2018). Consensus on wound antisepsis: update 2018 skin pharmacol. *Physiology* 31, 28–58. doi: 10.1159/000481545

Lapping-Scott, H., Burton, S., and Stoodley, P. (2014). Revealing a world of biofilms–the pioneering research of bill costerton. *Nat. Rev. Microbiol.* 12, 781–787. doi: 10.1038/nrmicro3343

Lenselink, E., and Andriessen, A. (2011). A cohort study on the efficacy of a polyhexanide-containing biocellulose dressing in the treatment of biofilms in wounds. *J. Wound Care.* 20, 534–536. doi: 10.12968/jowc.2011.20.11.534

Lo, S. F., Chang, C. J., Hu, W. Y., Hayter, M., and Chang, Y. T. (2009). The effectiveness of silver-releasing dressings in the management of non-healing chronic wounds: a meta-analysis. *J. Clin. Nurs.* 18, 716–728. doi: 10.1111/j.1365-2702.2008.02534.x

Loeffler, M. W., Schuster, H., Bühler, S., and Beckert, S. (2013). Wound fluid in diabetic foot ulceration: more than just an undefined soup? *Int. J. Low Extrem. Wounds.* 12, 113–129. doi: 10.1177/1534734613489989

Magill, S. S., Edwards, J. R., Bamberg, W., Beldavs, Z. G., Dumyati, G., Kainer, M. A., et al. (2014). Multistate point-prevalence survey of health care-associated infections. *N. Engl. J. Med.* 370, 1198–1208.

Norman, G., Dumville, J. C., Moore, Z. E., Tanner, J., Christie, J., and Goto, S. (2016). Antibiotics and antiseptics for pressure ulcers. *Cochrane Database Syst. Rev.* 4, CD011586.

O'Meara, S., Al-Kurdi, D., Ologun, Y., Ovington, L. G., Martyn-St James, M., and Richardson, R. (2013). Antibiotics and antiseptics for venous leg ulcers. *Cochrane Database Syst. Rev.* 23:CD003557. doi: 10.1002/14651858.CD003557

O'Meara, S., Cullum, N., Majid, M., and Sheldon, T. (2000). Systematic reviews of wound care management: (3) antimicrobial agents for chronic wounds; (4) diabetic foot ulceration. *Health Technol. Assess.* 4, 1–237.

Percival, S. L., Mayer, D., Kirsner, R. S., Schultz, G., Weir, D., Roy, S., et al. (2019a). Surfactants: role in biofilm management and cellular behaviour. *Int. Wound J.* 16, 753–760. doi: 10.1111/iwj.13093

Percival, S. L., Mayer, D., Malone, M., Swanson, T., Gibson, D., and Schultz, G. (2017a). Surfactants and their role in wound cleansing and biofilm management. *J. Wound Care.* 26, 680–690. doi: 10.12968/jowc.2017.26.11.680

Percival, S. L., Mayer, D., and Salisbury, A. M. (2017b). Efficacy of a surfactant-based wound dressing on biofilm control. *Wound Repair. Regen.* 25, 767–773. doi: 10.1111/wrr.12581

Percival, S. L., McCarty, S. M., and Lipsky, B. (2015). Biofilms and wounds: an overview of the evidence. *Adv. Wound Care* 4, 373–381. doi: 10.1089/wound.2014.0557

Percival, S. L., Salisbury, A. M., and Chen, R. (2019b). Silver, biofilms and wounds: resistance revisited. *Crit. Rev. Microbiol.* 45, 223–237. doi: 10.1080/1040841X.2019.1573803

Phillips, P. L., Yang, Q., Davis, S., Sampson, E. M., Azeke, J. I., Hamad, A., et al. (2015). Antimicrobial dressing efficacy against mature *Pseudomonas aeruginosa* biofilm on porcine skin explants. *Int. Wound J.* 12, 469–483. doi: 10.1111/iwj.12142

Rembe, J. D., Fromm-Dornieden, C., Böhm, J. K., and Stuermer, E. K. (2018). The influence of human acute wound fluid (AWF) on the antibacterial efficacy of different antiseptic polyurethane foam dressings: an in-vitro analysis. *Wound Repair. Regen.* 26, 27–35. doi: 10.1111/wrr.12612

Rembe, J. D., Huelsboemer, L., Besser, M., and Stuermer, E. K. (2020). Anti-biofilm activity of antimicrobial hypochlorous wound irrigation solutions compared to common wound antiseptics and bacterial resilience in a novel in-vitro human plasma biofilm model (hpBIOM). *Front. Microbiol.* 11:564513. doi: 10.3389/fmicb.2020.564513

Roche, E. D., Woodmansey, E. J., Yang, Q., Gibson, D. J., Zhang, H., and Schultz, G. S. (2019). Cadexomer iodine effectively reduces bacterial biofilm in porcine wounds ex vivo and in vivo. *Int. Wound J.* 16, 674–683.

Shukla, S. K., Sharma, A. K., Gupta, V., Kalonia, A., and Shaw, P. (2020). Challenges with wound infection models in drug development. *Curr. Drug Targets* 21, 1301–1312. doi: 10.2174/1389450121666200302093312

Sibbald, R. G., Coutts, P., and Woo, K. Y. (2011). Reduction of bacterial burden and pain in chronic wounds using a new polyhexamethylene biguanide antimicrobial foam dressing-clinical trial results. *Adv. Skin. Wound Care.* 24, 78–84. doi: 10.1097/01.ASW.0000394027.82702.16

Storm-Versloot, M. N., Vos, C. G., Ubbink, D. T., and Vermeulen, H. (2010). Topical silver for preventing wound infection. *Cochrane Database Syst. Rev.* 3:CD006478.

Stuermer, E. K., Besser, M., Brill, F. H. H., Geffken, M., Plattfaut, I., Severing, A. L., et al. (2021). Comparative analysis of biofilm models to determine the efficacy of antimicrobials. *J. Hyg. Environ. Health.* 234:113744.

To, E., Dyck, R., Gerber, S., Kadavil, S., and Woo, K. Y. (2016). The effectiveness of topical polyhexamethylene biguanide (PHMB) agents for the treatment of chronic wounds: a systematic review. *Surg. Technol. Int.* 29, 45–51.

Wiegand, C., Abel, M., Ruth, P., Elsner, P., and Hipler, U. C. (2015). pH influence on antibacterial efficacy of common antiseptic substances. *Skin Pharmacol. Physiol.* 28, 147–158. doi: 10.1159/000367632

Wu, L., Norman, G., Dumville, J. C., O'Meara, S., and Bell-Syer, S. E. (2015). Dressings for treating foot ulcers in people with diabetes: an overview of systematic reviews. *Cochrane Database Syst. Rev.* 7: CD010471.

Conflict of Interest: The authors declare that the research was conducted in the absence of any commercial or financial relationships that could be construed as a potential conflict of interest.

frontiers in Microbiology

ORIGINAL RESEARCH
published: 19 May 2021
doi: 10.3389/fmicb.2021.658373

Understanding How Staphylococcal Autolysin Domains Interact With Polystyrene Surfaces

*Radha P. Somarathne[1], Emily R. Chappell[1], Y. Randika Perera[2], Rahul Yadav[1], Joo Youn Park[3] and Nicholas C. Fitzkee[1]**

[1] Department of Chemistry, Mississippi State University, Mississippi State, MS, United States, [2] Department of Biochemistry, Chemistry, and Center for Structural Biology, Vanderbilt University, Nashville, TN, United States, [3] Department of Comparative Biomedical Sciences, College of Veterinary Medicine, Mississippi State University, Mississippi State, MS, United States

OPEN ACCESS

Edited by:
Mark Smeltzer,
University of Arkansas for Medical Sciences, United States

Reviewed by:
Jeffrey Lee Bose,
University of Kansas Medical Center, United States
Lichong Xu,
Pennsylvania State University, United States
Carla Renata Arciola,
Rizzoli Orthopedic Institute (IRCCS), Italy

***Correspondence:**
Nicholas C. Fitzkee
nfitzkee@chemistry.msstate.edu
orcid.org/0000-0002-8993-2140

Specialty section:
This article was submitted to Antimicrobials, Resistance and Chemotherapy, a section of the journal Frontiers in Microbiology

Received: 25 January 2021
Accepted: 19 April 2021
Published: 19 May 2021

Citation:
Somarathne RP, Chappell ER, Perera YR, Yadav R, Park JY and Fitzkee NC (2021) Understanding How Staphylococcal Autolysin Domains Interact With Polystyrene Surfaces. Front. Microbiol. 12:658373. doi: 10.3389/fmicb.2021.658373

Biofilms, when formed on medical devices, can cause malfunctions and reduce the efficiency of these devices, thus complicating treatments and serving as a source of infection. The autolysin protein of *Staphylococcus epidermidis* contributes to its biofilm forming ability, especially on polystyrene surfaces. R2ab and amidase are autolysin protein domains thought to have high affinity to polystyrene surfaces, and they are involved in initial bacterial attachment in *S. epidermidis* biofilm formation. However, the structural details of R2ab and amidase binding to surfaces are poorly understood. In this study, we have investigated how R2ab and amidase influence biofilm formation on polystyrene surfaces. We have also studied how these proteins interact with polystyrene nanoparticles (PSNPs) using biophysical techniques. Pretreating polystyrene plates with R2ab and amidase domains inhibits biofilm growth relative to a control protein, indicating that these domains bind tightly to polystyrene surfaces and can block bacterial attachment. Correspondingly, we find that both domains interact strongly with anionic, carboxylate-functionalized as well as neutral, non-functionalized PSNPs, suggesting a similar binding interaction for nanoparticles and macroscopic surfaces. Both anionic and neutral PSNPs induce changes to the secondary structure of both R2ab and amidase as monitored by circular dichroism (CD) spectroscopy. These changes are very similar, though not identical, for both types of PSNPs, suggesting that carboxylate functionalization is only a small perturbation for R2ab and amidase binding. This structural change is also seen in limited proteolysis experiments, which exhibit substantial differences for both proteins when in the presence of carboxylate PSNPs. Overall, our results demonstrate that the R2ab and amidase domains strongly favor adsorption to polystyrene surfaces, and that surface adsorption destabilizes the secondary structure of these domains. Bacterial attachment to polystyrene surfaces during the initial phases of biofilm formation, therefore, may be mediated by aromatic residues, since these residues are known to drive adsorption to PSNPs. Together, these experiments can be used to develop new strategies for biofilm eradication, ensuring the proper long-lived functioning of medical devices.

Keywords: biofilms, autolysin proteins, polystyrene nanoparticles, medical implants, surface chemistry

INTRODUCTION

Staphylococcus epidermidis is a very common pathogen known to cause a variety of infections, including those involving medical implants and devices (McCann et al., 2008; Büttner et al., 2015; Zheng et al., 2018). The cell wall of *S. epidermidis* contains protein, nucleic acid, and peptidoglycan components (Büttner et al., 2015), and a major protein component of the cell wall is the peptidoglycan hydrolase, autolysin (AtlE). The AtlE protein plays an essential role in bacterial cell wall cleavage and is therefore critical during cell division (Nega et al., 2020). The R2ab and amidase domains in AtlE are responsible for enzyme targeting in the septum region (Yamada et al., 1996). AtlE is post-translationally cleaved between the R2 and R3 domains, resulting in a construct containing the amidase enzyme and the R1 and R2 repeats (Amidase-R1-R2). The protein is non-covalently associated with the cell wall through interactions between the R1 and R2 repeats and lipoteichoic acid (LTA) (Zoll et al., 2012). The native structures of both R2ab and amidase have been solved by Zoll et al. (2010, 2012) but the structure of the LTA-complexed protein is not currently known. In addition, AtlE is known to take part in its primary attachment to surfaces, especially to polystyrene surfaces (Houston et al., 2011). Both amidase and R2ab are required for *S. epidermidis* to be biofilm positive on polystyrene surfaces (Heilmann et al., 1997; Zoll et al., 2012).

Biofilms are assemblies of microbial cells present in a highly structured community, with the ability to attach to surfaces and form colonies that are associated with a extracellular polymeric matrix (Sandal et al., 2007). Biofilm formation occurs in three steps – attachment, maturation and dispersion (Crouzet et al., 2014). In the attachment stage, microorganisms adhere on to non-biological surfaces by non-specific hydrophobic interactions (Dunne, 2002). Biofilms have many unfavorable effects on public health, especially since they infect medical implants in the body such as heart valves and catheters (Trautner and Darouiche, 2004). In fact, they account for more than half of microbial infections (Jamal et al., 2018). They can also form on a variety of biological surfaces such as the urinary tract, skin, and most commonly on teeth (Saini et al., 2011). *S. epidermidis*, being an opportunistic pathogen, can attach onto polymeric devices and cause harm to both healthy and immunocompromised patients. There are three basic components that are basic, vital components in biofilm formation – microbes, extracellular matrix, and a surface (Donlan, 2002). If any of these components are removed, biofilm formation would not happen. However, biofilm formation is a fairly complex process that cannot be restricted to merely these three main components. Many other factors such as the type of organism, surface, genetic variations, and other environmental factors serve a purpose in biofilm formation (Steenackers et al., 2016; Ponomareva et al., 2018).

Preventing biofilm formation is imperative for the optimum function of biomedical implants and diagnostic equipment. Polystyrene is an important surface for these applications, because it is abundant in the medical field, and because it is amenable to surface modification. While polystyrene is not currently used in implantable medical devices (Sastri, 2010), it is a common component of medical diagnostic equipment (Loos et al., 2014), and biofilms are observed to form readily on untreated polystyrene surfaces (Kaplan et al., 2004). These biofilms can lead to complications associated with device failure (Gominet et al., 2017). Primary adhesion of bacteria to abiotic surfaces is usually facilitated by non-specific interactions. Polystyrene is amenable to surface conditioning, an approach that can be used to alter these interactions, reducing biofilm formation through surface pretreatment (Lorite et al., 2011). However, conditioning remains challenging because it requires an understanding of the molecular interactions involved in surface adhesion. Some conditioners tend to hinder biofilm growth by killing bacterial cells (Zhang et al., 2013; Percival et al., 2014), emphasizing the importance of understanding adsorption to abiotic surfaces. Therefore, it is of high interest to understand how molecules interact with polystyrene surfaces: not only is this knowledge relevant for understanding biofilm formation on many medical diagnostic tools, it is also important for preventing biofilms through surface conditioning.

In this study, we explore the behavior of the R2ab and amidase domains on polystyrene surfaces. In addition to examining these proteins' behavior with macroscopic surfaces, such as cell plates, we explore how these protein domains interact with carboxylate functionalized, polystyrene nanoparticles (PSNPs). Nanoparticles have a large surface-to-volume ratio, and they can be functionalized to remain suspended in solution at high concentrations (Fang et al., 2009). Moreover, nanoparticles of diameter 15 nm and larger are several orders of magnitude larger than small protein domains like R2ab and amidase, making them a fair approximation for a flat surface. Our group (Wang et al., 2014; Woods et al., 2016), and others (Lacerda et al., 2010; Gunawan et al., 2014; Satzer et al., 2016) have found that protein binding occurs independently of nanoparticle curvature for nanoparticles larger than 15 nm. However, surface functionalization and protein identity can lead to curvature-dependent effects (Gagner et al., 2011; Perera et al., 2019; Visalakshan et al., 2020), and this remains an area of active investigation. By studying both R2ab and amidase on a nanoparticles and flat surfaces, we aim to understand the structural behavior of these proteins when adsorbed to surfaces and to understand the broader principles of protein-surface interactions. Ultimately, we have analyzed the interaction of the autolysin proteins R2ab and amidase with both polystyrene surfaces and nanoparticles to achieve a better understanding of these interactions and how they compare. In the long term, this could lead to novel potential solutions for eradicating biofilms formed on medical devices.

MATERIALS AND METHODS

Protein Expression and Purification

Plasmids encoding the sequence for R2ab and amidase domains were synthesized by Life Technologies, Inc. (Carlsbad, CA, United States) and transformed into a pET-15b vector; these sequences were identical to the sequences used previously (Zoll et al., 2010, 2012; Büttner et al., 2014). Both vectors were transformed into *Escherichia coli* BL21(DE3) cell. Transformed

cells containing the R2ab plasmid were grown overnight at 37°C for 16 h in LB media. This starter culture was then used to inoculate 1L of LB media, at an initial OD_{600} of 0.05. When this larger culture reached an OD_{600} of 0.5–0.7, it was induced using 0.5 mM isopropyl β-d-1-thiogalactopyranoside (IPTG), and the culture was allowed to incubate overnight at 25°C. The cells were then harvested by spinning them for 30 min at 8,000 × *g* and the pellets were resuspended in lysis buffer (150 mM NaCl, 20 mM HEPES pH 7.5, 40 mM imidazole). The resuspended cells were sonicated at 45% power, thrice with 2 min continuous pulsing, followed by 2 min rest, for a total process time of 6 min. The resulting lysate was centrifuged at 32,000 × *g* for 30 min at 4°C. R2ab was collected from the soluble fraction and purified through a 5 mL Nickel HisTrap FF column (Cytiva Life Sciences, Marlborough, MA, United States) that was equilibrated with lysis buffer. The bound protein was eluted using a gradient of elution buffer (150 mM NaCl, 20 mM HEPES pH 7.5, 800 mM Imidazole). Thrombin was added to the protein after quantification to remove the histidine tag, and then dialyzed in dialysis buffer (150 mM NaCl, 20 mM HEPES pH 7.5, 20 mM Imidazole) overnight. Thrombin was removed from the protein using benzamidine beads (Cytiva Life Sciences). After centrifuging and filtering the beads, the supernatant was run once more through a 5 mL Nickel HisTrap FF column to obtain tag-free protein. Finally, the purified protein was run through a Superdex 26/600 75 column, equilibrated using gel filtration buffer (50 mM NaCl, 20 mM sodium phosphate pH 6.5). Purified R2ab protein was lyophilized and stored at −80°C. Purification of amidase was performed similarly, except that the lysis buffer used, contained 50 mM sodium phosphate, pH 7.4, 300 mM NaCl and 25 mM imidazole, and the protein was eluted using 50 mM sodium phosphate, pH 7.4, 300 mM NaCl 400 mM imidazole.

Nanoparticle Preparation and Characterization

Carboxyl-functionalized polystyrene nanoparticles with a nominal diameter of 20 nm were purchased from Thermo Fisher (catalog #C37261, lot #1688129; Eugene, OR, United States). The manufacturer-listed nanoparticle diameter is 28 ± 6 nm by transmission electron microscopy (TEM); this was confirmed by dynamic light scattering (DLS) using an Anton Paar Litesizer 500, where the hydrodynamic diameter was observed to be 40 nm. The stock solution concentration was 4% (w/v) total solids. The number of carboxyl groups per nanoparticle (59 COOH groups per particle), determined by titration, was taken from the manufacturer's certificate of analysis for this lot. Neutral, non-functionalized polystyrene nanospheres were obtained from Polysciences (catalog #08691-10, lot #A774113; Warrington, PA, United States). According to manufacturer's specification, these non-functionalized spheres contain a slight anionic charge from the presence of sulfate esters. Prior to mixing with proteins, all nanoparticles were dialyzed against 1 L of buffered solution, and the pH of PSNP solutions was confirmed after dialysis.

Biofilm Assays

To determine the effects of the R2ab and amidase domains on biofilm formation of *S. epidermidis*, biofilm assays were performed as described previously and outlined below (Merritt et al., 2005; Billings et al., 2013). Briefly, different wells in a flat-bottomed 96-well polystyrene plate (Thermo Fisher, catalog #15041), were coated with 100 μL 0.1 mg/ml of either R2ab, amidase, or bovine serum albumin (BSA) (negative control). For protein coating, each of these proteins in gel filtration buffer (specified above) was added to a well to incubate overnight at 4°C. After incubation, the protein solution was removed by pipetting. To prepare the bacterium inoculum, *S. epidermidis* strain 1301 (available on request), a biofilm producing strain, was inoculated from a stab culture in 1 mL of Brain Heart Infusion (BHI) media at 37°C, overnight with shaking (Harris et al., 2016). To each coated well, 100 μL of fresh BHI media was added, followed by 2 μL of the overnight seed culture. The plate was allowed to incubate statically at 37°C for 72 h, allowing biofilms to form. Following the incubation and removal of the excess cells with three washings of 100 μL of PBS buffer (removed by pipetting), the biofilms were fixed with 100 μL of 100% methanol at room temperature for 10 min and stained with 100 μL 0.1% w/v crystal violet stain in water (B12525, Thermo Fisher Scientific). The biofilms were washed three times with PBS buffer as above to remove excess crystal violet stain, and 100 μL of 30% acetic acid was used to solubilize the cell bound crystal violet. Biofilm formation was monitored by measuring optical density of each well using a SpectraMax 4 plate reader at 570 nm.

Antimicrobial Assay

To determine the antimicrobial properties of the R2ab and amidase and amidase domains, R2ab and amidase were added to cultures of *S. epidermidis* in 96 well polystyrene plates. An overnight seed culture of *S. epidermidis* strain 1301 was prepared in BHI media as described above. Then, 2 μL of this seed culture was added to 100 μL of fresh BHI media in the 96-well plate. R2ab and amidase (stock concentration of 100 μM) in gel filtration buffer were then added to the culture, followed by pipette mixing. The bacterial culture was monitored for a period of 24 h by measuring the OD_{600} every hour, at a temperature of 37°C, using a Cytation5 plate reader.

Dynamic Light Scattering and Zeta Potential Measurements

Varying concentrations of proteins, starting from 1 μM, were added to 40 nM of nanoparticles, to a final volume of 50 μL. After nanoparticle – protein mixture was incubated at room temperature for 1 h, the samples were centrifuged at 15,000 × *g* for 10 min. The supernatant was discarded, and the sample pellet was washed three times with 10 mM sodium phosphate (pH 7.0), to remove any free protein in the solution. The pellet was then resuspended in the same buffer and the sample was transferred to a Low Volume Univette (Anton Paar). All measurements were obtained using an Anton Paar Litesizer 500 DLS at 25°C, and the data was processed using the Kalliope software.

Circular Dichroism Spectropolarimetry

The circular dichroism (CD) measurements were carried out using a Jasco 1500 CD spectrometer at 25°C. The measurements

were performed at a path length of 1 mm using a quartz cuvette. In order to determine how the secondary structure of both the proteins change in the presence of nanoparticles, all the protein solutions were made containing the same concentration of R2ab and amidase (3 μM) with increasing concentrations of nanoparticles present in the mixture. A lower concentration (0.6 μM) was used for BSA; this concentration was reduced because fewer BSA molecules are predicted to bind to PSNPs, and saturation of the surface is expected to occur at a lower concentration. Similarly, while the total number of proteins per nanoparticle monolayer changes dramatically with protein size, the total mass of protein in a monolayer remains roughly the same, justifying a lower molar concentration of BSA (**Supplementary Table 1**). A BSA concentration of 0.6 μM (or 0.04 mg/mL) is approximately the same in mg/mL as the 3 μM used for R2ab and Amidase (0.05 and 0.08 mg/mL, respectively). The buffer for all solutions was 10 mM sodium phosphate (pH 7.0). Between each sample measurement, the cuvette was carefully cleaned. Far-UV spectra were collected between 180 and 260 nm, with the scan rate set at 10 nm min^{-1} at a bandwidth of 1 nm using 4 s as the integration time. Spectra were smoothed using Savitzky-Golay filter set to a window size of 17. The data was analyzed, and the decomposition process was carried out using Jasco's Spectra Manager software suite.

Limited Proteolysis

The pattern of proteolytic digestion was tested on both R2ab and amidase in the presence and absence of polystyrene nanoparticles. In the experiments without nanoparticles, 0.5 mg/ml of proteins were incubated with 0.01 mg/ml of chymotrypsin (Amresco) (chymotrypsin: protein ratio 1:50) for 30 min at 22°C. Mixtures of proteins and nanoparticles were generated by adding PSNPs to a final (molar) nanoparticle to protein ratio of 1:190 for R2ab and 1:170 for amidase. These ratios were determined based on previous calculations of surface coverage (Wang et al., 2014). For digests containing PSNPs, chymotrypsin was added after mixing the proteins and nanoparticles, and allowing it to incubate for 1 h. The reactions were stopped by adding SDS-PAGE sample buffer (Bio-Rad) and heating the samples for 5 min at 95°C. For each experiment, a control sample of chymotrypsin was used, and a parallel sample of proteins without any chymotrypsin was analyzed and compared on 16.5% Tris–Tricine gels (Bio-Rad). The proteolytic products were visualized via silver staining due to low intensity of fragments.

RESULTS

R2ab and Amidase on Surfaces Hinders Biofilm Formation but Not Bacterial Growth

To examine the effects of the R2ab and amidase domains on biofilm formation, we tested their effect on biofilm formation on polystyrene plates. We used *S. epidermidis* strain 1301, which is able to form dense biofilms on polystyrene surfaces. After treating the 96-well plates with either R2ab and amidase, a significant reduction in biofilm was observed, as monitored by crystal violet staining (**Figure 1**) (O'Toole, 2011). The absorbance at 570 nm reflects the amount of biofilm present prior to fixation and staining. As expected, the highest absorbance was obtained for the untreated wells, where cells grew unhindered in BHI media. All treatments produced a statistically significant decrease in biofilm formation, including treatment with the negative control, BSA ($p = 0.0047$). This decrease occurs because protein adsorption is a general phenomenon (Andrade and Hlady, 1986). However, in wells that had been pre-treated with either R2ab or amidase, the growth of biofilms was reduced by a substantially larger amount, a nearly three-fold reduction ($p < 0.0001$). This suggests that R2ab and amidase are far more effective than typical proteins in adsorbing to a polystyrene surface, preventing bacterial attachment and subsequent biofilm formation.

While R2ab and amidase may hinder biofilm formation, it is also possible that they slow bacterial growth. To determine whether this is the case, we added R2ab and amidase to the growth media of *S. epidermidis* strain 1301 and monitored the bacterial growth curves, measuring the OD_{600} at fixed intervals. Over a period of 24 h the growth curve of *S. epidermidis* was monitored in BHI media containing increasing protein concentrations for both R2ab and amidase domains. These curves were compared to curves where no proteins were added to the media (**Figure 2**). Some differences in growth curves were observed between cells treated with proteins and those without;

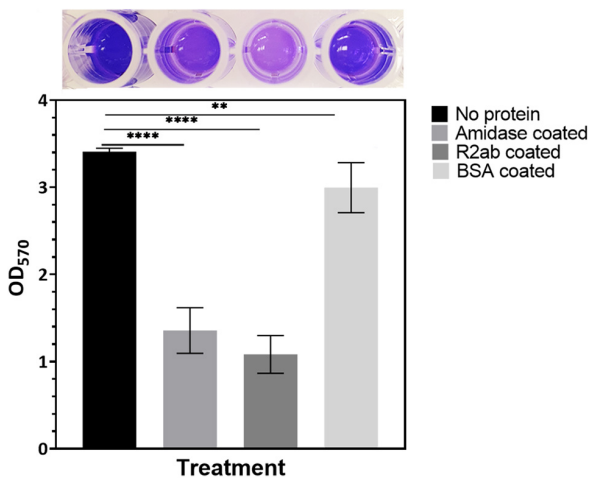

FIGURE 1 | The effect of protein treatment on biofilm formation. Wells were pre-coated with either no protein (control), amidase, R2ab, or BSA, followed by growth conditions favoring biofilm formation, which was monitored by crystal violet staining and measurement of absorbance at 570 nm. The BSA-coated plate showed only a slight reduction in biofilm growth relative to no treatment, but plates treated with amidase and R2ab domains show a much larger reduction. A typical row from a stained, 96-well plate is shown above each corresponding column to display the results of crystal violet staining. The error bars for each data point represent the standard error of the mean for $N = 8$ samples. A one-way ANOVA test [$F(3,28) = 217.2$, $p < 0.0001$] with Tukey's post hoc analysis was performed to determine the levels of significance (**$p < 0.005$, ****$p < 0.0001$).

however, this likely reflects small changes in the number of initial cells used to inoculate each well. Indeed, significant variability was observed for when each well reached log phase. In no case did the added R2ab or amidase lower the final OD_{600} for the cultures, and in several cases, the final cell density was increased. Moreover, as indicated by representative growth curves (**Figures 2A,C**), the doubling time did not appear to be affected by the addition of increasing concentrations of R2ab or amidase. At 18 h, differences between the OD_{600} values for each cultures were all statistically significant (**Figures 2B,D**, measured using one-way ANOVA). However, there was no apparent dose-response for treatment with either R2ab or amidase, and in many cases the treated cells grew to a higher OD_{600}. These data indicate that R2ab and amidase have no antimicrobial properties that could contribute to the stunted biofilm formation observed in **Figure 1**.

In the pre-treatment experiments, the R2ab and amidase domains were removed from each well, leaving only the proteins that had adsorbed to the polystyrene surface. The concentration of proteins in solution if desorption occurred is therefore expected to be much less than 10 μM. However, our bacterial growth experiments show no consistent effect on cell division for concentrations of protein in solution up to 10 μM. Together, these results strongly suggest a mechanism whereby biofilm formation is blocked by adsorption of R2ab and amidase to the polystyrene surface, and not a mechanism where cell density is reduced by the presence of these domains in solution.

R2ab and Amidase Domains Strongly Interact With Polystyrene Nanoparticles

Performing biophysical experiments of proteins on macroscopic, flat polystyrene surfaces is extremely challenging because of the low surface-volume ratio of flat surfaces and the corresponding small number of proteins adsorbed. Nanoparticles have a very high surface to volume ratio, and titration of nanoparticles into

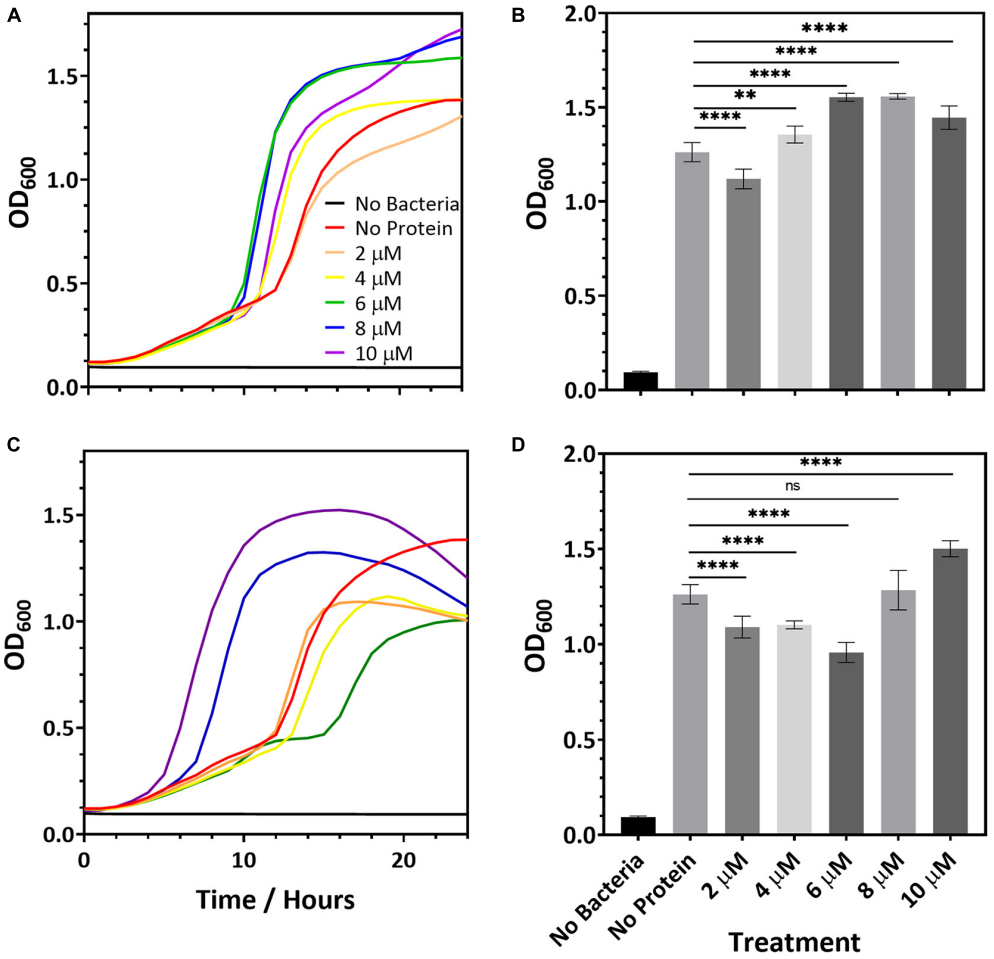

FIGURE 2 | Representative microbial growth curves in the presence of R2ab **(A)** and amidase **(C)**. Growth curves are shown for *S. epidermidis* when the media was mixed with **(A,B)** R2ab or **(C,D)** amidase. Concentrations added for each protein domain are 0 μM (red), 2 μM (orange), 4 μM (yellow), 6 μM (green), 8 μM (blue), and 10 μM (purple). The black curve shows a control with no bacteria added. Panels **(B,D)** show the average and standard deviation of OD_{600} at 18 h for R2ab and amidase, respectively, for the different treatments ($N = 8$). A one-way ANOVA test [**(B)**: $F(5, 42) = 120.4$, $p < 0.0001$ and **(D)**: $F(5, 41) = 77.51$, $p < 0.0001$] with Tukey's post hoc analysis was performed to determine the levels of significance between groups (n.s. is not significant; $^{**}p < 0.005$ and $^{****}p < 0.0001$).

solution allows for the controlled addition of surface binding sites in an experiment. While the effects of curvature (Gagner et al., 2011; Woods et al., 2016) and surface functionalization (Dominguez-Medina et al., 2016) play a significant role in nanoparticle-surface interactions, these effects can be minimized by using proteins that are much smaller than the nanoparticles in question and by minimizing surface functionalization. To explore the structural consequences of adsorption for the R2ab and amidase domains, we examined their behavior in the presence of spherical 20 nm (nominal diameter) carboxylate functionalized polystyrene nanoparticles (PSNPs). When protein solubility conditions permitted, we also examined protein adsorption to neutral, non-functionalized PSNPs. These nanoparticles are substantially larger than either protein domain, and hundreds of copies of each protein could fit in a monolayer on each nanoparticle (138 and 150 proteins per nanoparticle for R2ab and amidase, respectively; see **Supplementary Table 1**) (Wang et al., 2014), suggesting that, from the perspective of each protein domain, the surface is effectively flat. PSNPs have been used extensively in protein binding measurements (Baier et al., 2011; Contado et al., 2019; Kihara et al., 2019), providing fruitful information on protein binding, corona formation, and structural changes that occur upon adsorption. While the molecular similarities between PSNP adsorption and macroscopic adsorption remain unclear, we hypothesize that the processes are related, and we set out to explore the behavior of R2ab and amidase when adsorbed to PSNP surfaces, both with and without COOH functionalization.

To examine the interactions between the R2ab and amidase domains with PSNPs, DLS profiles were measured as the protein domains were titrated into the solutions containing PSNPs. A large interaction was observed for R2ab and amidase, as monitored by the dramatic shift in hydrodynamic diameter (**Supplementary Figure 1**). The hydrodynamic diameter of the carboxylate PSNPs alone was found to be 42.1 ± 0.1 nm; R2ab increased this value to 3,600 ± 300 nm, and amidase-coated PSNPs had an apparent hydrodynamic diameter of 670 ± 30 nm. However, the shift for BSA was much smaller, which had a final hydrodynamic diameter of only 48.5 ± 0.3 nm. The same trend was observed for neutral, non-functionalized PSNPs (**Supplementary Figure 1**). No visible aggregation was observed for any of the proteins under these conditions, suggesting that dynamic association of protein domains on the PSNP surfaces was occurring, as opposed to the formation of insoluble protein-nanoparticle conjugates. The interaction occurred at very low protein concentrations, indicating that the binding between both domains and the surface was rather strong. This is similar to what was observed in a prior study of PSNP-protein interactions in bovine α-lactalbumin, which reported strong but dynamic interactions in protein adsorption, associated with increases in hydrogen-deuterium exchange rates (Engel et al., 2004). Based on the significant increase in hydrodynamic diameter measured by DLS, R2ab, and amidase interact with PSNPs to a greater degree than BSA. This is consistent with the idea that R2ab and amidase domains interact with polystyrene surfaces in a uniquely strong way.

Zeta potential measurements for PSNPs coated with amidase and R2ab also reflect a strong interaction (**Figure 3**). Zeta potential measures the electric potential between at the slipping plane surrounding a surface and reflects the surface charge of a surface (Jiang et al., 2009). The zeta potential for both titrations starts at a negative zeta potential value for the bare carboxylate PSNPs, reflecting their net negative charge from carboxylic acid groups. The mV values become positive as the proteins are added in increasing concentrations. Initially, the variation of zeta potential is reasonably even; however, at higher concentrations of proteins, the zeta potential becomes fairly constant and the titration curve flattens out. The R2ab and amidase domains have theoretical isoelectric points of 9.7 and 6.8, respectively, and they are expected to decrease the net surface charge of carboxylate PSNPs as they adsorb. Assuming monolayer surface coverage, both proteins are expected to completely saturate the surface of 40 nM of PSNPs when 3–4 μM protein is present (Wang et al., 2014), and for titrations of both protein domains, the surface potential of PSNPs appears to be neutralized at this level of saturation. On the other hand, the BSA negative control does not induce a strong change in zeta potential as it is added (**Figure 3**), even though the degree of saturation is far greater when 4 μM is present, since far fewer molecules of BSA are able to bind in a single monolayer of a PSNP based on geometric considerations. Together, the DLS and zeta potential experiments reveal a strong interaction between amidase domains and PSNP surfaces that doesn't appear to be present for other proteins like BSA. This is consistent with our biofilm assays on macroscopic polystyrene surfaces.

Polystyrene Nanoparticles Alter the Secondary Structure of Autolysin Domains

To further understand the behavior of proteins in the presence of a polystyrene surface, we used CD to monitor changes in

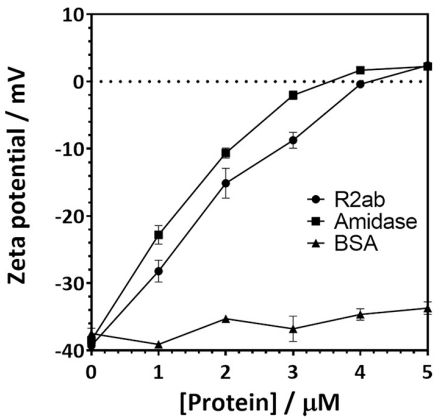

FIGURE 3 | Zeta potential changes when carboxylate functionalized PSNPs are titrated with autolysin domains. The zeta potential of 20 nm (nominal diameter) carboxylate-functionalized polystyrene nanospheres increases when R2ab or amidase domains are added to solution, but very little change is seen for BSA. Error bars represent the standard deviation for $N = 3$ experiments, and lines connecting each point are added as a guide to the eye.

protein secondary structure as PSNPs were added (**Figure 4**). The magnitude of the CD signal decreases as PSNP concentration is increased for both the R2ab and amidase. However, the behavior of both proteins differs slightly. The R2ab domain exhibits a uniform decrease in magnitude as PSNPs are added (**Figure 4A**). This type of scaling behavior could result from one of two phenomena: First, if protein-PSNP conjugates were sedimenting over time, the amount of protein in solution would decrease, leading to a lower signal compared to the non-interacting reference. Fewer protein molecules would then be present in solution, which would scale the molar residue ellipticity in the presence of PSNPs. Second, it is possible that the secondary structure is changing in such a way as to reduce the CD signal, even while the total protein concentration in the optical path is remaining constant. A combination of both effects is also possible; however, we believe that secondary structure changes are the primary cause for the spectra in **Figure 4**. This is because no aggregation is observed in the cuvette and the spectra are stable for at least an hour. The samples were prepared having the same total protein concentration, so the scaling observed is not simply a dilution effect. In these experiments, the R2ab is in excess of the predicted nanoparticle binding sites, even at the highest nanoparticle concentration of 20 nM. Therefore, it is likely that the changes in R2ab, while uniform across all wavelengths, reflect a change in secondary structure. The behavior of the amidase domain is different, and this spectrum is not uniformly scaled as the spectrum for R2ab is. Instead, the spectral shape for amidase changes, giving rise to isodichroic points at 205 nm and potentially near 230 nm. The lower signal to noise of the 20 nM titration point for amidase likely reflects increased scattering as larger agglomerates form, similar to what was observed in the DLS experiments. This behavior also suggests a secondary structure change in the amidase domain in the presence of PSNPs, and the isodichroic points indicate that a two-state transition may be occurring. The third protein investigated, BSA, shows a very minor change compared to the other two proteins. Structural changes in BSA, if present, are very marginal, and this is consistent previous observations of BSA on carboxylate-functionalized polystyrene nanospheres (Fleischer and Payne, 2014).

These experiments were also repeated on neutral, non-functionalized PSNPs to test whether the carboxylate groups on the PSNP surface were influencing the protein structure. CD is sensitive to scattering in the far-UV range, and we found that the neutral PSNPs would aggregate and give poor signal at high protein concentrations. This made collection of CD data more challenging under these conditions. Nevertheless, trends in the CD spectra were consistent for R2ab, amidase, and BSA collected with neutral PSNPs (**Supplementary Figure 2**). Importantly, R2ab and amidase looked very similar on neutral PSNPs as they did on carboxylate functionalized PSNPs, whereas BSA showed very little change on both neutral and carboxylate coated surfaces. In addition, the spectral changes for R2ab and amidase were remarkably consistent with those shown in **Figure 4**: the R2ab spectrum exhibited a uniform scaling behavior, and the amidase spectrum became flatter in the presence of non-functionalized PSNPs. The carboxylate PSNPs used in these experiments,

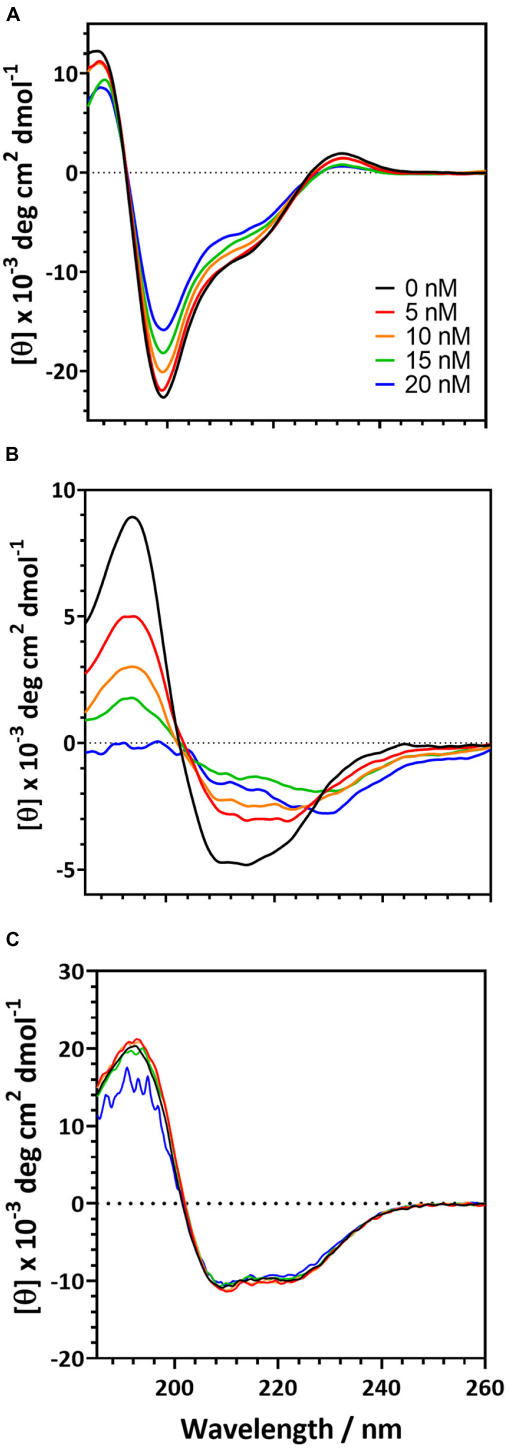

FIGURE 4 | Circular dichroism spectra for the of autolysin domains and a negative control in the presence of carboxylate functionalized PSNPs. R2ab **(A)** and amidase **(B)** exhibit changes in their CD spectra when nanoparticle concentrations are increased. In the absence of nanoparticles (black curve), both domains exhibit a well-defined secondary structure. As nanoparticles are increased to 5 nM (red), 10 nM (orange), 15 nM (green), and 20 nM (blue), secondary structure changes become evident. The same changes are not observed for BSA **(C)**, whose spectrum remains fairly constant as PSNP concentration is altered.

therefore, appear to induce similar (albeit not identical) behavior to what is observed for neutral, non-functionalized PSNPs, and this makes sense given the number density of COOH groups on the surface (see section "Discussion").

Secondary structure analysis supports the interpretation given above (**Table 1**) (Greenfield and Fasman, 1969; Johnson, 1990). Upon singular value decomposition (SVD) analysis, the proteins experience quantitative changes in their secondary structure. The R2ab domain consists of primarily β-strands (Zoll et al., 2012), and this is reflected in the initial estimates of secondary structure. Similarly, the SVD analysis of the free amidase domain reflects its α/β fold (Zoll et al., 2010). Thus, in the absence of nanoparticles, both R2ab and amidase appear to be folded, with secondary structure content that agrees with their three-dimensional protein structures. This is also true for the BSA control. Upon interaction with the PSNPs, R2ab and amidase seem to lose their secondary structure, and adopt a different conformation on the PSNP surface. For R2ab, it is observed that the values for helix and turn are absent. Predictably, these values do not change due to the interaction with PSNPs, but the β-sheet content decreases. Amidase, on the other hand, consists of three well defined secondary structure components, namely, helix, sheet and turn – with helices making up for more than half of the total secondary structure of the protein. In the presence of PSNPs, all three secondary structure compositions decrease, indicating that the protein may lack regular secondary structure when bound to the nanoparticle surface. Observations in loss of secondary structure are very common and can occur due to variations in temperature (Lighezan et al., 2016) and due to interaction with surfaces (Ghosh et al., 2016). BSA, as expected, does not exhibit the same magnitude of changes observed for R2ab and amidase, and its structural decomposition is the same to within 10% for all secondary structure categories.

One must use care when performing structural analysis on proteins interacting with nanoparticle surfaces using CD. As stated above, the samples are likely a mixture of protein conformations, some of which are adsorbed and some of which are free in solution. However, SVD analysis methods were developed for pure, structurally homogeneous proteins with a well-known concentration (Johnson, 1990). Importantly, CD-based secondary structure assignment cannot be performed on mixtures of folded and unfolded proteins (Toumadje and Johnson, 1995). Therefore, these methods may not apply to rapidly interconverting mixtures of folded, unfolded, and adsorbed proteins, where the populations of each species are not known. While our analysis in **Table 1** provides evidence that the secondary structure is indeed changing for R2ab and amidase, the precise percentages are not likely to be accurate in this analysis, and therefore our values for the secondary structure in the presence of PSNPs should be interpreted as an *apparent* fractional secondary structure.

Together, the changes in the CD spectral signatures, along with the secondary structure analysis, support a model where the autolysin domains interact with PSNP surface and (at least partially) unfold upon interaction. BSA, our control protein, does not appear to behave in this way, and the structural factors that make R2ab and amidase such effective polystyrene binders remain unclear. Previous work using saturation-transfer difference NMR has shown that aromatic groups can interact strongly with PSNP surfaces (Zhang et al., 2017; Zhang and Casabianca, 2018), and these are abundant in the core of these globular domains. R2ab and amidase unfolding on the PSNP surface is therefore likely mediated by these aromatic-surface interactions, and these interactions could potentially mediate the initial attachment of *S. epidermidis* bacteria during biofilm formation on polystyrene.

TABLE 1 | Apparent secondary structure of R2ab, amidase, and BSA in the absence and presence of carboxylate PSNPs, averaged over four independent experiments.

Protein	Helix (%)	Sheet (%)	Turn (%)	Other (%)
R2ab domain				
0 nM PSNPs	0	84.6	0	15.4
20 nM PSNPs	0	67.2	0	32.7
Amidase domain				
0 nM PSNPs	53.2	14.8	23.7	8.3
20 nM PSNPs	44.6	11.4	19.2	24.8
BSA domain				
0 nM PSNPs	76.2	0	12.9	10.9
20 nM PSNPs	69.6	4.4	13.2	12.8

Limited Proteolysis Reactions

While the spectroscopic changes we observe reflect global perturbations to protein structure, it is not clear whether any favored conformations exist when R2ab or amidase interact with the PSNP surface. To investigate this question, we performed limited proteolysis of autolysin domains in the presence of PSNPs using chymotrypsin. Because of the solubility challenges faced above with neutral PSNPs, these experiments were performed only with carboxylate functionalized PSNPs. Limited proteolysis can be used to monitor changes in exposed sites in the presence and absence of nanoparticles (Iwamoto et al., 2013; Dal Cortivo et al., 2018; Duan et al., 2019; McClain et al., 2020). If a cleavage site is protected in the presence of PSNPs, the pattern of proteolytic fragments observed on an SDS-PAGE gel will change relative to the pattern observed with no nanoparticles. Limited proteolytic reactions were compared with the uncleaved domains and with chymotrypsin to verify the nature of any ghost bands, if present. Clear differences in the cleavage patterns of both proteins were observed with and without nanoparticles (**Figure 5**). Due to the high sensitivity of silver staining, even less abundant populations of cleaved products were visible indicating the interaction of both R2ab and amidase with polystyrene nanoparticles. Under identical conditions, more complete cleavage was observed in the presence of PSNPs, suggesting a destabilization of these proteins when interacting with polystyrene surfaces. In addition, several low-molecular weight bands in both R2ab and amidase were stabilized. These bands likely correspond to protein fragments that have adsorbed to the PSNP surface and are partially protected from proteolysis. Chymotrypsin cleaves primarily at aromatic amino acids, which are known to favorably interact

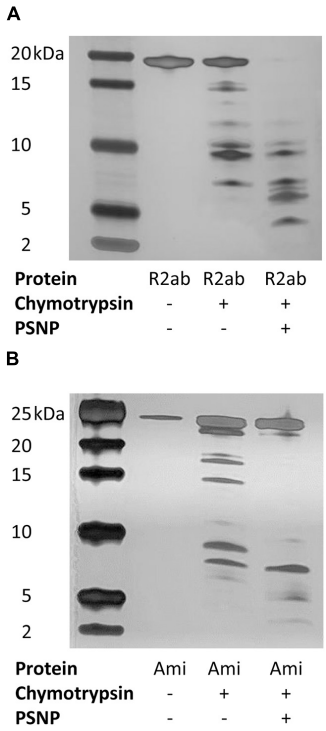

FIGURE 5 | Limited proteolysis of autolysin domains. Representative silver-stained products of chymotrypsin cleavage of R2ab **(A)** and amidase [Ami, **(B)**] domains in the presence and absence of carboxylate functionalized PSNPs. The leftmost lane contains markers, and molecular weights are labeled. Limited proteolysis is more complete in the presence of PSNPs for both proteins, suggesting partial unfolding in the presence of nanoparticles.

with PSNPs (Zhang and Casabianca, 2018). Therefore, significant alterations of chymotrypsin cleavage in the presence of PSNPs is anticipated and may reflect specific favorable conformations of R2ab and amidase on the nanoparticle surface.

DISCUSSION

When proteins encounter surfaces in solution of any type, there is a strong tendency for those proteins to adsorb to the surface. However, the similarities and differences between nanoparticle binding and macroscopic surface binding remain largely uninvestigated. Experiments have been performed to characterize binding to polystyrene nanoparticles (Kokkinopoulou et al., 2016; Contado et al., 2019), and several experiments have investigated protein adsorption to flat surfaces (Roach et al., 2006; Ngandu Mpoyi et al., 2016). In some cases, a significant influence from surface curvature is observed (Gagner et al., 2011), but in others, no effect seems to be observed. Nanoparticle surface functionalization also likely plays a significant role (Pelaz et al., 2015).

While studies of corona formation on nanoparticles abound, however, experiments comparing nanoparticle coronas with binding on macroscopic surfaces are far fewer. One reason for this is that surface functionalization on nanoparticles is often very different than what is found on macroscopic surfaces, hindering a direct comparison. Another reason is that rigorous, biophysical characterization of protein binding to flat surfaces is technically difficult: The surface to volume ratio for a flat surface is much smaller than it is for a nanoparticle, and flat surfaces are not amenable to many types of biophysical spectroscopies. For example, it would be impossible to perform the CD analysis used here on proteins adsorbed to a transparent flat surface; there is simply not enough detectable signal for such a measurement. Some methods, like attenuated total reflection Fourier transform infrared spectroscopy (Wang et al., 2006) and quartz crystal microbalance measurements (Reimhult et al., 2008) can be used to monitor proteins adsorbed to polystyrene, but these do not typically report on a protein's global structure. Direct comparisons between nanoparticle binding and macroscopic, flat surface binding are therefore challenging, even though the soluble nature of many nanoparticles make them an attractive target for protein-surface interaction studies.

In this work, we investigated two domains of staphylococcal AtlE, a protein known to bind to polystyrene surfaces (Houston et al., 2011). We sought to compare protein-surface binding using three scenarios: (1) the flat surface of polystyrene well plates, (2) the curved surface of neutral, non-functionalized PSNPs, and (3) the curved surface of carboxylate-functionalized anionic PSNPs. Although the PSNPs are curved, the radius of curvature is far larger than the characteristic radius of gyration for amidase and R2ab (16.3 and 17.7 Å, respectively) (Wang et al., 2014). This suggests that proteins encounter an effectively flat surface when adsorbing to these PSNPs. The major difference between the surfaces is the functionalization: With a zeta potential of −40 mV, the carboxylate functionalized PSNPs used here have a surface density of approximately 60 COOH groups per particle. This number is zero on the neutral, non-functionalized PSNPs and the polystyrene plates. The number of COOH groups is significant, and their presence makes carboxylate-PSNPs much more soluble than they would be otherwise; however, these groups could potentially interfere with protein adsorption. Our rationale for including carboxylate functionalized PSNPs was based on geometric considerations: Specifically, R2ab is expected to occlude approximately 980 $Å^2$ of surface based on its radius of gyration, and amidase is expected to occlude approximately 840 $Å^2$. For comparison, on average one carboxylic acid group is found for each 4,300 $Å^2$ on the carboxylate-PSNP surface (using the manufacturer's lot-specific certificate of analysis). Thus, there will be far fewer acidic groups on the surface than directly adsorbed proteins. Moreover, other ionic species in solution will also be drawn to the PSNP surface, and this will tend to screen electrostatic interactions through a Debye-Hückel effect, potentially making protein adsorption less dependent on the PSNP functionalization. Our goal in this work was to establish what similarities (if any) exist between AtlE's role in surface binding and biofilm formation and its ability to interact with PSNPs. Including both anionic, carboxylate functionalized PSNPs and neutral, non-functionalized PSNPs allowed us to control for the presence of COOH groups, even though the neutral nanoparticles suffered from significant problems with solubility at high protein concentrations.

While the importance of AtlE in polystyrene surface binding has been established (Heilmann et al., 1997; Houston et al., 2011), surprisingly, we find that both domains bind tightly to PSNPs as well. The R2ab and amidase domains, when adsorbed to a polystyrene surface, significantly hinder *S. epidermidis* biofilm formation in a way that other proteins, like serum albumin, cannot (**Figure 1**). This is likely because the R2ab and amidase domains, when present, occlude the polystyrene surface in the well plate, preventing the bacteria's own R2ab and amidase from binding. In other words, pre-coating the polystyrene with recombinant R2ab and amidase prevents the bacteria-attached AtlE and other components, such as polysaccharide intercellular adhesin (PIA) or extracellular DNA, from encountering any free polystyrene surface area. This demonstrates that these domains interact directly with the surface and out-compete R2ab and amidase from the bacteria, reducing the bacteria's ability to attach to surfaces. The interaction with the surface is sufficiently strong enough to withstand multiple washes and overnight incubation, and the bacterial growth experiments demonstrate that the effect is attributable to surface attachment alone as opposed to an antimicrobial effect. To our knowledge, this study is the first to show a direct, competitive effect between AtlE domains for surface binding; moreover, it demonstrates that both domains bind polystyrene surfaces strongly enough to hinder bacterial attachment. Thus, when a polystyrene surface is precoated with the autolysin domains, the surface is masked by the proteins, and the microbes cannot recognize the polystyrene well plate as a surface for colonization.

Interestingly, the R2ab and amidase domains also bind PSNPs very tightly. The average particle diameter for this lot of PSNPs is 28 $\pm$ 6 nm by TEM. Based on the size of the proteins and surface area of the nanoparticles, geometric considerations predict that a well-packed protein monolayer on a 28 nm PSNP contains approximately 250 R2ab molecules and 300 amidase molecules (Wang et al., 2014). The experiments performed in this work were done at conditions at or below this stoichiometry, and zeta potential measurements appeared to stabilize by this point, suggesting that the interaction is very strong. While zeta potential is less informative for neutral, non-functionalized PSNPs, both neutral and carboxylate PSNPs show a significant increase in hydrodynamic diameter by DLS, which also indicates a strong interaction. At this point, it remains unclear whether this interaction with PSNPs is mediated by similar molecular interactions as are seen in the flat polystyrene surfaces. Nevertheless, a strong interaction is observed between the AtlE domains and all three types of surfaces: carboxylate PSNPs, neutral PSNPs, and flat polystyrene. The common theme for all of these is polystyrene, and therefore the modes of interaction are likely to be similar.

Both R2ab and amidase are proteins with a highly ordered structure (Zoll et al., 2010, 2012). This is evident from the secondary structure, as monitored by CD, in the absence of PSNPs. In this study, we observed significant conformational changes of both R2ab and amidase upon interaction with PSNPs. Importantly, key secondary structure elements are lost when the proteins interact with nanoparticles, and an increase in coil is observed. Such measurements are difficult to interpret quantitatively, since the solution in the presence of PSNPs likely contains a mixture of free and bound states, where the nanoparticle-bound states are partially denatured. However, adsorption to a polystyrene surface appears to disrupt the structure of both proteins. Once again, a similar trend is seen regardless of the surface functionalization, as neutral PSNPs exhibit the same qualitative changes as observed for the more soluble carboxylate functionalized PSNPs. Quantifying the changes for the neutral PSNPs is difficult because of scattering and protein solubility of these nanoparticles, and slight differences in the CD spectra may reflect small changes in how R2ab and amidase bind to neutral polystyrene; nevertheless, the similarities between the CD spectra are striking (**Figure 4** vs. **Supplementary Figure 2**). Structural perturbations in PSNP-adsorbed proteins have been observed before: Engel et al. (2002) observed near-complete unfolding of α-lacalbumin when adsorbed to polystyrene spheres, and Salvati et al. (2013) observed less extensive structural changes in adsorbed transferrin. There appears to be a range of behaviors that are likely influenced not only by the PSNP surface itself, but also the protein structure and stability (Woods et al., 2016; Perera et al., 2019). The increased disorder observed for the AtlE domains likely exposes hydrophobic and aromatic groups, which can interact favorably with the PSNP surface (Zhang et al., 2017; Zhang and Casabianca, 2018).

The destabilization of the R2ab and amidase domains is further highlighted by enhanced limited proteolysis in the presence of carboxylate PSNPs. Limited proteolysis is an irreversible process which can be employed to obtain structural information on protein interactions, and it has been applied to study the interactions between folded proteins and nanoparticles (Iwamoto et al., 2013; Dal Cortivo et al., 2018; Duan et al., 2019). Limited proteolysis is a label-free method, employing a short digestion step where proteases cleave at specific accessible residues present in the folded protein (Brownridge and Beynon, 2011). If unfolding occurs in the presence of nanoparticles, the number of solvent accessible amino acids would change, potentially altering the number of proteolytic cleavage sites. Indeed, this is what is observed for R2ab and amidase: proteolysis is accelerated in the presence of PSNPs, and when nanoparticle fragments are present, fragments of smaller size are generated during a limited chymotrypsin digest (**Figure 5**). This result not only confirms the structural changes observed by CD, but the absence of any large fragments in PSNP digest suggests the protein is uniformly destabilized over the entire sequence. In other words, no stable subdomains appear to be protected from proteolysis when PSNPs are present.

CONCLUSION

In this study we present several approaches for examining the interaction between the domains of AtlE and polystyrene surfaces. While AtlE is known to be important in S. *epidermidis* attachment to biofilm surfaces, we have demonstrated that both the amidase and R2ab domains are capable of binding polystyrene tightly and can significantly reduce biofilm formation when

applied to a polystyrene surface. The mechanism appears to be that these domains pre-coat the surface, preventing binding from bacteria-associated AtlE. Importantly, this effect is much reduced for serum albumin, a negative control. To study the potential structural and biophysical consequences of protein adsorption, we employed anionic, carboxylate functionalized and neutral, non-functionalized PSNPs, which increase the surface-to-volume ratio and allow for spectroscopic and proteolytic characterization of the corona of adsorbed protein. Both AtlE domains also bind tightly to PSNPs, and structural changes are observed that suggest the proteins partially unfold upon binding to polystyrene surfaces. Importantly, the structural changes detected by CD are similar for both carboxylate and non-functionalized PSNPs, suggesting that the modes of binding for AtlE domains may also be similar for different surface types. AtlE provides a useful and biomedically relevant test case for studying surface binding because of its involvement in pathogenic biofilms and its strong interaction with polystyrene. However, additional work is needed to investigate other proteins, focusing on adsorption mechanisms to nanoparticle surfaces and to chemically related macroscopic surfaces. If general similarities are observed, then nanoparticles may prove to be a useful tool for studying how proteins interact with many different types of surfaces.

DATA AVAILABILITY STATEMENT

The original contributions presented in the study are included in the article/**Supplementary Material**, further inquiries can be directed to the corresponding author.

AUTHOR CONTRIBUTIONS

RS, YP, and NF conceived and designed the experiments. RS, EC, RY, JP, and NF performed the experiments. RS, EC, YP, and NF wrote and edited the manuscript. All authors contributed to the article and approved the submitted version.

FUNDING

This work was supported by the National Institute of Allergy and Infectious Diseases of the National Institutes of Health under grant number R01AI139479 and the National Science Foundation under grant number MCB 1818090. This work was also supported in part by grants from the Center for Biomedical Research Excellence in Pathogen-Host interactions and National Institute of General Medical Sciences, NIH (1P20GM103646-01A1). The content is solely the responsibility of the authors and does not necessarily represent the official views of the National Institutes of Health or National Science Foundation.

SUPPLEMENTARY MATERIAL

The Supplementary Material for this article can be found online at: https://www.frontiersin.org/articles/10.3389/fmicb.2021.658373/full#supplementary-material

REFERENCES

Andrade, J. D., and Hlady, V. (1986). "Protein adsorption and materials biocompatibility: a tutorial review and suggested hypotheses," in *Biopolymers/Non-Exclusion HPLC*, ed. K. Dusek (Berlin: Spinger-Verlag), doi: 10.1007/3-540-16422-7_6

Baier, G., Costa, C., Zeller, A., Baumann, D., Sayer, C., Araujo, P. H. H., et al. (2011). BSA adsorption on differently charged polystyrene nanoparticles using isothermal titration calorimetry and the influence on cellular uptake. *Macromol. Biosci.* 11, 628–638. doi: 10.1002/mabi.201000395

Billings, N., Millan, M. R., Caldara, M., Rusconi, R., Tarasova, Y., Stocker, R., et al. (2013). The extracellular matrix component Psl provides fast-acting antibiotic defense in *Pseudomonas aeruginosa* biofilms. *PLoS Pathogens* 9:e1003526. doi: 10.1371/journal.ppat.1003526

Brownridge, P., and Beynon, R. J. (2011). The importance of the digest: proteolysis and absolute quantification in proteomics. *Methods* 54, 351–360. doi: 10.1016/j.ymeth.2011.05.005

Büttner, F. M., Zoll, S., Nega, M., Götz, F., and Stehle, T. (2014). Structure-function analysis of *Staphylococcus aureus* amidase reveals the determinants of peptidoglycan recognition and cleavage. *J. Biol. Chem.* 289, 11083–11094. doi: 10.1074/jbc.M114.557306

Büttner, H., Mack, D., and Rohde, H. (2015). Structural basis of *Staphylococcus epidermidis* biofilm formation: mechanisms and molecular interactions. *Front. Cell. Infect. Microbiol.* 5:14. doi: 10.3389/fcimb.2015.00014

Contado, C., Mehn, D., Gilliland, D., and Calzolai, L. (2019). Characterization methods for studying protein adsorption on nano-polystyrene beads. *J. Chromatogr. A* 1606:460383. doi: 10.1016/j.chroma.2019.460383

Crouzet, M., Le Senechal, C., Brözel, V. S., Costaglioli, P., Barthe, C., Bonneu, M., et al. (2014). Exploring early steps in biofilm formation: set-up of an experimental system for molecular studies. *BMC Microbiol.* 14:253. doi: 10.1186/s12866-014-0253-z

Dal Cortivo, G., Wagner, G. E., Cortelletti, P., Padmanabha Das, K. M., Zangger, K., Speghini, A., et al. (2018). Luminescent and paramagnetic properties of nanoparticles shed light on their interactions with proteins. *Sci. Rep.* 8:3420. doi: 10.1038/s41598-018-21571-y

Dominguez-Medina, S., Kisley, L., Tauzin, L. J., Hoggard, A., Shuang, B., Indrasekara, A. S. D. S., et al. (2016). Adsorption and unfolding of a single protein triggers nanoparticle aggregation. *ACS Nano* 10, 2103–2112. doi: 10.1021/acsnano.5b06439

Donlan, R. M. (2002). Biofilms: microbial life on surfaces. *Emerg. Infect. Dis* 8, 881–890. doi: 10.3201/eid0809.020063

Duan, Y., Liu, Y., Coreas, R., and Zhong, W. (2019). Mapping molecular structure of protein locating on nanoparticles with limited proteolysis. *Anal. Chem.* 91, 4204–4212. doi: 10.1021/acs.analchem.9b00482

Dunne, W. M. (2002). Bacterial adhesion: seen any good biofilms lately? *Clin. Microbiol. Rev.* 15, 155–166. doi: 10.1128/CMR.15.2.155-166.2002

Engel, M. F. M., van Mierlo, C. P. M., and Visser, A. J. W. G. (2002). Kinetic and structural characterization of adsorption-induced unfolding of bovine alpha -lactalbumin. *J. Biol. Chem.* 277, 10922–10930. doi: 10.1074/jbc.M106005200

Engel, M. F. M., Visser, A. J. W. G., Mierlo, C. P. M., and van. (2004). Conformation and orientation of a protein folding intermediate trapped by adsorption. *Proc. Natl. Acad. Sci. U S A.* 101, 11316–11321. doi: 10.1073/pnas.0401603101

Fang, C., Bhattarai, N., Sun, C., and Zhang, M. (2009). Functionalized nanoparticles with long-term stability in biological media. *Small (Weinheim an Der Bergstrasse, Germany)* 5, 1637–1641. doi: 10.1002/smll.200801647

Fleischer, C. C., and Payne, C. K. (2014). Secondary structure of corona proteins determines the cell surface receptors used by nanoparticles. *J. Phys. Chem. B* 118, 14017–14026. doi: 10.1021/jp502624n

Gagner, J. E., Lopez, M. D., Dordick, J. S., and Siegel, R. W. (2011). Effect of gold nanoparticle morphology on adsorbed protein structure and function. *Biomaterials* 32, 7241–7252. doi: 10.1016/j.biomaterials.2011.05.091

Ghosh, G., Gaikwad, P. S., Panicker, L., Nath, B. B., and Mukhopadhyaya, R. (2016). Unfolding and inactivation of proteins by counterions in protein-nanoparticles interaction. *Colloids Surfaces. B, Biointerfaces* 145, 194–200. doi: 10.1016/j.colsurfb.2016.04.053

Gominet, M., Compain, F., Beloin, C., and Lebeaux, D. (2017). Central venous catheters and biofilms: where do we stand in 2017? *APMIS: Acta Pathologica, Microbiologica, et Immunologica Scandinavica* 125, 365–375. doi: 10.1111/apm.12665

Greenfield, N. J., and Fasman, G. D. (1969). Computed circular dichroism spectra for the evaluation of protein conformation. *Biochemistry* 8, 4108–4116. doi: 10.1021/bi00838a031

Gunawan, C., Lim, M., Marquis, C. P., and Amal, R. (2014). Nanoparticle–protein corona complexes govern the biological fates and functions of nanoparticles. *J. Mater. Chem. B* 2, 2060–2083. doi: 10.1039/C3TB21526A

Harris, L. G., Murray, S., Pascoe, B., Bray, J., Meric, G., Magerios, L., et al. (2016). Biofilm morphotypes and population structure among *Staphylococcus epidermidis* from commensal and clinical samples. *PLoS One* 11:e0151240. doi: 10.1371/journal.pone.0151240

Heilmann, C., Hussain, M., Peters, G., and Götz, F. (1997). Evidence for autolysin-mediated primary attachment of *Staphylococcus epidermidis* to a polystyrene surface. *Mol. Microbiol.* 24, 1013–1024. doi: 10.1046/j.1365-2958.1997.4101774.x

Houston, P., Rowe, S. E., Pozzi, C., Waters, E. M., and O'Gara, J. P. (2011). Essential role for the major autolysin in the fibronectin-binding protein-mediated *Staphylococcus aureus* biofilm phenotype. *Infect. Immun.* 79, 1153–1165. doi: 10.1128/IAI.00364-10

Iwamoto, N., Shimada, T., Umino, Y., Aoki, C., Aoki, Y., Sato, T.-A., et al. (2013). Selective detection of complementarity-determining regions of monoclonal antibody by limiting protease access to the substrate: nano-surface and molecular-orientation limited proteolysis. *Analyst* 139, 576–580. doi: 10.1039/C3AN02104A

Jamal, M., Ahmad, W., Andleeb, S., Jalil, F., Imran, M., Nawaz, M. A., et al. (2018). Bacterial biofilm and associated infections. *J. Chin. Med. Assoc.* 81, 7–11. doi: 10.1016/j.jcma.2017.07.012

Jiang, J., Oberdörster, G., and Biswas, P. (2009). Characterization of size, surface charge, and agglomeration state of nanoparticle dispersions for toxicological studies. *J. Nanoparticle Res.* 11, 77–89. doi: 10.1007/s11051-008-9446-4

Johnson, W. C. (1990). Protein secondary structure and circular dichroism: a practical guide. *Proteins: Struct. Funct. Bioinform.* 7, 205–214. doi: 10.1002/prot.340070302

Kaplan, J. B., Ragunath, C., Velliyagounder, K., Fine, D. H., and Ramasubbu, N. (2004). Enzymatic detachment of *Staphylococcus epidermidis* biofilms. *Antimicrob. Agents Chemother.* 48, 2633–2636. doi: 10.1128/AAC.48.7.2633-2636.2004

Kihara, S., van der Heijden, N. J., Seal, C. K., Mata, J. P., Whitten, A. E., Köper, I., et al. (2019). Soft and hard interactions between polystyrene nanoplastics and human serum albumin protein corona. *Bioconjug. Chem.* 30, 1067–1076. doi: 10.1021/acs.bioconjchem.9b00015

Kokkinopoulou, M., Simon, J., Mailaender, V., Lieberwirth, I., and Landfester, K. (2016). "Characterizing the protein corona of polystyrene nanoparticles," in *Proceedings of the European Microscopy Congress 2016: Proceedings*, (Atlanta, GA: American Cancer Society), 71–72.

Lacerda, S. H. D. P., Park, J. J., Meuse, C., Pristinski, D., Becker, M. L., Karim, A., et al. (2010). Interaction of gold nanoparticles with common human blood proteins. *ACS Nano* 4, 365–379. doi: 10.1021/nn9011187

Lighezan, L., Georgieva, R., and Neagu, A. (2016). The secondary structure and the thermal unfolding parameters of the S-layer protein from *Lactobacillus salivarius*. *Eur. Biophys. J.: EBJ* 45, 491–509. doi: 10.1007/s00249-016-1117-2

Loos, C., Syrovets, T., Musyanovych, A., Mailänder, V., Landfester, K., Nienhaus, G. U., et al. (2014). Functionalized polystyrene nanoparticles as a platform for studying bio–nano interactions. *Beilstein J. Nanotechnol.* 5, 2403–2412. doi: 10.3762/bjnano.5.250

Lorite, G. S., Rodrigues, C. M., de Souza, A. A., Kranz, C., Mizaikoff, B., and Cotta, M. A. (2011). The role of conditioning film formation and surface chemical changes on *Xylella fastidiosa* adhesion and biofilm evolution. *J. Colloid Interface Sci.* 359, 289–295. doi: 10.1016/j.jcis.2011.03.066

McCann, M. T., Gilmore, B. F., and Gorman, S. P. (2008). Staphylococcus epidermidis device-related infections: pathogenesis and clinical management. *J. Pharm. Pharmacol.* 60, 1551–1571. doi: 10.1211/jpp/60.12.0001

McClain, S. M., Ojoawo, A. M., Lin, W., Rienstra, C. M., and Murphy, C. J. (2020). Interaction of alpha-synuclein and its mutants with rigid lipid vesicle mimics of varying surface curvature. *ACS Nano* 14, 10153–10167. doi: 10.1021/acsnano.0c03420

Merritt, J. H., Kadouri, D. E., and O'Toole, G. A. (2005). Growing and analyzing static biofilms. *Curr. Protocols Microbiol.* Chapter 1:Unit–1B.1. doi: 10.1002/9780471729259.mc01b01s00

Nega, M., Tribelli, P. M., Hipp, K., Stahl, M., and Götz, F. (2020). New insights in the coordinated amidase and glucosaminidase activity of the major autolysin (Atl) in *Staphylococcus aureus*. *Commun. Biol.* 3:695. doi: 10.1038/s42003-020-01405-2

Ngandu Mpoyi, E., Cantini, M., Reynolds, P. M., Gadegaard, N., Dalby, M. J., and Salmerón-Sánchez, M. (2016). Protein adsorption as a key mediator in the nanotopographical control of cell behavior. *ACS Nano* 10, 6638–6647. doi: 10.1021/acsnano.6b01649

O'Toole, G. A. (2011). Microtiter dish biofilm formation assay. *J. Visual. Exp. JVE* 47:2437. doi: 10.3791/2437

Pelaz, B., del Pino, P., Maffre, P., Hartmann, R., Gallego, M., Rivera-Fernández, S., et al. (2015). Surface functionalization of nanoparticles with polyethylene glycol: effects on protein adsorption and cellular uptake. *ACS Nano* 9, 6996–7008. doi: 10.1021/acsnano.5b01326

Percival, S. L., Suleman, L., Francolini, I., and Donelli, G. (2014). The effectiveness of photodynamic therapy on planktonic cells and biofilms and its role in wound healing. *Future Microbiol.* 9, 1083–1094. doi: 10.2217/fmb.14.59

Perera, Y. R., Hill, R. A., and Fitzkee, N. C. (2019). Protein interactions with nanoparticle surfaces: highlighting solution NMR techniques. *Israel J. Chem.* 59, 962–979. doi: 10.1002/ijch.201900080

Ponomareva, A. L., Buzoleva, L. S., and Bogatyrenko, E. A. (2018). Abiotic environmental factors affecting the formation of microbial biofilms. *Biol. Bull.* 45, 490–496. doi: 10.1134/S106235901805014X

Reimhult, K., Petersson, K., and Krozer, A. (2008). QCM-D analysis of the performance of blocking agents on gold and polystyrene surfaces. *Langmuir: ACS J. Surfaces Colloids* 24, 8695–8700. doi: 10.1021/la800224s

Roach, P., Farrar, D., and Perry, C. C. (2006). Surface tailoring for controlled protein adsorption: effect of topography at the nanometer scale and chemistry. *J. Am. Chem. Soc.* 128, 3939–3945. doi: 10.1021/ja056278e

Saini, R., Saini, S., and Sharma, S. (2011). Biofilm: a dental microbial infection. *J. Nat. Sci. Biol. Med.* 2, 71–75. doi: 10.4103/0976-9668.82317

Salvati, A., Pitek, A. S., Monopoli, M. P., Prapainop, K., Bombelli, F. B., Hristov, D. R., et al. (2013). Transferrin-functionalized nanoparticles lose their targeting capabilities when a biomolecule corona adsorbs on the surface. *Nat. Nanotechnol.* 8, 137–143. doi: 10.1038/nnano.2012.237

Sandal, I., Hong, W., Swords, W. E., and Inzana, T. J. (2007). Characterization and comparison of biofilm development by pathogenic and commensal isolates of *Histophilus somni*. *J. Bacteriol.* 189, 8179–8185. doi: 10.1128/JB.00479-07

Sastri, V. R. (2010). "Chapter 6 - commodity thermoplastics: polyvinyl chloride, polyolefins, and polystyrene," in *Plastics in Medical Devices*, ed. V. R. Sastri (Norwich: William Andrew Publishing), 73–119. doi: 10.1016/B978-0-8155-2027-6.10006-6

Satzer, P., Svec, F., Sekot, G., and Jungbauer, A. (2016). Protein adsorption onto nanoparticles induces conformational changes: particle size dependency, kinetics, and mechanisms. *Eng. Life Sci.* 16, 238–246. doi: 10.1002/elsc.201500059

Steenackers, H. P., Parijs, I., Foster, K. R., and Vanderleyden, J. (2016). Experimental evolution in biofilm populations. *FEMS Microbiol. Rev.* 40, 373–397. doi: 10.1093/femsre/fuw002

Toumadje, A., and Johnson, W. C. (1995). Systemin has the characteristics of a poly(L-proline) II type helix. *J. Am. Chem. Soc.* 117, 7023–7024. doi: 10.1021/ja00131a034

Trautner, B. W., and Darouiche, R. O. (2004). Role of biofilm in catheter-associated urinary tract infection. *Am. J. Infect. Control* 32, 177–183. doi: 10.1016/j.ajic.2003.08.005

Visalakshan, R. M., García, L. E. G., Benzigar, M. R., Ghazaryan, A., Simon, J., Mierczynska-Vasilev, A., et al. (2020). The influence of nanoparticle shape on protein corona formation. *Small* 16:2000285. doi: 10.1002/smll.202000285

Wang, A., Vangala, K., Vo, T., Zhang, D., and Fitzkee, N. C. (2014). A three-step model for protein–gold nanoparticle adsorption. *J. Phys. Chem. C* 118, 8134–8142. doi: 10.1021/jp411543y

Wang, J., Chen, X., Clarke, M. L., and Chen, Z. (2006). Vibrational spectroscopic studies on fibrinogen adsorption at polystyrene/protein solution interfaces: hydrophobic side chain and secondary structure changes. *J. Phys. Chem. B* 110, 5017–5024. doi: 10.1021/jp0534683

Woods, K. E., Perera, Y. R., Davidson, M. B., Wilks, C. A., Yadav, D. K., and Fitzkee, N. C. (2016). Understanding protein structure deformation on the surface of gold nanoparticles of varying size. *J. Phys. Chem. C* 120, 27944–27953. doi: 10.1021/acs.jpcc.6b08089

Yamada, S., Sugai, M., Komatsuzawa, H., Nakashima, S., Oshida, T., Matsumoto, A., et al. (1996). An autolysin ring associated with cell separation of *Staphylococcus aureus*. *J. Bacteriol.* 178, 1565–1571. doi: 10.1128/jb.178.6.1565-1571.1996

Zhang, A., Mu, H., Zhang, W., Cui, G., Zhu, J., and Duan, J. (2013). Chitosan coupling makes microbial biofilms susceptible to antibiotics. *Sci. Rep.* 3:3364. doi: 10.1038/srep03364

Zhang, Y., and Casabianca, L. B. (2018). Probing amino acid interaction with a polystyrene nanoparticle surface using Saturation-Transfer Difference (STD)-NMR. *J. Phys. Chem. Lett.* 9, 6921–6925. doi: 10.1021/acs.jpclett.8b02785

Zhang, Y., Xu, H., Parsons, A. M., and Casabianca, L. B. (2017). Examining binding to nanoparticle surfaces using Saturation Transfer Difference (STD)-nmr spectroscopy. *J. Phys. Chem. C* 121, 24678–24686. doi: 10.1021/acs.jpcc.7b08828

Zheng, Y., He, L., Asiamah, T. K., and Otto, M. (2018). Colonization of medical devices by *Staphylococci*. *Environ. Microbiol.* 20, 3141–3153. doi: 10.1111/1462-2920.14129

Zoll, S., Pätzold, B., Schlag, M., Götz, F., Kalbacher, H., and Stehle, T. (2010). Structural basis of cell wall cleavage by a staphylococcal autolysin. *PLoS Pathogens* 6:e1000807. doi: 10.1371/journal.ppat.1000807

Zoll, S., Schlag, M., Shkumatov, A. V., Rautenberg, M., Svergun, D. I., Götz, F., et al. (2012). Ligand-Binding properties and conformational dynamics of autolysin repeat domains in staphylococcal cell wall recognition. *J. Bacteriol.* 194, 3789–3802. doi: 10.1128/JB.00331-12

Conflict of Interest: The authors declare that the research was conducted in the absence of any commercial or financial relationships that could be construed as a potential conflict of interest.

frontiers in Microbiology

ORIGINAL RESEARCH
published: 28 May 2021
doi: 10.3389/fmicb.2021.646303

Bacterial Biofilm Growth on 3D-Printed Materials

Donald C. Hall Jr.[1,2†], *Phillip Palmer*[2], *Hai-Feng Ji*[1], *Garth D. Ehrlich*[2,3] *and Jarosław E. Król*[2*†]

[1] Department of Chemistry, Drexel University, Philadelphia, PA, United States, [2] Center for Advanced Microbial Processing and Center for Surgical Infections and Biofilms, Institute for Molecular Medicine and Infectious Disease, Department of Microbiology and Immunology, Philadelphia, PA, United States, [3] Department of Otolaryngology-Head and Neck Surgery, Drexel University College of Medicine, Philadelphia, PA, United States

Recent advances in 3D printing have led to a rise in the use of 3D printed materials in prosthetics and external medical devices. These devices, while inexpensive, have not been adequately studied for their ability to resist biofouling and biofilm buildup. Bacterial biofilms are a major cause of biofouling in the medical field and, therefore, hospital-acquired, and medical device infections. These surface-attached bacteria are highly recalcitrant to conventional antimicrobial agents and result in chronic infections. During the COVID-19 pandemic, the U.S. Food and Drug Administration and medical officials have considered 3D printed medical devices as alternatives to conventional devices, due to manufacturing shortages. This abundant use of 3D printed devices in the medical fields warrants studies to assess the ability of different microorganisms to attach and colonize to such surfaces. In this study, we describe methods to determine bacterial biofouling and biofilm formation on 3D printed materials. We explored the biofilm-forming ability of multiple opportunistic pathogens commonly found on the human body including *Escherichia coli*, *Pseudomonas aeruginosa*, and *Staphylococcus aureus* to colonize eight commonly used polylactic acid (PLA) polymers. Biofilm quantification, surface topography, digital optical microscopy, and 3D projections were employed to better understand the bacterial attachment to 3D printed surfaces. We found that biofilm formation depends on surface structure, hydrophobicity, and that there was a wide range of antimicrobial properties among the tested polymers. We compared our tested materials with commercially available antimicrobial PLA polymers.

Keywords: biofilm, antimicrobial properties, 3D printing, bacterial infections, 3D structures, surface topology, PLA polymer

OPEN ACCESS

Edited by:
Mark Smeltzer, University of Arkansas for Medical Sciences, United States

Reviewed by:
Devendra Dusane, Nationwide Children's Hospital, United States
Lichong Xu, Pennsylvania State University, United States

***Correspondence:**
Jarosław E. Król
jek322@drexel.edu

† These authors have contributed equally to this work

Specialty section:
This article was submitted to Antimicrobials, Resistance and Chemotherapy, a section of the journal Frontiers in Microbiology

Received: *26 December 2020*
Accepted: *04 May 2021*
Published: *28 May 2021*

Citation:
Hall DC Jr, Palmer P, Ji H-F, Ehrlich GD and Król JE (2021) Bacterial Biofilm Growth on 3D-Printed Materials. Front. Microbiol. 12:646303. doi: 10.3389/fmicb.2021.646303

INTRODUCTION

Biofouling is the process of microorganisms attaching to solid inanimate surfaces as biofilms. It is estimated that biofouling costs billions of dollars per year and is a problem within many fields of science and industry, including the medical fields (Vladkova, 2009; Gule et al., 2016). One of the most recent areas impacted by biofouling is 3D-printed materials. 3D printed materials have become common in medical settings, especially in the area of prosthetic limbs (Poologasundarampillai and Nommeots-Nomm, 2017; Paul et al., 2018; Sun, 2018). Such 3D-printed prosthetics have not yet been studied for their ability to reduce biofilm attachments

nor their overall antimicrobial properties. This contrasts with conventional prosthetic limbs, which have been studied and developed to have antibiofilm and antimicrobial properties (Nablo et al., 2001).

The major cause of biofouling in the medical setting is bacterial cell attachment (Bixler Gregory and Bhushan, 2012; Harding and Reynolds, 2014; Damodaran and Murthy, 2016; Zander and Becker, 2018). Biofilms can be considered as a multicellular phase of growth in the life cycle of bacteria (Donlan, 2002; Sauer et al., 2002; Kostakioti et al., 2013). Once cells first attach to a surface, they extrude a matrix and develop cooperative behaviors resulting in the development of multicellular biofilm form. Often biofilms are metabolically resistant to antibiotics and antimicrobials, sometimes up to 1,000 × their planktonic counterparts (Hall-Stoodley et al., 2008; Wolcott and Ehrlich, 2008; Ito et al., 2009) due to triggering of the stringent response (Hall et al., 2020) and other gene expression changes (Costerton et al., 2007; Lewis, 2008; Wood et al., 2013). Bacterial biofilms are also the hot spots for horizontal gene transfer events, especially multidrug resistance plasmid conjugation (Król et al., 2011; Król et al., 2013). This makes the eradication of biofilms difficult in a medical setting as they can only be removed by physical means. These facts make it necessary to understand all aspects of medical devices being used in these medical settings. 3D printing has been utilized in casts, prosthetics, food products, and containers. All these applications have the potential for allowing biofilm development due to their proximity to bacteria and food sources.

Use of 3D-printed prosthetics is increasing because of their relative cost-effectiveness compared to that of conventional prosthetic devices (Zuniga et al., 2015; Choonara et al., 2016). While the average conventional prostatic can cost upwards of U.S. $50,000, a 3D-printed prosthetic can be made for less than U.S. $1000 (TASOM Engineers, 2018). This significant reduction in cost is due to the ability to quickly adapt models for the user's needs (Manero et al., 2019). 3D-printed models can be easily switched out when parts are damaged and as children grow.

Because 3D-printed materials are being used more frequently as medical materials, there is an overwhelming need to develop antifouling 3D-printing materials. There are many materials already on the market that utilize the simple method of impregnating the polymer filament with nanoparticles, fibers, or metal flakes (Zuniga, 2018). However, methods of studying and understanding biofilm formation and antimicrobial properties of 3D-printed materials are lacking.

The resolution on 3D printers is improving rapidly and high-resolution printers are affordable even as desktop devices. The resolution at which a typical extruder printer operates is 200 μm between layers and all polymers lead to an inherent surface roughness upon printing. These rough surfaces can provide an ideal environment for the initial attachment of bacteria and subsequent formation of biofilms (Mitik-Dineva et al., 2009).

In this study, we worked with several common polylactic acid (PLA) polymers doped with various materials and printed using a common extruder 3D printer. We report several polymers that have antifouling properties and develop a model for studying biofilm formation on these materials. We compare surface properties, roughness, and hydrophobicity in regard to the attachment and amount of biofilms. We also report several novel techniques to map and understand how biofilms attach to 3D printed materials. Notably, we developed surface analysis of biofilms using 3D optical profilometry to study the biofilm points of attachment and to gain understanding of how the surface roughness of 3D-printed materials contributes to biofilm attachment.

MATERIALS AND METHODS

PLA polymers (**Table 1**) were used with a MakerBot Replicator2 3D printer (MarkerBot, New York, NY, United States) (standard settings: 0.2 mm, 15% infill) to print standard (3 × 1 inch) slides, rings (outer diameter, 15 mm; inner diameter, 10 mm; height, 15.25 mm), and pins (head diameter, 10 mm; pin diameter, 5.5 mm; height, 15-17 mm) designed by a SketchUP Pro2018 (**Supplementary Figure 1**). Plastic (Rinzl) and glass microscope slides (Fisherbrand) were purchased from Amazon and Fisher Scientific, respectively. All STL files are available upon request.

Surface Characterization

Surface Free Energy – Hydrophobicity

The Dataphysics (Charlotte, NC, United States) Optical Contact Angle OCA 15EC measuring system was used with MilliQ® water to measure surface wettability. The surface angle of 1 μL drop was recorded in 4 different locations along the 3D printed slides and controls.

TABLE 1 | 3D polymers used in this study.

Material	Manufacturer	Composition	Abbreviation
Brass 3D Printer Filament	Yoyi 3D	33- 40% metal powder and 67-60% PLA	BRS
Copper 3D Printer Filament	Yoyi 3D	33% metal powder and 67% PLA	CU
Aluminum 3D Printer Filament	Yoyi 3D	33% metal powder and 67% PLA	AL
3D Printer Filament Frosted Bronze	AMOLEN	20% metal powder and 80% PLA	BRZ
Carbon Fiber Black	3D Solutech	70% PLA and 30% carbon fiber.	CF
3D PLA Wood color	AmazonBasic	70% polymer and 30% wood.	WD
Black Soft PLA	MatterHackers		SoftPLA
Silver Metal 3D Printer PLA Filament	3D Solutech	Silver Dye (no metal infill)	PLAS
Antimicrobial polymers			
Purement	Purement BnK Chemical Company	Copper	Pur
PLActive	Copper3D	Copper	PLAc
Antibacterial PLA	XYZ Printing	Silver ions	XYZ

Surface Topography – Contact and Optical Profilometers

A Mitutoyo (Kanagawa, Japan) JS210 contact profilometer was used to analyze surface properties of the materials using standard parameters like JIS, VDA, ISO-1997 and ANSI. Standard linear (2D) parameters (Ra, Rq, Rz, Rp, Rv, Rsk, Rku, Rc, RSm, RDq, Rmr, Rdc, Rt, Rk, Rpk, Rvk) (**Supplementary Table 1**) were examined and the averages from 4 horizontal and vertical reads were calculated.

A Leica (Leica United States) DVM6 digital microscope and MountainsMap® ver.7.4 (Digital Surf SARL, France) were used to collect and analyze 3D images. Standard surface 3D parameters S (Sq, Ssk, Sku, Sp, Sv, Sz, Sa, Sz, Smr, Smc, Sxp, Sdc) (**Supplementary Table 2**) and 2D parameters R (Rp, Rv, Rz, Rc, Rt, Ra, Rq, Rdc, Rsk, Rku, Rmr) were measured and averages were calculated based on at least 3 pictures and 3 profiles.

Bacterial Growth - Viability Assay

Printed out 3D rings were sterilized for 30 min in 70% ethanol followed by washing twice in sterile water or autoclaving in MilliQ® water (15 min) or just a dry cycle (15 min-sterilization/10min-drying). Rings were placed in 24-well plates (**Supplementary Figure 1B**). Eight hundred microliters of 100-fold diluted overnight (18 h) cultures of *Escherichia coli C, Pseudomonas aeruginosa* PA01*, and Staphylococcus aureus* ATCC 25923 in LB Miller medium were aliquoted into the wells. Plates were placed in Tecan (Tecan Inc., United States) Infinite 200Pro plate reader executing 15 min shaking and OD_{600} read cycles at 37°C for 18 h.

Bacterial Adhesion

Overnight cultures (25 mL) of bacterial strains in LB Miller medium were transferred into 50-mL conical Falcon tubes (**Supplementary Figure 2**). Slides were sterilized with 75% ethanol for 30 min following by washing twice in sterile water. Slides were incubated with bacterial cultures for 2 h at 37°C and shaken at 50 rpm. Planktonic cells were washed out by submerging the slides 4 times in 50 mL phosphate-buffered saline (PBS). Biofilm bacteria were detached from the surface by vortexing 3 min at 1,000 rpm (Mini-G, SPEX-Sample-Prep) in 25 mL PBS. Serial dilutions were plated by a drop-titer method on LB agar plates. Colonies (CFU) were counted after overnight incubation at 37°C.

Biofilm Assay

Printed pins were sterilized (autoclaved 15 min/10 min) and placed into 500 μL of 100x dilutions of bacterial overnight cultures in 48-well plates (Corning United States). Biofilms were grown for 3 days at 37°C (50 rpm) in Forma Model 3,950 incubator (> 90% humidity). Pins were submerged in the culture entire time and no change in liquid level was observed. After 3 days pins were removed and bacterial cell densities (OD_{600}) were measured in the medium. Pins were washed twice in PBS and placed into 700 μL BacTiter-Glo™ Reagent (Promega) (Herten et al., 2017) for 15 min. Two hundred microliters were transferred into 96-well white plates and the luminescence was measured using a Tecan Infinite 200Pro plate reader (integration time 1,000 s). Pins submerged in the sterile media were used as a control and these values were subtracted from the biofilm luminescence. Luminescence of the reagent was used as the control. Experiments were run in triplicate.

Biofilm Microscopic Analyses

A Leica DVM6 Digital Microscope was used to collect pictures of 3D-printed slides with and without bacterial biofilms. Biofilms were grown on 3D printed slides in 50 mL Falcon tubes as described in the Bacterial Adhesion section. After 3-day incubation at 37°C (50 rpm) biofilm-containing slides were washed two times with 1 × PBS solution. The entire slide was then fixed in 3% glutaraldehyde solution overnight at 4°C. After the fixation step, the slide was washed two times with distilled water and dried in a laminar flow hood for a period of 24 h. 3D projections were made using the MountainsMap® ver.7.4.

Statistical Analyses

All experiments were conducted at least in triplicates. A standard unpaired t-test was used in the case of simple two-group comparisons. Two-way analysis of variance (ANOVA) was performed on the biofilm data. MountainsMap® ver.7.4. statistics module was used to analyze pictures.

RESULTS

Material Characterization

Hydrophobicity

Eight different PLA 3D materials (**Table 1**) were used for analyzing their bacterial biofouling properties. Some of them were supplemented with metals such as copper (CU), brass (BRS), bronze (BRZ), and aluminum (AL). These polymers were chosen as some of these metals (CU, BRS, and BRZ) have a long history of reported antimicrobial properties (Dollwet, 1985; Grass et al., 2011). The SketchUP Pro 2018 designed slides stereolithography files (STL) were printed using a MakerBot Replicator2 3D printer. To characterize the material hydrophobicity, we measured surface free energy using the OCA-15EC optical contact angle measurement system (Dataphysics). The contact angles of water droplets were measured and compared among all polymers (**Figure 1**). All printed materials showed higher contact angles than the glass slide control (**Figure 1**). Most of the polymers except SoftPLA (112.9° ± 1.34°) showed similar contact angles (74.07° ± 2.7°). SoftPLA also showed higher hydrophobicity than plastic (**Figure 1**).

Surface Analyses

Contact Profilometry

To characterize the surfaces of the printed slides, we first used a Mitutoyo JS210 contact profilometer. The standard unit is equipped with a 5-μm radius stylus tip, which contacts the surface with 4-mN measuring force and measures 39 different parameters. For each printout, we conducted two kinds of measurements: perpendicular (**Figure 2**, black) and

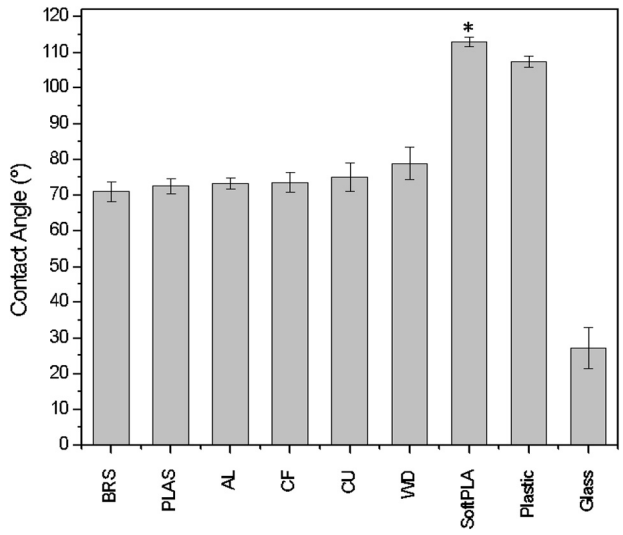

FIGURE 1 | Contact angle/wettability of water droplets on 3D printouts. AL, BRS, BRZ, CF, CU, PLAS, SoftPLA, WD (**Table 1**). Controls are glass and plastic microscope slides. Statistical difference with other PLA polymers (*).

parallel (**Figure 2**, red) with the extruded layers. The graphical representation clearly showed differences in both profiles. In the cross-section, each polymer showed a clear and defined profile (**Figure 2**, black).

Analyzing the cross-section profiles (**Figure 2**, black), we concluded that brass (BRS) (B) and SoftPLA (G) showed a high degree of similarity. A second pair was formed by aluminum (AL) (A) and bronze (BRZ) (C). Copper (CU) (E) was similar to PLA (PLAS) (F), while wood PLA (WD) (H) and carbon fiber PLA (CF) (D) polymers showed similarity to each other. However, analysis of the selected standard R parameters did not confirm these observations (**Supplementary Figure 3**). Although cross-section profiles showed interesting patterns, they represent macro-structures with R parameters ranging from several to more than a hundred micrometers (**Figure 2**, black and **Supplementary Figure 4**). These profiles did not show the real microstructure of the materials, which we thought might be more important for bacterial attachment and biofilm formation. Better, more relevant micro-profiles were obtained analyzing patterns parallel with the printing (**Figure 2**, red). Using R parameters of the profiles, we ranked polymers and found that the four metal-filled polymers were grouped in the middle, while "pure" PLA polymers showed lower R values. On the other hand, both WD and CF polymers showed much higher, statistically significant R values, indicating their much more complex surface structures (**Figures 2I,J**).

Non-contact Profilometry

A Leica DVM6 3D digital microscope was utilized for surface profiling of 3D printed slides. Original pictures (**Figure 3A**) were taken, and 3D projections were modeled and analyzed using Mountains Map software (**Figure 3B**). Optical profilometry revealed the true picture of the printouts. We noticed distinct structures on the surface such as knots on the WD polymer, and fibers on the CF polymer, flakes of metal on CU, BRS, BRZ, and AL, and dye in the PLAS polymer (**Figures 3A,B**). There were slight difficulties in imaging and 3D projecting materials that are translucent or reflect light such as wood, carbon fiber, and bronze.

Analyzing parameters calculated by the MountainsMap® software, we noticed that all R parameters showed lower values compared with those obtained with the contact profilometer (**Supplementary Figure 5**). Also, the standard deviation values were higher in the case of the optical profilometer.

In addition to linear (2D) R parameters, optical profilometry allows for calculation of areal (3D) parameters (Gadelmawla et al., 2002; Blateyron, 2006). Surface texture parameters have a prefix that is the capital letter S (Blateyron, 2013; Pagani et al., 2017). There are many S parameters which can be divided into height parameters (Sq, Ssk, Sku, Sp, Sv, Sz, Sa), functional parameters (Smr, Smc, Sxp), amplitude parameters (Sa, Sq, Sz, Ssk, Sku, Sp, Sv, St), area and volume parameters (Smr, Sdc), 3D parameters (St, Sp, Sv, Sq, Sa, Ssk, Sku, SWt) are precisely defined by ISO, EUR, and ASME (International, European and American Organizations) (Deltombe et al., 2014). Using these parameters, we have shown that each of the 3D printouts had specific and unique characteristics (**Supplementary Table 2**).

Biological Effects

Effect of Polymers on Bacterial Growth

To analyze the effect of the 3D polymers on microorganisms, we used 3 different bacterial species: *Escherichia coli* strain C (Król et al., 2019), *Pseudomonas aeruginosa* strain PA01, and *Staphylococcus aureus* ATCC 25923. These species represent major groups of human skin and hair colonizers (Kerk et al., 2018) and in some conditions may turn into opportunistic or major pathogens (Chiller et al., 2001; Cogen et al., 2008). 3D printed rings were sterilized and loaded into 24-well plates with bacterial cultures (**Supplementary Figures 1B,D**). Analyzing bacterial growth, we noticed that all the polymers induced reduction in bacterial growth (**Figure 4A-C**). The greatest bacteriostatic effect was observed in the case of the *E. coli* strain where all polymers showed statistically significant reductions of growth (**Table 2**). Similar changes in the growth curves were also observed for *P. aeruginosa* and *S. aureus* (**Figures 4B,C**). All but the PLAS, WD, and SoftPLA polymers had statistically significant effects on growth of *P. aeruginosa*, but in the case of *S. aureus* only the BRS showed a significant effect on cell density after 24 h of growth (**Table 2**).

Biofilm Formation: Bacterial Attachment to Polymers

Biofilm Formation on 3D Printed Slides

Bacterial attachment is the first step in biofilm formation (Feng et al., 2015). There is increasing evidence that bacterial attachment and subsequent biofilm formation are significantly impacted by surface topography. For surfaces with topographic features at the micrometric scale, comparable with the size of prokaryotic cells, cells tend to position themselves such that they

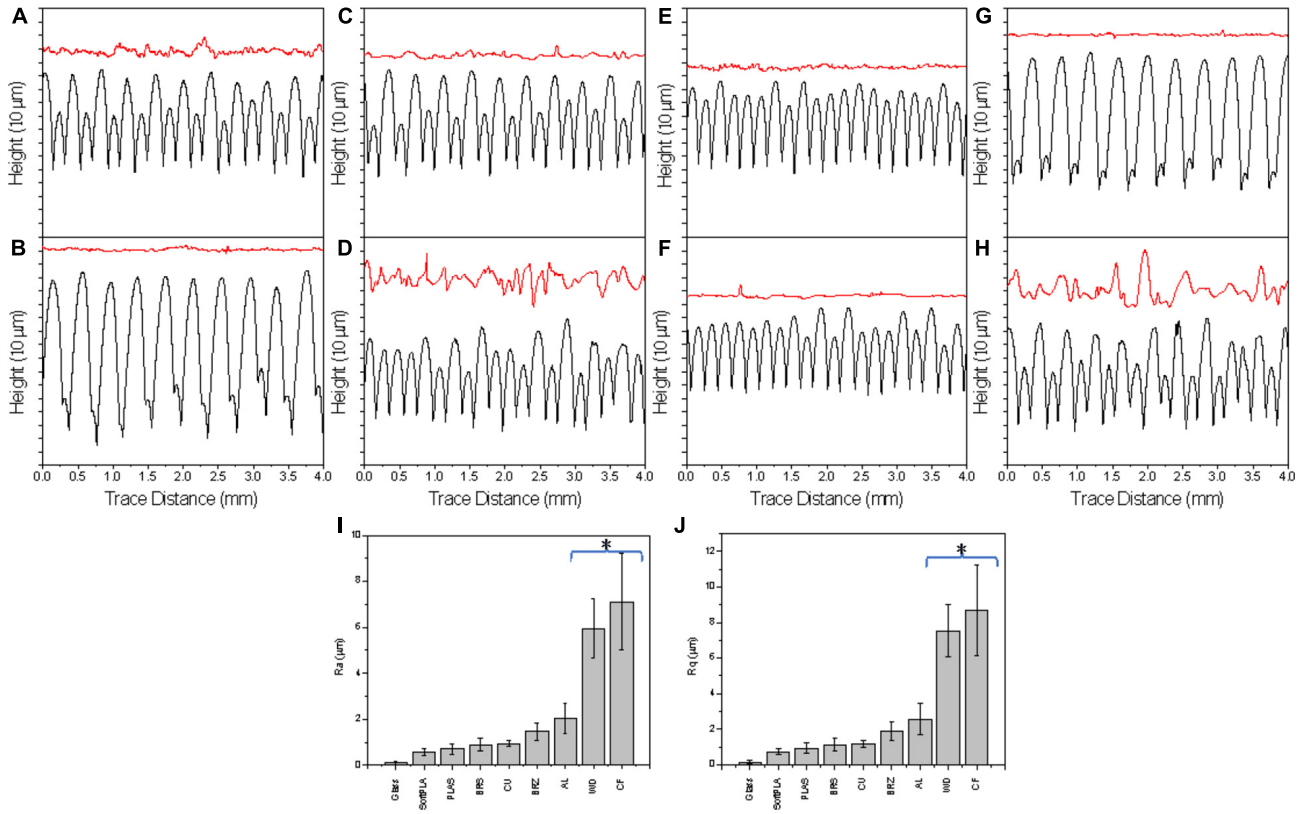

FIGURE 2 | The surface profiles of 3D printed slides perpendicular (black, bottom) and parallel (red, top) the layers (representative of 4 measurements); Selected R parameters: Ra **(I)** and Rq **(J)** of surface along the 3D printouts. Polymers were ranked by ascending values. A glass microscope slide was used as a control. AL **(A)**, BRS **(B)**, BRZ **(C)**, CF **(D)**, CU **(E)**, PLAS **(F)**, SoftPLA **(G)**, WD **(H)**. (*) Statistically different group.

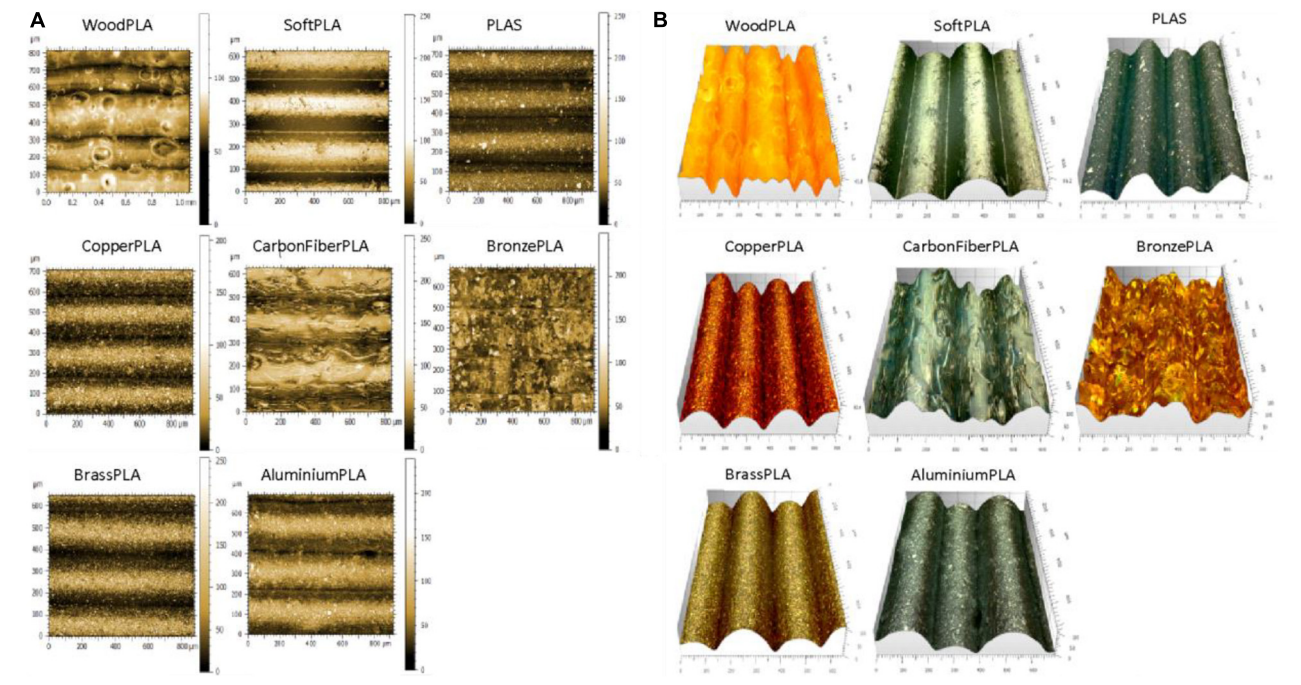

FIGURE 3 | Digital microphotography of 3D printouts **(A)** and their 3D projections **(B)**.

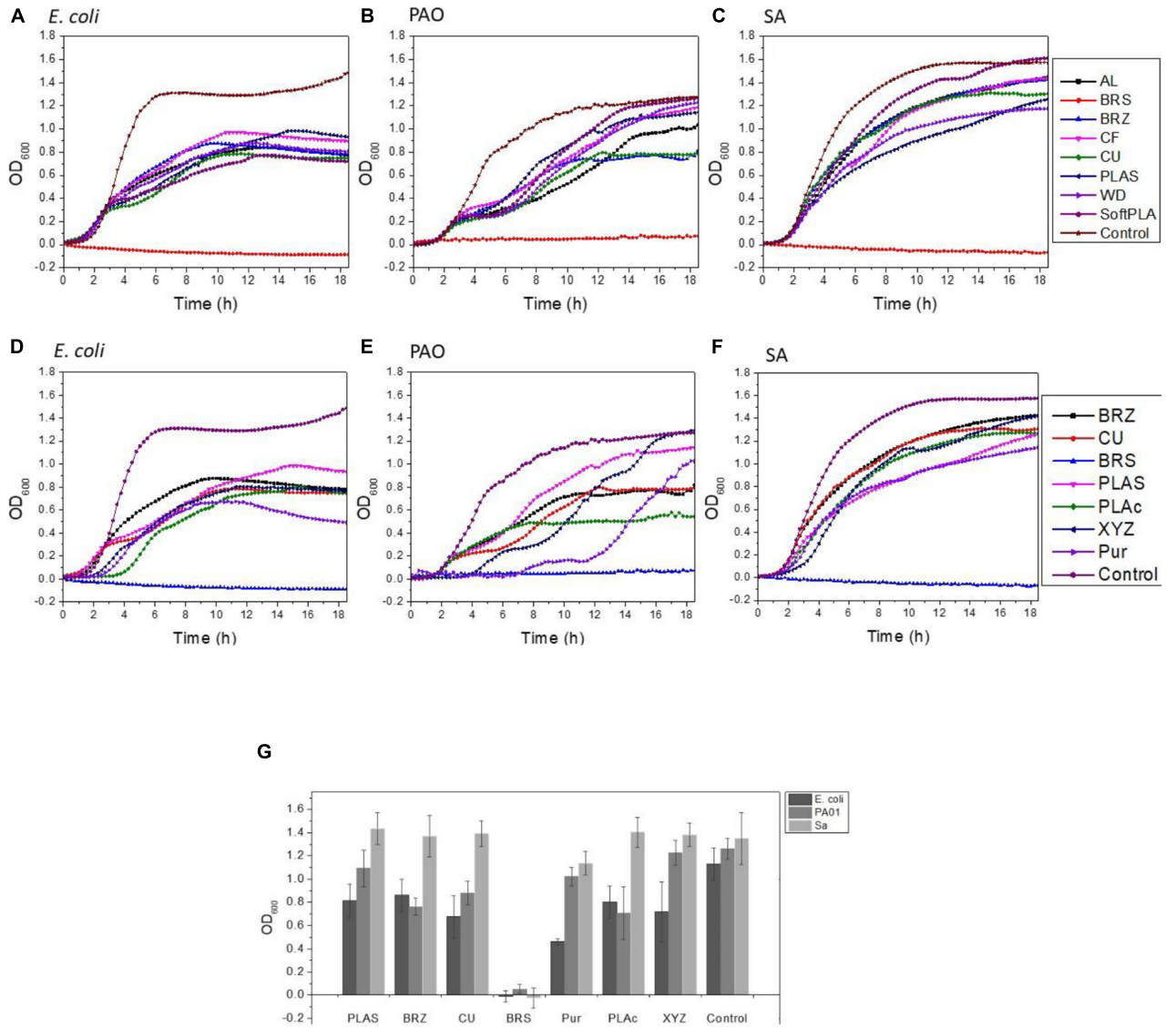

FIGURE 4 | Effect of polymers on bacterial growth **(A–C)** and comparison of antimicrobial properties **(D–G)** of tested polymers. **(A,D)** *E. coli* C **(B,F)** *P. aeruginosa* PA01, **(C,F)** *S. aureus* ATCC 25923. **(G)** Number of bacteria (OD_{600}) after 24-h growth with tested antimicrobial polymers and selected controls. Data obtained from 3-6 experiments with printed rings.

maximize contact area with the surface, which favors attachment (Mitik-Dineva et al., 2009; Bixler Gregory and Bhushan, 2012; Kostakioti et al., 2013).

Printed 3D slides were submerged in bacterial cultures of *E. coli* C (approximately 1.58×10^9), *P. aeruginosa* PA01 (1.95×10^9), and *S. aureus* ATCC 25823 (1.99×10^9). After 2 h, approximately 0.01% to 3% of the initial bacteria were found attached to the surface (**Figures 5A-C**). In the case of *E. coli,* polymers were grouped based on the efficiency of attachment into 4 statistically significant groups (**Figure 5A**). The first group contained BRS with approximately 6.5×10^6 attached cells. The second group with 9.3×10^6 to 1.09×10^7 attached cells consisted of CF, CU, and SoftPLA. The differences between polymers within that group were also statistically significant. The third group with 1.49 to 1.67×10^7 bacteria contained the AL, BRZ, and PLAS polymers although both AL and BRZ are statistically different from PLAS. The final group was represented by the WD polymer with approximately 1.9×10^7 attached cells which is statistically different from all other polymers.

Pseudomonas aeruginosa showed the highest number of attached bacteria. In this case, the polymers could be divided to 3 groups (**Figure 5B**). The first group contains BRS, CU, and SoftPLA (3.6 to 4.0×10^7). The second group consists of the CF, WD, AL, and PLAS polymers with 4.7 to 5.0×10^7 attached bacteria. In this group, only the 2 latter polymers showed statistically significant differences compared to the first group. BRZ polymer formed the last group (6.15×10^7), which was statistically different from the others.

TABLE 2 | Bacterial cell density (OD_{600}) measured after 24 h of growth at 37°C.

Polymer	*E. coli* C	*P. aeruginosa* PA01	*S. aureus* ATCC 25923
AL	0.82 ± 0.14*	0.98 ± 0.07*	1.31 ± 0.18
BRS	−0.00925 ± 0.047*	0.05 ± 0.04*	−0.02 ± 0.086*
BRZ	0.86 ± 0.14*	0.76 ± 0.075*	1.37 ± 0.18
CF	0.66 ± 0.067*	0.96 ± 0.19*	1.46 ± 0.13
CU	0.67 ± 0.18*	0.88 ± 0.1*	1.39 ± 0.11
PLAS	0.81 ± 0.14*	1.09 ± 0.16	1.43 ± 0.14
SoftPLA	0.75 ± 0.24*	0.99 ± 0.2	1.30 ± 0.15
WD	0.64 ± 0.18*	1.15 ± 0.17	1.42 ± 0.15
Control	1.13 ± 0.14	1.26 ± 0.08	1.35 ± 0.22

Data represent average values from 5-6 independent experiments. Statistically significant $p < 0.05$ (*) differences to the control.

S. aureus showed the lowest attachment levels to the polymers in this experiment, with only 0.15% to 1% of initial bacteria attached. Three groups of polymers could be distinguished (**Figure 5C**). The first group with AL, WD, CF, and BRZ showed 6.6 to 7.9 × 10^5 attached cells. In the second group with CU, PLAS and BRS polymers and almost 2 times more attached bacteria (1.2 to 1.6 × 10^6), only the latter showed statistically significant differences as compared to the first group. The SoftPLA formed the last group with statistically significantly more attached cells (2.16 × 10^6).

Biofilm Formation on 3D Printed Pins

To test biofilm using a semi-high-throughput method, the 3D pins were designed to fit a standard 48-well plate (see **Supplementary Figure 1** & "Materials and Methods"). Pins were incubated with the tested bacteria for 3 days and then optical cell density of bacterial cultures were measured in the wells and amount of bacteria attached to the pins was tested by the BacTiter-Glo™ Microbial Cell Viability Assay (**Figures 5D-F**). Pins submerged in the sterile media were used as controls.

For all 3 tested bacterial species, the least amount of biofilm formation with the lowest corresponding cell density was found in the case of the BRS polymer (**Figures 5D-F**). For *P. aeruginosa* and *S. aureus,* the next most inhibitory polymer was BRZ and it was ranked 3rd in *E. coli*. Other metal-filled polymers, CU and AL, were ranked 2nd, 3rd, and 4th and 4th, 6th, and 3rd with *E. coli*, *P. aeruginosa,* and *S. aureus,* respectively. The polymers showing highly structured surfaces such as WD (ranked 7th, 8th, and 6th) and CF (ranked 5th, 4th, and 7th) and the most hydrophobic polymer SoftPLA (ranked 5th, 7th, and 8th) were on the other side, with the highest amount of biofilm (**Figures 5D-F**).

Digital 3D Microscopy for Biofilm Analysis

Microscopic observation and analysis are the most common techniques for visualizing biofilms (Lawrence and Neu, 1999). Analysis methods include standard bright field imaging though increasingly expensive epifluorescence, confocal, atomic force,

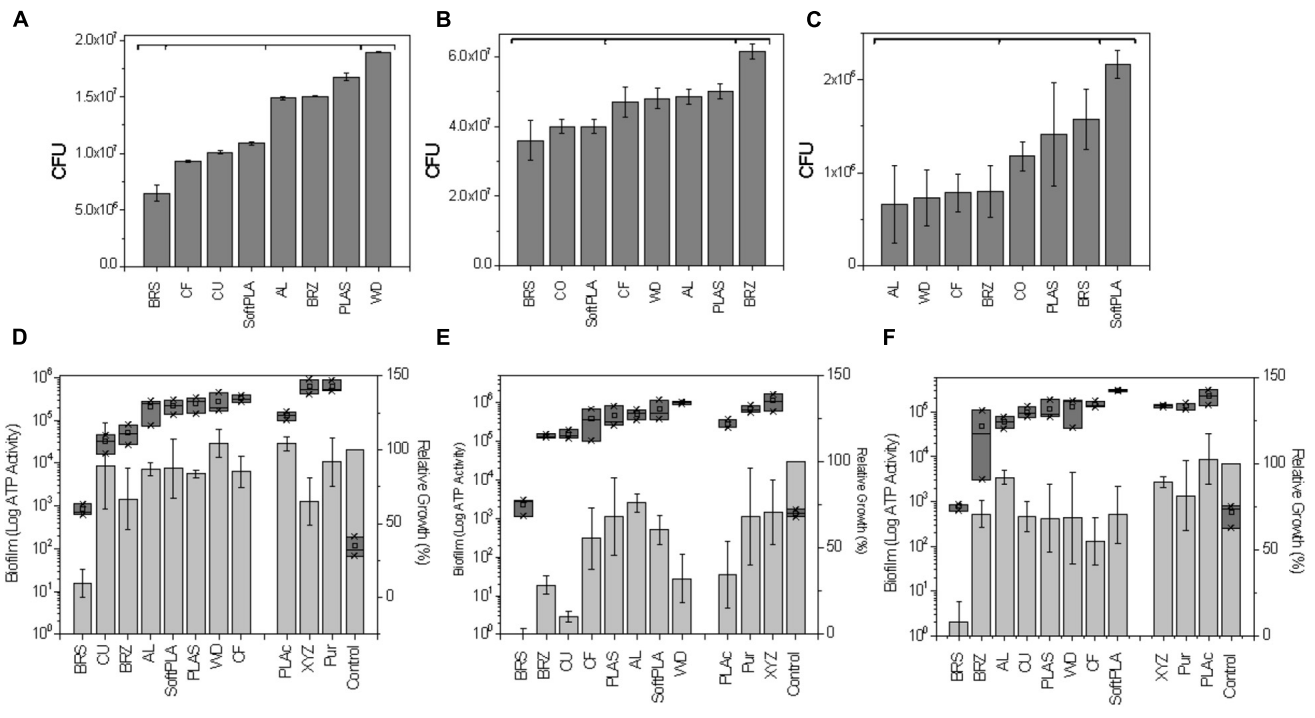

FIGURE 5 | Effect of polymers on bacterial attachment after 2-h attachment **(A–C)** and biofilm formation on 3D printed pins **(D–F). (A,D)** *E. coli* C **(B,E)** *P. aeruginosa* PA01, **(C,F)** *S. aureus* ATCC 25823. **(A–C)** Number of bacterial CFU after 2 h attachment to 3D printed slides (see **Supplementary Figure 2** for graphical protocol). Statistically different groups ($p \leq 0.05$) marked by horizontal brackets. **(D–F)** Relative cell densities to pinless control (100%) are represented by gray bars. Amount of biofilm as the total ATP amount from lysed biofilm cells attached to pins are presented as dark gray blocks (Log_{10}). Polymers are ranked by amount of biofilm. Data represents an average from 3 replicates.

and electron microscopes. To collect the data, biofilms must be prepared on special surfaces (transparent glass or plastics), treated with special dyes (CV or fluorescent dyes), or fixed, dehydrated, and covered with electron scattering heavy metals. 3D printouts are highly structured and non-transparent and therefore cannot be simply analyzed by standard microscopic techniques. We used a 3D Digital Leica DMV6 microscope to visualize biofilms attached to the 3D printed slides (**Figure 6** and **Supplementary Figure 6**). We noticed that in most cases biofilms were at the thickest in between the layers of the 3D printed materials (**Figure 6A**). In the second mode of growth, the entire surface was covered by bacterial biofilm (**Figure 6B**). Finally, we observed that in some settings bacteria formed bridges between the highest parallel layers (**Figure 6C**). Using 3D projections and MountainView, we observed that generally bacterial biofilm growth tended to make the 3D printed surface smoother, i.e., the bacteria fill in the valleys (**Figure 6**, bottom panel).

Comparison of Antimicrobial Properties of Studied Polymers With Commercially Available Antimicrobial Polymers

In this work, we noticed that some of the tested polymers showed bacteriostatic effect on microbes. Recently, 3 antimicrobial PLA polymers have been released to the market: Purement Antimicrobial PLA, Copper 3D PLActive Antibacterial Nanocomposite, and YXZPrinting Antibacterial PLA (**Table 1**). All of these materials claim to be antibacterial. PLActive has U.S. Food and Drug Administration and European Union certificates, as well as results of studies from laboratories in the United States and Chile claiming the bactericidal effect against *E. coli* DH5α and an *S. aureus* MRSA strain[1]. XYZPrinting PLA is impregnated with silver ions as the antimicrobial compound. These silver ions create reactive oxygen species according to the manufacturer. PLActive Copper 3D filament's method of action has been described as "copper oxide nanocomposite infused PLA." We compared the antimicrobial properties of these commercially available antimicrobial polymers to those of our test polymers.

In growth curve experiments, we noticed no difference between the PLActive polymer and normal PLAS (**Figures 4D-F**). Growth kinetics for XYZPrinting and Purement Antimicrobial polymers depended greatly on the bacterial strain. In the case of *E. coli* C, we saw a slight delay in growth and low final cell density (**Figures 4D,G**). However, the differences in cell densities between Purement and PLAS or BRZ were statistically significant, but they were not significantly different from the third tested polymer, CU (**Figure 4G**). In *P. aeruginosa,* both polymers showed a 2- to 4-h delay in growth; however, the final cell density after 17 h was not affected (**Figures 4E,G**). In the case of S. *aureus,* only a slight lag phase was observed, with no significant changes in final cell densities (**Figures 4F,G**). None of the tested antimicrobial polymers could compare with BRS in terms of its antimicrobial properties (**Figure 4**).

Next, we compared biofilm formation on the antimicrobial polymers and our previously tested ones (**Figures 5D-F**). In the case of *E. coli* C, the PLActive showed the least amount of biofilm formation, which was statistically significant compared to BRS, CU, and BRZ. Both the XYZPrinting and Purement polymers showed the highest amounts of biofilm formation and were statistically higher than PLActive, AL, SoftPLA, and PLAS but not the WD and CF polymers (**Figure 5D**).

We showed that the BRS, BRZ, and CU polymers were the most inhibitory for *P. aeruginosa* biofilm formation. Tests with the three commercial antimicrobial polymers showed that none of them were more efficient in PA biofilm inhibition. Again, the least amount of biofilm formed was observed on the PLActive polymer; however, it was not statistically better than the CU polymer and only slightly better than the BRZ polymer (**Figure 5E**). The amount of biofilm on the PLActive polymer was statistically less only when compared to WD. Purement also did not prevent biofilm formation and resulted in more biofilm growth than all test polymers except WD ($p = 0.03$); BRS, BRZ. and CU were all statistically better than the Purement polymer for inhibiting PA biofilm growth. The XYZPrinting antimicrobial polymer showed the highest amount of *P. aeruginosa* biofilm; however, statistical differences again were observed only with BRS, BRZ, and CU (**Figure 5E**).

The smallest differences in biofilm formation on 3D polymers were observed in the case of *S. aureus* (**Figure 5F**) which also was the poorest of the bacterial species in the adhesion experiments. The least amount of biofilm was formed on BRS and the highest on SoftPLA. Both polymers were statistically different from the others except SoftPLA and PLActive.

To conclude, none of the commercial antimicrobial polymers were better than our metal-filled polymers BRS, BRZ, and CU and the differences between the remaining polymers were not really striking.

DISCUSSION

Since its development in the early 1980s, 3D printing technology has become ever more popular in many fields of science and industry (Liaw and Guvendiren, 2017; Ngo et al., 2018; Hao and Lin, 2020). At the same time, the development of antibiotic-resistant bacterial pathogens is a real threat in the healthcare industry (Lin et al., 2015). Biofilms, surface-attached bacterial aggregation, have been found to be 1000 × more resistant to antibiotics than their planktonic counterparts (Mah and O'Toole, 2001; Hall-Stoodley et al., 2008). Biofilms have been noted as emerging problems in medicine, especially on medical devices and implants (Braxton et al., 2005; Ehrlich et al., 2005a,b, 2014; Stoodley et al., 2005; Fux et al., 2006; Wolcott and Ehrlich, 2008; Nowatzki et al., 2012; Palmer et al., 2014; Srivastava et al., 2019). During the current COVID-19 pandemic, the shortage of personal protection equipment (PPE) enforced the usage of 3D printed technology to produce face shields and facemasks (Flanagan and Ballard, 2020; Swennen et al., 2020). Because of the increased use of 3D printing in the medical fields, we decided to take a closer look at the properties of available polymers and their interactions with common biofilm-forming bacteria.

[1]https://copper3d.com/

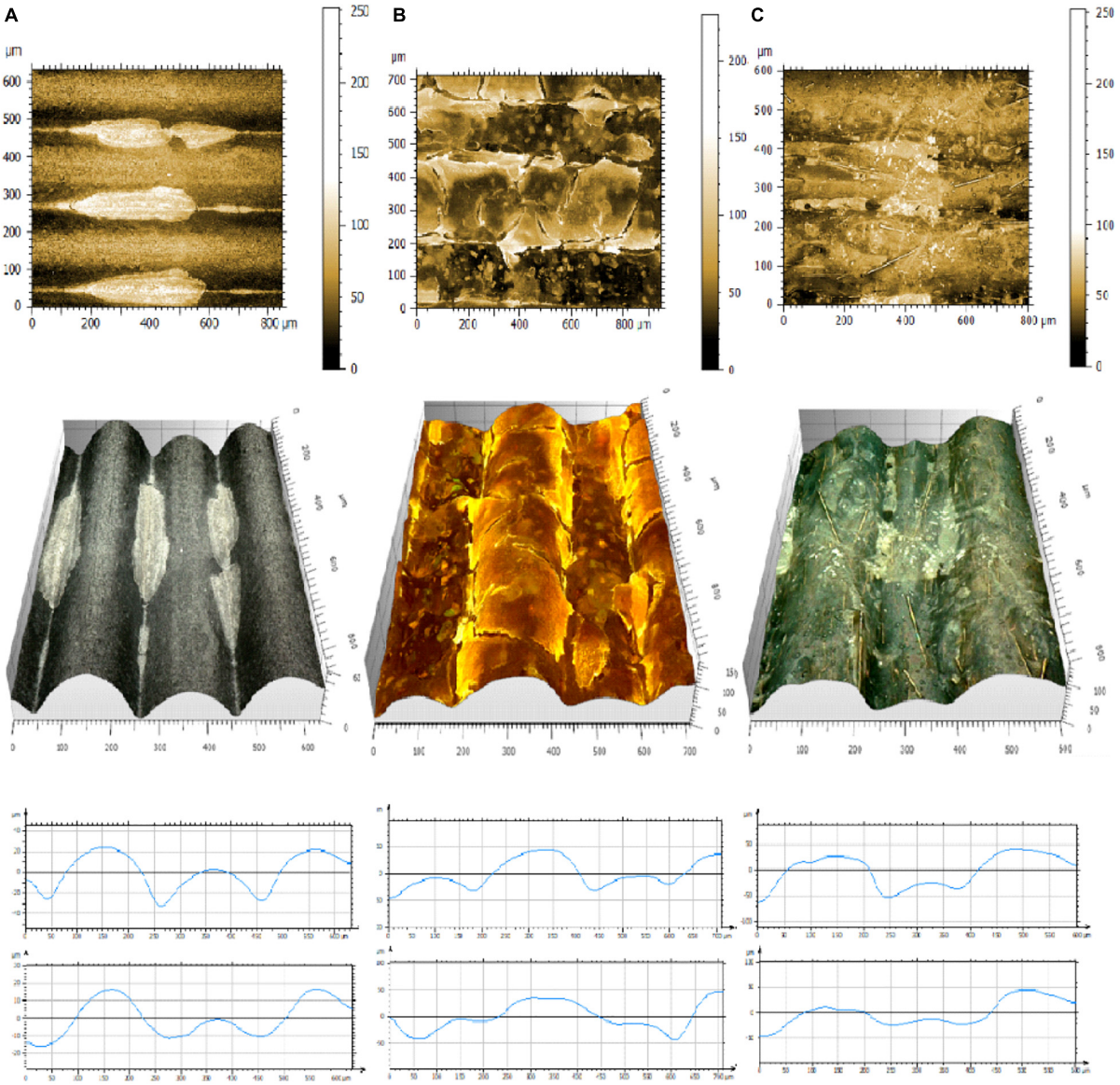

FIGURE 6 | Pictures of representative biofilms formed on 3D printed materials. **(A)** *E. coli* C on SoftPLA, **(B)** *S. aureus* ATCC25823 in CU, **(C)** *P. aeruginosa* PA01 on CF. Upper panel: 2D pictures, Center panel: 3D projections, Bottom panel: projections of profiles without (upper) and with biofilms (lower) generated by MountainView software.

PLA polymers were our main focus as they are made from natural resources, can be enzymatically degraded, and are safe for humans (Conn et al., 1995).

Several of our tested polymers have been filled with metals/alloys such as copper, brass, bronze, and aluminum. Copper, brass, and bronze have a long history of being used as antimicrobial agents (Dollwet, 1985; Grass et al., 2011) while aluminum has no or limited effect on bacterial growth (Varkey, 2010). PLA with carbon fibers and wood represented a second group of polymers with more structured surfaces, while PLA with silver dye was used as a PLA-only control. We used optical contact angle measurements to analyze the hydrophobicity of the prints and both surface contact and optical profilometry to analyze their surface. While hydrophobicity measurements were very straight forward, we faced some problems using both surface and optical profilometers. It was noted that all cross-section profiles tested by the Mitutoyo JS210 contact profilometer gave distinct patterns, but their lines were relatively smooth (**Figure 2**, black). That indicated that the big structural changes across the 3D printout hid the true micro-surface properties, which were revealed by along-layer profile measurements (**Figure 2**, red; **Figures 2I-L**). We also noticed that although the printer layer height was set to 200 µm, the R_{Sm} (mean peak width) parameter showed a large variation from 156 µm to almost 400 µm, indicating a limited precision of contact profilometry (**Supplementary Figure 4**).

Optical profilometry is a rapid, non-destructive, and non-contact surface metrology technique. An optical profiler is a type of microscope in which light from a lamp is split into two paths by a beam splitter and each light beam is used in forming topographic information (Wang et al., 2017). The optical profilometers have been used in material science and industry for decades. A different kind of 3D microscopy was used to analyze biological materials. These methods used expensive and sophisticated equipment like confocal microscopy (Lawrence and Neu, 1999; Palmer and Sternberg, 1999). Unfortunately, old profilometers (like Zygo®) and confocal microscopes are too precise or require fluorescent dyes and cannot really be used in the case of 3D printouts. Recent progress in imaging technology allowed construction of 3D digital optical microscopes such as Zeiss SmartZoom 5 (Zeiss, United States), Hirox RH-8800 (Hirox, United States), Keyence VR-5000, and VHX-7000 (Keyence, United States) and Leica DVM6 (Leica, United States). These microscopes combine a high magnification (up to 7,000×) with high resolution and sophisticated software to provide 3D capabilities. We have tested some of these instruments and found Leica, Keyence, and Hirox most suitable for our studies (**Supplementary Figures 6-8**). Unfortunately, 3D digital microscopy faces some problems. 3D projecting materials that are very dark, translucent, or reflect light, such as wood, carbon fiber, and bronze, are hard to image using 3D digital microscopy (see **Figure 3** and **Supplementary Figures 6-8**). Even if the pictures represent the true structures, 3D projections and surface R and S parameters do not always reflect it. More work must be done to improve this technique, such as coatings to reduce glare and lighting issues.

Three common human-associated bacterial species (*E. coli* strain C, *P. aeruginosa* PA01, and *S. aureus* ATCC25823) were employed to test the effect of 3D printouts on growth, attachment, and biofilm formation. Using 24-well plates with 3D printed rings we were able to test relatively fast and simply the effect of polymers on planktonic growth, showing that almost all polymers affect the growth. The differences might be attributed to the bacteriostatic properties of the polymers, as well as to the increased surface area, which sequesters some planktonic cells. We believe these sequestered cells are part of the first step of biofilm formation (Costerton et al., 1995; Donlan, 2002; Bixler Gregory and Bhushan, 2012; Feng et al., 2015). Two hours of interactions between printouts and 10^9 bacterial cells was not enough to kill the bacteria or reduce the number of bacteria in the culture as we observed in the growth experiments. Therefore, attachment should be affected by other parameters, i.e., surface roughness and hydrophobicity (Merritt and An, 2000; Mitik-Dineva et al., 2009). To analyze bacterial attachment, we used 3D printed slides partially submerged in the water. As adhesion to the surface is higher at the air-liquid interface we used this model to get a better idea of these complex interactions between bacteria and 3D printouts.

In the case of *E. coli,* the highest number of attached cells was observed on the wood polymer, which was ranked the second-most rough material (**Figures 2**, **5**). In the case of *P. aeruginosa,* the correlation between material roughness and cell attachment is not that straightforward. We speculate that *Pseudomonas,* with its "slime" and other extracellular appendages, overcame those surface parameters and maybe used its own factors for successful attachment (Chang, 2018). In the case of *S. aureus,* the highest number of attached cells was observed in the case of SoftPLA, which showed the smoothest surface of all tested polymers (**Figure 2**). On the other hand, the hydrophobicity of the SoftPLA surface was by far the highest of the tested polymers (**Figure 1**). Recently, Forson and colleagues showed that *S. aureus* has a much higher attachment rate to silanized glass (water contact angle, 96° ± 8°) than substrates with lower hydrophobicity (Forson et al., 2020).

While analyzing biofilm formation on 3D printouts, we realized that 3 principal parameters (antibacterial properties, surface structure, and hydrophobicity of the polymers) play important roles. All 3 (or 4) metal-filled polymers with their antimicrobial properties showed the least amount of biofilm formed for all 3 bacteria species (**Figures 5D-F**). On the other hand, most rough surfaces (carbon fiber and wood) were almost always the most supportive of biofilm growth. Additionally, in the case of *P. aeruginosa* and more importantly *S. aureus,* high surface hydrophobicity (SoftPLA) played the major role in biofilm formation.

In the biofilm image analyses, it was not surprising that we observed that most of the biofilms filled the grooves between printed layers. In a several cases, the biofilms formed bridges between higher layers. *P. aeruginosa* and *S. aureus* covered the surfaces more completely than *E. coli*. This observation might be related to shear force, which even at a low level (50 rpm) triggers a mechanism of finding a safe niche. The latter is related to the bacterial properties as both *P. aeruginosa* and *S. aureus* are the ultimate biofilm formers. Although, the grooves in 3D printouts can be smoothed, the process for PLA polymers is not that easy as for the ABS and other polymers and requires additional time and effort.

The antimicrobial properties of the polymers play a crucial role in reducing biofilm formation. The first antimicrobial PLA polymer with different concentrations of silver nanoparticles was developed in 2013; however, the fibers (not printouts) were tested only against planktonic cells (Erem et al., 2013). Currently, a few antibacterial polymers are available on the market. Here we tested 3 out of 5 of these polymers. The price of these antimicrobial polymers is usually 3 to 4 times higher than the standard and metal-filled polymers tested in this work. The exact composition of antimicrobial polymers is usually not revealed, and all provided information is vague. Although we noticed slight antimicrobial properties of these polymers, they were not statistically different from metal filled brass, copper, and bronze PLA polymers. The greatest antimicrobial and antibiofilm activity were observed in the case of BRS PLA polymer (**Figures 4**, **5D-F**). According to the manufacturer, this polymer contains about 40% metal.

To the best of our knowledge, this is the first report describing biofilm formation on 3D printed surfaces, with as many as 8 standard and 3 antimicrobial PLA polymers, as well as 3 of the most prevalent human colonizers: *E. coli*, *P. aeruginosa,* and *S. aureus*. We hope that the methods described here might set some standards for developing and testing new antimicrobial

polymers with different bacterial species and this research may lead to reducing the chances of bacterial infections spread by 3D printed devices.

DATA AVAILABILITY STATEMENT

The original contributions presented in the study are included in the article/**Supplementary Material**, further inquiries can be directed to the corresponding author/s.

AUTHOR CONTRIBUTIONS

DH and JK designed the study, performed the experiments and analyses, wrote the original draft, and edited the manuscript. PP performed experiments, analyzed data, and edited the manuscript. GE supported the project and edited the entire manuscript. H-FJ supported the project. All authors read and approved the final version of the manuscript.

FUNDING

This work was supported by a gift from Dr. James Truchard, the Drexel University College of Arts and Sciences, The Center for Advanced Microbial Processing, The Center for Surgical Infections and Biofilms, Drexel University College of Medicine start-up funding provided to GE, and NIH NIDCD R01 DC 02148.

ACKNOWLEDGMENTS

We thank Miller Microscopes (Leica), Steve Bucks (Hirox-USA), and Mark LaMarre (Keyence) for supplying 3D digital microscopes and Digital Surf for supplying a demo version of the MountainMap® software. We also thank Jocelyn Hammond for editing, proofreading, and comments on the manuscript.

SUPPLEMENTARY MATERIAL

The Supplementary Material for this article can be found online at: https://www.frontiersin.org/articles/10.3389/fmicb.2021.646303/full#supplementary-material

Supplementary Figure 1 | Designed 3D slides, rings, and pins **(A)**, rings in 24 well plate **(B)**.

Supplementary Figure 2 | Schematic representation of adsorption experiment. 1: 3D slide placed in overnight culture of bacteria; 2: 2 h incubation at 37°C, 50 rpm; 3&4: washing in sterile PBS; 5: Shaking 3 min 1000 rpm on Mini-G, SPEX-Sample-Prep; 6: Dilutions were plated by drip titration method.

Supplementary Figure 3 | Selected Mitutoyo R parameters on cross-sections of printouts ranked ascendant (average data from 4 measurements). Ra - Arithmetic mean deviation of the roughness profile; Rq - Root-mean-square (RMS) deviation of the roughness profile; Rz - Maximum Height of roughness profile; Rp - Maximum peak height of the roughness profile; Rv - Maximum valley depth of the roughness profile.

Supplementary Figure 4 | RSm (mean peak width) parameters on cross-sections of printouts (average data from 4 measurements).

Supplementary Figure 5 | Selected R parameters on cross-sections of printouts (average data from 9 measurements). Ra - Arithmetic mean deviation of the roughness profile; Rq - Root-mean-square (RMS) deviation of the roughness profile; Rz - Maximum Height of roughness profile; Rp - Maximum peak height of the roughness profile; Rv - Maximum valley depth of the roughness profile; Rc - Mean height of the roughness profile elements.

Supplementary Figure 6 | Pictures of representative biofilms formed by *E. coli* C, *P. aeruginosa* PA01, and *S. aureus* ATCC25823 on 3D printed materials. Upper panel: 2D pictures, Center panel: 3D projections, Bottom panel: projections of profiles without (upper) and with biofilms (lower) generated by MountainView® software.

Supplementary Figure 7 | 3D projections of selected printouts obtained with Keyence VHX-7000 Laser Scanning Confocal Microscope. From left top: CU, SoftPLA, WD, CF, BRS, BRZ.

Supplementary Figure 8 | 3D projections of selected printouts obtained with Hirox KH8700 microscope. From left top: CU, WD, SoftPLA, PLAS, BRS. Bottom: *P. aeruginosa* and *S. aureus* biofilms on CU (left and right, respectively).

Supplementary Table 1 | Most commonly used surface parameters.

Supplementary Table 2 | Characteristics of the 3D printouts generated by MountainMap® software.

REFERENCES

Bixler Gregory, D., and Bhushan, B. (2012). Biofouling: lessons from nature. *Philos. Trans. R. Soc. A Math. Phys. Eng. Sci.* 370, 2381–2417. doi: 10.1098/rsta.2011.0502

Blateyron, F. (2006). 3D Imaging and Analysis F Blateyron. *A Calcutta Imaging & Microsc.* 8, 42–43.

Blateyron, F. (2013). "The areal field parameters" in *Characterisation of Areal Surface Texture*, eds R. Leach (Berlin: Springer), 15–43.

Braxton, E. E., Ehrlich, G. D., Hall-Stoodley, L., Stoodley, P., Veeh, R., Fux, C., et al. (2005). Role of biofilms in neurosurgical device-related infections. *Neurosurg. Rev.* 28, 249–255. doi: 10.1007/s10143-005-0403-8

Chang, C.-Y. (2018). Surface Sensing for Biofilm Formation in *Pseudomonas aeruginosa*. *Front. Microbiol.* 8:2671. doi: 10.3389/fmicb.2017.02671

Chiller, K., Selkin, B. A., and Murakawa, G. J. (2001). Skin microflora and bacterial infections of the skin. *J. Investig. Dermatol. Symp. Proc.* 6, 170–174. doi: 10.1046/j.0022-202x.2001.00043.x

Choonara, Y. E., du Toit, L. C., Kumar, P., Kondiah, P. P. D., and Pillay, V. (2016). 3D-printing and the effect on medical costs: a new era? *Expert Rev. Pharm. Outcomes Res.* 16, 23–32. doi: 10.1586/14737167.2016.1138860

Cogen, A. L., Nizet, V., and Gallo, R. L. (2008). Skin microbiota: a source of disease or defence? *Br. J. Dermatol.* 158, 442–455. doi: 10.1111/j.1365-2133.2008.08437.x

Conn, R. E., Kolstad, J. J., Borzelleca, J. F., Dixler, D. S., Filer, L. J., Ladu, B. N., et al. (1995). Safety assessment of polylactide (PLA) for use as a food-contact polymer. *Food Chem. Toxicol.* 33, 273–283. doi: 10.1016/0278-6915(94)00145-E

Costerton, J. W., Lewandowski, Z., Caldwell, D. E., Korber, D. R., and Lappin-Scott, H. M. (1995). Microbial biofilms. *Annu. Rev. Microbiol.* 49, 711–745. doi: 10.1146/annurev.mi.49.100195.003431

Costerton, W., Veeh, R., Shirtliff, M., Pasmore, M., Post, C., and Ehrlich, G. (2007). The application of biofilm science to the study and control of chronic bacterial infections. *J. Clin. Investig.* 112, 1466–1477. doi: 10.1172/JCI20365

Damodaran, V. B., and Murthy, N. S. (2016). Bio-inspired strategies for designing antifouling biomaterials. *Biomater. Res.* 20:18. doi: 10.1186/s40824-016-0064-4

Deltombe, R., Kubiak, K., and Bigerelle, M. (2014). How to select the most relevant 3D roughness parameters of a surface. *Scanning* 36, 150–160. doi: 10.1002/sca.21113

Dollwet, H. H. A. (1985). Historic uses of copper compounds in medicine. *Trace Elem. Med.* 2, 80–87.

Donlan, R. M. (2002). Biofilms: microbial life on surfaces. *Emerg. Infect. Dis.* 8, 881–890. doi: 10.3201/eid0809.020063

Ehrlich, G. D., Hu, F. Z., Shen, K., Stoodley, P., and Post, J. C. (2005a). Bacterial plurality as a general mechanism driving persistence in chronic infections. *Clin. Orthop. Relat. Res.* 437, 20–24. doi: 10.1097/00003086-200508000-00005

Ehrlich, G. D., Hu, F. Z., Sotereanos, N., Sewicke, J., Parvizi, J., Nara, Pl, et al. (2014). What role do periodontal pathogens play in osteoarthritis and periprosthetic joint infections of the knee? *J. Appl. Biomater. Funct. Mater.* 12, 13–20.

Ehrlich, G. D., Stoodley, P., Kathju, S., Zhao, Y., McLeod, B. R., Balaban, N., et al. (2005b). Engineering approaches for the detection and control of orthopaedic biofilm infections. *Clin. Orthop. Relat. Res.* 437, 59–66. doi: 10.1097/00003086-200508000-00011

Erem, A. D., Ozcan, G., Erem, H. H., and Skrifvars, M. (2013). Antimicrobial activity of poly(l-lactide acid)/silver nanocomposite fibers. *Textile Res. J.* 83, 2111–2117. doi: 10.1177/0040517513481875

Feng, G., Cheng, Y., Wang, S.-Y., Borca-Tasciuc, D. A., Worobo, R. W., and Moraru, C. I. (2015). Bacterial attachment and biofilm formation on surfaces are reduced by small-diameter nanoscale pores: how small is small enough? *NPJ Biofilms Microb.* 1:15022. doi: 10.1038/npjbiofilms.2015.22

Flanagan, S. T., and Ballard, D. H. (2020). 3D printed face shields: a community response to the COVID-19 global pandemic. *Acad. Radiol.* 27, 905–906.

Forson, A. M., van der Mei, H. C., and Sjollema, J. (2020). Impact of solid surface hydrophobicity and micrococcal nuclease production on Staphylococcus aureus Newman biofilms. *Sci. Rep.* 10:12093. doi: 10.1038/s41598-020-69084-x

Fux, C. A., Quigley, M., Worel, A. M., Post, C., Zimmerli, S., Ehrlich, G., et al. (2006). Biofilm-related infections of cerebrospinal fluid shunts. *Clin. Microbiol. Infect.* 12, 331–337.

Gadelmawla, E. S., Koura, M., Maksoud, T., Elewa, I., and Soliman, H. (2002). Roughness parameters. *J. Mater. Process. Technol.* 123, 133–145. doi: 10.1016/S0924-0136(02)00060-2

Grass, G., Rensing, C., and Solioz, M. (2011). Metallic copper as an antimicrobial surface. *Appl. Environ. Microbiol.* 77, 1541–1547.

Gule, N. P., Begum, N. M., and Klumperman, B. (2016). Advances in biofouling mitigation: a review. *Crit. Rev. Environ. Sci. Technol.* 46, 535–555. doi: 10.1080/10643389.2015.1114444

Hall, D. C. Jr., Król, J. E., Cahill, J. P., Ji, H.-F., and Ehrlich, G. D. (2020). The development of a pipeline for the identification and validation of small-molecule rela inhibitors for use as anti-biofilm drugs. *Microorganisms* 8:1310. doi: 10.3390/microorganisms8091310

Hall-Stoodley, L., Nistico, L., Sambanthamoorthy, K., Dice, B., Nguyen, D., Mershon, W. J., et al. (2008). Characterization of biofilm matrix, degradation by DNase treatment and evidence of capsule downregulation in Streptococcus pneumoniae clinical isolates. *BMC Microbiol.* 8:173. doi: 10.1186/1471-2180-8-173

Hao, B., and Lin, G. (2020). 3D printing technology and its application in industrial manufacturing. *IOP Conf. Ser. Mater. Sci. Eng.* 782:022065. doi: 10.1088/1757-899x/782/2/022065

Harding, J. L., and Reynolds, M. M. (2014). Combating medical device fouling. *Trends Biotechnol.* 32, 140–146. doi: 10.1016/j.tibtech.2013.12.004

Herten, M., Bisdas, T., Knaack, D., Becker, K., Osada, N., Torsello, G. B., et al. (2017). Rapid in vitro quantification of s. aureus biofilms on vascular graft surfaces. *Front. Microbiol.* 8:2333. doi: 10.3389/fmicb.2017.02333

Ito, A., Taniuchi, A., May, T., Kawata, K., and Okabe, S. (2009). Increased antibiotic resistance of *Escherichia coli* in mature biofilms. *Appl. Environ. Microbiol.* 75, 4093–4100. doi: 10.1128/aem.02949-08

Kerk, S. K., Lai, H. Y., Sze, S. K., Ng, K. W., Schmidtchen, A., and Adav, S. S. (2018). Bacteria display differential growth and adhesion characteristics on human hair shafts. *Front. Microbiol.* 9:2145. doi: 10.3389/fmicb.2018.02145

Kostakioti, M., Hadjifrangiskou, M., and Hultgren, S. J. (2013). Bacterial biofilms: development, dispersal, and therapeutic strategies in the dawn of the postantibiotic era. *Cold Spring Harb. Perspect. Med.* 3:a010306. doi: 10.1101/cshperspect.a010306

Król, J. E., Hall, D. C. Jr., Balashov, S., Pastor, S., Sibert, J., McCaffrey, J., et al. (2019). Genome rearrangements induce biofilm formation in *Escherichia coli* C - an old model organism with a new application in biofilm research. *BMC Genomics* 20:767. doi: 10.1186/s12864-019-6165-4

Król, J. E., Nguyen, H. D., Rogers, L. M., Beyenal, H., Krone, S. M., and Top, E. M. (2011). Increased transfer of a multidrug resistance plasmid in *Escherichia coli* biofilms at the air-liquid interface. *Appl. Environ. Microbiol.* 77, 5079–5088.

Król, J. E., Wojtowicz, A. J., Rogers, L. M., Heuer, H., Smalla, K., Krone, S. M., et al. (2013). Invasion of E. coli biofilms by antibiotic resistance plasmids. *Plasmid* 70, 110–119.

Lawrence, J. R., and Neu, T. R. (1999). "Confocal laser scanning microscopy for analysis of microbial biofilms," in *Methods in Enzymology*, eds J. Abelson, M. Simon, G. Verdine, and A. Pyle (Cambridge, MA: Academic Press), 131–144.

Lewis, K. (2008). "Multidrug tolerance of biofilms and persister cells," in *Bacterial Biofilms*, ed. T. Romeo (Berlin: Springer), 107–131.

Liaw, C.-Y., and Guvendiren, M. (2017). Current and emerging applications of 3D printing in medicine. *Biofabrication* 9:024102. doi: 10.1088/1758-5090/aa7279

Lin, J., Nishino, K., Roberts, M. C., Tolmasky, M., Aminov, R. I., and Zhang, L. (2015). Mechanisms of antibiotic resistance. *Front. Microbiol.* 6:34. doi: 10.3389/fmicb.2015.00034

Mah, T. F., and O'Toole, G. A. (2001). Mechanisms of biofilm resistance to antimicrobial agents. *Trends Microbiol.* 9, 34–39. doi: 10.1016/s0966-842x(00)01913-2

Manero, A., Smith, P., Sparkman, J., Dombrowski, M., Courbin, D., Kester, A., et al. (2019). Implementation of 3D printing technology in the field of prosthetics: past, present, and future. *Int. J. Environ. Res. Public Health* 16:1641. doi: 10.3390/ijerph16091641

Merritt, K., and An, Y. H. (2000). "Factors influencing bacterial adhesion," in *Handbook of Bacterial Adhesion: Principles, Methods, and Applications*, eds Y. H. An and R. J. Friedman (Totowa, NJ: Humana Press), 53–72.

Mitik-Dineva, N., Wang, J., Truong, V. K., Stoddart, P., Malherbe, F., Crawford, R. J., et al. (2009). *Escherichia coli*, *Pseudomonas aeruginosa*, and *Staphylococcus aureus* attachment patterns on glass surfaces with nanoscale roughness. *Curr. Microbiol.* 58, 268–273. doi: 10.1007/s00284-008-9320-8

Nablo, B. J., Chen, T.-Y., and Schoenfisch, M. H. (2001). Sol-gel derived nitric-oxide releasing materials that reduce bacterial adhesion. *J. Am. Chem. Soc.* 123, 9712–9713. doi: 10.1021/ja0165077

Ngo, T. D., Kashani, A., Imbalzano, G., Nguyen, K. T. Q., and Hui, D. (2018). Additive manufacturing (3D printing): a review of materials, methods, applications and challenges. *Composites Part B Eng.* 143, 172–196. doi: 10.1016/j.compositesb.2018.02.012

Nowatzki, P. J., Koepsel, R. R., Stoodley, P., Min, K., Harper, A., Murata, H., et al. (2012). Salicylic acid-releasing polyurethane acrylate polymers as anti-biofilm urological catheter coatings. *Acta Biomater.* 8, 1869–1880. doi: 10.1016/j.actbio.2012.01.032

Pagani, L., Qi, Q., Jiang, X., and Scott, P. J. (2017). Towards a new definition of areal surface texture parameters on freeform surface. *Measurement* 109, 281–291.

Palmer, M. P., Altman, D. T., Altman, G. T., Sewecke, J. J., Ehrlich, G. D., Hu, F. Z., et al. (2014). Can we trust intraoperative culture results in nonunions?. *J. Orthop. Trauma* 28, 384–390.

Palmer, R. J., and Sternberg, C. (1999). Modern microscopy in biofilm research: confocal microscopy and other approaches. *Curr. Opin. Biotechnol.* 10, 263–268. doi: 10.1016/S0958-1669(99)80046-9

Paul, G. M., Rezaienia, A., Wen, P., Condoor, S., Parkar, N., King, W., et al. (2018). Medical applications for 3D printing: recent developments. *Mol. Med.* 115, 75–81.

Poologasundarampillai, G., and Nommeots-Nomm, A. (2017). "3 - Materials for 3D printing in medicine: metals, polymers, ceramics, hydrogels," in *3D Printing in Medicine*, ed. D. M. Kalaskar (Woodhead Publishing), 43–71.

Sauer, K., Camper, A. K., Ehrlich, G. D., Costerton, J. W., and Davies, D. G. (2002). *Pseudomonas aeruginosa*displays multiple phenotypes during development as a biofilm. *J. Bacteriol.* 184, 1140–1154. doi: 10.1128/jb.184.4.1140-1154.2002

Srivastava, A., Chandra, N., and Kumar, S. (2019). "The role of biofilms in medical devices and implants," in *Biofilms in Human Diseases: Treatment and Control*, eds S. Kumar, N. Chandra, L. Singh, M. Z. Hashmi, and A. Varma (Cham: Springer International Publishing), 151–165.

Stoodley, P., Kathju, S., Hu, F. Z., Erdos, G., Levenson, J. E., Mehta, N., et al. (2005). Molecular and imaging techniques for bacterial biofilms in joint arthroplasty infections. *Clin. Orthop. Relat. Res.§* 437, 31–40.

Sun, Z. (2018). 3D printing in medicine: current applications and future directions. *Quant. Imaging Med. Surg.* 8, 1069–1077. doi: 10.21037/qims.2018.12.06

Swennen, G. R. J., Pottel, L., and Haers, P. E. (2020). Custom-made 3D-printed face masks in case of pandemic crisis situations with a lack of commercially available FFP2/3 masks. *Int. J. Oral Maxillof. Surg.* 49, 673–677. doi: 10.1016/j.ijom.2020.03.015

TASOM Engineers (2018). *3-D Printing to Lower Prosthetic Costs: Frost & Sullivan*. Available from: https://aabme.asme.org/posts/3-d-printing-to-lower-prosthetic-costs (accessed July 19, 2019).

Varkey, A. J. (2010). Antibacterial properties of some metals and alloys in combating coliforms in contaminated water. *Sci. Res. Essays* 5, 3834–3839.

Vladkova, T. (2009). "Surface modification approach to control biofouling," in *Marine and Industrial Biofouling*, eds H.-C. Flemming, P. S. Murthy, R. Venkatesan, and K. Cooksey (Berlin: Springer), 135–163.

Wang, Y., Xie, F., Ma, S., and Dong, L. (2017). Review of surface profile measurement techniques based on optical interferometry. *Optics Lasers Eng.* 93, 164–170. doi: 10.1016/j.optlaseng.2017.02.004

Wolcott, R. D., and Ehrlich, G. D. (2008). Biofilms and chronic infections. *JAMA* 299, 2682–2684. doi: 10.1001/jama.299.22.2682

Wood, T. K., Knabel, S. J., and Kwan, B. W. (2013). Bacterial persister cell formation and dormancy. *Appl. Environ. Microbiol.* 79, 7116–7121. Epub 2013/09/13. doi: 10.1128/AEM.02636-13 PubMed

Zander, Z. K., and Becker, M. L. (2018). Antimicrobial and antifouling strategies for polymeric medical devices. *ACS Macro Lett.* 7, 16–25. doi: 10.1021/acsmacrolett.7b00879

Zuniga, J., Katsavelis, D., Peck, J., Stollberg, J., Petrykowski, M., Carson, A., et al. (2015). Cyborg beast: a low-cost 3d-printed prosthetic hand for children with upper-limb differences. *BMC Res. Notes* 8:10. doi: 10.1186/s13104-015-0971-9

Zuniga, M. J. (2018). 3D printed antibacterial prostheses. *Appl. Sci.* 8:1651. doi: 10.3390/app8091651

Conflict of Interest: The authors declare that the research was conducted in the absence of any commercial or financial relationships that could be construed as a potential conflict of interest.

frontiers in Microbiology

ORIGINAL RESEARCH
published: 09 June 2021
doi: 10.3389/fmicb.2021.645180

2-Heptylcyclopropane-1-Carboxylic Acid Disperses and Inhibits Bacterial Biofilms

Zoe L. Harrison[1†], Rukhsana Awais[1†], Michael Harris[1], Babatunde Raji[2], Brian C. Hoffman[2], Daniel L. Baker[2] and Jessica Amber Jennings[1]*

[1] Department of Biomedical Engineering, University of Memphis, Memphis, TN, United States, [2] Department of Chemistry, University of Memphis, Memphis, TN, United States

OPEN ACCESS

Edited by:
Rustam Aminov,
University of Aberdeen,
United Kingdom

Reviewed by:
Diane McDougald,
University of Technology Sydney,
Australia
Wolf-Rainer Abraham,
Helmholtz Center for Infection Research, Helmholtz Association of German Research Centers (HZ),
Germany
Shi-qi An,
University of Southampton,
United Kingdom

***Correspondence:**
Jessica Amber Jennings
jjnnings@memphis.edu

[†] These authors have contributed equally to this work and share first authorship

Specialty section:
This article was submitted to Antimicrobials, Resistance and Chemotherapy, a section of the journal Frontiers in Microbiology

Received: 22 December 2020
Accepted: 29 April 2021
Published: 09 June 2021

Citation:
Harrison ZL, Awais R, Harris M, Raji B, Hoffman BC, Baker DL and Jennings JA (2021) 2-Heptylcyclopropane-1-Carboxylic Acid Disperses and Inhibits Bacterial Biofilms. Front. Microbiol. 12:645180. doi: 10.3389/fmicb.2021.645180

Fatty-acid signaling molecules can inhibit biofilm formation, signal dispersal events, and revert dormant cells within biofilms to a metabolically active state. We synthesized 2-heptylcyclopropane-1-carboxylic acid (2CP), an analog of *cis*-2-decenoic acid (C2DA), which contains a cyclopropanated bond that may lock the signaling factor in an active state and prevent isomerization to its least active *trans*-configuration (T2DA). 2CP was compared to C2DA and T2DA for ability to disperse biofilms formed by *Staphylococcus aureus* and *Pseudomonas aeruginosa*. 2CP at 125 μg/ml dispersed approximately 100% of *S. aureus* cells compared to 25% for C2DA; both 2CP and C2DA had significantly less *S. aureus* biofilm remaining compared to T2DA, which achieved no significant dispersal. 2CP at 125 μg/ml dispersed approximately 60% of *P. aeruginosa* biofilms, whereas C2DA and T2DA at the same concentration dispersed 40%. When combined with antibiotics tobramycin, tetracycline, or levofloxacin, 2CP decreased the minimum concentration required for biofilm inhibition and eradication, demonstrating synergistic and additive responses for certain combinations. Furthermore, 2CP supported fibroblast viability above 80% for concentrations below 1 mg/ml. This study demonstrates that 2CP shows similar or improved efficacy in biofilm dispersion, inhibition, and eradication compared to C2DA and T2DA and thus may be promising for use in preventing infection for healthcare applications.

Keywords: biofilm, dispersal, *Staphylococcus aureus*, *Pseudomonas aeruginosa*, diffusible signaling factors, 2-decenoic acid, anti-biofilm agents

INTRODUCTION

A biofilm is an aggregate of microbial cells that attaches to various surfaces, including tissue and medical implants (Stoodley et al., 2013; Saeed et al., 2019). Almost 80% of human infections are caused by the development of biofilms by pathogenic bacterial strains such as *Staphylococcus aureus*, *Staphylococcus epidermis*, *Pseudomonas aeruginosa*, and *Escherichia coli* (Brady et al., 2006). The attachment of these and other bacterial strains to implant or tissue surfaces to form biofilms poses a particular risk for recurring infections, as the cells within a biofilm are resistant to both antibiotics and immune cell clearance (Bauer and Grosso, 2013). The recalcitrance of biofilms to treatment is multifactorial, owing in part to secretion of exopolymeric substances (EPS) and

alteration of the bacterial metabolic state (Flemming et al., 2016). EPS secretion enhances bacterial attachment, resistance to mechanical stresses, and facilitation of nutrient transport and may limit diffusion of antimicrobials and immune cell penetration (Molin and Tolker-Nielsen, 2003; Czaczyk and Myszka, 2007; Flemming, 2016). Immobilized subgroups of bacterial cells within the biofilm have decreased metabolic activity and can increase the minimum inhibitory concentration of antibiotics up to 1,000 times higher for biofilms compared to planktonic bacteria (Keren et al., 2004). These and other complexities associated with biofilm infections have led to extensive research of their mechanism of action and potential novel treatments.

Although current clinical treatments for biofilm infections typically include debridement of infected tissue and prescription of high-dose systemic antibiotics, there are a number of non-antibiotic methods currently being studied for their potential to prevent and treat biofilms. Some of these therapies include natural-derived molecules targeting specific aspects of the biofilm life cycle. Enzymes such as glycoside hydrolases and proteases disperse biofilm bacteria by degrading the EPS (Jennings et al., 2015). Antimicrobial peptides (AMPs) typically have cationic amphipathic structures that can disrupt bacterial cell membranes to inhibit biofilms (Batoni et al., 2016). Hydrophobic D-amino acids are secreted by bacteria prior to dispersal of biofilms and have been shown to inhibit biofilm growth *in vitro* and *in vivo*, although their mechanism of action remains unclear (Hochbaum et al., 2011). Some types of bacteria also secrete biosurfactant molecules called rhamnolipids (Nickzad and Déziel, 2014), which inhibit bacterial attachment to surfaces and trigger degradation of the EPS during dispersal. Sugar alcohols like mannitol and erythritol have been shown to stimulate metabolism of bacteria that causes awakening of dormant cells and increased susceptibility to antibiotics (Pace et al., 2019). AMPs and the sugar alcohol mannitol have been shown to eradicate both *P. aeruginosa* and *S. aureus* infections when combined with typical concentrations of antibiotics (Barraud et al., 2013; Dosler and Karaaslan, 2014; de Breij et al., 2016; Pace et al., 2019), although neither of these methods have been attempted clinically.

A class of medium-chain fatty-acid molecules has been shown to induce dispersion of preformed biofilms and inhibit biofilm formation (Davies and Marques, 2009; Ryan and Dow, 2011; Jennings et al., 2012). These specific medium-chain fatty acids are members of a family of diffusible signal factors (DSF) in bacteria. DSF are secreted by bacteria to function in cell–cell communication or quorum sensing (Solano et al., 2014). One well-studied DSF molecule is *cis*-2-decenoic acid (C2DA), which is released by *P. aeruginosa* and has been shown to inhibit biofilm formation and to disperse established biofilms of multiple strains (Davies and Marques, 2009). However, other studies have shown difficulty in reproducing these results, with less than 10% dispersion of *S. aureus* and *Acinetobacter baumannii* strains at 400 μM concentration (Su et al., 2011). It has been observed that some of these fatty-acid signaling factors revert dormant bacterial cells to a metabolically active state (Marques et al., 2014), which in combination with antimicrobials could decrease bacterial viability (Allison et al., 2011; Rahmani-Badi et al., 2014; Masters et al., 2016; Saeed et al., 2019). Moreover, these compounds have cross-kingdom efficacy in that they have been shown to inhibit and disperse biofilms formed by multiple types of microorganisms, including gram-positive bacteria, gram-negative bacteria, and fungi (Wang et al., 2004). C2DA was also shown to inhibit *S. aureus* growth at a concentration of 500 μg/ml and to prevent biofilm formation at a concentration of 125 μg/ml, with neither concentration showing cytotoxic effects in fibroblasts (Jennings et al., 2012). Dispersal and inhibition effects may be mediated by activation of gene pathways that control motility, metabolism, and persistence (Amari et al., 2013; Rahmani-Badi et al., 2015b). While mechanisms of action remain unclear (Jennings et al., 2012), recent work shows that the *cis*-conformation of this molecule increases membrane permeability and could allow for entry of more small-molecule antibiotics into the cells as compared to the less active *trans*-isomer (Masters et al., 2016).

Activity of DSF molecules appears to be dependent on the conformation of atoms around the point of unsaturation at carbon 2. *cis*-Alkenes may isomerize to *trans*- when exposed to light, elevated temperature, or radiation (Dugave and Demange, 2003). These conditions, one or more of which may be used in the fabrication and/or sterilization of medical devices or therapeutics, can lead to isomerization of the alkene portion of the fatty-acid DSF (Tipnis and Burgess, 2018). In this study, we have developed chemical routes for synthesis of a cyclopropanated analog, 2-heptylcyclopropane-1-carboxylic acid (2CP), that locks this molecule into a *cis*-like configuration. This configuration eliminates the potential for *cis*/*trans*-isomerization and oxidative degradation that is possible for C2DA when exposed to light, heat, and radiation. We evaluated the hypothesis that 2CP disperses and inhibits biofilm using *in vitro* assays of *S. aureus* and *P. aeruginosa* biofilm dispersion. These were chosen as representative specimens as *S. aureus* is a major pathogen in bone infection, and *P. aeruginosa* is prevalent in soft tissue infection; both strains selected for this study are clinically derived. We further evaluated the combination of 2CP with antibiotics to identify synergistic and additive responses through minimum biofilm inhibitory concentration (MBIC) and minimum biofilm eradication concentration (MBEC) assays compared to C2DA and T2DA. We compared compatibility with mammalian cells at concentrations active against biofilms for all three 2-decenoic acid analogs and compared preliminary stability of 2CP to C2DA in an accelerated ultraviolet light-driven degradation scenario.

MATERIALS AND METHODS

Synthesis of C2DA and 2CP

A common synthetic approach using a single starting material was used to generate C2DA *via* Jones oxidation and then Lindlar reduction, and 2CP *via* Lindlar reduction, Simmons–Smith cyclopropanation, and finally Jones oxidation (**Supplementary Figure 1**). ^{1}HNMR was performed to determine whether 2CP had been synthesized with a "*cis*-like" conformation (**Supplementary Figures 2, 3**). T2DA was purchased from Cayman Chemical and was used without purification.

Dispersion

Dispersion assays were performed to compare the dispersion activity of each analog against 7-day biofilms. 2CP (stabilized version of C2DA) was compared with C2DA (active, positive control) and T2DA (inactive/active, negative control). Each well of a 96-well plate was seeded with 150 μl of bacterial culture (*S. aureus*, UAMS-1, or *P. aeruginosa*, PA-ATCC 27317) and incubated for 7 days at 37°C to result in biofilms. Media [Tryptic Soy Broth (TSB)] was changed after careful aspiration every 24 h. On day 7, each well was again carefully aspirated and then received 195 μl of TSB and 5 μl of fatty-acid stock ranging in concentration from 0 to 500 μg/ml. Fatty-acid concentrations were made in absolute ethanol; thus, the final ethanol concentration in wells was 2.5%. The plates were incubated for 24 h at 37°C, then turbidity was measured at 540 nm. Turbidity readings were performed using a Biotek Synergy™ H1 microplate reader, with increased turbidity readings indicating a higher number of viable bacterial cells. Afterward, the media was aspirated and the plate was washed three times using phosphate-buffered saline (PBS). The relative percentage of attached cells as compared to non-treated controls were measured using BacTiter-Glo™ (Promega) Luciferase assay for ATP production, with higher percentages indicating a higher quantity of attached biofilm cells.

Inhibition

Synergy assays were performed to determine the effects of 2CP when used in combination with various antimicrobials against gram-positive *S. aureus* and gram-negative *P. aeruginosa*. Tobramycin (MP Biomedicals, Irvine, CA, United States), tetracycline (MP Biomedicals, Irvine, CA, United States), and levofloxacin (Alfa Aesar, Tewksbury, MA, United States) were chosen for evaluation based on prior work, demonstrating their synergistic effects with C2DA (Masters et al., 2016). A checkerboard assay was prepared in 96-well plates with increasing antibiotic concentration on the horizontal axis and increasing 2CP concentration on the vertical axis. Tested concentrations of 2CP, C2DA, and T2DA ranged from 0 to 4,000 μg/ml. Antibiotic concentrations tested ranged from 0 to 2,500 μg/ml. Each plate was then inoculated with *S. aureus* (UAMS-1) or *P. aeruginosa* (PA-ATCC 27317) overnight growths for a final dilution of 1 in 50 or 1 in 200, respectively, and incubated overnight. Inhibition was defined as a lack of visible growth after a 24-h incubation period.

The fractional inhibitory concentration index (FICI) was used to determine synergistic, additive, or antagonistic responses between the three antibiotics and three fatty acids. To calculate the FICI, the MIC of the antibiotic when combined with fatty acids was divided by the MIC of the antibiotic alone and added to the MIC of fatty acid when combined with antibiotics and divided by the MIC of fatty acid when applied alone (Equation 1). FICI values less than or equal to 0.5 indicate synergy, values between 0.5 and 1 indicate additivity, values between 1 and 2 indicate indifference, and values above 2 indicate antagonism (Equation 1) (European Committee for Antimicrobial Susceptibility Testing (EUCAST) of the European Society of Clinical Microbiology and Infectious Dieases (ESCMID), 2000).

$$FICI = \frac{MIC_{ABX(C)}}{MIC_{ABX(S)}} + \frac{MIC_{FA(C)}}{MIC_{FA(S)}}$$

Equation 1. FICI calculation using the concentrations of antibiotics (ABX) and fatty acids (FA) alone (S) and in combination (C).

Eradication

Bacteria (*S. aureus*, UAMS-1, or *P. aeruginosa*, PA-ATCC 27317) were grown overnight in TSB by incubation at 37°C. One milliliter of bacterial solution was diluted in 9 ml of TSB. An amount of 150 μl of the bacterial stock solution was seeded into each well of a 96-well MBEC™ Biofilm Inoculator plate, followed by overnight incubation at 37°C to form the biofilm. The next day, the medium from each well was carefully aspirated, allowing the biofilm to remain both on the pegs of the top plate and the bottom of the wells. Stocks of tobramycin, tetracycline, and levofloxacin as well as varying concentrations of C2DA, T2DA, and 2CP were added to the wells. Tested concentrations of 2CP, C2DA, and T2DA ranged from 0 to 4,000 μg/ml. Antibiotic concentrations tested ranged from 0 to 2,500 μg/ml. These plates were incubated at 37°C for 24 h. The next day, the pegged lids were removed and added to new plates containing 150 μl of sterile TSB in each well. Plates were sonicated for 5 min at 40 kHz (Fisher Scientific Ultrasonic Bath, 9.5 l) to remove the viable bacteria attached to the peg surface and then incubated for 24 h. Turbidity was measured by reading absorbance at 540 nm for bacterial growth in the presence of fixed concentrations of the antibiotics with varying concentrations of 2CP, C2DA, and T2DA. MBECs were determined by the lowest concentration that had no turbid growth after treatment and sonication.

The fractional biofilm eradication concentration (FBEC) index was used to determine synergistic, additive, or antagonistic responses between the three antibiotics and three fatty acids. The FBEC index was determined in an identical method to the FICI: the MBEC of the antibiotic when combined with fatty acids was divided by the MBEC of the antibiotic alone and added to the MBEC of fatty acid when combined with antibiotics and divided by the MBEC of fatty acid when applied alone (Equation 2). FBEC index values less than or equal to 0.5 indicate synergy, values between 0.5 and 1 indicate additivity, values between 1 and 2 indicate indifference, and values above 2 indicate antagonism.

$$FBEC = \frac{MBEC_{ABX(C)}}{MBEC_{ABX(S)}} + \frac{MBEC_{FA(C)}}{MBEC_{FA(S)}}$$

Equation 2. FBEC index calculation using the concentrations of antibiotics (ABX) and fatty acids (FA) alone (S) and in combination (C).

Cytocompatibility

NIH-3T3 fibroblasts were seeded (1×10^4 cells/cm^2) in 24-well plates in Dulbecco's modified Eagle's medium (DMEM) supplemented with 10% fetal bovine serum and 100 μg/ml Normocin (Invivogen, San Diego, CA, United States) for 24 h at 37°C and 5% CO_2. 2CP, C2DA, and T2DA were added in

varying concentrations from 0 to 1,000 μg/ml in ethanol for a final ethanol concentration of 2.5%. Controls with no ethanol addition were also used to normalize percentage viability. Plates were incubated for 24 h, after which cell viability was measured using CellTiter-Glo® (Promega, Madison, WI, United States).

Stability of C2DA and 2CP

Oxidative degradation and isomerization of C2DA and 2CP were assessed using negative-ion LC-MS to quantify the loss of each parent DSF following exposure to the photoinitiator Irgacure 2959 (Sigma-Aldrich, St. Louis, MO, United States). Aqueous solutions (10 ml total volume, 10% final methanol concentration) of C2DA and 2CP (200 ng/μl) were prepared from methanolic stocks. Irgacure was also prepared as a methanolic stock with final concentrations varying from 0, 0.05, and 0.1% (w/v). Solutions of C2DA or 2CP with and without the initiator were then exposed to UV at 365 nm for up to 4 h using a Spectrolinker XL-1500 UV crosslinker (Westbury, NY, United States). Triplicate samples (200 μl) were taken at timepoints between 0 and 240 min and were extracted by the method of Bligh and Dyer. The chloroform extracts were then dried and resuspended in 4 ml of HPLC-grade water. Samples (10 μl) were analyzed *via* negative-ion LC-ESI-MS, using a Thermo Fisher Hypersil BDS C18 column and an isocratic mobile phase of 55: 45 (v/v) methanol: aqueous ammonium hydroxide (10 μM). Peak areas for molecular anions of C2DA and 2CP were quantified using calibration curves using decanoic acid as an internal standard. The concentration of each sample was calculated, and the change in concentration of 2CP and C2DA over time was tracked.

Statistical Analysis

Statistical analysis was performed using SigmaPlot (Systat Software Inc., San Jose, CA, United States) and GraphPad Prism 7.2 software (GraphPad Software Incorporation, La Jolla, CA, United States). Data was assessed first by performing the Shapiro–Wilk normality test, followed by the Brown–Forsythe equal variance test. If both passed, data was further analyzed with one-way analysis of variance (ANOVA) followed by Holm–Sidak *post-hoc* analysis to detect significant between experimental groups ($\alpha = 0.05$). If normality and equal variance were not passed, data was analyzed using Kruskal–Wallis ANOVA on ranks, followed by the Tukey *post-hoc* test.

RESULTS

Dispersion

2CP at 125 μg/ml dispersed approximately 100% of *S. aureus* biofilms grown for 24 h, compared to wells treated with C2DA which had 75% of biofilm remaining compared to untreated controls; T2DA-treated biofilms did not show any dispersion at this concentration. At concentrations of 62.5 μg/ml and above, both 2CP and C2DA had significantly less *S. aureus* biofilm remaining in wells compared to wells treated with T2DA ($p < 0.05$), which showed no significant dispersal (**Figure 1A**) and was statistically similar to the non-ethanol control group. 2CP concentrations ranging from 15.625 to 500 μg/ml dispersed approximately 40–60% of *P. aeruginosa* biofilm, which was comparable to the dispersion activity of C2DA and T2DA at the same concentrations. Statistical differences between *P. aeruginosa* dispersion between fatty-acid analogs were only observed between 2CP and T2DA at only the 62.5-μg/ml concentration ($p > 0.05$) (**Figure 1B**).

Inhibition

The fatty-acid 2CP inhibited bacterial growth at high concentrations, inhibiting *S. aureus* at 1 mg/ml and *P. aeruginosa* growth at 4 mg/ml. Various concentrations of 2CP were shown to effectively reduce the MIC of tested antibiotics against both strains by at least 50%, with the exception of only tetracycline and *S. aureus*. Tobramycin was found to have additive effects with 2CP, C2DA, and T2DA against *S. aureus* growth, although 2CP had the lowest FICI score of 0.31, compared to 1.0 for C2DA and T2DA (**Table 1**). Tetracycline and levofloxacin were found to have additive effects with all three fatty acids against *S. aureus* growth. Similarly, tobramycin and tetracycline were additive with all three fatty acids for *P. aeruginosa* inhibition (**Table 2**). Although additive effects were found for levofloxacin combined with 2CP against *P. aeruginosa*, indifference or no effect was observed when combined with C2DA or T2DA.

Eradication

The fatty-acid 2CP was not capable of eradicating *P. aeruginosa* biofilm when applied alone but at the concentration of 1,000 μg/ml was sufficient to eradicate *S. aureus*. Various concentrations of 2CP were shown to effectively reduce the MBEC of tobramycin, tetracycline, and levofloxacin against both strains by at least 50%. Tobramycin and tetracycline were found to have additive effects with all three fatty-acid analogs against *S. aureus* growth, although combining 2CP or C2DA with levofloxacin it had synergistic effects in eradication of biofilm (**Table 3**). Tobramycin and levofloxacin were synergistic with 2CP for eradication of *P. aeruginosa* (**Table 4**). Tetracycline did not result in eradication of *P. aeruginosa* biofilm at the highest concentration studied, which could not be increased in these assays due to solubility limitations.

Cytocompatibility

2CP at concentrations at 500 μg/ml in 2.5% ethanol, as well as lower concentrations, promoted fibroblast cell viability above 70% compared to non-ethanol controls, in accordance with the ISO 109935 Biological Evaluations of Medical Devices standard when evaluating biomaterials against fibroblasts. There were no statistically significant differences in cytotoxicity between 2CP and C2DA for any concentration studied; T2DA at concentrations of 500 μg/ml had slightly more viable cells remaining compared to C2DA and 2CP but significantly lower cell viability at concentrations of 1,000 μg/ml (**Figure 2**).

Stability of 2CP and C2DA

The stability of C2DA and 2CP was determined during short-term exposure to the UV-activated photoinitiator Irgacure 2959. This system was used to mimic both oxidative degradation and

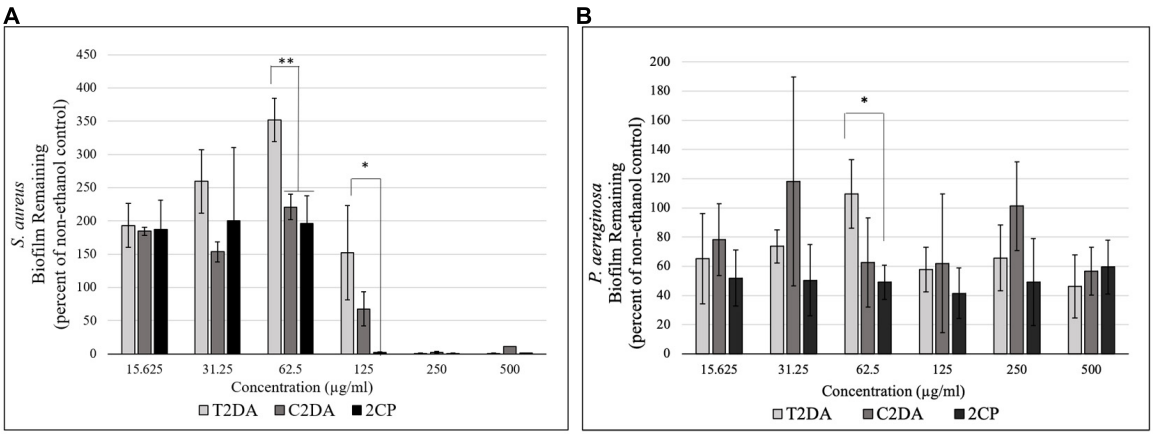

FIGURE 1 | Graph showing the percentage of **(A)** *S. aureus* and **(B)** *P. aeruginosa* biofilm remaining after 1 h of exposure to T2DA, C2DA, and 2CP. Asterisks represent significantly less biofilm remaining compared to T2DA (*$p < 0.05$, **$p < 0.01$), detected by one-way ANOVA with the Holm–Sidak *post-hoc* test. Data represent mean ± standard deviation.

TABLE 1 | *S. aureus* fractional inhibitory concentration index values.

	MBIC for 2CP (alone) (μg/ml)	MBIC for 2CP (combined) (μg/ml)	MBIC for antibiotic (alone) (μg/ml)	MBIC for antibiotic (combined) (μg/ml)	FICI	Interpretation
S. aureus						
Tobramycin	1000.0	31	4.0	2.0	0.531	Additive
Tetracycline	1000.0	63	1.0	1.0	1.06	Indifferent
Levofloxacin	1000.0	500	1.0	0.3	0.8	Additive
	MBIC for C2DA (alone) (μg/ml)	**MBIC for C2DA (combined) (μg/ml)**	**MBIC for antibiotic (alone) (μg/ml)**	**MBIC for antibiotic (combined) (μg/ml)**	**FICI**	**Interpretation**
Tobramycin	1000.0	500	4.0	2.0	1.0	Additive
Tetracycline	1000.0	250	1.0	0.5	0.75	Additive
Levofloxacin	1000.0	250	1.0	0.5	0.75	Additive
	MBIC for T2DA (alone) (μg/ml)	**MBIC for T2DA (combined) (μg/ml)**	**MBIC for antibiotic (alone) (μg/ml)**	**MBIC for antibiotic (combined) (μg/ml)**	**FICI**	**Interpretation**
Tobramycin	1000.0	500	4.0	2.0	1.0	Additive
Tetracycline	1000.0	250	1.0	0.5	0.75	Additive
Levofloxacin	1000.0	250	1.0	0.5	0.75	Additive

Minimum biofilm inhibitory concentration (MBIC) for 2CP, C2DA, and T2DA against S. aureus when treated alone or combined with tobramycin, tetracycline, or levofloxacin. MBIC of each antibiotic against S. aureus alone is also included. These values were used in Equation 1 to determine the fractional inhibitory concentration index for each fatty acid/antibiotic combination. FICI values less than or equal to 0.5 indicate synergy, values between 0.5 and 1 indicate additivity, values between 1 and 2 indicate indifference, and values above 2 indicate antagonism.

UV-induced isomerization of the *cis*-alkene in C2DA. C2DA was completely consumed by the combination of UV and initiator (0.05% Irgacure, half-life ∼20 min, complete degradation by 60 min, 0.1% Irgacure half-life ∼10 min, complete degradation by 30 min) (**Figure 3**). C2DA showed no degradation to UV alone out to 4 h of exposure. In contrast, 2CP showed no degradation to either UV alone or UV plus initiator out to 4 h.

DISCUSSION

A synthetic strategy for reliable synthesis of C2DA, T2DA, and 2CP is demonstrated using a combination of Lindlar reduction, Jones oxidation, and cyclopropanation to make all three targets. Our work demonstrates increased activity against *S. aureus* with a cyclopropyl isostere replacing the double bond to attain structural similarity. Chemical mimics or analogs of fatty acids like 2CP may be used in therapeutics for prevention or treatment of biofilm-based infections (Davies and Marques, 2009). Delivered locally or applied topically, 2CP may inhibit formation of biofilms or increase eradication of biofilms on implants or tissue, especially when combined with antibiotic administration. The cyclopropanated analogs have reduced isomerization and degradation when exposed to UV in the presence of a photoinitiator and thus may have better shelf stability. Further, as 2CP is an analog of natural diffusible

TABLE 2 | *P. aeruginosa* fractional inhibitory concentration index values.

	MBIC for 2CP (alone) (μg/ml)	MBIC for 2CP (combined) (μg/ml)	MBIC for antibiotic (alone) (μg/ml)	MBIC for antibiotic (combined) (μg/ml)	FICI	Interpretation
P. aeruginosa						
Tobramycin	4,000	31	0.5	0.25	0.508	Additive
Tetracycline	4,000	1,000	32	16	0.75	Additive
Levofloxacin	4,000	1,000	4.0	2	0.75	Additive
	MBIC for C2DA (alone) (μg/ml)	**MBIC for C2DA (combined) (μg/ml)**	**MBIC for antibiotic (alone) (μg/ml)**	**MBIC for antibiotic (combined) (μg/ml)**	**FICI**	**Interpretation**
Tobramycin	4,000	125	0.5	0.25	0.531	Additive
Tetracycline	4,000	500	32	16	0.625	Additive
Levofloxacin	4,000	4,000	4.0	4.0	2.0	Indifferent
	MBIC for T2DA (alone) (μg/ml)	**MBIC for T2DA (combined) (μg/ml)**	**MBIC for antibiotic (alone) (μg/ml)**	**MBIC for antibiotic (combined) (μg/ml)**	**FICI**	**Interpretation**
Tobramycin	4,000	125	0.5	0.3	0.631	Additive
Tetracycline	4,000	1,000	32	16	0.75	Additive
Levofloxacin	4,000	4,000	4.0	4.0	2.0	Indifferent

Minimum biofilm inhibitory concentration (MBIC) for 2CP, C2DA, and T2DA against P. aeruginosa when treated alone or combined with tobramycin, tetracycline, or levofloxacin. MBIC of each antibiotic against P. aeruginosa alone is also included. These values were used in Equation 1 to determine the fractional inhibitory concentration index for each fatty acid/antibiotic combination. FICI values less than or equal to 0.5 indicate synergy, values between 0.5 and 1 indicate additivity, values between 1 and 2 indicate indifference, and values above 2 indicate antagonism.

TABLE 3 | *S. aureus* FBEC index values.

	MBEC for 2CP (alone) (μg/ml)	MBEC for 2CP (combined) (μg/ml)	MBEC for antibiotic (alone) (μg/ml)	MBEC for antibiotic (combined) (μg/ml)	FBEC	Interpretation
S. aureus						
Tobramycin	1,000	31.25	2.5	1.25	0.531	Additive
Tetracycline	1,000	125	1.25	0.625	0.625	Additive
Levofloxacin	1,000	250	1	0.25	0.5	Synergistic
	MBEC for C2DA (alone) (μg/ml)	**MBEC for C2DA (combined) (μg/ml)**	**MBEC for antibiotic (alone) (μg/ml)**	**MBEC for antibiotic (combined) (μg/ml)**	**FBEC**	**Interpretation**
Tobramycin	1,000	125	2.5	1.25	0.625	Additive
Tetracycline	1,000	500	1	0.25	0.75	Additive
Levofloxacin	1,000	125	1	0.25	0.375	Synergistic
	MBEC for T2DA (alone) (μg/ml)	**MBEC for T2DA (combined) (μg/ml)**	**MBEC for antibiotic (alone) (μg/ml)**	**MBEC for antibiotic (combined) (μg/ml)**	**FBEC**	**Interpretation**
Tobramycin	1,000	125	2.5	1.25	0.625	Additive
Tetracycline	1,000	500	1	0.25	0.75	Additive
Levofloxacin	1,000	500	1	0.25	0.75	Additive

Minimum biofilm eradication concentration (MBEC) for 2CP, C2DA, and T2DA against S. aureus biofilm when treated alone or combined with tobramycin, tetracycline, or levofloxacin. MBEC of each antibiotic against S. aureus alone is also included. These values were used in Equation 2 to determine the fractional inhibitory concentration index for each fatty acid/antibiotic combination. FBEC index values less than or equal to 0.5 indicate synergy, values between 0.5 and 1 indicate additivity, values between 1 and 2 indicate indifference, and values above 2 indicate antagonism.

signaling factor molecules, presence of this fatty acid is not likely to drive bacterial resistance due to selective pressure, although this has not been evaluated in the current study.

The tolerance of biofilms to antimicrobials and persistence of biofilm infections can cause unique challenges for the treatment of infections. Numerous methods are adopted for the disruption, inhibition, and eradication of biofilms. 2CP showed dispersal of biofilms, although at higher concentrations than were observed in studies of C2DA by Davies and Marques (2009). Potential reasons for these discrepancies may include use of different commercial suppliers or synthetic routes. C2DA isolated from biological spent media may also be enantiopure, which may explain the higher activity of chloroform-extracted media used in studies by Davies and Marques (2009). We are currently working to separate the two 2CP enantiomers *via* conversion to diastereomeric analogs using chiral alcohols, although this work was done

TABLE 4 | *P. aeruginosa* fractional eradication concentration index values.

	MBEC for 2CP (alone) (μg/ml)	MBEC for 2CP (combined) (μg/ml)	MBEC for antibiotic (alone) (μg/ml)	MBEC for antibiotic (combined) (μg/ml)	FBEC	Interpretation
P. aeruginosa						
Tobramycin	>4,000	250	500	150	0.363	Synergistic
Tetracycline	>4,000	ND	ND	ND	ND	ND
Levofloxacin	>4,000	250	312	78	0.313	Synergistic
	MBEC for C2DA (alone) (μg/ml)	**MBEC for C2DA (combined) (μg/ml)**	**MBEC for antibiotic (alone) (μg/ml)**	**MBEC for antibiotic (combined) (μg/ml)**	**FBEC**	**Interpretation**
Tobramycin	>4,000	250	2500	625	0.313	Synergistic
Tetracycline	>4,000	ND	ND	ND	ND	ND
Levofloxacin	>4,000	500	312	78	0.375	Synergistic
	MBEC for T2DA (alone) (μg/ml)	**MBEC for T2DA (combined) (μg/ml)**	**MBEC for antibiotic (alone) (μg/ml)**	**MBEC for antibiotic (combined) (μg/ml)**	**FBEC**	**Interpretation**
Tobramycin	>4,000	250	2,500	625	0.313	Synergistic
Tetracycline	>4,000	ND	ND	ND	ND	ND
Levofloxacin	>4,000	500	312	78	0.375	Synergistic

Minimum biofilm eradication concentration (MBEC) for 2CP, C2DA, and T2DA against P. aeruginosa biofilm when treated alone or combined with tobramycin, tetracycline, or levofloxacin. MBEC of each antibiotic against P. aeruginosa alone is also included. These values were used in Equation 2 to determine the fractional inhibitory concentration index for each fatty acid/antibiotic combination. FBEC index values less than or equal to 0.5 indicate synergy, values between 0.5 and 1 indicate additivity, values between 1 and 2 indicate indifference, and values above 2 indicate antagonism.

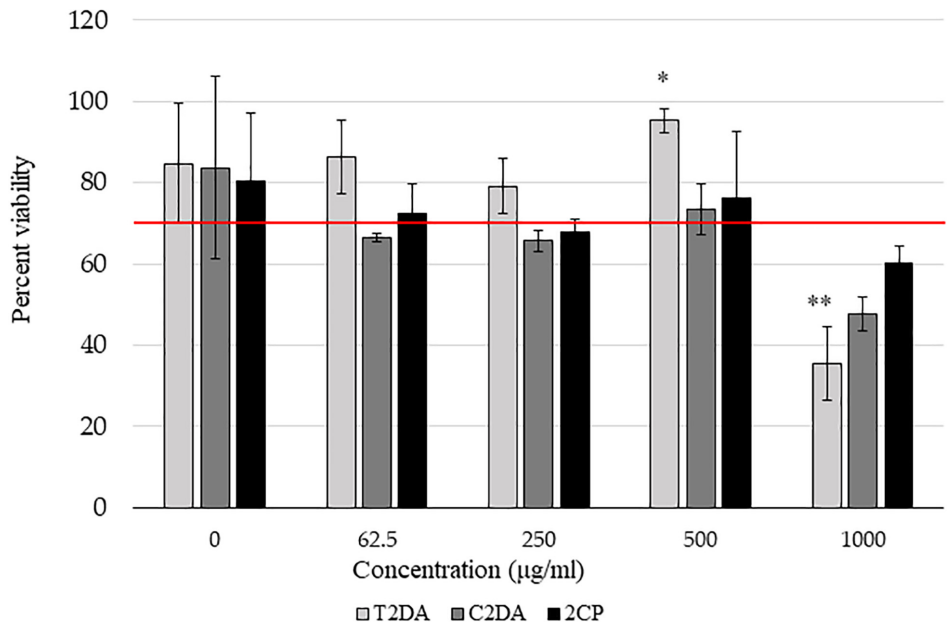

FIGURE 2 | NIH-3T3 cytocompatibility assay results showing the percentage of viable cells compared to non-ethanol controls 24 h after addition of fatty acids. Asterisks represent significant differences between the other groups (*$p < 0.05$, **$p < 0.01$), detected by one-way ANOVA with the Holm–Sidak *post-hoc* tests. Data represent mean ± standard deviation.

using the racemic mixture. Furthermore, methods to quantify biofilms vary greatly between previous studies, which may further explain differences seen in effective concentrations. Rahmani-Badi et al. observed two- to three-fold increases in the number of planktonic cells of mixed species biofilms after treatment with 310 nM C2DA in models of catheter infection and dental plaque removal (Rahmani-Badi et al., 2014, 2015a). The activity of the *trans*-isomer against *P. aeruginosa* is consistent with studies by Davies et al. where T2DA showed dispersal activity in the concentration range reported here, although the C2DA analog dispersed biofilms at a much lower concentration (Davies and Marques, 2009). T2DA is also known as a Streptococcal DSF (SDSF), produced by *Streptococcus mutans* with inhibitory effects on fungal hyphae (Vílchez et al., 2010).

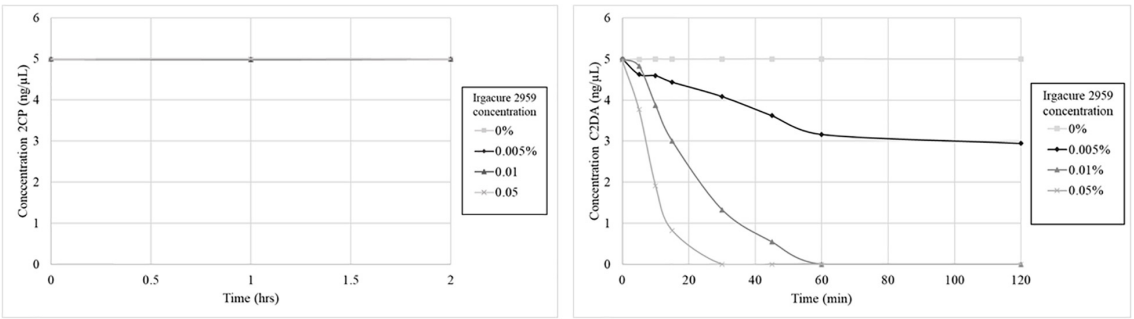

FIGURE 3 | Graphs show 2CP (left) and C2DA (right) short term solution stability over time (4 h total, 2 h shown) and concentration dependence of DSF stability when challenged with UV and the photoinitiator Irgacure.

DSF molecules are known to have mechanisms of action that differ between strains at least in the site of action, external or internal to the cell. In *Xanthomonas* and *Pseudomonas*, DSF binds to specific transmembrane protein receptors and activates genetic transcription (Van Houdt and Michiels, 2010; Rahmani-Badi et al., 2015b; Ryan et al., 2015; Suppiger et al., 2016). In *Burkholderia cenocepacia*, DSF diffuse across the membrane to bind to cytosolic proteins to activate transcriptional changes (Suppiger et al., 2016). Cui et al. (2019) developed a DSF analog that was capable of interfering with *Burkholderia cenocepacia* quorum sensing and virulence, demonstrating its potential as a novel antibacterial agent. Similarly, Huedo et al. (2019) developed DSF that could interfere with quorum sensing of both *Stenotrophomonas maltophilia* and *Burkholderia cepacia*. Su et al. (2011) synthesized 4,5-disubstituted-2-aminoimidazole-triazole conjugates that inhibited *S. aureus* at micromolar concentrations and *Acinetobacter baumannii* at slightly higher concentrations, with dispersal and inhibition activity two orders of magnitude greater than C2DA. While mechanisms of action for DSF are not entirely elucidated, our cyclopropyl analog has a similar structure to C2DA and other DSF molecules and thus may have similar biological interactions with receptors and cell membranes. In one dispersal study, Rahmani-Badi et al. (2015b) have identified protein transcription changes occurring in *P. aeruginosa* upon stimulation with C2DA, identifying a cluster of genes implicated in sensing and responding to fatty-acid signals, including regulation of pathogenicity factor (rpf) proteins. It has also been shown that the histidine kinase PA1396 in *P. aeruginosa* is a major factor in DSF function; certain DSF analogs are able to block the ability of PA1396 to autophosphorylate, which subsequently reduces biofilm formation and antibiotic tolerance both *in vitro* and *in vivo* (An et al., 2019). Previous research has also demonstrated that C2DA increased membrane permeability of *P. aeruginosa* and *S. aureus* (Masters et al., 2016), which may occur by substitution of membrane phospholipids by fatty acid or by stimulating proton-motive force at the membrane (Meylan et al., 2017). Compared to enzymatic dispersal agents such as enzymatic hydrolases that degrade the EPS matrix (Fleming et al., 2017), 2-decenoic acid analogs appear to act at the cellular level and do not directly affect EPS (Marques et al., 2015).

In order to have clinical relevance as a prophylactic agent, biofilm inhibitors should also prevent planktonic bacterial growth and attachment to surfaces. Previous work has shown that C2DA has additive or synergistic growth- and biofilm-inhibitory effects with many common antibiotics including vancomycin, linezolid, tetracycline, amikacin, and ciprofloxacin (Marques et al., 2015; Masters et al., 2016; Harris et al., 2017). The present study indicates that 2CP maintains additive or synergistic effects with these antibiotics against both gram-positive and gram-negative pathogens. Similar results have been observed with drugs that target quorum sensing pathways, thereby keeping bacteria in the more susceptible planktonic state (Christensen et al., 2012; Yang et al., 2012; Roy et al., 2013). C2DA, T2DA, and the synthetic analog 2CP may be advantageous compared to antibiotic drugs because they are a natural part of the biofilm regulatory process, thereby reducing the risk of pathogens acquiring resistance (Rahmani-Badi et al., 2015b). While it has not been determined whether combining 2-decenoic acids or their analogs decrease or increase the likelihood of antimicrobial resistance, combinatorial effects should improve the efficacy of prophylactic antibiotic therapy by preventing bacterial attachment and reducing the amount of drug needed for bacterial clearance. The tobramycin–2CP combination is especially promising due to the low concentration of 2CP needed for inhibition or eradication of both bacterial strains, as well as the prevalence of tobramycin in many current local drug delivery systems.

Use of biofilm dispersal agents in the absence of antimicrobials could lead to negative effects on the host, including seeding of further infection sites and septicemia (Fleming and Rumbaugh, 2018). The present study found that 2CP increased susceptibility of established biofilms to eradication by antimicrobials, which may be due to its activity in stimulating dormant bacterial cell metabolism, which plays a major role in the antimicrobial tolerance of bacteria within biofilms (Del Pozo and Patel, 2007). Although the current study did not specifically select for persister cell populations, studies of C2DA have shown that it can revert persister cell status by increasing the respiratory activity of the cells (Marques et al., 2014). Studies by Marques et al. also demonstrated that in contrast with other metabolites such as sugars that awaken persister cells (Allison et al., 2011),

C2DA is not used by bacteria as a carbon source for growth (Marques et al., 2014). The 2CP analog would not be expected to be utilized as a carbon source and further would have increased structural stability that would improve long-term storage and sterilization for healthcare applications. Biomaterial systems for co-delivery of antimicrobials and fatty-acid biofilm-disrupting agents have included direct application (Sepehr et al., 2014), biopolymer particles or sponges (Jennings et al., 2012), or implant coatings (Harris et al., 2017). While we did not study persister phenotypes specifically, future studies may explore the effects of this molecule on persisters.

For healthcare applications, targeting biofilm disruption without adverse effects on tissue is critical for the development of therapeutics for treating biofilm-based infection. We observed that the cyclopropyl moiety did not change the biocompatibility profile, with similar results to previous evaluations of cellular viability responses (Jennings et al., 2012; Rawson et al., 2014). A limitation of the current study is the use of a fibroblast cell line for preliminary evaluation of biocompatibility. Other studies of bone cell lines have shown that below certain concentration thresholds, fatty-acid biofilm inhibitors did not interfere with bone cell viability or mineralization (Harris et al., 2017). In an *in vivo* evaluation or orthopedic infection, a similar molecule C2DA applied to implants in phosphatidylcholine coatings was found to inhibit biofilm formation and no adverse events or increased inflammation in tissue were observed (Harris et al., 2017). Our preliminary stability evaluation indicates that 2CP is stable in environmental extremes, which may be favorable for sterilization or incorporation into controlled delivery systems. Longer-term and milder degradation experiments are currently underway to confirm enhanced the shelf stability of 2CP. Expanded preclinical evaluations, including studies on inflammatory cell effects, bone cell response, and *in vivo* infection models, are needed to fully evaluate the potential of 2CP as a clinical therapeutic. Another limitation of this study is the use of microtiter plate-based assays; while they were adequate for this pilot study, future studies will include additional biofilm assays to confirm results, in addition to experiments that may specifically identify effects of 2CP on gene expression and phenotype as well as sensing mechanisms for different bacteria. Evaluation of 2CP activity in dynamic conditions such as bioreactor culture could complement these results. While this study established preliminary efficacy against two representative strains of bacteria, future studies may also incorporate mixed cultures of different strains of bacteria as well as fungi.

We have demonstrated a successful synthetic route for cyclopropanated analogs of 2-decenoic acid, replacing the double bond in *cis*-configuration with a cyclopropyl ring. This analog had similar or improved bioactivity in biofilm dispersal, inhibition, and eradication. Additive and synergistic effects when 2CP is combined with antimicrobials may be clinically useful in applications to treat implant-associated infection, dental plaque removal, or surface decontamination. Future work will explore methods for sustained delivery, evaluate long-term stability and activity, and expand preclinical investigations to determine potential as a clinical therapeutic.

DATA AVAILABILITY STATEMENT

The raw data supporting the conclusions of this article will be made available by the authors, without undue reservation.

AUTHOR CONTRIBUTIONS

JJ and DB conceived this idea and determined the methodology. BR synthesized the fatty acids and performed the chemical analysis and validation. ZH, RA, and MH conducted the biofilm studies and performed the bacteriological analysis. BH performed the stability evaluation and all authors contributed to the original draft preparation. ZH, JJ, and DB reviewed and edited the final forms of this manuscript. JJ and DB acquired the funding, were administrators of this project, and supervised the other authors.

FUNDING

This research was supported by the FedEx Institute of Technology with a development grant under award no. 241109 and the National Institute of Arthritis and Musculoskeletal and Skin Disease of the National Institute of Health (NIH) under award no. R01 AR066050.

ACKNOWLEDGMENTS

We acknowledge the assistance of Landon Choi, Emily Coleman, and Stasianne Mallin in performing the laboratory experiments.

SUPPLEMENTARY MATERIAL

The Supplementary Material for this article can be found online at: https://www.frontiersin.org/articles/10.3389/fmicb.2021.645180/full#supplementary-material

REFERENCES

Allison, K. R., Brynildsen, M. P., and Collins, J. J. (2011). Metabolite-enabled eradication of bacterial persisters by aminoglycosides. *Nature* 473, 216–220. doi: 10.1038/nature10069

Amari, D. T., Marques, C. N., and Davies, D. G. (2013). The putative enoyl-coenzyme a hydratase DspI is required for production of the *Pseudomonas aeruginosa* biofilm dispersion autoinducer cis-2-decenoic acid. *J. Bacteriol.* 195, 4600–4610. doi: 10.1128/jb.00707-13

An, S.-Q., Murtagh, J., Twomey, K. B., Gupta, M. K., O'Sullivan, T. P., Ingram, R., et al. (2019). Modulation of antibiotic sensitivity and biofilm formation in *Pseudomonas aeruginosa* by interspecies signal analogues. *Nat.Commun.* 10:2334.

Barraud, N., Buson, A., Jarolimek, W., and Rice, S. A. (2013). Mannitol enhances antibiotic sensitivity of persister bacteria in *Pseudomonas aeruginosa* biofilms. *PLoS One* 8:e84220. doi: 10.1371/journal.pone.0084220

Batoni, G., Maisetta, G., and Esin, S. (2016). Antimicrobial peptides and their interaction with biofilms of medically relevant bacteria. *Biochim. Biophys. Acta* 1858, 1044–1060. doi: 10.1016/j.bbamem.2015.10.013

Bauer, T., and Grosso, M. (2013). The basic science of biofilm and its relevance to the treatment of periprosthetic joint infection. *Orthop. Knowl. Online J.* 11, 12–20.

Brady, R. A., Leid, J. G., Camper, A. K., Costerton, J. W., and Shirtliff, M. E. (2006). Identification of *Staphylococcus aureus* proteins recognized by the antibody-mediated immune response to a biofilm infection. *Infection Immun.* 74, 3415–3426. doi: 10.1128/iai.00392-06

Christensen, L. D., van Gennip, M., Jakobsen, T. H., Alhede, M., Hougen, H. P., Høiby, N., et al. (2012). Synergistic antibacterial efficacy of early combination treatment with tobramycin and quorum-sensing inhibitors against *Pseudomonas aeruginosa* in an intraperitoneal foreign-body infection mouse model. *J. Antimicrob. Chemother.* 67, 1198–1206. doi: 10.1093/jac/dks002

Cui, C., Song, S., Yang, C., Sun, X., Huang, Y., Li, K., et al. (2019). Disruption of quorum sensing and virulence in *Burkholderia cenocepacia* by a structural analogue of the cis-2-dodecenoic acid signal. *Appl. Environ. Microbiol.* 85, e00105–e00119.

Czaczyk, K., and Myszka, K. (2007). Biosynthesis of extracellular polymeric substances (EPS) and its role in microbial biofilm formation. *Pol. J. Environ. Stud.* 16, 799–806.

Davies, D. G., and Marques, C. N. (2009). A fatty acid messenger is responsible for inducing dispersion in microbial biofilms. *J. Bacteriol.* 191, 1393–1403. doi: 10.1128/jb.01214-08

de Breij, A., Riool, M., Kwakman, P. H., de Boer, L., Cordfunke, R. A., Drijfhout, J. W., et al. (2016). Prevention of *Staphylococcus aureus* biomaterial-associated infections using a polymer-lipid coating containing the antimicrobial peptide OP-145. *J. Control. Release* 222, 1–8. doi: 10.1016/j.jconrel.2015.12.003

Del Pozo, J., and Patel, R. (2007). The challenge of treating biofilm—associated bacterial infections. *Clin. Pharmacol. Ther.* 82, 204–209. doi: 10.1038/sj.clpt.6100247

Dosler, S., and Karaaslan, E. (2014). Inhibition and destruction of *Pseudomonas aeruginosa* biofilms by antibiotics and antimicrobial peptides. *Peptides* 62, 32–37. doi: 10.1016/j.peptides.2014.09.021

Dugave, C., and Demange, L. (2003). Cis- trans isomerization of organic molecules and biomolecules: implications and applications. *Chem. Rev.* 103, 2475–2532. doi: 10.1021/cr0104375

European Committee for Antimicrobial Susceptibility Testing (EUCAST) of the European Society of Clinical Microbiology and Infectious Dieases (ESCMID). (2000). Terminology relating to methods for the determination of susceptibility of bacteria to antimicrobial agents. *Clin. Microbiol. Infect.* 6, 503–508. doi: 10.1046/j.1469-0691.2000.00149.x

Fleming, D., and Rumbaugh, K. (2018). The consequences of biofilm dispersal on the host. *Sci. Rep.* 8:10738.

Fleming, G., Aveyard, J., Fothergill, J. L., McBride, F., Raval, R., and D'Sa, R. A. (2017). Nitric oxide releasing polymeric coatings for the prevention of biofilm formation. *Polymers* 9:601. doi: 10.3390/polym9110601

Flemming, H.-C. (2016). "The perfect slime–and the 'dark matter'of biofilms," in *The Perfect Slime: Microbial Extracellular Polymeric Substances*, eds H.-C. Flemming, T. R. Neu, and J. Wingender (Heidelberg, NY: Springer), 1–14.

Flemming, H.-C., Wingender, J., Szewzyk, U., Steinberg, P., Rice, S. A., and Kjelleberg, S. (2016). Biofilms: an emergent form of bacterial life. *Nat. Rev. Microbiol.* 14, 563–567. doi: 10.1038/nrmicro.2016.94

Harris, M. A., Beenken, K. E., Smeltzer, M. S., Haggard, W. O., and Jennings, J. A. (2017). Phosphatidylcholine coatings deliver local antimicrobials and reduce infection in a murine model: a preliminary study. *Clin. Orthop. Relat. Res.* 475, 1847–1853. doi: 10.1007/s11999-016-5211-7

Hochbaum, A. I., Kolodkin-Gal, I., Foulston, L., Kolter, R., Aizenberg, J., and Losick, R. (2011). Inhibitory effects of D-amino acids on *Staphylococcus aureus* biofilm development. *J. Bacteriol.* 193, 5616–5622. doi: 10.1128/jb.05534-11

Huedo, P., Kumar, V. P., Horgan, C., Yero, D., Daura, X., Gibert, I., et al. (2019). Sulfonamide-based diffusible signal factor analogs interfere with quorum sensing in Stenotrophomonas maltophilia and Burkholderia cepacia. *Future Med. Chem.* 11, 1565–1582. doi: 10.4155/fmc-2019-0015

Jennings, J. A., Courtney, H. S., and Haggard, W. O. (2012). Cis-2-decenoic acid inhibits *S. aureus* growth and biofilm in vitro: a pilot study. *Clin. Orthop. Relat. Res.* 470, 2663–2670. doi: 10.1007/s11999-012-2388-2

Jennings, L. K., Storek, K. M., Ledvina, H. E., Coulon, C., Marmont, L. S., Sadovskaya, I., et al. (2015). Pel is a cationic exopolysaccharide that cross-links extracellular DNA in the *Pseudomonas aeruginosa* biofilm matrix. *Proc. Natl. Acad. Sci.* 112, 11353–11358. doi: 10.1073/pnas.1503058112

Keren, I., Kaldalu, N., Spoering, A., Wang, Y., and Lewis, K. (2004). Persister cells and tolerance to antimicrobials. *FEMS Microbiol. Lett.* 230, 13–18. doi: 10.1016/s0378-1097(03)00856-5

Marques, C. N., Davies, D. G., and Sauer, K. (2015). Control of biofilms with the fatty acid signaling molecule cis-2-decenoic acid. *Pharmaceuticals* 8, 816–835. doi: 10.3390/ph8040816

Marques, C. N., Morozov, A., Planzos, P., and Zelaya, H. M. (2014). The fatty acid signaling molecule cis-2-decenoic acid increases metabolic activity and reverts persister cells to an antimicrobial-susceptible state. *Appl. Environ. Microbiol.* 80, 6976–6991. doi: 10.1128/aem.01576-14

Masters, E., Harris, M., and Jennings, J. (2016). Cis-2-decenoic acid interacts with bacterial cell membranes to potentiate additive and synergistic responses against biofilm. *J. Bacteriol. Mycol.* 3, 1031–1038.

Meylan, S., Porter, C. B., Yang, J. H., Belenky, P., Gutierrez, A., Lobritz, M. A., et al. (2017). Carbon sources tune antibiotic susceptibility in *Pseudomonas aeruginosa* via tricarboxylic acid cycle control. *Cell Chem. Biol.* 24, 195–206. doi: 10.1016/j.chembiol.2016.12.015

Molin, S., and Tolker-Nielsen, T. (2003). Gene transfer occurs with enhanced efficiency in biofilms and induces enhanced stabilisation of the biofilm structure. *Curr. Opin. Biotechnol.* 14, 255–261. doi: 10.1016/s0958-1669(03)00036-3

Nickzad, A., and Déziel, E. (2014). The involvement of rhamnolipids in microbial cell adhesion and biofilm development–an approach for control? *Lett. Appl. Microbiol.* 58, 447–453. doi: 10.1111/lam.12211

Pace, L. R., Harrison, Z. L., Brown, M. N., Haggard, W. O., and Jennings, J. A. (2019). Characterization and anti-biofilm activity of mannitol-chitosan blended paste for local antibiotic delivery system. *Mar. Drugs* 17:517. doi: 10.3390/md17090517

Rahmani-Badi, A., Sepehr, S., and Babaie-Naiej, H. (2015a). A combination of cis-2-decenoic acid and chlorhexidine removes dental plaque. *Arch. Oral Biol.* 60, 1655–1661. doi: 10.1016/j.archoralbio.2015.08.006

Rahmani-Badi, A., Sepehr, S., Fallahi, H., and Heidari-Keshel, S. (2015b). Dissection of the cis-2-decenoic acid signaling network in *Pseudomonas aeruginosa* using microarray technique. *Front. Microbiol.* 6:383. doi: 10.3389/fmicb.2015.00383

Rahmani-Badi, A., Sepehr, S., Mohammadi, P., Soudi, M. R., Babaie-Naiej, H., and Fallahi, H. (2014). A combination of cis-2-decenoic acid and antibiotics eradicates pre-established catheter-associated biofilms. *J. Med. Microbiol.* 63, 1509–1516. doi: 10.1099/jmm.0.075374-0

Rawson, M., Haggard, W., and Jennings, J. A. (2014). Osteocompatibility of biofilm inhibitors. *Open Orthop. J.* 8, 442. doi: 10.2174/1874325001408010442

Roy, V., Meyer, M. T., Smith, J. A., Gamby, S., Sintim, H. O., Ghodssi, R., et al. (2013). AI-2 analogs and antibiotics: a synergistic approach to reduce bacterial biofilms. *Appl. Microbiol. Biotechnol.* 97, 2627–2638. doi: 10.1007/s00253-012-4404-6

Ryan, R. P., An, S. Q., Allan, J. H., McCarthy, Y., and Dow, J. M. (2015). The DSF family of cell-cell signals: an expanding class of bacterial virulence regulators. *PLoS Pathog.* 11:e1004986. doi: 10.1371/journal.ppat.1004986

Ryan, R. P., and Dow, J. M. (2011). Communication with a growing family: diffusible signal factor (DSF) signaling in bacteria. *Trends Microbiol.* 19, 145–152. doi: 10.1016/j.tim.2010.12.003

Saeed, K., McLaren, A. C., Schwarz, E. M., Antoci, V., Arnold, W. V., Chen, A. F., et al. (2019). 2018 international consensus meeting on musculoskeletal infection: summary from the biofilm workgroup and consensus on biofilm related musculoskeletal infections. *J. Orthop. Res.* 37, 1007–1017. doi: 10.1002/jor.24229

Sepehr, S., Rahmani-Badi, A., Babaie-Naiej, H., and Soudi, M. R. (2014). Unsaturated fatty acid, cis-2-decenoic acid, in combination with disinfectants or antibiotics removes pre-established biofilms formed by food-related bacteria. *PLoS ONE* 9:e101677. doi: 10.1371/journal.pone.0101677

Solano, C., Echeverz, M., and Lasa, I. (2014). Biofilm dispersion and quorum sensing. *Curr. Opin. Microbiol.* 18, 96–104. doi: 10.1016/j.mib.2014.02.008

Stoodley, P., Hall-Stoodley, L., Costerton, B., DeMeo, P., Shirtliff, M., Gawalt, E., et al. (2013). "5 – biofilms, biomaterials, and device-related infections," in *Handbook of Polymer Applications in Medicine and Medical Devices*, eds K. Modjarrad and S. Ebnesajjad (Oxford: William Andrew Publishing), 77–101.

Su, Z., Peng, L., Worthington, R. J., and Melander, C. (2011). Evaluation of 4,5-disubstituted-2-aminoimidazole-triazole conjugates for antibiofilm/antibiotic resensitization activity against MRSA and *Acinetobacter baumannii*. *Chemmedchem* 6, 2243–2251. doi: 10.1002/cmdc.201100316

Suppiger, A., Aguilar, C., and Eberl, L. (2016). Evidence for the widespread production of DSF family signal molecules by members of the genus *Burkholderia* by the aid of novel biosensors. *Environ. Microbiol. Rep.* 8, 38–44. doi: 10.1111/1758-2229.12348

Tipnis, N. P., and Burgess, D. J. (2018). Sterilization of implantable polymer-based medical devices: a review. *Int. J. Pharm.* 544, 455–460.

Van Houdt, R., and Michiels, C. W. (2010). Biofilm formation and the food industry, a focus on the bacterial outer surface. *J. Appl. Microbiol.* 109, 1117–1131. doi: 10.1111/j.1365-2672.2010.04756.x

Vílchez, R., Lemme, A., Ballhausen, B., Thiel, V., Schulz, S., Jansen, R., et al. (2010). Streptococcus mutans inhibits Candida albicans hyphal formation by the fatty acid signaling molecule trans−2−decenoic acid (SDSF). *Chembiochem* 11, 1552–1562. doi: 10.1002/cbic.201000086

Wang, L. H., He, Y., Gao, Y., Wu, J. E., Dong, Y. H., He, C., et al. (2004). A bacterial cell–cell communication signal with cross−kingdom structural analogues. *Mol. Microbiol.* 51, 903–912. doi: 10.1046/j.1365-2958.2003.03883.x

Yang, Y.-X., Xu, Z.-H., Zhang, Y.-Q., Tian, J., Weng, L.-X., and Wang, L.-H. (2012). A new quorum-sensing inhibitor attenuates virulence and decreases antibiotic resistance in *Pseudomonas aeruginosa*. *J. Microbiol.* 50, 987–993. doi: 10.1007/s12275-012-2149-7

Conflict of Interest: The authors declare that the research was conducted in the absence of any commercial or financial relationships that could be construed as a potential conflict of interest.

frontiers in Microbiology

ORIGINAL RESEARCH
published: 21 June 2021
doi: 10.3389/fmicb.2021.662149

One-Pot Microwave-Assisted Synthesis of Carbon Dots and *in vivo* and *in vitro* Antimicrobial Photodynamic Applications

María Paulina Romero[1,2], Fernanda Alves[1], Mirian Denise Stringasci[1], Hilde Harb Buzzá[1], Heloísa Ciol[1], Natalia Mayumi Inada[1] and Vanderlei Salvador Bagnato[1,3]*

[1] São Carlos Institute of Physics, University of São Paulo, São Carlos, Brazil, [2] Departamento de Materiales, Facultad de Ingeniería Mecánica, Escuela Politécnica Nacional, Quito, Ecuador, [3] Hagler Fellow, Texas A&M University, College Station, TX, United States

OPEN ACCESS

Edited by:
Jessica Amber Jennings, University of Memphis, United States

Reviewed by:
Reza Ghiladi, North Carolina State University, United States
Guilherme T. P. Brancini, University of São Paulo, Brazil

***Correspondence:**
María Paulina Romero
maria.romerom@epn.edu.ec

Specialty section:
This article was submitted to Antimicrobials, Resistance and Chemotherapy, a section of the journal Frontiers in Microbiology

Received: *31 January 2021*
Accepted: *12 May 2021*
Published: *21 June 2021*

Citation:
Romero MP, Alves F, Stringasci MD, Buzzá HH, Ciol H, Inada NM and Bagnato VS (2021) One-Pot Microwave-Assisted Synthesis of Carbon Dots and in vivo and in vitro Antimicrobial Photodynamic Applications. Front. Microbiol. 12:662149. doi: 10.3389/fmicb.2021.662149

Carbon-based photosensitizers are more attractive than the other ones based on their low cost, high stability, broadband of light absorption, tunable emission spectra, high quantum yield, water solubility, high resistance to metabolic degradation, and selective delivery. These properties allow multiple applications in the field of biology and medicine. The present study evaluated *in vitro* and *in vivo* the antimicrobial photodynamic effect of a one-pot microwave produced C-DOTS based on citric acid. The *in vitro* assays assessed the effectiveness of illuminated C-DOTS (C-DOTS + light) against *Staphylococcus aureus* suspension and biofilm. The concentrations of 6.9 and 13.8 mg/mL of C-DOTS and light doses of 20 and 40 J/cm^2 were able to reduce significantly the microorganisms. Based on these parameters and results, the *in vivo* experiments were conducted in mice, evaluating this treatment on wounds contaminated with *S. aureus*. The viability test showed that C-DOTS–mediated photodynamic inactivation reduced 10^4 log of the bacteria present on the skin lesions. These results, altogether, showed that antibacterial photodynamic therapy using C-DOTS is a promising and viable treatment for Gram-positive bacteria-infected wounds.

Keywords: carbon dot, photodynamic therapy, antibacterial photodynamic therapy (aPDT), carbon-based materials, carbon-based photosensitizer, antibacterial materials, *Staphylococcus aureus*, nanomedicine

INTRODUCTION

During the coronavirus disease 2019 (COVID-19) pandemic, 50% of the COVID-19 victims had a secondary bacterial (Chen et al., 2020) or fungal (Cox et al., 2020) infection. Coinfections also played an important role in other global pandemics. In the 1918 influenza outbreak, most of the deaths were due to a subsequent bacterial infection, mainly of them caused by *Streptococcus pneumonia*. In 2009, the failure results in the treatment of H1N1 influenza pandemic were also associated with bacterial coinfections (Resistencia a los antibióticos, 2020). Because of the importance of coinfections in the severity of global diseases and also associated with the emergence

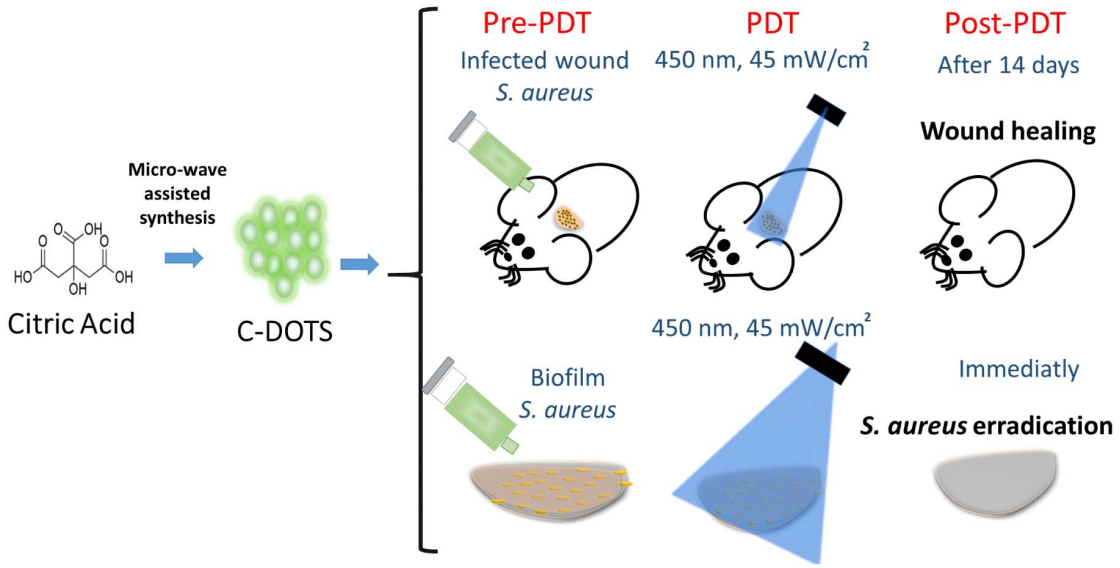

GRAPHICAL ABSTRACT | Brief description of the procedures carried out in this study. *In vivo* and *in vitro* antibacterial photodynamic therapy (aPDT) studies, where aPDT mediated by C-DOTS and blue LED light against *S. aureus* was evaluated.

of bacterial resistance to antibiotics (Tablan et al., 2004; Gordon and Lowy, 2008), the search for new, efficient, and cheap mechanisms for bacterial control is needed.

Staphylococcus aureus is one of the most common and problematic bacteria that is able to develop antibiotic resistance. *S. aureus* is a Gram-positive bacterium commonly isolated from skin and oropharyngeal tract of healthy individuals and is responsible for superficial infections, pneumonia, and sepsis (Tablan et al., 2004; Gordon and Lowy, 2008). This bacterium has the ability to form biofilm, which is considered a high virulence factor that facilitates the infection in the host. Biofilms are a complex microbial community, where microorganisms produce an extracellular matrix (ECM) to protect them (Donlan, 2002; Donlan and Costerton, 2002).

The chemical composition and characteristics of Gram-positive bacteria, such as *S. aureus*, form a cationic ECM, which determines different relationships between the matrix and the environment. The matrix exhibits a highly hydrated structure with hydrophilic and hydrophobic groups. These characteristics protect the biofilm from dehydration and antimicrobial agents. Moreover, biofilms show a dynamic and complex architecture that is able to adapt according to environmental and internal changes. The presence of water channels provides nutrient and oxygen transportation through the biofilm and also enables cell-to-cell communication via quorum sensing molecules (Donlan, 2002; Donlan and Costerton, 2002). All these features make biofilms the hardest microbial organization to be inactivated by all types of antimicrobial drugs, playing an important role for disease control, and they are a challenge for healthcare professionals.

Nanotechnological approaches are a powerful tool for microbial control, mainly when they are associated with antibacterial photodynamic therapy (aPDT) and involve the use of carbon-based materials such as graphene, graphene oxide (GO), reduced GO, carbon quantum dot (C-DOTS), and graphene quantum dots (GQDs). Carbon-based materials are attractive for their low cost and high stability and emerged as a new class of broad−spectrum antimicrobial agents (Karahan et al., 2018).

Antibacterial photodynamic therapy has been proposed as a technique to treat clinical relevant infectious diseases, such as dental biofilms, ventilator-associated pneumonia, chronic wound infections, oral candidiasis, and chronic rhinosinusitis (Hu et al., 2018). It has been demonstrated that aPDT has a great potential for inactivating many classes of microorganisms, and it has the advantage of being minimally invasive and having low incidence of side effects, and it is suitable for rapid and repetitive application (Maisch, 2009; Yin et al., 2015; Cieplik et al., 2018).

Antimicrobial PDT involves the combination of a non-toxic photosensitizer and a light in an appropriate wavelength, which interact with the molecular oxygen-producing reactive oxygen species (ROS) that are able to selectively kill microbial cells. The ROS may include radical ions, such as superoxide ($O_2^{\cdot-}$), hydroxyl radical ($^{\cdot}OH$), and/or singlet oxygen ($^1O_2$), and their production has been associated with the type I and/or type II photodynamic effects (Dolmans et al., 2003). *In vitro* and *in vivo* aPDT studies have demonstrated a substantial reduction of biofilms, in which the ROS are produced during photoactivation and attack adjacent targets, including proteins, lipids, and nucleic acids present within the biofilm matrix, on the cell surface and inside the microbial cells (Hu et al., 2018; Dong et al., 2020).

Carbon-based photosensitizers such as fullerene, GO, GQD, and graphitic carbon nitride have demonstrated low photosensitization efficiency, poor water solubility, or complex synthetic conditions, restricting their biological applications (Luo et al., 2014; Nie et al., 2020). On the other hand, C-DOTS

presents effective photodynamic action, with the advantage of being non-toxic, photostable, and versatile and having high quantum yield (Dong et al., 2020).

Several authors have studied the antibacterial effects of C-DOTS, under blue and white light irradiation against different bacteria cells (Dong et al., 2018; Li et al., 2018; Marković et al., 2018; Travlou et al., 2018). Nie et al. (2020) synthesized CQDs based on citric acid and 1,5-diaminonaphthalene in relation 1:2. aPDT studies demonstrated good results of this treatment for the inactivation of Gram-negative (*Escherichia coli*) and Gram-positive (*S. aureus*) bacteria upon visible light illumination ($\lambda \geq 420$ nm, 65 ± 5 mW/cm^2; 60 min) (Nie et al., 2020). Sidhu et al. (2017) also synthesized C-DOTS based on citric acid with penicillin adsorbed or covalently attached to the C-DOTS. Authors demonstrated *in vitro* that both compounds under light irradiation exhibited activity against *S. aureus*, multidrug-resistant *E. coli*, *E. coli*, and methicillin-resistant *S. aureus* (Sidhu et al., 2017).

Other works have developed C-DOTS/photosensitizing nanocomposites (Du et al., 2016; Achadu and Nyokong, 2017; Nwahara et al., 2018) and C-DOTS/polymer (Marković et al., 2019; Bayoumy et al., 2020; Kováčová et al., 2020) with antibacterial activity. These studies have shown good results; however, there is no *in vitro and in vivo* C-DOTS study covering a very simple, cheap, and straightforward synthesis and its effective application as a photosensitizer in aPDT.

In general, C-DOTS are prepared via bottom-up syntheses using pyrolysis or carbonization of some organic precursors (citric acid, L-glutamic acid, and glucose) (Dong et al., 2012; Wu et al., 2013; Li et al., 2017). The carbonization of organic precursors through hydrothermal treatment has been used through the microwave-assisted and autoclave techniques, and they have been used in different biomedical applications. Besides that, their production occurs from abundant and inexpensive precursors, favoring their broad and low-cost application (Kumawat et al., 2017). The aim of the present work involved the simple one-pot hydrothermal synthesis, characterization of C-DOTS, and the evaluation of its aPDT effectiveness *in vitro* and *in vivo* against *S. aureus*. Only citric acid was used as the sole carbon source to prepare C-DOTS based on the preparation of C-DOTS via a standard microwave procedure, enabling its facile synthesis, being considered a cheap and green material with promising biomedical applications.

MATERIALS AND METHODS

Synthesis and Characterization of C-DOTS

The water-soluble C-DOTS were prepared via microwave from the hydrothermal treatment of citric acid. First, 100 g of citric acid was dissolved 100 mL of deionized water in a glass beaker. Then, this solution was irradiated in a common microwave (Panasonic, Brazil) at high potency, for 8 min in an open atmosphere. The color of the liquid changed from colorless to pale yellow and strong yellow, indicating the formation of C-DOTS (Dong et al., 2012). Then, C-DOTS were purified by repeated dialysis in ultrapure water for 2 days (double dialyses bag molecular weight 1,300 Da). Finally, the solution was dried using a hot-air oven (Phoenix Luferco, Araraquara, Brazil) to produce solid structures of C-DOTS.

The C-DOTS sample was characterized by tapping-mode atomic force microscopy (Bruker Dimension Icon AFM) and transmission electron microscopy (TEM, JEOL–JEM2100 LaB6 HR operated at 200 kV). For TEM characterization, samples were prepared by dropping the C-DOTS solution on ultrathin carbon film-coated copper grid, 300 meshes. The luminescence emission measurements were performed at room temperature on a Cary Eclipse, Agilent technology spectrofluorometer, and a Varian Cary® 50 UV-VIS system spectrophotometer.

Other techniques, including infrared spectroscopy [Agilent Technologies, Cary 630 Fourier transform infrared spectroscopy (FTIR)], Raman spectroscopy (Renishaw RM2000, laser HeNe, and 632.8-nm wavelength), and XRD spectroscopy (BRUKER APEX II Duo, two-copper, and molybdenum microsources, and low-temperature OXFORD system), were adopted to characterize the C-DOTS. In addition, the charge and size were evaluated by zeta potential and DLS measurements (Brookhaven Instruments Corporation MODELO: 90 plus particle size analyzer wavelength 659 nm).

In vitro C-DOTS–mediated aPDT

Bacterial Suspension and Treatment

The *S. aureus* standard strain from the American Type Culture Collection (25923) was maintained in brain–heart infusion (BHI, Kasvi, São José dos Pinhais, Brazil) supplemented with glycerol (40%) at −20°C. The strain was reactivated by transferring 1 mL of the stock cultures to a tube containing 9 mL of BHI media and incubated at 37°C overnight. This culture was used to prepare bacterial suspension in phosphate-buffered saline (PBS). The suspension was standardized at an optical density of 0.2 arbitrary units (a.u.), determined in a spectrophotometer (Varian Cary® 50 UV-Vis Spectrophotometer-Agilent, Santa Clara, CA, United States), which is equivalent to 10^8 cells/mL. Then, 2 mL of bacterial suspension was transferred to a centrifuge tube for centrifugation [3,000 revolutions/min (rpm), 10 min]. The supernatant was removed, and 2 mL of C-DOTS solution with 0.345, 3.45, or 6.9 mg/mL diluted in PBS was added.

An aliquot of 0.5 mL of the resultant solution was transferred to a 24-well plate and incubated for 40 min at 37°C protected from light. Then, the plate was irradiated with blue light (450 nm; 40 mW/cm^2) at the fluencies of 0, 20, 40, and 60 J/cm^2, corresponding to irradiation times of 0, 8.3, 16.7, and 25 min, respectively. To determine cell survival, aliquots of the contents of each sample were serially diluted 10-fold in sterile saline. Aliquots of each serial dilution were plated in duplicate over the surfaces of BHI agar, and all plates were aerobically incubated at 37°C for 24 h. Then, the colony-forming units per milliliter (CFU/mL) were calculated. Control groups consisted of untreated bacteria suspension, the isolated application of light, and bacterial incubation with C-DOTS in the dark. Experiments were performed in five replicates for each experimental group on three different occasions.

Biofilm Formation and Treatment

The standardized bacterial suspension was prepared at the same conditions described previously, and it was used to form biofilm (10^8 cells/mL) in PBS. For this, 1 mL of cell suspension was transferred to a 24-well plate and incubated at 37°C under agitation (75 rpm) for 90 min (adhesion phase). After the adhesion period, samples were carefully washed twice with 1 mL of saline to remove unbound cells and metabolites. Then, 1 mL of tryptic soy broth (TSB) was added in each well, and plates were maintained at 37°C in a shaker incubator (75 rpm) for 24 h. After this period, TSB culture medium was removed, and 1 mL of fresh medium was added. The plates were maintained at 37°C under agitation for a further 24 h, completing 48 h of biofilm formation (maturation stage). After this period, the content of each well was removed, and biofilms were washed twice with 1 mL of saline.

After the biofilm formation, 1 mL of PBS/C-DOTS solution at the concentrations of 3.45, 6.9, or 13.8 mg/L was added to the biofilms. Samples were incubated for 40 min at 37°C protected from light, and irradiated with blue light (450 nm; 40 mW/cm^2) at the fluencies of 0, 20, 40, and 60 J/cm^2, corresponding to irradiation times of 0, 8.3, 16.7, and 25 min, respectively.

After treatments, biofilms were detached by rubbing the pipette tip for 30 s on the bottom of the wells. Aliquots of the contents of each sample were serially diluted 10-fold in sterile saline. Duplicate 25-μL aliquots were spread over the surface of BHI agar plates. Control groups consisted of biofilms and light, biofilms and C-DOTS in the dark, and untreated biofilms.

All plates were aerobically incubated at 37°C for 24 h, and the CFU/mL values were calculated. Experiments were performed in five replicates for each experimental group on three different occasions.

In vivo C-DOTS–Mediated aPDT

All experimental procedures were approved by the Institutional Animal Care and Use Committee (protocol 7658051218) of Sao Carlos Institute of Physics. The induction of skin wounds in Swiss mice was performed using the methodology proposed by Takakura et al. (2003) and Mima et al. (2010) with some modifications. The animals were immunosuppressed by two subcutaneous injections of prednisolone at a dose of 100 mg/kg of body weight using the medication methylprednisolone acetate 40 mg/mL. Immunosuppression was performed on the first and fifth days of the experiment.

On the second day of the experiment, the animals were anesthetized with an intraperitoneal injection of ketamine (30 mg/kg) and xylazine (13 mg/kg) solution in addition to diazepam injection at the dose of 5 mg/kg. The animals were trichotomized, and the wound was produced on the skin with a 3-mm-diameter punch. After wound procedure, 50 μL of bacterial suspension standardized at 108 cell/mL was added on the wound.

On the seventh day of the experiment and, therefore, after 6 days of bacterial inoculation, the animals were anesthetized with ketamine and xylazine solution (same concentration) and divided into four groups, with three animals in each group, as follows: control, only light, C-DOTS, and C-DOTS + light (aPDT). Mice of aPDT group received topical application of 50 μL of C-DOTS at a concentration of 13.8 mg/mL for 40 min in the dark and after incubation; LED illumination was performed with 60 J/cm^2 (28 min) at the wavelength of 450 nm. Other animals received only the application of C-DOTs or light in the same parameters, and the control group received no treatment.

Immediately after applying the treatments, the microorganisms were collected using a sterile swab soaked in a saline solution that was scrubbed for 30 s over the wound. The collection was subjected to serial dilutions (10^0–10^5) and plated in duplicate on the BHI agar medium. Plates were incubated for 24 h at 37°C, and after this period, CFU/mL values were calculated. A second collection was also performed 7 days after the treatments, following the same procedure.

Colony-forming units per milliliter values were transformed into base-10 logarithms and were evaluated for the distribution and homogeneity of variance among the groups evaluated. One-way analysis of variance followed by the Tukey test was applied for multiple comparisons ($p = 0.05$).

RESULTS AND DISCUSSION

Characterization of the C-DOTS

Atomic force microscopy and TEM were used to visualize the size, morphology, and structure of C-DOTS. The AFM images of C-DOTS shown in **Figures 1A,B** present the height profile along the small lines and indicate the thickness of the C-DOTS is in the range of 1.5–4.5 nm.

A TEM image of the C-DOTS is shown in **Figure 2a**. In **Figure 2b**, the size of C-DOTS is shown, which is equivalent to 3.75 and 4.18 nm. The mean diameter of the C-DOTS is 3.81 nm. The high-resolution TEM showed the lattice fringes with a lattice spacing around 0.35 ± 0.02 nm (**Figure 2c**), which corresponds to the lattice fringes of (0 0 2) planes (Zhou et al., 2007; Dong et al., 2013). In addition, the fast Fourier transform (FFT) pattern (**Figure 2d**) reveals that these structures are crystalline. Both AFM and TEM demonstrated that C-DOTS have circular shape with a diameter range of 1.5–4.5 nm and with a crystalline structure belonging to the carbon family. This result is comparable with the results found by Tang et al. (2016) and Van Tam et al. (2014).

To investigate the difference in oxygen-related functional groups on C-DOTS, FTIR spectra (**Figure 3A**) were performed. The presence of the carbonyl group (C=O 1706 cm^{-1}) and the hydroxyl group (–OH 3,444 cm^{-1}) was observed, and C-DOTS showed absorption of stretching vibration C–H at 2,986 cm^{-1} and stretching vibration of –CH_2 at 1,399 cm^{-1}. Additionally, the C-DOTS showed absorption of stretching vibration C–O at 1,170 cm^{-1} and C–OH at 1,080 cm^{-1} (Kumawat et al., 2017). These results corroborate with those obtained by Dong et al. (2012), where GQDs and GO were synthesized based on the carbonization of citric acid. The analysis of FTIR spectrum suggested that GQDs contain incomplete carbonization of citric acid, compared to the GO, which exhibits complete carbonization of it.

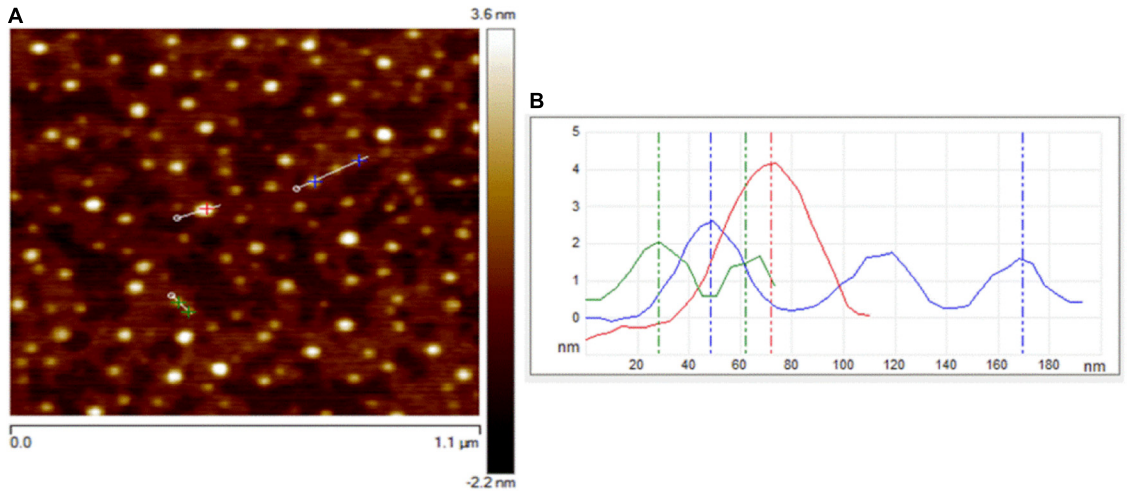

FIGURE 1 | AFM images of C-DOTS. **(A)** AFM image of C-DOTS deposited on a mica substrate. **(B)** The height profiles along the lines of the panel from C-DOTS.

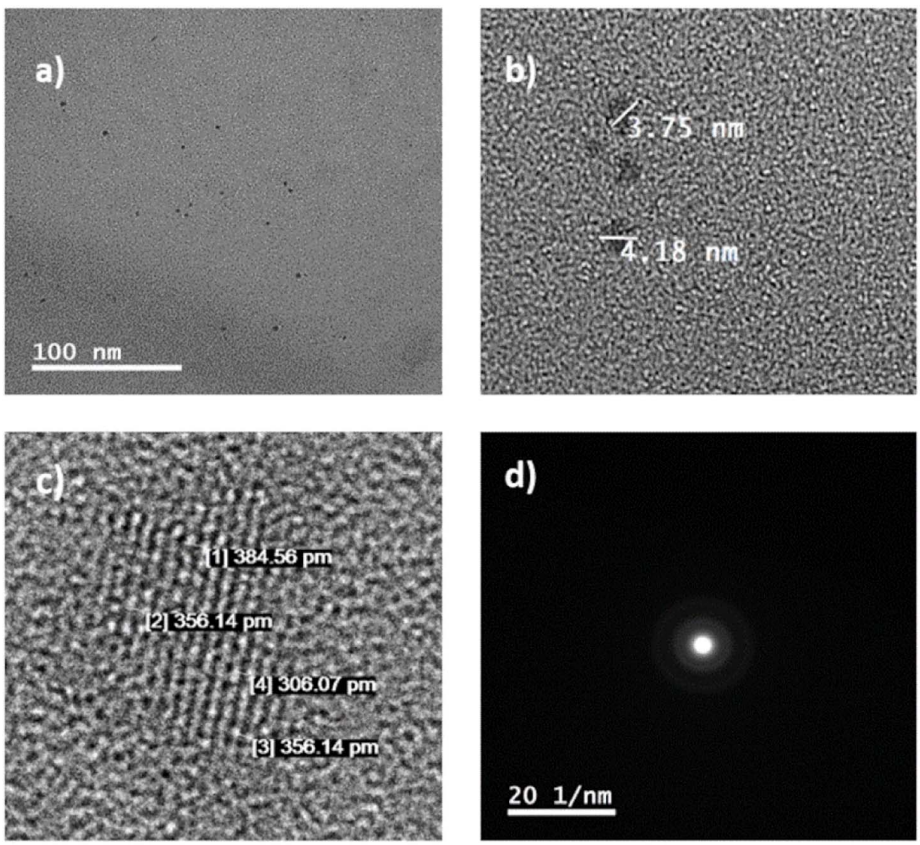

FIGURE 2 | (a,b) C-DOTS TEM images. **(c,d)** High-resolution TEM images and corresponding 2D FFT image.

The XRD pattern of C-DOTS (**Figure 3B**) revealed a single broad diffraction peak at $2\theta = 26^{\circ}$ that corresponded to the crystal lattice distance of (0 0 2) ($d_{002} = 0.34$ nm), and demonstrated a well-ordered lamellar structure with layered regularity (Dang et al., 2016).

The presence of oxygen-related functional groups on C-DOTS also creates disorders as defects and creates different hybridized atoms in the graphitic carbon skeleton, where both types of hybridized carbon atoms (sp_2 and sp_3) are prevalent. The XRD results are consistent with the Raman spectrum of C-DOTS.

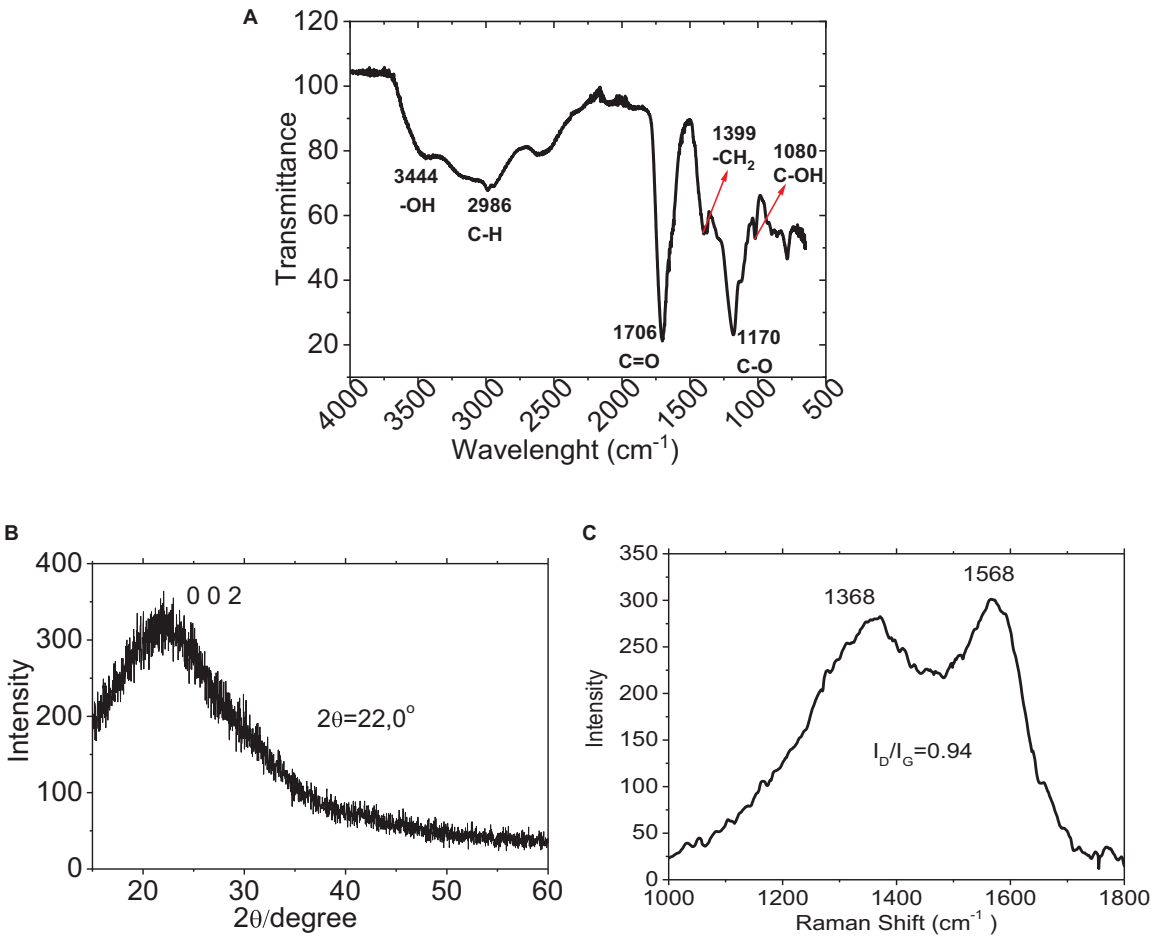

FIGURE 3 | Characterization of C-DOTS. **(A)** FTIR spectrum of C-DOTS. **(B)** XRD pattern for the C-DOTS. **(C)** Raman spectrum of C-DOTS.

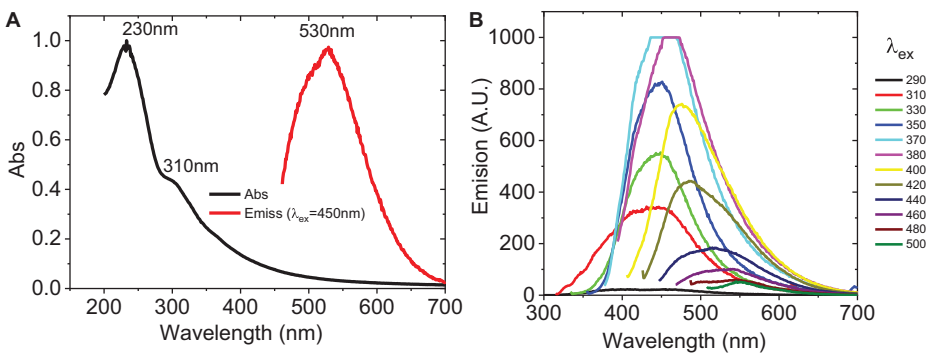

FIGURE 4 | Optical properties of C-DOTS. **(A)** UV-VIS spectra (black line) and emission spectra (red line). λ_{ex} = 450 nm, λ_{em} = 530 nm. Images above: C-DOTS solution (yellow) without irradiation and C-DOTS emitting light green light when irradiated with 350-nm light. **(B)** Emission spectra of C-DOTS. Excitation wavelength from 290 to 500 nm (side frame) with their respective emission spectra (same color).

Figure 3C shows the Raman spectrum of C-DOTS, where the D-band (related to sp_3 hybridized carbon atoms and the presence of structural defects) and the G-band (associated with sp_2 hybridized carbon atoms) are characteristic of carbon-based material. The ID/IG ratio for C-DOTS is equivalent to 0.94, which indicates that the C-DOTS present high crystallinity and disorder in the skeleton of C-DOTS.

UV-VIS absorbance spectra and photoluminescence (PL) emission were obtained. **Figure 4A** indicates that C-DOTS have an absorption band at $\lambda < 240$ nm (characteristic of the $\pi-\pi^*$

transitions of aromatic bonds C=C) and another smaller band around 310 nm, which belongs to the n–π^* transition of C=O or the COOH group (Liu and Kim, 2015; Tang et al., 2016). The PL spectra are generally broad and dependent on the excitation wavelength (Shen et al., 2011). **Figure 4B** shows that C-DOTS have the highest luminescence in the visible part of the spectrum, with the maximum emission intensity approximately at 450 nm ($\lambda_{ex} = 370$ nm), then it is reduced and shifted at higher wavelengths to approximately 548 nm ($\lambda_{ex} = 500$ nm), and it is consistent with previous fluorescence analysis (Li et al., 2010; Pan et al., 2010; Ristic et al., 2014).

Stability Analysis of C-DOTS

Stability is the main characteristic of the C-DOTS that depends on the nature of the environment in which they are exposed. Poor stability leads to aggregation and deterioration of lattice attributed to a disturbance of fluorescence properties (Sidhu et al., 2017). To investigate the stabilities of the C-DOTS by photo-oxidation and PL properties, they were examined over 24 h in the presence of blue light (Xenon lamp of Cary Eclipse, Agilent technology spectrofluorometer) with $\lambda_{exc} = 450$ nm and $\lambda_{emis} = 530$ nm (**Figure 5A**). It was shown that in the presence of light, a very small decrease in the fluorescence intensity was observed, and it is consistent with previous stability analysis (Wang et al., 2017; Dager et al., 2019).

The stability of C-DOTS when the temperature was increased is shown in **Figure 5B**. It was observed that, increasing the temperature, there is a decrease in the fluorescence emission. Surprisingly, at 70°C, the fluorescence intensity of the C-DOTS decreased only 36.20%. Unlike amorphous C-DOTS, the crystalline structure of the C-DOTS synthesized in the present study could explain their excellent photostability (Liu et al., 2017; Nie et al., 2020). The C-DOTS solution in water remains without any precipitation, and its fluorescence emission intensity was maintained after 90 days, keeping it in the dark.

PHOTODYNAMIC EFFECTS

C-DOTS-Mediated aPDT in the Inactivation of Planktonic and Biofilm Cultures of *S. aureus*

Biofilm is a microbial community embedded in a self-produced extracellular polymeric matrix (ECM) attached to a biological or non-biological surface. Compared to planktonic cells, biofilm exhibits specific physiological and metabolic states (Hu et al., 2018). According to Karunakaran et al. (2011), the biofilm is formed with three elements: the ECM, the microbial cells, and the intracellular biomolecules (Karunakaran et al., 2011). During aPDT-mediated biofilm inactivation, oxidative damage occurs from extracellular polymeric substances (EPS) to intracellular biomolecules (Barra et al., 2015).

The colony count method demonstrated a significant reduction in the number of CFU/mL in *S. aureus* in both planktonic and biofilm cultures exposed to C-DOTS photoexcited by light at 450 nm and 40 mW/cm^2 (**Figure 6**). The decrease in log (CFU/mL) can be observed as a function of the dose of blue light delivered to the planktonic culture (0, 20, 40, and 60 J/cm^2) and the C-DOTS concentration (345 μg/mL, 3.45 mg/mL, 6.9 and 13.8 mg/mL). As expected at higher C-DOTS concentrations, the log (CFU/mL) reduction was greater, and when the concentration of 6.9 mg/mL was applied, the total elimination of *S. aureus* suspension was achieved. For the biofilm cultures (**Figure 6B**), twice of the C-DOTS concentration was used (13.8 mg/mL) compared to the planktonic culture, in order to obtain complete elimination of the *S. aureus* bacteria. For both systems mentioned previously, the complete elimination of the *S. aureus* bacteria was obtained using the light dose of 40 J/cm^2.

The dose–response curve is a relationship among the viability reduction of planktonic and biofilm cultures, C-DOTS concentrations, and the light delivery of 450 nm 40 mW/cm^2. Because of the variability among the bacteria cells, the dose–response curve has a sigmoid shape (Romero et al., 2020). The threshold dose shows the distribution formed by the response of the bacterial to C-DOTS and light around a maximum dose of light, Dp. This curve was obtained by deriving the dose–response curve.

The dose–response curves and their corresponding threshold dose distribution of *S. aureus* planktonic (**Figure 7A**) and biofilm (**Figure 7B**) were evaluated. These curves were obtained from the results of colony counting of planktonic and biofilm of *S. aureus* in the presence of C-DOTS as a direct killing effect. The fitting of the inverse of standard colony counting (loss of the viability) curve was performed in the Origin8 program using a sigmoidal curve.

The loss of viability distribution was characterized by the width. **Figure 7A** is showing a measure at half maximum (full-width half-maximum) and their peak center, which corresponds to the maximal dose amplitude. de Faria et al. (2018) argued that quantifying tolerance in a population of bacteria is a measure of how heterogeneous the population of bacteria is with respect to the threshold dose. This variability is related to the tolerance (de Faria et al., 2018).

Parameter is summarized in **Supplementary Figure 1A** and is shown as a function of the C-DOTS concentration, where the higher the concentration of C-DOTS, the lower the value. This means that a small dose of light is required to eliminate a great amount of bacterial population. This behavior was observed in planktonic and biofilm cultures. For the analysis of the parameter, the concentration of 345 μg/mL in the planktonic culture was eliminated as it was an incomplete curve where its respective value was not distinguished.

The highest value corresponds to the biofilm *S. aureus* + C-DOTS; this indicates that the biofilm has the strongest resistance condition in relation to the planktonic culture. The planktonic culture is the most sensitive for both concentrations of C-DOTS. It is interesting to note that when doubling the concentration of C-DOTS for both cultures (**Supplementary Figure 1B**), the value is reduced 2.5 times for planktonic form and 2 times for the biofilm. This means that with higher concentrations in both cultures, the difference in sensitivity is significant. In summary, the planktonic culture showed a better response to C-DOTS

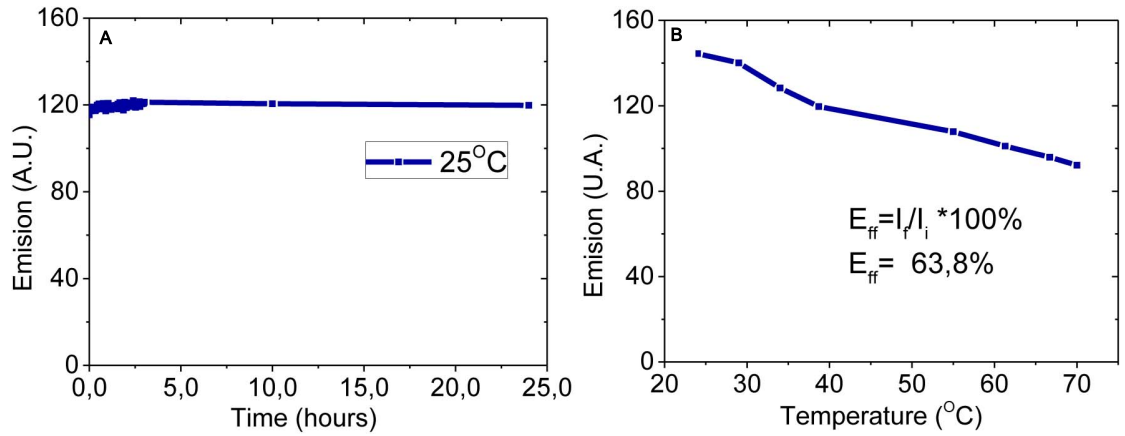

FIGURE 5 | Stability analysis of C-DOTS. **(A)** Twenty-four hours of photoirradiation at constant temperature (25°C). **(B)** Photoirradiation based on temperature, from 25 to 70°C. λex = 450 nm, λem = 530 nm, pH 5.5.

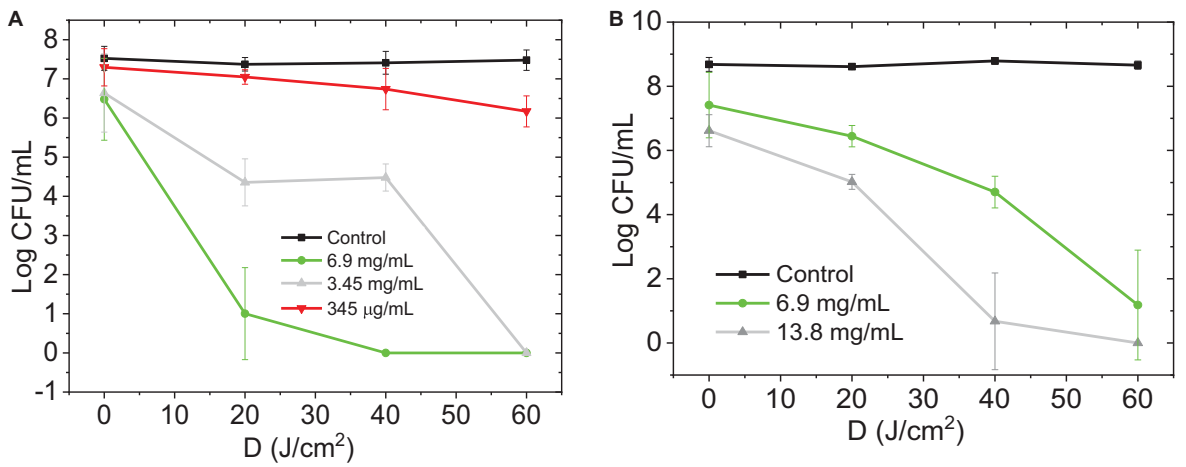

FIGURE 6 | Photoexcited C-DOTS reduce the number of bacterial colonies (log CFU/mL) based on the light dose 450 nm, 40 mW/cm^2 delivered. **(A)** Planktonic *S. aureus* + C-DOTS. **(B)** Biofilm of *S. aureus* + C-DOTS. The "control" group refers to the bacteria + light system. The group "0 J/cm^2" corresponds to the bacteria + C-DOTS system, where it was observed that the C-DOTS by themselves decreased the bacterial population in 10^2 CFU/mL.

concentration compared to the biofilm. All control groups had the same order of magnitude (1×10^8 CFU/mL) from the initial standardized suspensions.

Planktonic culture needs C-DOTS concentrations lower than 6.9 mg/mL to achieve total bacterial killing, whereas concentrations greater than it were required to the biofilm. Biofilm can tolerate antibiotic levels 10–1,000 times higher than their planktonic counterparts (Ceri et al., 1999). The biofilm living form is a protective lifestyle that allows pathogenic bacteria and fungi to survive in hostile environments (Hall-Stoodley et al., 2004). In the clinical area, biofilms lead to infections that are difficult to eradicate, as microbes are protected from the attack of the host defense system and exhibit antimicrobial resistance (Hu et al., 2018). For this reason, the results obtained in the present study are of great importance, as aPDT with C-DOTS was able to inactivate even biofilm communities.

The relative variability of ΔD/Dp is shown in **Supplementary Figure 2A**, and in both cases, ΔD/Dp decreased with the increase in C-DOTS concentration; in higher concentrations of C-DOTS, there was a more homogeneous response of *S. aureus* bacteria to 450 nm irradiation (40 mW/cm^2 LED light), with a minimal variability of response. In both cultures, plankton and biofilm, the response to the presence of C-DOTS and blue light presented similar values of ΔD/Dp for low and high concentrations (**Supplementary Figure 2B**), concluding that both cultures have a similar response to C-DOTS–mediated aPDT.

C-DOTS-Mediated aPDT Zeta Potential and DLS

To confirm the electrostatic interactions, the zeta potentials of bacterial cells were evaluated after treatments. The zeta potential of C-DOTS and *S. aureus* and *S. aureus* + C-DOTS were

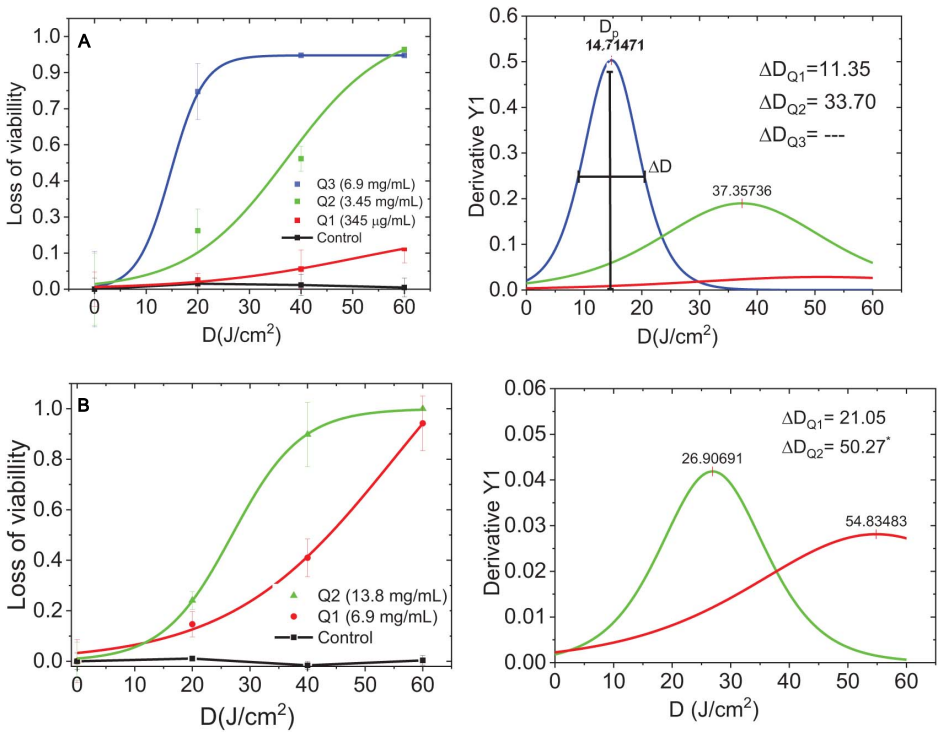

FIGURE 7 | Dose-response curves and threshold dose distribution. **(A)** Planktonic *S. aureus* + C-DOTS. **(B)** Biofilm of *S. aureus* + C-DOTS. Dp is the maximum dose of delivery light, ΔD [full-width half-maximum (FWHM)] is the threshold dose distribution curves obtained from the dose–response curves. *The FWHM value found of the complete curve.

−22.09 and −31.60 mV, respectively, but the zeta potential of *S. aureus* + C-DOTS + light was −15.33 and 4.5 mV as shown in **Supplementary Figures 3A–D**. It was shown that the zeta potential of the bacteria may be attributed to the cell surface components of Gram-positive bacteria, in the case of *S. aureus* (Ran et al., 2019).

These results indicate that the photodynamic effect produced a charge change in the bacteria + C-DOTS + light solution, tending to be positive. The hydrodynamic sizes of the *S. aureus*, *S. aureus* + C-DOTS, and *S. aureus* + C-DOTS + light was 966.2, 1,018.6, and 1,064 nm, respectively (**Supplementary Figure 3E**). A small difference was observed between maximum sizes of the studied solutions, but a greater distribution of sizes was observed for the bacteria + C-DOTS + light, with larger sizes than the bacteria + C-DOTS. These values lead to the conclusion that in the illumination to obtain the photodynamic effect (elimination of bacteria), there is formation of aggregates in the solution.

Ran et al. (2019) synthetized carbon dots prepared by the solvothermal treatment of dimethyloctadecyl[3-(trimethoxysilyl)propy]ammonium chloride (Si-QAC CDs) and quaternized carbon dots without long alkyl chains (termed TTPAC CDs). The zeta potentials of *S. aureus* bacteria after the treatment with TTPAC CDs and Si-QAC CD-treated (incubated for 2 h) indicated a higher binding affinity between the Si-QAC CDs and the bacterial surfaces. Especially, the similar zeta potentials of the bacterial cells at the CD concentrations of 30 and 50 μg/mL suggested that the *S. aureus* bacteria were well coated by the CDs at a concentration of 30 μg/mL or higher (Ran et al., 2019).

From the results obtained in the present study, due to the presence of light, the zeta potential increased, as observed by Ran et al. (2019). It suggests that the presence of light in the *S. aureus* + C-DOTS solution allows a greater binding affinity between C-DOTS and bacterial surfaces, allowing total elimination of bacteria observed in **Figure 6A**.

The C-DOTS concentrations evaluated in the present study were between 0 and 6.9 mg/mL, and compared to the concentrations of various types of C-DOTS used by other authors (between 0 and 1 mg/mL) (Yang et al., 2016, Yang et al., 2019; Ran et al., 2019), the concentration of C-DOTS used in this study was approximately seven times higher. This could be explained by the traces of citric acid in which they were duly purified in the stage of the synthesis of C-DOTS. In *in vitro* studies developed in HDFn fibroblasts cell line (**Supplementary Information 1**), it is observed that at a concentration of 6.9 mg/mL, cell survival decreases to approximately 40% for a light dose of 63 J/cm^2 and 450-nm irradiation. Concluding that at concentrations greater than and equal to 6.9 mg/mL, cellular cytotoxicity is already observed under the effect of aPDT. This effect was observed using 38 and 63 J/cm^2 of light doses, after 4 and 24 h of aPDT.

In vivo C-DOTS Antimicrobial Activity

The use of C-DOTS as an antimicrobial agent *in vivo* was investigated with and without light. The "control" group was

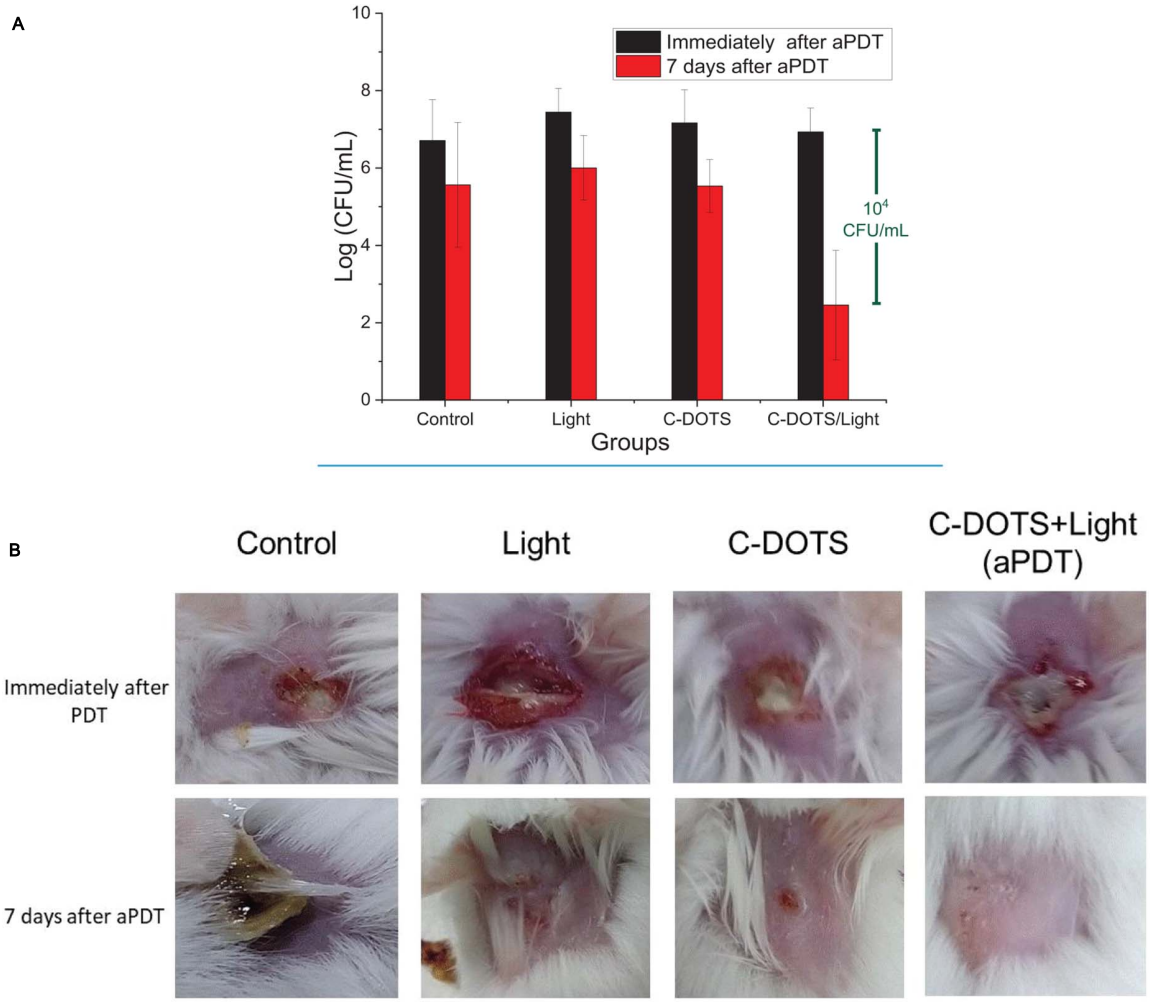

FIGURE 8 | *In vivo* aPDT. **(A)** Log (CFU/mL) of *S. aureus* bacteria in mouse immediately aPDT (black blocks) and 7 days after the procedures (red blocks) in control, light, C-DOTS, and C-DOTS + light (aPDT) groups ($n = 3$). **(B)** Photographs of mice wounds infected with *S. aureus*. Same groups as panel **(A)** ($n = 3$). The C-DOTS concentration was 6.9 mg/mL; the wound was infected with 10^8 cells/mL of bacteria suspension; the LED light was applied with the dose of 60 J/cm^2 (28 min) at 450 nm.

performed to analyze the natural processes of infection healing in wound contaminated with *S. aureus*. The "light" group was performed to confirm that the light parameters used did not cause any damage in the contaminated wound.

Bacteria were collected from the wound immediately and 7 days after all procedures to obtain the effectiveness of each group. Immediately after the procedures, there was no great difference among the groups ($p \geq 0.05$), as shown in **Figure 8A**, where all groups presented colony counts in the same order of magnitude (1×10^7 CFU/mL). However, on day seven post-treatment, a significant reduction of the viability was observed in the C-DOTS + light group. The control groups (no treatment, light, and C-DOTS) showed 1×10^6 CFU/mL, whereas the C-DOTS + light group showed in the order of 10^2 CFU/mL, resulting in a reduction of 10^4 log CFU/mL (**Figure 8A**). A small reduction was observed in the "control" (only bacteria in lesion), "light" (bacteria + light), and "C-DOTS" (bacteria + C-DOTS in dark) groups. This reduction may be attributed to immune system of the animals that combated the infection by itself.

The induced infection on the skin of mice also showed different features after 7 days of the procedures. The lesions in the control group had a large crust with a very purulent aspect. The light and C-DOTS groups exhibited small wounds (**Figure 8B**). However, a complete response and good healing were observed in the C-DOTS + light group, as shown in **Figure 8B**. The skin of all mice was completely recovered after 21 days (with and without treatment). When evaluating the cytotoxic effects of aPDT in HDFn fibroblasts cell line (**Supplementary Information 1**), it was observed that at the concentration of 6.9 mg/mL, there is a cell survival of approximately 35%; this survival is reduced by increasing the concentration of C-DOTS. However, it was demonstrated that *in vivo* the C-DOTS concentration used (6.9 mg/mL) had no visible effect (**Figure 8B**).

The antimicrobial mechanism of C-DOTS–mediated aPDT was caused by the production of ROS, which leads to oxidative stress as described by Marković et al. (2019) and Zhang et al. (2018). The generation and clearance of ROS in bacterial cells are balanced in normal conditions; however, the excessive production of ROS favors the oxidation of the cells. This unbalanced state produces oxidative stress, which damages the components of bacteria. The mechanisms of action include the adhesion of C-DOTS to the bacterial surface, the photoinduced production of ROS, the disruption and penetration of the bacterial cell wall/membrane, and the induction of oxidative stress with damages to DNA/RNA, leading to alterations or inhibitions of important gene expression and oxidative damages to proteins and other intracellular biomolecules (Al Awak et al., 2017; Li et al., 2018).

Some articles have described that photoactivate C-DOTS and other nanoparticles can transfer electron or energy to oxygen or biomolecules generating cytotoxic-free radicals and ROS (Ipe et al., 2005; Yaghini et al., 2009). Besides the death of microorganisms, there is some evidence that aPDT can stimulate the host immune system, which contributes to the healing process, as observed in the better aspect of lesions 7 days after C-DOTS + light treatment (Castano et al., 2006).

Antibacterial photodynamic therapy using traditional PS is often limited by its high cost, mainly in developing and/or underdeveloped countries. With the results obtained in this article, we are proposing C-DOTS as nanomaterials whose synthesis is cheap, easy, and green (there is no generation of toxic waste). These advantages make C-DOTS attractive to be used as photosensitizer in aPDT for antibacterial control.

CONCLUSION

In summary, we developed C-DOTS from citric acid through a facile microwave-assisted synthesis, and it was evaluated in association with blue light to mediate aPDT *in vitro* and *in vivo* against *S. aureus*. The C-DOTS aqueous solutions exhibited strong fluorescence under 450-nm light and fluorescence emission stability for 24 h of continuous irradiation and also after 90 days of being stored in the dark. The *in vitro* study demonstrated that C-DOTS–mediated aPDT was able to eliminate *S. aureus* suspension and biofilm. The *in vivo* study was conducted based on the *in vitro* study. Seven days after the aPDT procedure on the mice contaminated wounds, a 10^4 log of reduction in the *S. aureus* population compared to the controls and complete healing of the tissue were observed. The use of C-DOTS as a photosensitizer in aPDT proved to be promising in the treatment of biofilms and infected wounds, making these water-soluble C-DOTS a simple, cheap, and efficient agent for aPDT both for *in vitro* and *in vivo* studies.

DATA AVAILABILITY STATEMENT

The original contributions presented in the study are included in the article/**Supplementary Material**, further inquiries can be directed to the corresponding author.

ETHICS STATEMENT

The animal study was reviewed and approved by CEUA N 7658051218.

AUTHOR CONTRIBUTIONS

MR: synthesis of carbon dots, development of *in vitro* studies in *S. aureus* bacterial cells, and manuscript writing. FA: development of studies in biofilms and English language review. MS and HB: development of *in vivo* studies (mice) and English language review. HC: development of *in vitro* studies on epithelial cells. NI and VB: guide in the conception, design of the work, analysis, and interpretation of data. All authors contributed to the article and approved the submitted version.

FUNDING

This work was supported by CePOF (São Paulo Research Foundation—FAPESPgrant 2013/07276-1), National Institute of Optics and Photonics—INCT (National Council for Research and Development—CNPq grant465360/2014-9 and São Paulo Research Foundation - FAPESPgrant 2014/50857-8), and Escuela Politécnica Nacional Quito- Ecuador.

ACKNOWLEDGMENTS

We thank Cristina Cecibel Garzón Romero for the support given in the C-DOTS synthesis. We also thank the Buzza scholarship by São Paulo Research Foundation – FAPESP grant 2016/14033-6.

SUPPLEMENTARY MATERIAL

The Supplementary Material for this article can be found online at: https://www.frontiersin.org/articles/10.3389/fmicb.2021.662149/full#supplementary-material

REFERENCES

Achadu, O. J., and Nyokong, T. (2017). Application of graphene quantum dots functionalized with thymine and thymine-appended zinc phthalocyanine as novel photoluminescent nanoprobes. *New J. Chem.* 41, 1447–1458. doi: 10.1039/c6nj03285k

Al Awak, M. M., Wang, P., Wang, S., Tang, Y., Sun, Y. P., and Yang, L. (2017). Correlation of carbon dots' light-activated antimicrobial activities and fluorescence quantum yield. *RSC Adv.* 7, 30177–30184. doi: 10.1039/c7ra05397e

Barra, F., Roscetto, E., Soriano, A. A., Vollaro, A., Postiglione, I., Pierantoni, G. M., et al. (2015). Photodynamic and antibiotic therapy in combination to

fight biofilms and resistant surface bacterial infections. *Int. J. Mol. Sci*. 16, 20417–20430. doi: 10.3390/ijms160920417

Bayoumy, A. M., Refaat, A., Yahia, I. S., Zahran, H. Y., Elhaes, H., Ibrahim, M. A., et al. (2020). Functionalization of graphene quantum dots (GQDs) with chitosan biopolymer for biophysical applications. *Opt. Quantum Electron*. 52:16. doi: 10.1007/s11082-019-2134-z

Castano, A. P., Mroz, P., and Hamblin, M. R. (2006). Photodynamic therapy and anti-tumour immunity. *Nat. Rev. Cancer* 6, 535–545. doi: 10.1038/nrc1894

Ceri, H., Olson, M. E., Stremick, C., Read, R. R., Morck, D., and Buret, A. (1999). The Calgary Biofilm Device: new technology for rapid determination of antibiotic susceptibilities of bacterial biofilms. *J. Clin. Microbiol*. 37, 1771–1776. doi: 10.1128/jcm.37.6.1771-1776.1999

Chen, N., Zhou, M., Dong, X., Qu, J., Gong, F., Han, Y., et al. (2020). Epidemiological and clinical characteristics of 99 cases of 2019 novel coronavirus pneumonia in Wuhan, China: a descriptive study. *Lancet* 395, 507–513. doi: 10.1016/S0140-6736(20)30211-7

Cieplik, F., Deng, D., Crielaard, W., Buchalla, W., Hellwig, E., Al-Ahmad, A., et al. (2018). Antimicrobial photodynamic therapy – what we know and what we don't. *Crit. Rev. Microbiol*. 44, 571–589. doi: 10.1080/1040841X.2018.1467876

Cox, M. J., Loman, N., Bogaert, D., and O'Grady, J. (2020). Co-infections: potentially lethal and unexplored in COVID-19. *Lancet Microbe* 1:e11. doi: 10.1016/s2666-5247(20)30009-4

Dager, A., Uchida, T., Maekawa, T., and Tachibana, M. (2019). Synthesis and characterization of Mono-disperse Carbon Quantum Dots from Fennel Seeds: photoluminescence analysis using Machine Learning. *Sci. Rep*. 9:14004. doi: 10.1038/s41598-019-50397-5

Dang, H., Huang, L.-K., Zhang, Y., Wang, C.-F., and Chen, S. (2016). Large-Scale Ultrasonic Fabrication of White Fluorescent Carbon Dots. *Ind. Eng. Chem. Res.* 55, 5335–5341.

de Faria, C. M. G., Inada, N. M., Vollet-Filho, J. D., and Bagnato, V. S. (2018). A threshold dose distribution approach for the study of PDT resistance development: a threshold distribution approach for the study of PDT resistance. *J. Photochem. Photobiol. B*. 182, 85–91. doi: 10.1016/j.jphotobiol.2018.03.022

Dolmans, D. E., Fukumura, D., and Jain, R. K. (2003). Photodynamic therapy for cancer. *Nat. Rev. Cancer* 3, 380–387. doi: 10.1038/nrc1071

Dong, X., Bond, A. E., Pan, N., Coleman, M., Tang, Y., Sun, Y. P., et al. (2018). Synergistic photoactivated antimicrobial effects of carbon dots combined with dye photosensitizers. *Int. J. Nanomedicine* 13, 8025–8035. doi: 10.2147/IJN.S183086

Dong, X., Liang, W., Meziani, M. J., Sun, Y. P., and Yang, L. (2020). Carbon dots as potent antimicrobial agents. *Theranostics* 10, 671–686. doi: 10.7150/thno.39863

Dong, Y., Pang, H., Yang, H. B., Guo, C., Shao, J., Chi, Y., et al. (2013). Carbon-based dots co-doped with nitrogen and sulfur for high quantum yield and excitation-independent emission. *Angew. Chem. Int. Ed. Engl.* 52, 7800–7804. doi: 10.1002/anie.201301114

Dong, Y., Shao, J., Chen, C., Li, H., Wang, R., Ch, Y., et al. (2012). Blue luminescent graphene quantum dots and graphene oxide prepared by tuning the carbonization degree of citric acid. *Carbon* 50, 4738–4743. doi: 10.1016/j.carbon.2012.06.002

Donlan, R. M. (2002). Biofilms: microbial life on surfaces. *Emerg. Infect. Dis*. 8, 881–890. doi: 10.3201/eid0809.020063

Donlan, R. M., and Costerton, J. W. (2002). Biofilms: survival mechanisms of clinically relevant microorganisms. *Clin. Microbiol. Rev*. 15, 167–193. doi: 10.1128/CMR.15.2.167-193.2002

Du, D., Wang, K., Wen, Y., Li, Y., and Li, Y. Y. (2016). Photodynamic Graphene quantum dot: reduction condition regulated photoactivity and size dependent efficacy. *ACS Appl. Mater. Interfaces* 8, 3287–3294. doi: 10.1021/acsami.5b11154

Gordon, R. J., and Lowy, F. D. (2008). Pathogenesis of Methicillin-Resistant *Staphylococcus aureus* Infection. *Clin. Infect. Dis.* 46, S350–S359. doi: 10.1086/533591

Hall-Stoodley, L., Costerton, J. W., and Stoodley, P. (2004). Bacterial biofilms: from the natural environment to infectious diseases. *Nat. Rev. Microbiol*. 2, 95–108. doi: 10.1038/nrmicro821

Hu, X., Huang, Y. Y., Wang, Y., Wang, X., and Hamblin, M. R. (2018). Antimicrobial photodynamic therapy to control clinically relevant biofilm infections. *Front. Microbiol*. 9:1299. doi: 10.3389/fmicb.2018.01299

Ipe, B. I., Lehnig, M., and Niemeyer, C. M. (2005). On the generation of free radical species from quantum dots. *Small* 1, 706–709. doi: 10.1002/smll.200500105

Karahan, H. E., Wiraja, C., Xu, C., Wei, J., Wang, Y., Wang, L., et al. (2018). Graphene Materials in antimicrobial nanomedicine: current status and future perspectives. *Adv. Healthc. Mater*. 7:e1701406. doi: 10.1002/adhm.201701406

Karunakaran, E., Mukherjee, J., Ramalingam, B., and Biggs, C. A. (2011). "Biofilmology": a multidisciplinary review of the study of microbial biofilms. *Appl. Microbiol. Biotechnol*. 90, 1869–1881. doi: 10.1007/s00253-011-3293-4

Kováčová, M., Špitalská, E., Markovic, Z., and Špitálskı, Z. (2020). Carbon Quantum dots as antibacterial photosensitizers and their polymer nanocomposite applications. *Part. Part. Syst. Charact*. 37:1900348. doi: 10.1002/ppsc.201900348

Kumawat, M. K., Thakur, M., Gurung, R. B., and Srivastava, R. (2017). Graphene Quantum dots for cell proliferation, nucleus imaging, and photoluminescent sensing applications. *Sci. Rep*. 7:15858. doi: 10.1038/s41598-017-16025-w

Li, H., He, X., Kang, Z., Huang, H., Liu, Y., Liu, J., et al. (2010). Water-soluble fluorescent carbon quantum dots and photocatalyst design. *Angew. Chem. Int. Ed. Engl.* 49, 4430–4434. doi: 10.1002/anie.200906154

Li, H., Huang, J., Song, Y., Zhang, M., Wang, H., Lu, F., et al. (2018). Degradable Carbon dots with broad-spectrum antibacterial activity. *ACS Appl. Mater. Interfaces* 10, 26936–26946. doi: 10.1021/acsami.8b08832

Li, K., Liu, W., Ni, Y., Li, D., Lin, D., Su, Z., et al. (2017). Technical synthesis and biomedical applications of graphene quantum dots. *J. Mater. Chem. B* 5, 4811–4826. doi: 10.1039/c7tb01073g

Liu, M. L., Yang, L., Li, R. S., Chen, B., Liu, H., and Huang, C. Z. (2017). Large-scale simultaneous synthesis of highly photoluminescent green amorphous carbon nanodots and yellow crystalline graphene quantum dots at room temperature. *Green Chem*. 19, 3611–3617. doi: 10.1039/c7gc01236e

Liu, Y., and Kim, D. Y. (2015). Ultraviolet and blue emitting graphene quantum dots synthesized from carbon nano-onions and their comparison for metal ion sensing. *Chem. Commun*. 51, 4176–4179. doi: 10.1039/c4cc07618d

Luo, P. G., Yang, F., Yang, S. T., Sonkar, S. K., Yang, L., Broglie, J. J., et al. (2014). Carbon-based quantum dots for fluorescence imaging of cells and tissues. *RSC Adv*. 4, 10791–10807. doi: 10.1039/c3ra47683a

Maisch, T. A. (2009). New Strategy to destroy antibiotic resistant microorganisms: antimicrobial photodynamic treatment. *Mini Rev. Med. Chem*. 9, 974–983. doi: 10.2174/138955709788681582

Marković, Z. M., Jovanović, S. P., Mašković, P. Z., Danko, M., Mičušík, M., Pavlović, V. B., et al. (2018). Photo-induced antibacterial activity of four graphene based nanomaterials on a wide range of bacteria. *RSC Adv*. 8, 31337–31347. doi: 10.1039/c8ra04664f

Marković, Z. M., Kováčová, M., Humpolíček, P., Budimir, M. D., Vajď'ak, J., Kubát, P., et al. (2019). Antibacterial photodynamic activity of carbon quantum dots/polydimethylsiloxane nanocomposites against *Staphylococcus aureus*, *Escherichia coli* and *Klebsiella pneumoniae*. *Photodiagnosis Photodyn. Ther*. 26, 342–349. doi: 10.1016/j.pdpdt.2019.04.019

Mima, E. G., Pavarina, A. C., Dovigo, L. N., et al. (2010). Susceptibility of Candida albicans to photodynamic therapy in a murine model of oral candidosis. *Oral Surg. Oral Med. Oral Pathol. Oral Radiol. Endod*. 109, 392–401. doi: 10.1016/j.tripleo.2009.10.006

Nie, X., Jiang, C. H., Wu, S., Chen, W., Pengfei, L. V., Wang, Q., et al. (2020). Carbon quantum dots: a bright future as photosensitizers for *in vitro* antibacterial photodynamic inactivation. *J. Photochem. Photobiol. B Biol.* 206, 1–10.

Nwahara, N., Nkhahle, R., Ngoy, B. P., Mack, J., and Nyokong, T. (2018). Synthesis and photophysical properties of BODIPY-decorated graphene quantum dot-phthalocyanine conjugates. *New J. Chem*. 42, 6051–6061. doi: 10.1039/c8nj00758f

Pan, D., Zhang, J., Li, Z., and Wu, M. (2010). Hydrothermal route for cutting graphene sheets into blue-luminescent graphene quantum dots. *Adv. Mater*. 22, 734–738. doi: 10.1002/adma.200902825

Ran, H. H., Cheng, X., Bao, Y. W., Hua, X.-W., Gao, G., Zhang, X., et al. (2019). Multifunctional quaternized carbon dots with enhanced biofilm penetration and eradication efficiencies. *J. Mater. Chem. B* 7, 5104–5114. doi: 10.1039/c9tb00681h

Resistencia a los antibióticos (2020). Available online at: https://www.who.int/es/news-room/fact-sheets/detail/resistencia-a-los-antibióticos (accessed June 7, 2020).

Ristic, B. Z., Milenkovic, M. M., Dakic, I. R., Todorovic-Markovic, B. M., Milosavljevic, M. S., Budimir, M. D., et al. (2014). Photodynamic antibacterial effect of graphene quantum dots. *Biomaterials* 35, 4428–4435. doi: 10.1016/j.biomaterials.2014.02.014

Romero, M. P., Marangoni, V. S., de Faria, C. G., Leite, I. S., Silva, C. C. C. E., Maroneze, C. M., et al. (2020). Graphene oxide mediated broad-spectrum antibacterial based on bimodal action of photodynamic and photothermal effects. *Front. Microbiol.* 10:2995. doi: 10.3389/fmicb.2019.02995

Sidhu, J. S., Pandiyan, T., Kaur, N., and Singh, N. (2017). The Photochemical degradation of bacterial cell wall using penicillin-based carbon dots: weapons Against Multi-Drug Resistant (MDR) Strains. *ChemistrySelect* 2, 9277–9283. doi: 10.1002/slct.201701810

Shen, J., Zhu, Y., Chen, C., Yang, X., and Li, C. (2011). Facile preparation and upconversion luminescence of graphene quantum dots. *Chem. Commun*. 47, 2580–2582. doi: 10.1039/c0cc04812g

Tablan, O. C., Anderson, L. J., Besser, R., Bridges, C., and Hajjej, R. (2004). *Guidelines for Preventing Health-Care–Associated Pneumonia. MMWR*. Available online at: https://www.cdc.gov/mmwr/preview/mmwrhtml/rr5303a1.htm (accessed January 19, 2021).

Takakura, N., Sato, Y., Ishibashi, H., et al. (2003). A novel murine model of oral candidiasis with local symptoms characteristic of oral thrush. *Microbiol. Immunol*. 47, 321–326. doi: 10.1111/j.1348-0421.2003.tb03403.x

Tang, D., Liu, J., Yan, X., and Kang, L. (2016). Graphene oxide derived graphene quantum dots with different photoluminescence properties and peroxidase-like catalytic activity. *RSC Adv*. 6, 50609–50617. doi: 10.1039/c5ra26279h

Travlou, N. A., Giannakoudakis, D. A., Algarra, M., Labella, A. M., Rodríguez-Castellón, E., and Bandosz, T. J. (2018). S- and N-doped carbon quantum dots: surface chemistry dependent antibacterial activity. *Carbon* 135, 104–111. doi: 10.1016/j.carbon.2018.04.018

Van Tam, T., Trung, N. B., Kim, H. R., Chung, J. S., and Choi, W. M. (2014). One-pot synthesis of N-doped graphene quantum dots as a fluorescent sensing platform for Fe3+ ions detection. *Sens. Actuators B Chem*. 202, 568–573. doi: 10.1016/j.snb.2014.05.045

Wang, H., Sun, C., Chen, X., Zhang, Y., Colvin, V. L., Rice, Q., et al. (2017). Excitation wavelength independent visible color emission of carbon dots. *Nanoscale* 9, 1909–1915. doi: 10.1039/c6nr09200d

Wu, X., Tian, F., Wang, W., Chen, J., Wu, M., and Zhao, J. X. (2013). Fabrication of highly fluorescent graphene quantum dots using L-glutamic acid for in vitro/in vivo imaging and sensing. *J. Mater. Chem. C* 1, 4676–4684. doi: 10.1039/c3tc30820k

Yaghini, E., Seifalian, A. M., and MacRobert, A. J. (2009). Quantum dots and their potential biomedical applications in photosensitization for photodynamic therapy. *Nanomedicine* 4, 353–363. doi: 10.2217/nnm.09.9

Yang, J., Zhang, X., Ma, Y. H., Gao, G., Chen, X., Jia, H. R., et al. (2016). Carbon Dot-based platform for simultaneous bacterial distinguishment and antibacterial applications. *ACS Appl. Mater. Interfaces* 8, 32170–32181. doi: 10.1021/acsami.6b10398

Yang, J., Gao, G., Zhang, X., Ma, Y. H., Chen, X., and Wu, F. G. (2019). One-step synthesized carbon dots with bacterial contact-enhanced fluorescence emission property: fast Gram-type identification and selective Gram-positive bacterial inactivation. *Carbon* 146, 827–839. doi: 10.1016/j.carbon.2019.02.040

Yin, R., Agrawal, T., Khan, U., Gupta, G. K., Rai, V., Huang, Y. Y., et al. (2015). Antimicrobial photodynamic inactivation in nanomedicine: small light strides against bad bugs. *Nanomedicine* 10, 2379–2404. doi: 10.2217/nnm.15.67

Zhang, J., Lu, X., Tang, D., Wu, S., Hou, X., Liu, J., et al. (2018). Phosphorescent Carbon dots for highly efficient oxygen photosensitization and as photo-oxidative nanozymes. *Appl. Mater. Interfaces* 10, 40808–40814.

Zhou, J., Booker, C., Li, R., Zhou, X., Sham, T. K., Sun, X., et al. (2007). An electrochemical avenue to blue luminescent nanocrystals from multiwalled carbon nanotubes (MWCNTs). *J. Am. Chem. Soc*. 129, 744–745. doi: 10.1021/ja0669070

Conflict of Interest: The authors declare that the research was conducted in the absence of any commercial or financial relationships that could be construed as a potential conflict of interest.

frontiers in Microbiology

ORIGINAL RESEARCH
published: 26 August 2021
doi: 10.3389/fmicb.2021.631248

Adaptation of the Start-Growth-Time Method for High-Throughput Biofilm Quantification

Lara Thieme[1,2†], Anita Hartung[1†], Kristina Tramm[1], Julia Graf[1], Riccardo Spott[1], Oliwia Makarewicz[1] and Mathias W. Pletz[1]*

[1] Institute for Infectious Diseases and Infection Control, Jena University Hospital/Friedrich-Schiller-University, Jena, Germany,
[2] Leibniz Center for Photonics in Infection Research, Jena University Hospital/Friedrich-Schiller-University, Jena, Germany

OPEN ACCESS

Edited by:
Lauren B. Priddy,
Mississippi State University,
United States

Reviewed by:
Devendra Dusane,
Nationwide Children's Hospital,
United States
Carlos Montez Wells,
University of Memphis, United States

***Correspondence:**
Lara Thieme
Lara.Thieme@med.uni-jena.de

† These authors have contributed equally to this work and share first authorship

Specialty section:
This article was submitted to Antimicrobials, Resistance and Chemotherapy, a section of the journal Frontiers in Microbiology

Received: 19 November 2020
Accepted: 29 July 2021
Published: 26 August 2021

Citation:
Thieme L, Hartung A, Tramm K, Graf J, Spott R, Makarewicz O and Pletz MW (2021) Adaptation of the Start-Growth-Time Method for High-Throughput Biofilm Quantification. Front. Microbiol. 12:631248. doi: 10.3389/fmicb.2021.631248

Colony forming unit (CFU) determination by agar plating is still regarded as the gold standard for biofilm quantification despite being time- and resource-consuming. Here, we propose an adaption of the high-throughput Start-Growth-Time (SGT) method from planktonic to biofilm analysis, which indirectly quantifies CFU/mL numbers by evaluating regrowth curves of detached biofilms. For validation, the effect of dalbavancin, rifampicin and gentamicin against mature biofilms of *Staphylococcus aureus* and *Enterococcus faecium* was measured by accessing different features of the viability status of the cell, i.e., the cultivability (conventional agar plating), growth behavior (SGT) and metabolic activity (resazurin assay). SGT correlated well with the resazurin assay for all tested antibiotics, but only for gentamicin and rifampicin with conventional agar plating. Dalbavancin treatment-derived growth curves showed a compared to untreated controls significantly slower increase with reduced cell doubling times and reduced metabolic rate, but no change in CFU numbers was observed by conventional agar plating. Here, unspecific binding of dalbavancin to the biofilm interfered with the SGT methodology since the renewed release of dalbavancin during detachment of the biofilms led to an unintended antimicrobial effect. The application of the SGT method for anti-biofilm testing is therefore not suited for antibiotics which stick to the biofilm and/or to the bacterial cell wall. Importantly, the same applies for the well-established resazurin method for anti-biofilm testing. However, for antibiotics which do not bind to the biofilm as seen for gentamicin and rifampicin, the SGT method presents a much less labor-intensive method suited for high-throughput screening of anti-biofilm compounds.

Keywords: biofilms, high-throughput biofilm susceptibility testing, BBC, VISA hypothesis, dalbavancin

INTRODUCTION

Microbial communities that are surrounded by a matrix of extracellular polymeric substance are commonly defined as biofilms (Hall-Stoodley et al., 2012). Biofilms represent the preferred life-form of pathogenic bacteria, following that they play a key role in many infectious diseases such as endocarditis, osteomyelitis, urinary tract infections and joint and soft tissue infections (Flemming et al., 2016). Increased antibiotic tolerance and/or resistance are one of the major

hallmarks of biofilm-associated infections (Stewart, 2002). Since biofilm-embedded bacteria are usually genetically susceptible but phenotypically resistant, biofilm susceptibility is not predictable by the study of planktonic cells. Currently, biofilm-associated antibiotic tolerance is not addressed by microbiological routine diagnostics and treatment of biofilm-associated infections is guided by planktonic MIC testing, resulting in therapy failure and relapses. A multitude of biofilm susceptibility testing methods has been suggested, but none has so far reached a balance between the simplicity of a high-throughput method and the complex representation of the *in vivo* biofilm situation (Azeredo et al., 2017; Coenye et al., 2018; Magana et al., 2018). Further, standardization of the existing methods, including consistent interpretation of results and according recommendations, is lacking (Cruz et al., 2018; Thieme et al., 2019).

Colony forming unit (CFU) determination by agar plating is still regarded as the gold standard among bacterial quantification methods, including biofilms (Azeredo et al., 2017). Since agar-plating is time- and resource-consuming, we aimed to indirectly depict CFU/mL numbers by a culture-based method. Therefore, we adapted the recently published Start-Growth-Time (SGT) method to anti-biofilm testing, which allows a rapid quantification of the absolute and relative number of live cells in a high throughput manner (Hazan et al., 2012). The principle is comparable to the methodology of quantitative PCR calculations. After treatment, the biofilms are dispersed, diluted and regrown under continuous measurement of the optical density (OD) to obtain growth curves. The lag-phases of these growth curves are proportional to the number of cells in the dispersed biofilms, i.e., the more efficient the anti-biofilm treatment, the less CFU/mL, the longer the lag-phase. The SGT of each sample is defined as the time required to reach a defined OD threshold within the early to midst log-phase of the culture (Hazan et al., 2012). The growth delay of the treated growth curves, i.e., the respective SGTs, can be correlated to the quantity of CFU/mL reduction in comparison to the untreated control by CFU-SGT-standard curves of the same untreated strain. This minimizes the standard agar-plating procedure to a limited number of plates while simultaneously allowing the indirect measurement of CFU reduction of up to 96 samples.

To compare the CFU reduction results obtained with the novel SGT method with those obtained by conventional agar plating and resazurin metabolic assay, we treated mature biofilms of *Staphylococcus aureus* and *Enterococcus faecium*—which are one of the main pathogens causing biofilm-associated infections such as endocarditis and prosthetic joint infections—with serial concentrations of the antibiotics dalbavancin, rifampicin and gentamicin. Dalbavancin is a novel lipoglycopeptide with so far limited knowledge on biofilm eradication capability (Neudorfer et al., 2018), while the bactericidal antibiotics gentamicin and rifampicin were shown to exhibit anti-biofilm activity against Gram-positive biofilms (Sandoe et al., 2006; Coraça-Huber et al., 2012; Zimmerli and Sendi, 2019). The methods applied for biofilm quantification accessed different features of the viability status of the cells, i.e., the cultivability (CFU agar plating), growth behavior (SGT) and the metabolic activity (resazurin assay).

MATERIALS AND METHODS

Bacterial Strains and Antibiotics

The clinical *S. aureus* isolates (MSSA: SA4733 and SA1642, MRSA: SA4002) and *E. faecium* isolates (VSE: EF24498 and EF12713, VRE: EF17129) were obtained from the Institute of Medical Microbiology at Jena University Hospital, Germany. Test solutions of dalbavancin (Correvio GmbH, Bielefeld, Germany), rifampicin (Sigma Aldrich, St. Louis, United States) and gentamicin (TCI Europe, Zwijndrecht, Belgium) were prepared freshly for each experiment.

Biofilm Formation and Antibiotic Treatment

For biofilm maturation, 200 μL of 0.5 McFarland bacterial cultures were incubated in 96-well microtiter plates for 48 h at 37°C in a humidified chamber. *S. aureus* isolates were grown in Müller-Hinton (MH) broth and *E. faecium* isolates in Todd-Hewitt (TH) broth (both obtained from Sigma Aldrich, St. Louis, United States). For antibiotic treatment, the supernatants with planktonic cells were removed carefully, antibiotic solution with selected concentrations were prepared in the respective media and 200 μL per well were added to the biofilm. Pure media was used as growth control. Biofilms were incubated for additional 24 h at 37°C. Then, supernatant was removed and biofilms were washed two times with 0.9% NaCl before analyzing the biofilm reduction with the different methods. Each experiment was done in triplicates. To compare the different quantification methods, the biofilm bactericidal concentration (BBC), which is the lowest concentration of an antibiotic reducing 99.9% of biofilm-embedded bacteria (3 $\log_{10}$ reduction in CFU/mL) compared to the growth control (Macià et al., 2014), was determined for each antibiotic and strain by each method.

CFU Determination by Agar Plating

The washed biofilms were scraped off the wells via vigorous scraping with a 100 μL pipette (i.e., the pipette tip was moved with pressure in all directions of the well's bottom) and pipetting up and down, and resuspended in fresh MH or TH broth. For serial 10-fold dilution, 50 μL of each biofilm were transferred in MH or TH broth and vortexed to homogenize the biofilm debris. From selected dilutions, 100 μL were plated on MH or TH agar plates. After incubation of 18 h, colony forming units (CFU_{AGAR}) were counted and bactericidal effects were calculated in relation to the untreated control biofilms.

Resazurin Assay

Biofilm analysis by resazurin metabolism was adopted from Van den Driessche et al. (2014). Hundred microliter of a 10^{-2} dilution (taken from the previously prepared dilution series for agar plating) were added to a new 96-well microtiter plate and mixed with 10 μL alamarBLUE cell viability reagent (Thermo Fisher Scientific, Dreieich, Germany). Fluorescence was measured every 10 min for 18 h with a microtiter plate reader (Infinite M200pro, Tecan, Switzerland). Measurements were done at 37°C and with subsequently shaking for optimized growth conditions. For each

isolate, a dilution series of a control biofilm was simultaneously measured to create a resazurin standard curve. The time to reach maximum fluorescence (t_{max}) was determined for each biofilm. The t_{max} and the CFU_{AGAR} of the tested dilution series were correlated by linear regression to set-up a standard curve and to determine the detection limit for each strain. From this standard curve, the CFU_{RESA} of the treated and untreated biofilms were calculated by the corresponding t_{max} and subtracted from each other (ΔCFU_{RESA}).

Start-Growth-Time Method

Biofilms were washed twice with 0.9% NaCl, resuspended in fresh media and dispersed via vigorous scraping with a 100 µL pipette (Cruz et al., 2018). Dispersed biofilms were diluted 1:10 in fresh media and regrown in 96-well microtiter plates. The optical density was measured every 10 min at 600 nm for 18 h at 37°C in a microtiter plate reader under shaking conditions (Sunrise, Tecan, Switzerland). The SGT of each sample was defined as the time required to reach an $OD_{600\ nm}$ threshold that was set at the start to midst of the logarithmic phase, depending on the resulting growth curves. For the relative comparison of treated and untreated samples, the absolute size of the $OD_{600\ nm}$ threshold was not decisive but the unification for all samples. SGT values were normalized to the controls by the formula $\Delta SGT = SGT_{treated} - SGT_{control}$. To assess the linearity between SGT and CFU_{AGAR} values and thereby the detection limit for each strain, a standard curve was performed on every run. Therefore, SGTs of a serial diluted control biofilm and, in parallel, CFU_{AGAR} counts were determined. The CFU_{SGT} reduction due to antibiotic treatment was calculated by the standard curve $\log_{10}$ CFU_{AGAR} (x-axis) versus SGT (y-axis), whereby the SGT time span correlating to 1 $\log_{10}$ CFU difference was given by the slope of the linear regression. The resulting $\log_{10}$ CFU reduction was calculated by $\Delta\log_{10} CFU_{SGT} = \Delta SGT/slope$.

RESULTS

To verify the new high-throughput method from Hazan et al. (2012) for biofilm quantification, we recorded the growth curves of a dilution series of resuspended biofilms for each isolate. As on planktonic level time-lagged growth curves for biofilms could be observed in correlation to the CFU input (**Figure 1**). Comparable to a quantitative PCR, a specific OD threshold was defined within the midst of the exponential growth of the control biofilms. By this method, we received a linear correlation of SGT and CFU from 10^6 to 10^0 (**Figure 1**). The level of detection reached down to 2 CFU/well for both species whereby the level of detection and the detection range varied between experiments and isolates, especially for *E. faecium* (**Supplementary Material**).

After calibration, we used the SGT method for analyzing the BBC of dalbavancin and gentamicin for *E. faecium* isolates (**Figure 2**). According to the SGT method, a 3 $\log_{10}$ CFU reduction was achieved at 128 mg/L of dalbavancin (**Figure 2A**). By contrast, agar plating revealed only a CFU reduction of < 1 $\log_{10}$ CFU at the highest dalbavancin concentration tested, thereby not achieving the required 3 $\log_{10}$ CFU reduction for the BBC (**Figure 2A**).

On closer inspection, it was striking that the regrowth of the former dalbavancin-treated biofilms started at the same time like the controls but had a slower growth kinetic (**Figure 2A**, zoom). This changed growth behavior might be due to a reduced metabolism after antibiotic treatment. Therefore, we checked our results by resazurin assays as described by Van den Driessche et al. (2014). In parallel to the SGT method, a standard curve was performed within the experiment to calculate the CFU to the respective resazurin t_{max} value (**Supplementary Material**). The BBC determined by the SGT method (BBC_{SGT}) was consistent ($\pm$ 1x BBC) with the BBC measured by the resazurin assay (BBC_{RESA}) for dalbavancin at 256 mg/L (**Figure 2A** and **Table 1**).

For gentamicin-treated *E. faecium* biofilms, the SGT method revealed no anti-biofilm effect for all tested concentrations and showed no change in growth behavior (**Figure 2B**). The CFU determination by agar plating and resazurin obtained the same results (**Figure 2B** and **Table 1**). For the other two *E. faecium* isolates, BBC results obtained by all three methods were in accordance as well (**Table 1** and **Supplementary Material**).

To test whether the changed growth behavior observed in the SGT method is strain- or antibiotic-dependent, we analyzed *S. aureus* biofilms by all three methods using dalbavancin and rifampicin. In contrast to *E. faecium*, dalbavancin-treated biofilms showed normal time-lagged growth curves or no growth at all (**Figure 3A**). By the SGT method, we calculated a 3 $\log_{10}$ CFU reduction already at 8 mg/L while with agar plating there was nearly no CFU reduction detectable for all concentrations (**Figure 3A**). However, the BBC_{RESA} was again in line with the BBC_{SGT} (**Figure 3A** and **Table 1**). Similar results were seen for rifampicin-treated *S. aureus* biofilms (**Figure 3B** and **Table 1**). The BBC_{SGT} and BBC_{RESA} were both reached at 4 mg/L of rifampicin, whereas no BBC could be determined by agar plating since none of the tested rifampicin concentrations obtained a 3 $\log_{10}$ CFU reduction (**Figure 3B**).

DISCUSSION

In the presented study, the principle of the recently published, easy-to-use SGT-method was transferred from planktonic to biofilm-embedded cells, and compared to established, more labor-intensive methods. To integrate the SGT-method into the pool of already established methods for quantification of biofilm-embedded cells, biofilm bactericidal effects of three different antibiotics against mature *S. aureus* and *E. faecium* biofilms were measured by resazurin staining, agar plating and the SGT method. All methods are based on determination of CFU/mL values, either directly (agar plating) or indirectly via CFU/mL-calibrated standard curves (SGT, resazurin). While the SGT data correlated well with the results obtained by the resazurin assay, they only partially correlated with the results obtained by conventional agar plating. This led to a partial mismatch between the SGT/resazurin-derived BBCs (BBC_{SGT} and BBC_{RESA}) and the current gold-standard, agar plating-derived BBCs (BBC_{AGAR}), questioning the utility of the novel

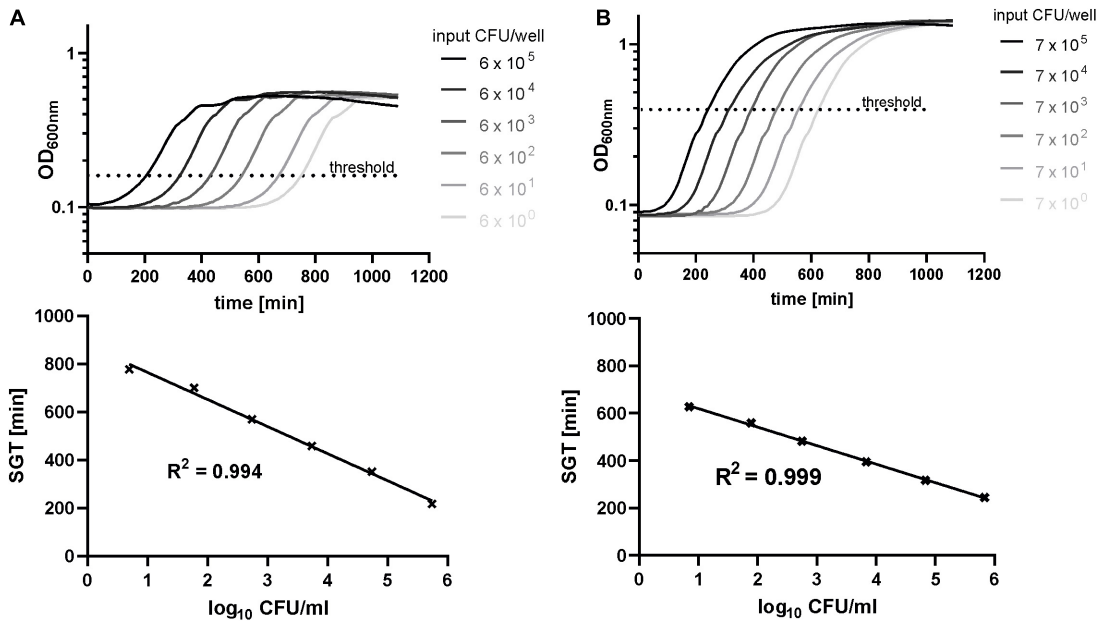

FIGURE 1 | Standard curves determined by the SGT method and agar plating for exemplary isolates of *E. faecium* **(A)** and *S. aureus* **(B)** biofilms. The optical density at 600 nm was recorded for 18 h for a dilution series of resuspended biofilms (48 h of growth). Simultaneously, CFU numbers were determined by agar plating.

SGT-method—and of the well-established resazurin assay - for quantifying biofilm reducing effects.

Since gentamicin and rifampicin testing in contrast to dalbavancin testing resulted in comparable BBC values by all three methods, we arrived at the hypothesis that the SGT-method might only be well-suited for measuring the effect of certain antibiotic classes. We first thought about a classification into bactericidal/bacteriostatic antibiotics, but this categorization is usually based on planktonic cells and poorly transferable to biofilm-embedded cells (Pankey and Sabath, 2004). Biofilms resemble stationary-phase cultures with strongly reduced cell division rates, following that they are less susceptible to cell-wall active agents such as dalbavancin compared to planktonic cells, where cell wall active agents usually exhibit bactericidal effects. In contrast, the mode of actions of gentamicin and rifampicin do not require actively dividing cells since they target transcriptional and translational processes. Whether the mode of action of the antibiotics, i.e., whether they target growth-arrested or actively dividing cells, influences the utility of the SGT method for determining biofilm reducing effects requires further testing.

Another possible explanation for the discrepancy between BBC_{SGT} and BBC_{AGAR} values might be due to the method-related comparison of two different time-points of bacterial growth. While the agar plating method assesses the number of CFUs in the stationary phase after 24 h of growth, the SGT method pictures the regrowth of the former biofilm-embedded cells over time, with the SGT values theoretically being calculated in the midst of the logarithmic phase. However, instead of being parallel and lagged to the untreated growth control as seen for gentamicin treatment, some antibiotic treatment-derived growth curves showed a significantly slower increase with reduced cell doubling times and without distinct growth phases, as seen for dalbavancin-treated *E. faecium* biofilms. Here, the reduced growth kinetics of the cells led to higher SGT values since the $OD_{600\ nm}$ threshold was reached later. As a consequence, the higher SGT values were falsely interpreted as lower number of cells leading to an overestimation of antibiotic bactericidal efficacy by the SGT method. To analyze whether the recovery from antibiotic-induced stress is also accompanied by a decreased CFU development on agar plates, we checked the number of CFUs formed on agar plates in 1 h intervals for a period of 14 h. The hypothesis hereby was that the colonies of growth kinetic-altered samples appear later and might show an altered phenotype, e.g., formation of small colony variants, but finally result in the same number of cells as the untreated control. However, no difference in the time point of CFU appearance or shape, size and color could be observed between treated and untreated samples (data not shown). Changes in colony formation were generally hard to depict though since both *E. faecium* and *S. aureus* form relatively small colonies.

As indicated by high SGT and low resazurin values, dalbavancin seemed to be able to slow down the bacterial metabolism, thereby reducing the redox potential of the cells and changing the growth behavior. However, these cells were still cultivable as reflected by unchanged CFU_{AGAR} numbers. For *E. faecium* EF17129 no effect of dalbavancin was expected since this isolate shows a vanA-VRE genotype, which exhibits high-level resistance to dalbavancin (Biedenbach et al., 2009). Bacteria use different strategies for survival during exposure to antibiotics, namely resistance, tolerance and persistence (Brauner et al., 2016). Resistance describes the inherited ability of bacteria to grow, i.e., to proliferate, at high concentrations of an antibiotic

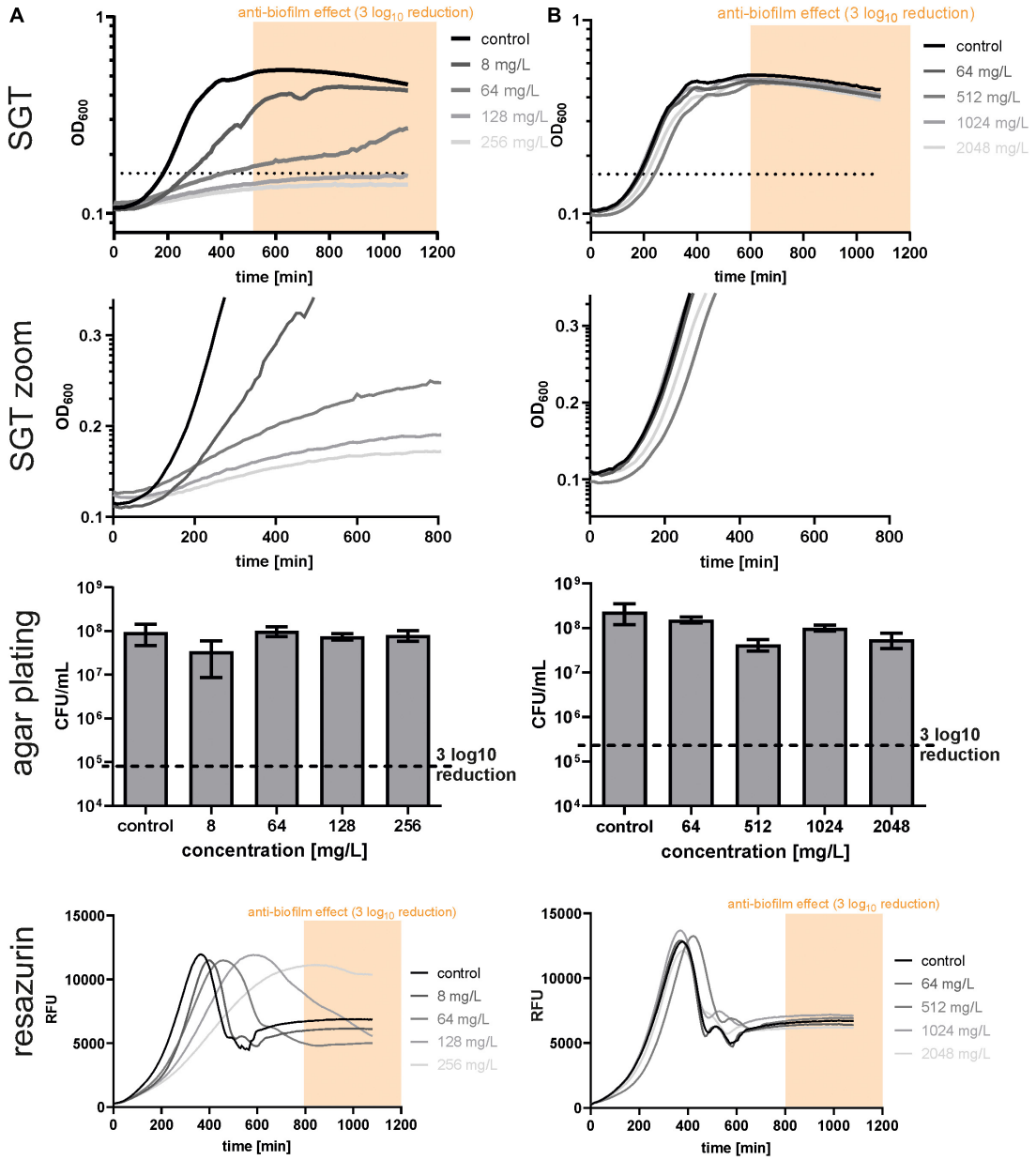

FIGURE 2 | Determination of biofilm bactericidal effects with the three different methods in EF17129 biofilms treated with dalbavancin **(A)** and gentamicin **(B)**. The yellow or orange window ("anti-biofilm effect") indicates the area with an at least 3 $\log_{10}$ reduction in CFU compared to the untreated control. The black dotted line indicates the OD threshold for SGT determination.

irrespective of the duration of treatment due to gene mutations. In contrast, tolerant cells survive high antibiotic concentrations by transiently slowing down essential bacterial processes at the cost of loss of cell proliferation. Once the transient trigger for tolerance is removed, cells do recover and growth can continue. While resistance and tolerance are attributes of the whole bacterial population, persistence is only attributable to a subpopulation (typically around 1%) of clonal cells. Persistent cells can survive at high concentrations of antibiotics whereas the majority of the clonal bacterial population is rapidly killed (Lewis, 2010). While antibiotic-resistant bacteria can form biofilms, the survival strategies characteristic for biofilms are antibiotic tolerance and persister cell formation (Stewart, 2002). We therefore hypothesized that the altered growth kinetics observed in growth curves of dalbavancin-treated biofilms were caused by the physiological rearrangements necessary to leave the tolerant state once the antibiotic had been removed and the biofilms were re-transferred to the planktonic phase. To test this hypothesis, we performed time-kill measurements of biofilm-derived planktonic cells (i.e., cells which have been grown into

TABLE 1 | Comparison of biofilm bactericidal concentration (BBC) values obtained by different methods for biofilm quantification.

Antibiotic	Strain		Calculated BBC (mg/L)		
			SGT (= BBC_{SGT})	Resazurin (= BBC_{RESA})	Agar plating (= BBC_{AGAR})
Dalbavancin	*S. aureus*	4002	8	16	>32
		4733	4	2	>8
		1642/1	4	4	>8
	E. faecium	24498	8	8	>16
		12713	2	16	>64
		17129	128	256	>256
Rifampicin	*S. aureus*	4002	4	4	>8
		4733	0.125	0.125	>16
		1642/1	2	2	>8
Gentamicin	*E. faecium*	24498	64	64	64
		12713	128	128	128
		17129	>2,048	>2,048	>2,048

The BBC is defined as the lowest concentration leading to 99.9% eradication of the biofilm (= 3 log_{10} CFU/mL reduction). SGT, Start-Growth-Time.

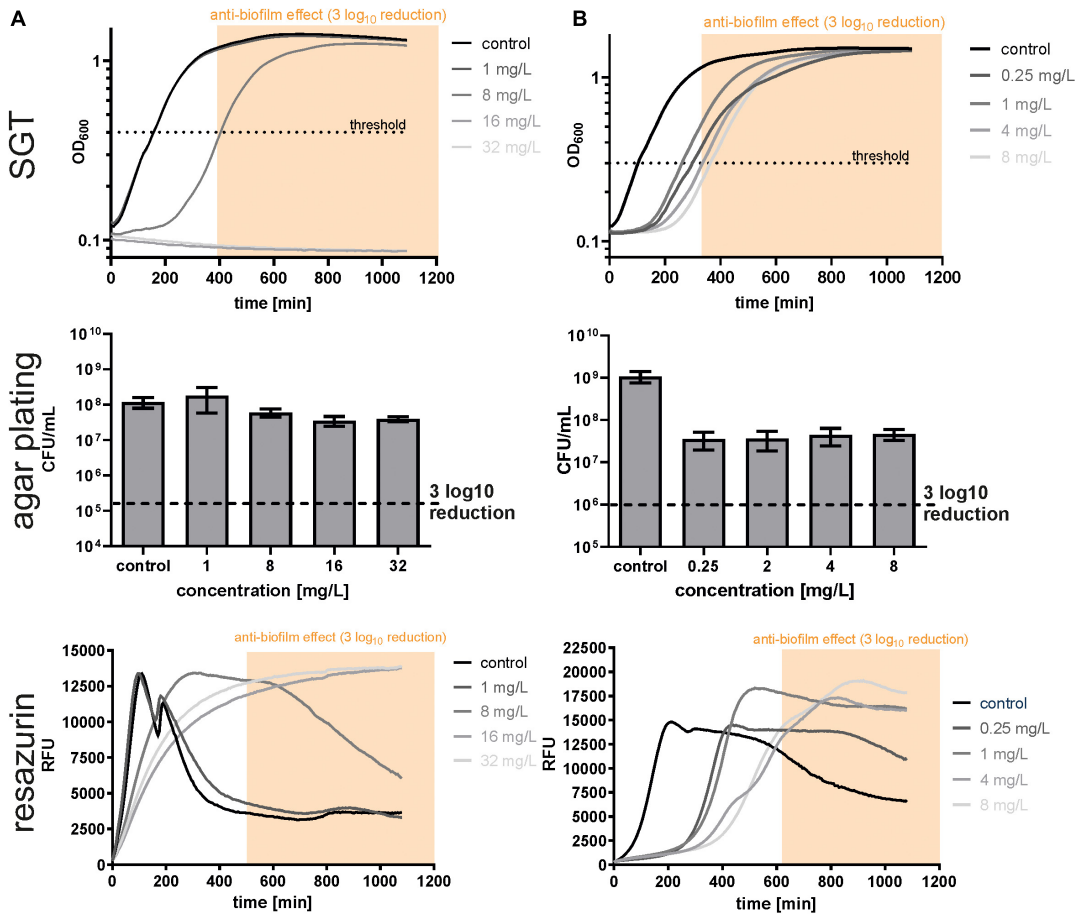

FIGURE 3 | Determination of biofilm bactericidal effects with the three different methods in SA4002 biofilms treated with dalbavancin **(A)** and rifampicin **(B)**. The yellow window ("anti-biofilm effect") indicates the area with an at least 3 log_{10} reduction in CFU compared to the untreated control.

biofilms, have been treated and then were re-transferred into the planktonic phase for recording of the growth curves) versus non-biofilm, conventional planktonic cells treated with 20x $MIC_{DALBAVANCIN}$ to determine the so-called minimal duration of killing (MDK). The $MDK_{99\%}$ describes the time amount needed to kill 99% of the bacterial population and is derived by plotting

viable CFUs against time (Hazan et al., 2014; Brauner et al., 2016). While the MIC is used as a standardized metric to measure antibiotic resistance, the MDK has been suggested as a metric for measurement of tolerance and persistence. If truly tolerant cells had emerged due to treatment of the biofilms, a higher $MDK_{99\%}$ would have been expected for the biofilm-derived planktonic cells compared to the non-biofilm, conventional planktonic cells. However, no difference in the $MDK_{99\%}$ was observed for both cell types indicating no physiological differences and no tolerance effects (data not shown).

A further explanation for the altered growth kinetics of dalbavancin-treated biofilms might be the transient uptake of glycopeptide molecules in the cell wall of Gram-positive organisms, as described for vancomycin-intermediate *S. aureus*. Vancomycin molecules were shown to bind not only to their main target, namely d-alanyl-d-alanine residues of cell wall precursors, but also to excess free d-alanyl-d-alanine residues randomly distributed in the cell wall of *S. aureus* (Cui et al., 2006). These second targets of vancomycin lead to clogging and cell wall thickening, preventing vancomycin to reach its true target at the growing peptidoglycan chain, thus mediating resistance (Cui et al., 2003). Since dalbavancin as a glycopeptide targets d-alanyl-d-alanine residues as well, a similar mechanism where *E. faecium* absorbs single dalbavancin molecules in its cell wall is possible (Zhanel et al., 2010). Upon transfer from the biofilm to the planktonic phase in the SGT method processing, the cell wall-residing dalbavancin molecules might be released again in the media due to renewed cell division, leading to delayed growth and altered growth kinetics. To verify this hypothesis, we performed again a SGT measurement with *E. faecium* and *S. aureus* biofilms after dalbavancin treatment (**Supplementary Figure 9**). To check for dalbavancin residues in the biofilm as well as in the cell wall, we collected the supernatant of the resuspended biofilm cells at different time points during their cell growth. After collection, standardized amounts of fresh bacterial cells were added to each supernatant and possible growth-inhibitory effects were analyzed similar to MIC testing. For *E. faecium*, a significant growth delay was only observed for the cells which had been treated with the supernatant taken from 128 mg/L dalbavancin treatment at time point 0 h, indicating the release of sufficient dalbavancin directly out of the biofilm upon resuspension to interfere with bacterial growth (**Supplementary Figure 9A**). No change in growth was observed for the cells treated with the other supernatants, implicating no release of dalbavancin molecules out of the cell wall. In contrast, experiments with *S. aureus* indicated the release of dalbavancin of both, the biofilm and the cell wall, confirming above hypothesis (**Supplementary Figure 9B**). Since for agar plating only high dilutions were evaluated to allow for CFU counting, released dalbavancin molecules were diluted as well, therefore no change in CFU numbers or cell growth was seen although the same effect is likely present. Importantly, the adherence of dalbavancin to the biofilm and the cell wall does not only lead to false positive anti-biofilm effects with the SGT method (and consequently to a mismatch between BBC_{SGT} and BBC_{AGAR}) but also with the resazurin method. Resazurin is a stable redox indicator which's highly fluorescent reduction product resorufin can be easily and rapidly measured after 30–120 min of cell contact and is proportional to the number of metabolically active cells (Azeredo et al., 2017). Since the linear range between resorufin and CFU numbers is restricted to 10^6–10^8 CFU/mL, the conventional resazurin-based viability assay fails to depict a 3 $\log_{10}$ reduction required for BBC calculation (Sandberg et al., 2009). We therefore used a recently published optimized method determining the time needed to reach the maximum fluorescence extending the linear range to 10^3–10^8 CFU/mL (Van den Driessche et al., 2014). While this new approach claims to accurately reflect CFU numbers as determined by agar plating, our results indicate that this was not true for dalbavancin. Here, dalbavancin residues in the biofilm interfered as well with the actual methodology resulting in falsely lowered metabolic activity and therefore overestimation of the anti-biofilm effect. Since resazurin is being increasingly used to study microbial biofilms (Azeredo et al., 2017), researchers should be aware of a potential correlation bias for some antibiotics.

In conclusion, the adherence of dalbavancin to the biofilm and cell wall led to false positive anti-biofilm effects with the SGT method, since the altered growth kinetics and consequential high SGT values were not due to the initial treatment of the biofilm but due to a renewed antibiotic challenge of the biofilm-resuspended planktonic cells during regrowth. The application of the SGT method for anti-biofilm testing is therefore not suited for antibiotics which stick to the biofilm and/or to the cell wall. Since it remains unknown for which antibiotic-biofilm combinations such effects occur, a prior testing before high-throughput application of the SGT method for measurement of CFU reduction is mandatory for anti-biofilm testing. It is important to note that we adapted the SGT method for Gram-positive biofilms only; it remains unclear whether Gram-negative biofilms show the same tendency to transiently uptake glycopeptide molecules in the biofilm matrix and/or in the cell wall as observed for Gram-positive biofilms in this study. Further studies are necessary to adapt the SGT method to Gram-negative biofilms and to find a solution for counteracting the adherence effect of dalbavancin to the biofilm, i.e., to avoid an unintended, renewed antibiotic challenge. However, if a comparison of CFU_{SGT} with CFU_{AGAR} for a specific antibiotic exhibits a good correlation, CFU_{SGT} as a much less labor-intensive method may be used for high-throughput screening as required for microbiological routine testing.

DATA AVAILABILITY STATEMENT

The original contributions presented in the study are included in the article/**Supplementary Material**, further inquiries can be directed to the corresponding author/s.

AUTHOR CONTRIBUTIONS

LT conceptualized the article, designed, performed the experiments, analyzed, interpreted the data, wrote, and revised

the manuscript. AH designed, performed the experiments, analyzed, interpreted the data, and wrote the methods and results part of the manuscript. KT, JG, and RS revised and critically discussed the article. OM and MP revised the manuscript for important intellectual content. All authors read and approved the final manuscript.

FUNDING

This work was supported by the Federal Ministry of Education and Research, Germany (Grant Nos. 01KI1501 and 13N15467).

ACKNOWLEDGMENTS

We thank Correvio for providing us with dalbavancin infusion powder.

SUPPLEMENTARY MATERIAL

The Supplementary Material for this article can be found online at: https://www.frontiersin.org/articles/10.3389/fmicb.2021.631248/full#supplementary-material

REFERENCES

Azeredo, J., Azevedo, N. F., Briandet, R., Cerca, N., Coenye, T., Costa, A. R., et al. (2017). Critical review on biofilm methods. *Crit. Rev. Microbiol.* 43, 313–351.

Biedenbach, D. J., Bell, J. M., Sader, H. S., Turnidge, J. D., and Jones, R. N. (2009). Activities of dalbavancin against a worldwide collection of 81,673 gram-positive bacterial isolates. *Antimicrob. Agents chemother.* 53, 1260–1263. doi: 10.1128/aac.01453-08

Brauner, A., Fridman, O., Gefen, O., and Balaban, N. Q. (2016). Distinguishing between resistance, tolerance and persistence to antibiotic treatment. *Nat. Rev. Microbiol.* 14, 320–330. doi: 10.1038/nrmicro.2016.34

Coenye, T., Goeres, D., Van Bambeke, F., and Bjarnsholt, T. (2018). Should standardized susceptibility testing for microbial biofilms be introduced in clinical practice? *Clin. Microbiol. Infect.* 24, 570–572. doi: 10.1016/j.cmi.2018.01.003

Coraça-Huber, D. C., Fille, M., Hausdorfer, J., Pfaller, K., and Nogler, M. (2012). *Staphylococcus aureus* biofilm formation and antibiotic susceptibility tests on polystyrene and metal surfaces. *J. Appl. Microbiol.* 112, 1235–1243. doi: 10.1111/j.1365-2672.2012.05288.x

Cruz, C. D., Shah, S., and Tammela, P. (2018). Defining conditions for biofilm inhibition and eradication assays for Gram-positive clinical reference strains. *BMC Microbiol.* 18:173. doi: 10.1186/s12866-018-1321-6

Cui, L., Iwamoto, A., Lian, J. Q., Neoh, H. M., Maruyama, T., Horikawa, Y., et al. (2006). Novel mechanism of antibiotic resistance originating in vancomycin-intermediate Staphylococcus aureus. *Antimicrob. Agents Chemother.* 50, 428–438. doi: 10.1128/aac.50.2.428-438.2006

Cui, L., Ma, X., Sato, K., Okuma, K., Tenover, F. C., Mamizuka, E. M., et al. (2003). Cell wall thickening is a common feature of vancomycin resistance in *Staphylococcus aureus*. *J. Clin. Microbiol.* 41, 5–14. doi: 10.1128/jcm.41.1.5-14.2003

Flemming, H. C., Wingender, J., Szewzyk, U., Steinberg, P., Rice, S. A., and Kjelleberg, S. (2016). Biofilms: an emergent form of bacterial life. *Nat. Rev. Microbiol.* 14, 563–575. doi: 10.1038/nrmicro.2016.94

Hall-Stoodley, L., Stoodley, P., Kathju, S., Høiby, N., Moser, C., Costerton, J. W., et al. (2012). Towards diagnostic guidelines for biofilm-associated infections. *FEMS Immunol. Med. Microbiol.* 65, 127–145. doi: 10.1111/j.1574-695x.2012.00968.x

Hazan, R., Maura, D., Que, Y. A., and Rahme, L. G. (2014). Assessing *Pseudomonas aeruginosa* Persister/antibiotic tolerant cells. *Methods Mol. Biol.* 1149, 699–707. doi: 10.1007/978-1-4939-0473-0_54

Hazan, R., Que, Y. A., Maura, D., and Rahme, L. G. (2012). A method for high throughput determination of viable bacteria cell counts in 96-well plates. *BMC Microbiol.* 12:259. doi: 10.1186/1471-2180-12-259

Lewis, K. P. (2010). Persister cells. *Annu. Rev. microbiol.* 64, 357–372.

Macià, M. D., Rojo-Molinero, E., and Oliver, A. (2014). Antimicrobial susceptibility testing in biofilm-growing bacteria. *Clin. Microbiol. Infect.* 20, 981–990. doi: 10.1111/1469-0691.12651

Magana, M., Sereti, C., Ioannidis, A., Mitchell, C. A., Ball, A. R., Magiorkinis, E., et al. (2018). Options and limitations in clinical investigation of bacterial biofilms. *Clin. Microbiol. Rev.* 31, e00084–16.

Neudorfer, K., Schmidt-Malan, S. M., and Patel, R. (2018). Dalbavancin is active in vitro against biofilms formed by dalbavancin-susceptible enterococci. *Diagn. Microbiol. Infect. Dis.* 90, 58–63. doi: 10.1016/j.diagmicrobio.2017.09.015

Pankey, G. A., and Sabath, L. D. (2004). Clinical relevance of bacteriostatic versus bactericidal mechanisms of action in the treatment of Gram-positive bacterial infections. *Clin. Infect. Dis.* 38, 864–870. doi: 10.1086/381972

Sandberg, M. E., Schellmann, D., Brunhofer, G., Erker, T., Busygin, I., Leino, R., et al. (2009). Pros and cons of using resazurin staining for quantification of viable *Staphylococcus aureus* biofilms in a screening assay. *J. Microbiol. Methods* 78, 104–106. doi: 10.1016/j.mimet.2009.04.014

Sandoe, J. A., Wysome, J., West, A. P., Heritage, J., and Wilcox, M. H. (2006). Measurement of ampicillin, vancomycin, linezolid and gentamicin activity against enterococcal biofilms. *J. Antimicrob. Chemother.* 57, 767–770. doi: 10.1093/jac/dkl013

Stewart, P. S. (2002). Mechanisms of antibiotic resistance in bacterial biofilms. *Int. J. Med. Microbiol.* 292, 107–113. doi: 10.1078/1438-4221-00196

Thieme, L., Hartung, A., Tramm, K., Klinger-Strobel, M., Jandt, K. D., Makarewicz, O., et al. (2019). MBEC versus MBIC: the lack of differentiation between biofilm reducing and inhibitory effects as a current problem in biofilm methodology. *Biol. Proced. Online* 21:18.

Van den Driessche, F., Rigole, P., Brackman, G., and Coenye, T. (2014). Optimization of resazurin-based viability staining for quantification of microbial biofilms. *J. Microbiol. Methods* 98, 31–34. doi: 10.1016/j.mimet.2013.12.011

Zhanel, G. G., Calic, D., Schweizer, F., Zelenitsky, S., Adam, H., Lagacé-Wiens, P. R., et al. (2010). New lipoglycopeptides: a comparative review of dalbavancin, oritavancin and telavancin. *Drugs* 70, 859–886. doi: 10.2165/11534440-000000000-00000

Zimmerli, W., and Sendi, P. (2019). Role of rifampin against staphylococcal biofilm infections in vitro, in animal models, and in orthopedic-device-related infections. *Antimicrob. Agents Chemother.* 63, e01746–18.

Conflict of Interest: The authors declare that the research was conducted in the absence of any commercial or financial relationships that could be construed as a potential conflict of interest.

Publisher's Note: All claims expressed in this article are solely those of the authors and do not necessarily represent those of their affiliated organizations, or those of the publisher, the editors and the reviewers. Any product that may be evaluated in this article, or claim that may be made by its manufacturer, is not guaranteed or endorsed by the publisher.

Frontiers in Microbiology

Explores the habitable world and the potential of microbial life

The largest and most cited microbiology journal which advances our understanding of the role microbes play in addressing global challenges such as healthcare, food security, and climate change.

Discover the latest Research Topics

See more →

Frontiers

Avenue du Tribunal-Fédéral 34
1005 Lausanne, Switzerland
frontiersin.org

Contact us

+41 (0)21 510 17 00
frontiersin.org/about/contact